AD609458

AFOSR Sci. Doc. 64-1340

RESEARCH ON ELECTROMAGNETIC PLASMA ACCELERATION

Final Report, Contract AF 49(638)-759

Submitted to

United States Air Force
Office of Scientific Research
Office of Aerospace Research
Washington, D. C.

COPY 2 OF 3
HARD COPY $.4.95
MICROFICHE $.2.25
494P

June 1964

Prepared by

Space Sciences Laboratories
LITTON SYSTEMS, INC.
Beverly Hills, California

DDC
RECEIVED
DEC 31 1964
DDC-IRA A

(A. S. Penfold and R. M. Rosen, authors)

ARCHIVE COPY

AFOSR Sci. Doc. 64-1340

RESEARCH ON ELECTROMAGNETIC PLASMA ACCELERATION

Final Report, Contract AF 49(638)-759

Submitted to

United States Air Force
Office of Scientific Research
Office of Aerospace Research
Washington, D. C.

June 1964

Prepared by

Space Sciences Laboratories
LITTON SYSTEMS, INC.
Beverly Hills, California

(A. S. Penfold and R. M. Rosen, authors)

CONTENTS

1. INTRODUCTION AND SUMMARY. 1

2. EXPERIMENTS WITH A PULSED ACCELERATOR 5

2.1 General Description of the Accelerator. 6
2.2 The Mechanical Arrangement. 7
2.3 The Magnetic Field 11
2.4 The Gas Injector. 15
2.5 Early Difficulties 19
2.6 The Acceleration Process 20
2.7 Results. 23
2.8 Concluding Remarks 54

3. THEORETICAL CONSIDERATIONS 57

3.1 Introductory Remarks. 57
3.2 The Electromagnetic Field Components 61
3.3 Single-Particle Equations of Motion 63
3.4 Single-Particle Motion in a Rapidly Oscillating Field . . . 67
3.5 Particle-Particle Interactions 70
3.6 The Boltzmann Equation 73
3.7 Moments of the Boltzmann Equation 77
3.8 Simplifications of the Moment Equations 83
3.9 Angular Momentum Considerations. 85
3.10 Determination of $\langle K^{\mathcal{E}} \rangle$. 87
3.11 Plasma Current 89
3.12 The Slow Flow Approximation 97
3.13 Self-Fields. 100
3.14 A Passive Analog for Plasma. 109
3.15 Comparison of Plasma Accelerators 110
3.16 High-Frequency Plasma Containment 115
3.17 Motion of a Pinched Plasma Torus 115
3.18 Concluding Remarks. 120

CONTENTS (cont)

4. DESIGN OF A CW ACCELERATOR 123

4.1 Magnetic Field Design. 123
4.2 Electrical Design of the Mark II 146

APPENDIX A Electrical Timing of the Mark I Accelerator

APPENDIX B Epoxy Encapsulation Technique

APPENDIX C Particle Motion in an Axially Symmetric Magnetic Field

APPENDIX D A Model for the Motion of a Rarified Plasma in an Axially Symmetric Magnetic Field

APPENDIX E Two-Fluid Model for the Motion of a Rarified Plasma Accelerated by Induction

APPENDIX F Determining Axially Symmetric Magnetic Field Patterns

APPENDIX G A Resistor-Mesh Analog Board

APPENDIX H Mechanical Design of the Mark II Accelerator

APPENDIX I Power Source Modification

APPENDIX J Control and Monitoring Methods

APPENDIX K Design of a Current-Forcing Transformer

APPENDIX L Analysis of a Ring Coupling-Circuit

APPENDIX M Zener Diodes as Temperature-Sensing Devices

APPENDIX N Shielding Against Capacitive Electric Fields

APPENDIX P A Single-Phase Induction Plasma Accelerator

PREFACE

This document is the final report of contract AF49Δ638)-759 entitled "Research on Electromagnetic Plasma Acceleration." The report covers the period of time from 15 December 1959 to 31 October 1963. The work was performed in the Space Sciences Laboratory of Litton Systems Inc., located in Beverly Hills California. Dr. Alan S. Penfold was the Principal Investigator. The document bears the Litton publication number 3484.

1. INTRODUCTION AND SUMMARY*

Research on the acceleration of plasma by traveling magnetic fields was initiated at the Space Sciences Laboratory of Litton Systems in January 1957. The initial effort was aimed at the production of high-speed plasma tori by means of a traveling magnetic field produced by a series of one-turn coils energized in time-sequence by a set of spark-gap-discharged capacitors. This earliest work was described in a final report (AF49(638)-345) dated September 30, 1959.

These early results were sufficiently encouraging to justify additional effort (Contract AF 49(638)-759) which was entered upon in December 1959. The present document is the final report on this work. The earliest part of the new work included modifications to the pulsed accelerator, development of diagnostic techniques, and a more detailed theoretical analysis of the induction acceleration phenomenon.

By September 1961 the pulsed accelerator (Mark I) was operating satisfactorily, and pinched plasma tori were being produced in a repeatable fashion. In general the following observations were made:

1. The tori remained pinched over the observable flight path (about 24 inches)
2. The measured speeds were $\sim 10^5$ meters/second
3. The appearance of the tori were independent of the gas used (H, He, N_2, A)
4. Their mass was estimated to be $> 6 \times 10^{-12}$ kg
5. The tori carried strong circulating currents
6. It was found to be possible to focus them to some extent

*The research effort upon which this report is based was supported by USAF, Office of Aerospace Research, Office of Scientific Research under contract AF49(638)-759.

7. Successive tori had opposite magnetic moments
8. Two to three tori accompanied each capacitor-bank discharge
9. Phosphoresence of target materials was observed
10. Some plasma instability was seen
11. The experimental results had good reproducibility.

Details of these results are included in this report.

Concurrent with the experimental effort, an attempt was made to devise a theoretical treatment for the behavior of rarified plasma in a cylindrically symmetric magnetic field.

This theoretical treatment started with a set of assumptions regarding the general types of plasma to be considered. These were:

1. Low density
2. High electron engergy
3. Axial symmetry

These assumptions simplify the equations of motion since they can treat the plasma as a fluid in which the particles do not interact. Later, restrictions are applied to account for particle-particle interactions.

Under the above-cited assumptions, the equations were seen to be in a form such that the particle velocity components could be obtained by taking a spatial gradient of a single scalar quantity. This quantity was given the name "inductive potential" (V) since it arose through magnetic effects. As described in Section 3 the inductive potential was of considerable value in providing a mental picture of the motion. The work on single-particle motion using the inductive potential treatment was published in an AFOSR Technical Note[6] in 1960, and since then the theoretical effort was directed toward the inclusion of corrections for particle-partical interactions and the application of the theory to the design of a CW accelerator. This effort is described in Sections 3 and 4.

During the summer of 1961, sufficient understanding of the subject was available to permit the conceptual design of a continuously operating device; that is, a traveling field accelerator (Mark II) operating with polyphase excitation on a CW basis using radio-frequency power supplies. The advantages of this type of device over a pulsed device were evident, and acquisition of suitable power sources was initiated.

In the fall of 1961 the laboratory acquired from the United States Navy, six surplus TBC radio transmitters. Their installation and modification as well as the design and construction of suitable monitoring and control equipment was finally completed by January 1963. During this period the design of the new Mark II accelerator was also completed, and construction was well under way. Enough was known about the kind of circuitry necessay for the production of continuous traveling waves to anticipate the problems introduced by the plasma interaction with these circuits. The design and construction of this circuitry, with sufficient flexibility and control to accomplish the required adjustment of circuit parameters, was accomplished in 1963.

2. EXPERIMENTS WITH A PULSED ACCELERATOR

The first two years of work herein reported were devoted to a study of the formation and acceleration of toroidal plasmoids, formed and held in shape by the confining action of their own magnetic fields. One of the primary objects of the research was to prove, beyond reasonable doubt, that such pinched plasma toroids could be formed and that they had more than a fleeting existence measured on a time scale comparable to the useful operating time of the accelerator, which was 8 microseconds per discharge of the associated capacitor bank.

The basic mechanical and electrical design of the accelerator was already frozen at the beginning of the contract period and the apparatus was at hand. This work was accomplished on a former contract (AF49(638)-345). Neither the basic mechanical design nor the basic electrical design were changed much during the contract, but the control and monitoring equipment was greatly improved.

The accelerator can in no sense be described as a steady-state device. Every aspect of the plasma behavior is transitory and not amenable to steady-state analysis. Definitive proof of correct operation depended heavily on two commercial developments which occurred:

1. The development of a fast and reliable Kerr cell shutter.
2. The development of fast (3000 and 10,000 speed) polaroid film.

The accelerator was designed to prove a principle rather than to be an efficient device. The magnetic field strength was chosen with the idea in mind that to err on the side of too strong a field was better than to have a field not strong enough to produce the desired phenomena. Now there are theoretical reasons for believing that the field need not be stronger than a few hundred gauss but at the time of the choice (1958) no such reasons existed and a field of 3-4 thousand gauss seemed reasonable.

At this point it is probably well to distinguish rather carefully between this accelerator and another, related but distinctly different type, sometimes called a "traveling piston" or "delay line" accelerator. In the former, gas is introduced into the accelerating structure close to one end where the field ionizes, shapes, and accelerates it. The plasma is trapped in the field at one or more locations and forces act in such a way as to try to maintain the position of the plasma with respect to the moving field. On the other hand, in the traveling piston device the accelerator tube is initially filled with a low density gas, usually already weakly ionized. The magnetic field begins to grow at one end of the device and a magnetic front moves along, ionizing additional gas, and sweeping gas along like a piston moving down the tube.

2.1 GENERAL DESCRIPTION OF THE ACCELERATOR

At the heart of the accelerator is a 6-inch diameter pyrex tube with a gas injector at one end and vacuum pumps at the other. In normal operation the ambient pressure in the tube is about 10^{-4} Torr.

Surrounding the pyrex tube, at the gas injector end, is a series of one-turn coils each of which is connected to an energy-storage capacitor through a spark-gas switch.

Upon operation, a short burst of gas is admitted to the tube from the gas injector. The gas moves down the tube at sonic speed (about 300 meter/sec) and at a pressure of about 2×10^{-2} Torr. When the gas front is somewhere in the vicinity of the second or third coil the spark-gap switches are triggered, one at a time, in carefully-controlled sequence. Currents flow in the coils and for a few microseconds the resulting magnetic field has the form of a repetitive wave, traveling with uniform acceleration, away from the gas injector.

The objective is to form a toroidal plasma and trap it in the magnetic field. Since the field accelerates uniformly the plasma is also accelerated. When the plasma reaches the end of the coil system its momentum carries it forward, out of the field, and into a section of the tube where measuring apparatus is located.

The whole action takes but a few microseconds.

2.2 THE MECHANICAL ARRANGEMENT

The accelerator was assembled on the framework shown in Figure 2-1. A pyrex tube (not shown in Figure 2-1) seals to the vacuum pump at the bottom of the frame and extends, up the axis of the frame, for a distance of about four feet. The gas injector rests on the top of the tube and a vacuum seal is made. The electrical components shown to the right in Figure 2-1 are the control console and the high-voltage power supply. The cables which carried the high voltage (30 kilovolts) from the power supply to the energy-storage capacitors can be seen emerging from the upper section of the power supply unit and entering a metal trough near the ceiling. The high voltage was carried on RG 8/U cable and there was never a cable failure.

The brackets bolted to the accelerator frame were used to attach the energy-storage capacitors.

A total of twenty energy-storage capacitors were purchased, but most of the good data was taken with nineteen in operation. One failed early in the program. The capacitors were special low-inductance units capable of withstanding a sudden 100% reversal of voltage. The capacitor sizes varied with location on the accelerator and a listing of the sizes is given in Appendix A.

Each capacitor was connected to a one-turn coil through a low inductance transmission line and a spark-gap switch. Several of these coil-capacitor assemblies are shown in Figure 2-2. Each of the units shown in Figure 2-2 is equipped with a high-voltage pulse transformer which triggers the spark-gap.

The pyrex accelerator tube fits through the coils. The capacitors are arranged around the accelerator tube so that the coils line up with a one-inch coil-to-coil spacing. Figure 2-3 shows the capacitors mounted on the accelerator frame. The lower end of the aligned array of coils is seen at the center of the frame.

Details concerning the coil-capacitor assemblies are given in Appendix A.

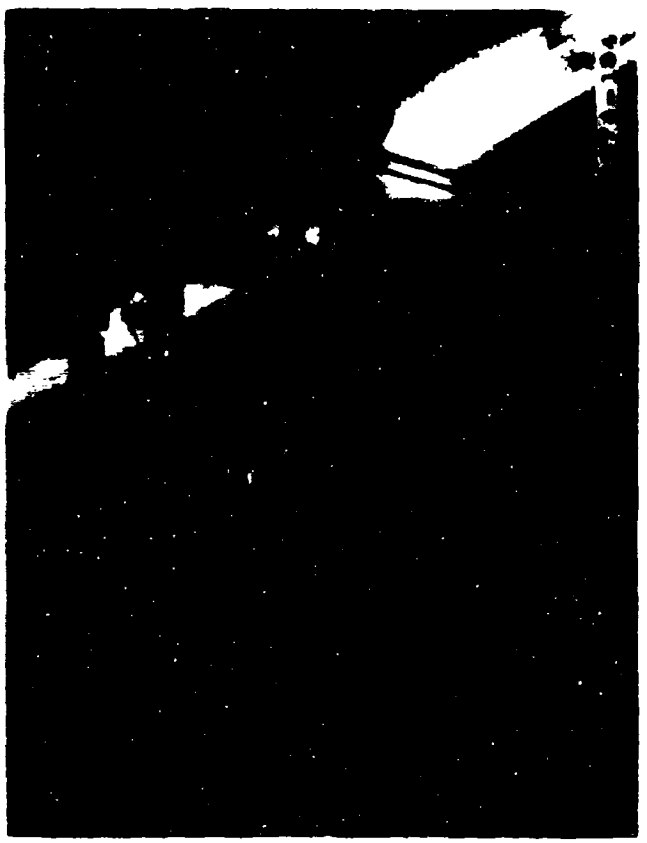


Figure 2-1. Accelerator Frame

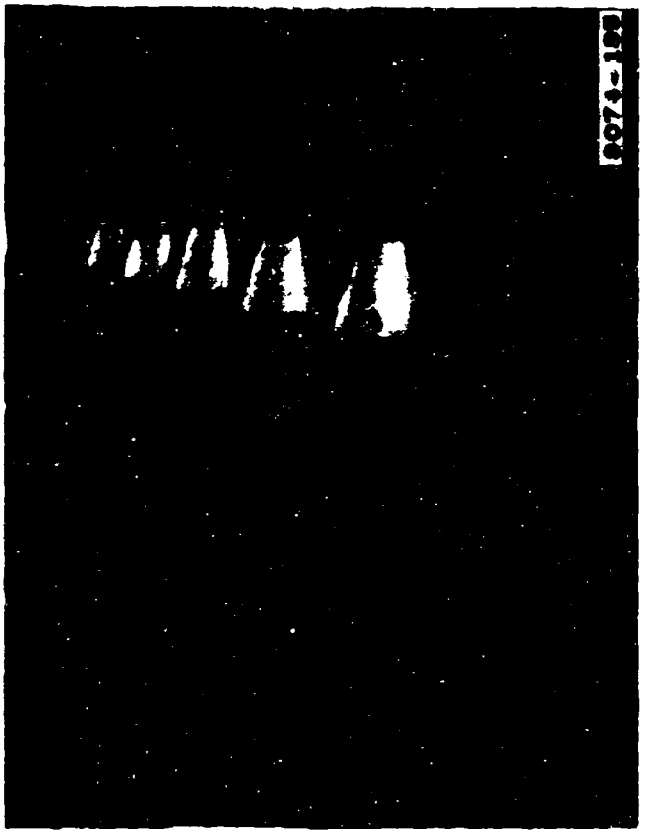


Figure 2-2. Coil-Capacitor Assemblies

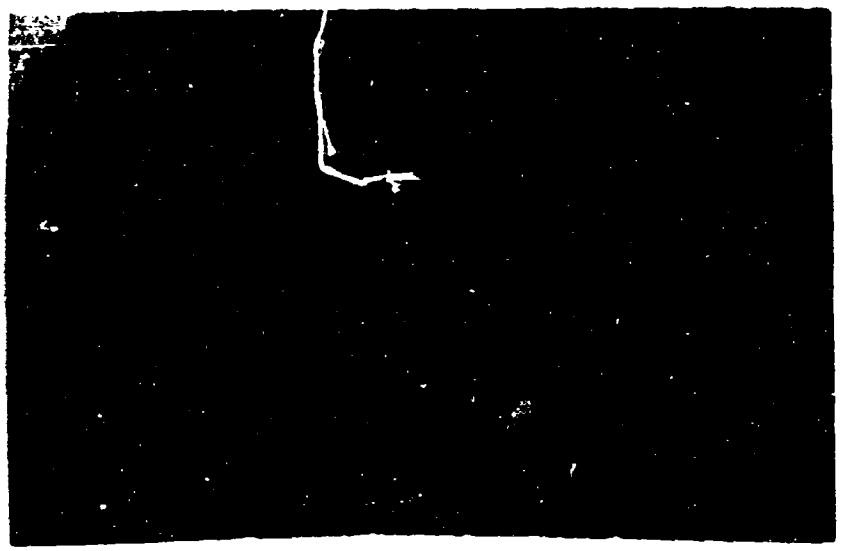


Figure 2-3. Energy Storage Capacitors Mounted on Accelerator

2.3 THE MAGNETIC FIELD

Each coil-capacitor assembly constituted an L-C ringing circuit with a Q (unloaded with plasma) of 3 to 4. Figure 2-4 shows some typical coil voltage waveforms. The net magnetic field in the accelerator tube was formed from the superposition of the field from each separate coil. Figure 2-5 shows the relative coil currents 9 microseconds after the spark gap of coil #2 fires. A sketch of the probable appearance of the corresponding magnetic field is shown at the top of Figure 2-5. There are three locations where the field is predominantly radial. These will be called field confluences. Notice that the field confluences occur at locations where the coil-currents are instantaneously zero or nearly zero. Thus, the position of the zero-current coils, as a function of time, gives the travel of the field confluences.

The axial force on the plasma is proportional to the strength of the radial component of the magnetic field, and this is strongest at the field confluences. In-between the field confluences the radial component becomes zero, and the axial accelerating forces become zero also. Thus, one expects the plasma to be located near the field confluences.

Figure 2-6 shows the timing scheme which was found to be the most satisfactory. The position-versus-time behavior of the first six current zeroes are plotted. The plot was constructed from a knowledge of the ringing frequency of each coil-capacitor combination (see Appendix A for a listing of these). The timing scheme is constructed in such a way that the 1st current zero (i.e., the first field confluence) moves smoothly along the accelerator with constant acceleration, eventually reaching a speed of 1.21×10^5 meters/second. The first plasma torus is expected to follow this curve.

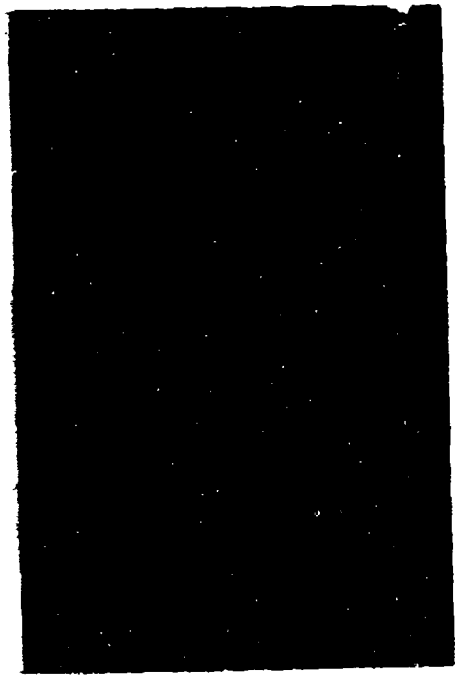


Figure 2-4. Typical Coil Voltage Wave Forms; 20 kv/div

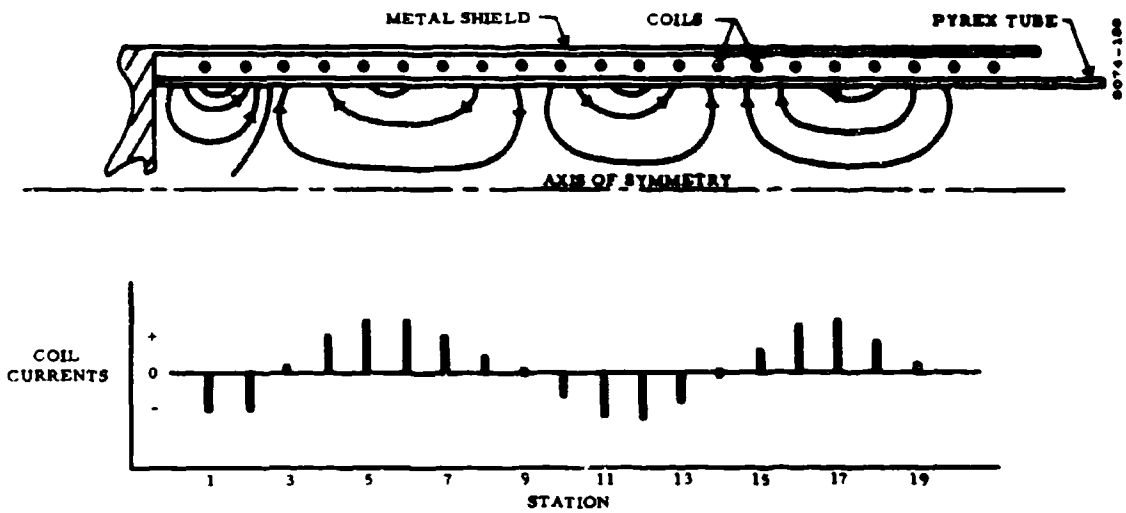


Figure 2-5. Top: Sketch of Magnetic Field Pattern Bottom: Coil Currents at 9 μsec.

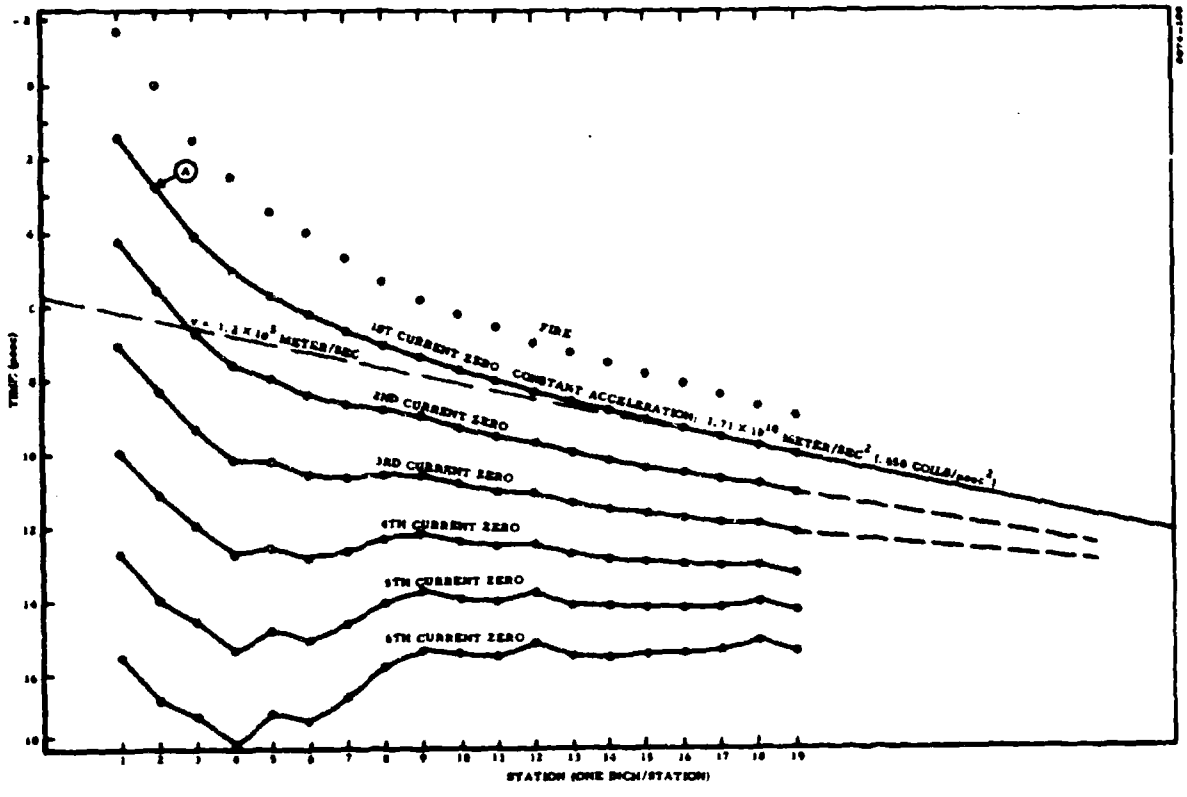


Figure 2-6. Accelerator Timing Scheme

The succeeding field confluences do not move so smoothly since unit-to-unit variations in ringing frequency prevent this. In fact, a backwards acceleration is evident in the 4th, 5th, and 6th confluences. This backwards acceleration will carry plasma towards the injector end of the machine. A clash of forward and backward moving plasma will take place in the vicinity of station 5; and, according to Figure 2-6, such a clash should occur every 2-3 microseconds, beginning about 14 microseconds after the firing of #1 spark gap.

A collimated photomultiplier was directed towards Station 5 in an attempt to observe the light from the gas clashes. Typical results are shown in the oscillograms of Figure 2-7. In these oscillograms #1 spark gap fired about 5 microseconds from the beginning of the trace.

According to Figure 2-6 one should expect 2-3 tori per operation of the machine. This was the number observed. Note, however, that the several tori tend to converge as they leave the field because the first travels slower than the succeeding two.

A grounded metal shield surrounded each coil. The net magnetic field generated by the coil was due to the superposition of two currents; the one in the coil and the image current in the metal shield (the metal shield will not pass magnetic fields of the frequency used here). The purpose of the shield was to force the field towards the axis to improve the radial containment of plasma. The action is shown in the sketch of Figure 2-8.

2.4 THE GAS INJECTOR

A cross section of the gas injector is shown in Figure 2-9. A double-valve system was used in order to minimize the effects of gas leakage so that a low ambient pressure could be maintained in the accelerator tube.

Gas, typically at 1-2 atmospheres of pressure, enters Chamber B through passage A (refer to Figure 2-9). The passage between Chamber B and Chamber E is a small-diameter hole, D, which is normally sealed by the solenoid-actuated plunger C. In turn, Chamber E is sealed by the rotating Plate F. The latter has two holes which, twice every revolution, open Chamber E to the accelerator. When one hole lines up with Chamber E the other lines up with the photo-diode and lamp. The photo-diode provides a pulse to which the timing of the entire acceleration sequence



Figure 2-7. Evidence of Gas Clash (10 μsec/div)

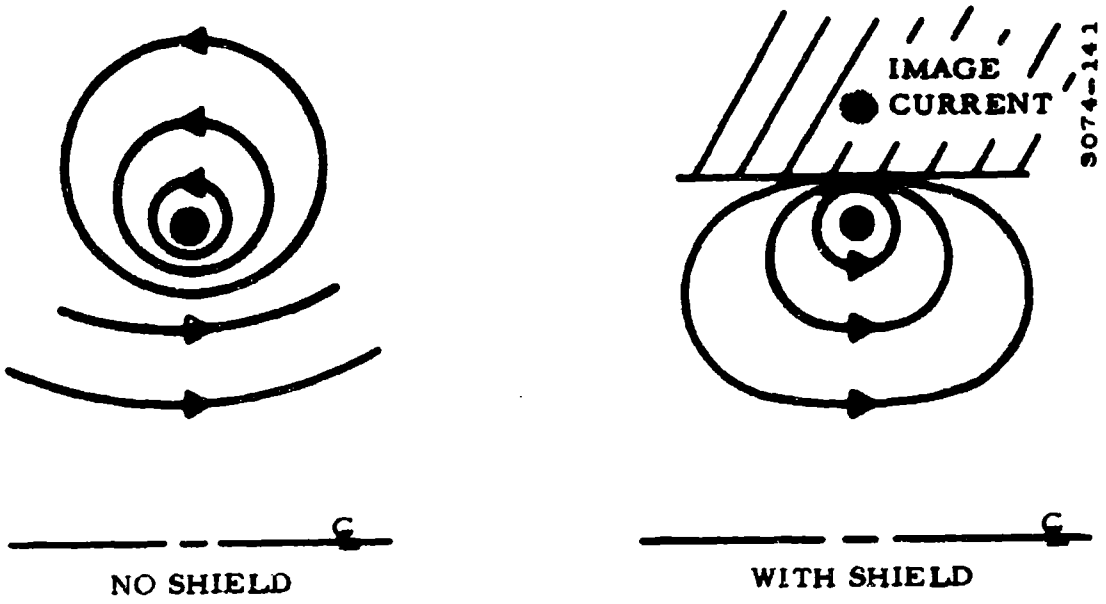


Figure 2-8. Action of the Coil Shield

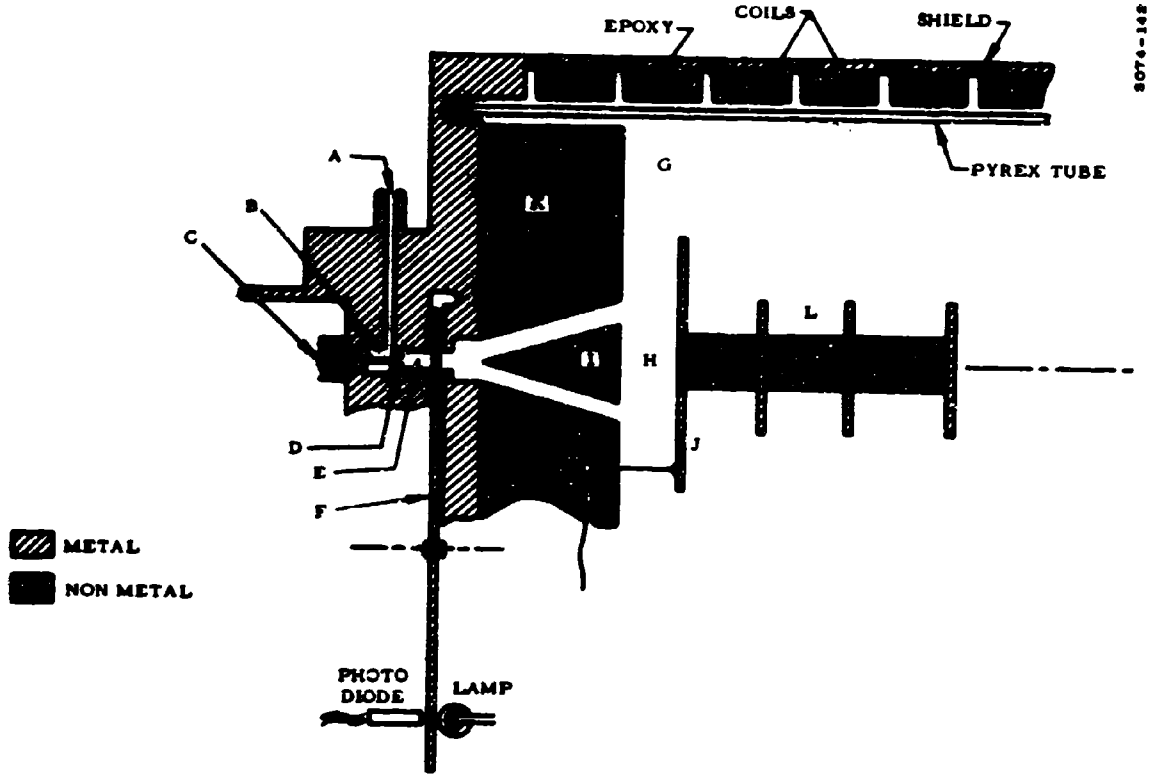


Figure 2-9. Gas Injector

is referred. A small channel at the periphery of the rotating plate accepts gas which tries to leak by. The channel is scavenged by a small oil-diffusion pump.

When the accelerator is operated the sequence of events is the following: 1) a pulse from the photo-diode actuates a timing circuit; 2) 2-3 milliseconds later (when the hole in F no longer lines up with Chamber E) plunger C operates and gas enters Chamber E; 3) the next time a hole in F aligns with E the gas passes to the accelerator and, simultaneously, another pulse from the diode starts the spark-gap-timing sequence.

The double-valve system just described was found to be necessary. The holes in F define the length of the gas burst (600 microseconds). It is likely that less than 1% of the injected gas is caught by the magnetic field as toroids. The remaining gas is ionized and heated. It passes down the accelerator tube and arrives at the end of the coil structure some 25 microseconds after the tori (according to Kerr cell pictures).

This large mass of uncontrolled, heated, gas made the use of a ballistic target (for determining the momentum of the tori) impractical.

The purpose of the structures labelled I, J, K, etc. will be explained later.

The gas injector shown in Figure 2-9 was the one in use at the end of the Mark I experiments.

2.5 EARLY DIFFICULTIES

Considerable difficulty was experienced with the coil-capacitor assemblies and many failures occurred during the first year of the program. These failures were due to:

1. Tiny bubbles in the epoxy insulation of the coil rings and the high power transmission lines. At certain places the electric field strength exceeded 80 volts per 0.001-inch. This is a sufficiently large field to cause ionization breakdown inside a small bubble, leading to deterioration of the epoxy and eventual failure of the insulation.

2. Electro-mechanical shock of the insulation. The coil currents exceeded 100,000 amperes and the resulting high stresses, suddenly applied, led to insulation failure.

The first difficulty was overcome by the development of an efficient vacuum-molding technique. The details are given in Appendix B. The second difficulty was overcome by the use of an epoxy of high impact strength. It should be noted that manufacturers' specifications on strength do not apply to impact loading. The tensile and compressive strength of the epoxy which was finally chosen was relatively low even though its impact strength was high.

Electrical interaction between the separate coil-capacitor assemblies, through the timing circuitry, was also a serious problem. The problem and the method of solution are discussed in detail in Appendix A.

Malfunction of the spark gap switches was a serious problem during the first year of the contract and considerable effort was directed towards overcoming the difficulties. The problem was eventually brought under control but it was never completely eliminated. The seriousness of the problem can be understood through an example. Suppose the reliability of an individual spark gap is 99% (i. e., the jitter in the firing time is less than the critical amount for 99 out of 100 operations of the gap). When the net reliability of 19 such gaps is computed it is found that a misfire of the accelerator is expected once in 5 firings. If the gap reliability falls to 90% only 1 firing in 10 will be proper.

2. 6 THE ACCELERATION PROCESS

The peak value of the radial magnetic field varied by a factor of 2:1 between Coil #1 and Coil #19 due to the decrease in size of the energy-storage capacitors. Near Coil #1 the peak field was about 3000 gauss.

Refer now to Figure 2-9. Gas enters the accelerator tube when the injector is actuated and flows to, and beyond, region G. It is prevented from getting close to #1 coil by the non-metallic piece K. When spark gap #1 fires, the rising magnetic field induces an electric field in region G which ionizes some of the gas, driving it downward and to the right. Subsequently, the magnetic field of Coil #1 is used as a kind of buffer to ensure that the bulk of the ionized gas will be caught at a field confluence as required.

Coil #2 is fired as the field from #1 reaches its peak value. The gas is in close contact with #2 coil and an intense ring-current-discharge occurs. The ionized material is driven radially inward towards the axis

of symettry of the accelerator and a hot, high-pressure region is created near H. The conical plug, I, prevents the hot gas from re-entering the injector. At the conclusion of this phase the field from #2 coil is maximum and the field from #1 coil is zero and beginning to reverse. At this time spark gap #3 is triggered. As the field of #1 coil begins to rise again, and that from #2 begins to fall, a field confluence is formed. During this formation time the induced electric fields are strong and additional ionization occurs. Some of the gas becomes magnetically-trapped near the field confluence.

At the time when the field of #2 coil goes to zero (its first current zero) the fields from Coil #1 and Coil #3 are at maximum amplitude and the point labelled A on the timing diagram (Figure 2-6) has been reached. The field confluence subsequently moves as shown on the timing diagram.

To understand the actions described above one must remember that an increasing field drives plasma radially inward whereas a decreasing field pulls it out towards the coils. This general tendancy can be understood with the aid of the "inductive potential" concept discussed in Section 3 of this report.

The cylinder-and-disc assembly L is added to trap gas which is driven towards the axis of symmetry to the left of the disc J.

Were it not for the baffle system shown, the gas would be ionized, driven to the axis, and squirted along the axis much like toothpaste being squeezed from a tube.

Disc J is connected to a several-thousand volt power supply so that a preionizing glow-discharge can be formed between J and the rotating disc F. Experimentally, preionization was found to be required.

A photograph of the baffle system is shown in Figure 2-10.

It was also experimentally observed that no discharge occurred at all when the pressure at G was lower than 3×10^{-4} Torr.

The magnetic field of the accelerator is not quite strong enough to accelerate ions directly, but strong electron-ion coupling forces come into play. These are discussed in Section 3.

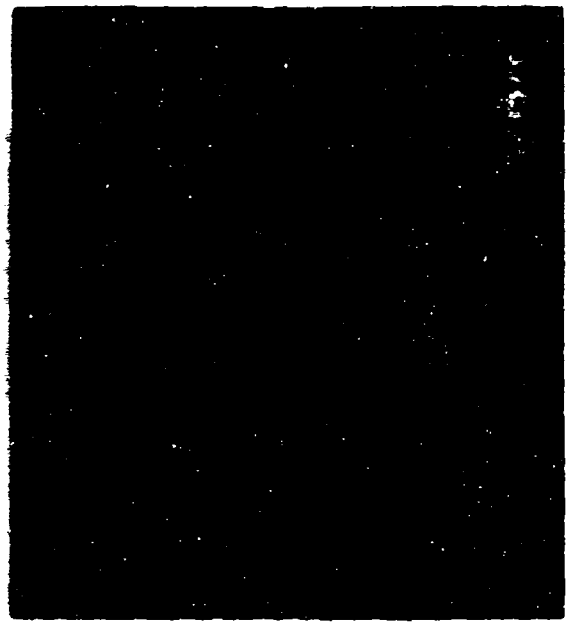


Figure 2-10. Injector Baffle System

The acceleration of the first field confluence is 1.7×10^{10} meter/square-second and the speed at coil #19 is 1.2×10^{5} meter/second (12 cm per microsecond). Nitrogen ions moving at this speed have a directed kinetic energy of 1000 electron-volts.

2.7 RESULTS

The diagnostic technique most frequently employed was to allow the accelerated plasma to strike a flat surface and to photograph the results. Figure 2-11 illustrates a typical result obtained at the beginning of the contract period (time exposure; ASA 200; f/22). The outlines of the impact target (non-metal) can be dimly seen. A mass of luminous plasma lies over and on the target surface. The luminosity is greatest at the center (on the axis of the accelerator) and no evidence of a toroidal shape can be seen. In approximately one case in 20 the light was more concentrated and luminous near the edges of the target than at the center, providing some evidence for the existence of toroids. The shot-to-shot variations in performance were great at this time in the program (January 1960).

Several carefully-collimated photomultiplier tubes were employed in an attempt to observe the light from the fast-moving gas. However, the oscillograms obtained had insufficiently-definite features to be interpreted with any assurance. The hot, relatively slow-moving gas which came from the accelerator after the real time of interest was easily observed but the evidence for prompt, fast-moving toroids was questionable. Single turn loops of wire were used in an attempt to detect the self magnetic field of the plasma. Here again the results were ambiguous.

A microwave doppler system was employed to measure the speed of the plasma. This system could not be operated satisfactorily due to electrical interference from the accelerator.

Subsequent improvements were made in all these areas and the gas injector was subjected to a vigorous development program. A fast-acting Kerr cell shutter was obtained in August 1960.

A photograph of the impact target is shown in Figure 2-12. A small, well-shielded, single-turn loop has been added. The loop-shield material is a copper tube. Later, a short piece of copper tube was added at right-angles to the support stem of the loop (that is parallel to the surface of



Figure 2-11. Plasma on Surface of Impact Target

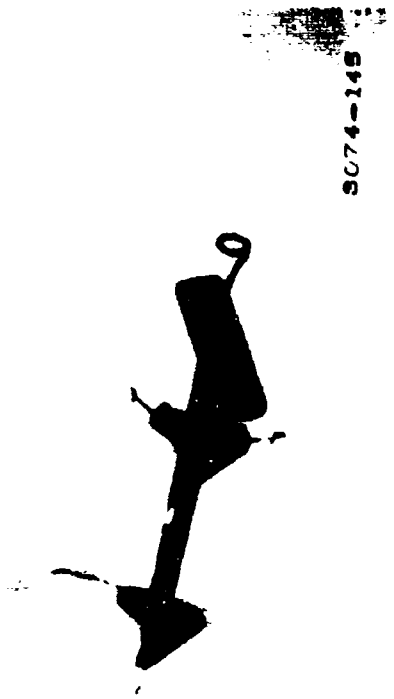


Figure 2-12. Impact Stage with Shielded One-turn Loop Mounted

impact target) The Kerr-cell photographs shown in Figures 2-13 through 2-19 were obtained.

Figure 2-13 shows a Kerr cell photograph (10 μsec shutter time; ASA 3000; effective aperture was f/3.9) of the target discussed above. The Kerr-cell shutter was set to open 2 microseconds before the expected arrival of the first toroid and to close 10 microseconds later (this performance was verified experimentally). All events recorded in Figure 2-13 are due to plasma which travelled from #1 coil to the target position with a speed in excess of 4×10^4 meter/sec; a figure which is one third the ultimate field speed in the accelerator.

Subsequent examination of the cross-bar on the target showed that the luminous trails hanging from it are probably largely composed of ablated copper. The width of the trails can be judged from the fact that the bar is 12.5 cm across. It is obvious that the bar was hit by a fast-moving plasma which could have been toroidal in shape.

Figure 2-14 shows a similar picture with evidence of the effects of more than one toroid. Figure 2-15 shows more than one impact also but the trails are not symmetric about the search coil. None of these pictures reveal any evidence of the path of the plasma before impact. Apparently, it moves too quickly and makes too little light. The photomultiplier monitors recorded no signals large enough to extend unmistakedly above the background noise.

Figure 2-16 shows the result of an impact with the search coil itself. Several such events were recorded.

Figure 2-17 shows a rather curious fact. Besides being relatively intense the plasma has somehow gotten in under the coil without striking it. Figure 2-18 shows the same event on a time exposure. In the original photo some thin, individually-luminous trails of ablated material can be discerned.

Figure 2-19 provided the explanation for the event discussed above. In the original photo a faint luminous cone can be seen converging on the search coil, indicating that the plasma came to a focus at the search coil. For this picture the ambient pressure in the accelerator was 2 or 3 times higher than in the previous pictures; enough so that the moving plasma left faint evidence of its path.

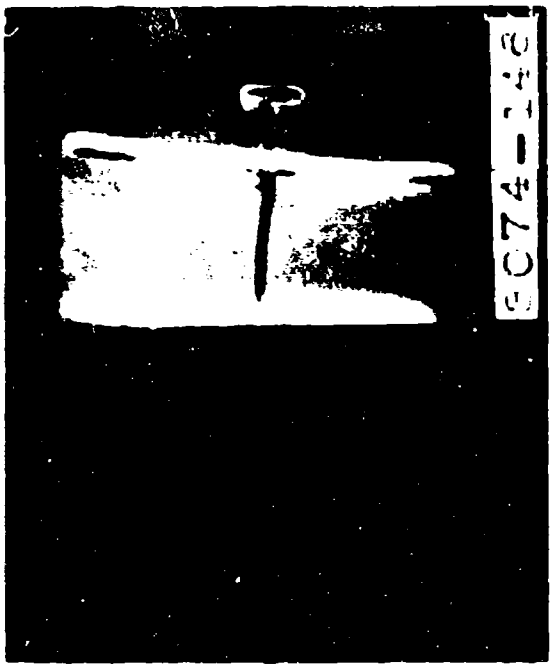


Figure 2-13. Kerr-Cell Photo

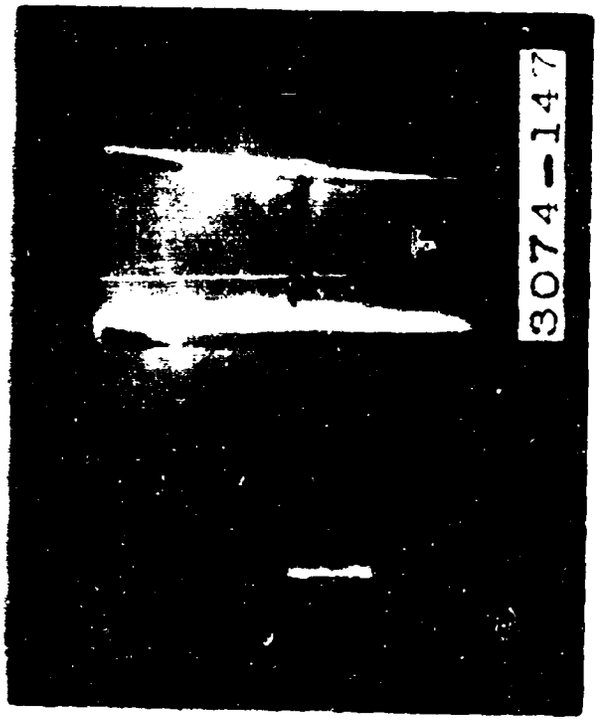


Figure 2-14. Kerr-Cell Photo

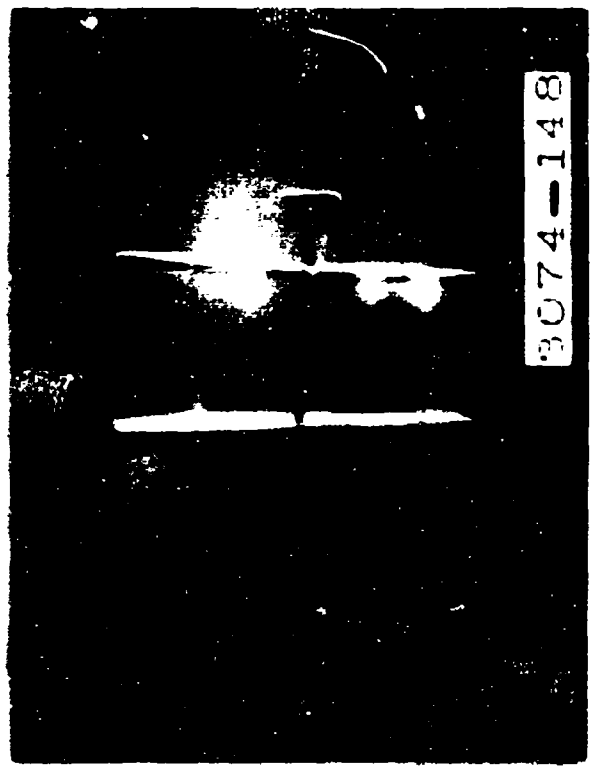


Figure 2-15. Kerr-Cell Photo

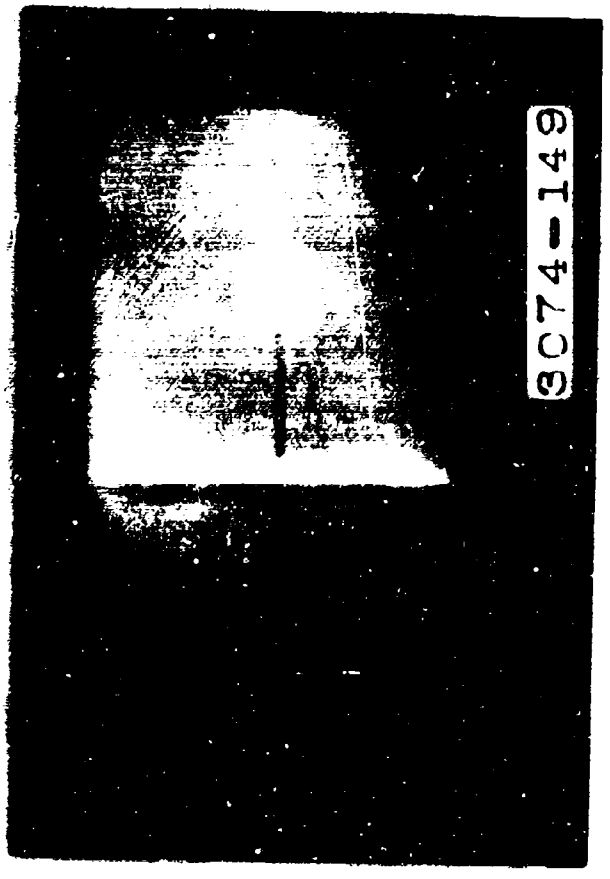


Figure 2-16. Kerr-Cell Photo



Figure 2-17. Kerr-Cell Photo



Figure 2-18. Time Exposure of Event in Figure 2-17

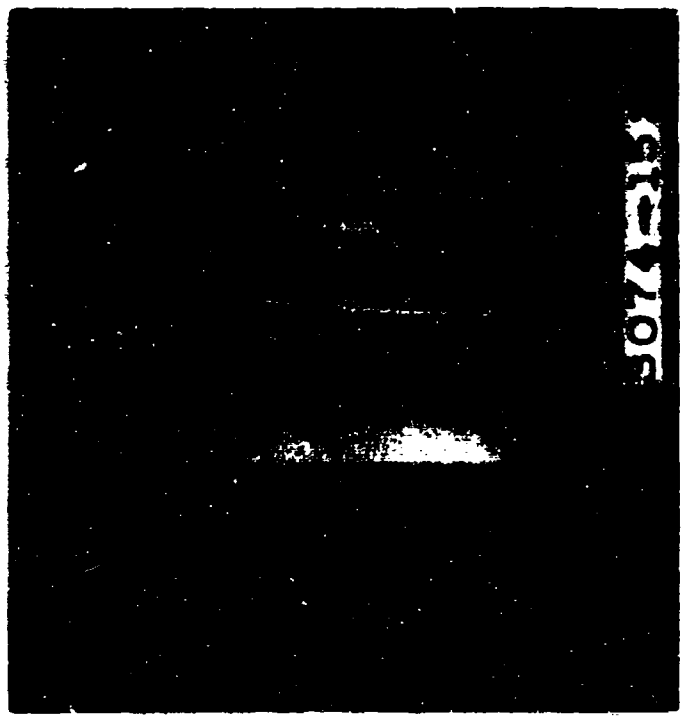


Figure 2-19. Kerr-Cell Photo

Figure 2-16 can now be explained as the result of a plasmoid which came to a focus a short distance above the search coil. In the case of Figure 2-17 the focal point lay under the search coil.

Signals were recorded by the search coil. The oscillograms are fuzzy with high frequency noise and are not plain enough to reproduce here. However, the signals indicated toroids with both right-handed and left-handed ring-currents. A rough estimate of the ring currents was made from the coil signals and it was concluded that the plasmoids contained currents of several hundred amperes. When the search coil was struck by the plasma the resulting signals could not be interpreted.

The horn of the microwave doppler system can be seen towards the lower edge of each photograph. The signals from this device indicated beating of several doppler frequencies. The results were generally not capable of interpretation. However, on one or two occasions a clean signal was obtained. The calculated speed, on these occasions, was 1×10^5 meters/second with a probable error of 30%. This offers evidence that the plasma was attaining the same speed as the traveling field of the accelerator.

The problems with shielding the doppler system proved not to be amenable to any standard shielding technique. A solution was obtained by physically moving the transmitter-receiver parts of the circuit some 30 feet away from the accelerator. This remote station is shown in Figure 2-20.

The experiments employed nitrogen, hydrogen, and argon. Definite evidence of toroids were found only in the case of nitrogen and hydrogen. Argon was not tried extensively, however.

In the light of the successes described above a new impact target was constructed. A rear view of this target is shown in Figure 2-21 and a front view is shown in Figure 2-22. In the rear view the white object is a teflon slider which carried the search coil. A mechanism was arranged so that the search coil could either be in working position (as shown) or retracted down behind the target. The microwave horn is also visible.

The top surface of the target was approximately half-round as shown in the top view of Figure 2-23. A series of slots were located close to the flat edge as shown. In Figure 2-22 it can be seen that the slots were



Figure 2-20. Microwave Doppler System

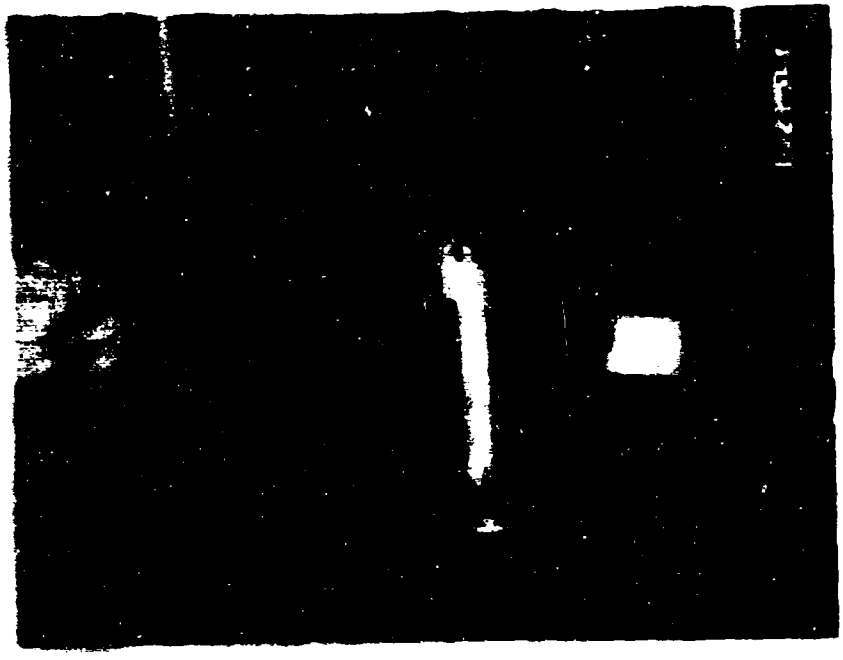


Figure 2-21. Rear View — Impact Target



Figure 2-22. Front View — Impact Target



Figure 2-23. Top View — Impact Target

deep. They were fronted with a transparent plate so that a camera could look into them. The top of the target was also pitted with a series of shallow drill holes. The purpose of these was to provide a series of traps for luminous, relatively slowly moving, ablated material.

It was hoped that the fast plasmoids would break up on the target and that parts of them would enter the slots, penetrating deeply and showing their presence by strong luminosity. This did not happen. No deep-penetrating luminosity was ever observed in the slots. In fact, the luminosity which was observed was fairly uniformly distributed with no one slot being brighter than the others. The slots were viewed through the Kerr cell shutter.

Simultaneous with these attempts, time-exposure pictures were taken of the top of the target through a periscope. One of the periscope pictures is shown in Figure 2-24. A faint ring-shaped pattern of light is evident on the top surface of the target.

The Kerr cell was moved to the periscope position and a series of pictures like Figure 2-24a were obtained. The Kerr cell shutter opened 16 microseconds after #1 spark gap fired and closed 10 microseconds later. It is seen that the view was not improved by the use of the Kerr cell.

When the opening of the Kerr cell was delayed an additional 10 microseconds photographs were obtained which showed a luminous ring on the top surface of the target as shown in Figures 2-25 and 2-26. Examination of these photos, and others like them, revealed that the luminescense was not due to gas on the surface of the target, but was contained in the target material itself. Delaying the Kerr cell opening had allowed the view-obscuring gas to move away.

Rings were observed with hydrogen, helium, nitrogen, and argon.

Evidence of the impact of more than one torus was found, as is shown in Figures 2-27 and 2-28.

In the case of argon some difficulty was experienced since the gas appeared to move very slowly once it had struck the target. In fact, the gas flowed over the edges of the target like water over a falls, as is shown in Figure 2-29. Argon also produced the unexplained result shown in Figure 2-30. Attempts were made to delay the Kerr cell shutter

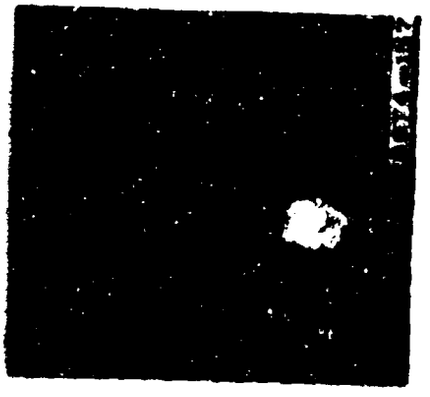


Figure 2-24. Time Exposure Photo of Top of Target



Figure 2-24a. Kerr Cell Photo (10 μsec shutter speed)

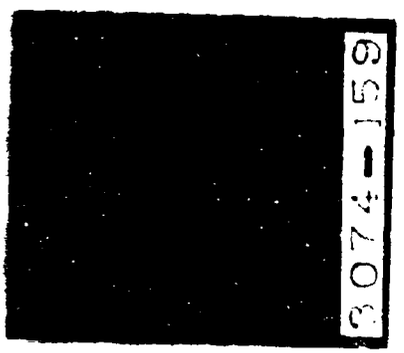


Figure 2-25. Kerr Cell Photo

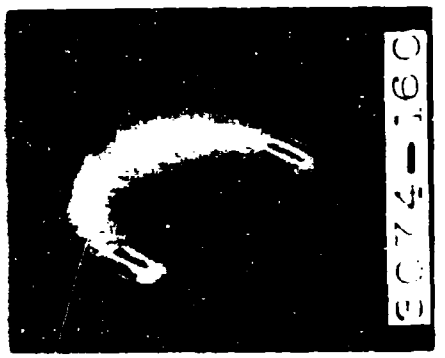


Figure 2-26. Kerr Cell Photo

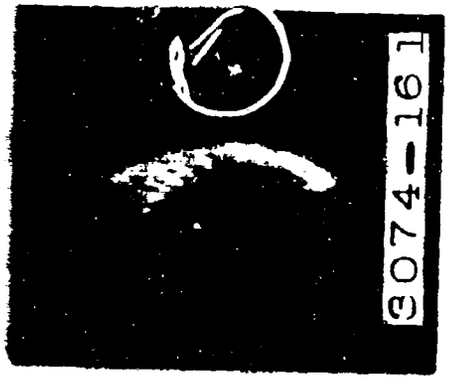


Figure 2-27. Kerr Cell Photo

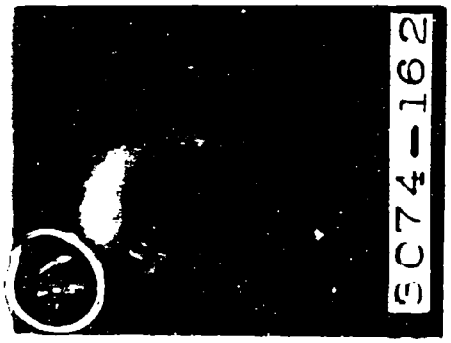


Figure 2-28. Kerr Cell Photo

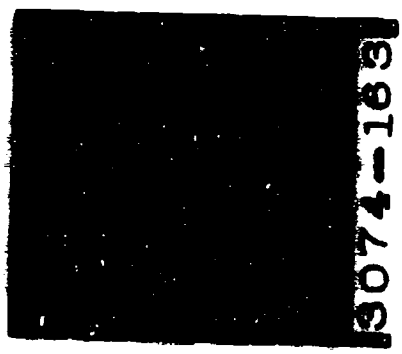


Figure 2-29. Argon; Kerr Cell Photo



Figure 2-30. Argon; Kerr Cell Photo

still further but these attempts met with failure. A hot mass of gas, moving down the accelerator (as discussed earlier) obscured the view again.

Evidence for various forms of pinch instabilities was obtained as shown in Figures 2-31 through 2-34 and also in Figure 2-27 (radial striations).

In general, the rings were 12 cm. in diameter and 1 cm. wide.

The exact color of the luminescence was not determined but it lies in the visible range (~2 ev quantum energy). A measurement of the decay time was attempted but the large mass of hot gas, mentioned earlier, rendered the attempt unsuccessful. It is only known that the decay time was longer than 30 microseconds. Non-linear time-dependent saturation effects in the film were tested for by varying the f-number of the cameras. They were found to be absent.

Properly exposed pictures of the rings were obtained with 3000 ASA polaroid film at a lens setting of f/11. The transmission factor for the Kerr Cell was 1/4. If the diagnostic surface is considered to be a diffuse radiator then the known response of the (panchromatic) film can be used to estimate the power going to make visible light during the shutter time. The estimate is 180 watts. It is difficult to estimate the efficiency with which the directed kinetic energy of the plasma ions (700 electron volts in the case of nitrogen) is converted into visible light quanta (2 to 3 electron volt quanta). The efficiency of N_2 discharges, Hg discharges, and carbon arcs for converting electrical energy into visible light is about 5 percent but it is felt that the efficiency here must be less than this. The decay time of the phosphorescence is also not know, but experimental results show that it is longer than 30 microseconds. From the efficiency mentioned above, the decay time mentioned above, the toroid velocity before impact, and the fact that three toroids are formed each time the machine is operated, the mass of a toroid may be estimated. The calculations yield 0.006 micrograms per toroid and, for the case of nitrogen, 2.5×10^{14} atoms per toroid. These numbers must be regarded as lower limits and they may, in fact, be an order of magnitude too small.



Figure 2-31. Kerr Cell Photo

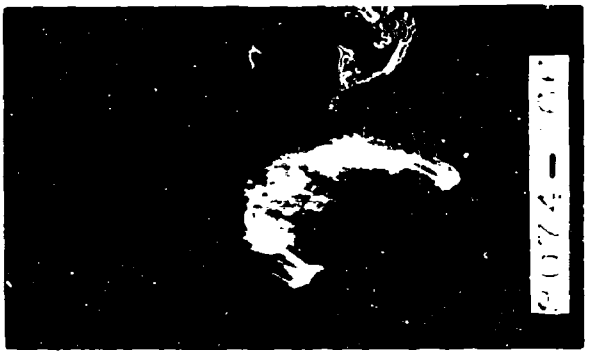


Figure 2-32. Kerr Cell Photo



Figure 2-33. Kerr Cell Photo



Figure 2-34. Kerr Cell Photo

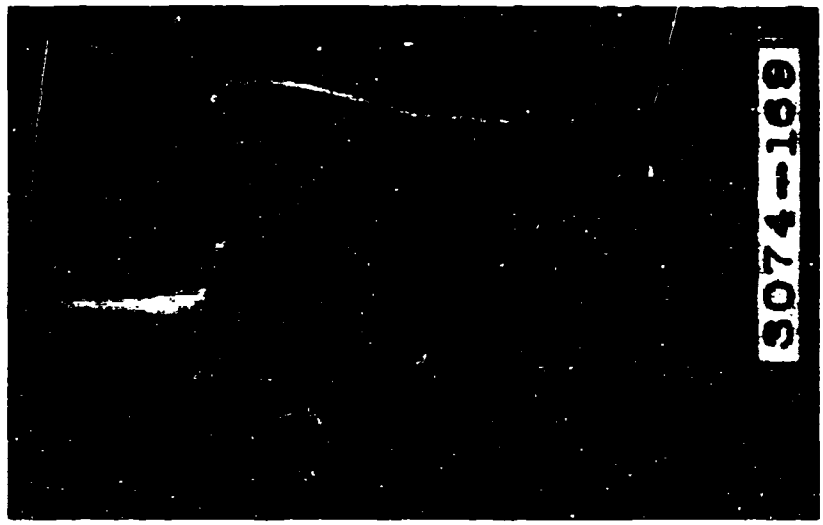


Figure 2-34a. Photomultiplier Signals for Time-of-Flight Analysis

Analysis of the signals from two collimated photomultipliers gave an estimate of the speed of the plasmoids based on a time-of-flight calculation. The result was 10^5 meters/second with a probable error of ±20%. A typical oscillogram is shown in Figure 2-34.

When a toroid reaches the end of the accelerator coil system it must tear loose from the field. In doing so the pinch may be greatly enhanced. The state of the toroids as observed in free flight is, in general, different from their state during acceleration.

After the tests the top surface of the target (which had been coated with black paint) was examined for surface damage. The pattern shown in Figure 2-23 was observed. This pattern corresponds reasonably well with some of the luminous patterns which were photographed.

For these, and other, tests the inside surface of the accelerator tube was also painted black to prevent the intense light from the injector region from interfering with the photography. Otherwise the accelerating tube tended to act like a light pipe; lighting up brilliantly and making observations very difficult.

Surface damage, taking the form of rings of discoloration, was observed on the walls of the accelerator tube near the injector end. These rings are visible in the top view of the tube shown in Figure 2-35. The position of the rings was carefully measured and they were found to occur exactly midway between the one-turn accelerating coils. This is not surprising. However, there was only a ring for every second coil pair. No explanation for this is available.

2.8 CONCLUDING REMARKS

The pulsed character of the accelerator, with all its attendant difficulties, lessens the possibilities of obtaining good quantitative data on the characteristics of the toroids. Sufficient measurements to permit a power balance calculation could not be obtained.

Some of the measurements indicated that the toroids were coming to a focus. At other times the tendency seemed to be absent. Although the accelerator timing was modified slightly between these measurements there was no good explanation for the difference in behavior. The change had not been purposely sought.



Figure 2-35. Evidence Surface Damage on Walls of Accelerator

For these reasons the contract effort was redirected in the fall of 1961 and work was begun on a continuously-operating traveling field accelerator designed to produce a continuous stream of pinched toroids. By this time, also, theoretical understanding had progressed to the point where it was realized that:

1. Toroid formation could be enchanced by using a gas of high atomic number.
2. The desired action could be achieved by a short accelerator; one which possessed no more than one electrical wavelength.
3. The magnetic field could be much weaker.
4. The magnetic field need not accelerate. That is, a constant speed design could be used.

A description of the work on this new accelerator (designated Mark II) is contained in Section 4 of this report. A presentation of theoretical ideas is given in Section 3; the next section.

3. THEORETICAL CONSIDERATIONS

3.1 INTRODUCTORY REMARKS

An important phase of the contract work was the attempt to gain a theoretical understanding of the behavior of plasma in electrodeless magnetic field configurations such as a traveling wave. In these cases the magnetic field is time dependent, and the plasma experiences an electric field due to the process of induction as described by Maxwell's equations. The arrangement of the coils used to produce the field can be chosen from a virtually endless variety of possibilities, but the work on this contract, was restricted to systems in which a straight line can be drawn which passes through the center of each coil. That is, the work was limited to systems with axial symmetry.

The primary process for energy input to the plasma is through the induced electric field; and this field closes on itself. Thus, there is a strong tendency to form ring currents in the plasma, and, because of the symmetry of the field, the ring currents center about the axis of the coil system. When the ring currents are sufficiently strong they produce fields of their own which tend to counteract the field from the coils (the skin effect) and to interact with the plasma current in such a way as to pull the plasma together (the pinch effect). When the geometry and the plasma conditions are right the plasma will react to the pinch effect by forming itself into well-defined tori. The conditions for formation of such tori and their subsequent behavior in the magnetic field and while emerging from the magnetic field were of major interest in the contract work.

It will be shown later in this section that the formation of tori can be accomplished only if the characteristic time for current decay due to Joule heating is relatively long, and for this condition to be satisfied the plasma must have a relatively low density. Consequently, the theoretical considerations concern the behavior of low-density plasma for which the mean free path is of the order of, or larger than, the diameter of the coil system and for which the well-developed subject of fluid mechanics has questionable application.

The frequency at which the coil system is operated in a traveling wave plasma accelerator is determined by the speed to which the plasma must be accelerated and by the physical size of the machine itself. Typically, the operating frequency lies in the range from 100 kilocycles to 1 megacycle. At these frequencies the current which can be made to flow in the coils is limited by the inductance of the coil-system and its associated circuitry, and with power supplies of reasonable voltage (less than 50,000 volts, for example) it is found that the magnetic field strengths which can be obtained are less than 0.5 weber/sq-meter (5000 gauss). Such fields are too weak to accelerate the ions to any reasonable speed. The electrons, however, are strongly affected by such fields and they attempt to keep up with the moving field lines. In doing so, they tend to separate from the ions. This separation is prevented by strong electric fields which immediately develop because of space-charge effects. The ions are accelerated by this field. In the language commonly used to describe $j \times B$ channel accelerators one would say that the ions are accelerated by the Hall voltage. On a time-averaged basis no Hall currents flow even though there may be instantaneous Hall currents due to electron oscillations.

In order to account for the actions described above a two-fluid plasma model is needed. In such a model, as will be shown later, energy is exchanged between the ions and the electrons. If the plasma beam from the accelerator contains ions of axially directed kinctic energy, E, then somewhere back in the accelerator there are electrons with azimuthaliy directed kinetic energy, E. A study of the Joule-heating process shows that it is reasonable to expect, in addition, random thermal energies on the order of E. Since E is typically larger than 100 electron volts, rather long electron-ion collision times can be expected so that the relation between current and induced voltage is not described by Ohm's law.

In summary, the characteristics of the plasma that are of great importance to a theoretical description are:

1. Low density
2. High electron energy
3. Axial symmetry

These characteristics make it feasible to base the theoretical model on the single-particle equations of motion with corrections for particle-particle interactions rather than on the fluid-flow equations with corrections for single-particle effects. In actual fact neither the extreme viewpoint of collisionless motion nor that of collision-dominated motion is

correct. The real situation lies somewhere between; probably closer to the former for cases of interest to this program.

Already at the beginning of the contract period a study of the motion of single-charged particles in axially symmetric magnetic fields was under way, in an attempt to reduce the equations to a tractable form. Although the force law is the well-known Lorentz force, the complexity of the equations causes difficulty in forming an adequate mental picture of the process, and without such a picture it is difficult to proceed with assurance to the task of introducing the additional complications of particle-particle interactions.

The first major theoretical step was taken in the summer of 1960 when it was realized that a theorem on angular momentum, well-known in the field of electron optics for static, axially symmetric magnetic fields and known as Busche's theorem, could be generalized to include time-dependent magnetic fields of arbitrary time dependence. Shortly thereafter it was found that the radial and axial particle motions could be obtained by taking the spatial gradient of a single, scalar quantity that has the properties and dimensions of a voltage, and — since it arose through magnetic effects — it was given the name inductive potential. Through the use of this potential a mental picture of the motion of charged particles in fields of considerable complication could be obtained. In the special case when the inductive potential is not time-dependent, the radial and axial motions of particles are the same as the motion of a small ball moving, without friction, over a landscape whose contours of elevation are similar to the contours of the inductive potential.

The picture above led to the realization that certain regions of the magnetic field would be forbidden to a given particle on the basis of energy considerations alone. This realization, coupled with the recall that the magnetic field of the earth is axially symmetric, led to a re-examination of some of the early work by Störmer[1] on the "allowed and forbidden regions" of cosmic ray particles. Thus it was discovered that, without naming it as such, Störmer had made use of the inductive potential concept and that the origins of the concept dated at least as early as 1936.

The authors are indebted to Morton Levine, of the Cambridge Research Laboratories, for pointing out to them the use of the inductive potential concept by Rajchman and Cherry,[2] in 1947, for the design of high-energy, circular electron accelerators.

In early 1961 it was learned that the concept had been employed by G. Schmidt, at Stevens Institute of Technology, for the study of a plasma betatron[3] and that he had interest in applying the same concept to plasmas in general. Some of the latter work has been published[4,5].

The early work on single-particle motion that was performed on this contract was published in 1960 as an AFOSR Technical Note [6], and the investigations were then directed toward the inclusion of particle-particle interactions. An ad hoc model was developed which satisfied the basic requirement of a plasma (that of charge neutrality) and brought to light the processes of energy exchange between electrons and ions in the plasma through the medium of space-charge forces. This model was described in an AFOSR Technical Note, also published in the summer of 1960.[7] Subsequently, the model was used to calculate plasma motion and energy in a sinusoidally driven theta-pinch. The work was performed with the aid of an analog computer, and a paper [8] was presented at the annual meeting of the ARS in the fall of 1960.

A great deal of the information contained in the three reports mentioned above is not duplicated in the main text of this report. Consequently, for completeness, they are included as Appendices C, D, and E.

By the fall of 1961 the motion of a collisionless, pinched plasma torus in a traveling magnetic field was well enough understood to have considerable influence on the design of a CW accelerator (the Mark II accelerator). These influences are discussed in some detail toward the end of this section and also in Section 4.

During the summer of 1962 an attempt was made to use the theory to analyse the performance of a single-phase, 2-Mc, funnel-shaped plasma accelerator on which experimental work had already been done. This work led to the development of the principle of slow flow which is discussed later in this section and, as well, represented the first attempts to take account of the effects of thermal expansion in low-density plasma accelerators. It is now felt that the thermal effects were not handled in a completely proper fashion; but, in spite of this, the work represented a major step in the theoretical development. It is included in this report as Appendix P.

Since then, the theoretical effort has been directed toward fitting the model into a Boltzmann formalism in order that a firm connection between the single-particle and the many-particle picture can be established.

In the course of the work many different references have been employed, but especially frequent use has been made of books by Brown,[9] Delcroix,[10] Jeans,[11] Kennard,[12] Linhart,[13] and Spitzer.[14]

3.2 THE ELECTROMAGNETIC FIELD COMPONENTS

The MKS system of units is used throughout along with a right-handed cylindrical coordinate system with unit vectors $\hat{r}$, $\hat{\theta}$, and $\hat{z}$. The system of plasma and fields is assumed to be, at all times, symmetrically distributed with respect to the z-axis of the coordinate system in such a way that the field strengths and the plasma properties do not depend on the angle θ.

Extensive use is made of the scalar quantity, Φ, which is the magnetic flux expressed in units of the weber. There are two reasons why the flux is used rather than the magnetic field strength: first, it appears in the equations naturally as the entity representing the magnetic effects; and second, since it is a scalar quantity, the net flux is due to the additive effect of the flux from all the field-producing coils of the magnetic system. By the term "flux at a point" we shall mean the value of the following quantity:

$$\Phi(r, z, t) = 2\pi \int_0^r dr' r' B_z(r', z, t) \tag{3.1}$$

where B_z (r, z, t) is the axial component of the field strength at position r, z, and time t. The meaning of the flux at the point r, z is the following:

> If a circle is drawn through r, z which has its center at position z on the axis of symmetry, then Φ is the total number of field lines that pass through the circle at the instant of time t.

The equation for Φ can be derived from Maxwell's equations and is found to be

$$\frac{\partial}{\partial r}\left(\frac{1}{r}\frac{\partial \Phi}{\partial r}\right) + \frac{1}{r}\frac{\partial^2 \Phi}{\partial z^2} = -2\pi \mu_o j_\theta \tag{3.2}$$

where j_θ is the density of current in the azimuthal direction and μ_o is the permeability of free space ($4\pi \times 10^{-7}$ henry/meter).

The electromagnetic effects can be described through the use of a vector potential, $\vec{A}$, and a scalar potential (or voltage), X. Because of the assumed symmetry the functional dependences of the two potentials are

$$\vec{A} = \hat{\theta} A_\theta (r, z, t) \tag{3.3}$$

$$X = X (r, z, t) \tag{3.4}$$

Both of these potentials must be interpretated as the net effect of the applied fields and those generated by the plasma itself. It will be a consequence of the theoretical model that the scalar potential that exists in the plasma depends only on the magnetic potential and the thermal properties of the plasma.

The magnetic field components are found by taking the curl of the vector potential. Then the axial field component can be used in Eq. (3.1) to compute the flux. It is found that the flux and the vector potential are related in the following way:

$$\Phi = 2\pi r A_\theta \tag{3.5}$$

and that the field components are

$$B_r = -\frac{1}{2\pi r} \frac{\partial \Phi}{\partial z} \tag{3.6}$$

$$B_z = \frac{1}{2\pi r} \frac{\partial \Phi}{\partial r} \tag{3.7}$$

The electric field is computed from

$$\vec{E} = -\frac{\partial \vec{A}}{\partial t} - \text{grad } X \tag{3.8}$$

and, as a result, the electric field components are

$$E_r = -\frac{\partial X}{\partial r} \tag{3.9}$$

$$E_z = -\frac{\partial X}{\partial z} \tag{3.10}$$

$$E_\theta = -\frac{1}{2\pi r}\frac{\partial \Phi}{\partial t} \tag{3.11}$$

It is to be noted that the azimuthal component of the electric field is determined by the behavior of the flux. This is the electric field of induction.

3.3 SINGLE-PARTICLE EQUATIONS OF MOTION

The charge of a particle will be taken to be equal to Ze, where e is the absolute value of the charge of an electron and Z has values -1, 0, 1, 2,... depending on whether the particle is an electron (or negative ion), a neutral, or an ion. The three-dimensional position vector will be denoted by $\vec{R}$. The equation of motion for a particle of mass M, in the fields defined in Section 3.2 is

$$M\frac{d^2\vec{R}}{dt^2} = Ze\left[\frac{d\vec{R}}{dt} \times \vec{B} + \vec{E}\right] \tag{3.12}$$

This equation is valid as long as the particle has no collisions and is moving at nonrelativistic speeds. The azimuthal component of Eq. (3.12) can be written down and simplified through the use of Eq. (3.6) and (3.7). The result, which is a generalization of Busche's theorem of electron optics, is

$$\frac{d(Mr^2\dot{\theta})}{dt} = -\frac{Ze}{2\pi}\frac{d\Phi}{dt} \tag{3.13}$$

If the angular momentum of the particle (with respect to the z-axis) is denoted by J and the azimuthal component of momentum is denoted by P_θ then since

$$J \equiv rP_\theta \equiv r(Mr\dot{\theta}) \tag{3.14}$$

the integral of Eq. (3.13) can be written as

$$P_\theta (r, z, t) = - \frac{Ze}{2\pi} \left[\frac{\Phi - K}{r} \right] \tag{3.15}$$

where K is a constant whose value is

$$K = \frac{2\pi}{Ze} J(0) + \Phi(0) \tag{3.16}$$

The notation in the equation above has the following meaning: the position of the particle at time t_o is assumed to be r_o, z_o, and the flux at this point and time is denoted by $\Phi(0)$. Similarily, the angular momentum is denoted by $J(0)$. So long as the only forces that act on the particle are those that arise from the particular set of fields discussed in Section 3.2, the quantity K is a constant of the motion. If the particle is in a field-free region at time t_o, then K can be interpreted as being directly proportional to the angular momentum at time t_o.

The equations of motion for the radial and axial directions, obtained from Eq. (3.12) are:

$$M \frac{d^2 r}{dt^2} = \frac{Ze}{2\pi M} \frac{P_\theta}{r} \frac{\partial \Phi}{\partial r} + \frac{P_\theta^2}{Mr} - Ze \frac{\partial X}{\partial r} \tag{3.17}$$

$$M \frac{d^2 z}{dt^2} = \frac{Ze}{2\pi M} \frac{P_\theta}{r} \frac{\partial \Phi}{\partial z} - Ze \frac{\partial X}{\partial z} \tag{3.18}$$

It is obvious that one can substitute Eq. (3.15) into Eqs. (3.17) and (3.18). When this is done it is found that the resulting equations can be written in a particularly simple and useful form. In order to achieve simplicity of notation a new coordinate system is defined. This coordinate system is cartesian, rather than cylindrical, and employs unit vectors (relating to r and z) of $\hat{a}_r$ and $\hat{a}_z$, respectively. In this system the position vector will be denoted by $\vec{S}$ and the velocity vector by $\vec{W}$. Two gradient operators will also be defined. The relations are shown below.

$$\vec{S} \equiv \hat{a}_r\, r + \hat{a}_z\, z \tag{3.19}$$

$$\vec{W} \equiv \hat{a}_r\, \dot{r} + \hat{a}_z\, \dot{z} \equiv \hat{a}_r\, W_r + \hat{a}_z\, W_z \tag{3.20}$$

$$\vec{Q} \equiv M\vec{W} \tag{3.21}$$

$$\nabla_s \equiv \hat{a}_r \frac{\partial}{\partial r} + \hat{a}_z \frac{\partial}{\partial z} \tag{3.22}$$

$$\nabla_w \equiv \hat{a}_r \frac{\partial}{\partial W_r} + \hat{a}_z \frac{\partial}{\partial W_z} \tag{3.23}$$

In this notation Eq. (3.17) and (3.18) become combined into the following single equation:

$$M \frac{d\vec{W}}{dt} = -Ze\, \nabla_s \left[V + X\right] \tag{3.24}$$

It is obvious from the form of Eq. (3.24) that the term

$$V \equiv \frac{Ze}{8\pi^2 M} \left(\frac{\Phi - K}{r}\right)^2 \tag{3.25}$$

stands on exactly the same basis as X and can therefore be interpreted as a potential; herein called the inductive potential. Since X arises through the accumulation of charges and is therefore associated with capacitive effects, the two potentials will be distinguished by calling X a capacitive potential. A plot of contours of constant V can be made. Such a plot generally yields a great deal of information about the motion of the particle in the r and z directions. The azimuthal position, which is usually of no particular importance, can be obtained by integrating Eq. (3.15).

If one forms the vector dot product of Eq. (3.24) with $\vec{W}$, the following result is obtained:

$$\frac{d}{dt}\left[\frac{M}{2}\vec{W}\cdot\vec{W} + Ze\,(V + X)\right] = Ze\,\frac{\partial (V + X)}{\partial t} \tag{3.26}$$

By making reference to Eq. (3. 15) and (3. 25) one finds that the term on the left-hand side of the equation above is equal to the total kinetic energy, E, of the particle. Hence, the result

$$\frac{dE}{dt} = Ze \frac{\partial (V + X)}{\partial t} \qquad (3.27)$$

When V and X are not time-dependent, Eq. (3. 27) yields the fact that the kinetic energy of the particle is a constant of the motion, and Eq. (3. 26) yields the fact that

$$\frac{M}{2} W^2 + Ze (V + X) = \text{constant} \qquad (3.28)$$

If the particle is in a field that moves through space at a uniform rate, without change of strength (i. e. a traveling field) then Eq. (3. 27) and (3. 28) are valid in a frame of reference that moves with the field. The flux must satisfy the differential equation, (3. 2), and therefore cannot be arbitrarily chosen. However, the basic characteristics of the particle motion are not influenced by the fine details of the flux pattern, and simple analytical forms can be chosen which, while they do not satisfy Eq. (3. 2) exactly, give the desired information about the particle. One can proceed in this way to establish the shape of the field which will yield a certain desired type of motion. Then, the actual configuration of coils and currents which produce a field of the determined shape can be found by cut-and-try methods with the aid of a passive analog computer. A suitable computer for this purpose is described in Appendix G of this report.

The following information about V is worth noting:

1. The unit of V is the volt
2. For a particle of given charge, V never changes sign no matter what the value of the field or the position of the particle
3. The sign of V depends on the charge of the particle, and as a result, a given magnetic field pattern accelerates positive and negative particles in the same direction
4. The magnitude of V is related to the square of the flux and, therefore, for a given configuration of coils, to the square of the current flowing in the coils

5. If the flux has the same sign as K, then there may exist a flux contour within the field along which V is zero. Such a contour will act as an equilibrium line for the motion and is closely related to the locus of "guiding centers" of the particle motion as viewed in the cartesian coordinate system that has been defined.

While the inductive potential concept is very useful for studying the curved trajectories followed by a particle in a magnetic field, the description of straight-line motion is rather obscure. For example, suppose $\Phi = \Phi(0)$ everywhere so that, according to Eq. (3.6) and (3.7), the magnetic field is zero. Then Eq. (3.24) yields the following two equations from which the radial and axial positions of the particle may be found

$$\ddot{r} = \frac{J(0)^2}{M^2} \frac{1}{r^3} \tag{3.29}$$

$$\ddot{z} = 0 \tag{3.30}$$

Consider a particle moving at constant speed in a field-free region as shown in Figure 3-1. The angular momentum of the particle is constant with a value $J(0) = Mbv$, where b is the impact parameter and v is the speed. The equation of motion for the z-direction clearly is the same as Eq. (3.30). For the radial motion one finds

$$\dot{r} = v \cos \theta \tag{3.31}$$

$$\ddot{r} = \frac{b^2 v}{r^2 \sqrt{r^2 - b^2}} \dot{r} = \frac{v^2 b^2}{r^3} \tag{3.32}$$

This last equation is the same as Eq. (3.29), and one concludes that Eq. (3.29) and (3.30) represent straight-line motion in real space. In the coordinate system used here the motion can be represented on a potential diagram such as that of Figure 3-2. The horizontal line, oAA', is drawn at a height equal to the total kinetic energy of the particle. The point, o, is a turning-point of the motion.

3.4 SINGLE-PARTICLE MOTION IN A RAPIDLY OSCILLATING FIELD

The particular utility of the inductive potential in the case where the flux is not a function of time, and in the case where the flux arises from

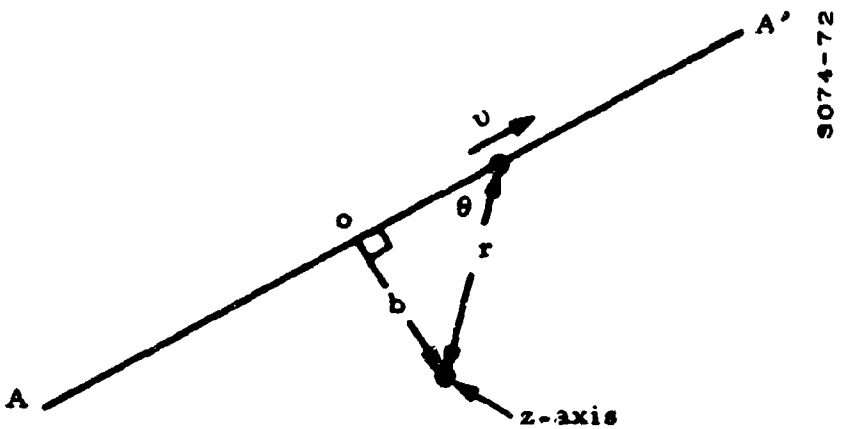


Figure 3-1. Parameters of the Straight-Line Motion of a Particle

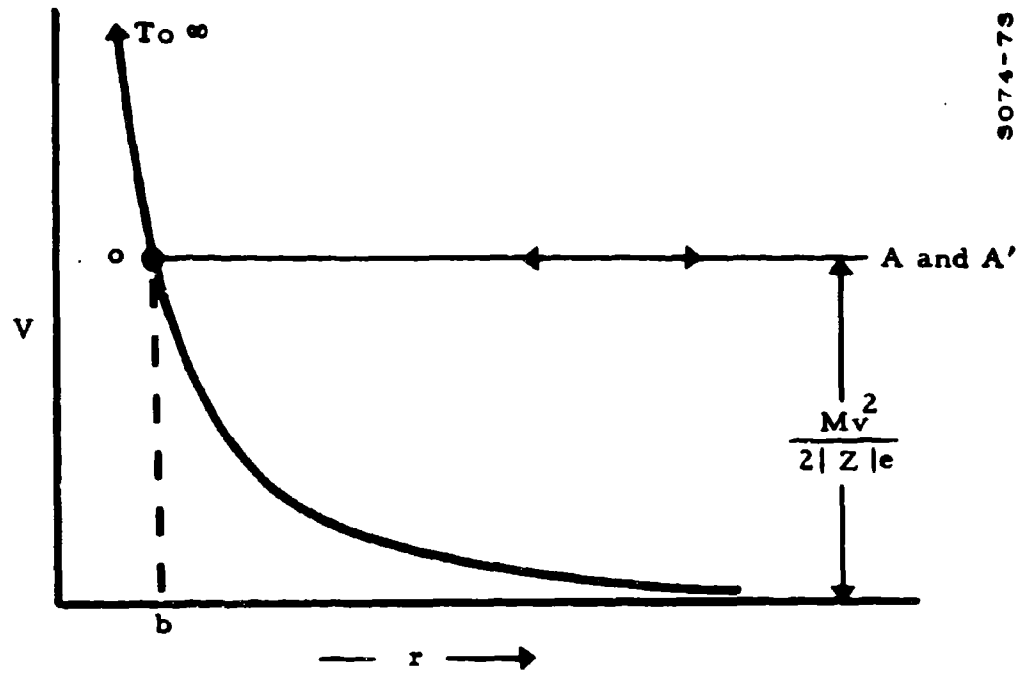


Figure 3-2. Inductive Potential Representation of Straight-Line Motion

a uniform traveling wave, has been discussed. The potential concept is equally useful when the flux is a rapidly oscillating function of time. The required condition is:

$$\omega >> \omega_c \tag{3.33}$$

where ω is the circular frequency of the field and ω_c is the cyclotron frequency of the particle in the field. The cyclotron frequency is $\frac{e|Z|B}{M}$, where B is the peak value of the magnetic field strength at the position of the particle. The validity of the criterion has been checked both by theoretical investigation and by computer calculation in certain special cases.

When the condition expressed by Eq. (3.33) is valid, and only the general features of the motion are required, it is permissible to use the time-averaged value of V in Eq. (3.28). Since the flux is assumed to have an oscillatory behavior the time-averaged value of V is

$$\langle V \rangle_t \equiv \frac{Ze}{8\pi^2 M} \left[\frac{\langle \phi^2 \rangle_t + K^2}{r^2} \right] \tag{3.34}$$

A criterion similar to the one expressed by Eq. (3.33) exists for a plasma. It will be discussed later in this section.

3.5 PARTICLE-PARTICLE INTERACTIONS

When a particle moves in a field in the presence of other particles the equations of motion must be modified to include the interactions. Although, in general, the situation is extremely complicated, a good deal of progress can be made by recognizing just two general types of interactions: stochastic interactions and steady interactions.

The stochastic interactions are those that result from the relatively close encounters between two or three particles at one time. One characteristic of these interactions is that the resultant force on a particle exhibits significantly large random fluctuations. Another characteristic is that the instantaneous values of the forces for several similar particles in the same neighborhood of the plasma are quite different. The hard-sphere scattering events and the Coulomb scattering events are stochastic processes.

The steady interactions are those that result from the distant interactions between one particle and a great many others at one time. A characteristic of these interactions is that the resultant force is steady, with very small random fluctuations. In addition, similar particles in the same neighborhood of the plasma experience the same force at any given instant of time. The self-field effects are steady interactions, and both space-charge forces and pinch forces must be included.

The stochastic interactions can be formally included in the equations of motion by adding a stochastic force, $\vec{\delta}$. The steady interactions can be included by interpreting Φ and X to be the net quantities arising from both applied- and self-fields. This can be done provided the plasma has the same type of symmetry as the applied fields. Only this case will be considered here.

The equations of motion which result from these amendment are

$$P_\theta = -\frac{Ze}{2\pi}\left[\frac{\Phi - K}{r}\right] \tag{3.35}$$

$$M\frac{d\vec{W}}{dt} = -Ze\,\nabla_s\left|V + X\right| + \vec{\delta}_s \tag{3.36}$$

where

$$V \equiv \frac{Ze}{8\pi^2 M}\left[\frac{\Phi - K}{r}\right]^2 \tag{3.37}$$

$$K \equiv \frac{2\pi}{Ze}\left[J(0) + \int_{t_o}^{t} dt\; r\,(t)\,\delta_\theta\right] + \Phi(0) \tag{3.38}$$

$$\vec{\delta}_s \equiv \hat{a}_r\,\delta_r + \hat{a}_z\,\delta_z \tag{3.39}$$

These equations have changed from those given previously in that Φ and X must be interpretated as representing net effects, a stochastic force has appeared in the radial-axial equation, and K has become a stochastic function of time. The integral in Eq. (3.38) represents the torque experienced by the particle in the time t_o to t.

Consider the situation illustrated in Figure 3-3. A particle, gyrating in a magnetic field experiences an elastic scattering collision at the point

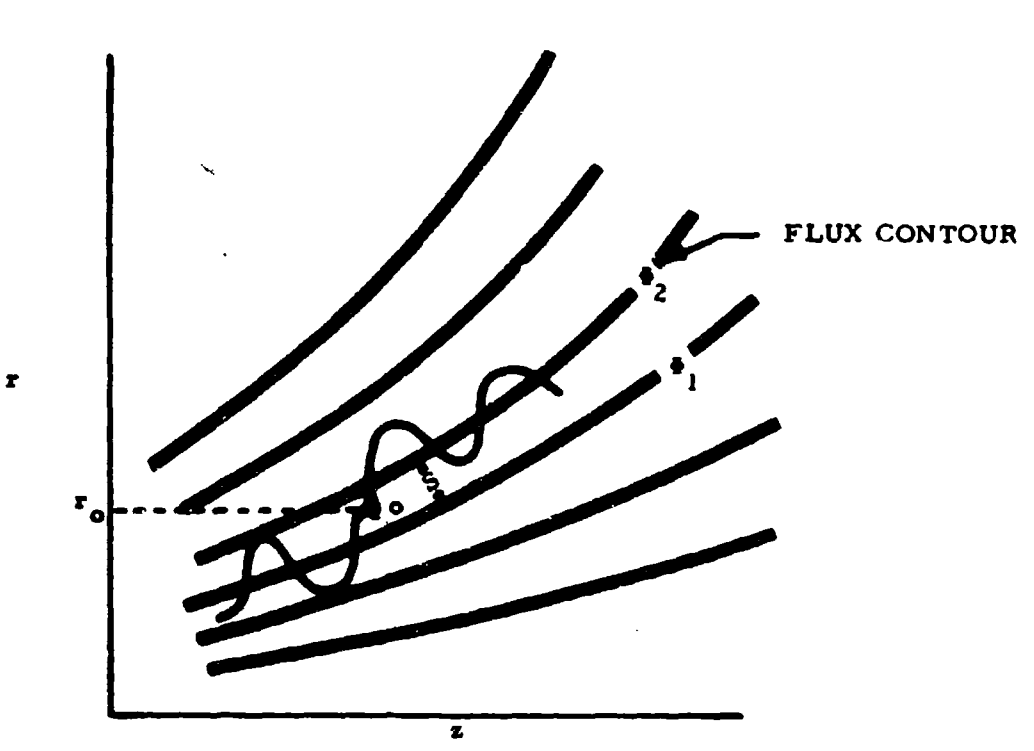


Figure 3-3. Representation of a Scattering Event

o. Prior to the event the gyrations center on the flux contour, labeled Φ_1; and after the event they center on the contour, Φ_2. At point o the two contours are separated by a distance S. We wish to compute the maximum value that S can have.

Let us assume that the particle had a value of K equal to K_1 before the collision and K_2 after the collision. Since the gyrations center on the flux lines Φ_1 and Φ_2, it follows that these lines must closely correspond to zero values for the inductive potential. Therefore, one can write

$$K_1 - K_2 \approx \Phi_1 - \Phi_2 \tag{3.40}$$

The maximum change in azimuthal momentum that can occur in a single elastic scattering event is 2Mv, where v is the speed of the particle. This fact, used with Eq. (3.35) and (3.40), yields the result

$$|\Phi_1 - \Phi_2| \leq \frac{4\pi M r_o v}{|Z| e} \tag{3.41}$$

If the change in K is reasonably small, one can write that

$$|\Phi_1 - \Phi_2| \approx 2\pi r_o BS \tag{3.42}$$

and finally, the result

$$S \leq \frac{2v}{(e|Z|B/M)} \tag{3.43}$$

is obtained. The quantity in the denominator of Eq. (3.43) is the cyclotron frequency so the equation states that S is smaller than twice the gyro radius, as might be expected.

3.6 THE BOLTZMANN EQUATION

The equations of motion that apply to the many-particle situation have been given in terms of a two-dimensional coordinate system. The independent variables are six in number: axial and radial position, axial and radial speed, time, and K. These variables are all that are necessary

for the specification of the position and the state of motion of the particle in the coordinate system used. Consequently one can define a distribution function

$$f(\vec{S}, \vec{W}, K, t) \tag{3.44}$$

for each type of particle in the field. The distribution function gives the density of particles in the five-dimensional space defined by the variables $\vec{S}$, $\vec{W}$, and K at the instant of time, t. The density of particles in the two-dimensional space S is:

$$n(\vec{S}, t) \equiv \int_{-\infty}^{\infty}\int\int f \, dW_r \, dW_z \, dK \tag{3.45}$$

The quantity n will be called the ring-density and is numerically equal to the number of particles in a torus of radius, r, and unit minor cross section. Such a torus is illustrated in Figure 3-4. The ordinary three-dimensional density will be denoted by n_o, and, because of the assumed symmetry, it is related to n in the following way:

$$n_o = \frac{1}{2\pi r} n \tag{3.46}$$

If Q is an arbitrary function of the independent variables, then the following average value of Q can be defined:

$$\langle Q(\vec{S}, t)\rangle \equiv \langle Q\rangle \equiv \frac{1}{n} \int_{-\infty}^{\infty}\int\int Qf \, dW_r \, dW_z \, dK \tag{3.47}$$

For subsequent discussions the dispersed components of W_r, W_z, K, and P_θ will be needed. These are defined by the following equations:

$$w_r = W_r - \langle W_r\rangle \tag{3.48}$$

$$w_z = W_z - \langle W_z\rangle \tag{3.49}$$

$$k = K - \langle K\rangle \tag{3.50}$$

$$p_\theta = P_\theta - \langle P_\theta\rangle \tag{3.51}$$

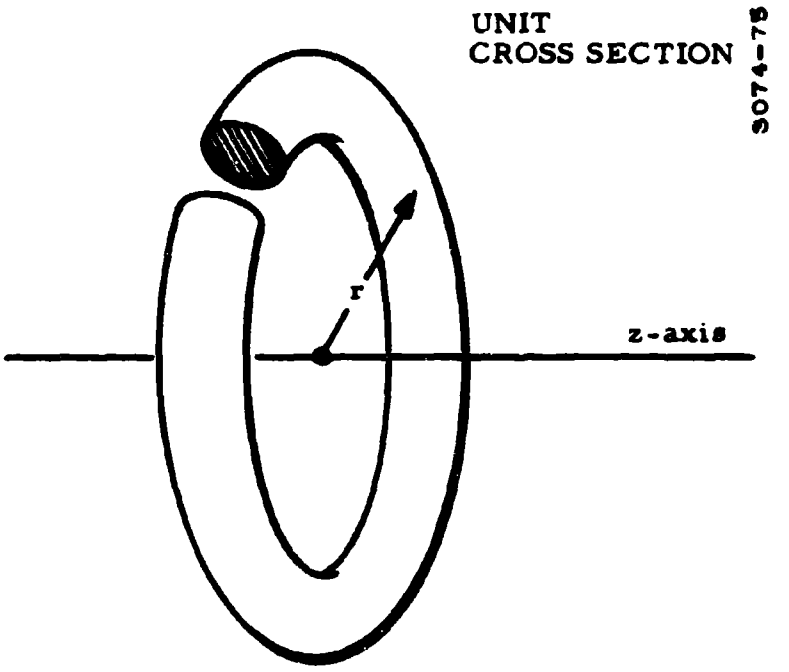


Figure 3-4. Representation of a Torus to Illustrate the Concept of Ring Density

Then, the dispersions of W_r, W_z, and K are

$$\langle W_r W_r \rangle - \langle W_r \rangle \langle W_r \rangle = \langle w_r w_r \rangle \tag{3.52}$$

$$\langle W_z W_z \rangle - \langle W_z \rangle \langle W_z \rangle = \langle w_z w_z \rangle \tag{3.53}$$

$$\langle KK \rangle - \langle K \rangle \langle K \rangle = \langle kk \rangle = \left(\frac{2\pi r}{Ze}\right)^2 \langle p_\theta p_\theta \rangle \tag{3.54}$$

The significance of these equations lies in the fact that the dispersions are very closely related to the temperature. In particular it should be noted that the dispersion of K is related to the temperature in the azimuthal direction.

The average total energy of a particle can be found from the above equations and Eq. (3.28). One finds

$$\langle E_T \rangle = \frac{M}{2} \langle \vec{W} \cdot \vec{W} \rangle + \frac{Z^2 e^2}{8\pi^2 M} \left[\frac{\Phi - \langle K \rangle}{r}\right]^2 + ZeX + \frac{M}{2}\left[\langle w_r w_r \rangle + \langle w_z w_z \rangle + \frac{\langle p_\theta p_\theta \rangle}{M^2}\right] \tag{3.55}$$

The last term in this equation can be interpreted as the "temperature" of the gas even though the system is far from thermal equilibrium. Also one must admit the possibility that the temperature is different in each of the three coordinate directions.

A differential equation for f can be derived by considering the flow in and out of a five-dimensional volume element in the $\vec{S}$, $\vec{W}$, K space. The derivation proceeds in a manner entirely analogous to that of the usual Boltsmann equation.[11, 12] Insofar as the flow in and out of the elemental volume is concerned, K must be regarded as a constant since it only changes stochastically. The equation obtained is:

$$\frac{\partial f}{\partial t} + \vec{W} \cdot \nabla_s f - \frac{Ze}{M} \nabla_s (V + X) \cdot \nabla_w f = \left.\frac{\partial f}{\partial t}\right|_c \tag{3.56}$$

The operators, ∇_s and ∇_w, have been previously defined. The right-hand side is the time rate of change of f due to stochastic particle-particle interactions. It is the collision term and may have either positive or negative values.

The collision term can be rewritten in terms of a collision frequency, ν, in order to make the role of the term more evident. Thus:

$$\left.\frac{\partial f}{\partial t}\right|_c \equiv \nu f \tag{3.57}$$

The collision term includes the effects of those processes that create or destroy particles, such as ionization processes, recombination processes, and electron attachment processes. In general $<\nu>$ is not equal to zero, but when the above-mentioned processes are in equilibrium one can set $<\nu>$ equal to zero.

3.7 MOMENTS OF THE BOLTZMANN EQUATION

Eq. (3.56) is the Boltzmann equation for the particular coordinate system and type of symmetry that has been assumed. The scalar potential, X, which appears must be regarded as an unknown quantity because its value will be determined almost entirely by the plasma itself. As conditions in the plasma change, X will change in such a way that charge neutrality is maintained. In order to evaluate X one must consider the coupling between several equations like Eq. (3.56); one equation refers to the electrons and the others refer to the ions. The evaluation of X can be done with the aid of certain moments of Eq. (3.56).

If Q is an arbitrary function of the variables of the problem, then it can be shown that:

$$\frac{\partial n <Q>}{\partial t} - n\left<\frac{\partial Q}{\partial t}\right> + \nabla_s \cdot \left|n <\vec{W} Q>\right| - n <\vec{W} \cdot \nabla_s Q> + \frac{Ze}{M} n <\nabla_s (V + X) \cdot \nabla_w Q> = n <\nu Q> \tag{3.58}$$

This equation is similar to one discussed by Jeans.[11]

An equation for the conservation of ring-density results if Q is set equal to unity. The equation is

$$\frac{\partial n}{\partial t} + \nabla_s \cdot [n \langle \vec{W} \rangle] = n \langle \nu \rangle \tag{3.59}$$

This equation is analogous to the well-known equation for the conservation of mass. Two other important equations are obtained by setting Q equal to K and to M $\vec{W}$. The results are

$$\frac{D\langle K \rangle}{Dt} = \langle \nu k \rangle - \frac{1}{n} \nabla_s \cdot [n \langle \vec{w} k \rangle] \tag{3.60}$$

$$\frac{D M \langle \vec{W} \rangle}{Dt} = -Ze \langle \nabla_s (V + X) \rangle + M \langle \nu \vec{w} \rangle - \frac{M}{n} \nabla_s \cdot [n \langle \vec{w} \vec{w} \rangle] \tag{3.61}$$

The operator D/Dt, which occurs frequently, is defined as follows:

$$\frac{D}{Dt} \equiv \frac{\partial}{\partial t} + \langle \vec{W} \rangle \cdot \nabla_s \tag{3.62}$$

It signifies the rate of change along the path of flow in the gas, and it is sometimes called the hydrodynamic derivative.

In the moment equations the terms containing $\langle \nu k \rangle$ and $\langle \nu \vec{w} \rangle$ are associated with frictional drag forces, and the terms containing $\langle k \vec{w} \rangle$ and $\langle \vec{w}\, \vec{w} \rangle$ express the effects of diffusive spatial transport of gas. The latter effects include pressure forces and viscous forces. The term $\langle \vec{w}\, \vec{w} \rangle$ is a second-order tensor, and $\nabla_s \cdot [n \langle \vec{w} w \rangle]$ stands for the following sequence of matrix multiplications:

$$\nabla_s \cdot [n \langle \vec{w}\, \vec{w} \rangle] \equiv \begin{bmatrix} \frac{\partial}{\partial r} & \frac{\partial}{\partial z} \end{bmatrix} \begin{bmatrix} n & 0 \\ 0 & n \end{bmatrix} \begin{bmatrix} \langle w_r w_r \rangle & \langle w_r w_z \rangle \\ \langle w_z w_r \rangle & \langle w_z w_z \rangle \end{bmatrix} \begin{bmatrix} \hat{a}_r \\ \hat{a}_z \end{bmatrix} \tag{3.63}$$

We now turn to a detailed examination of the second of the two moment equations, Eq. (3.61). The first term on the right-hand side expresses the effects of electromagnetic forces and can be written as the sum of two terms, as follows:

$$- Ze \langle \nabla_s (V + X) \rangle = - Ze \langle \nabla_s V \rangle - Ze \nabla_s X \qquad (3.64)$$

Note that the last term in the equation above does not contain an average since X has the same value for all particles in a given neighborhood of the space.

Through the use of Eq. (3.37) and (3.54), along with the notation of Eq. (3.47), one can write Eq. (3.61) as follows:

$$\frac{DM\langle \vec{w} \rangle}{Dt} = \frac{-(Ze)^2}{8\pi^2 M} \left[\lim_{S' \to S} \nabla_s \left(\frac{\Phi - \langle K(S', t) \rangle}{r} \right)^2 \right]$$

$$- Ze \nabla_s X + M \langle \nu \vec{w} \rangle + \frac{\langle p_\theta p_\theta \rangle}{M} \nabla_s \ln r - \frac{M}{n} \nabla_s \left[n \langle \vec{w}\vec{w} \rangle \right] \qquad (3.65)$$

Let us consider, for the moment, a particle in free flight and use a cylindrical coordinate system as the frame of reference. Choose the reference system so that the particle is approaching the axis with an impact parameter, b. As viewed from the axis the particle appears to approach, pass within a distance, b, and then recede. Thus, when viewed from the axis, the particle appears to be accelerating radially outward, despite the fact that it has constant velocity. In fact, all particles in the system appear to be accelerating radially outward except those which have an impact parameter of zero. This process is represented by the second last term on the right-hand side of Eq. (3.65). For a gas in motional equilibrium this acceleration must be balanced by an equal, but opposite, acceleration. It will be shown later that the desired balancing acceleration is hidden in the last term of Eq. (3.65).

The moment equations that have been derived refer to one type of particle only. In order to treat a plasma one has to consider a similar set of equations for each type of particle in the plasma. The various equations will be distinguished from one another by the use of the superscripts e, i, and o, referring, respectively, to electrons, ions, and neutrals. The electron mass will be written as m, so that $M^e \equiv m$.

Gross charge neutrality of the plasma requires that:

$$n^e = \sum_i Z^i n^i \tag{3.66}$$

where the summation extends over all the ion species that are present.

In order to proceed with the analysis a basic assumption is made. The assumption is:

> The radial and axial current density in the plasma, $\vec{j}_S$, is zero at all times.

This assumption limits the discussion in two ways: first, it precludes any study of plasma oscillations; and second, it precludes all situations where metallic electrodes are in direct electrical contact with the plasma. The current density, $\vec{j}_S$, is defined as follows:

$$\vec{j}_S \equiv e \sum_i Z^i n^i \langle \vec{w} \rangle^i - e n^e \langle \vec{w} \rangle^e = 0 \tag{3.67}$$

From this equation it follows that:

$$\frac{D\langle \vec{w} \rangle^e}{Dt} = \sum_i \left[\frac{Z^i n^i}{n^e} \frac{D\langle w \rangle^i}{Dt} \right] \tag{3.68}$$

Through the use of Eq. (3.68) and a series of equations like (3.65), it is possible to find a value for X. This value of X is the one that must exist in order to satisfy the basic assumption of neutrality. It depends only on the properties of the plasma and the magnetic effects and not at all on any applied electric fields. The effects of the latter are counteracted near the boundries of the plasma by narrow electrical sheaths in which the assumption of charge neutrality is not valid. The sheaths are of the order of a Debye length in thickness: a very small distance for most plasmas dealt with in the laboratory.

It is found that the equation for X contains terms that are small enough to be neglected. These terms can be neglected provided $m << M^i$ and $m << M^i/Z^i$ for all ion species in the plasma. However, the result must

retain terms which are first-order in m/M^i. The task of writing the equation is simplified by the use of the following notation:

$$( )_a \equiv \frac{\sum_i ( ) \, Z^i n^i}{n^e} \tag{3.69}$$

One finds:

$$\begin{aligned} e \nabla_s X = & \left\{1 - m\left(\frac{Z^i}{M^i}\right)_a\right\} \left\{\frac{e^2}{8\pi^2 m} \lim_{S' \to S} \nabla_s \left(\frac{\Phi - \langle K(S',t)\rangle^e}{r}\right)^2 \right. \\ & - m\left[\langle \nu \vec{w}\rangle^e - \left(\langle \nu \vec{w}\rangle^i\right)_a\right] \\ & - m\left[\frac{\langle p_\theta p_\theta\rangle^e}{m^2} - \left(\frac{\langle p_\theta p_\theta\rangle^i}{M^i M^i}\right)_a\right] \nabla_s \ln r \\ & \left. + m\left[\frac{\nabla_s \cdot (n^e \langle \vec{w}\vec{w}\rangle^e)}{n^e} - \left(\frac{\nabla_s \cdot (n^i \langle \vec{w}\vec{w}\rangle^i)}{n^i}\right)_a\right]\right\} \end{aligned} \tag{3.70}$$

The equation above, when substituted back into Eq. (3.65), yields equations of motion for the ions and the electrons. Again certain terms may be dropped because they are very small.

For electrons

$$\frac{D\, m \langle \vec{w} \rangle^e}{Dt} = -\left(\frac{Z^i}{M^i}\right)_a \frac{e^2}{8\pi^2} \lim_{S' \to S} \left[\nabla_s \left(\frac{\Phi - \langle K(S',t) \rangle^e}{r} \right)^2 \right]$$

$$+ m \left[\left(\langle \nu \vec{w} \rangle^i \right)_a + m \left(\frac{Z^i}{M^i} \right)_a \langle \nu \vec{w} \rangle^e \right]$$

$$+ m \left[\left(\frac{\langle p_\theta p_\theta \rangle^i}{M^i M^i} \right)_a + m \left(\frac{Z^i}{M^i} \right)_a \frac{\langle p_\theta p_\theta \rangle^e}{m^2} \right] \nabla_s \ln r \qquad (3.71)$$

$$- m \left[\left(\frac{\nabla_s \cdot (n^i \langle \vec{w}\vec{w} \rangle^i)}{n^i} \right)_a + m \left(\frac{Z^i}{M^i} \right)_a \frac{\nabla_s \cdot (n^e \langle \vec{w}\vec{w} \rangle^e)}{n^e} \right]$$

For ions

$$\frac{DM^i \langle \vec{w} \rangle^i}{Dt} = -\frac{Z^i e^2}{8\pi^2 m} \lim_{S' \to S} \left[\nabla_s \left(\frac{\Phi - \langle K(S',t) \rangle^e}{r} \right)^2 \right]$$

$$+ \left[M^i \langle \nu \vec{w} \rangle^i + m Z^i \langle \nu \vec{w} \rangle^e \right]$$

$$+ \left[\frac{\langle p_\theta p_\theta \rangle^i}{M^i} + Z^i \frac{\langle p_\theta p_\theta \rangle^e}{m} \right] \nabla_s \ln r \qquad (3.72)$$

$$- \left[\frac{M^i}{n^i} \nabla_s \cdot (n^i \langle \vec{w}\vec{w} \rangle^i) + \frac{m Z^i}{n^e} \nabla_s \cdot (n^e \langle \vec{w}\vec{w} \rangle^e) \right]$$

The following points concerning these two equations are worth noting:

1. The effect of the magnetic forces on the ions depends inversely as the electron mass; whereas, the effect of the magnetic forces on the electrons depends inversely on the mass-to-charge ratio of the average ion.

2. The quantity $\langle K \rangle^e$ appears in the equations, but the corresponding quantity for the ions does not appear.

The assumptions that have been made in order to derive these equations are:

1. Axial symmetry of the fields, the density, the temperature, and the distribution of ion species
2. Zero net current in the axial and radial directions
3. Zero net charge density.

The various effects that are included in the equations are:

1. Magnetic forces
2. Electron-ion space charge coupling
3. Ionization, recombination, electron attachment, and charge exchange
4. Electron-ion-neutral collisional drag
5. Centrifugal effects
6. Tensor pressure and temperature effects
7. Viscous effects.

The equations, as they stand, are complicated and difficult to apply. Additional simplifying assumptions can be made which reduce the equations to a more manageable form; but, in the process, the ability to treat certain phenomena is given up. These simplifications are considered next.

3.8 SIMPLIFICATIONS OF THE MOMENT EQUATIONS

Viscous effects are almost always neglected in plasma problems, probably more because of the mathematical difficulty of including them than the fact that they are not important. Further study is needed in this area; but, for the present, they will be ignored. Simplifications result when viscous forces are ignored. For example:

$$\frac{1}{n^i} \nabla_s \cdot (n^i \langle \vec{w}\vec{w} \rangle^i) = \frac{1}{n^i} \nabla_s (n^i \langle \vec{w}.\vec{w} \rangle^i) \qquad (3.73)$$

where n_o is the ordinary three-dimensional density. Eq. (3.72) becomes the following:

$$\frac{DM^i \langle \vec{w} \rangle^i}{Dt} = -\frac{Z^i e^2}{8\pi^2 m} \lim_{S' \to S} \left[\nabla_s \left(\frac{\Phi - \langle K(S',t) \rangle^e}{r} \right)^2 \right]$$

$$+ \left[M^i \langle \nu \vec{w} \rangle^i + m Z^i \langle \nu \vec{w} \rangle^e \right]$$

$$+ M^i \left[\left(\frac{\langle P_\theta P_\theta \rangle^i}{M^i M^i} - \langle w_r w_r \rangle^i \right) + \frac{m Z^i}{M^i} \left(\frac{\langle P_\theta P_\theta \rangle^e}{m^2} - \langle w_r w_r \rangle^e \right) \right] \nabla_s \ln r \qquad (3.74)$$

$$- \frac{M^i}{n_o^i} \nabla_s \left(n_o^i \langle \vec{w} \cdot \vec{w} \rangle^i \right) - \frac{m Z^i}{n_o^e} \nabla_s \left(n_o^e \langle \vec{w} \cdot \vec{w} \rangle^e \right)$$

where:

$$\langle \vec{w} \cdot \vec{w} \rangle = \langle w_r w_r \rangle + \langle w_z w_z \rangle \qquad (3.75)$$

Tensor effects still remain in Eq. (3.74). For example, the third term on the right-hand side vanishes if the "temperature" in the azimuthal direction is the same as the "temperature" in the radial direction; otherwise it does not. It is quite certain that, when the gas density is low and the mean-free-path for collisions is large, tensor effects play a significant role. However, the situation has not yet been studied in any detail, and there is very little work by other authors to act as a guide.

When the temperature in the three directions is taken to be the same, Eq. (3.74) becomes.

$$\frac{DM^i \langle \vec{w} \rangle^i}{Dt} = -\frac{Z^i e^2}{8\pi^2 m} \lim_{S' \to S} \left[\nabla_s \left(\frac{\Phi - \langle K(S',t) \rangle^e}{r} \right)^2 \right]$$

$$+ M^i \langle \nu \vec{w} \rangle^i + m Z^i \langle \nu \vec{w} \rangle^e \qquad (3.76)$$

$$- k_b \left[\frac{\nabla_s (n_o^i T^i)}{n_o^i} + Z^i \frac{\nabla_s (n_o^e T^e)}{n_o^e} \right]$$

where k_b is the Boltzmann constant and T is the temperature. In order to use this equation, or any of those like it, a knowledge of $<K>^e$ is required; and this knowledge can be obtained from Eq. (3.60). Before examining the latter it is worth pointing out that the equation for X (Eq. (3.70) can be inserted directly into the equations of motion for a single particle. For example, if one puts Eq. (3.70) into Eq. (3.36), ignores tensor effects, and drops small terms, an equation for the motion of a single ion can be obtained. It is

$$M^i \frac{d\vec{W}}{dt} = -\frac{(Z^i e)^2}{8\pi^2 M^i} \nabla_s \left(\frac{K}{r}\right)^2 + \vec{\delta}_s$$

$$- \frac{Z^i e^2}{8\pi^2 m} \left[\lim_{S' \to S} \nabla_s \left(\frac{\Phi - <K(S', t)>^e}{r} \right)^2 \right] \qquad (3.77)$$

$$+ Z^i m <\nu \vec{w}>^e - \frac{Z^i k_b}{n_o^e} \nabla_s (n_o^e T^e)$$

If the plasma consists only of electrons and singly-charged ions then, since X guarantees that the ions and electrons flow together, it will be true that

$$M^i <\nu \vec{w}>^i + m Z^i <\nu \vec{w}>^e = 0 \qquad (3.78)$$

so that Eq. (3.76) can be further simplified.

3.9 ANGULAR MOMENTUM CONSIDERATIONS

The quantity $<K>^e$ that appears frequently in the equations is intimately related with the average angular momentum of the electrons. Information concerning the behavior of $<K>^e$ can be obtained from Eq. (3.60). If, as before, the viscous term is neglected, and if use is made of Eq. (3.35), (3.50), and (3.51) then one finds that

$$\frac{D<K>}{Dt} = \frac{2\pi r}{Ze} <\nu p_\theta> \qquad (3.79)$$

An equation like the above can be written for each species present. Collisions cannot change the total angular momentum of the particles in a localized region of the space, so:

$$\sum_i n^i \langle \nu\ p_\theta \rangle^i + n^e \langle \nu\ p_\theta \rangle^e = 0 \qquad (3.80)$$

This condition, when combined with a series of equations like (3.79) yields the following result:

$$\sum_i n^i Z^i \frac{D\langle K \rangle^i}{Dt} - n^e \frac{D\langle K \rangle^e}{Dt} = 0 \qquad (3.81)$$

or, using Eq. (3.35):

$$\sum_i n^i \frac{D\langle P_\theta \rangle^i}{Dt} + n^e \frac{D\langle P_\theta \rangle^e}{Dt} = 0 \qquad (3.82)$$

If n^i/n^e is a constant (along the path of flow) for each species present then Eq. (3.82) becomes

$$\sum \frac{n^i}{n^e} \langle P_\theta \rangle^i + \langle P_\theta \rangle^e = \text{constant along the flow path} \qquad (3.83)$$

The assumption that n^i/n^e is a constant is rigorously true when the plasma consists of singly charged ions and no neutrals. It is also very nearly correct in those cases where the plasma has no net flow and is sinusoidally excited at a frequency so high that it cannot follow the instantaneous variations of the field pattern.

When Eq. (3-83) holds, the net angular momentum is proportional to n^e, along the path of the flow; and, if zero in the beginning, it remains zero.

The contribution from the ions to the current flowing in the plasma can be neglected, because the ions move very slowly compared to the electrons. The current in the plasma is in the azimuthal direction only. The current density in the asimuthal direction, j_θ, is:

$$j_\theta = -en_o^e \frac{\langle P_\theta \rangle^e}{m} = -\frac{e^2 n_o^e}{2\pi rm} \left[\Phi - \langle K \rangle^e \right] \qquad (3.84)$$

3.10 DETERMINATION OF $\langle K \rangle^e$

When Eq. (3.79) is specialized so as to refer to electrons, it becomes

$$\frac{D\langle K\rangle^e}{Dt} = -\frac{2\pi r}{e}\langle \nu\, p_\theta\rangle^e = -\frac{2\pi r}{e}\left[\langle \nu\, P_\theta\rangle^e - \langle \nu\rangle^e \langle P_\theta\rangle^e\right] \tag{3.85}$$

The effects of ionization, recombination, and electron attachment will be ignored; so we set $\langle \nu \rangle^e = 0$. The remaining collision term can be written in terms of the characteristic times for collisions between electrons and the other constituents of the plasma. Thus:

$$\langle \nu\, P_\theta\rangle^e = -\sum_i \left[\frac{\frac{M^i}{M^i+m}\langle P_\theta\rangle^e - \frac{m}{M^i+m}\langle P_\theta\rangle^i}{\tau_{ei}}\right] \tag{3.86}$$

where τ_{ei} represents the average time for an electron to be scattered through 90° by interaction with particles of the $i^{\underline{th}}$ type. Since $m \ll M^i$ for all of the heavy particles, the equation becomes simplified, and one finally obtains

$$\frac{D\langle K\rangle^e}{Dt} = \frac{2\pi r}{e}\,\frac{\langle P_\theta\rangle^e}{\tau} \tag{3.87}$$

where

$$\tau = \left[\sum_i \frac{1}{\tau_{ei}}\right]^{-1} \tag{3.88}$$

The quantity, τ, will be referred to as the collision time. Using Eq. (3.35) one now obtains a differential equation for $\langle K \rangle^e$. It is

$$\frac{D\langle K\rangle^e}{Dt} + \frac{\langle K\rangle^e}{\tau} = \frac{\Phi}{\tau} \tag{3.89}$$

In general, τ will vary with time and with position so that it cannot be set equal to a constant. However, if it does not change much in the course of one or two collisions; that is if

$$\frac{D\tau}{Dt} \ll 1 \tag{3.90}$$

then the equation obtained by integrating Eq. (3.89) with τ constant is meaningful. One obtains

$$\langle K \rangle^e = \langle K \rangle^e_{t=t_o} e^{-\left(\frac{t-t_o}{\tau}\right)} + \frac{1}{\tau} \int_{t_o}^{t} e^{-\left(\frac{t-t'}{\tau}\right)} \Phi_{t=t'} \, dt' \tag{3.91}$$

where the integration must be performed along the path of the flow.

The general effect of collisions is found by letting Φ be independent of time and assuming no flow. Then:

$$\langle K \rangle^e = \langle K \rangle^e_{t=t_o} e^{-\left(\frac{t-t_o}{\tau}\right)} + \Phi \left(1 - e^{-\left(\frac{t-t_o}{\tau}\right)}\right) \tag{3.92}$$

After a time of the order of 2τ, one finds that $\langle K \rangle^e$ has become equal to Φ. This means that the magnetic term has disappeared from the equations of motion (equations such as Eq. (3.77)) and the plasma may be said to be completely imbedded in the magnetic field.

On the other hand, if Φ oscillates with angular frequency, ω; if the flow is slow; and if

$$\omega\tau \gg 1 \tag{3.93}$$

then

$$\langle K \rangle^e \approx \langle K \rangle^e_{t=t_o} e^{-\left(\frac{t-t_o}{\tau}\right)} \tag{3.94}$$

After a time of the order of 2τ one finds that $\langle K \rangle^e = 0$. By slow flow one means that

$$\tau \langle \vec{W} \rangle \cdot \nabla_s \Phi \ll \Phi \tag{3.95}$$

and

$$\frac{1}{\omega} \langle \vec{W} \rangle \cdot \nabla_s \Phi \ll \Phi \tag{3.96}$$

If the variation of Φ along the path of the flow is approximately linear then, after a time of the order of τ, one finds that

$$\langle K \rangle^e = \Phi(t-\tau) \equiv \Phi - \frac{D\Phi}{Dt} \tau \tag{3.97}$$

provided that $\omega\tau \ll 1$. This is the opposite extreme to the situation described by Eq. (3.94).

3.11 PLASMA CURRENT

The current in the plasma flows in the azimuthal direction only and is described by Eq. (3.84). Combining this with Eq. (3.89) yields a differential equation that can be written in the following way:

$$\ell \frac{Dj_\theta}{Dt} + \rho j_\theta = -\frac{1}{2\pi r} \frac{D\Phi}{Dt} \tag{3.98}$$

where

$$\ell \equiv \frac{m}{e^2 n_o^e} \text{ (henry-meter)} \tag{3.99}$$

$$\rho \equiv \frac{m}{e^2 n_o^e \tau} \text{ (ohm-meter)} \tag{3.100}$$

The quantities ℓ and ρ can be called the specific inductance and the specific resistance of the plasma, respectively. The conductivity of the plasma is equal to $1/\rho$.

The azimuthal electric field seen by the plasma, E_θ(plasma), is the quantity that appears on the left-hand side of the equation.

$$E_\theta(\text{plasma}) = - \frac{1}{2\pi r} \frac{D\Phi}{Dt} \tag{3.101}$$

Eq. (3.98) can be represented by an equivalent electrical network that consists of a generator, an inductor, and a resistor. The circuit is shown in Figure 3-5.

In reality both ℓ and ρ are variable quantities, so the circuit is a non-linear one. However, a great deal of information about plasma can be obtained by assuming them to be constant, or a least slowly varying.

The characteristic time constant of the circuit is ℓ/ρ and this is seen to be equal to the collision time, τ. The energy stored in the inductor is related to the inductive potential of the average electron, $V^{<e>}$, in the following way:

$$\frac{1}{2} \ell j_\theta^2 = e n_o^e V^{<e>} \tag{3.102}$$

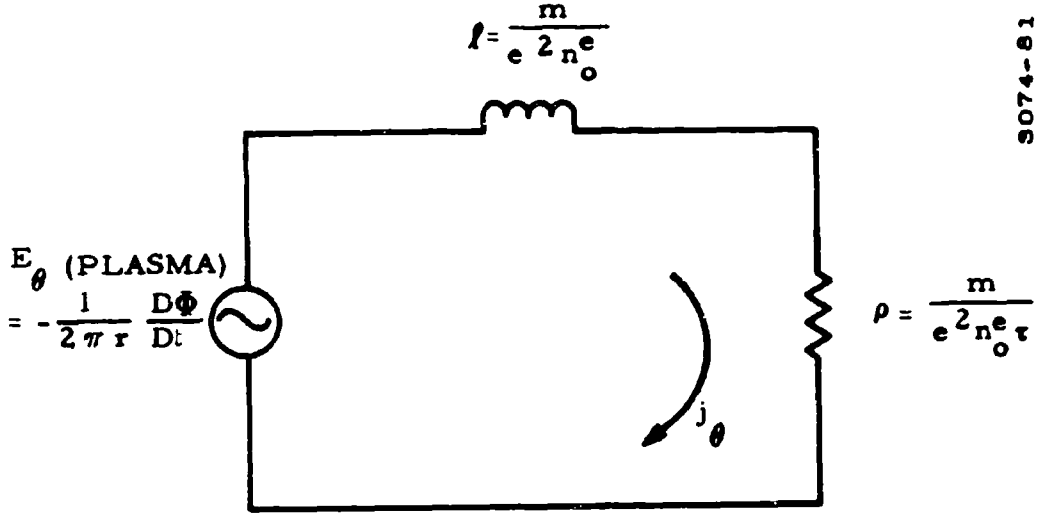
where

$$V^{<e>} = \frac{e}{8\pi^2 m} \left[\frac{\Phi - <K>^e}{r} \right]^2 \tag{3.103}$$

The terms in Eq. (3.102) have units of joules/cubic-meter. From Eq. (3.35) one learns that $V^{<e>}$ is equal to the azimuthally directed kinetic energy of the average electron. Hence:

$$\frac{1}{2} \ell j_\theta^2 = \frac{1}{2} n_o^e \frac{\left(<P_\theta>^e\right)^2}{m} \tag{3.104}$$

In accord with this relation one sees that the energy stored in ℓ is, in reality, inertially stored energy (just as a flywheel may be regarded as storing energy).


$\ell = \frac{m}{e^2 n_o^e}$
E_θ (PLASMA)
$= -\frac{1}{2\pi r}\frac{D\Phi}{Dt}$
$\rho = \frac{m}{e^2 n_o^e \tau}$
j_θ
3074-81

Two states for a plasma can be distinguished:

1. When the impedance offered by ℓ is larger than that offered by ρ, the current flow is inductively controlled. In that case the plasma may be described as being inertially dominated. Then j_θ tends to be in phase with $\dot{\Phi}$ and 90° out of phase with E_θ. Collisions play a minor role.
2. When the effects of ρ are larger than those of ℓ the plasma may be described as resistively dominated. The current tends to be in phase with E_θ and 90° out of phase with $\dot{\Phi}$. Ohm's law applies.

In either case the instantaneous rate at which azimuthal kinetic energy is converted to randomised energy (joule heating) is P, where

$$P = j_\theta^2 \rho \text{ (watt/cubic-meter)} \tag{3.105}$$

With the aid of Eq. (3.102) the result above may be expressed in terms of $V^{<e>}$. The relationship is:

$$P = 2e n_o^e \frac{V^{<e>}}{\tau} \tag{3.106}$$

Thus, the average electron experiences an instantaneous loss of directed energy which is equal to $2V^{<e>}$ electron-volts in a time interval equal to τ, provided $\omega\tau \ll 1$. Eq. (3.106) is a useful relationship. In many cases $V^{<e>}$ is determined by the desired performance characteristics of a device (e.g., the desired kinetic energy required for the beam from an accelerator), and Eq. (3.106) can be used to make a quick estimate of the electron temperatures that will be generated during the acceleration process. The value of $V^{<e>}$ at a given place in the plasma is directly related to the square of the current flowing in the field-producing coils, so P varies as I^2_{coil}, and the joule heating appears as a resistive loss as far as the exciting circuits are concerned.

At this time it is interesting to investigate the values of τ that can be obtained in a plasma of various gases. The mean kinetic energy of the electrons in the plasma, the gas density, and the degree of ionization are the factors which determine τ for a given gas. The mean kinetic energy is conveniently expressed in units of one electron-volt, and the

density is conveniently expressed in terms of the pressure of the gas at room temperature. The latter quantity will be denoted by P_o and will be expressed in units of one micron (10^{-3} Torr).

Figures 3-6, 3-7, and 3-8 show the relationship between collision time, degree of ionization, gas pressure (referred to 20C), and electron energy for gases of mercury, argon, and air respectively. The data were assembled from information given by Brown[9] and Spitzer[14] with multiple ionization being neglected. Because of this neglect the data should not be applied to a plasma in equilibrium with its own recombination processes (Saha equilibrium); and, in any case, the curve for a fully-ionized gas is not accurate above an electron energy of about 15 ev.

In each figure a dashed line is shown, separating the graph into two regions. The region between the dashed line and the curve for zero percent ionization is dominated by electron-neutral collisions. The region between the dashed line and the 100 percent curve is dominated by electron-ion collisions.

It is an interesting fact that, for each gas, the curves converge and cross over each other at one particular value of electron energy. This value varies from 17 ev for argon to 23 ev for air.

The parameter, $\omega\tau$, has appeared several times as a characteristic parameter that separates the inertially dominated plasma state from the resistively dominated state. For a mercury plasma with a mean electron energy of 18 ev (the energy at which the curves of Figure 3-6 converge) the value of $\omega\tau$ is larger than unity provided the pressure satisfies the following relation with the exciting frequency f ($f = \omega/2\pi$):

$$f\ (\mathrm{Mc}) > 2.2\ P_o\ (\mathrm{micron}) \qquad (3.107)$$

This example illustrates the general rule that the gas pressure must be low and the frequency of excitation high before plasma in an inertially dominated state can be produced. Referring once again to the equivalent circuit of Figure 3-5 one sees that values of $\omega\tau$ larger than one correspond to the "Q" of the circuit being larger than unity. One can therefore say that an inertially dominated plasma is a high-Q plasma.

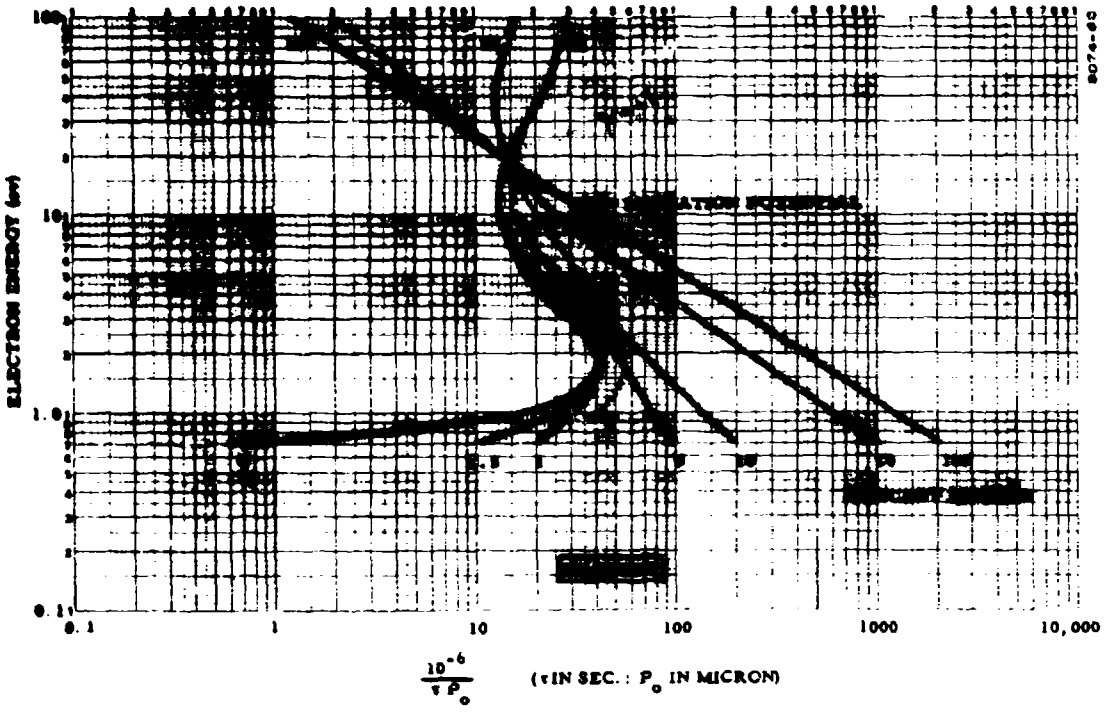


Figure 3-6. Graph for Determining Electron Collision Time in Mercury Gas

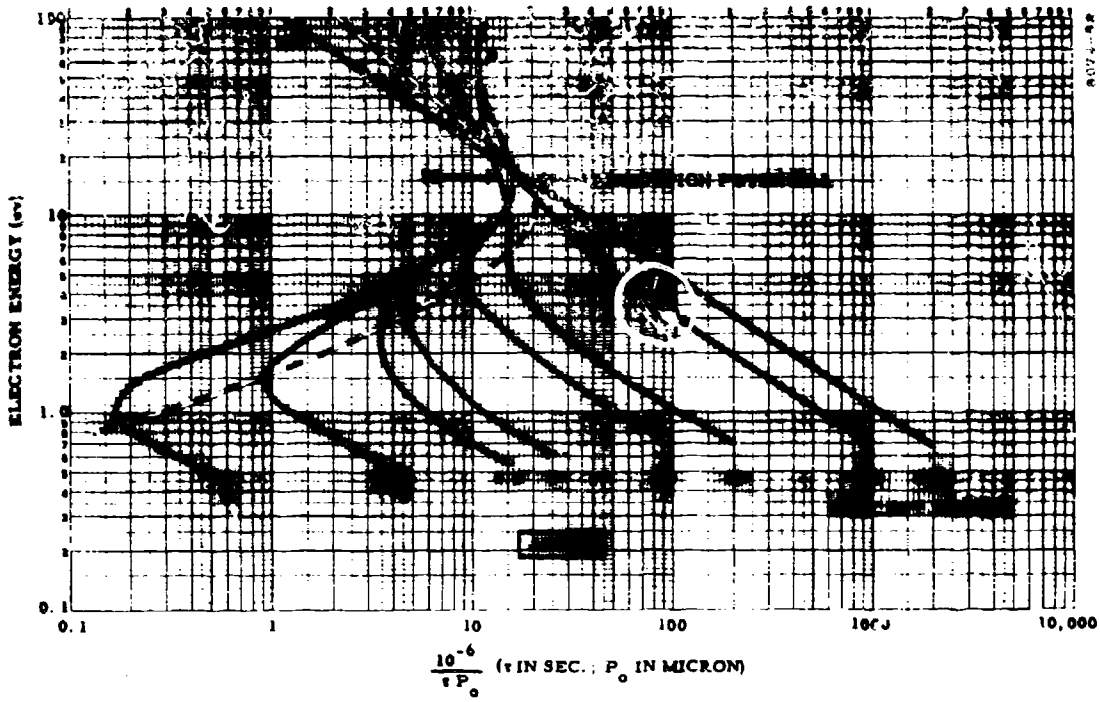


Figure 3-7. Graph for Determining Electron Collision Time in Argon Gas

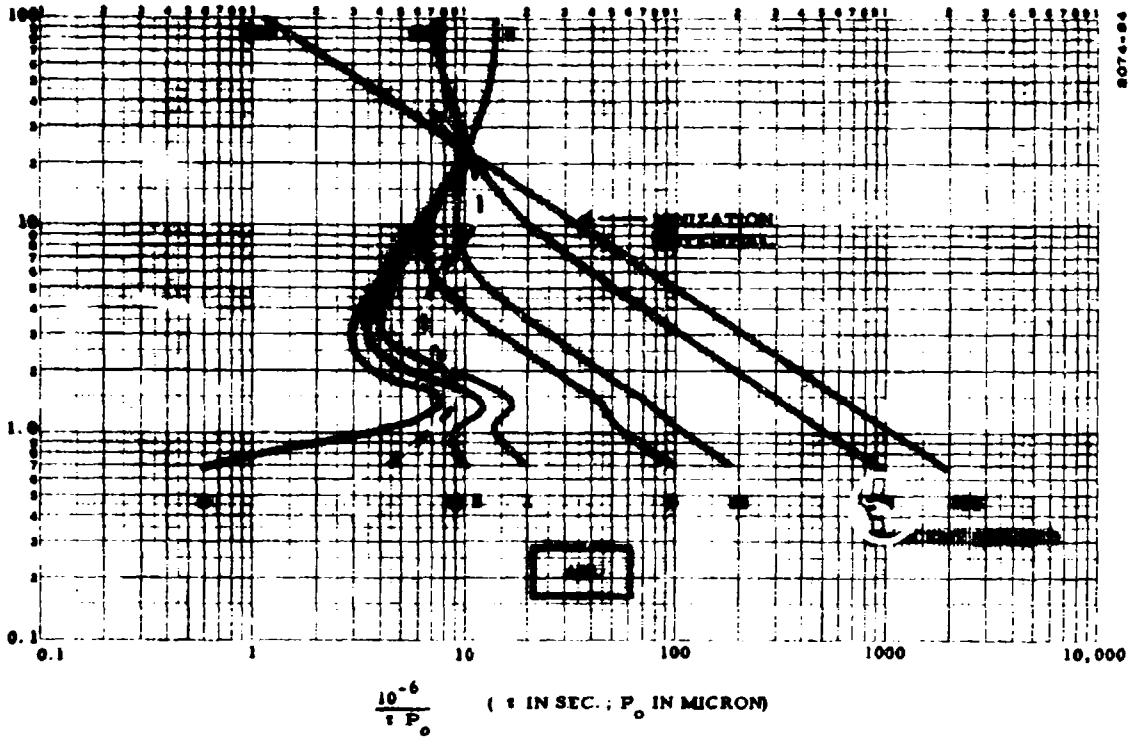


Figure 3-8. Graph for Determining Electron Collision Time in Air

3.12 THE SLOW FLOW APPROXIMATION

The equivalent circuit can be used to good advantage when the motion of the plasma is slow. The exact definition of "slow" will be given later. We consider a magnetic field produced by a set of coils, all operating at a circular frequency, ω, but in different phase relations. If $\Phi_n(\vec{S})$ denotes the flux produced by the n^{th} coil, and ϕ_n denotes the (constant) phase of the coil, then the flux at any position is:

$$\Phi = \sum_n \Phi_n \sin(\omega t + \phi_n) \tag{3.108}$$

this can be written as:

$$\Phi = \Phi_o \sin(\omega t + \phi) \tag{3.109}$$

where

$$\Phi_o = \left[\left(\sum_n \Phi_n \cos\phi_n\right)^2 + \left(\sum_n \Phi_n \sin\phi_n\right)^2\right]^{1/2} \tag{3.110}$$

$$\phi = \tan^{-1} \frac{\sum_n \Phi_n \sin\phi_n}{\sum_n \Phi_n \cos\phi_n} \tag{3.111}$$

It is, therefore, seen that the form for Φ expressed by Eq. (3.109) is a very general one. For a field that travels in the positive z-direction with uniform speed, v_f, the value of ϕ becomes:

$$\phi = -\omega \frac{z}{v_f} \tag{3.112}$$

and if the amplitude of the field is uniform, then Φ_o is a function of radius but not of z. For convenience in the analysis we take

$$\Phi = \Phi_o e^{j(\omega t + \phi)} \tag{3.113}$$

and, at the end of the analysis, suppress the real part of the answer and accept only the imaginary part.

The conditions for slow flow can now be defined. They are:

1. The change in ϕ in a time τ, or in a time $1/\omega$, is approximately linear
2. The change in Φ_o in a time τ, or in a time $1/\omega$, is approximately linear
3. The percentage change in Φ_o in a time τ, or in a time $1/\omega$, is smaller than 50 percent.

For convenience the reference time will be taken to be t = 0. Then, because of the first condition, we can write

$$\phi(t) = \phi(o) + \left[\langle \vec{W} \rangle^e \cdot \nabla_s \phi \right] t \tag{3.114}$$

where the bracketed term is understood to be evaluated at t = 0. Similarly, the second condition allows the following equation:

$$\Phi_o(t) = \Phi_o(o) + \left[\langle \vec{W} \rangle^e \cdot \nabla_s \Phi_o \right] t \tag{3.115}$$

The third condition allows the last equation to be written in exponential form. If this is done, then:

$$\Phi = \Phi_o(o)\, e^{j\left(\omega' t + \phi(o)\right)} \tag{3.116}$$

where $\Phi_o(o)$ and $\phi(o)$ are constants, and where

$$\omega' = \omega + \left[\langle \vec{W} \rangle^e \cdot \nabla_s \phi \right] - j \left[\langle \vec{W} \rangle^e \cdot \frac{\nabla_s \Phi_o}{\Phi_o} \right] \tag{3.117}$$

It is seen that ω' plays the role of a doppler-shifted frequency. Also

$$\frac{D\Phi}{Dt} = j\omega' \Phi$$

From the network of Figure 3-5 one can easily determine the steady-state current, and it is obvious that the steady state is reached in a time on the order of 2τ. The steady-state current is

$$j_\theta = -\frac{1}{2\pi r}\,\frac{j\omega'}{\rho + j\omega' \ell}\,\Phi \tag{3.118}$$

This current will be closely equal to the current in the plasma, provided the conditions of slow flow are satisfied. When the imaginary part of Eq. (3.118) is taken, the equation for the current in the plasma becomes the following:

$$j_\theta = -\frac{e^2 n_o^e}{2\pi r m}\left\{\left(\frac{\cos\alpha}{\cos\beta}\right)\Phi_o \sin(\omega t - \phi + \alpha - \beta)\right\} \tag{3.119}$$

where:

$$\alpha = \tan^{-1}\left[\frac{1 + \left(\langle\vec{W}\rangle^e \cdot \frac{\nabla_s \Phi_o}{\Phi_o}\right)\tau}{\omega\tau + \left(\langle\vec{W}\rangle^e \cdot \nabla_s\phi\right)\tau}\right] \tag{3.120}$$

$$\beta = \tan^{-1}\left[\frac{\left(\langle\vec{W}\rangle^e \cdot \frac{\nabla_s \Phi_o}{\Phi_o}\right)\tau}{\omega\tau + \left(\langle\vec{W}\rangle^e \cdot \nabla_s\phi\right)\tau}\right] \tag{3.121}$$

For the uniform traveling field previously discussed $\beta \approx 0$ and α becomes

$$\alpha = \tan^{-1}\frac{1}{\omega\tau\left(1 - \frac{\langle W_z\rangle^e}{v_f}\right)} \tag{3.122}$$

If all the field-producing coils are operating at the same phase, then ϕ is a constant.

The values of $\langle K \rangle^e$ that correspond to j_θ can be determined from Eq. (3.84). One finds

$$\Phi - \langle K \rangle^e = \frac{\cos \alpha}{\cos \beta} \Phi_o \sin (\omega t - \phi + \alpha - \beta) \tag{3.123}$$

3.13 SELF-FIELDS

The self-fields in a plasma include electric fields due to space-charge accumulation and magnetic fields (along with their associated induced electric fields) due to current flow. The electric fields due to space-charge accumulation have already been accounted for in the calculation of X (Section 3.7). The self-fields due to current flow will now be considered.

Formally one can write that the flux at any point in the plasma, Φ, is

$$\Phi = \Phi_c + \Phi_p \tag{3.124}$$

where Φ_c is the flux produced by the coil system and Φ_p is the flux produced by the plasma. The latter is the net flux at the point due to the current flow throughout the plasma. One can write that

$$\Phi_p(S) = \iint_{-\infty}^{\infty} M(S, S') \, j_\theta (S') \, dS' \tag{3.125}$$

where the integral extends over the entire r-z plane. The quantity $M(S, S')$ is the coefficient of mutual inductance between the point S and the point S'. and it is a geometrical quantity. If metal surfaces or ferrites are present, M must include image-current effects.

In a similar way Φ_c can be written as an integral of the current density in the coil system. Alternatively, the total flux, Φ, may be found by solution of Eq. (3.2).

The magnetic field associated with Φ_c is sometimes called the "vacuum field"; a term which implies that it is the field that would exist if the plasma were removed. This terminology hides the fact that, in practice, Φ_c is affected by the presence of the plasma since the current that flows in the field-producing coils is determined by all of the following factors:

1. The voltages of the power sources
2. The internal impedances of the power sources
3. The electrical properties of the coil system
4. The electrical properties of the plasma
5. The electrical coupling between the coils and the plasma.

In this discussion Φ_c will be called the applied flux: the flux produced by a definite system of currents in the coils.

The equivalent circuit of Figure 3-5 may be modified to include, at least on a formal basis, the self-field effects. Figure 3-5 becomes modified to Figure 3-9.

Except in special cases the computation of self-fields is very difficult and must be performed with the aid of Eq. (3.2). The self-fields lead to the skin-effect and to the pinch-effect.

Refer to Figure 3-9 and consider sinusoidal excitation. The self-field effects may be represented by an equivalent circuit element that is either an inductor, a resistor, a capacitor, or a combination of these elements depending on the relative phase between Φ_p and j_θ. The well-known skin effect is resistive in character if it occurs in a collision-dominated system. When the system is inertially dominated ($\omega l/\rho$ is large) a skin-effect can also exist; but it is inductive in character, since j_θ is in phase with $-\Phi_p$.

The motion of a reasonably well-defined plasma torus is a problem of relative simplicity and one that is amenable to the methods presented here. The process by which such a torus is formed in the first place is, on the other hand, relatively complicated and not yet fully understood.

Consider a torus of radius, r, whose axis of symmetry coincides with the z-axis (like the torus shown in Figure 3-4). Let the torus contain N^e electrons and have a minor cross section of A units of area. An increment of A will be denoted by dA. Thus:

$$N^e = 2\pi r \iint n_o{}^e \, dA \qquad (3.126)$$

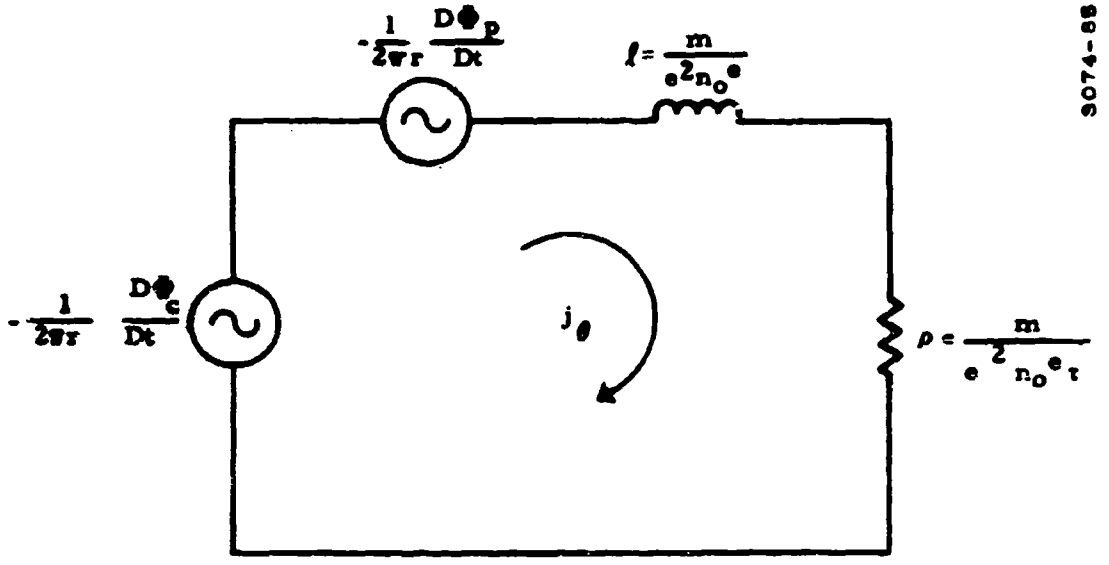


Figure 3-9. Equivalent Electric Circuit for a Plasma

If A is much smaller than πr^2 the self-flux, Φ_p, will be very nearly the same for all particles in the torus; and, if the total current in the torus is I_θ, and the self-inductance of the torus is L, then:

$$\Phi_p \approx L \iint j_\theta \, dA = L I_\theta \tag{3.127}$$

For a torus, L is approximately equal to the following:

$$L = \mu_o r \left[\ln \frac{14r}{\sqrt{A}} - 2 \right] \text{(henry)} \tag{3.128}$$

In a typical experimental situation where $r = 0.05$ meter and $A \approx 10^{-4}$ square-meter, the value of L is 0.15 microhenry.

An equation for the total current flowing in the torus can be obtained by integrating Eq. (3.98) over the cross-sectional area of the torus, A. If it is assumed that Φ_c varies but little over the area in question and that the minor radius is small compared to the major radius, then one obtains

$$\iint \frac{Dj_\theta}{Dt} dA + \iint \frac{j_\theta}{\tau} dA = - \frac{e^2 N^e}{4\pi^2 r^2 m} \frac{D\Phi_c}{Dt} - \frac{e^2}{2\pi r m} \iint n_o{}^e \frac{D\Phi_p}{Dt} dA \tag{3.129}$$

The following restricting assumptions will be made:

1. The pinch is in equilibrium so that any changes in currents and self-fields are predominantly due to the motion of the torus (as a whole) in the applied field.
2. The mean collision time for the average electron is constant over area, A.
3. The self-flux is nearly constant over area, A.

Then, with the aid of Eq. (3.127) one finds that

$$(L + \ell_t) \frac{DI_\theta}{Dt} + \rho_t I_\theta = - \frac{D\Phi_c}{Dt} \tag{3.130}$$

where

$$\ell_t = \frac{4\pi^2 r^2 m}{N^e e^2} \text{ (henry)} \tag{3.131}$$

$$\rho_t = \frac{4\pi^2 r^2 m}{N^e e^2 \tau} \text{ (ohm)} \tag{3.132}$$

In these equations ρ_t is the total resistance of the torus and ℓ_t is an intrinsic inductance, a quantity that expresses the inertial effects. The equivalent electrical circuit for Eq. (3.130) is shown in Figure 3-10.

Two effects are immediately obvious from this circuit:

1. The "Q" of the plasma has been increased from a value $\ell/\rho = \tau$ to a value $(L + \ell_t)/\rho_t = (1 + L/\rho_t)\,\tau$.
2. For large values of N^e the effects of L completely override the inertial effects.

In accord with the second point one recognizes a third state of plasma: a state in which the current flow is governed by inductive effects.

Thus one can distinguish

1. Inertially controlled plasma
2. Inductively controlled plasma
3. Resistively controlled plasma

From Eq. (3.84) one determines that

$$I_\theta = -\frac{(\Phi_c - \langle\langle K \rangle^\theta\rangle^L)}{L + \ell_t} \tag{3.133}$$

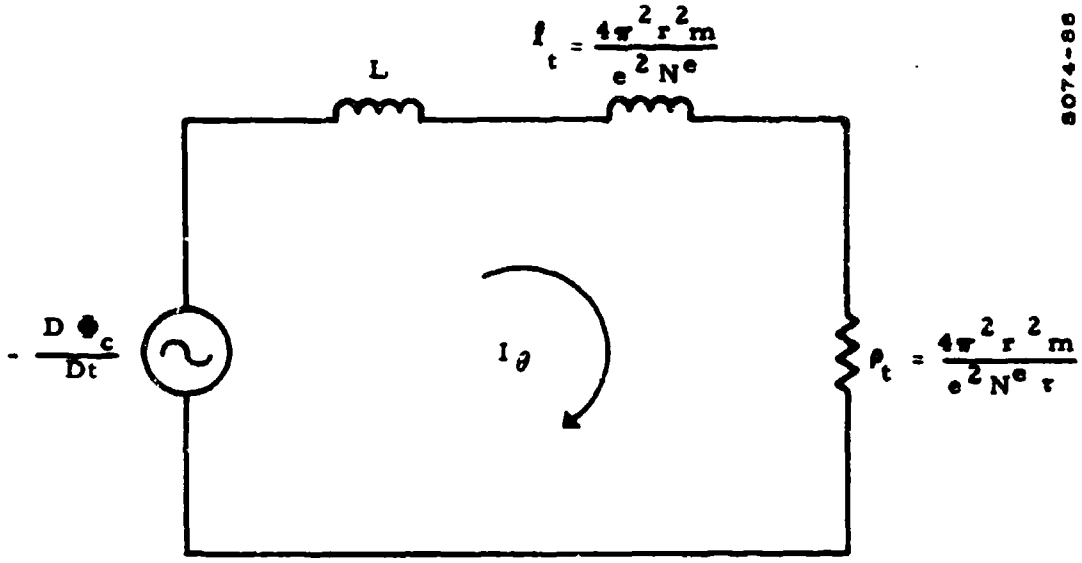


Figure 3-10. Equivalent Electric Circuit for a Torus

where

$$\langle\langle K\rangle^{e}\rangle^{L} \equiv \frac{\iint n_o^{\,e} \langle K\rangle^{e}\, dA}{\iint n_o^{\,e}\, dA} \tag{3.134}$$

Similarily, from Eq. (3.35) one finds that

$$\langle\langle P_\theta\rangle^{e}\rangle^{L} = \frac{e}{2\pi r}\left(\frac{\ell_t}{L+\ell_t}\right)\left(\Phi_c - \langle\langle K\rangle^{e}\rangle^{L}\right) \tag{3.135}$$

The energy stored in ℓ_t is equal to $1/2\ \ell_t\ I_\theta^{\,2}$, and using Eqs. (3.133) and (3.135) one finds that

$$\frac{1}{2}\,\ell_t\, I_\theta^{\,2} = N^e\,\frac{\left(\langle\langle P_\theta\rangle^{e}\rangle^{L}\right)^2}{2m} \tag{3.136}$$

Thus, the energy stored in ℓ_t is equal to the kinetic energy of azimuthal motion summed over all the particles in the torus.

The energy storage is shared between the flywheel effect of inertia and the field set up by current flow in the inductance, L.

The total energy stored is

$$\frac{1}{2}\,(\ell_t + L)\, I_\theta^{\,2} = eV^L \tag{3.137}$$

where

$$V^L = \frac{1}{2e}\,\frac{\left(\Phi - \langle\langle K\rangle^{e}\rangle^{L}\right)^2}{L+\ell_t}\ \text{(volt)} \tag{3.138}$$

It will be shown later that the motion of the torus as a whole can be determined from V^L, and that V^L is the inductive potential of the torus. In Eq. (3.138) V^L has been written in such a way that it is expressed in units of one volt.

With the aid of the equivalent circuit given in Figure 3-10, an equation can be derived for I_θ in the approximation of slow flow. The derivation proceeds exactly as before and one finds

$$I_\theta = - \frac{1}{\ell_t} \left| \left(\frac{\cos \alpha'}{\cos \beta'} \right) \Phi_{co} \sin (\omega t - \phi + \alpha' - \beta' \right| \qquad (3.139)$$

where Φ_{co} is the amplitude of the applied flux, and α', β' are the same as α and β (see Eq. (3.120) and (3.121)), except they contain $\tau (1 + L/\ell_t)$ in place of just τ.

The total flux acting on particles near the center of the pinch is approximately given by

$$\Phi \text{ (in pinch)} = \Phi_c \text{ (at pinch)} + \Phi_p \qquad (3.140)$$

With the aid of Eq. (3.127) and (3.133) one finds

$$\Phi \text{ (in pinch)} = \frac{\ell_t}{L + \ell_t} \Phi_c \text{ (at pinch)} + \frac{L}{L + \ell_t} \langle\langle K \rangle^e \rangle^L \qquad (3.140)$$

If one accepts, for the present time, the idea that V^L is the potential that determines the motion of the torus as a whole, then the flux contour corresponding to $V^L = 0$ corresponds to the equilibrium line of the motion of the torus (if the motion is essentially collisionless). One can substitute into Eq. (3.140) the value for $\langle\langle K \rangle^e \rangle^L$ derived from Eq. (3.138), and the following interesting equation results:

$$\Phi \text{ (in pinch)} = \frac{\ell_t}{L + \ell_t} \Phi_c \text{ (at pinch)} + \frac{L}{L + \ell_t} \Phi_c \text{ (at } V^L = 0) \qquad (3.141)$$

Notice that as the pinch gets stronger (i.e., as L gets larger and larger compared to ℓ_t) the first term on the right-hand side goes to zero and one finds that

$$\Phi \text{ (in pinch)} \rightarrow \Phi_c \text{ (at } V^L = 0); \text{ as } \frac{L}{\ell_t} \rightarrow \infty \qquad (3.142)$$

This result justifies the name "trapped flux" for the quantity $\langle\langle K \rangle^e \rangle^L$.

Consider now the effective time constant for decay of current in the torus:

$$\tau_{eff} = \tau \left[1 + \frac{L}{\ell_t}\right] \tag{3.143}$$

The mean collision time, τ, can be written as follows:

$$\tau = \frac{1}{n_o^e} \left[F_1 + \frac{1-\epsilon}{\epsilon} F_2\right]^{-1} \tag{3.144}$$

where ϵ is the fraction ionized and F_1, F_2 are functions of the mean electron energy. The first function, F_1, describes the effects of Coulomb collisions between electrons and ions and the second describes the effects of electron-neutral collisions. Singly ionized ions are assumed. The curves plotted in Figures 3-6 to 3-8 are related to $F_1 + \frac{1-\epsilon}{\epsilon} F_2$ by a constant multiplicative factor. Then:

$$\tau_{eff} = \tau + \frac{L e^2 N^e}{4\pi^2 r^2 m n_o^e} \left[F_1 + \frac{1-\epsilon}{\epsilon} F_2\right]^{-1} \tag{3.145}$$

We define the "critical" number of electrons, N^e_{crit}, to be that number for which $\ell_t = L$. It is the number at which the inductive effects become equal to the inertial effects.

$$N^e_{crit} = \frac{4\pi^2 r^2 m}{e^2 L} = 1.5 \times 10^9 \frac{r^2}{L} \tag{3.146}$$

Using the parameters given before for the determination of L (i.e., r = 0.05 meter, etc), the critical number is found to be

$$N^e_{crit} = 2.5 \times 10^{13} \text{ electrons/torus} \tag{3.147}$$

One can also define a critical density, N^e_{crit}, by dividing N^e_{crit} by $2\pi rA$, the volume of the torus. This quantity appears in Eq. (3.145) since

$$\tau_{eff} \approx 2\pi rA \left[\frac{1}{N^e} + \frac{1}{N^e_{crit}}\right]\left[F_1 + \frac{1-\epsilon}{\epsilon} F_2\right]^{-1}$$

$$\approx \frac{1}{\tau} + \frac{1}{\tau\ (\text{at } n^e_{crit})} \qquad (3.148)$$

Clearly, if $N^e \gg N^e_{crit}$ the mean time for decay of current in the torus is governed by N^e_{crit} and not at all by N^e. One should remember that, no matter what the value of τ_{eff}, collisions are still taking place at a rate $1/\tau$. However, each collision results in a decrease in current and therefore, in the self-field, and this decrease causes an induced electric field which accelerates electrons and tends to compensate.

For a torus 0.05 meter in diameter with a cross section of 10^{-4} square-meter the critical density is 8×10^{17} electrons/cubic meter. This corresponds to a pressure (referred to room temperature) of 0.22 micron.

For mercury vapor at an electron energy of 18 ev, the corresponding collision time, as obtained form Figure 3-6, is 3.3 microseconds.

The rate of Joule heating in the torus is, P^L, where

$$P^L = I_\theta^2 \rho_t = \frac{2e\ V^L}{\tau_{eff}} \qquad (3.149)$$

This result should be compared to the equation obtained for the density of Joule heating without self-field effects (Eq. (3.106)).

3.14 A PASSIVE ANALOG FOR PLASMA

The equivalent electric circuits that have been derived suggest that a two-dimensional array of passive circuit elements can be found that will serve as an analog for plasma. This is, in fact, the case; and such an analog is discussed in Appendix G of this report.

However, that analog uses resistors to represent the inertial effects of the plasma (collisionless effects) and capacitors to represent the resistive effects (collisional effects). In order to demonstrate the connection between that analog and the equivalent circuits used here consider, Eq. (3.98).

Assume no flow and integrate over time. The result is

$$\ell j_\theta + \rho \int j_\theta \, dt = - \frac{1}{2\pi r} \Phi \tag{3.150}$$

If the right-hand side is taken to represent a voltage, then the equivalent circuit shown in Figure 3-11 is obtained. This demonstrates the connection.

3.15 COMPARISON OF PLASMA ACCELERATORS

The purpose of this section is to compare the operation of several types of plasma accelerators insofar as the magnetic effects are concerned. The comparison will be restricted to the slow-flow approximation.

It is assumed that, due to the action of "hard sphere" and charge-exchange scattering, the heavy particles are all strongly coupled to each other so that $\langle \vec{W} \rangle$ is the same for all of them. Then the percentage mixture of ions, electrons, and neutrals is constant. Let x^i be the fractional content of heavy particles of type i, x^e be the number of electrons per heavy particle (either ions or neutrals), and n_o be the heavy particle density. Then:

$$\sum_i x^i = 1 \tag{3.151}$$

$$\sum_i Z^i x^i = x^e \tag{3.152}$$

$$n_o = n_o^i \Big/ x^i \tag{3.153}$$

In addition, define

$$\langle M \rangle \equiv \sum_i x^i M^i \tag{3.154}$$

$$\langle \vec{W} \rangle \equiv \frac{\sum_i x^i M^i \langle \vec{W} \rangle^i}{\langle M \rangle} \tag{3.155}$$

$$T \equiv \sum_i x^i T^i + x^e T^e \tag{3.156}$$

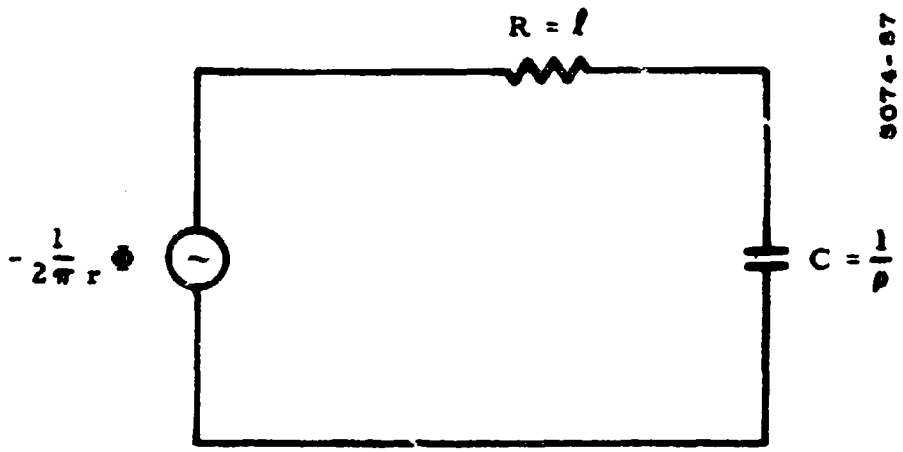


Figure 3-11. An Alternative Electrical Analog for Plasma

By combining a series of equations like Eq. (3.76) the following equation is obtained:

$$\langle M \rangle \frac{D\langle \vec{W} \rangle}{Dt} = -\frac{x^e e^2}{8\pi^2 m} \lim_{S' \to S} \left[\nabla_s \left(\frac{\Phi - \langle K(S't) \rangle^e}{r} \right)^2 \right] - k_b \frac{\nabla_s (n_o T)}{n_o} \quad (3.157)$$

The first term on the right-hand side can be evaluated, in the slow-flow approximation, by using the result expressed by Eq. (3.123). Since the flow is assumed to be slow enough so that the plasma experiences small changes in both phase and amplitude of the field in one collision time, and in one cycle time, one can time-average the result. This achieves a great simplification without harming the result to any extent. One finds

$$\left[\lim_{S' \to S} \nabla_s \left(\frac{\Phi - \langle K(S',t) \rangle^e}{r} \right)^2 \right]_{\substack{\text{time} \\ \text{average}}} = \frac{1}{2} \frac{\cos^2 \alpha}{\cos^2 \beta} \Phi_o^2 \nabla_s \frac{1}{r^2}$$

$$+ \frac{1}{r^2} \frac{\cos \alpha}{\cos \beta} \left[\frac{\cos (\alpha - \beta)}{2} \nabla_s \Phi_o^2 - \sin (\alpha - \beta) \Phi_o^2 \nabla_s \phi \right] \quad (3.158)$$

where α and β are given by Eq. (3.120) and (3.121), respectively.

It is sufficiently accurate for the present to set $\beta = 0$. In addition we limit ourselves to changes in ϕ that accord with a field traveling in the +z direction with uniform speed, v_f. Then

$$\left[\lim_{S' \to S} \nabla_s ( )^2 \right]_t = \frac{1}{2} (\cos^2 \alpha) \Phi_o^2 \nabla_s \frac{1}{r^2}$$

$$+ \frac{1}{2r^2} \left[(\cos^2 \alpha) \nabla_s \Phi_o^2 + \frac{\omega}{v_f} (\sin 2\alpha) \Phi_o^2 \nabla_s z \right] \quad (3.159)$$

where

$$\alpha \approx \tan^{-1} \frac{1}{\omega\tau} \left[\frac{1}{1 - \frac{\langle W_z \rangle}{v_f}} \right] \quad (3.160)$$

The first term on the right-hand side of Eq. (3.159) represents a radial blow-out. The second is the acceleration due to magnetic effects.

It is interesting to evaluate the quantity in brackets in the last term of Eq. (3.159) for various cases. The results are shown in Table III-1 where, for the sake of easy comparison $\langle W_z \rangle$ has been taken equal to zero.

TABLE III-1

VALUE OF BRACKETED TERM IN EQ. (3.159)

Type of Plasma	Uniphase Field ($v_f \to \infty$)	Uniform Traveling Field
Inertially Dominated ($\omega\tau \gg 1$)	$\frac{1}{2} \nabla_s \Phi_o^2$	$\frac{2}{v_f \tau} \Phi_o^2 \nabla_s z$
Collisionally Dominated ($\omega\tau \ll 1$)	$\frac{(\omega\tau)^2}{2} \nabla_s \Phi_o^2$	$\frac{2(\omega\tau)^2}{v_f \tau} \Phi_o^2 \nabla_s z$
Mixed ($\omega\tau \approx 1$)	$\frac{1}{4} \nabla_s \Phi_o^2$	$\frac{1}{v_f \tau} \Phi_o^2 \nabla_s z$

It is seen from Table III-1 that the changes that occur with changes in $\omega\tau$ are the same for the two types of fields. In order to have a uniphase accelerator with the same magnetic effects as a traveling field accelerator, in each of the three cases, one would require

$$\Phi_o^2 \text{ (traveling field)} = \frac{v_f \tau}{4} \left| \nabla_s \Phi_o^2 \text{ (uniphase)} \right| \qquad (3.161)$$

Now we observe that $\nabla_s \Phi_o^2$ can be written as Φ_o^2/λ, where λ is the characteristic distance over which Φ_o decreases. Then Eq. (3.161) becomes

$$\Phi_o \text{(traveling field)} \approx \sqrt{\frac{v_f \tau}{4\lambda}}\, \Phi_o \text{ (uniphase)} \qquad (3.162)$$

This equation shows that traveling field and uniphase accelerators may require about the same flux when τ is large. However, when τ is small (collisionally dominated plasma) the traveling field type of accelerator requires much less flux than the uniphase type.

These results depend on the slow-flow approximation. One requirement of the slow-flow approximation is that the plasma remain in the field for a time long compared to $1/\omega$, and the question is: How can this be guaranteed?

Equation (3.157) can be rewritten so that the mass that appears on the left-hand side is the same as the mass that appears in the magnetic term. This mass is $\sqrt{<M>m}$, and it is the effective mass of the plasma particles (insofar as magnetic effects are concerned). The plasma will remain in the field for a time long compared to $1/\omega$ if

$$\omega >> \frac{eB}{\sqrt{<M>m}} \equiv \omega_c \tag{3.163}$$

where ω_c is the cyclotron frequency for a particle of mass, $\sqrt{<M>m}$.

Now, let us consider a uniphase system ($v_f \to \infty$). Observe that Eq. (3.159) can be written as follows:

$$\left[\lim_{S' \to S} \nabla_s \left(\quad\right)^2\right]_t = \frac{1}{2}\left(\cos^2 a\right) \nabla_s \left(\frac{\Phi_o}{r}\right)^2 \tag{3.164}$$

Specializing this to the case $\omega\tau >> 1$ allows one to write Eq. (3.157) in the following way:

$$<M> \frac{D<\vec{W}>}{Dt} = - e \nabla_s V^P - k_b \frac{\nabla_s (n_o T)}{n_o} \tag{3.165}$$

where V^P is the effective inductive potential. It is given by:

$$V^P = \frac{x^e e}{16\pi^2 m} \nabla_s \left(\frac{\Phi_o}{r}\right)^2 \text{ (volt)} \tag{3.166}$$

The use of V^P is valid providing $\omega\tau \gg 1$ and providing the condition expressed by Eq. (3.163) is satisfied. It is not necessary to satisfy the condition

$$\frac{\langle \vec{W} \rangle \cdot \nabla_s \Phi_o}{\Phi_o} \tau < 1 \tag{3.167}$$

Eq. (3.165) might be further simplified by assuming an adiabatic relation between n_o and T, but this will not be done here.

3.16 HIGH-FREQUENCY PLASMA CONTAINMENT

If the coil system is chosen correctly (for example: a mirror geometry), and is excited at a sufficiently high frequency, then plasma containment results. Assume:

1. That $\omega\tau \gg 1$
2. That $\langle \vec{W} \rangle \approx 0$
3. That approximate thermal equilibrium is established.

Then Eq. (3.165) yields an equation for the particle density. It is

$$n_o = n_o(0)\, e^{-eV^P/k_bT} \tag{3.168}$$

where $n_o(0)$ is the maximum density that occurs. This equation, or one essentially like it but written for the electron density alone, can be used in the equation for j_θ (Eq. (3.84)), and the latter can be inserted into Eq. (3.2). A nonlinear equation for Φ results; which, if solved, gives the total flux present (applied flux plus self-flux).

3.17 MOTION OF A PINCHED PLASMA TORUS

The flow of current in a pinched plasma torus was considered in Section 3.13. The motion of such a torus, as a whole, will be considered here.

If Eq. (3.157) is integrated over the cross section, A, of the torus, and if use is made of Eq. (3.84), then one finds that

$$\frac{N_o}{r}\langle M\rangle\frac{D\langle\vec{W}\rangle}{Dt}=\frac{I_\theta}{r}\nabla_s\Phi_c$$

$$+\left[\frac{2\pi m}{e^2}\nabla_s \ln r\right]\iint\frac{j_\theta^2}{n_o e}\,dA$$

$$+\frac{1}{r}\iint(j_\theta\nabla_s\Phi_p)\,dA$$

$$-2\pi k_b\iint\nabla_s\left[n_o T\right]\,dA \qquad (3.169)$$

where N_o is the total number of heavy particles in the torus, Φ_p is the self flux, and I_θ is the total current. It has been assumed that r has the same value for all the particles and that Φ_c (the applied flux) varies but little over the area A.

Consider the term

$$\iint(j_\theta\,\nabla_s\,\Phi_p)\,dA$$

This term contains a contribution to the pinch forces and also a radial blow-out force (a hoop expansion force). The situation has been treated by Linhart[13]. The self-flux, Φ_p, consists of two parts

$$\Phi_p=\Phi_p'+\Phi_p'' \qquad (3.170)$$

The contours of Φ_p'' are symmetric circles around the current of the torus, and the corresponding magnetic field is of the Bennett type.[19] This field is responsible for the pinch forces.

On the other hand, the contours of Φ'_p are parallel to the z-axis (at least for positions near the torus), and the corresponding field is a uniform one. In the notation used here, the results of Linhart[13] are:

$$\nabla_s \Phi'_p = \frac{I_\theta}{2} \nabla_s L \tag{3.171}$$

where L is the inductance of the torus (see Eq. (3.128)).

In order that the pinch be stable the pinch forces and the pressure forces must be balanced. Therefore

$$\frac{1}{r} \iint \left(j_\theta \nabla_s \Phi''_p \right) dA = 2\pi k_b \iint \nabla_s (n_o T)\, dA \tag{3.172}$$

If T is assumed to be constant over the area A (a good assumption only when the pinch is very strong) then Eq. (3.172) yields the result

$$I_\theta^2 = \frac{4N_o}{\mu_o r} k_b T \tag{3.173}$$

This equation is identical (except for units) to the well-known pinch equation stated, for example, by Spitzer.[14]

Once the pinch is established and is quasi-stable, the temperature changes are due to Joule heating. An expression for the Joule heating has been given in Eq. (3.149) and one can use this to write that

$$I_\theta^2 = \frac{N_o}{\rho_t} k_b \frac{dT}{dt} \tag{3.174}$$

where ρ_t is the resistance of the torus.

Equations (3.173) and (3.174) can be combined, and the result can be expressed in terms of quantities already defined. The result is:

$$\frac{dT}{dt} = \frac{T}{\tau''} \tag{3.175}$$

where τ'' is a characteristic heating time. It is given by:

$$\tau'' = \tau \frac{N^e}{N^e_{crit}} \left[4 \ln \frac{14r}{\sqrt{A}} - 8 \right]^{-1} \tag{3.176}$$

where τ is the mean collision time, N^e is the number of electrons in the torus, and N^e_{crit} is the critical number of electrons (see Eq. (3.147)). If N^e is much larger than the critical number, and if the collision processes are dominated by Coulomb collisions, then it is found that

$$\tau'' \propto A \tag{3.177}$$

and that τ'' is independent of n^e_o, the election density in the torus.

Now, if we assume the validity of Eq. (3.172), and if use is made of Eq. (3.171) and of the intrinsic inductance, ℓ_t, then Eq. (3.169) becomes

$$N_o \langle M \rangle \frac{D\langle \vec{W} \rangle}{Dt} = I_\theta \nabla_s \Phi_c$$

$$+ \frac{N_o}{4\pi r} \left[\nabla_s \ell_t \right] \iint \frac{j^2_\theta}{n_o} \, dA \tag{3.178}$$

$$+ \frac{I^2_\theta}{2} \nabla_s L$$

When a pinch is well formed (a strong pinch) the current flow is near the skin of the torus. Consequently

$$\frac{1}{2\pi r} \iint \frac{j_\theta^2}{n_o} dA < \frac{I_\theta^2}{N_o} \tag{3.179}$$

However, when the pinch is well formed the last term in Eq. (3.178) is more important than the next-to-last term. Therefore, little error is made by assuming Eq. (3.179) to be an equality. Then Eq. (3.178) becomes

$$N_o <M> \frac{D <\vec{W}>}{Dt} = - e \nabla_s V^L \tag{3.180}$$

where V^L is the inductive potential that describes the motion of the torus as a whole

$$V^L = \frac{i}{2e} \frac{\left(\Phi_c - <<K>^e>^L\right)^2}{L + \ell_t} \text{ (volt)} \tag{3.181}$$

In deriving this result Eq. (3.133) has been used. This result is identical to Eq. (3.138), and it justifies the statements, made earlier, about V^L.

If V^L is not an explicit function of time then

$$\frac{N_o <M>}{2e} <\vec{W}> \cdot <\vec{W}> + V^L = \text{constant of motion} \tag{3.182}$$

and the flux necessary to achieve a given value of $<\vec{W}>$ can be computed.

For a uniform traveling field Φ_c is independent of time in the moving reference frame of the field and V^L will be approximately time independent if the change of $<<K>^e>^L$ with collisions is slow enough.

The tendency of a torus to expand radially is contained in V^L.

$$V^L \propto \frac{1}{r^2} \quad (\text{if } \ell_t << L) \tag{3.183}$$

$$V^L \propto \frac{1}{r} \quad (\text{if } \ell_t >> L) \tag{3.184}$$

From this it is seen that the tendency toward radial blow-out changes as a pinch forms.

The motion of a single charged particle in the pinch can be investigated with the aid of the equations that have been developed. The work is not yet complete, and no detail will be given here.

3.18 CONCLUDING REMARKS

The chance of being able to form a pinched torus in a traveling-field accelerator is enhanced by using a plasma of high atomic number. This can be proved with the aid of the pinch equation. The pinch forces vary like I_θ^2, but it has been shown that I_θ^2 is equal to $2e\, V^L/(L + \ell_t)$. Now, in the frame of reference of the moving field $eV^L + 1/2 <M> W^2$ is an approximate constant of the motion, so the maximum value of V^L experienced by the torus, must be equal to the value $1/2 <M> v_f^2$, where v_f is the speed of travel of the field. At this maximum value the torus reaches a turning point of its motion. Combining these ideas leads to the following condition for pinch formation:

$$<M> v_f^2 > \frac{4L}{\mu_o r}\left(1 + \frac{\ell_t}{L}\right) kT \tag{3.185}$$

Now L is proportional to $\mu_o r$ so this term is essentially constant, depending on r only logarithmically. It has also been shown that ℓ_t/L is proportional to N^e_{crit}/N^e and that T increases exponentially. Eq. (3.185) states that the chances of pinching are improved if:

1. $<M>$ is large
2. $N^e > N^e_{crit}$

REFERENCES

1. Störmer, C.; Astrophysica Norvegica, II (1936).
2. Rajchman J. A. and Cherry W. H.; Jor. of Franklin Institute, 243, 261 (1947).
3. Schmidt G.; Physics of Fluids, 5, 994 (1962).
4. Sinnir J. and Schmidt G.; Physics of Fluids, 6, 841 (1963).
5. Wells D. R. and Schmidt G.; Physics of Fluids, 6, 418 (1963).
6. Penfold A. S.; AFOSR TN 60-841 (1960).
7. Penfold A. S.; AFOSR TN 60-961 (1960).
8. Penfold A. S.; "Two-Fluid Model for the Motion of a Rarified Plasma"; paper presented at the Annual Meeting of the ARS, Washington D. C., December 1960.
9. Brown S. C.; Basic Data of Plasma Physics, John Wiley and Sons Inc. (1959).
10. Delcroix J. L.; Introduction to the Theory of Ionized Gases, Interscience Publishers Inc., New York (1960).
11. Jeans J. H.; The Dynamical Theory of Gases; Dover Publications, Inc. (1954).
12. Kennard E. H.; Kinetic Theory of Gases, McGraw-Hill Book Company, Inc. (1938).
13. Linhart J. G.; Plasma Physics; North-Holland Publishing Co., Amsterdam (1960).
14. Spitzer, L.; Physics of Fully Ionized Gases; Interscience Publishers, Inc.; New York (1956).

4. DESIGN OF A CW ACCELERATOR

This section deals with the experimental aspects of traveling-wave plasma acceleration with a CW device. Section 4.1 is concerned with the design of the traveling wave field and discusses qualitatively the type of acceleration process expected. Section 4.2 deals with the actual production of this field and indicates the main problems encountered and their solution.

4.1 MAGNETIC FIELD DESIGN

The objective of this section is to describe the design of a traveling-wave field with the following two major properties:

1. The radius of radial stability of the inductive potential, V^L, lies in the annular accelerating region of the field.
2. The field shape is correct to oppose the tendancy for radial blow-out of a plasma torus discussed at the end of Section 3.

Many field configurations resulting from a variety of coil-and-ferrite combinations were calculated. Only the result of those trials will be given.

4.1.1 The Magnetic Field of the Mark II

The magnetic field of the Mark II is derived assuming complete cylindrical symmetry and a current system that is infinite in the cylindrical-coordinate z-direction.

We write the current density, $\vec{j}$:

$$\vec{j} = \hat{\theta}\, j(r) \sin\left(\omega t - \frac{\omega}{v_f} z\right) \qquad (4.1)$$

This represents a wave traveling in the +z-direction with a speed, v_f.

With this current the magnetic field components will be B_r and B_z, and there is an induced electric field E_θ. These are derivable from a vector potential $\vec{A}$ given by:

$$\vec{A} = \hat{\theta}\, R(r) \sin\left(\omega t - \frac{\omega}{v_f} z\right) \tag{4.2}$$

since

$$\vec{B} = \text{curl } \vec{A}; \text{ and } \vec{E} = -\frac{\partial \vec{A}}{\partial t} \tag{4.3}$$

This form for $\vec{A}$ is justified later by showing that the fields derived from it satisfy all relevant boundary conditions.

From Eq. (4.2) and (4.3) one obtains

$$B_r = \frac{\omega}{v_f} R(r) \cos\, \omega \left(t - \frac{z}{v_f}\right) \tag{4.4}$$

$$B_z = \frac{1}{r} \frac{\partial}{\partial r} (r\, R(r)) \sin \omega \left(t - \frac{z}{v_f}\right) \tag{4.5}$$

$$E_\theta = -\omega R(r) \cos \omega \left(t - \frac{z}{v_f}\right) = -v_f B_r \tag{4.6}$$

The fields must also staisfy:

$$\text{curl } \frac{\vec{B}}{\mu} = \vec{j} + \epsilon \frac{\partial \vec{E}}{\partial t} \tag{4.7}$$

where we assume only homogeneous media of permeability, μ, and dielectric constant, ϵ.

Substituting Eq. (4.4), (4.5) and (4.6) into Eq. (4.7) one finds

$$-\frac{\partial}{\partial r} \frac{1}{r} \frac{\partial}{\partial r} (rR) + \left(\frac{\omega}{v_f}\right)^2 R + \mu j(r) - \mu\epsilon\omega^2 R = 0 \tag{4.8}$$

and collecting terms

$$\frac{\partial^2 R}{\partial r^2} + \frac{1}{r}\frac{\partial R}{\partial r} - \left[\left(\frac{\omega}{v_f}\right)^2 (1-\mu\epsilon v_f^2) + \frac{1}{r^2}\right] R = \mu j(r) \qquad (4.9)$$

Now

$$1 - \mu\epsilon v_f^2 = 1 - \left(\frac{\mu}{\mu_o}\right)\left(\frac{\epsilon}{\epsilon_o}\right)\left(\frac{v_f}{c}\right)^2$$

where c is the speed of light.

If we let μ be as high as 1000 μ_o, and let $\epsilon = \epsilon_o$ and $v_f \cong 5 \times 10^4$ meters/sec, then

$$\frac{\mu\epsilon}{\mu_o \epsilon_o}\left(\frac{v_f}{c}\right)^2 \cong 3 \times 10^{-5}$$

so this "radiation" term can always be neglected in our case (where $v_f/c \ll 1$).

Finally:

$$\frac{\partial^2 R}{\partial r^2} + \frac{1}{r}\frac{\partial R}{\partial r} - \left(\left(\frac{\omega}{v_f}\right)^2 + \frac{1}{r^2}\right) R = \mu j(r) \qquad (4.10)$$

The situations of interest are ones for which the driving currents can be considered as sheet currents, so j(r) is a series of δ-functions. Eq. (4.10) will be solved using the homogeneous equation and introducing j(r) as a boundary condition.

With this the solution of the homogeneous form of Eq. (4.10) is:

$$R(r) = AI_1(\rho) + B K_1(\rho) \qquad (4.11)$$

where

$$\rho = \frac{\omega}{v_f} r \qquad (4.12)$$

and I_1 and K_1 are hyperbolic Bessel functions of order one. The following properties are of interest*.

$$\left.\begin{aligned} \frac{d}{d\rho}\,\rho\, I_1(\rho) &= \rho\, I_o(\rho) \\ \frac{d}{d\rho}\,\rho\, K_1(\rho) &= -\rho\, K_o(\rho) \end{aligned}\right\} \qquad (4.13)$$

and

$$I_1(\rho)\, K_o(\rho) + I_o(\rho)\, K_1(\rho) = \frac{1}{\rho}$$

where I_o and K_o are hyperbolic Bessel functions of order zero. Figure 4-1 is a plot of these four functions.

We now write the fields in terms of the solution Eq. (4.11), using Eq. (4.13)

$$\left.\begin{aligned} B_r &= \frac{\omega}{v_f}\left[AI_1 + BK_1\right]\cos\omega\left(t - \frac{z}{v_f}\right) \\ B_z &= \frac{\omega}{v_f}\left[AI_o - BK_o\right]\sin\omega\left(t - \frac{z}{v_f}\right) \\ E_\theta &= -\omega\left[AI_1 + BK_1\right]\cos\omega\left(t - \frac{z}{v_f}\right) \end{aligned}\right\} \qquad (4.14)$$

The magnetic flux Φ defined by:

$$\Phi(r, z, t) = 2\pi \int_0^r r' B_z\,(r', z, t)\, dr' \qquad (4.15)$$

is given by

$$\Phi = 2\pi r\left[AI_1 + BK_1\right]\sin\omega\left(t - \frac{z}{v_f}\right) \qquad (4.16)$$

*See References 4 and 5 of Appendix N.

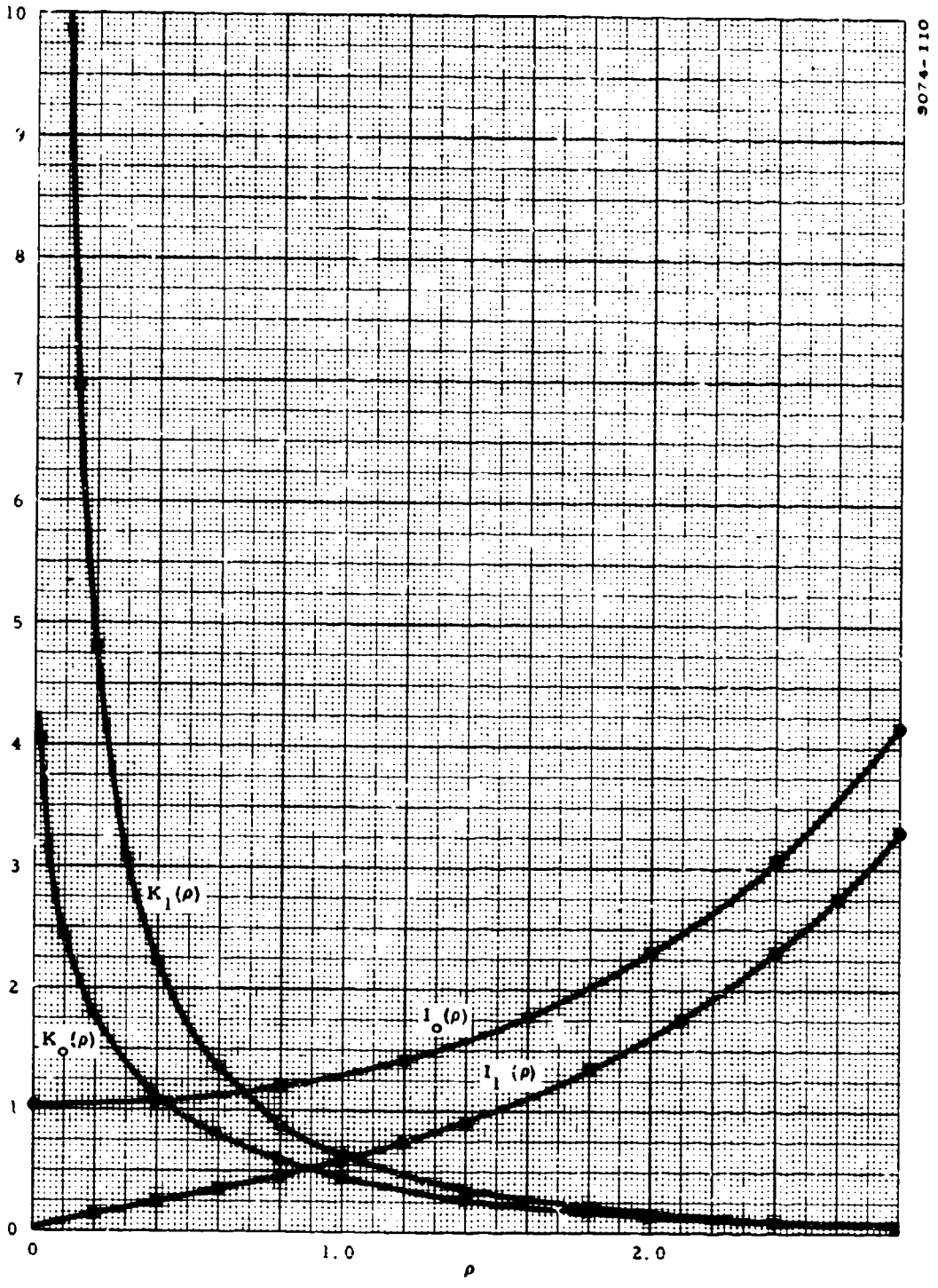


Figure 4-1. Plot of Zeroth- and First- Order Hyperbolic Bessel Functions

We now specialize to a particular geometry. It will be convenient to solve the problem for two different geometries and then to superimpose the separate solutions to obtain the final solution.

Figure 4-2 shows the first geometry to which Eq. (4.14) is applied.

In region (2)

$$B_r^{(2)} = \frac{\omega}{v_f}\left[A^{(2)} I_1 + B^{(2)} K_1\right] \cos \nu$$

$$B_z^{(2)} = \frac{\omega}{v_f}\left[A^{(2)} I_o - B^{(2)} K_o\right] \sin \nu \qquad (4.17)$$

where $\nu \equiv \omega\,(t - \frac{z}{v_f})$ and the superscript refers to region (2). At $\rho = \frac{\omega}{v_f} r_1 \equiv \rho_1$, B_z is zero because of the assumption $\mu = \infty$.

Therefore:

$$A^{(2)} I_o(\rho_1) = B^{(2)} K_o(\rho_1) \qquad (4.18)$$

In region (3) one must discard the I_o and I_1 parts of the solution as they become infinitely large as r becomes large.

Then, in region (3)

$$B_r^{(3)} = \frac{\omega}{v_f} B^{(3)} K_1 \cos \nu$$

$$B_z^{(3)} = -\frac{\omega}{v_f} B^{(3)} K_o \cos \nu \qquad (4.19)$$

At the boundary between regions (2) and (3)

$$\left.\begin{aligned} B_r^{(2)} &= B_r^{(3)} \\ \text{and} \qquad & \\ B_z^{(2)} - B_z^{(3)} &= \mu_o J_o \sin \nu \end{aligned}\right\} \qquad (4.20)$$

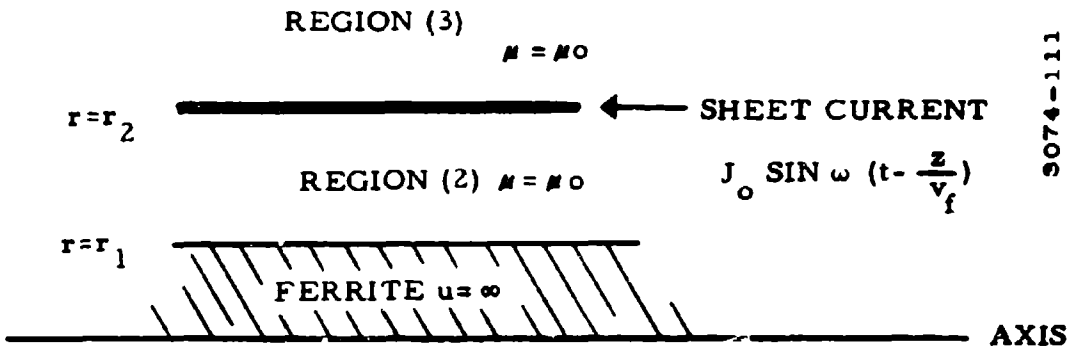


Figure 4-2. Geometry A

Using these boundary conditions and Eq. (4.16) one arrives finally at the flux in region (2)

$$\Phi^{(2)} = \frac{2\pi \mu_o J_o}{(\frac{\omega}{v_f})^2} \left[I_o(\rho_1) K_1(\rho_2) \rho_2 \right] \rho \, a(\rho) \sin \nu \qquad (4.21)$$

where

$$a(\rho) \equiv \frac{I_1(\rho)}{I_o(\rho_1)} + \frac{K_i(\rho)}{K_o(\rho_1)} \qquad (4.22)$$

We now consider the second geometry shown in Figure 4-3.

By the methods used in solving Eq. (4.10) for geometry A, one arrives at the flux in region (2) for geometry B.

$$\Phi^{(2)} = \frac{2\pi \mu_o J_i}{(\frac{\omega}{v_f})^2} \rho \frac{K_1(\rho)}{K_o(\rho_1)} \sin (\omega t - \frac{\omega}{v_f} z - \phi) \qquad (4.23)$$

Note that the current, J_i, may be phase-shifted with respect to J_o by an amount, ϕ.

We now superimpose the solutions of geometries A and B; and the flux in region (2), which is to be the plasma-accelerating region, is given by:

$$\Phi = \frac{2\pi \mu_o J_i}{(\frac{\omega}{v_f})^2} \left[\rho \, \gamma(\rho) \sin (\nu - \phi) + X \rho \, a(\rho) \sin \nu \right] \qquad (4.24)$$

where $a(\rho)$ is defined by Eq. (4.22), and

$$\gamma(\rho) \equiv \frac{K_1(\rho)}{K_o(\rho_1)} \qquad (4.25a)$$

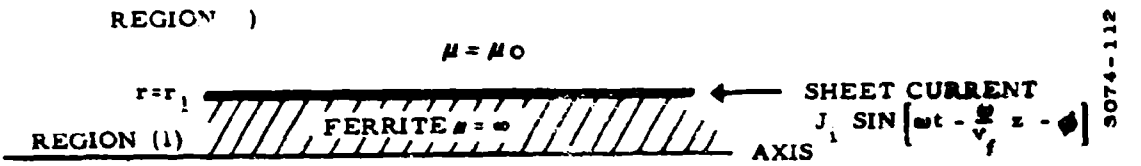


Figure 4-3 Geometry B

and

$$\chi \equiv \frac{J_o}{J_i} \rho_2 I_o(\rho_1) K_1(\rho_2) \qquad (4.25b)$$

At this point in the analysis it is apropos to list some of the values chosen for the field parameters.

1. Field velocity: $v_f = 5 \times 10^4$ meters/sec

2. Frequency: $f = \frac{\omega}{2\pi} = 250,000$ cycles/sec

   There is a certain arbitrariness about both choices (1) and (2). The field velocity is quite arbitrary but is in the range of interest for certain applications. The frequency is not quite as arbitrary. Frequencies in the megacycle range offer numerous practical difficulties when operating sensitive diagnostic instruments in the vicinity of high-frequency fields. Frequencies below 50 kc demand rather bulky electrical equipment. Choices (1) and (2) taken together yield a wavelength that is quite reasonable (0.2 meter). In practice it was more convenient to choose a wavelength of 0.225 meter and a frequency of 240 kc. Therefore, the field elocity in the device is 5.4×10^4 meters/sec.

3. The Outer Current Radius, r_2: $r_2 = 0.084$ meter

   Since the region between the two currents is a vacuum channel, this choice allows the use of the largest standard tubing for the outer channel wall with sufficient space for cooling purposes.

4. The Inner Current Radius, r_1: $r_1 = 0.035$ meter

   This is small enough to give a reasonably wide channel and large enough for coil winding purposes.

The parameter, χ, in Eq. (4.24) is a field-shaping term, and it is found by trial that a value of 1.32 yields a good shape for the field. In addition Eq. (4.25) yields

$$\frac{J_o}{J_i} = 5 \qquad (4.26)$$

Putting these numbers into Eq. (4.24) we get

$$\Phi = 2.0 \times 10^{-9} J_o \left[\rho \gamma(\rho) \sin (\nu - \phi) + 1.32 \rho a(\rho) \sin \nu \right] \quad (4.27)$$

The field-shaping parameter is still left undetermined as is ϕ, the phase shift between the two currents. Computer analysis of the trajectory of particles in magnetic fields led to the conclusion that particles are turned, in a manner described closely by specular reflection, by a critical contour of the inductive potential, V^L. That is, if a particle of a given kinetic energy is sent into a stationary field, its subsequent turn-around and ejection can be described by saying that it specularly reflected off the potential line corresponding to its initial energy. The value of ϕ was chosen as 40°, since the field shape that resulted indicated that much more or much less shift would lead to forces driving the plasma toward the inner wall or the outer wall, respectively.

With this choice the field shape in the channel is determined, and the field is as shown in Figure 4-4.

Except for the zero flux line, the labeling of the flux lines is arbitrary, their actual values depending on the coil current.

Figure 4-5 is a plot of the single particle inductive potentials corresponding to the flux plot of Figure 4-4. The potential is in arbitrary units. The parameter that varies from one plot to another is the "trapped flux" parameter, K (see Section 3).

Figure 4-6 is a flux plot done on the analog computer (see Appendix G). The flux units are on an arbitrary scale. The real-space ordinate is in centimeters. The auxiliary ordinate is connected with the operation of the computer. This figure illustrates the fringing field of the accelerator. (The fringing field is not described by the equations that have been presented already.)

In the analytical derivation of the flux, certain ideal conditions were assumed.

1. Fields extending radially to infinity
2. Ferrite of $\mu = \infty$
3. Ferrite region extending to the axis of symmetry.

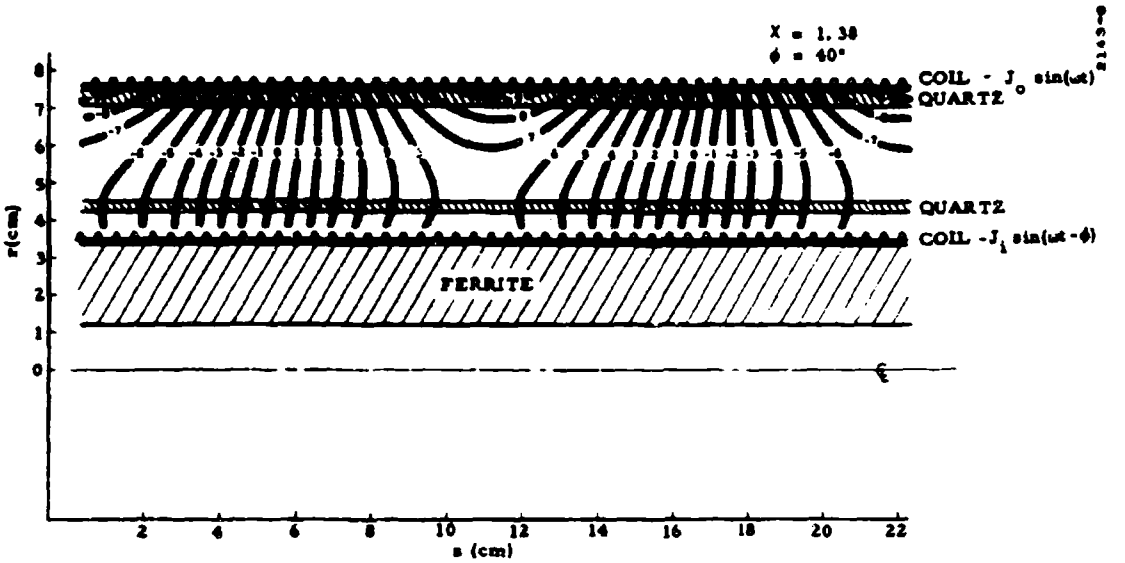


Figure 4-4. Calculated Magnetic Field Pattern of Accelerator

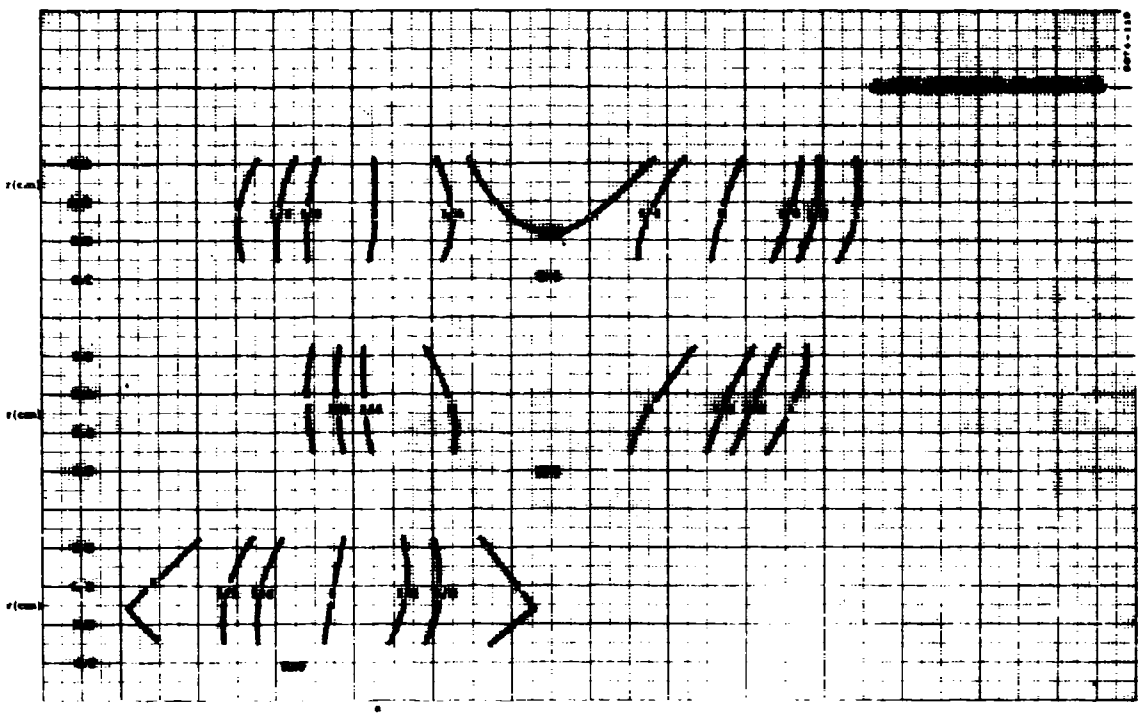


Figure 4-5. Plot of Inductive Potentials for Various Values of K

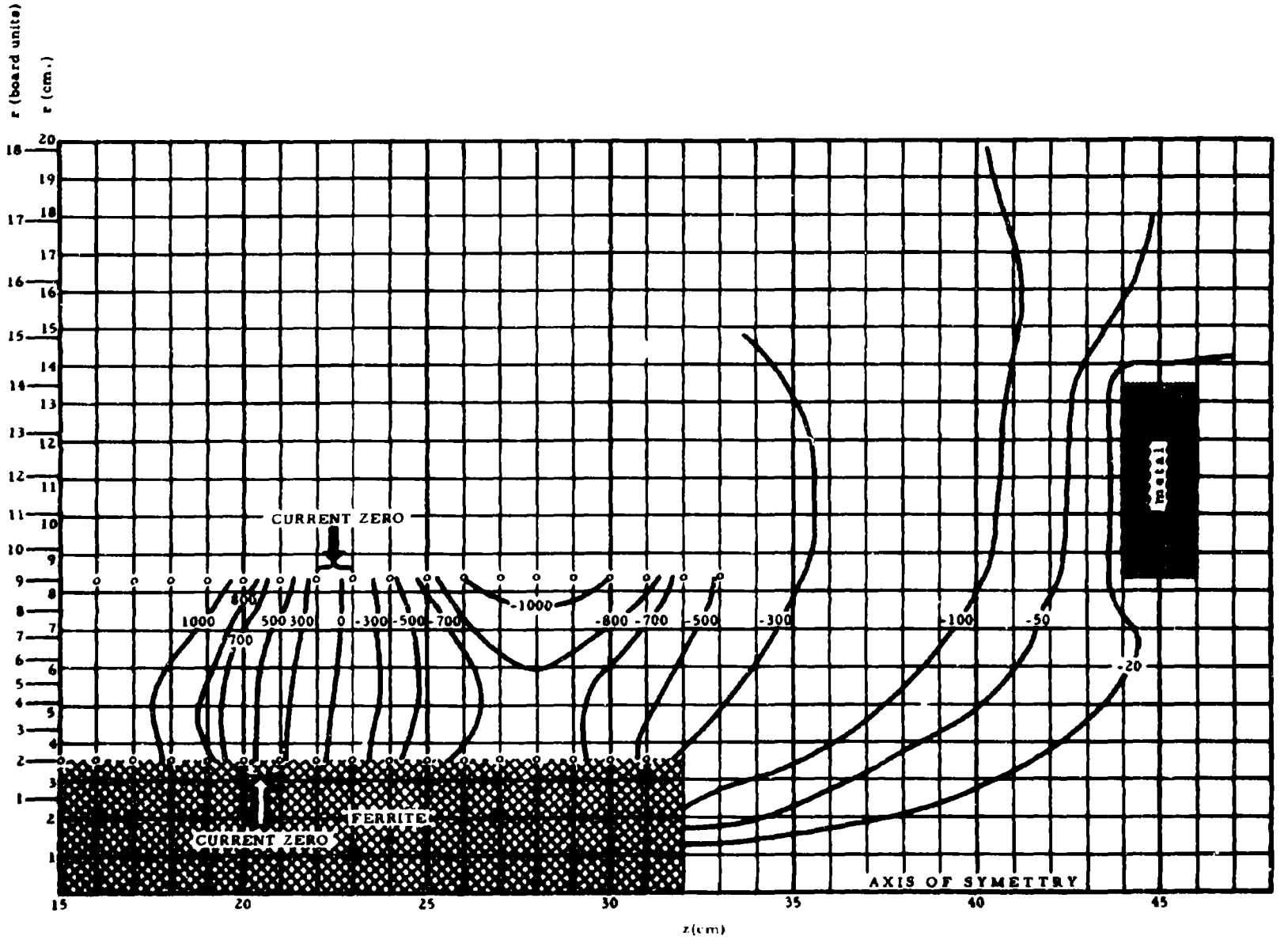


Figure 4-6 Analog Flux Plot, Mark II

In the device itself these assumptions are not met. (See Appendix H for detailed description.)

1. The fields are cutoff in the radial direction by a metal enclosure.
2. The ferrite has a finite μ.
3. There is a hole down the center of the ferrite to provide a cooling channel.

To estimate the extent of these conditions we consider the following geometry, geometry C (Figure 4-7).

Proceeding exactly as before one arrives at the radial function for this geometry. In region (2) we have

$$R^{(2)}(\rho) = \mu_o J_o r_2 \frac{I_o(\rho_1) K_1(\rho_2)}{C_w} \left[\frac{I_1(\rho)}{I_o(\rho_1)} + \delta \frac{K_1(\rho)}{K_o(\rho_1)} \right] \tag{4.28}$$

where

$$C_w = 1 + \frac{I_1(\rho_2) K_1(\rho_3)}{K_1(\rho_2) I_1(\rho_3)} \tag{4.29}$$

$$\delta = 1 - \frac{C_h}{\beta - 1} \frac{1}{\rho_1 I_1(\rho_1) K_o(\rho_1)} \tag{4.30}$$

$$C_h = \left[1 - \frac{I_1(\rho_o)}{\rho_1 I_1(\rho_1) I_o(\rho_1) K_1(\rho_o)} \right]^{-1} \tag{4.31}$$

The effect of the outer metal shield is given by C_w, and the effect of the finite permeability and the void of the ferrite is given by δ and C_h.

These various corrections are discussed below.

1. C_w (The Outer Wall Correction) — C_w-1 is plotted against r_3/r_2 for various ρ_2 of interest (see Figure 4-8). It can be seen that values of r_3/r_2 between 2 and 3 are needed in order that C_w be within a percent of unity. Notice that in the expression for the radial function that the role of C_w is a scaling factor, i.e., it has the effect of reducing the field strength everywhere without changing the shape of the field.

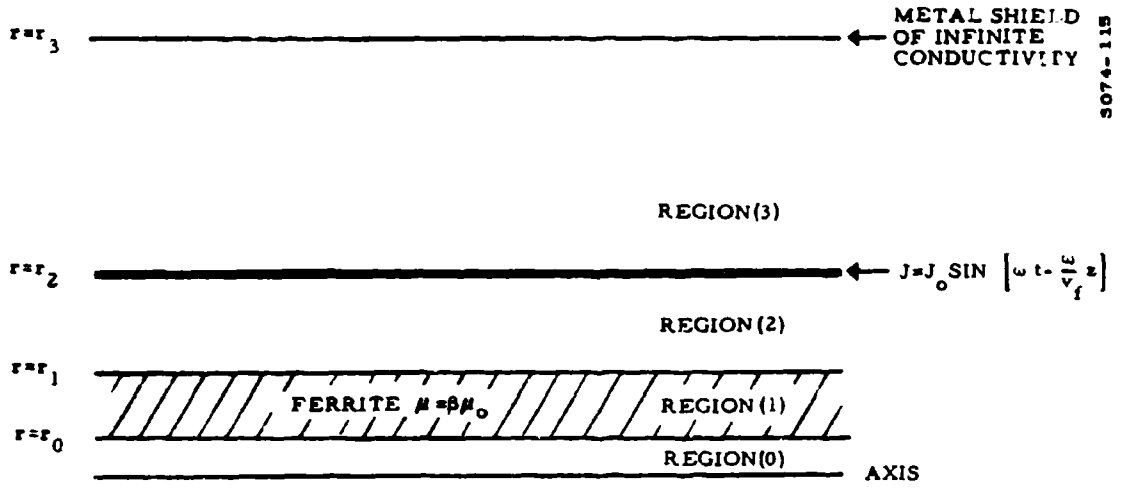


Figure 4-7. Geometry C

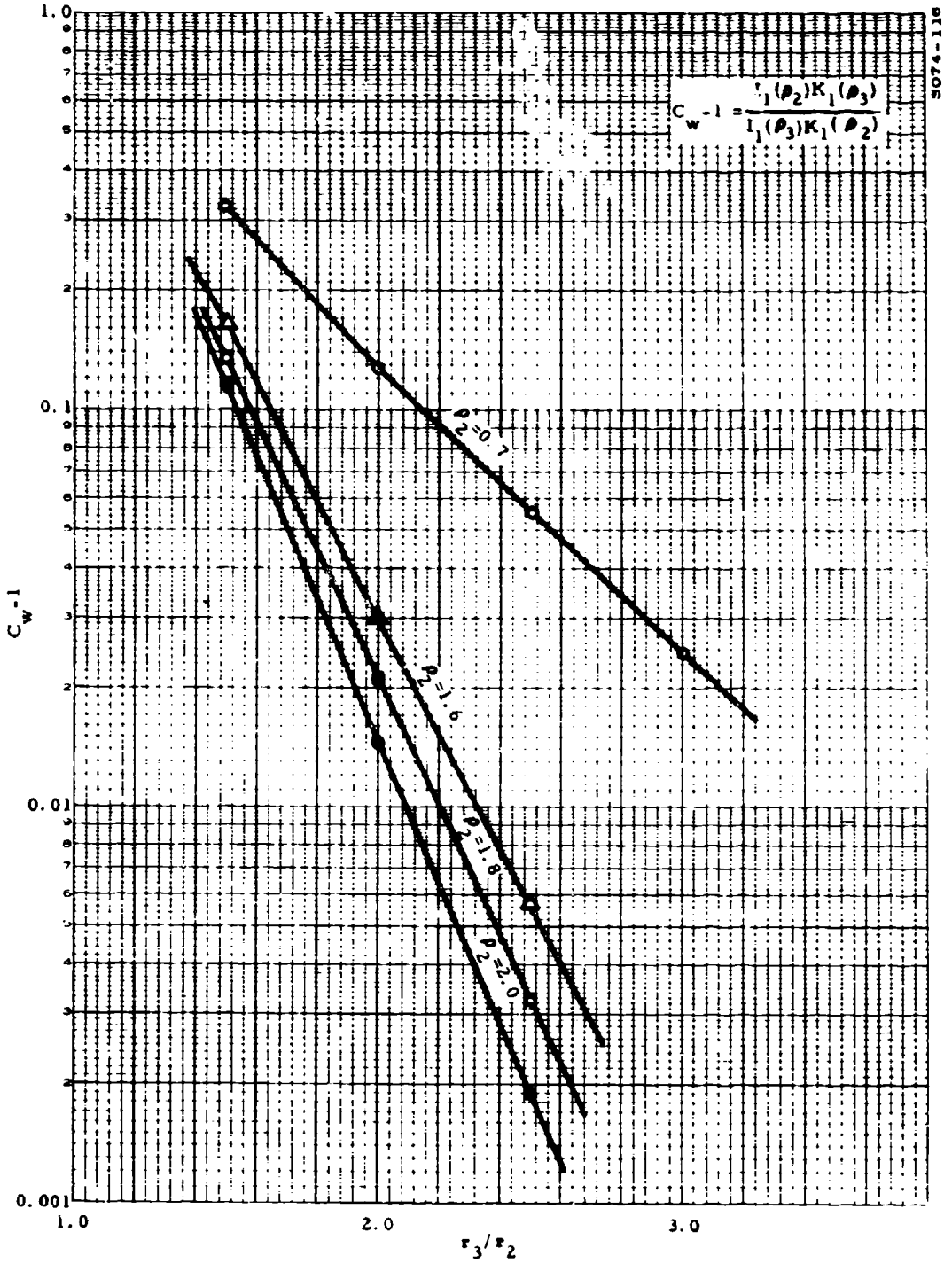


Figure 4-8. Plot of $C_w - 1$ vs r_3/r_2

2. C_h (The Hole Correction) — C_h is plotted against r_o/r_1 in Figure 4-9. From the expression for δ it can be seen that the effect of C_h is to degenerate the permeability of the ferrite, and thus the effect of the hole can be compensated for by using a ferrite of slightly higher permeability. The expression for C_h shows that it depends not only on the hole size but also on the outer radius of the ferrite. However it is found that over the range $\rho_1 = 0.6$ to $\rho_1 = 0.9$, C_h depends mostly on r_o/r_1. It is felt that r_o/r_1 should be kept smaller that about 0.4 in order to minimize its effect on the ferrite.

3. δ (The Ferrite Correction) — In Figure 4-10, $\frac{(\beta - 1)(1 - \delta)}{C_h}$ is plotted against ρ_1. Notice that in the expression for the radial function, δ affects only the second term and thus is not a simple scaling factor but tends to distort the function. Since the properties of the ferrites are temperature-sensitive, the value of δ must be close to unity to minimize this distortion.

It has been found possible to design the Mark II so as to avoid the above-cited effects to a good approximation. In what follows we assume all three corrections are negligible.

4.1.2 Acceleration Process

There are still several parameters of the device that have not been discussed, namely

1. Type of gas
2. Number of wavelengths along the accelerator
3. Mass flow rate
4. Power level
5. Coil currents.

These choices are intimately connected with the expected behavior of the plasma in the field.

Consider the neutral gas introduced at some point in the traveling field. The field sweeps through the gas, and, in the laboratory frame, there is an induced electric field, E_θ. Any electrons present will be accelerated, and the ionization of the gas will increase; the rate depending on E_θ, the density, recombination, etc. The heavy positive ions will lag,

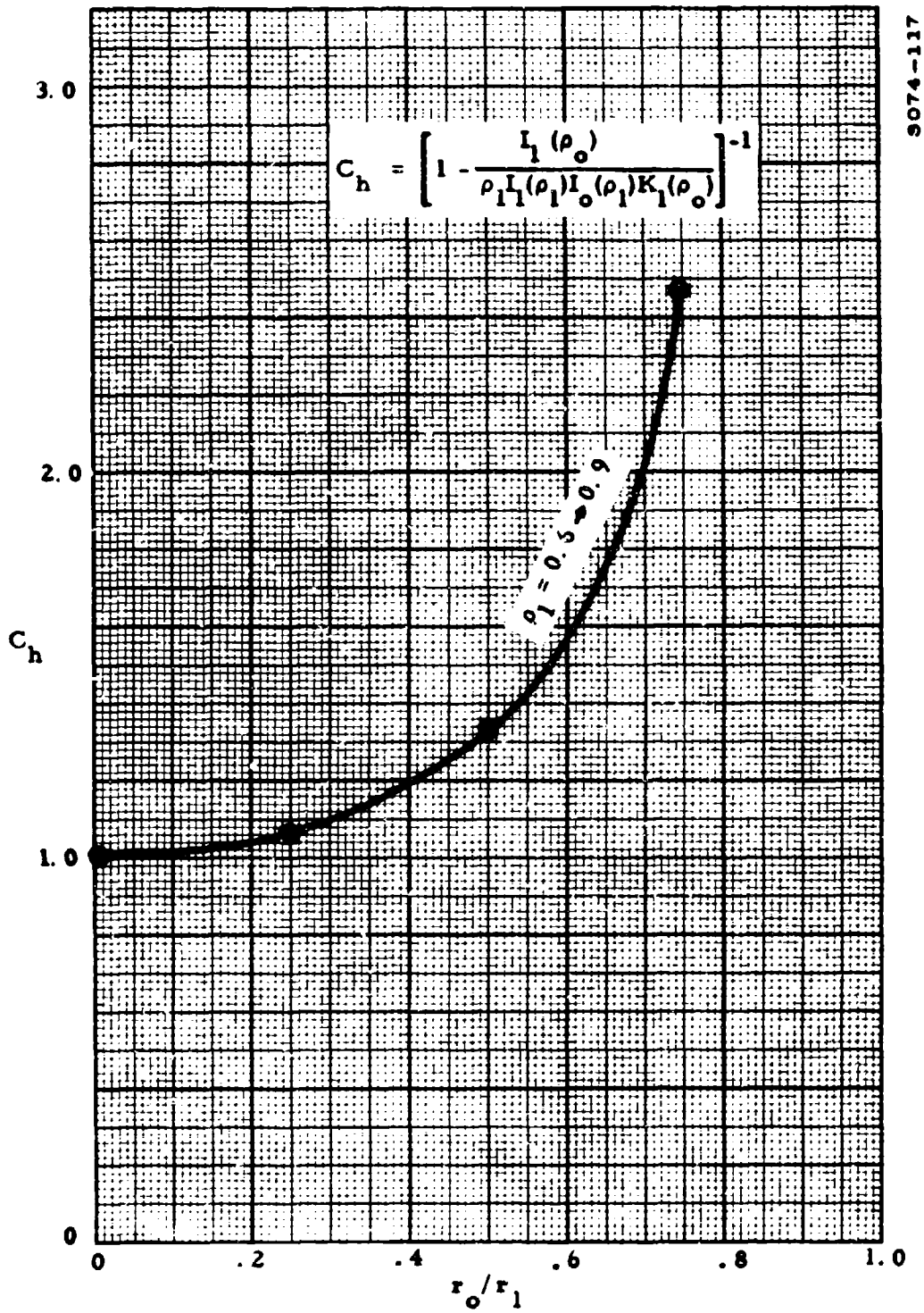


Figure 4-9. Plot of C_h vs r_o/r_1

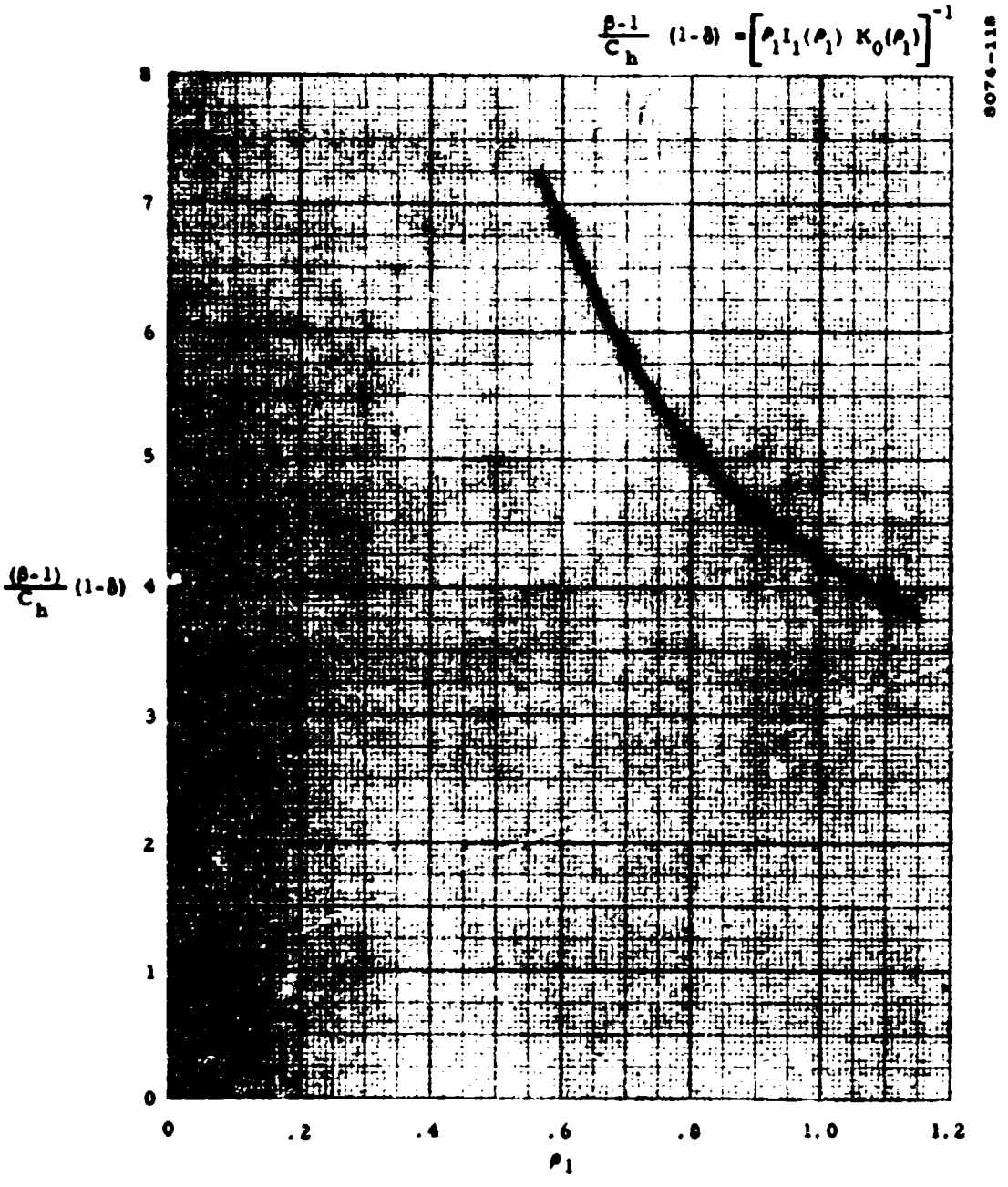


Figure 4-10. Plot of $(\beta-1)(1-\delta)/C_h$ vs ρ_1

and, as the gas will tend to be neutral, there will be a local buildup of electron current and positive ion density.

This current will tend to be destroyed by Joule heating, but the Coulomb cross section falls rapidly with increasing energy; so if the electron energy builds up fast enough, the current will be increased. At a certain point in the current buildup, the pinch forces will develop enough to form a plasma torus. In Section 3 it is shown that, over a period of time less than the current decay time due to heating, the motion of this torus can be described by the inductive potential, V^L, and we are interested in the acceleration process during this time only. In order to discuss the subsequent motion of the torus, one moves into the frame of reference of the field so that the magnetic field appears stationary, and the motion of the torus is governed by energy conservation; i. e., the sum of the kinetic energy of the torus at a point and the value of the potential at that point is a constant.

With this picture in mind the initial speed of the torus is $-v_f$; i. e., it appears from the field as if it were moving backward with the field speed. Suppose, for simplicity, that the torus was formed near the zero flux line of the field with K = 0. Then it is at the minimum of the potential. Moving backward, it loses kinetic energy and, provided the potential is high enough, reaches a turning point and reverses its motion. When it reaches the minimum potential again, it will have its initial speed but in the opposite direction. If now the field terminates, the torus will exit at this speed, which, in the laboratory frame, is twice the field speed. This effect is called the slingshot.

This type of process is clearly transient and cannot be described by the slow-flow analysis of Section 3. It is recognized that the picture above is highly idealized, and the rate of collisions cannot be ignored. Indeed the slingshot starts with a collision-dominated process. Still it is felt that this picture provides reasonable criteria for choosing the parameters mentioned at the beginning of this discussion. The choices that were made are:

1. Mercury is chosen because of its mass, low ionization energy, and ease of condensation. This latter property is not trivial in view of the mass flow rate used.
2. One wavelength was chosen, because more would not be of any use if the motion is as pictured.

3. The mass flow rate is calculated as follows:

f = field frequency = 2.4×10^{5} cycles/sec (chosen)

M^{i} = mass of the ion = 3.2×10^{-25} kg (mercury)

N = number of ions/toroid = 4.6×10^{13} (chosen)

Then

$\dot{M}$ = mass flow rate = $N M^{i} 2f = 7 \times 10^{-6}$ kg/sec $\cong$ 0.4 gm/min

The factor of 2 is used because a toroid should be formed every time a potential minimum appears, and this occurs twice every cycle of the field. The number of atoms per toroid, N, was chosen by calculating the critical number of ions in the torus (see Section 3) which is a lower limit for inductive behavior of the plasma ($\sim 2.5 \times 10^{13}$ ions) and multiplying this by a factor roughly estimated at two.

4. The power level is now determined by calculating the energy per second carried off by the plasma, assuming that the slingshot works. This is $2\dot{M} v_f^2 \cong 35$ kw.

5. The necessary coil current is estimated by setting V^{L} equal to the ion energy at the field speed (to effect the turning motion). The ion energy is 2.5 kev. Since V^{L} is related to the flux and the inductance of the toroid, the dimensions of the toroid must be estimated. Eq. (4.27) relates Φ to J_o. In the particular coil design chosen $J_o = 222\ I_o$, where I_o is the current in the coil (J_o is in units of amps/meter). The peak value of I_o is $\sim$ 70 amperes.

4.1.3 Field Measurements

The theory of the measurement of the magnetic field is developed in Appendix F. The search coil used in the Mark II is shown in Figure 4-11. It is comprised of a set of twelve fixed, coaxial, coplanar single-strand copper wires embedded in plexiglass, the wires being spaced one millimeter apart. The wires span almost the entire radial width of the channel. The second ring fixed to the search coil acts as an aligning guide. The ruler is marked off in steps of 0.5 centimeter, and a fiducial mark is fixed to the channel to allow known steps along the direction of the channel (z-direction).



Figure 4-11. Search Coil

To make a field map, the outer coil currents are set to have equal amplitudes (±5 percent) and correct phase (± three electrical degrees). The inner coil currents are then automatically correct (see Section 4.2.3) The search coil is positioned in the channel at a given z coordinate, and a wire is chosen. (This determines the r-coordinate.) The induced voltage in the wire is determined on an oscillogram, the oscilloscope being triggered from the master oscillator which controls the main coil currents. Time is measured from the start of the trace, so the oscillogram shows the induced voltage at a particular point from time, t = 0, to the end of the trace (usually one full cycle of the field). Particular care must be taken that the oscilloscope trigger, sweep, and gain controls remain the same throughout the entire run. A field plot for two different times is shown in Figure 4-12. To make this plot, a set of 80 oscillograms was taken. We chose a particular time and measured voltages, marking these down as a field of numbers on an r-z diagram. Equal voltage contours were then traced out, interpolating between measured points. Some of the excursions of the contour lines are undoubtedly due to a combination of measuring errors and the use of linear interpolation.

The main features of the field can be seen in Figure 4-12. The r scale is considerably stretched; the correct extent in real space is noted on the left. The general field shape is what would be expected, but the field lines do not have the correct forward tilt. Further tests have shown that no errors were made in wiring. There is no explanation for this effect at the time of writing, and more investigation is planned.

4.2 ELECTRICAL DESIGN OF THE MARK II

In this section we deal with the circuit problems involved in the production of the traveling wave field of the Mark II.

We start with the assumption that five power sources are available which are capable of polyphase voltage output (see Appendices I and J for details).

4.2.1 The Field Coils

The ideal polyphase field coil has an infinite number of phases. The real system is finite in axial extent, and only a finite number of electrical phases are available. A block diagram of the coil configuration is shown in Figure 4-13.

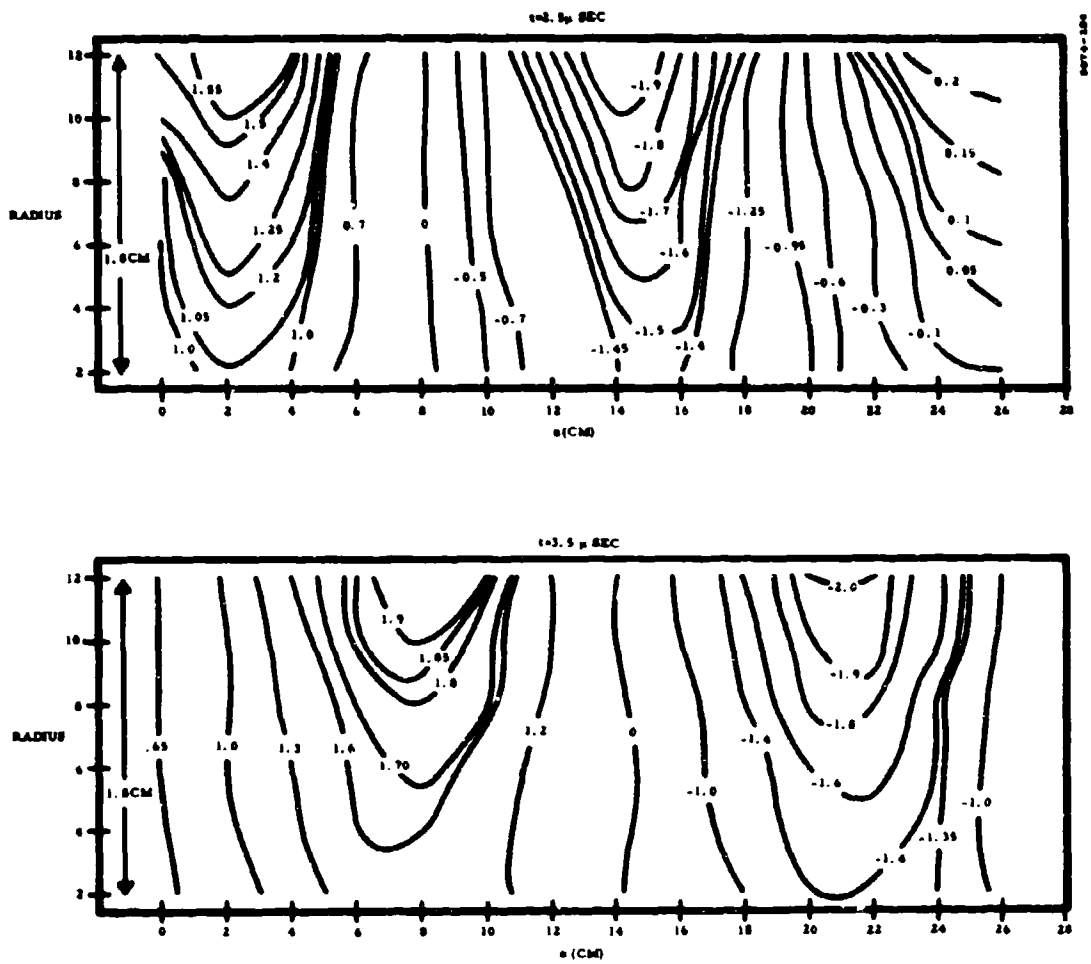


Figure 4-12. Flux Plots

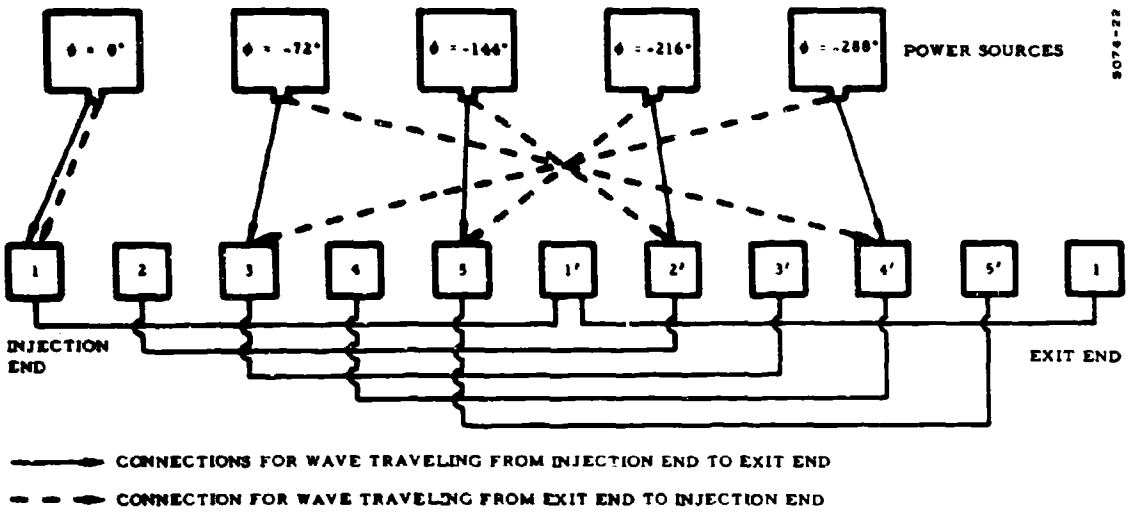


Figure 4-13. Outer Coil Phasing

Each of the blocks represents one coil group (see Appendix H for details). The primed and unprimed coil groups are identical, the only effective difference being that they are connected in such a way that the magnetic fields are 180° out of phase but have the same amplitude.

To find how to connect the coils to the power sources one writes a coil current wave moving uniformly in the +z direction (from the injection end to the exit end). If I is the current then

$$I = I_o e^{j\omega t} e^{-j\frac{2\pi z}{\lambda}} \tag{4.32}$$

where ω is the angular frequency of excitation and λ is the wavelength. The speed of the wave, v_f, is given by

$$v_f = \frac{\omega}{2\pi} \lambda$$

The speed is determined solely by the coil geometry, and if the coils are equally spaced the speed is uniform (neglecting end effects).

To avoid any confusion the point is made here that this has no relation to a delay line. The speed of the wave if forced upon the system and has nothing to do with pulses propagating naturally along the line of coils. The current is to be thought of as rising simultaneously in all the turns of a given coil group.

The coils are located at axial distances, $z_n = \frac{n\lambda}{10}$; n = 0, 1, . . 10. The current wave form for this finite array is given by:

$$I = I_o e^{j\omega t} e^{-j\frac{\pi n}{5}} \tag{4.33}$$

This is the desired current distribution, and we may write it in vector notation where degrees rather than radians are used:

$$\frac{\{I\}}{I_o} = \begin{bmatrix} e^{-j0} \\ e^{-j36} \\ e^{-j72} \\ e^{-j108} \\ e^{-j144} \\ e^{-j180} \\ e^{-j216} \\ e^{-j252} \\ e^{-j288} \\ e^{-j324} \\ e^{-j360} \end{bmatrix} \equiv \begin{bmatrix} e^{-j0} \\ e^{-j216} \\ -e^{-j72} \\ e^{-j288} \\ -e^{-j144} \\ e^{-j0} \\ -e^{-j216} \\ e^{-j72} \\ -e^{-j288} \\ e^{-j144} \\ -e^{-j0} \\ e \end{bmatrix} \qquad (4.34)$$

The second equivalent vector has been written because it is expressed in terms of phases that are available. This vector gives the prescribed hook-up of the coils. These connections are shown on Figure 4-13. For completeness, the connections for a backward traveling wave are noted. Such a backward traveling wave is useful in certain experiemental tests.

4.2.2 The Coupling Circuits

Since the power sources are Class-C-operated amplifiers, it was clear early in the design stage that the coils would have to be part of fairly high-Q resonant circuits. This is the usual load for amplifiers operating in this mode. The unusual feature is the polyphase operation into a load which is complicated by the existence of mutual inductances.

It is implicit in the meaning of a smoothly traveling wave produced by a polyphase coil system that the coils are coupled one to another by the field. If this were not so, and the coils were somehow uncoupled, the resulting field would only be a succession of separate pulses. The inherent mutual inductance is what makes tuning of the resonant coupling circuits difficult. The tuning problems become more difficult when one considers that the introduction of plasma, considered as a conducting medium, into the coil system will tend to lower the circuit inductances. This latter effect has been mitigated to some extent in the circuit network.

4.2.3 Inner Coil Drive

The theoretical design of the accelerator calls for two sets of field coils: an outer and an inner set. The current ratio outer to inner is 5, and the inner coil at a given axial position is phase-lagged 40° with respect to the outer coil at the same axial position. As will be shown,

it is easy to get a phase lag of 36° electrically, so the additional lag is obtained by mechanically shifting the outer coils along the axis of symmetry. The inner coil drive is obtained from the outer coils by transformer drive as shown in Figure 4-14. The transformers are discussed in Appendix K.

The notation of Figure 4-14 means, for example, that the fourth outer coil (counted from the injection end) drives the third inner coil. Five of these transformers were built.

4.2.4 Electrical Measurements

With this coupling method for the inner coils the accelerator is effectively a black box with five terminals connected to five power sources, the network chosen to connect the accelerator to the supplies is in Appendix L. In addition large inductances (called pad inductances) were connected in series with the outer coils. It is these pads that tend to isolate the power sources from the effects of the plasma, since fractional inductance changes of the circuits due to the plasma are minimized. Figure 4-15 shows the circuit used.

Figure 4-15 is one node of the five-phase version of the circuit analyzed in Appendix L.

The inductance matrix of this network was measured as follows:

1. All ring capacitors were disconnected
2. All the resonating capacitor branches were opened with the exception of the driver circuit
3. The driver branch was excited at 250 kc, and all open-circuit voltages at the other nodes were measured.
4. The self-inductances of all branches was measured by resonating them with a known capacity, C, at a known frequency, ω_o, and using

$$L = \frac{1}{\omega_o^2 C} \tag{4.35}$$

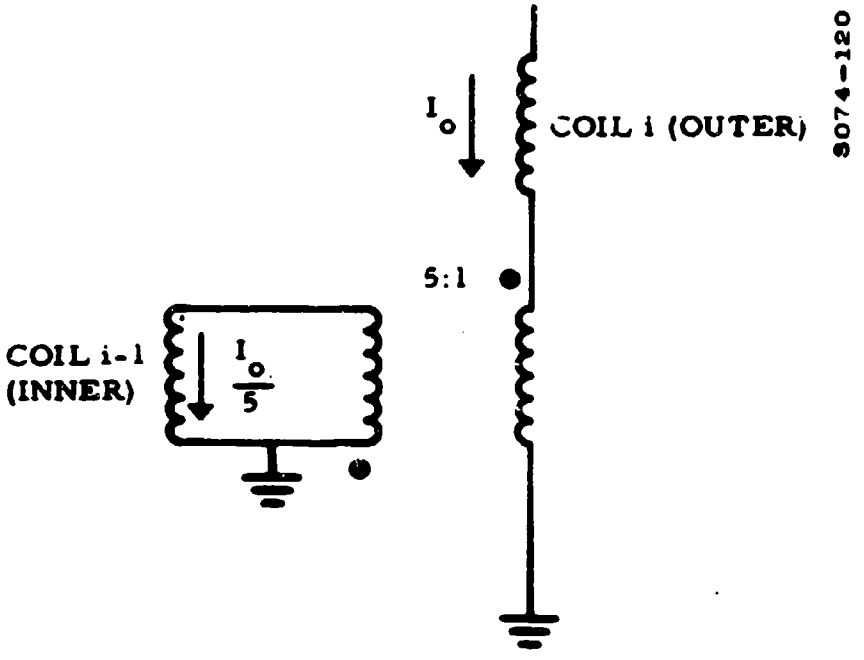


Figure 4-14. Coupling System for Inner Coils

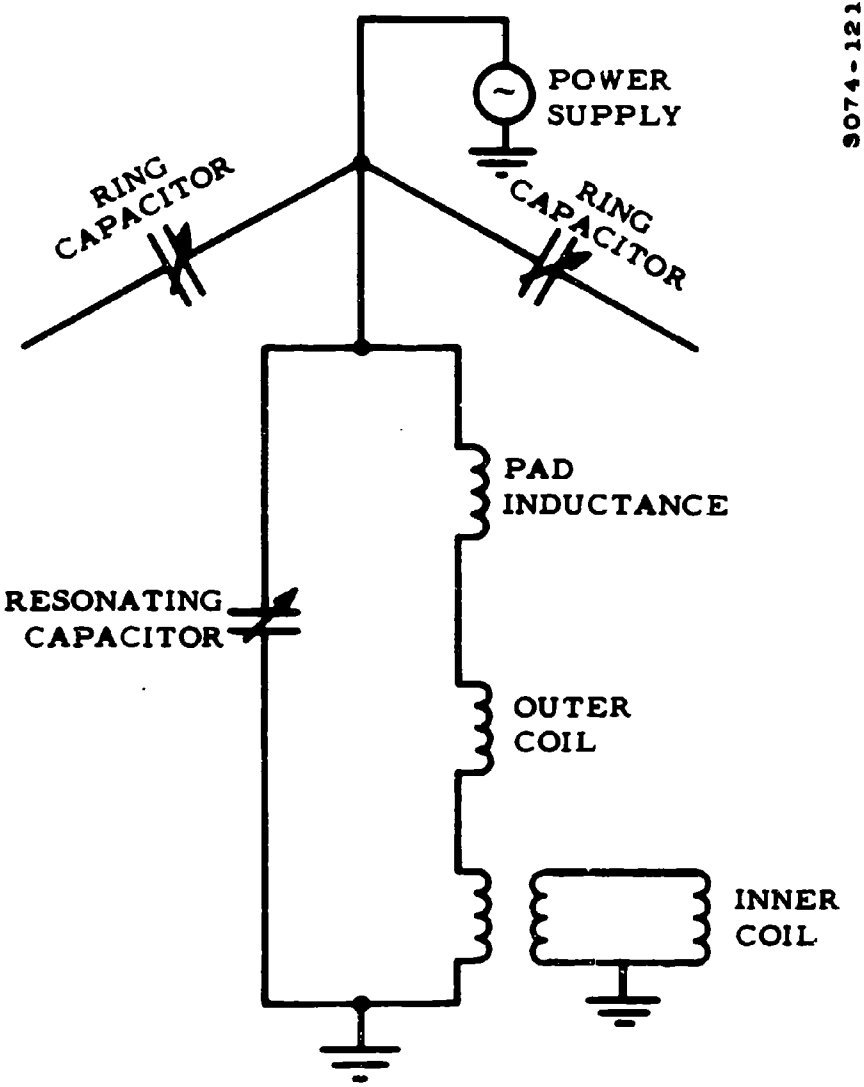


Figure 4-15. Schematic of One Node of Coupling Circuit

5. The mutual inductances were calculated from

$$M = L \frac{V_i}{V_o} \tag{4.36}$$

where V_i is the induced open-circuit voltage and V_o is the driving voltage. M was taken to be negative if the two voltages were 180° out of phase.

The real Q's of the system were measured by using the half-voltage points on the frequency response curve. The Q's looking into the nodes were all in the range 95 - 105. The real resistances R_i are derived from the Q measurements by

$$R = \frac{\omega L}{Q} \tag{4.37}$$

The inductance matrix so derived is given in Figure 4-16. The units of the matrix are microhenrys.

All the elements of the matrix were measured, and the matrix was symmetrized by averaging the corresponding off-diagonal elements, since, in principle, the matrix must be symmetrical. The larget deviation from the mean was about 15 percent.

As shown in Appendix L the "effective" inductances, ℓ_i, and the effective resistances, r_i, of the inductive branches must be calculated from the voltage-current relation.

$$\{E\} = \left(j\omega [M] + [R]\right)\{I\} \tag{4.38}$$

where $\{E\}$ and $\{I\}$ are the node voltage and inductive branch current vectors, $[M]$ is the inductance matrix and $[R]$ is the diagonal real resistance matrix.

The details of this calculation are shown in Appendix L.

PHASE		0°	-72°	-144°	-216°	-288°
	NODE	1	2	3	4	5
0°	1	90	4.54	-3.01	-3.51	3.82
-72°	2	4.54	90	6.03	-6.34	-5.77
-144°	3	-3.01	6.03	90	1.75	-5.95
-216°	4	-3.51	-6.34	1.75	90	6.26
-288°	5	3.82	-5.77	-5.95	6.26	90

8074-122

Figure 4-16. Inductance Matrix

Following is Table IV-1 which gives the results of the calculation.

TABLE IV-1

VALUES OF EFFECTIVE INDUCTANCE AND EFFECTIVE RESISTANCE

Node	ℓ (μhy)	r (ohm)
1	96.0	0.35
2	103.0	0.06
3	100.0	10.8
4	100.0	-7.6
5	102.0	5.2
		Sum = 8.8 ohms

The negative effective resistance indicates that one circuit is receiving energy from others through the mutual coupling. Of course the sum of the effective resistances is the total real-ohmic resistance of the network. It is the varied signs of these resistive elements that prevents the tuning of the device using simpler networks than the one in use.

There is another way of correcting for these mutual effects. That is to interconnect phases via transformers so that the mutually induced voltages are just canceled by the voltages introduced by the transformers. Since all phases interact with all other phases, this implies the use of ten transformers. This system would have the advantage of making all phases independent of the other phases but physically it requires considerably more electrical equipment.

Figure 4-17 is a photograph of the external circuitry.

PHASE		0°	-72°	-144°	-216°	-288°
	NODE	1	2	3	4	5
0°	1	90	4.54	-3.01	-3.51	3.82
-72°	2	4.54	90	6.03	-6.34	-5.77
-144°	3	-3.01	6.03	90	1.75	-5.95
-216°	4	-3.51	-6.34	1.75	90	6.26
-288°	5	3.82	-5.77	-5.95	6.26	90

9074-122

Figure 4-16. Inductance Matrix

Following is Table IV-1 which gives the results of the calculation.

TABLE IV-1

VALUES OF EFFECTIVE INDUCTANCE AND EFFECTIVE RESISTANCE

Node	ℓ (μhy)	r (ohm)
1	96.0	0.35
2	103.0	0.06
3	100.0	10.8
4	100.0	-7.6
5	102.0	5.2
		Sum = 8.8 ohms

The negative effective resistance indicates that one circuit is receiving energy from others through the mutual coupling. Of course the sum of the effective resistances is the total real-ohmic resistance of the network. It is the varied signs of these resistive elements that prevents the tuning of the device using simpler networks than the one in use.

There is another way of correcting for these mutual effects. That is to interconnect phases via transformers so that the mutually induced voltages are just canceled by the voltages introduced by the transformers. Since all phases interact with all other phases, this implies the use of ten transformers. This system would have the advantage of making all phases independent of the other phases but physically it requires considerably more electrical equipment.

Figure 4-17 is a photograph of the external circuitry.

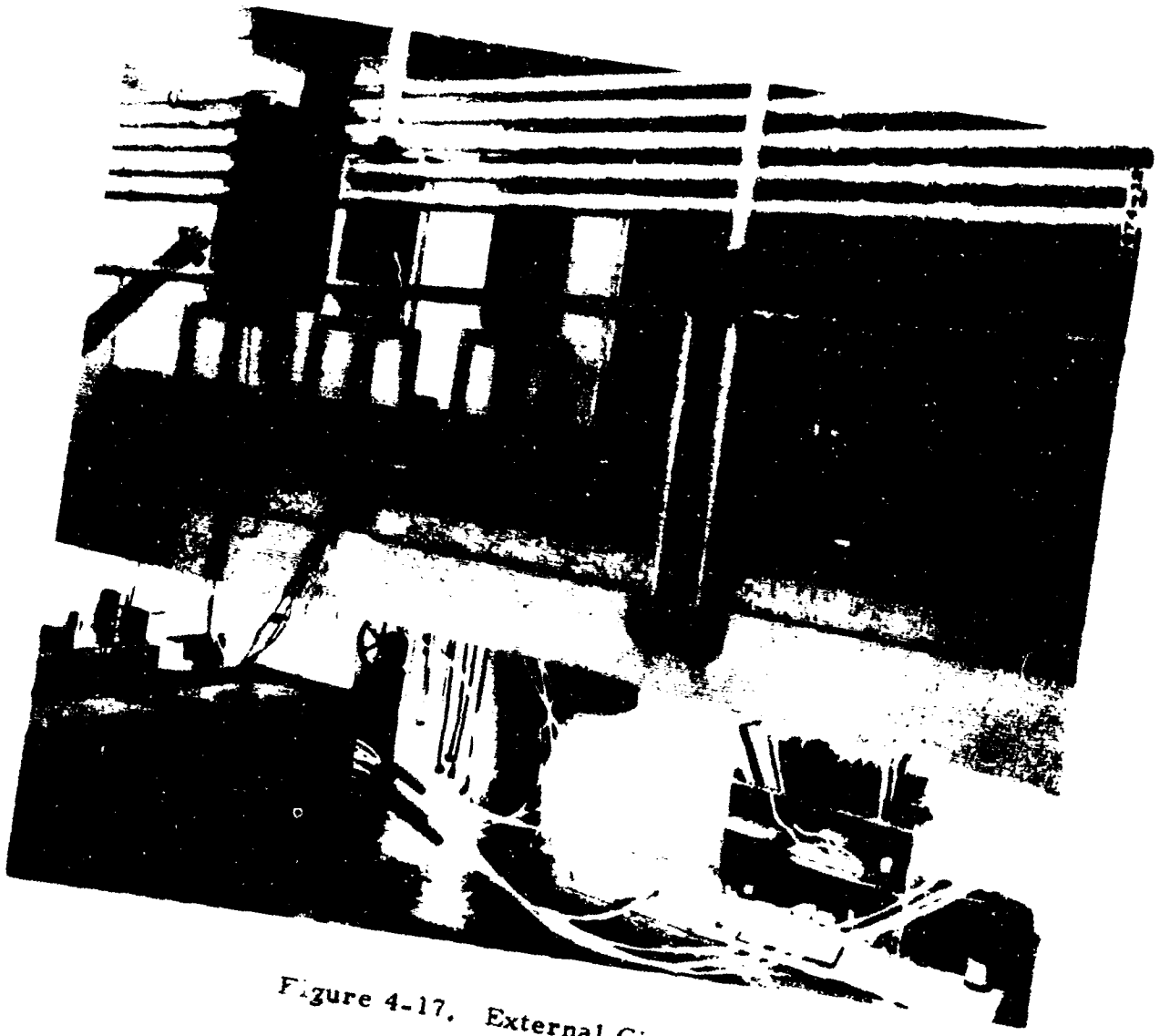


Figure 4-17. External Circuitry

APPENDIX A

ELECTRICAL TIMING OF THE MARK I ACCELERATOR

APPENDIX A

ELECTRICAL TIMING OF THE MARK I ACCELERATOR

1. INTRODUCTORY REMARKS

The magnetic field of the Mark I accelerator was produced by electrical currents in a series of one-turn coils which surrounded an evacuated pyrex tube. The plasma was formed and accelerated in the tube.

Each coil was connected, through a spark-gap switch, to a high-voltage energy-storage capacitor. Six of the coil-capacitor assemblies are shown in Figure A-1. The various components are:

A. Metal hoop surrounding the epoxy- encapsulated one-turn coil. One end of the coil is connected to A. The hoop carries a copper tube on its exterior surface through which a cooling fluid could be passed. The metal hoops were designed to nest into each other when the assemblies were mounted on the accelerator frame

B. Upper section of a 7-ohm coaxial transmission line. The space between the inner conductor of this line and the outer conductor (B) was filled with epoxy

C. Flange joining the upper and lower parts of the transmission line. This flange allowed the assembly to be separated into two parts

D. Hole that allowed a pulse transformer (not shown) to be connected to the center electrode of the three-element spark-gap switch located in the center conductor of the transmission line

E. Lower section of the 7-ohm transmission line (also epoxy insulated)



Figure A-1. Coil-Capacitor Assemblies

F. Insulated bushing surrounding a rod that connects to the center conductor of the transmission line. This rod provides the means for charging the energy storage capacitor

E. Energy storage capacitor. The brackets on the capacitor case allow the unit to be solidly attached to the accelerator frame.

The entire outer surface of each assembly was connected to ground when in operation. When the spark-gap switch was actuated the current passed from the capacitor to the center conductor of E, up the center conductor to the vicinity of the flange C, across the spark gap to the center conductor of B, through the narrow neck at the top of B to one end of the coil, through the coil to the metal hoop A, through the outer conductor of B and E to the case of the capacitor G.

A detailed account of the current flow has been given to illustrate the fact that the system is as well shielded as possible in order to minimize radiation of energy. In spite of these precautions the interference with electrical instruments was severe.

The capacitors were discharged in a carefully selected timing sequence. The entire current flow sequence was concluded in about 14 microseconds. The energy stored in the system was about 4800 joules, so the peak power level during the discharge exceeded 340 megawatts, and the peak flow of current in some of the coils exceeded 120,000 amperes.

The spark-gap firing sequence that was in use at the end of the Mark I experiments is shown in Table A-1.

The first column shows the capacitor numbers: numbers that corresponded to position in the sequence and also to the physical position of the corresponding coils. The coil-to-coil separation was one inch, so a one-to-one correspondence exists between capacitor number and the position of that coil. The second column gives the capacity as measured on a bridge operating at one kilocycle. The third column gives the time at which the spark-gap switches were fired. The fourth column gives the measured ringing frequency of each coil-capacitor assembly. The firing sequence was determined in a manner described in the main text.

2. TIMING PROBLEMS

Satisfactory operation of the accelerator was not achieved until the timing of the coil currents was determined and controlled to an accuracy

TABLE A-1

SPARK-GAP FIRING SEQUENCE

Capacitor No.	Capacity (μf)	Firing Time (microseconds)	Measured Ringing Frequency (kc)
1	2.99	0	178
2	2.95	1.41	178
3	2.57	2.91	192
4	2.51	3.91	194
5	1.78	4.82	220
6	1.54	5.41	228
7	1.47	6.09	250
8	1.20	6.71	286
9	1.00	7.26	314
10	0.83	7.63	330
11	0.80	7.97	334
12	0.672	8.41	368
13	0.659	8.62	370
14	0.600	8.95	370
15	0.532	9.27	394
16	0.466	9.57	416
17	0.451	9.84	440
18	0.431	10.15	460
19	0.408	10.42	472

of about ±0.15 microsecond. This accuracy was achieved only after a rather tedious series of empirically determined improvements. Serious difficulty was experienced in two areas:

1. The timing circuits themselves
2. The spark-gap switches

These problems and their solutions are discussed in detail in the following subsections.

2.1 THE TIMING CIRCUITS

There is no particular problem in devising a circuit that will supply a series of sharp pulses corresponding to the required spark-gap firing times; four or five circuit schemes come quickly to mind. Similarly there is no particular problem in constructing the circuits so that they do not mutually interact.

However, when No. 1 spark gap fires and coil current begins to flow and the power level reaches some 70 megawatts, the electrical noise generated in any and all electrical equipment in the vicinity is severe. This noise affects the timing of the remaining capacitors. When No. 2 spark gap fires the noise level is increased, and so on. Timing circuits, therefore, had to be devised that were unaffected by this noise. A solution was found in the form of LC ringing circuits for timing, with interstage coupling elements consisting of thyratrons.

Hard-vacuum tubes were used in the overall circuit but the design was such that their functions were completed prior to the firing of No. 1 spark gap. Subsequent to this firing the only active elements were the LC ringing circuits, the coupling thyratrons, and the gap-triggering pulse transformers. Circuit details are given later.

2.2 THE SPARK GAPS

The spark gaps were cylindrical aluminum pieces shaped (in cross section) as indicated in Figure A-2. They were three-element gaps with the center electrode biased to one-half the total gap voltage. The gaps fired spontaneously at about 33 kilovolts. Normal operation of the accelerator employed 28-30 kilovolts. The bias for the center electrode was obtained from a voltage divider as shown in Figure A-2. The method of connecting the triggering pulse transformer is also shown.

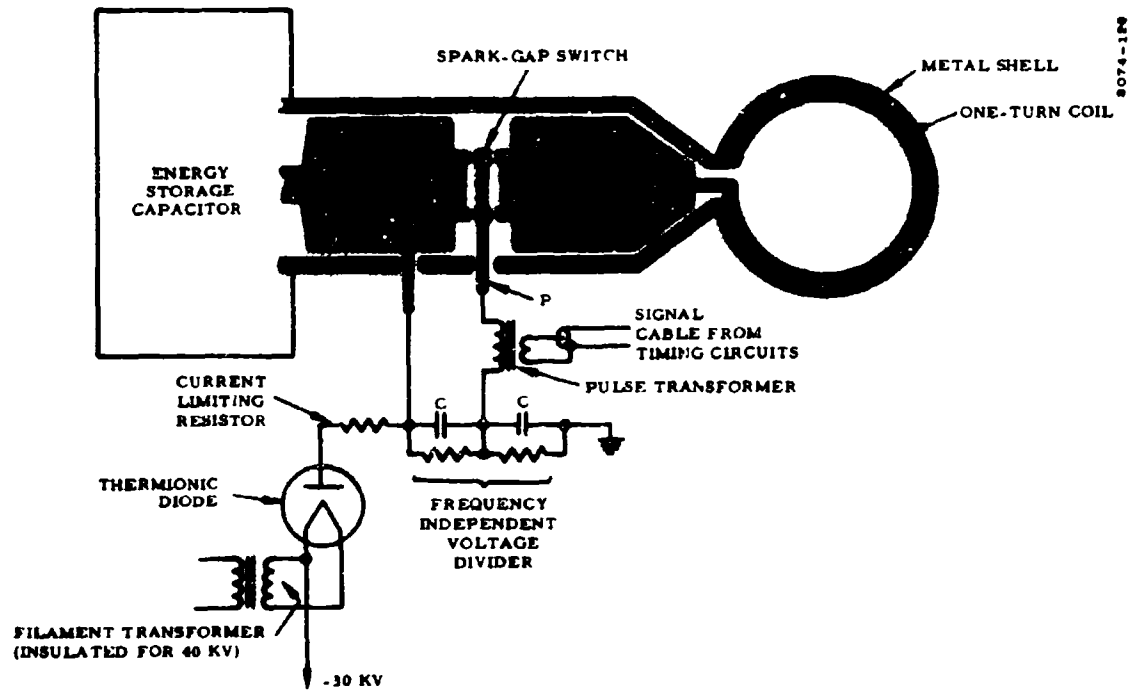


Figure A-2. Cross-Sectional Sketch of One Coil-Capacitor Assembly

The capacitors were charged from a common high-voltage power supply, each being connected to the supply through a thermionic diode and a current-limiting resistor as shown. When No. 1 spark-gap was fired, the power supply voltage was changed. The thermionic diodes acted as unidirectional switches to prevent the other stages from following this change.

No particular difficulty was experienced from the choice of aluminum for the spark gaps. There was no apparent tendency for the arc to seek out a preferred spot on the electrodes, indeed, the arc pits seemed to distribute themselves randomly over the surface of the electrodes.

Figure A-3 illustrates a problem that did develop. The photograph shows a view of one of the assemblies as seen from above flange C (refer to Figure A-1) looking down toward the center conductor of the transmission line E. One of the three spark-gap elements screws into the threaded part D (refer now to Figure A-3). A ribbed surface of insulating epoxy is shown as C. The hole, A, allows access to the pulse transformer which plugs into the middle electrode of the spark-gap (not shown). Flange B mates with the coil-carrying half of the assembly. The dark colored spots in the vicinity of A are arc pits. The arc had jumped the gap between the center electrode and the wall of the assembly in preference to jumping over its proper path; even though the former was four or five times the longer path.

After some study the difficulty illustrated in Figure A-3 was explained and corrected. The explanation involved the flow of cooling gas that was passed over the spark-gap assembly to prevent unwanted multiple-firing of the gaps. Three small tubes (shown at E in Figure A-3) squirted a flow of dry nitrogen over the gap electrodes. This flow left the spark-gap chamber through the hole, A. The pulse transformer lead, which projected through A, was an epoxy-insulated cylinder that fitted loosely into A, allowing adequate space for outflow of the dry nitrogen. Each time the gap was fired some aluminum vapor, carried along by the gas flow, was deposited on the epoxy insulation of the pulse transformer. After a time the deposition (even though barely visible to the critical eye) offered a path of lower resistance than did the spark gap, and the arc traveled directly to the walls, by-passing the coil. This behavior, even if it occurred on only one coil assembly per operation of the system, completely destroyed the ability of the accelerator to function properly.

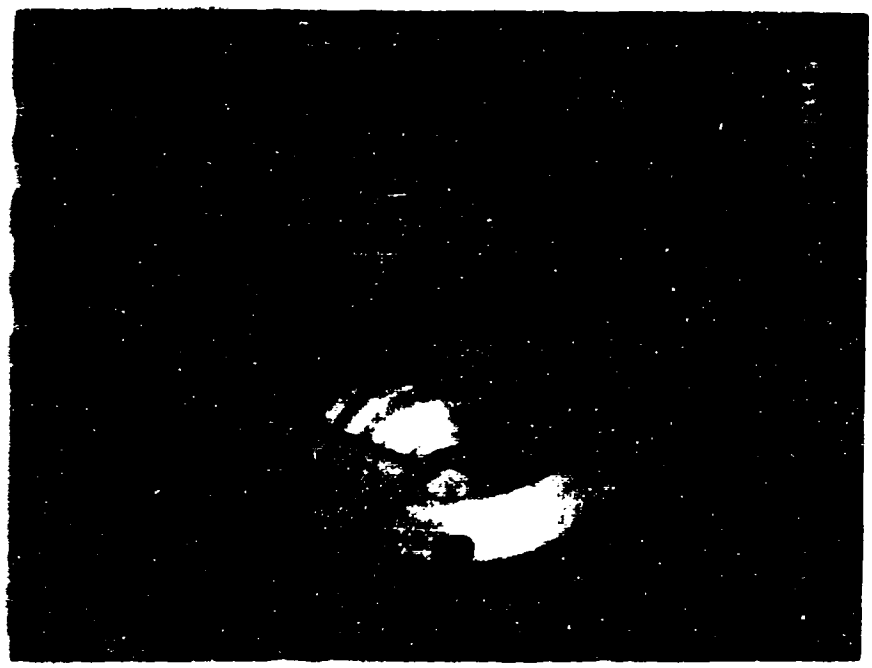


Figure A-3. Interior of a Spark Gap Chamber Showing Arc Pits on the Wall

Once assembled and mounted on the accelerator frame, the spark-gap chamber was not available to visual inspection. Hence, the difficulty was not discovered at an early time and it seriously affected the experimental progress. It was finally rectified by changing the direction and outflow path of the cooling gas.

The firing of the gaps can be monitored by a simple, insulated, wire probe hooked over the pulse transformer lead marked P (refer to Figure A-2). Typical oscillograms of the signal from this probe are shown in Figure A-4. The linear ramp is the output of the pulse transformer. The sudden end of the ramp indicates that the gap fired. In one of the three traces the gap is seen to fire earlier than in the others. These variations were never fully explained, but they were observed to occur frequently when the electrodes were new, clean, and polished but only infrequently after the electrodes had experienced several hundred operations with the full capacitor voltage applied. No capacitor voltage was applied in Figure A-4.

Figure A-5 shows the same spark-gap with high voltage applied to the associated energy-storage capacitor (and with the oscilloscope polarity reversed). Each trace is actually a superposition of three traces in order to measure the jitter of the firing time. The oscillograms show No. 2 spark gap with No. 1 already operating. The jitter is seen to be about ±0.1 microsecond, and the time of actual firing is seen to be quite difficult to determine. Nevertheless, such oscillograms, taken for each gap of the machine, had to be used to determine whether the timing was correct.

Tests were made to determine whether irradiation with ultraviolet light could stabilize the spark gaps and reduce the firing jitter. A significant improvement was not found.

Toward the end of the Mark I experiments the timing jitter seemed to be consistently less than ±0.07 microsecond and frequently less than ±0.03 microsecond.

The maximum repetition rate of the firing was less than one per minute.

3. THE TIMING AND CONTROL CIRCUITS

A schematic diagram of the major timing and control circuit is shown in Figure A-6. The circuit uses 2D21 thyratrons. The



Figure A-4. Oscillograms Showing Firing of Spark Gaps
(1 μ sec per Division, 20, 000 Volts per Division)



Figure A-5. Oscillograms Showing Firing of Spark Gaps
(With Capacitor High Voltage Applied)

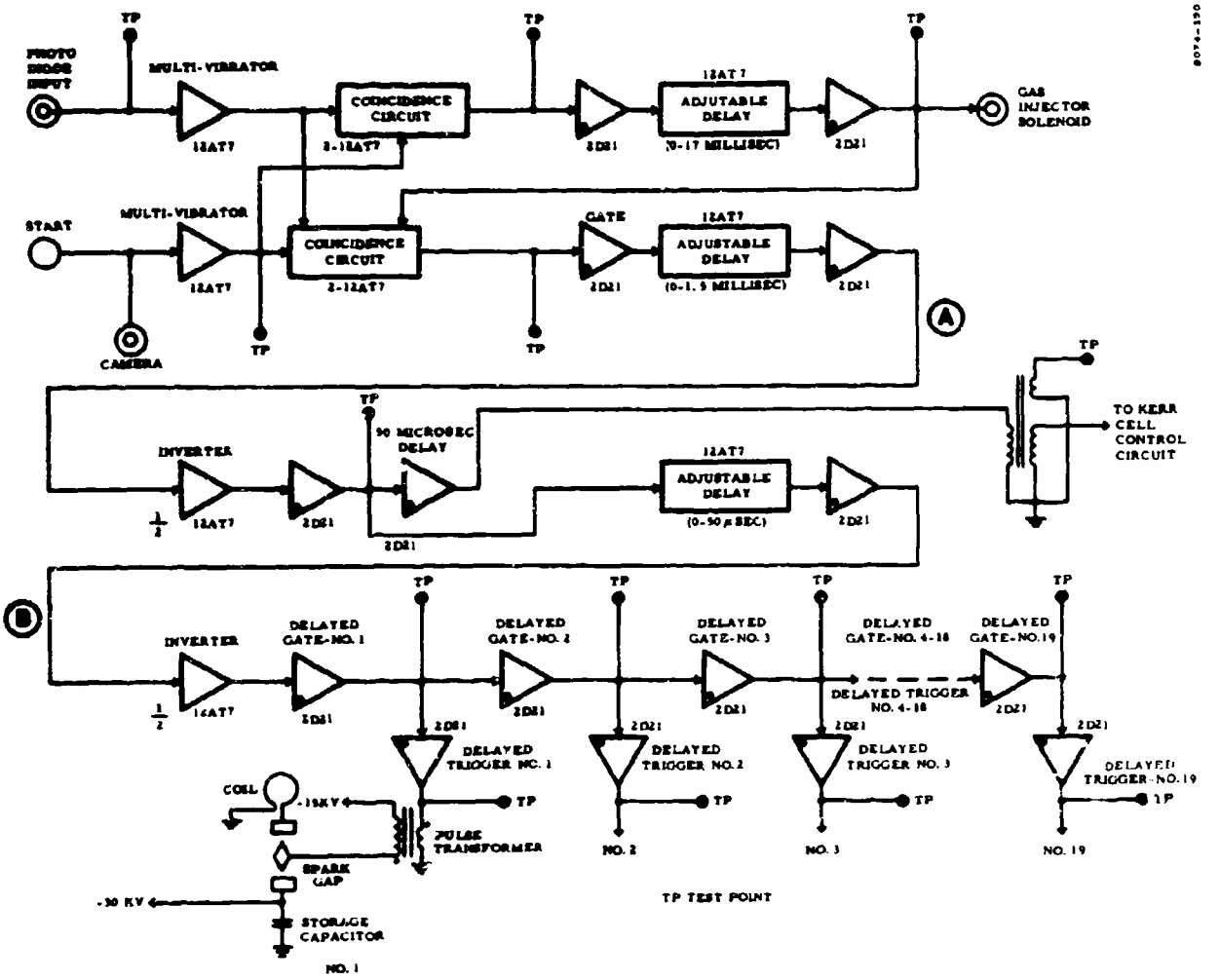


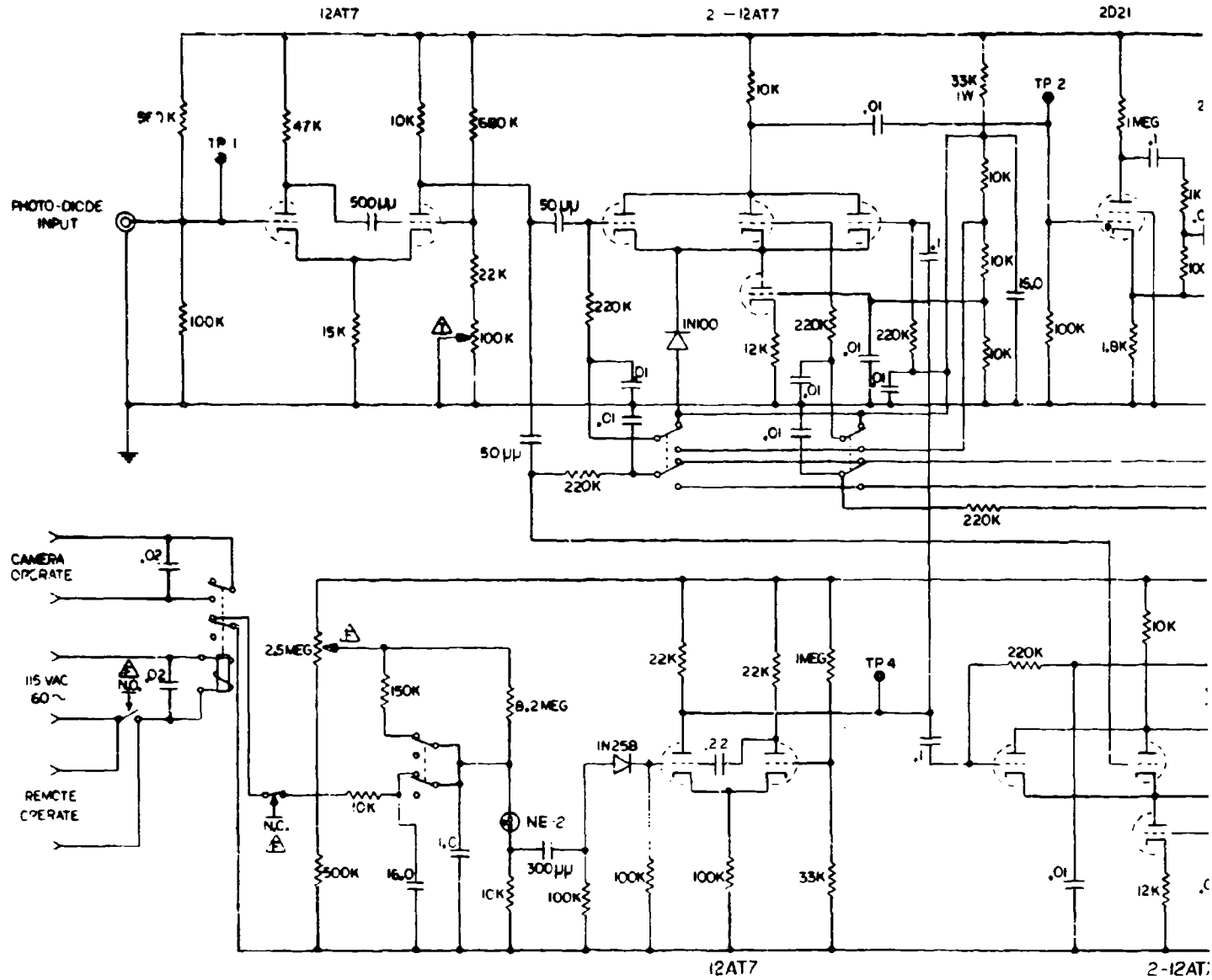
Figure A-6. Schematic of Timing and Control Circuit

adjustable delay generators are modified multivibrators. The fixed delay generators are LC ringing circuits. The action of the circuit is as follows:

1. When the start button is pushed all mechanical camera shutters are opened, the upper coincidence circuit is armed, and the lower one is partially armed.
2. The photodiode signal occurs when a rotating shutter in the gas injector is aligned with certain gas-conducting channels. This occurs every 17 milliseconds. Upon receipt of the first photodiode signal after being armed, the upper coincidence circuit actuates a sequence of events leading to loading of the gas injector of the accelerator. This sequence takes several milliseconds and when completed, a second arming signal is passed to the lower coincidence circuit to complete the arming of the latter.
3. The next photodiode signal coincides with injection of gas into the accelerator and causes the lower coincidence circuit to begin the coil-timing sequence and also causes actuation of the timing circuit for a Kerr cell camera shutter.
4. When the first coil fires the timing circuit for the second is actuated and so on.
5. The firing of the whole set of coils is variable with respect to the Kerr cell, the timing of the latter being fixed.

The section of the circuit down to the point marked (A) (Figure A-6) is shown in detail in Figure A-7. The section between (A) and (B) is shown in detail in Figure A-8 and the remainder in Figure A-9.

In connection with Figure A-9 it is to be noted that the 2D21 thyratrons in the coil-timing series draw some 50 amperes apiece when they operate. This is five times larger than the conventional rating of these tubes, but they nevertheless operate satisfactorily. No failure ever occurred.


12AT7
2 — 12AT7
2D21
PHOTO-DIODE INPUT
TP 1
TP 2
TP 4
47K
10K
680K
500µµ
50µµ
22K
100K
15K
220K
IN100
12K
.01
.1
33K 1W
1MEG
16.0
1.8K
CAMERA OPERATE
.02
115 VAC 60~
N.O.
.02
REMOTE OPERATE
N.C.
2.5MEG
150K
8.2MEG
10K
500K
1.0
NE-2
300µµ
IN258
.22
22K
1MEG
33K
12K
12AT7
2-12AT

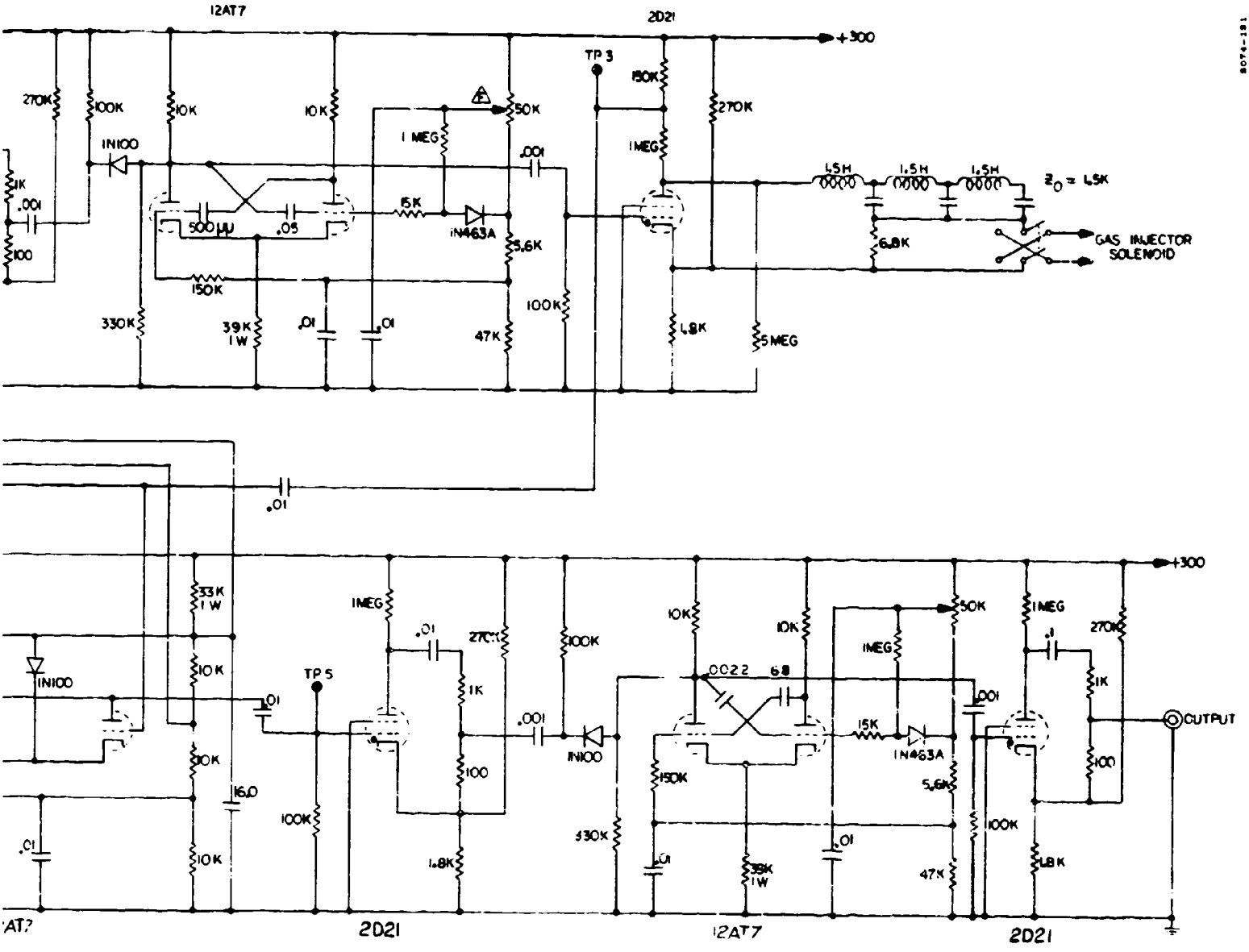
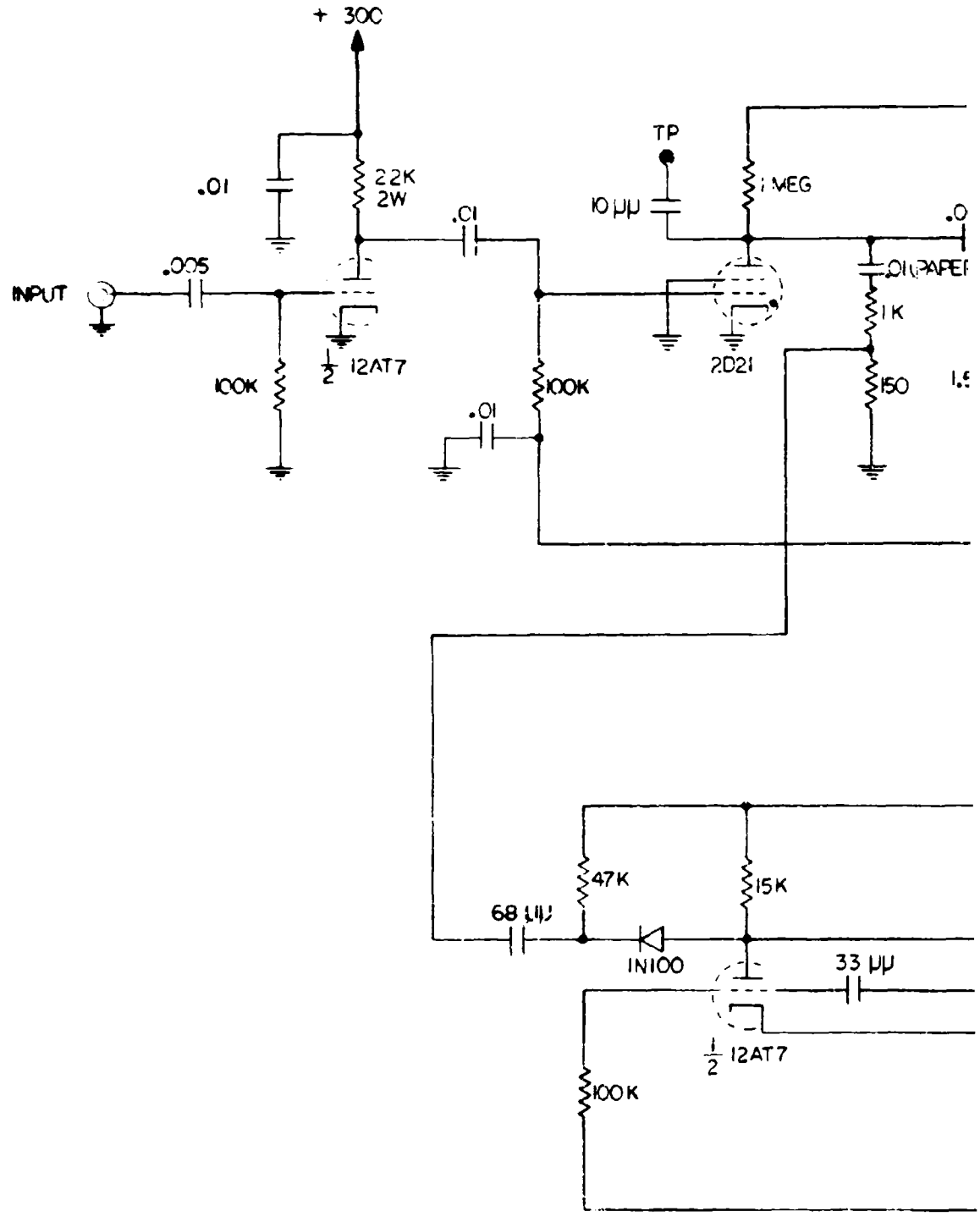


Figure A-7. Schematic of Timing Circuit


+ 300
.01
22K
2W
.01
TP
10 μμ
1 MEG
.005
INPUT
100K
½ 12AT7
100K
.01
2D21
1K
150
47K
15K
68 μμ
IN100
33 μμ
½ 12AT7
100K

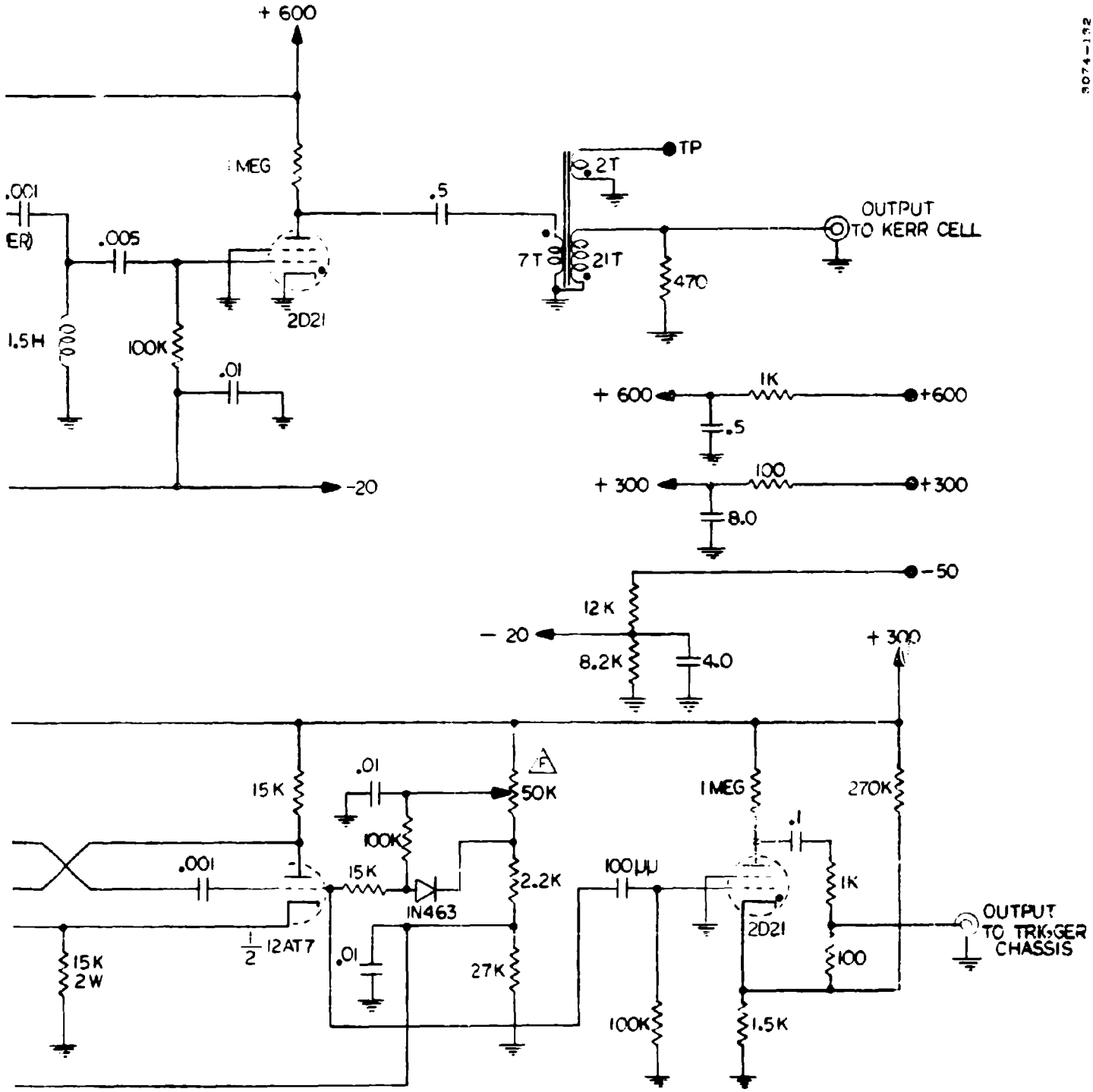
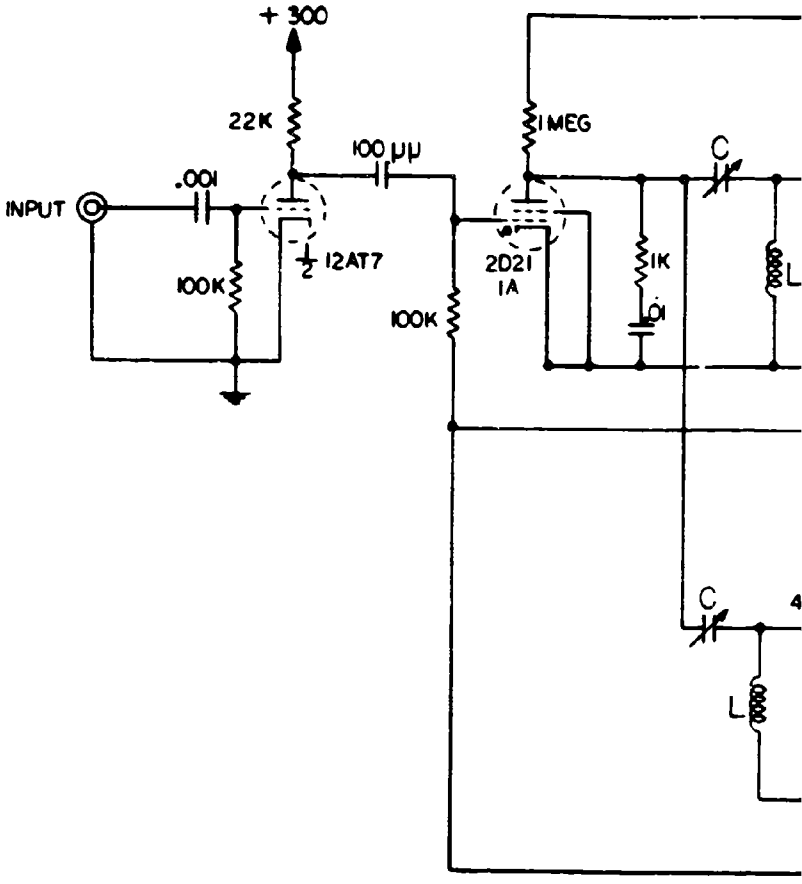
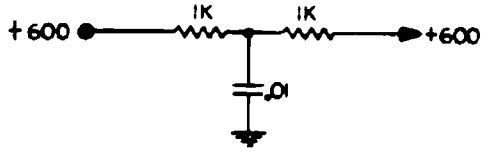
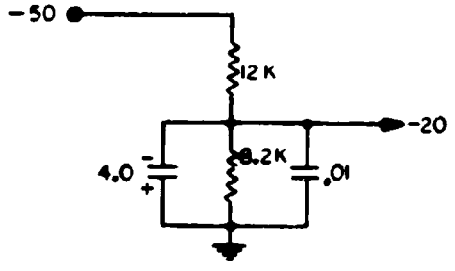


Figure A-8. Kerr Cell Timing Chassis Schematic


+ 300
22K
100 μμ
1 MEG
.001
INPUT
100K
1/2 12AT7
2D21
1A
1K
.01
100K
C
L
C
L


+600
1K
1K
+600
.01


-50
12K
-20
4.0
8.2K
.01

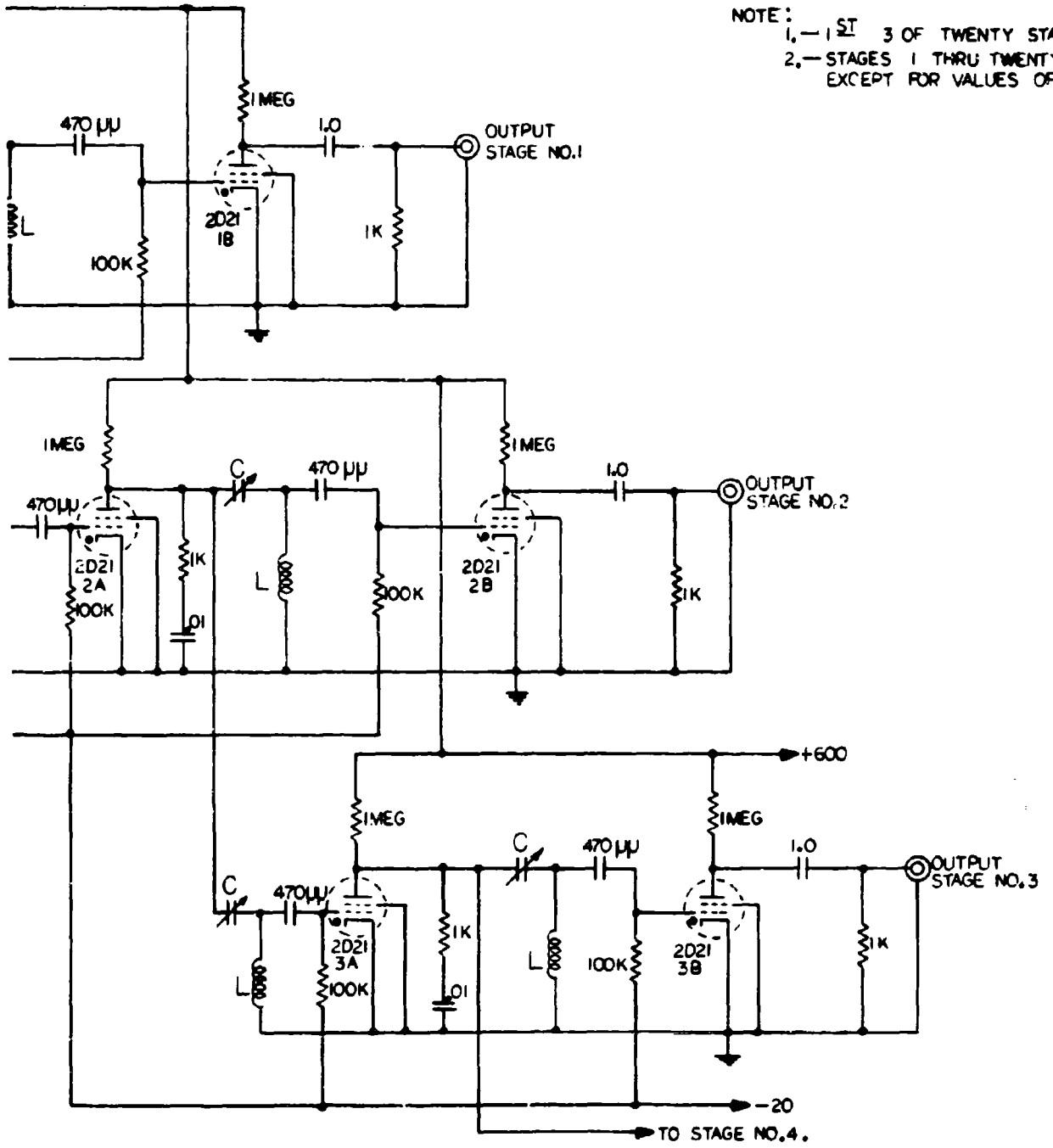


Figure A-9. Schematic of Trigger Circuits

APPENDIX B
EPOXY ENCAPSULATION TECHNIQUE

APPENDIX B

EPOXY ENCAPSULATION TECHNIQUE

1. DESCRIPTION OF THE PROBLEM

The design of the spark gap and its associated pulse transformer (Figure B-1) called for these parts to be encapsulated in an epoxy resin. In order to maintain proper spacing and alignment of the components and to achieve the desired electrical insulation, it was necessary to use an epoxy having the following properties:

1. Low shrinkage without internal stress
2. Good impact resistance
3. No breakdown despite 100% voltage reversal

After some investigation of commercial epoxies, a product (Scotchcast #235, Minneapolis Mining and Manufacturing) was found that, according to the manufacturers claims, had the desired properties and also had long pot life and low viscosity at pouring temperatures. The only undesirable property found was the toxicity of the fumes. A well-ventilated fume cupboard overcame this difficulty.

This epoxy (Scotchcast #235) was tested by potting six 0.025-inch spark gaps and subjecting them to sudden voltage changes of about 60 kv through the use of one of the accelerator stages. All six gaps passed these tests successfully.

2. THE SOLUTION

The use of epoxy required special techniques to avoid the presence of trapped gas bubbles that seriously affected the mechanical and electrical properties. A technique for outgassing the epoxy was developed after considerable effort. This technique involved the following steps.

1. Mix the two-component epoxy; pump, while stirring, to a hard vacuum (about 10 microns) for a period of at least one hour.

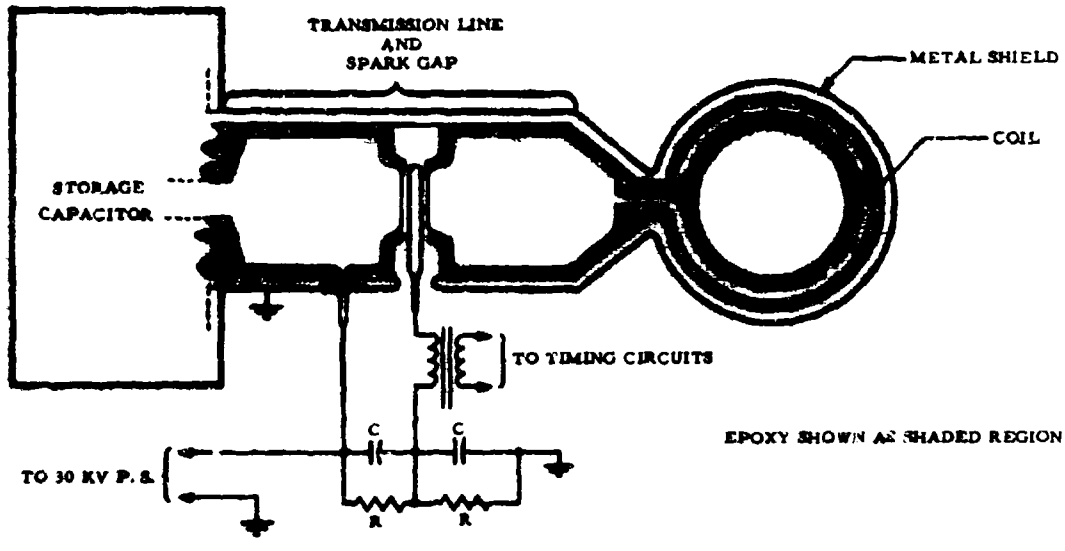


Figure B-1. Coil-Capacitor Assembly

During the pumping period the temperature of the epoxy is held to about 80 C.

2. Preheat the mold to 80 C.
3. Allow the epoxy to enter the mold only after it has flowed over a large area that exposes as much surface as possible to the vacuum.
4. Pour into the mold under vacuum, injecting the epoxy from the bottom of the mold.

The following components were potted separately by the above-cited procedure.

1. Coils (19 in all)
2. One-half of each transmission line (19 in all)
3. One-half of the transmission line potted and joined with epoxy to the storage capacitor (19 in all)
4. Pulse transformer required for each spark gap (19 in all)

The apparatus and procedure for encapsulation is described with the aid of Figure B-2, which shows the equipment used. Referring to Figure B-2, the epoxy enters through the preheated copper tube, A, runs into the baffled trough, B, and finally into the plastic tube, C, to the bottom of the mold. The lamp, E, provides a heat source to maintain the epoxy temperature as it runs over the baffled trough. The lamp, E, is an extremely important part of the apparatus and should not be omitted. The bell jar, F, which encloses the entire assembly, is pumped to the best vacuum that a mechanical pump can obtain. When the mold is full, the vacuum is broken and the plastic tube, C, is tied and cut. It remains on the mold until curing is complete. The coil molds proved to present the most serious problems because of the narrow neck between the coil and the transmission line cylinder. This was also the most critical section because of the high impact loading when the capacitor was discharged through the spark gap and coil.

Once the epoxy technique had been perfected there were no more failures due to bubbles in the molded material.

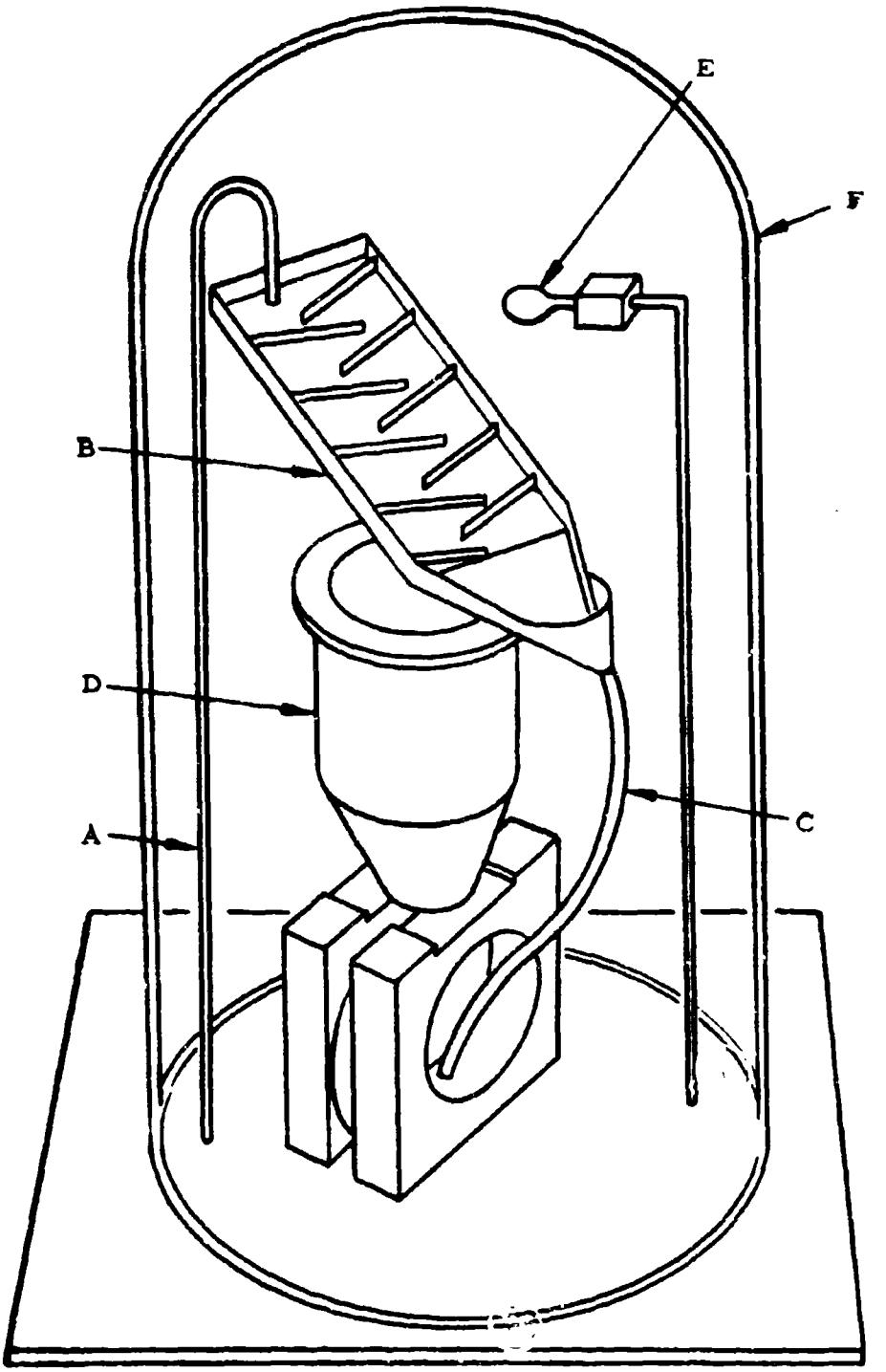


Figure B-2. Apparatus for Vacuum Pouring of Epoxy

APPENDIX C

PARTICLE MOTION IN AN AXIALLY SYMMETRIC MAGNETIC FIELD

NOTE

This appendix contains a reprinting of a document first published in 1960 as AFOSR TN 60-841 and subsequently issued as Litton TM 61-25.

The document represents a step in the development of a theoretical model. It contains information not included in the main text of this report.

Publication No. 2402

Technical Memorandum 61 - 25

PARTICLE MOTION IN AN AXIALLY SYMMETRIC MAGNETIC FIELD

by

Alan S. Penfold

June 1961

This document contains proprietary information of Litton Systems, Inc. Any reproduction, use and/or disclosure of this document and/or any portions thereof for purposes other than evaluation is expressly prohibited without the prior written consent of Litton Systems, Inc.

LITTON SYSTEMS, INC.
Space Sciences Laboratory
336 North Foothill Road, Beverly Hills, California

CONTENTS

I INTRODUCTION. 1

II PRELIMINARY CONSIDERATIONS 3

III PARTICLE EQUATIONS OF MOTION. 5

IV MOTION IN A STATIC FIELD 13

V MOTION IN A TIME-DEPENDENT FIELD 23

5.1 Introduction 23
5.2 Energy Transfer 27
5.3 Motion for ϕ (o) = 0 28
5.4 Motion for ϕ (o) $\neq$ 0 31

VI PARTICLE COLLISIONS 39

VII CONCLUDING REMARKS 41

FOREWORD

This technical memorandum presents a study by Alan S. Penfold, made under contract AF 49(638)-759 for the Air Force Office of Scientific Research. Its distribution provoked an extensive interest, as reflected in the numerous requests received for the document or for information from the document; therefore, it has been reprinted in technical memorandum form.

ABSTRACT

A description of the motion of charged particles in an electromagnetic field is given. The method can be applied whenever the field possesses a certain type of rotational symmetry about one axis. A cylindrical coordinate system is employed and the radial, axial, and circumferential motions of a particle are shown to be completely describable in terms of a scalar potential of position and time. The potential also depends on the initial angular momentum of the particle with respect to the axis of symmetry. One of the advantages of the description is that it allows an easy visualization of the primary features of the motion. When applied to a magnetic dipole field, the method is found to yield a potential which is very closely related to one which has already been used by Störmer. The application of the method to the initial phases of the ionization of a tenuous gas is discussed.

I INTRODUCTION

It will be shown that the motion of a charged particle in an electromagnetic field is, under certain circumstances, completely described by a scalar potential which depends on position and time, and also on the "launch" conditions of the particle. This potential gives rise to a type of electric field which couples directly to the charge of the particle. The potential applies equally well to static or to time-dependent fields and the latter may be either stationary or moving.

Through the use of the method a very considerable insight into the behavior of charged particles in an electromagnetic field can be achieved. Exact solutions to the equations of motion are, however, no easier to obtain by this method than by other methods.

The method is first developed and certain immediate results are discussed. The method is then applied to motion in a static magnetic field and some illustrative examples are given. Next, the method is applied to motion in time-dependent magnetic fields and particular attention is paid to the question of energy transfer from simple coil arrays to a particle moving near the coils. The application of the method to a determination of the initial phases in the electrical breakdown of a tenuous gas is discussed.

The MKS system of units is employed throughout.

The work to be discussed is actually a generalization of some results which have already been obtained by Störmer [1, 2]

II PRELIMINARY CONSIDERATIONS

Consider a cylindrical co-ordinate system with unit vectors $\hat{r}$, $\hat{\theta}$, $\hat{z}$ and take the z-axis as an axis of symmetry. Suppose an electromagnetic field pattern which is described by a vector potential, $\vec{A}$, and a scalar potential, X. These potentials are assumed to have the following form:

$$\vec{A} = \hat{\theta} A(r, z, t) \tag{1a}$$

$$X = X(r, z, t) \tag{1b}$$

From these potentials and the equations $\vec{B} = \text{Curl } \vec{A}$, $\vec{E} = -\partial\vec{A}/\partial t - \nabla X$ one obtains the field components

$$B_r(r, z, t) = -\frac{1}{r}\frac{\partial(rA)}{\partial z} \tag{2a}$$

$$B_z(r, z, t) = \frac{1}{r}\frac{\partial(rA)}{\partial r} \tag{2b}$$

$$E_r(r, z, t) = -\frac{\partial(X)}{\partial r} \tag{2c}$$

$$E_z(r, z, t) = -\frac{\partial(X)}{\partial z} \tag{2d}$$

$$E_\theta(r, z, t) = -\frac{\partial(A)}{\partial t} \tag{2e}$$

Equation (2b) can be integrated from r = 0 to r = r. The result, if B_z (r = 0) is finite, is:

$$rA \equiv \phi(r, z, t) = \int_0^r dr\, r B_z \tag{3}$$

From (2e) and (3) one obtains the usual equation

$$E_\theta = -\frac{1}{r} \frac{\partial(\phi)}{\partial t} \tag{4}$$

The above equations describe the field which will be employed throughout. Aside from a factor of 2π, the quantity ϕ is the flux which passes through a circle of radius r at position z and time t. It is also to be noted that the relationship, Div $\vec{A} = 0$, holds.

III PARTICLE EQUATIONS OF MOTION

For a particle of charge q and relativistic mass M, and momentum $\vec{P}$

$$\frac{d\vec{P}}{dt} = q\left[\vec{v} \times \vec{B} + \vec{E}\right] \tag{5}$$

and one obtains from this equation the component equations of the motion, which are:

$$\frac{dP_r}{dt} = \frac{q}{M} P_\theta B_z + \frac{P_\theta^2}{Mr} + qE_r \tag{6a}$$

$$\frac{dP_z}{dt} = -\frac{q}{M} P_\theta B_r + qE_z \tag{6b}$$

$$\frac{1}{r}\frac{d(rP_\theta)}{dt} = q\left[\dot{z} B_r - \dot{r} B_z + E_\theta\right] \tag{6c}$$

The last equation was derived from the fact that $\dot{r}P_\theta = r\dot{\theta}P_r$.

Substitution of equations (2) into equation (6c) results in:

$$\frac{d(rP_\theta)}{dt} = -q\left[\frac{\partial(rA)}{\partial z}\dot{z} + \frac{\partial(rA)}{\partial r}\dot{r} + \frac{\partial(rA)}{\partial t}\right] \tag{7}$$

The quantity in the square brackets in equation (7) is the total derivative of rA with respect to time, and hence the equation can be easily integrated. Before doing this, however, use is made of equation (3) by letting $\phi = rA$;

then, on integrating with r_o, z_o, t_o as the initial conditions, one obtains:

$$P_\theta = -\frac{q}{r}\left[\phi - \phi(o) - \frac{r_o P_\theta(o)}{q}\right] \qquad (8)$$

In the above equation $P_\theta(r_o, z_o, t_o)$ has been denoted by $P_\theta(o)$; and similar meaning is implied by the notation $\phi(o)$; because of the assumed symmetry, the initial value of θ does not appear explicitly.

Aside from a factor of 2π, $\phi(r, z, t)$ is the flux which the particle "encloses" to the axis of symmetry. Hence, equation (8) gives the result that the change in the angular momentum of a particle is proportional to the change in the amount of flux which the particle "encloses." Such a relationship for static fields is well-known in the field of electron optics where it is sometimes called Busche's theorem. Equation (8) is a generalization of this theorem to include time-dependent fields.

There are two types of electric fields present: an "inductive" field arising from the vector potential, $\vec{A}$; and a "capacitive" field arising from the scalar potential, X. It is interesting that neither field appears explicitly in the equation for P_θ. It should also be noted that the equation is relativistically correct.

Equation (8) is applicable to measuring the operating energy of a betatron. In such an application the momenta in the r and z directions are usually completely negligible and so $P_\theta(o)$ would equal the momentum of the electrons at injection and P_θ, the momentum as they strike the X-ray target. By integrating the voltage induced in two turns of wire ϕ and $\phi(o)$ can be obtained; one having the same radius as the injector filament, and the other having the same radius as the tip of the X-ray target.

Equations for the r and z motions of the particle can be determined by substituting equation (8) into equations (6a) and (6b). Before presenting the results, a scalar potential, V, will be defined because with this

definition, the results can be expressed in a compact and useful form,

$$V \equiv \frac{q}{2Mr^2}\left[\phi - \phi(0) - \frac{r_o P_\theta(o)}{q}\right]^2 \qquad (9)$$

The unit of V is the volt since the MKS system is being employed. V is unlike the usual type of scalar potential in that it depends explicitly on the initial angular momentum of the particle. In spite of this, it can be regarded as a real potential and not just a quantity having meaning only at the coordinates r, z, t of the particle. For example, it will be seen that -grad V is a type of electric field which couples to the particle through its charge, q, to produce motion in the r and z directions. The equations for this motion are derived by substituting equation (8) into equations (6a) and (6b) to obtain:

$$\frac{dP_r}{dt} = -q\frac{\partial}{\partial r}\left[V + X\right] \qquad (10a)$$

$$\frac{dP_z}{dt} = -q\frac{\partial}{\partial z}\left[V + X\right] \qquad (10b)$$

Inasmuch as V arises from the interaction of a charge with a magnetic field it can be called an "inductive potential." Because V is a potential it combines additively with the "capacitive potential" X.

Consider now an r - z plane on which is drawn a Cartesian coordinate system with unit vectors $\hat{a}_r$ and $\hat{a}_z$. The momentum of the particle in this system is denoted by $\vec{Q}$.

$$\vec{Q} = \hat{a}_r P_r + \hat{a}_z P_z \qquad (11)$$

This r - z plane is taken to coincide exactly with the plane $\theta = 0$ of the original cylindrical coordinate system, and it will be called the "plane of projected motion." If the coordinates of a particle in the original

system are r, θ, z then it has coordinates r, z in the projected system. Figure 1 shows these relations.

Equations (10) can be combined into a single vector equation in the projected system.

$$\frac{d\vec{Q}}{dt} = -q \operatorname{grad}(V + X) \tag{12}$$

The momentum perpendicular to $\vec{Q}$ has already been given by equation (8), but it can be re-expressed in terms of V.

$$\left| P_\theta \right| = \left[2Mq\, V \right]^{1/2} \tag{13}$$

The sign of P_θ can be determined by reference to equation (8).

A relativistically correct equation for the rate of change of the total energy, T, can easily be obtained. If c is the velocity of light, then:

$$T\frac{dT}{dt} = \frac{c^2}{2} \frac{d}{dt}\left[\vec{Q} \cdot \vec{Q} + P_\theta{}^2 \right] \tag{14}$$

Through the use of equations (12) and (13) one finds:

$$T\frac{dT}{dt} = Mqc^2 \left[\frac{1}{M} \frac{\partial (VM)}{\partial t} + \frac{\partial X}{\partial t} - \frac{dX}{dt} \right] \tag{15}$$

The equations just presented give a complete description for the motion of a charged particle in the electromagnetic field. In order to get a solution for the motion one must solve equation (12) and this is usually a difficult task. However, a knowledge of V and X allows one to draw contours of constant V + X on a projected coordinate system, and a study of these contours usually gives a good qualitative picture of the motion. Furthermore, it may also happen, that a study of these contours will suggest a suitable approximate method for obtaining a quantitative knowledge of the motion.

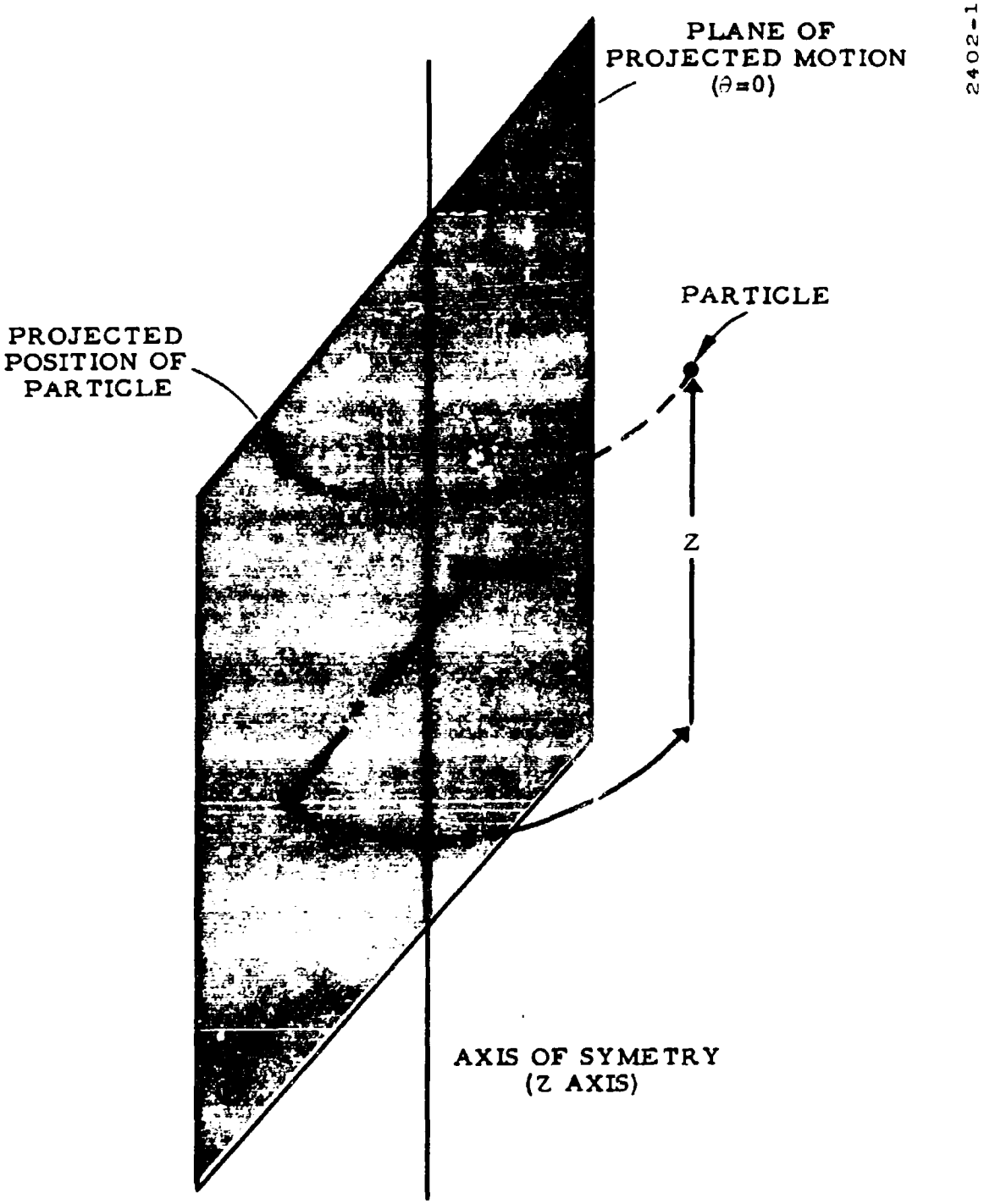


Figure 1. Diagram to Define the Plane of Projected Motion

In equation (9), which defines V, the sign of V is always the same as that of the charge of the particle. However, in equation (12), V is multiplied by q; thus the direction of the force which V exerts on a particle is independent of the sign of q. This is not true for motion in the θ-direction, however, as can be seen from equation (8).

In the original coordinate system, the minimum value for r is r = 0, which corresponds with the axis of symmetry of the fields. In the newly-defined, projected coordinate system r can assume negative values as well as positive ones. This situation can be handled in a very simple fashion by the definition

$$V(r, z, t) = V(-r, z, t) \tag{16}$$

which will be true if the defining equation for ϕ (equation (3)) is changed to:

$$\phi \equiv \int_0^{|r|} dr\, r\, B_z \tag{17}$$

In all situations of practical importance the magnetic field, B_z is finite on the axis of symmetry and so $\phi/r \to 0$ as $r \to 0$. The net result of this for the inductive potential is either

$$V \to 0 \qquad \text{as} \qquad r \to 0 \tag{18}$$

or

$$V \to \infty \qquad \text{as} \qquad r \to 0 \tag{19}$$

As can be seen from equation (9) the former value at r = 0 is obtained only if $\left[q\phi(o) + r_o P_\theta(o) \right] = 0$ which is a very special case. It is only for this case, furthermore, that the definition of V for negative values of r has any significance. In all other cases the particle can never pass through r = 0 because, for it to do so, it would have to have an infinite energy.

The capacitive potential, X, has been included in the formalism largely for reasons of completeness. In the discussions to follow X will frequently be set equal to zero and the discussions will concern the inductive potential only.

The relation between the inductive potential and the vector field potential, $\vec{A}$, is given through equations (3) and (9).

IV MOTION IN A STATIC FIELD

In the following discussions X is set equal to zero. If, in addition, $\vec{A}$ does not depend on time (therefore $\vec{B}$ does not depend on time) then equation (15) gives:

$$\frac{dT}{dt} = 0$$

This equation expresses the well-known result that the energy of a particle cannot be changed by a static magnetic field.

For convenience equation (9) defining V is given again:

$$V \equiv \frac{q}{2Mr^2}\left[\phi - \phi(o) - \frac{r_o P_\theta (o)}{q}\right]^2 \qquad (9)$$

One of the interesting features of V occurs when V = 0; this happens at all values of r and z for which:

$$\phi = \text{constant} = \phi(o) + \frac{r_o P_\theta (o)}{q}$$

The zero of V is also a minimum value and hence V has the form of a valley and the floor of this valley (V = 0) exactly follows a magnetic-field line.

The maximum value of V that can be reached by the particle occurs when $\vec{Q}$ is zero and all the motion is in the θ-direction. From equation (13), one finds V max to be:

$$V_{max} = \frac{1}{q}\left[\frac{T^2 - M_o^2 c^4}{2T}\right] \tag{20a}$$

where c is the velocity of light, M_o is the rest mass of the particle, and T is the total energy. If the energies are given in electron volts then the factor q^{-1} can be dropped and V_{max} is given in volts. If, during its motion in the potential valley, the particle ever reaches such a value of r and z that $V = V_{max}$ then $\dot{r} = \dot{z} = 0$ and so the particle is at a turning point. From (13), (14), and (20) it can be shown that

$$|\vec{Q}| = \left[2Mq(V_{max} - V)\right]^{1/2} \tag{20b}$$

Since the contour $V = 0$ is a field line, and since $\text{div}\,\vec{B} = 0$, it follows the contour closes on itself. This behavior is illustrated in Figure 2.

Figure 2 shows a sketch of V-contours as they appear around a solenoid for the case that $V = 0$ within the field pattern. As discussed above, the $V = 0$ contour closes on itself. Somewhere outside the coil there is a contour, $V = V_o$, which has a shape like that shown in Figure 2. A particle which begins its motion within the solenoid will, in general, eventually find its way to the outside region. It can then escape from the field if by equation (20)

$$V_{max} > V_o \tag{21}$$

but it is indefinitely trapped in the field if:

$$V_{max} < V_o \tag{22}$$

The point where the contour $V = V_o$ crosses itself is a saddle point. These facts are made clearer by a study of Figure 3 which shows two cross sections of the potential pattern. Figure 3a shows the cross

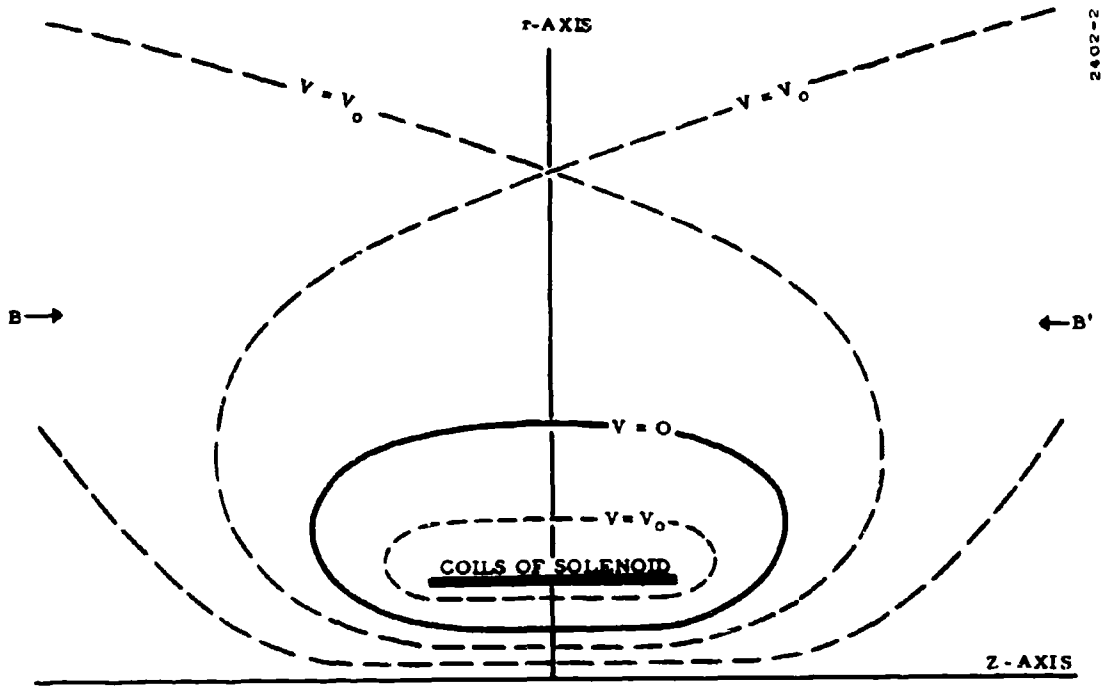
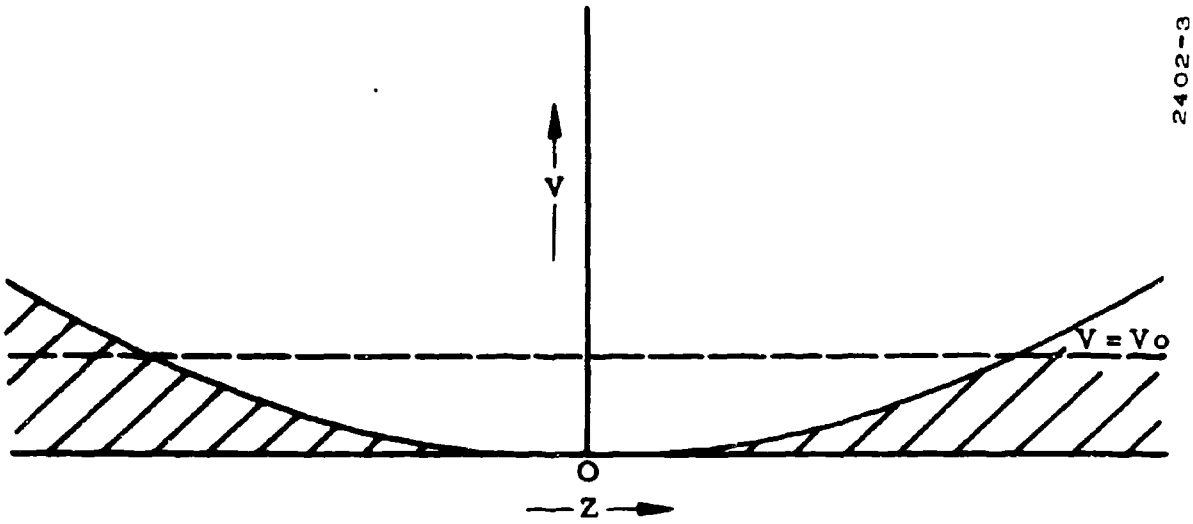
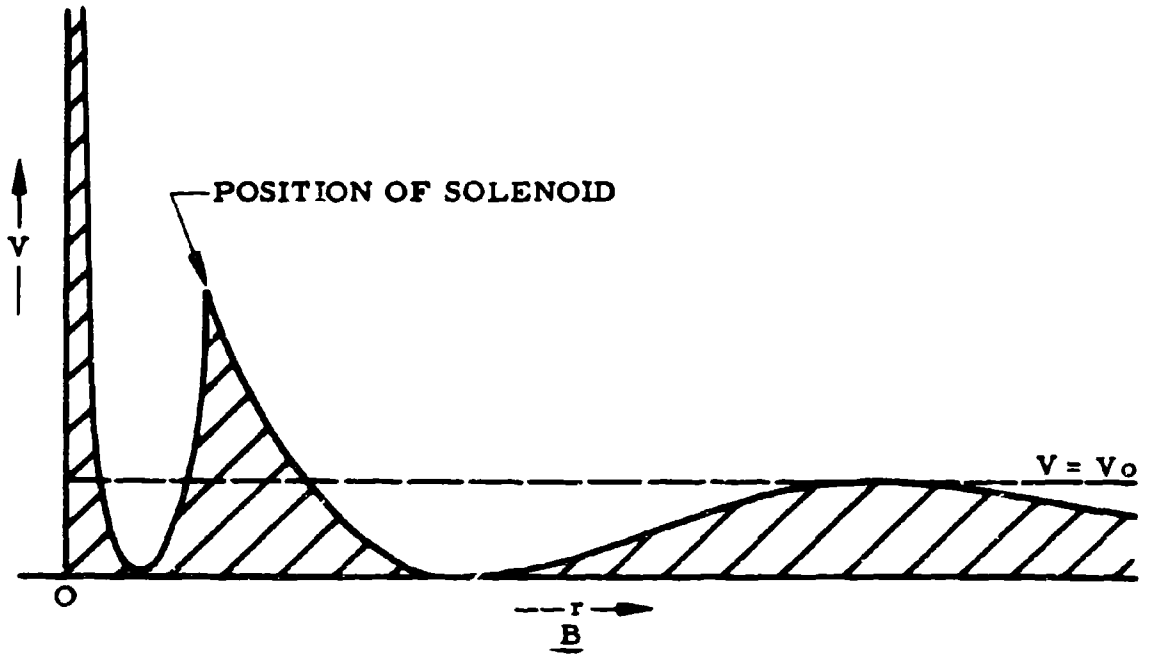


Figure 2. An Inductive Potential Pattern for a Solenoid



A



B

Figure 3. Cross Sections of an Inductive Potential Pattern for a Solenoid

section taken along the line BB' in Figure 2. Figure 3b shows a cross section taken along the line z = 0 in Figure 2.

Beside the type of potential pattern shown in Figure 2, there is another which can be obtained. This type occurs if V has a stationary value but no zero. A stationary value of V occurs if there is a point in the field at which the following conditions hold:

$$r^2 B_z = \phi - \phi(o) - \frac{r_o P_\theta (o)}{q} \tag{23a}$$

$$B_r = 0 \tag{23b}$$

Figure 4 shows a sketch of a potential pattern for the same solenoid as in Figure 2, but for the condition that V has a stationary value for which $V \neq 0$. The stationary point is seen to be a saddle point, and also it is seen that particles cannot now be trapped in the field.

When there is no place within the field at which V = 0 then, by equation (13), there is no place at which $P_\theta = 0$; hence, P_θ never changes sign. This in turn means that the particle can gyrate about the axis of symmetry, but it can never gyrate about an off-axis field line.

The various types of potential patterns which can occur for the solenoid of Figure 2 are listed in Table I. Although there are only two basic types, these can become modified by the presence of the solenoid.

The potential patterns shown in Figures 2 and 4 resemble, in many respects, the patterns which obtain for the field of a magnetic dipole (e.g. the earth's field). The major difference is that, for a dipole, there is no "inside" region - that is, no region where $r < r_{sol}$. There is, however, the possibility of having a saddle point as in the example of Figure 2 and, hence, there

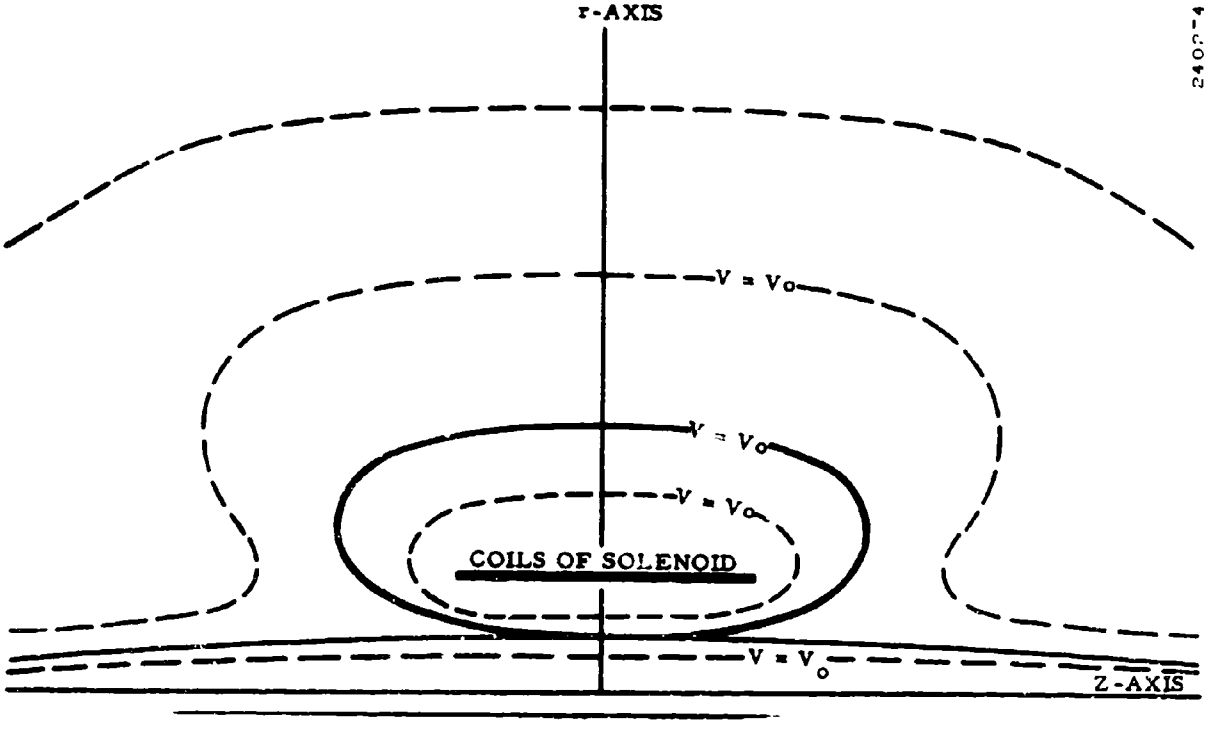


Figure 4. An Inductive Potential Pattern for a Solenoid

TABLE I

TYPES OF POTENTIAL PATTERNS WHICH CAN OCCUR FOR THE SOLENOID OF FIGURE I

All characteristics refer to the line Z = 0

$\frac{1}{\phi}\left[\phi(o) + \frac{r_o P_\theta(o)}{q}\right] < 0$		$\left[\phi(o) + \frac{r_o P_\theta(o)}{q}\right] = 0$		$\frac{1}{\phi}\left[\phi(o) + \frac{r_o P_\theta(o)}{q}\right] > 0$	
$r < r_{sol}$	$r > r_{sol}$	$r < r_{sol}$	$r > r_{sol}$	$r < r_{sol}$	$r > r_{sol}$
V has a stationary value $\neq 0$ for $0 < r < r_{sol}$	V has no stationary values	V = 0 at r = 0	V has no stationary values	V has a zero for $r_{sol} > r > 0$	V has a zero and a stationary value
V has a stationary value $\neq 0$ for $r = r_{sol}$				V has a zero at $r = r_{sol}$	V has a zero at $r = r_{sol}$ and a stationary value at $r > r_{sol}$
V has no stationary value				V has no stationary value	V may or may not have a stationary value

r_{sol} = value of r at solenoid

is the possibility of having particles trapped in the earth's field. In such a case particles can hit the earth's surface at positions near the magnetic poles.

For a dipole of strength "a" (i.e. the magnetic potential, A_θ, is $ar/(r^2 + z^2)^{3/2}$) the inductive potential is:

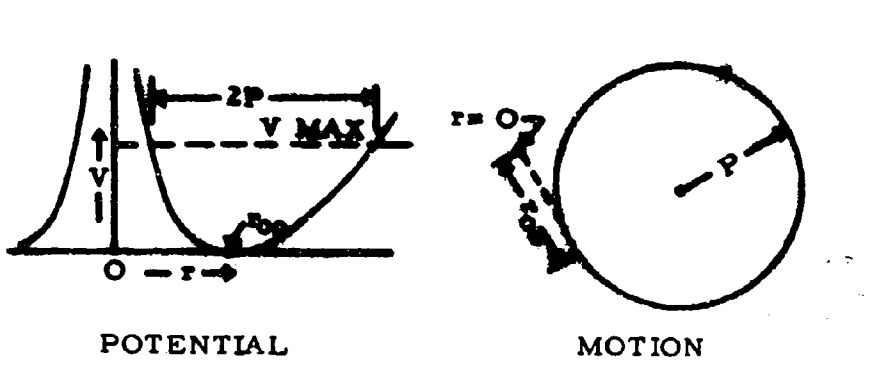
$$V = \frac{q}{2Mr^2}\left[\frac{ar^2}{(r^2 + z^2)^{3/2}} - \frac{ar_o^2}{(r_o^2 + z_o^2)^{3/2}} - \frac{r_o P_\theta(o)}{q}\right]^2 \qquad (24)$$

It is easily shown that this potential is very closely related to that which has been used by Stormer and others [1, 5, 6] to illustrate the orbits of cosmic-ray particles.

The inductive potential, drawn for the earth's field, makes very clear the various allowed and forbidden regions discussed by cosmic-ray physicists.

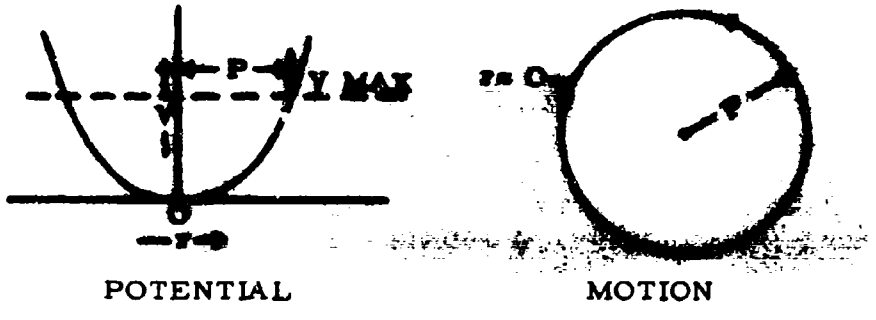
As another example of particle motion in a static magnetic field, a uniform field is considered in the z-direction ($B_r = 0$) with $\dot{z} = 0$. The inductive potential can have any of three forms. These three forms along with the corresponding particle motions are shown in Figure 5. The three potential forms are equivalent to the three major divisions shown in Table I. In each of Figures 5(a) to 5(c) the radius of curvature is denoted by the symbol P. The maximum value of V which the particle can reach, V_{max}, is given by equation (20a). The magnetic field is perpendicular to the plane of the paper in each of the three diagrams of the motion. It is evident from Figure 5(a) that a circle drawn about r = 0, whose radius is equal to the value of r for which V = 0, does not pass through the center of curvature of the motion.

It should be noted that there was nothing in the development leading to the inductive potential which stated that $\phi(o)$ could not be equal to zero.

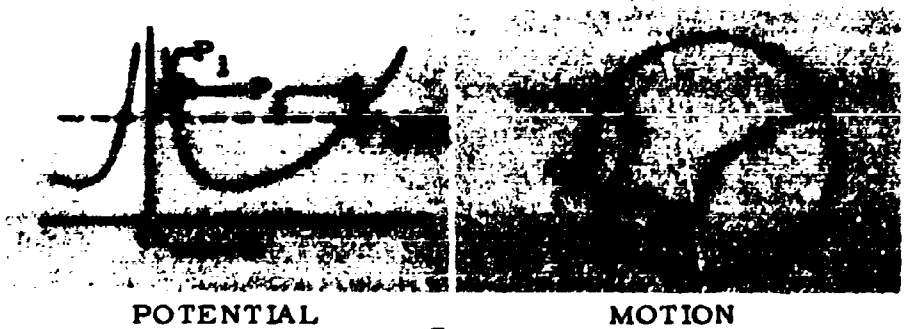


2402-5

A



B



C

Figure 5. Particle Motion in a Uniform Magnetic Field

If it is so, it means that the particle is outside the field pattern at $t = t_o$. Thus the inductive potential patterns may be used to investigate the focussing properties of magnetic fields.

The infinity which V possesses at r = 0 (except under special circumstances) gives rise to some conceptual difficulties. The infinity arises in part from the basic nature of cylindrical coordinate systems since V contains the quantity that is sometimes called a centrifugal potential. For example, if $\phi = 0$ everywhere then the motion is a straight line. However, even in this case, V has an infinity at r = 0 provided that $P_\theta(o) \neq 0$.

So far the capacitive potential, X, has been neglected. Its inclusion will not basically change the potential patterns, however, since X is undetermined to within an arbitary constant.

V MOTION IN A TIME-DEPENDENT FIELD

5.1 INTRODUCTION

The concept of the inductive potential that has been discussed for static fields can be applied, without change, to time-dependent fields. These can be either of two types: stationary fields, for which the time dependence is everywhere the same; or moving fields, for which the time dependence depends on position.

As before, the motion in the r and z directions is described by an inductive potential, V, which now depends explicitly on time. The induced electric field, $E = \frac{\partial}{\partial t}[\phi/r]$, is taken into account by the fact that the whole potential pattern translates. The particles are accelerated in much the same way as a marble, placed in the bottom of a bowl, is accelerated if the bowl is moved. Also, as before, there are two basic types of potential patterns - those for which zeros can exist, and those for which zeros cannot exist. The two examples which have been given (Figures 2 and 4) are valid for time-dependent fields and each can be regarded as a "snapshot" of a potential pattern taken at a given instant of time.

The velocity of the potential contour V will be denoted by $\vec{v}_V$ and will be taken to be, at all points, perpendicular to the contour. The velocity is easily derived and it is found to be:

$$\vec{v}_V = -\left[\frac{\partial V/\partial t}{|\text{grad } V|^2}\right] \text{grad } V \qquad (31)$$

The equation above gives the result that, when the field is increasing with time, the contour lines emerge from the field-producing elements and proceed away from them. The action is reversed when the field is decreasing with time.

An examination of equation (5) shows that, for time-dependent fields, the energy of a particle can change and hence its mass does not remain constant. This introduces a considerable complication because V now depends on velocity as well as position. In order to proceed further it will be assumed that the motions are nonrelativistic. When this assumption is made, the pertinent equations which describe the motion become:

$$V \equiv \frac{q}{2M_o r^2} \left[\phi - \phi(o) - \frac{r_o P_\theta(o)}{q} \right]^2 \tag{32}$$

$$\frac{d\vec{Q}}{dt} = - q \text{ grad } \left[V + X \right] \tag{33}$$

$$\frac{dT}{dt} = q \frac{\partial V}{\partial t} \tag{34}$$

$$V_{max} = \frac{T}{q} \tag{35}$$

$$|P_\theta| = \left[2qM_o V \right]^{1/2} \tag{36}$$

$$|\vec{Q}| = \left[2qM_o (V_{max} - V) \right]^{1/2} \tag{37}$$

The above equations are, respectively, the nonrelativistic forms of equations (9), (12), (15), (20a), (13), and (20b). The symbol M_o denotes the rest mass of the particle, and T the kinetic energy of the particle. It is noted, in passing, that a betatron operates in such a manner that the "stable orbit" occurs at a place where the inductive potential has a

stationary value at any given instant of time. Equations (23a) and (23b) give the conditions for V to have a stationary value. Equation (23a) is identical to the basic betatron equation and gives, in a generalized fashion, the condition that the flux through the orbit should be twice the "flux at the orbit." Further examination shows that the betatron stability conditions

$$\frac{1}{r}\,\frac{\partial(r B_z)}{\partial r} > 0 \quad (B_z \text{ is } +) \tag{38}$$

$$\frac{\partial B_r}{\partial z} > 0 \tag{39}$$

guarantee that the stable orbit corresponds to a minimum of the inductive potential and not to a saddle point as in the example of Figure 4.

There is such a variety of possibilities for particle motion that it is difficult to discuss it adequately in a few pages. For this reason, the subsequent discussion is based on certain simplifying assumptions. The main features of many of the conclusions that are reached have a validity that goes beyond the bounds set by the assumptions, however.

A problem of immediate interest is that of the dynamic behavior of electron-ion pairs in a tenuous gas, near the time of electrical breakdown, in a time-varying magnetic field. In this problem, there are two major complicating factors; elastic and inelastic collisions between the gas constitutents, and cooperative effects such as space-charge forces. The former is discussed in a later section of this manuscript whereas the latter will be left for another time.

Here, the discussion is kept to a single-particle point of view, which is, admittedly, a gross simplification but which, nevertheless, provides a

rather firm basis from which the more complex picture can be viewed. One of the advantages of the single-particle approach is that the role played by the inertia of the particles is clearly set forth.

The two simplifications to be made are the following:

a. The capacitive potential, X, is taken equal to zero.

b. The initial θ-momentum, $P_\theta(o)$, is taken equal to zero. This condition immediately limits the discussion to those potential patterns for which zeros can exist. It is implicitly assumed in the discussion that such a zero does, in fact, exist within the pattern.

Now returning to the equation for $\vec{v}_V$ (equation (31)) and making use of the above assumptions, equation (32), and also equations (2), (3), and (4) it can be shown that:

$$|\vec{v}_V| = \left| \frac{E_\theta}{\left[\left(B_z - \frac{\phi - \phi(o)}{r^2} \right)^2 + B_r^2 \right]^{1/2}} \right| \qquad (40)$$

This equation gives the interesting result that the contour V = 0 (i.e. $\phi = \phi(o)$ moves with a speed $E_\theta / |\vec{B}|$. However, the contour V = o exactly follows a magnetic field line (i.e. - lies on the surface of a flux tube) so that the magnetic-field lines corresponding to V = o move with this speed. The choice of $\phi(o)$ is arbitrary, furthermore, so that all the field lines move with speed $E_\theta / |\vec{B}|$.

This speed is just exactly the magnitude of the quantity which is called the "drift velocity" for particles in crossed $\vec{E}$ and $\vec{B}$ fields[2,4]. It is apparent that it is the zero of the inductive potential which moves with the drift velocity rather than the quantity which is called the "guiding center" of the motion. Even for motion in a uniform magnetic field the V = o line

does not coincide with the instantaneous center of curvature. This can be seen from Figure 5a by drawing an arc of radius r_{oo} about the point r = o. According to equation (40) the magnitude of the contour velocity, $|\vec{v}_V|$, exceeds the drift velocity if $|\phi| > |\phi(o)|$ and is less than the drift velocity otherwise. This means that the potential valley around the contour V = 0 gets steeper and steeper as the field strength increases.

5.2 ENERGY TRANSFER

This section considers the question: how much energy can be transferred from a magnetic field to a charged particle? The discussion will be confined to simple geometries and will remain within the scope of the simplifying assumptions made in the last section.

To begin with, consider equation (34). If one substitutes for $\partial V/\partial t$ the values from previous equations it is easily shown that, for a particle starting from rest at time to:

$$T = \frac{q^2}{M_o} \int_{t_0}^{t} dt \left(\frac{\phi - \phi(o)}{r}\right)\left(\frac{\partial \phi/\partial t}{r}\right) \qquad (41)$$

The integrand in equation (41) is identical with the product of the θ-velocity and the electric field (i.e. - it is identical with $qr\dot{\theta}E_\theta$). Thus, as could be expected, the energy which a particle acquires is governed by the voltage drop through which it moves. The role played by the magnetic field is that of a restrainer.

There is a considerable variety to the results which can be obtained - even within the framework defined by the simplifying assumptions which have been made. In order to illustrate this, a number of examples will be given. In all of these examples the time dependence of the field is taken to be everywhere the same. Thus, the vector potential (Equation (1a)) can be written as a function of r, z multiplied by a function of time:

$$\vec{A} = \hat{\theta} A'(r, z)\, f(t) \tag{42}$$

It is also convenient to take f(t) to be a ramp function. If γ denotes the rise time of the ramp, then:

$$\begin{aligned} f(t) &= 0 \quad \text{for } t < 0 \\ &= t/\gamma \quad \text{for } 0 < t < \gamma \\ &= 1 \quad \text{for } t > \gamma \end{aligned} \tag{43}$$

There are two cases to be considered: that for a particle which is present in the field at t = 0; and that for a particle which is not present until some time t > 0. The latter case is represented, for example, by either member of an electron-ion pair which is created in consequence of the prior acceleration of other particles.

5.3 MOTION FOR ϕ (o) = 0

If the particle is present at t = 0 then θ(o) = 0 and:

$$V = \frac{q}{2M_o} \left(\frac{\phi}{r}\right)^2 \tag{44}$$

Thus the potential is zero on the axis of symmetry and at infinity, and the motion of the particle is directed towards the zero. If one takes, as an example, a solenoid as in Figure 2, a particle that is originally at a distance less than the radius of the solenoid from the axis of symmetry will subsequently pass through the axis of symmetry.

If the field is brought on suddenly enough, the potential will jump from zero to a value given by equation (44) before the particle has had time to move significantly in either the r or z directions. Hence, it will acquire an energy (in electron volts) equal to the value acquired by the potential.

For example: take an electron initially at 0.1 meter and a uniform magnetic field in the z-direction of 1 weber/meter^2. Since the final radius of curvature is 0.05 meter, the electron will acquire an energy of 14.5 Mev. However, in order to transfer this amount of energy the field must be brought on in a time that is short compared to the cyclotron period for an electron in a field of 1 weber/meter^2; this time is 3.6×10^{-11} sec.

From equation (44), the energy which is acquired by the sudden application of a field depends inversely on the mass of the particle. In other words, a suddenly applied field imparts a fixed velocity to a particle-independent of its mass. This result is radically altered if the field is brought on slowly compared to a cyclotron period as will be shown next.

Consider, as above, a uniform field in the z-direction; let a particle be at $r = r_o$ at time $t = 0$, and let a field be turned on in accord with equations (43). The radial position of the electron at time t is found to be:

$$r = r_o \, \Gamma(3/4) \left(\frac{W}{2}\right)^{1/4} J_{-1/4}(W) \tag{45a}$$

where

$$W = \frac{q B_z}{4 M_o \gamma} \, t^2 \tag{45b}$$

In equation (45a) $J_{-1/4}(W)$ is the Bessel Function of order -1/4. The following remarks on energy transfer are limited to the interval of time between t = o and the time when the particle first reaches $r = 0$.

The particle remains at its starting radius for a considerable period of time and then heads inwards. The changeover from circumferential motion to radial motion takes place when the time is approximately equal to one half the instantaneous value of the cyclotron period at the

position of the particle.

The kinetic energy can be computed by using equations (32) and (34) and integrating graphically. It is found that all the energy has been acquired by the time

$$W = 2 \tag{46}$$

and that the energy acquired is:

$$T = 0.98\, E_\theta(r_o)\, r_o\, q \tag{47}$$

This last result is seen to be independent of the mass of the particle. This rather surprising result is obtained as long as equation (46) holds at sometime $t \leq \gamma$. Since, for a given geometry, $E_\theta(r)$ is directly proportional to the voltage applied to the field-producing coils it follows that the energy transfer is directly proportional to applied voltage.

The above calculation for the position as a function of time was done again with the use of a first order approximation for V. The result was:

$$r = r_o \left(1 - \frac{q}{12 M_o \gamma^2} (\text{grad } V)_o\, t^4 \right) \tag{48}$$

The subscript on (grad V) means to evaluate the quantity at $r = r_o$, $t = \gamma$. Equation (48) is assumed to hold until $(r_o - r) = (V/\text{grad } V)_o$ — a distance which, in the approximation, is the total distance over which acceleration takes place since V is taken to be zero for larger values of $(r_o - r)$. The following result is found for the total energy transferred.

$$T = 1.62\, q\, E_\theta(r_o) \left(\frac{V}{\text{grad } V} \right)_o \qquad (49)$$

For a uniform field $(V/\text{grad } V)_o = \frac{r_o}{2}$ and a comparison of equations (47) and (49) shows agreement to 20%. Thus, the approximate method gives very good results. Figure 6 shows how the energy is accumulated as a a function of distance traveled. In that figure $(r_o - r)$ is denoted by S, and $(V/\text{grad } V)_o$ by S_o. The reason for the excellence of the approximation is that most of the energy is accumulated before the particle has moved very far.

Equation (49) can be applied to fields which are not uniform provided the field gradients are not too severe. Figure 7 shows an example of a situation to which it is applicable. The data on Figure 7 were calculated from experimental measurements made with axially symmetric search coils[7]. The contours of constant ϕ (normalized to 1 at the outermost coil) are shown as solid lines. The contours of constant V (for $\phi(o) = 0$) are shown as dotted lines. The V-contours are normalized to 1 at the outermost coil. The field was produced by "in phase" currents flowing in the coils. The cross-hatched object is a small, metal disc. Figure 7 constitutes a "snapshot" of the ϕ and V contours at one instant of time. The V-contours have the same shape as contours of constant E_θ would have.

For most positions on Figure 7, the quantity $(V/\text{grad } V)_o$ has values between $\frac{r_o}{2}$ and r_o. Hence, the energy which can be transferred is not significantly different from the corresponding positions for a uniform axial field (i.e., positions having the same value of E_θ).

5.4 MOTION FOR $\phi(o) \neq 0$

The motion previously discussed was for the case $\phi(o) = P_\theta(o) = 0$ and, for this situation the zero contour of V does not move. Particle acceleration

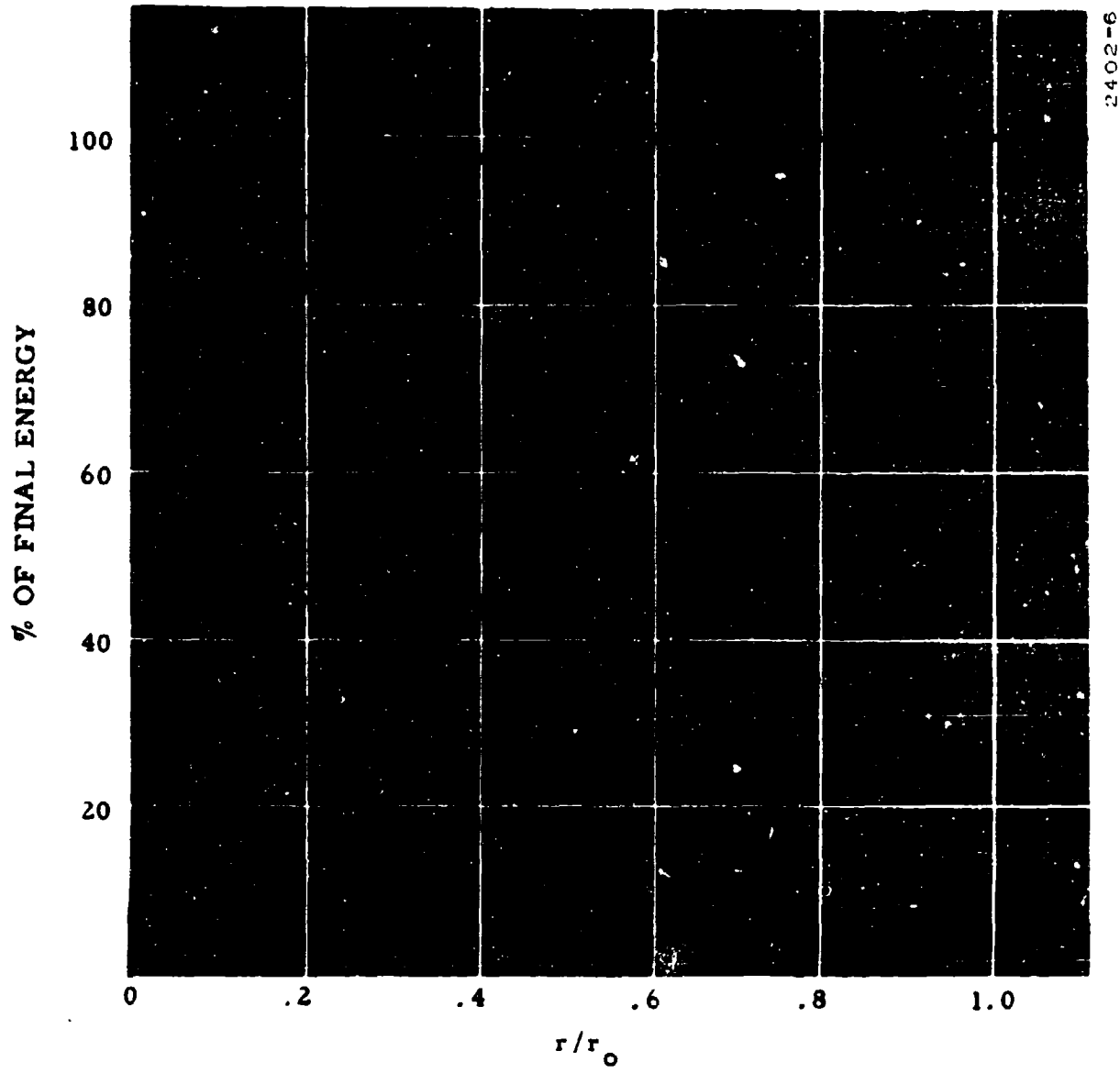


Figure 6. Accumulation of Kinetic Energy Versus Distance Traveled

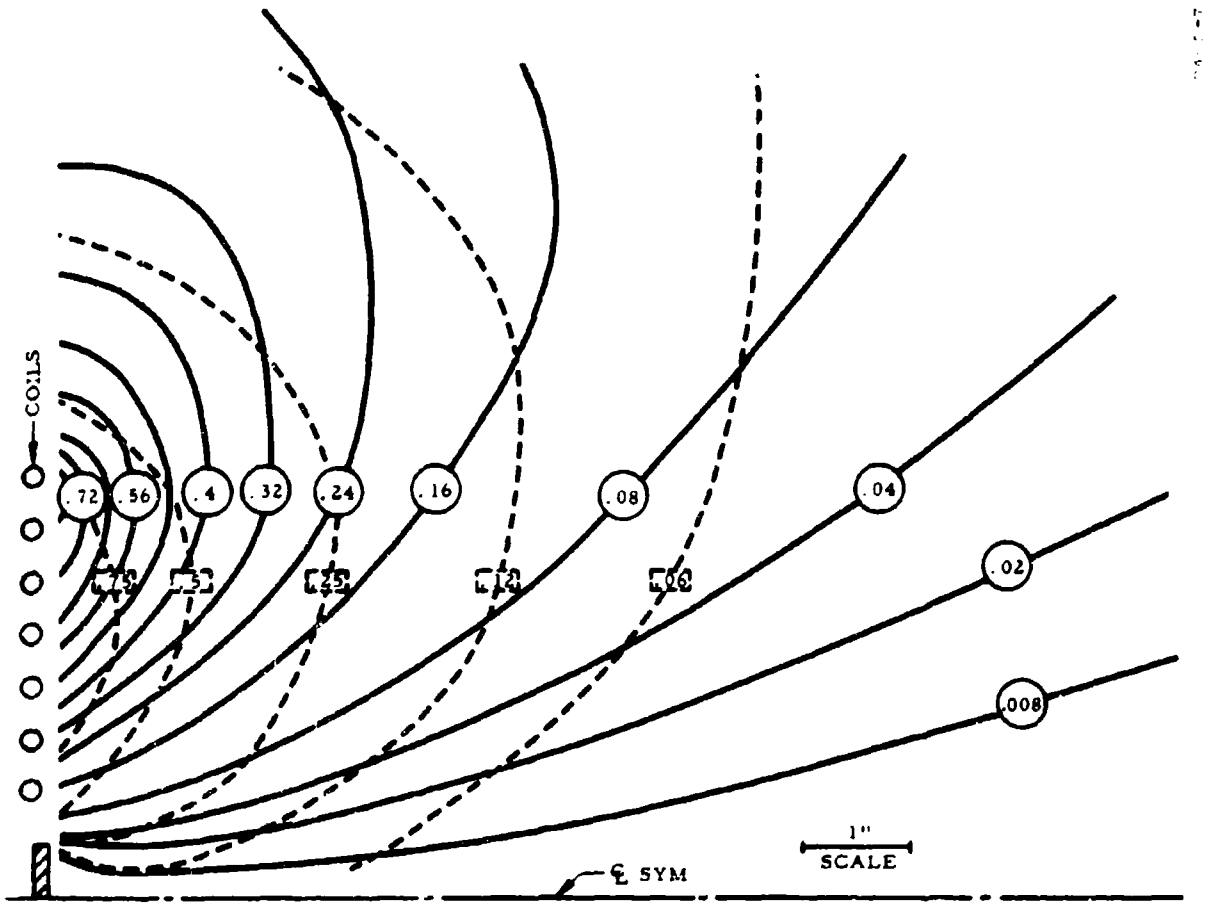


Figure 7. An Inductive Potential Pattern for a Set of Coils

is obtained because the slope of V increases as the field strength increases and vice versa.

When the restriction $\phi(o) = 0$ is removed a completely different accelerating mechanism appears. The particle always begins its motion from a point on the $V = 0$ contour (by virtue of the definition of $\phi(o)$). As the field strength increases the $V = 0$ contour moves (as previously discussed) and so a particle that is initially at rest at a point where $V = 0$ soon experiences a value of V different from zero and so is accelerated.

In terms of the concept of a potential valley, the accelerating mechanism are of two types:

a. The whole valley translates with respect to the particle.

b. The steepness of the valley changes with time.

In order to see the essential characteristics of these two acceleration mechanisms one can consider them separately even though they are, in fact, very strongly coupled.

In order to get a rough idea of the phenomena to be expected, we assume:

1. The potential valley has the form of a parabolic cylinder which oscillates in position, and without change of shape.

2. The potential valley has the form of a parabolic cylinder whose shape varies sinusoidally, but without change of position.

Assumption (1) leads to an equation of motion of the form:

$$\ddot{x} + K^2 x = K_o \sin \omega t \qquad (50)$$

whereas assumption (2) leads to:

$$\ddot{x} + \left[K_1^2 \sin^2 \omega t \right] x = 0 \qquad (51)$$

Equation (50) is a driven harmonic oscillator which resonates at $\omega = K$. Equation (51) is a Mathieu's equation.

In actual fact the two types of motion just described are coupled to each other and so the situation is very complicated indeed.

Equations like Mathieu's equation typically give rise to both stable and unstable motions [8,9]. An essential feature to the instabilities is that there are not just discrete values of driving frequency at which instabilities can occur but there are whole bands of frequencies which lead to unstable motions.

In regard to unstable motions, the question of stability versus instability involves very intimate connections between the exciting frequency of the field and the maximum field strength at any point. Therefore, for a field pattern which is very nonuniform, one might expect to find quite localized spots where the energy transfer can become large. This can lead, in the case of a gaseous discharge to quite localized rings of light.

It follows from the above argument that distinctive phenomena, such as rings of light, should be grossly affected by changes in the frequency of excitation of a field. Startling changes in the position of luminous rings found in electrodeless discharges have, in fact, been observed experimentally.

An example of a moving potential valley is given in Figure 8. The field-producing geometry is the same as for Figure 7, but in Figure 8, $\phi(0) \neq 0$. The potential valley shown by the solid contours was computed from the

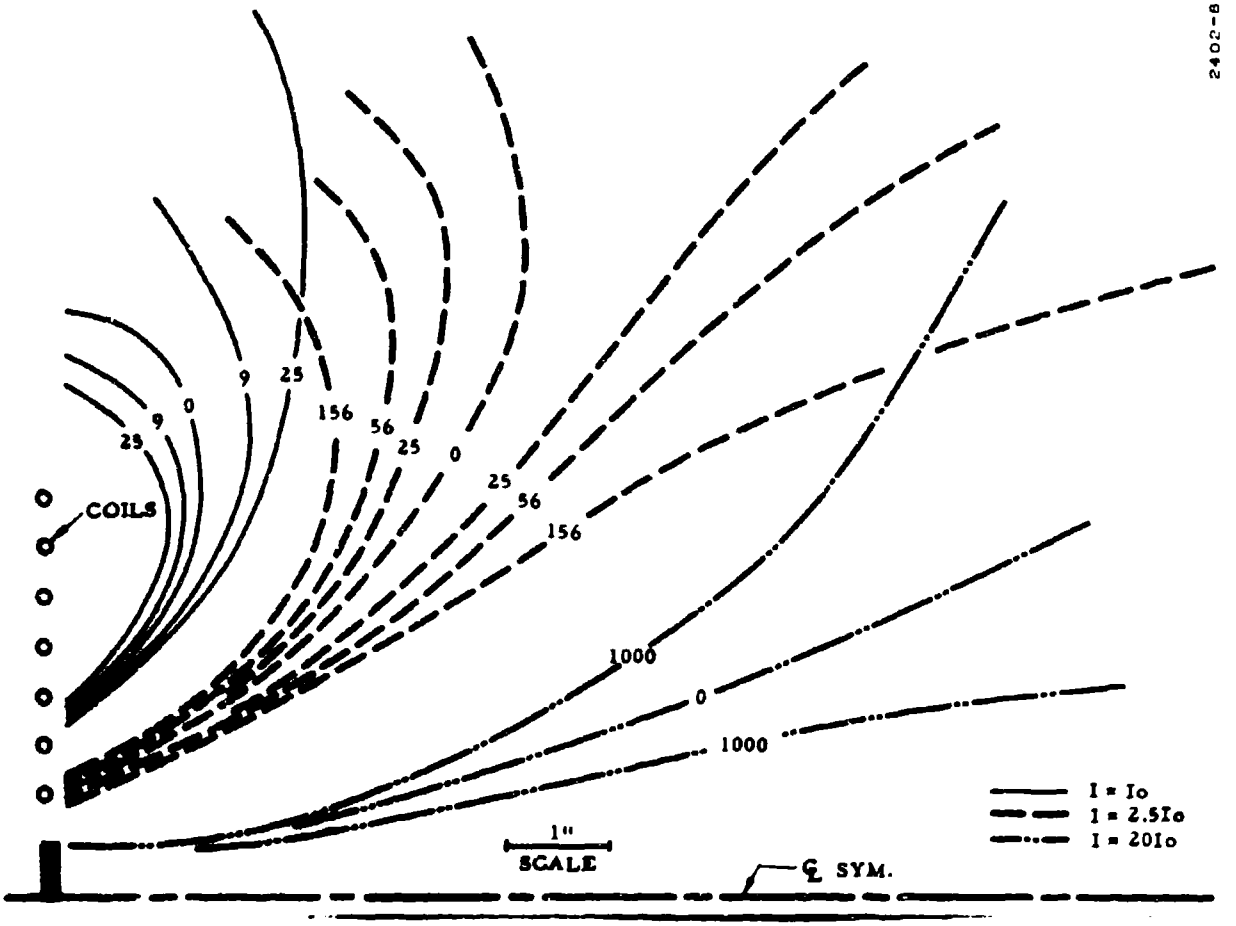


Figure 8. An Inductive Potential Pattern for a Set of Coils

ϕ-contours given on Figure 7 with $\phi(o)$ assumed to be 0.4; this potential valley corresponds to current I_o flowing in the coils. By the time the current has risen to a value $2.5\ I_o$, the potential valley has evolved to the position and shape shown by the dashed contours. At $I = 20 I_o$ the contours are given by the dotted lines. The numbers attached to the contours are relative values of V.

Figure 8 illustrates how the potential valley steepens as it evolves in time. If I decreases from the value $20 I_o$ then the potential valley simply retraces its path and the V = 0 contour is eventually swallowed up by the outermost coil (since it encloses the most flux). At I = 0 the potential has the form

$$\left[\phi(o)/r\right]^2$$

In order to illustrate the crucial role played by the mass of a particle, one can examine the extreme case of a particle of vanishingly small mass. Such a particle is capable of immediately responding to a force and so the motion consists of a translation at the field drift velocity plus a rotation around a field line (at V = 0) with a circumferential speed equal to the drift velocity. Hence, the velocity never exceeds twice the drift velocity at the position of the particle. If the particle mass is increased it becomes more and more able to depart from the contour and the motion becomes less and less that of a translation plus a rotation.

Because the mass, field strength, and field rise time are all determining factors to the motion of a particle, it is very difficult to make many generalized statements. Furthermore, the discussion has so far ignored the effects of particle collisions and cooperative phenomena. The next section discusses particle collisions.

VI PARTICLE COLLISIONS

It is expected that the description for the motion of isolated charged particles which has been given also has validity for the description of phenomena observed in tenuous gas discharges. There is an ever-increasing effort going into the study of gas breakdown and acceleration by magnetic induction, and often the symmetry is right for the present method.

One can only expect the present method to lead to valid conclusions for situations where the collision frequency is not large compared to the characteristic times for the motion of the ionized particles. Experimental observations seem to support the view that for gas pressures below about 10 microns the method may have application.

Suppose that a charged particle is present in the field geometry before the field is turned on (so $\phi(0) = 0$). Let the field be excited by current flowing in a set of coils and suppose that the current flow starts at $t = 0$ and is sinusoidal thereafter.

Initially the inductive potential for the particle has the form:

$$V(t) = \frac{q}{2 M_0} \left(\frac{\phi(t)}{r}\right)^2 \qquad (52)$$

The particle will move in a manner prescribed by the potential. Suppose that a collision occurs at time t_c. Equation (52) can be rewritten to apply to a time $t_c - \epsilon$ (i.e. just prior to the collision):

$$V = \frac{q}{2 M_0 r_{t_c}^{2-\epsilon}} \left[\phi(t) - \phi(t_c - \epsilon) - \frac{r_{t_c}^{-\epsilon} P_\theta(t_c - \epsilon)}{q} \right]^2 \qquad (53)$$

In equation (53), $\phi(t_c - \epsilon) = - \frac{r_{t_c}^{-\epsilon} P_\theta(t_c - \epsilon)}{q}$

This follows from equation (8). Now, consider the situation at time $t_c + \epsilon$ — that is, immediately after the collision. The collision does not change the position of the particle but only its direction of motion and its kinetic energy and possibly its charge. In particular the collision does not change the "enclosed" flux, $\phi(t_c - \epsilon)$. Hence, for times $t > t_c$ the potential has the form:

$$V(t>t_c) = \frac{q}{2 M_0 r^2} \left[\phi(t) - \phi(t_c - \epsilon) - \frac{r_{t_c}^{-\epsilon} P_\theta(t_c + \epsilon)}{q} \right]^2 \qquad (54)$$

A collision therefore corresponds to a sudden displacement of the inductive potential. The basic character of the motion after collision may be different from that of the motion before collision. In the example given, the motion is changed from one that does not have entrapped flux to one that does. A collision may change the potential pattern from one that does possess a zero contour to one that does not. A really radical change in V can only be caused by large-angle deflections of the particle or by highly inelastic collisions.

VII CONCLUDING REMARKS

It is convenient to separate possible collective effects into two classes: those which are capacitive in nature, such as space charge; and those which are inductive in nature such as the fields produced by the currents of particle motion. Since the magnetic field pattern produced by the latter has the same symmetries as the applied field it may be possible to gain a qualitative idea of their effects by an extension of the present method. This has not yet been done.

The present approach does lead to a rather simple model for describing the effects of strong space charges This model is discussed in another report[10]. It is felt that if collisions are rare, the present method, with space charge included, can be very helpful in explaining the behavior of a partially ionized gas as a condition of electrical breakdown is approached.

VIII ACKNOWLEDGEMENTS

The author would like to acknowledge the cooperation and assistance of Mr. Robert G. Cross.

REFERENCES

1. Heisenbert, W. Cosmic Radiation. Springer, 1943; Dover Publications, 1946.

2. Alfvén, H. Cosmical Electro-Dynamics. Oxford Press, 1950.

3. Fermi, E. Nuclear Physics. The University of Chicago Press, 1950.

4. Spitzer, L., Jr. Physics of Fully Ionized Gasses. London: Interscience Publishers, Inc., 1956.

5. Störmer, C. Astrophysica Norvegica, II (1936).

6. Malmfors, K. G. Ark. f. Mat., Astr., 0 Fysik, 32A, 1 (1945).

7. Penfold, A. S. Determining Axially Symmetric Magnetic Field Patterns, AFOSR TN-60-842 (1960).

8. Morse, P. and Feshbach, H. Methods of Theoretical Physics. New York: McGraw-Hill Book Co., 1953.

9. Morgenau, H. and Murphy, G. The Mathematics of Physics and Chemistry, D. Van Nostrand Co., Inc., 1943.

10. Penfold, A. S. A Model for the Motion of a Rarified Plasma, AFOSR TN-(to be assigned), 1960.

11. Jahnke, E. and Emde, F. Tables of Functions, Dover Publications, Inc., 1945.

APPENDIX D

A MODEL FOR THE MOTION OF A RARIFIED PLASMA IN AN AXIALLY SYMMETRIC MAGNETIC FIELD

NOTE

This appendix contains a document first published in 1960 as AFOSR TN 60-961 and subsequently issued as Litton TM 61-27.

The document represents a step in the dvelopment of a theoretical model. It contains information not included in the main text of this report.

Publication No. 2402A

Technical Memorandum 27

A MODEL FOR THE MOTION OF A RARIFIED PLASMA IN AN AXIALLY SYMMETRIC MAGNETIC FIELD

by

Alan S. Penfold

June 1961

This document contains proprietary information of Litton Systems, Inc. Any reproduction use and/or disclosure of this document and/or any portions thereof for purposes other than evaluation is expressly prohibited without the prior written consent of Litton Systems, Inc.

LITTON SYSTEMS, INC.
Space Sciences Laboratory
336 North Foothill Road, Beverly Hills, California

CONTENTS

I	INTRODUCTION	1
II	MOTION WITHOUT COULOMB FORCES	3
III	THE INCLUSION OF COULOMB FORCES	7
	3.1 Preliminary Remarks	7
	3.2 The Ion-pair Model	8
	3.3 Energy Transfer	12
	3.4 Motion in a Uniform Field	14
IV	CONCLUDING REMARKS	17
V	ACKNOWLEDGEMENTS	19
	REFERENCES	21

FOREWORD

This technical memorandum presents a study by Alan S. Penfold, made under contract AF49(638)-759 for the Air Force Office of Scientific Research. Its distribution provoked an extensive interest, as reflected in the numerous requests received for the document or for information from the document; therefore, it has been reprinted in technical memorandum form.

ABSTRACT

Equations of motion are derived for the charged constituents of a tenuous plasma immersed in a time-dependent, axially symmetric, magnetic field. An "ion-pair" model is employed which assumes strong coulomb forces. The motion of the ion-pair is shown to be closely related to that of an isolated positively charged particle whose mass is equal to the geometric mean of the ion and electron masses. Equations for the energy transferred from the field to the ion-pair are also derived.

I INTRODUCTION

Studies of the behavior of ionized gases in the presence of electromagnetic fields have shown many strange, and still unexplained, phenomena. In order to try to understand these it is necessary to adopt a model which attacks the problem from a simplified, and often extreme, point of view. One such approach is the "circuit model" in which the gas is regarded as analogous to a simple electrical circuit.

One then speaks of the resistivity of the gas, the inductance of the gas configuration, the mass of the configuration and so on. This approach is usually taken when one knows that there are very frequent collisions occuring between the constituent particles of the gas and when the self-fields of the gas currents are expected to be large. In fact, the very use of the concept of inductance is closely allied with the idea that one part of a circuit can react on the other parts through the self-fields which may be established.

There is a fundamental assumption implicit in the "circuit model" and that is the assumption that an infinite number of current carriers exist in the gas. In an ordinary electrical circuit the currents which flow are the result of many electrons, each moving along the wire very slowly. There is, effectively, an infinite supply of electrons and the kinetic energy associated with the current flow is negligibly small. This need not be true for a gas that is charge limited: in this case, high currents are obtained only by causing the charged constituents of the gas to move at high velocities. A significant amount of kinetic energy may be associated with large current-flow in a gas.

A second model which can be employed is a "single-particle" model. Here one works from the behavior of isolated, charged particles moving in the applied electromagnetic field. This approach can be expected to give meaningful results when collisions between the constituent particles of the gas are relatively infrequent and when the effects of self-fields are small. The effect of the inertia of the particles on the buildup of currents is automatically included in the model. In a previous report[1] (hereafter referred to as I) a method for describing the motion of isolated, charged particles in an electromagnetic field was developed. The method applies to fields which possess a certain kind of axial symmetry. It is the intent of the present report to extend the work of I to include the coupling of electrons to ions caused by coulomb forces.

Collective effects in a gas can be divided into two classes: those due to the accumulation of a net charge at points within the gas; those due to the fields produced as a consequence of current flow in the gas. The present report deals with the former effects. It is not yet known whether the method can be further extended so as to include the latter effects as well.

The results which are obtained when coulomb forces are included still require that the mean free path for collisions between the gas particles be large. It is therefore necessary to ask whether conditions can be realized where collisions are relatively unimportant and yet coulomb effects are very important. Most discussions of plasma physics emphasize a basic property of a plasma – its tendency toward macroscopic electrical neutrality[2,3,4]. An examination of this question is undertaken in Section III of this report and it is concluded that coulomb forces can be very important even though collisions are not.

The MKS system of units is used throughout this report.

II MOTION WITHOUT COULOMB FORCES

The particle motions will be described with respect to a cylindrical co-ordinate system with unit vectors $\hat{r}$, $\hat{\theta}$, $\hat{z}$. The z-axis is taken to be an axis of symmetry for the electromagnetic fields which are present. The field components are:

$$B_r(r, z, t)$$

$$B_z(r, z, t) \qquad (1)$$

$$E_\theta(r, z, t)$$

The required symmetry is defined by the form of the field components given above. It will be assumed that the electric field, E_θ, arises by induction. The magnetic flux (divided by 2π) which the circle (r, z) encloses about the axis of symmetry is denoted by ϕ, and is given by:

$$\phi = \int_0^r dr\, r\, B_z \qquad (2)$$

The following relations also hold:

$$\frac{\partial \phi}{\partial r} = r\, B_z \qquad (3a)$$

$$\frac{\partial \phi}{\partial z} = -r\, B_r \qquad (3b)$$

$$\frac{\partial \phi}{\partial t} = -r\, E_\theta \qquad (3c)$$

Suppose that a particle of charge q and mass M_o is at position r_o, θ_o, z_o at time t_o and has angular momentum J(o) with respect to the axis of symmetry. The value of ϕ corresponding to the initial position and time is denoted by $\phi(o)$. (The motion of the particle is assumed to be non-relativistic at all times.) At some later time, t, the particle will have a linear momentum whose components are P_r, P_θ, and P_z.

The "plane of projected motion" is defined to be a plane passing through the line $\theta = z = 0$ and the z-axis and containing a two-dimensional Cartesian coordinate system with unit vectors $\hat{a}_r$ and $\hat{a}_z$. The position and momentum of the particle, at time t, in this new coordinate system is:

$$\vec{S} = \hat{a}_r\, r + \hat{a}_z\, z \tag{4}$$

$$\vec{Q} = \hat{a}_r\, P_r + \hat{a}_z\, P_z \tag{5}$$

It was shown in I that the motion of the particle subsequent to time t_o is completely determined by a scalar potential, V, which was called an inductive potential. The equaticns of motion are the following:

$$\frac{d\vec{Q}}{dt} = -q \text{ grad } V \tag{6a}$$

$$\left|P_\theta\right| = \left[2M_o q\, V\right]^{1/2} \tag{6b}$$

where

$$V = \frac{q}{2M_o r^2}\left[\phi - \phi(o) - \frac{J(o)}{q}\right]^2 \tag{6c}$$

The unit of V is the volt and, as is evident from (6c), the minimum value which V can have is zero (for positive q).

The following relations for the kinetic energy, T, also hold:

$$\frac{dT}{dt} = q\frac{\partial V}{\partial t} \tag{7a}$$

$$T = q\,V_{max} \tag{7b}$$

The last equation can be taken to be the defining equation for V_{max}, the maximum value of V which can be reached by the particle. It follows from equations (6a) and (7b) that the kinetic energy, T′, in the plane of projected motion is:

$$T' = q\left[V_{max} - V\right] \tag{7c}$$

It was demonstrated in I that the contours of constant V are stationary if the magnetic field is independent of time, and move if the field depends on time. The contour V = ∪ (if it exists) moves with velocity $\frac{\vec{E}\times\vec{B}}{|B|^2}$

P_θ/q is negative if $\phi > \left[\phi(o) + \frac{J(o)}{q}\right]$ and positive if the reverse is true.

III THE INCLUSION OF COULOMB FORCES

3.1 PRELIMINARY REMARKS

The equations of motion that are given in the last section describe the behavior of isolated particles. They can be applied to the constituent particles of a plasma only if the plasma is extremely tenuous so that the neutralizing effect of coulomb forces can be neglected.

A rough idea of the importance of coulomb forces can be obtained in the following way. Imagine a sphere of radius R that contains an unbalanced charge $4\pi nqR^3/3$ due to the presence of n particles per unit volume, each particle with charge q. The potential at the surface of this sphere is:

$$V_c = \frac{nqR^2}{3\epsilon_o} \tag{8}$$

where ϵ_o is the permittivity of empty space. In a plasma, charge accumulation can occur only if the kinetic energy which the constituent particles can obtain is large enough to overcome the coulomb potential; e.g., equation (8). An approximate measure of the distance over which charge separation can occur can be obtained from equation (8), if V_c is interpreted as the kinetic energy (in electron volts) tending to separate electrons from ions in the plasma. It is important to remember that transient conditions are being considered and that the plasma is not necessarily in a state of thermal equilibrium.

Figure 1 gives a plot of R versus n for various values of V_c. As an example, consider a gas at 20° C and 1-micron pressure, which is suddenly ionized to the extent of 1%. Then, the electron density is about 4×10^{11}. If R = 0.5 cm is small compared to the dimensions of the magnetic-field-producing system then Figure 1 shows that charge separation will not be important unless separation energies higher than 75 Kev can be transferred to the charged particles by the field.

From a study of Figure 1 it can be seen that there exist conditions for which the influence of coulomb forces is very great while collisions are still relatively unimportant. Hence, it is useful to extend the methods of I to include coulomb forces even though particle collisions are not taken into account.

3.2 THE ION-PAIR MODEL

The effects of coulomb forces on a particle moving in a magnetic field are included by adding a term to the basic equation of motion as follows:

$$\frac{d\vec{P}}{dt} = q\left[\vec{v} \times \vec{B} + \vec{E}\right] + \vec{F}_c \qquad (9)$$

If equation (9) is written for an ion then $\vec{F}_c$ is the total force acting on the ion because of charge separations in the plasma. The important characteristics of this force are completely determined by the assumed symmetry of the magnetic and electric fields.

The fields have axial symmetry and if the plasma density is initially axially symmetric it will remain so for all time. Thus $\vec{F}_c$ has no component in the $\hat{\theta}$ direction and coulomb forces can affect only the r and z motions. The flow of charged particles in the θ direction is unimpeded.

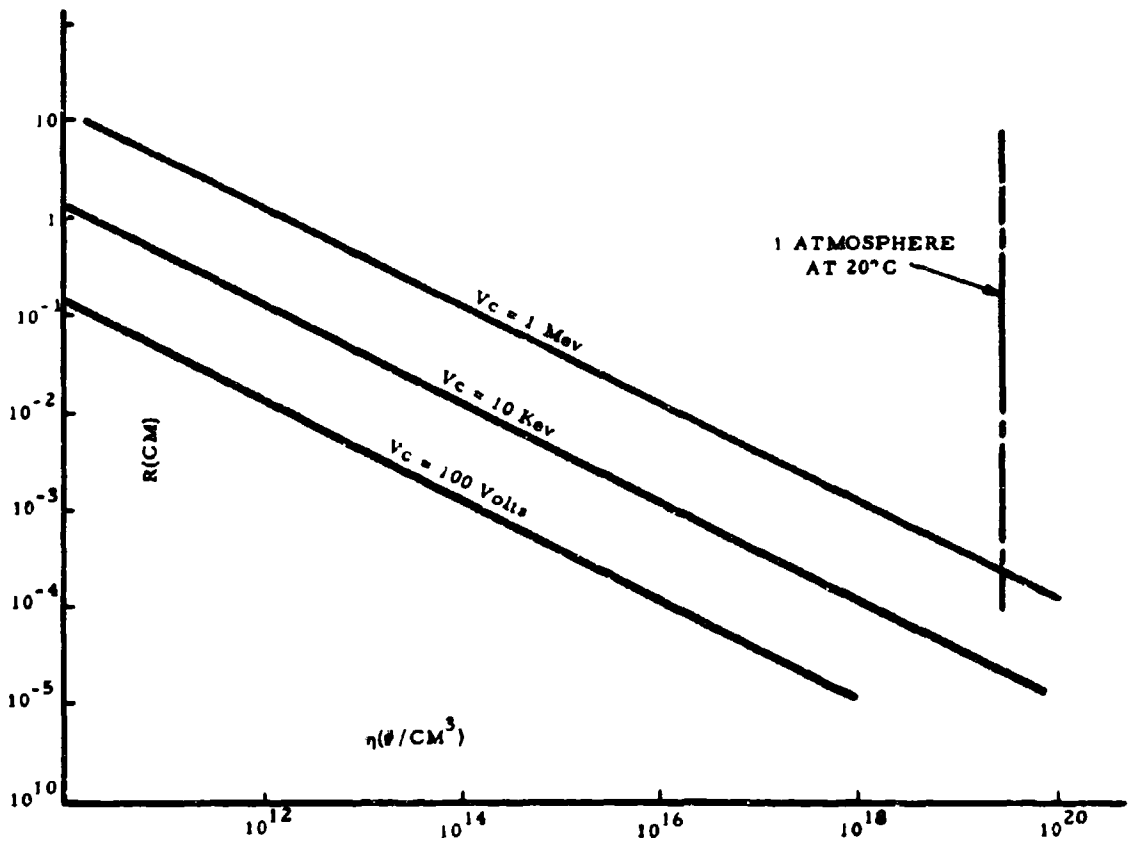


Figure 1. A Plot of Equation 8

Referred to the plane of projected motion [1] for which equations (6) are valid, the coulomb force has the following form:

$$\vec{F}_c \equiv q\vec{f} = q\left[\hat{a}_r f_r(r,z,t) + \hat{a}_z f_z(r,z,t)\right] \tag{10}$$

For simplicity it will be assumed that the plasma consists of: singly-charged ions of mass M_o and charge e; electrons of mass m_o and charge -e; and a tenuous un-ionized gas which affects the motion of the charges not at all. Macroscopic neutrality is assumed to exist at time t_o, and the charged particles are assumed to have negligible angular momentum at time t_o.

The motion of an ion in the projected coordinate system, subsequent to time t_o, under the influence of a time-dependent magnetic field plus coloumb forces is:

$$\frac{d^2}{dt^2}(M_o\vec{S}_i) = -e \text{ grad } V_i + e\vec{f} \tag{11a}$$

where

$$V_i = \frac{e}{2M_o r^2}\left[\phi-\phi(o)\right]^2 \tag{11b}$$

Equations (11) were obtained from equations (4), (6a), (6c), and (10).

A similar pair of equations holds for an electron:

$$\frac{d^2}{dt^2}(m_o\vec{S}_e) = e \text{ grad } V_e - e\vec{f} \tag{12a}$$

where

$$V_e = -\frac{e}{2m_o r^2}\left[\phi-\phi(o)\right]^2 \tag{12b}$$

If charge neutrality is preserved there will be in the vicinity of each ion, at every instant of time, an electron. The electron is, however, not bound to a particular ion but is free to exchange with other ions.

In the present case of axial symmetry such exchanges will be continually taking place in the θ direction and give rise to circulating currents as will be seen.

In order to describe the motion of the charged particles in the projected coordinate system an "ion pair" model will be employed. According to this model the plasma is assumed to consist entirely of neutral gas plus ion-electron pairs. Each ion is taken to be intimately bound to a "neutralizing electron" which moves with it at all times. In distinct contrast, in the direction perpendicular to the projected coordinate system (i. e. the θ direction) the ions and electrons are assumed to be completely unbound and free to move as the applied field dictates.

The proposed model assumes rigid coupling between ions and electrons in all but the θ-direction. In reality the coupling is not rigid and electron-ion oscillations will occur at the so-called plasma frequency[2]. These motions will not be considered in this report.

In accord with the ion-pair model introduced above one defines the position vector (in the projected coordinate system) of an ion-pair $\vec{S}_p$, as follows.

$$\vec{S}_p = \frac{M_o \vec{S}_i + m_o \vec{S}_e}{M_o + m_o} \tag{13}$$

An equation for the acceleration of $\vec{S}_p$ is obtained by adding equations (11a) and (12a) and dividing by $(M_o + m_o)$. When this is done the coulomb force term cancels out. In order to compare the result with that for an uncoupled ion and electron, it is desirable to have the result in the same form as equations (11) and (12). For this purpose we define an effective mass for the ion pair as follows:

$$M_p = \left[M_o m_o\right]^{1/2} \tag{14}$$

The resulting equation of motion for the ion pair is:

$$\frac{d^2}{dt^2}\left[M_p \vec{S}_p\right] = -e \text{ grad } V_p \qquad (15a)$$

where

$$V_p = \frac{e}{2M_p r^2}\left[\phi - \phi(o)\right]^2 \qquad (15b)$$

The last equations show that the r-z motion of the ion pair is exactly the same as it would be for an isolated particle of charge e and mass M_p (the geometric mean of the masses of the ion and the electron).

The momentum in the θ-direction can be found once $\vec{S}_p$ is known by solving equations (15). The ion and electron are not coupled in the θ-direction. The equations corresponding to (6b) are found to be:

$$\left|P_\theta(\text{ion})\right| = \left|P_\theta(\text{electron})\right| = \left[2M_p e V_p\right]^{1/2} \qquad (15c)$$

Hence each particle acquires the same θ-momentum as that acquired by an isolated particle of mass M_p. The net momentum in the θ-direction is always zero, however, since P_θ(ion) and P_θ(electron) have opposite sign.

3.3 ENERGY TRANSFER

The time rate of change of the kinetic energy T, of the ion plus electron is:

$$\frac{d\left[T(\text{ion}) + T(\text{elect})\right]}{dt} = \frac{M_o + m_o}{\left[M_o m_o\right]^{1/2}} e \frac{\partial V_p}{\partial t} \qquad (16)$$

The corresponding equation for a single, isolated particle of mass $M_p = \left[M_o m_o\right]^{1/2}$ and charge e does not have the mass ratio factor.

This is shown by equation (7a). For $M_o >> m_o$ the rate of energy accumulation is $\sim \left[M_o/m_o\right]^{1/2}$ times faster than for a particle of mass M_p. Since the r, z, and θ motions are, according to the ion-pair model, identical to those of a particle of mass M_p it can be concluded that, not only the rate of change of energy, but the energy is $\sim \left[M_o/m_o\right]^{1/2}$ times larger.

The mass ratio factor in equation (16) can be written as the sum of two terms:

$$\frac{M_o + m_o}{\left[M_o m_o\right]^{1/2}} = \left(\frac{M_o}{m_o}\right)^{1/2} + \left(\frac{m_o}{M_o}\right)^{1/2} \qquad (17)$$

It can be shown that the first term on the right hand side of equation (17) arises from the sum of:

a. The rotational kinetic energy of the <u>electrons</u> about the axis of symmetry of the magnetic field.

b. The translational kinetic energy (i.e. due to the r and z motions) of the <u>ions</u>.

The second term of equation (17) comes from the rotational energy of the ions and translational energy of the electrons. The ratio of the first term to the second term is > 1800 for all gases and so the motions (a) and (b) are overwhelmingly dominant. Energy exchange between (a) and (b) can take place through the action of the coulomb forces.

The electrons are held back by the ions and are thereby forced to remain in high-field regions longer than they otherwise would. Thus there is time for considerable betatron acceleration (i.e. induction acceleration) to occur. Subsequently, this rotational energy can be transferred to translational energy of the ions. This two-step process accounts for

the fact that the energy transferred to a tenuous plasma can be much larger than that which could be transferred if coulomb forces were absent.

3.4 MOTION IN A UNIFORM FIELD

As an example of the use of the equations which have been derived, consider the case of a uniform field which rises linearly in time.

$$B_r = 0 \tag{18a}$$

$$B_z = B_o \frac{t}{\tau} \quad (0 \leq t \leq \tau) \tag{18b}$$

Let $\phi(o) = J(o) = 0$ and consider an ion pair of hydrogen. If $Z = 0$ for all times then the equation of motion for r_p is:

$$\frac{d^2 r_p}{dt^2} + \left(\frac{eB_o}{2M_p \tau}\right)^2 t^2 r_p = 0 \tag{19}$$

The solution of this equation must be subject to the conditions $r_p = r_p(o)$ at $t = 0$ and $\dot{r}_p(o) = 0$ at $t = 0$.

The solution is found to be[5]:

$$r_p / r_p(o) = \Gamma(3/4) \left(\frac{W}{2}\right)^{1/4} J_{-1/4}(W) \tag{20a}$$

where:

$$W = \left(\frac{eB_o}{4M_p \tau}\right) t^2 \tag{20b}$$

and $J_{-1/4}$ is the Bessel Function of order - 1/4. Equation (20a) gives the motion in the projected coordinate system. The motion in the original cylindrical coordinate system is given by $|r_p|$. The θ-motions are found from equations (15c) and the results are:

$$\theta\,(\text{ion}) = -\left(\frac{m_o}{M_o}\right)^{1/2} W + \theta(o) \qquad (20c)$$

$$\theta\,(\text{electron}) = \left(\frac{M_o}{m_o}\right)^{1/2} W + \theta(o) \qquad (20d)$$

From equation (16) the kinetic energy is found to be:

$$T\,(\text{ion}) + T\,(\text{electron}) = \frac{M_o + m_o}{(M_o m_o)^{1/2}} \left(\frac{eB_o r_p(o)^2}{2\tau}\right) \int_o^W dW \left(\frac{r_p}{r_p(o)}\right)^2 \qquad (21)$$

For a hydrogen ion pair in a field, B_o, of 1 Weber/meter^2 with a rise time, τ, of 10^{-6} sec one finds that $W = 10^{15} t^2$.

Figure 2 shows the radial motion of the ion on an r/θ plot. The motion is shown by the solid line. During the time that the ion makes three passes through the axis of symmetry and rotates 11° the electron will have rotated 19,500°. The electron's path is not shown in Figure 2. The dotted line in Figure 2 shows the path which would be traveled by an isolated hydrogen ion (i.e. - no coulomb forces) in the same time interval as that encompassed by the solid line (8.7×10^{-8} sec).

Equations (20a) and (20b) give the result that the time at which the ion pair reaches the axis of symmetry is independent of the starting radius. This means that ionized material in the gas is swept up by the field into an ionized cylindrical shell of ever increasing density—which converges on the axis of symmetry. This is a collisionless "snow plow" effect. This action takes place in 4.3×10^{-8} sec.

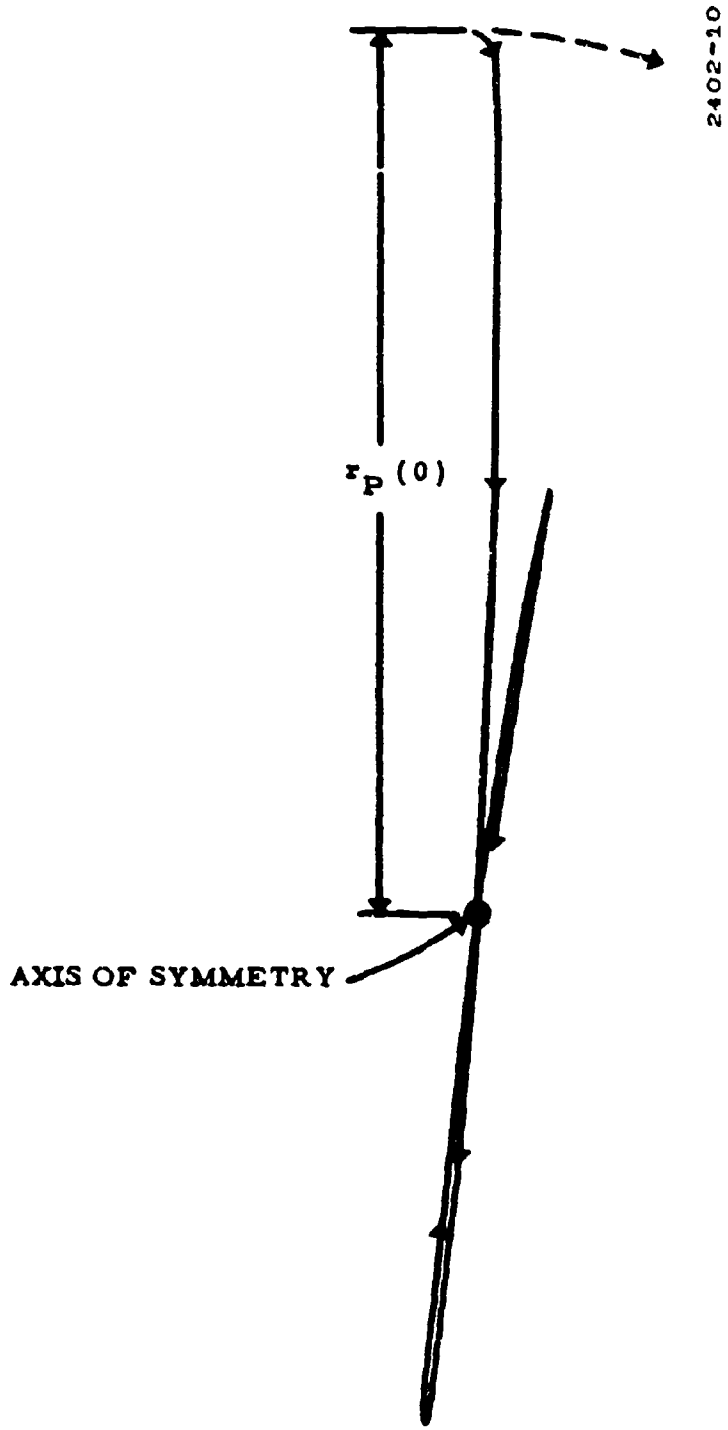


Figure 2. Motion in A Uniform Field

IV CONCLUDING REMARKS

It is concluded that the important results of coulomb forces are three in number. First, the translation of the massive ions in the field is much more rapid than for no coulomb forces ($\approx \left(M_o/m_o\right)^{1/4}$ more rapid). Second, the energy which can be transferred to the particles is much larger $\left(\approx (M_o/m_o)^{1/2} \text{ larger}\right)$ Third, the circulation of electrons about the axis of symmetry is much increased ($\approx \left(M_o/m_o\right)^{1/4}$ larger).

The latter result is very significant since it can lead to the relatively easy establishment of pinch effects. The tendency to pinch is proportional to the square of the gas current and hence it is increased by a factor of about $\left(M_o/m_o\right)^{1/2}$.

V ACKNOWLEDGEMENTS

The author would like to thank Mr. G. Fonda-Bonardi and Mr. R. G. Cross for help given during the course of the work reported here.

REFERENCES

1. A. S. Penfold, Particle Motion in an Axially Summetric Magnetic Field, AFOSR TN60-841 (1960)

2. L. Spitzer, Physics of Fully Ionized Gases, Interscience Publishers, Inc., New York (1956)

3. H. Alfvén, Cosmical Electrodynamics, Oxford Press (1948)

4. R. F. Post, Rev. Mod. Phys. 28, 338 (1956)

5. E. Jahnke and F. Emde, Tables of Functions, Dover Publications, Inc. (1945)

APPENDIX E

TWO-FLUID MODEL FOR THE MOTION OF A RARIFIED PLASMA ACCELERATED BY INDUCTION

Publication No. 1456

Technical Memorandum 10

TWO-FLUID MODEL FOR THE MOTION OF A RARIFIED PLASMA ACCELERATED BY INDUCTION

by
Alan A. Penfold

1 February 1961

This document contains proprietary information of Litton Systems, Inc. Any reproduction, use and/or disclosure of this document and/or any portions thereof for purposes other than evaluation is expressly prohibited without the prior written consent of Litton Systems, Inc.

LITTON SYSTEMS, INC.
Space Sciences Laboratory
336 North Foothill Road, Beverly Hills, California

CONTENTS

I	INTRODUCTION	1
II	MOTION WITHOUT COULOMB FORCES . . .	3
III	MOTION WITH COULOMB FORCES	7
IV	MOTION IN A UNIFORM FIELD	13
	BIBLIOGRAPHY	
	APPENDIX	

I INTRODUCTION

The problems of plasma physics are sufficiently complex that one must approach them from a simplified, and often extreme, point of view; in brief, one must adopt a model. On the basis of the model certain behavior characteristics of plasmas can be predicted; the approach is fruitful if a sufficient number of these characteristics are manifest in the behavior of a real plasma.

One such approach is the "circuit model" in which it is assumed that an infinite number of current carriers exists in the gas, and so the kinetic energy associated with current flow is negligibly small. Current flow can be stopped and started with no inertial lag. In accord with this model one deals with quantities like resistivity, inductance, total mass, viscosity, and so on.

A second model that can be employed is a "single particle" model. Here one works from the behavior of isolated, charged particles moving in the applied electromagnetic field, and the effects of the inertia of the particles on current build-up is automatically included. The single particle approach is expected to be valid in the limit of no collision—that is, in the limit of a rarified plasma.

The present paper uses a single particle model, and complete absence of close collisions is assumed. The model does not neglect the powerful neutralizing effects of coulomb forces, however. On the contrary, the coulomb forces are assumed to be so powerful that the plasma is macroscopically neutral at all times.

In addition to coulomb forces, the charged constituents of a plasma are affected by the magnetic fields produced as a consequence of current flow in the plasma. In a real plasma these self fields are often extremely important since they lead, for example, to the pinch effect. To the extent that the two-fluid model is developed in this paper, the effects of self fields will be neglected. However, it should be kept in mind that their effects can be included by a direct extension of the present

results. This is an area for future work. The present results do demonstrate how the condition of self-field dominance is approached, and also show that the role of self-fields is larger than might be suspected. This latter conclusion follows from the fact that, as will be shown, strong coulomb forces lead to a strong enhancement of the gas currents.

The present results are valid for fields having a certain kind of axial symmetry, and this symmetry will be defined in the following section of the paper. As an introduction to the problem one must first consider particle motion in the absence of coulomb forces. This is also done in the next section.

II MOTION WITHOUT COULOMB FORCES

When coulomb forces are not included, the motion of each ion and electron in the plasma is governed solely by its interaction with the applied electromagnetic field. All of the results that are presently desired can be obtained by assuming the applied field to consist only of a time-dependent magnetic field. In terms of a cylindrical coordinate system with unit vectors $\hat{r}$, $\hat{z}$, and $\hat{\theta}$, the required symmetry is obtained by restricting the field to an r-component, and a z-component, but no θ-component. In addition, since the field is varying with time, an induced electrical field exists which has only a θ-component. All motions are assumed to be nonrelativistic. The MKS system of units is used.

When the applied field has the symmetry that has been described, the equations of motion for a particle of mass m and charge q can be written in a particularly simple and compact form. The development leading to this particular form is given in the appendix of this Technical Memorandum. The r and z motions are given by:

$$m\ddot{r} = -q\frac{\partial V}{\partial r} \tag{1}$$

$$m\ddot{z} = -q\frac{\partial V}{\partial z} \tag{2}$$

where:

$$V = \frac{q}{2m}\left[\frac{\phi - \phi(o) - \frac{J(o)}{q}}{r}\right]^2 \tag{3}$$

and:

$$\phi = \int_0^r dr\ r\ B_z(r, z, t) \tag{4}$$

The quantity ϕ, which is defined by Eq. (4) is (aside from a factor of 2π) the magnetic flux enclosed to the axis of symmetry by a circle of radius r, located at position (r, z) at time t. The notation $\phi(0)$ is used to denote the value of ϕ at the position of the particle at time zero. The notation J(0) is used to denote the angular momentum of the particle with respect to the axis of symmetry at time zero.

V is a scalar potential whose gradient describes a vector field that acts in every way like an electric field. That is, V couples to the particle through the charge of the latter in the same way as a potential that describes an irrotational electric field. V differs from the usual type of scalar potential in that it depends explicitly on the initial state of the particle.

The equation that describes the θ-motion is the following:

$$P_\theta = mr\dot{\theta} = -q\left[\frac{\phi - \phi(0) - \frac{J(0)}{q}}{r}\right] \tag{5}$$

Equations for the energy of the particle at any time can be derived from (1) through (5). If E denotes the kinetic energy in electron volts, then:

$$E = \frac{m}{2q}(\dot{r}^2 + \dot{z}^2) + V \tag{6}$$

$$\frac{dE}{dt} = \frac{\partial V}{\partial t} \tag{7}$$

From (7) it is seen that the energy of a particle can change only if V is explicitly time dependent.

In order to get a qualitative idea about the motion of the particle, one can plot V for various instants of time. V can be regarded as a landscape over which the particle slides without friction - much like a small marble rolling about in a bowl of perhaps intricate shape.

It seems rather appropriate to give V the name "inductive potential" since it arises through the action of magnetic fields, and is the magnetic analogue of the "capacitive potential" due to the accumulation of charges. Störmer has already developed a formalism similar to that presented here for studying the orbits of charged particles moving in the earth's magnetic field [1]. This is a special case however, whereas the equations given here apply in general.

The quantity $\phi(o) + \frac{J(o)}{q}$, which appears in (3), is a constant for any given problem. It determines the nature and the scale of variation of V. It should be noted that if $\phi(o) + \frac{J(o)}{q} = 0$ then V usually approaches zero as r approaches zero. If $\phi(o) + \frac{J(o)}{q}$ is not equal to zero then V approaches infinity as r approaches zero - meaning that the particle can never pass through the axis of symmetry.

III MOTION WITH COULOMB FORCES

The tendency of a plasma toward macroscopic neutrality [2] is taken into account in the limit of strong neutralizing forces. Hence it is necessary to write two sets of equations like (1) through (7). In the first set all quantities are subscribed "i" -for ion; in the second all quantities are subscribed "e" - for electron. For simplicity, singly charged ions are assumed. The ion charge will be denoted by +e, the electron charge by -e.

The electrons are prevented from separating from the ions by an electric field (which arises from the slight charge separation that must occur in order to establish the field). The coulomb forces are described by this field. Since the equations of motion do not depend on θ - that is, there is axial symmetry - the coulomb electric field will have an r-component and a z-component, but no θ-component (provided there is axial symmetry at time zero). The plasma may be thought of as being composed of two interpenetrating, charged fluids with strong interactions in the r and z directions and no interactions in the θ-direction.

Equations analogous to Eq. (1) are written below - one for an electron, and one for an ion - with the coulomb field added.

$$m_e \ddot{r}_e = e \frac{\partial V_e}{\partial r_e} - eE_r \tag{8}$$

$$m_i \ddot{r}_i = -e \frac{\partial V_i}{\partial r_i} + eE_r \tag{9}$$

Since the plasma is to be macroscopically neutral, the ion and the electron densities are taken to be everywhere the same. This means, that in the vicinity of every ion, at every instant of time, there will be an electron. It will not be the same electron from time to time since free exchange can take place

in the θ-direction. As far as the radial and axial motions are concerned, however, the result is the same as though this free exchange were not taking place and one can think of an ion-electron pair. If the motions are described in terms of such pairs the requirement of macroscopic neutrality will be met, and at the same time no false restraints on the θ-motion will be imposed.

The center of gravity of a typical ion-electron pair can be defined as follows:

$$r = \frac{1}{m_e + m_i}\left[m_e r_e + m_i r_i\right] \tag{10}$$

$$z = \frac{1}{m_e + m_i}\left[m_e z_e + m_i z_i\right] \tag{11}$$

The equations of motion for r and z can be obtained through the use of Eqs. (10) and (11) along with equations like (8) and (9). Since the members of the pair are at nearly the same axial and radial position at all instants of time (though not necessarily at the same azimuthal position) they each experience the same applied field. This fact is used in evaluating V_i and V_e. The simplifying assumption $J_i(0) = J_e(0) = 0$ is also made*. The resulting equations of motion are:

$$m_p \ddot{r} = -e\frac{\partial V}{\partial r} \tag{12}$$

$$m_p \ddot{z} = -e\frac{\partial V}{\partial z} \tag{13}$$

where

$$m_p = \left[m_e m_i\right]^{1/2} \tag{14}$$

and, the inductive potential, V, is:

$$V = \frac{e}{\Sigma m_p}\left[\frac{\phi - \phi(o)}{r}\right]^2 \tag{15}$$

A comparison of these equations with Eqs. (1), (2), and (3) shows the two sets to be identical in form. Thus the r- and z- motions of a plasma pair are exactly the same as those of an isolated, positively charged particle of mass m_p - the

*Quite similar results are obtained if it is assumed that there is no initial net momentum in the azimuthal direction. This is expressed by $J_i(0) + J_e(0) = 0$.

geometric mean of the ion and electron masses. This fictitious particle can be called a "plasma particle."

The θ-equations of motion can be obtained directly from Eq. (5):

$$P_\theta(\text{ion}) = -P_\theta(\text{electron}) = -e\left[\frac{\phi - \phi(o)}{r}\right] \tag{16}$$

A comparison of Eq. (16) with Eq. (15) shows that one may also write the equations in the following way:

$$|P_\theta(\text{electron})| = |P_\theta(\text{ion})| = \left[2m_p e V\right]^{1/2} \tag{17}$$

It is immediately seen from Eq. (16) that there is never any net momentum in the θ-direction, because P_θ (electron) + P_θ (ion) = 0.

A consideration of the electric currents that can flow shows that there is never any current in the radial and axial directions, because the electrons and the ions move together at all times. However, in the θ-direction the electrons and ions move in opposite directions, so azimuthal currents will flow. However, since there is no net momentum in the azimuthal direction, and since the electron is much less massive than the ion, the ion current will always be negligibly small compared to the electron current.

The energy equations for an electron-ion pair can be found from Eqs. (12) through (17). The results are:

$$E = \frac{m_i + m_e}{\left[m_i m_e\right]^{1/2}}\left[\frac{m_p(\dot{r}^2 + \dot{z}^2)}{2e} + V\right] \tag{18}$$

$$\frac{dE}{dt} = \frac{m_i + m_e}{\left[m_i m_e\right]^{1/2}} \frac{\partial V}{\partial t} \tag{19}$$

In the expressions stated above the energy is given in electron volts. A comparison of these equations to the equations for a single isolated particle (Eqs. (6) and (7)) shows that the plasma equations are the same except for a factor, $\simeq \sqrt{\frac{m_i}{m_e}}$,

which appears in each. Since this factor is always large (it has a minimum value of 43), the ion-electron pair acquires much more energy than a single particle of mass m_p does.

During the motion of an ion-electron pair the energy is sometimes predominantly with the ion and sometimes predominantly with the electron. There is a continuing exchange of energy between the electron and the ion through the action of the coulomb forces that couple the two. When the motion is mostly axial or radial, the energy is with the ion; when the motion is mostly azimuthal, the energy is with the electron.

The energy acquired is higher than that for a single particle with mass m_p because of the impeding effect that the ions exert on the electrons. A betatron-like acceleration of the electrons results, and this energy is subsequently transferred to the ions.

According to the model that has been developed here, the coulomb effects are represented by an electric field. This field acts in a similar manner on both members of a pair, and the field arises predominantly from the presence of many other ions and electrons in the plasma. In a real plasma this field is not a "smooth" quantity but will have a rather "lumpy" nature - both with respect to the space variables and with respect to time. This is just another way of expressing the fact that there are collisions occurring between the plasma constituents. Such effects are not taken into account in the present treatment.

In order to map the inductive potential, V, for any given situation it is necessary to know the quantity ϕ. This quantity was defined by Eq. (4) where it was noted that it is closely related to the flux enclosed by a circle centered on the axis of symmetry. A map of contours of constant ϕ is also a map of the magnetic field lines[3]. It is relatively easy to make such a map for any given experimental situation[3].

A more detailed discussion of the present work may be found elsewhere[4,5].

In the following section some specific examples of results obtained for the present model are presented. These examples are for the particularly simple case of a uniform, axially-directed, magnetic field with a sinusoidal time variation. Even for this simple case a rather complicated variety of results is possible.

IV MOTION IN A UNIFORM FIELD

In this section a number of examples are given for the case of a uniform field in the z-direction. The strength of this field is taken to be:

$$B_z = B_o \sin \omega t \tag{20}$$

The equations of motion for an ion-electron pair that starts at radius r_o at time t_o can be written from the results that have been given. The equations can be put into a dimensionless form. The equation for the radial motion becomes:

$$\frac{d^2 a}{d\tau^2} = -a \sin^2 \lambda \tau + \frac{\sin^2 \omega t_o}{a^3} \tag{21}$$

The various quantities that appear in Eq. (21) are defined as follows:

$$a = r/r_o \tag{22}$$

$$\omega_c = eB_o/2m_p \tag{23}$$

$$\tau = \omega_c t \tag{24}$$

$$\lambda = \omega/\omega_c \tag{25}$$

$$E_m = \pi \omega B_o r_o^2 \tag{26}$$

The quantity ω_c is the cyclotron angular frequency for a particle of mass m_p and charge e gyrating in a field of strength B_o. (Note: the factor of 2 arises because the azimuth angle is measured from the axis of symmetry of the field rather than from the center of curvature of the particle gyration.) The quantity E_m is the peak voltage that would

appear on a one-turn loop of wire, of radius r_o, placed about the axis of symmetry. The equation for the total kinetic energy of the pair is:

$$E = \sqrt{\frac{m_i}{m_e}} \frac{E_m}{4\pi\lambda} \left[\left(\frac{da}{d\tau} \right)^2 + \left(a \sin \lambda\tau - \frac{\sin \omega t_o}{a} \right)^2 \right] \quad (27)$$

Solutions to (21) and (27) have been obtained for various values of the parameters λ and t_o with the aid of a digital differential analyzer. These solutions are discussed below.

Case 1: $t_o = 0$:

When t_o equals zero there is no field present at the time the particle motion begins. The inductive potential for this case has a simple parabolic form:

$$V = \frac{E_m}{4\pi\lambda} a^2 \sin^2 \lambda\tau \quad (28)$$

Equation (21) reduces to a Mathieu's equation, and standard theory predicts solutions that have three forms: periodic; nonperiodic and exponentially damped; or nonperiodic and exponentially undamped.

Figure 1 shows the solution obtained for the case $\lambda = 1/16$ over the time range encompassing the first full cycle of the applied field. It is seen that the pair passes repeatedly through the axis of symmetry and finally travels outward to large radial distances.

Since the solution depends only on r/r_o, all pairs in the plasma (no matter what particular value of r_o might apply) converge on the axis of symmetry at one time. For a real gas this convergence would lead to many particle collisions that would disrupt the motion shown in Figure 1. However, it is experimentally observed that the general features of the motion persist in spite of the influence of collisions.

Figure 2 shows the energy of the pair for the first half-cycle of the applied field. The curve for the total kinetic energy is smooth. Shown as a dotted line is the kinetic energy of the electron only, and it is seen that its energy oscillates from the full amount to almost zero during the action. There

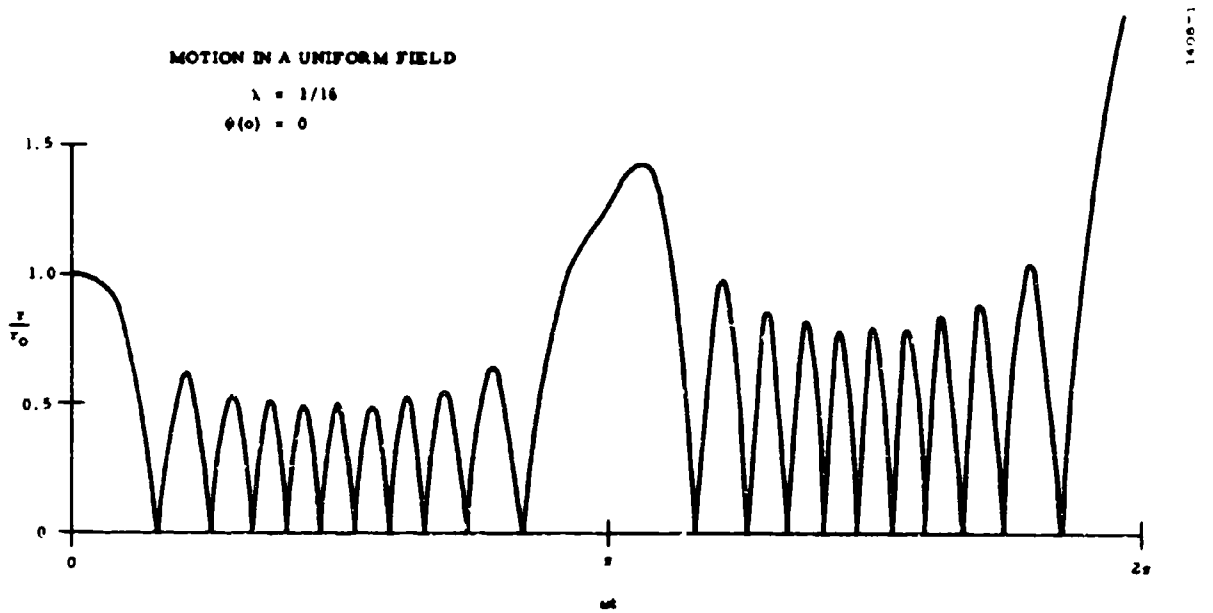


Figure 1. Motion in a Uniform Field, $\lambda = 1/16$, $\phi(o) = 0$

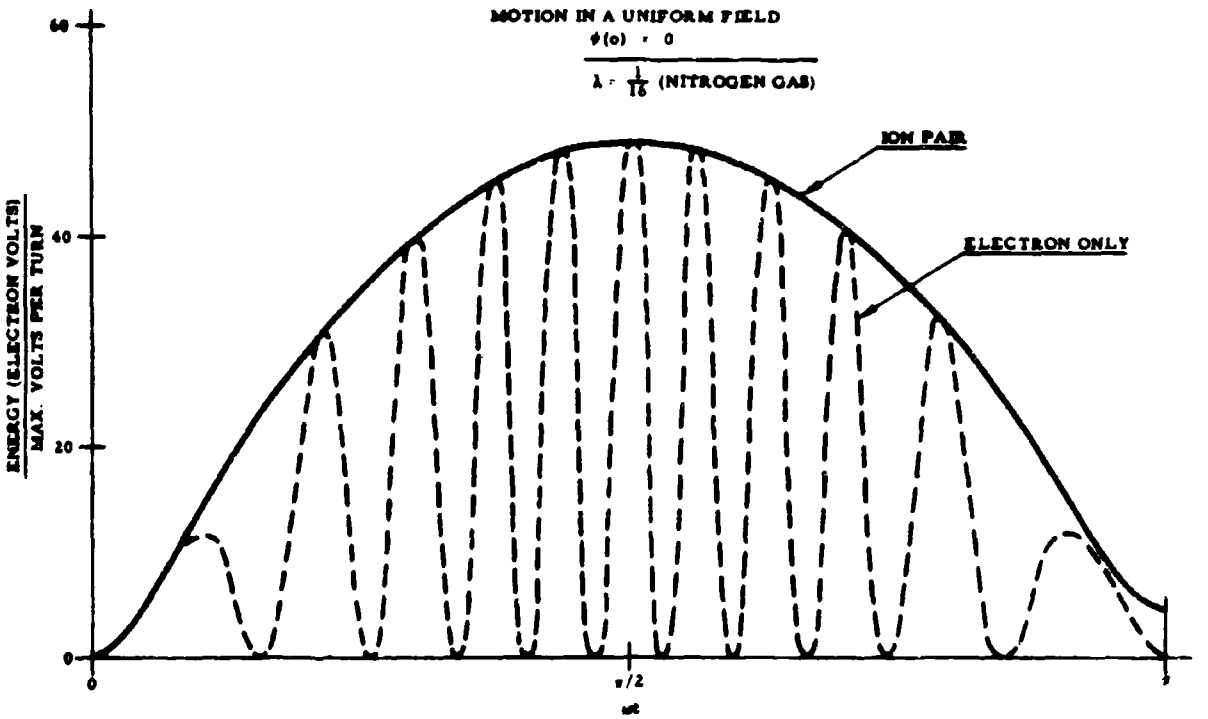


Figure 2. Motion in a Uniform Field, $\lambda = 1/16$, $\phi(o) = 0$ (Energy Plot)

is a continuing exchange of energy between the electron and the ion. At the end of the first half-cycle of the applied field most of the energy has been taken back by the field, and only a small amount remains with the pair. This follows from the fact that the induced electric field reverses its direction after the first quarter-cycle of the applied field.

Figure 3 shows the radial solution obtained for $\lambda = 1/4$, and Figure 4 shows the corresponding energy plot. The behavior is similar to that for $\lambda = 1/16$ except that the pair never reaches large radial displacements. The solution was actually obtained to 4-1/2 full cycles of the applied field with results similar to those shown.

The two graphs for energy were evaluated for the particular case of nitrogen.

Figure 5 summarizes the results of a number of computer runs for values of λ in the range 1/128 to 4. In all cases the maximum energy acquired by the pair during the first half cycle of the applied field occurred near phase $\pi/2$. These energies are shown in Figure 5 plotted against λ. The results apply to nitrogen gas. It is seen that the energy transfer can become large, because it is not too difficult to make a field for which the maximum volts per turn is several thousand. If the energy transfer gets larger than about 200,000 volts, it is no longer valid to consider the motion as nonrelativistic, since the electron mass will not remain constant. If the electron mass increases, the effective value of λ increases, and a limiting process sets in.

In order to apply the results of Figure 5 to deuterium gas, one must divide the ordinate scale by 2.64. It is still possible to be able to transfer energies in excess of 100,000 volts to the gas with typical laboratory fields. These energies are above the (D, D) fusion threshold, and one would expect to observe neutrons coming from the gas.

Case 2: $t_o > 0$:

This case arises if the pair is not created until the applied field has existed for a time, or if the pair has experienced a collision which causes flux to be "entrapped within its orbit".

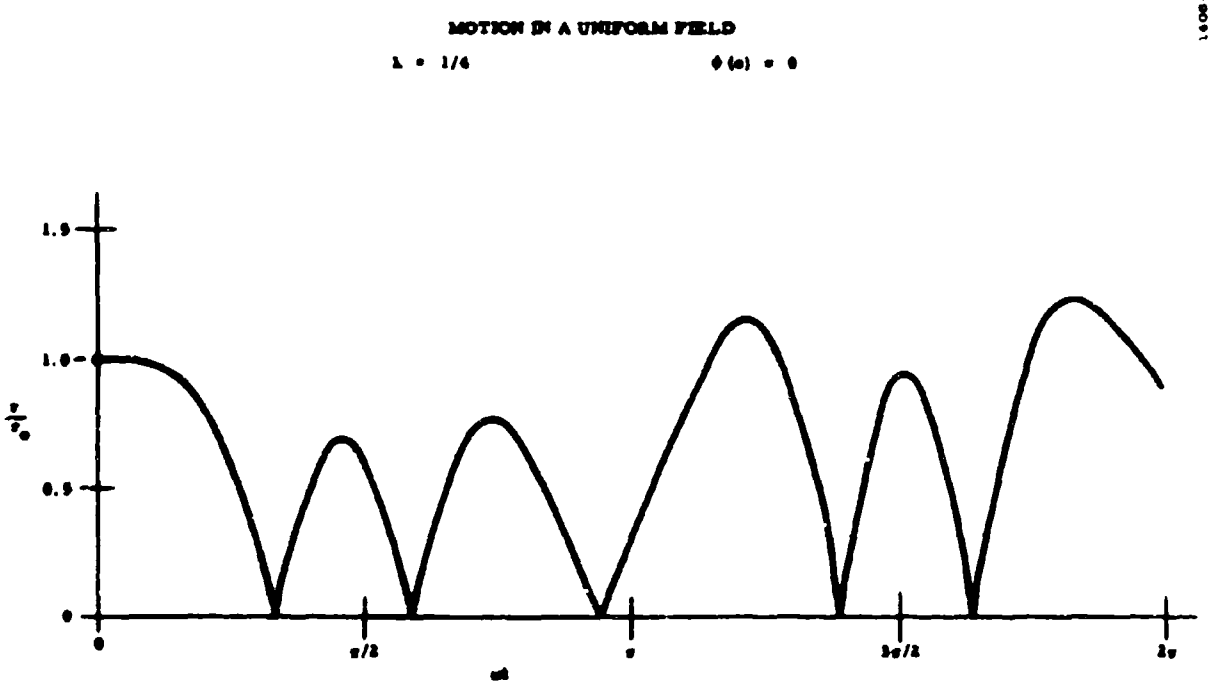


Figure 3. Motion in a Uniform Field, $\lambda = 1/4$, $\phi(o) = 0$

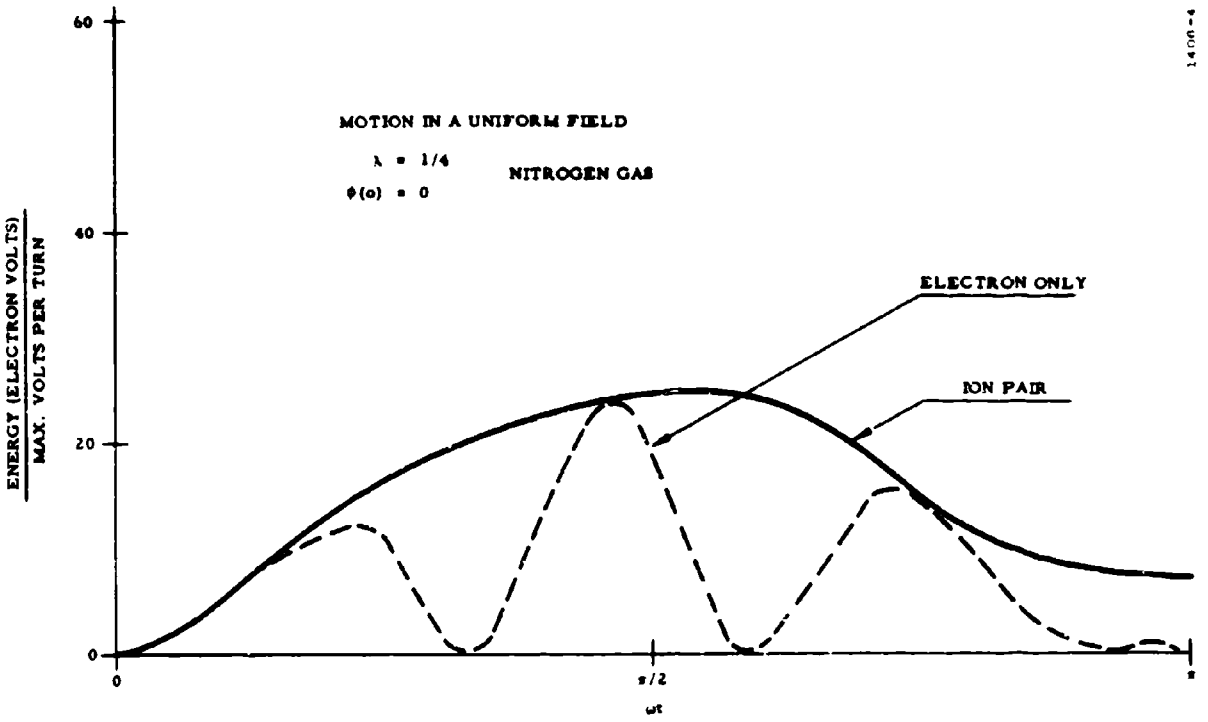


Figure 4. Motion in a Uniform Field, $\lambda = 1/4$, $\phi(o) = 0$ (Energy Plot)

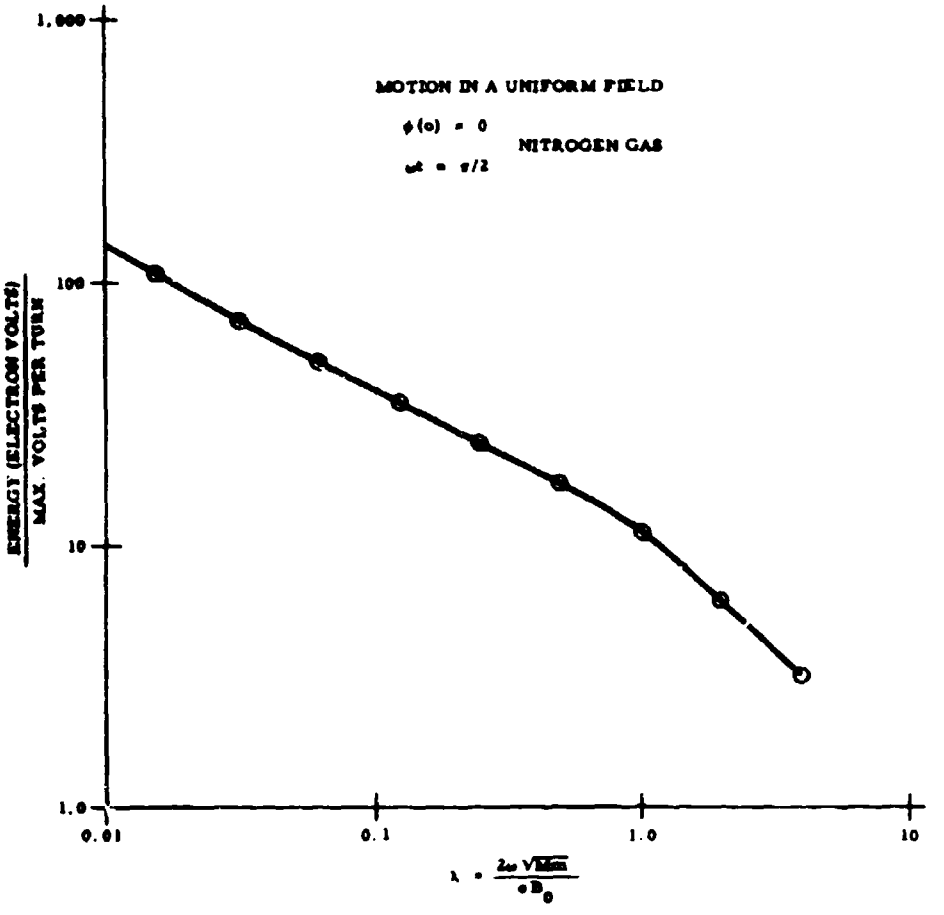


Figure 5. Summary of Computer Runs for Various Value of λ

The right hand side of Eq. (21) then possesses a singularity on the axis of symmetry, so the particles never pass through the axis of symmetry. The inductive potential now has the following form:

$$V = \frac{E_m}{4\pi\lambda}\left[a \sin \omega t - \frac{\sin \omega t_o}{a}\right]^2 \qquad (29)$$

Two cases must be distinguished: 1) during the first half cycle of the applied field the potential has a zero whose position depends on time; 2) during the second half-cycle of the applied field the potential has no zero. It is easily shown that for this latter case the potential has a minimum value whose position as a function of time is described by the same equation as for the potential zero during the first half-cycle.

Figure 6 shows the radial motion for two values of λ for the case $\sin \omega t_o = 1/4$, i.e., the initial field strength equals one-fourth of the maximum field strength. If the results of Figure 6 are interpreted for a single, isolated particle, the small oscillations would represent local gyrations around magnetic field lines, and these gyrations would take the form of almost circular paths in the r and θ directions. When the results are interpreted for an ion-electron pair, however, the motions are quite different. One must combine the results of Figure 6 (which represent the r motions) with the appropriate expressions for the azimuthal motions. These latter expressions are:

$$\frac{d\theta}{d(\omega t)} = \frac{1}{\lambda}\sqrt{\frac{m_i}{m_e}}\left[\sin \omega t - \frac{\sin \omega t_o}{a^2}\right] \qquad (30)$$

for the electron, and

$$\frac{d\theta}{d(\omega t)} = \frac{1}{\lambda}\sqrt{\frac{m_e}{m_i}}\left[\sin \omega t - \frac{\sin \omega t_o}{a^2}\right] \qquad (31)$$

for the ion.

It is now found (for typical values of the parameters) that the electron motion consists of a rapid circulation which encloses the axis of symmetry. On the other hand, the motion of the ions is almost completely radial with little circulation at all.

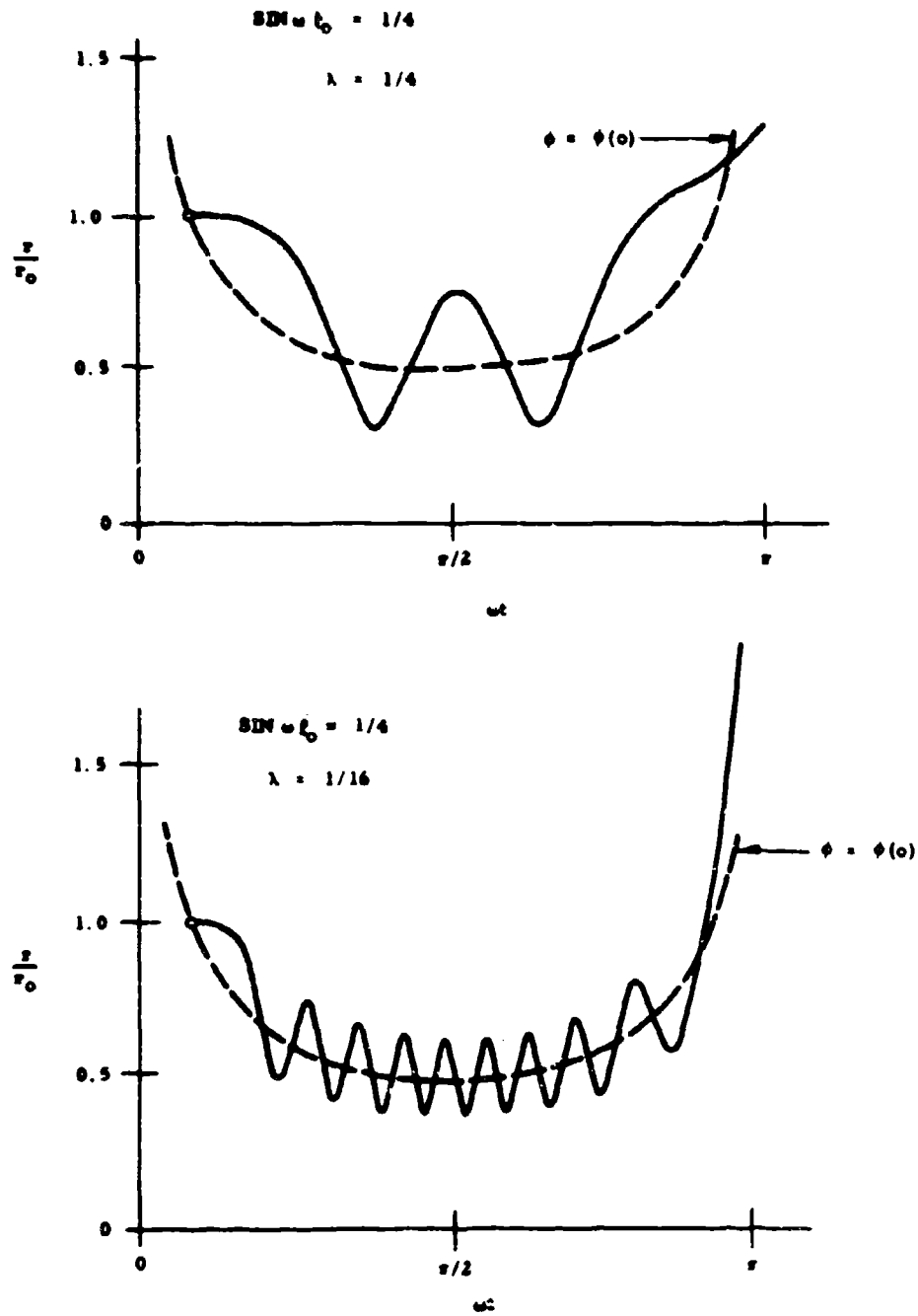


Figure 6. Motion in a Uniform Field, $\lambda = 1/4$, Sin $\omega t_o = 1/4$; $\lambda = 1/16$, Sin $\omega t_o = 1/4$

The dotted lines in Figure 6 indicate the position of the potential zero as a function of time. Each time the path crosses a dotted line, the electron currents reverse their direction.

Figure 7 shows the radial motion for the case $\lambda = 1/4$, $\sin \omega t_o = 1/2$. In this case the solution was extended into the time range encompassed by the second half-cycle of the applied field. The dotted line represents the position of the potential zero (during the first half-cycle) or the potential minimum (during the second half-cycle). The plot at the bottom of the figure shows the energy of the pair as a function of time. It is seen that the energy gets larger during the second half-cycle than during the first. This requires some explanation. If one examines the field conditions that must hold at a minimum of the inductive potential, one finds the following relation:

$$B_z r^2 = \phi - \phi(o) \qquad (32)$$

Recalling that ϕ represents the amount of flux enclosed to the axis of symmetry (aside from a factor of 2π), it is seen that (32) is identical to the equation that defines the location of the "stable orbit" for a betatron accelerator. Thus, during the second half-cycle of the applied field, a betatron type of acceleration prevails. Initially the energy is acquired by the electron, but it is subsequently shared with the ion. The energy graph of Figure 6 applies to nitrogen gas.

By the end of the second half-cycle of the applied field, the energy is largely taken back by the field, and the motion during the third half-cycle is essentially like that during the first.

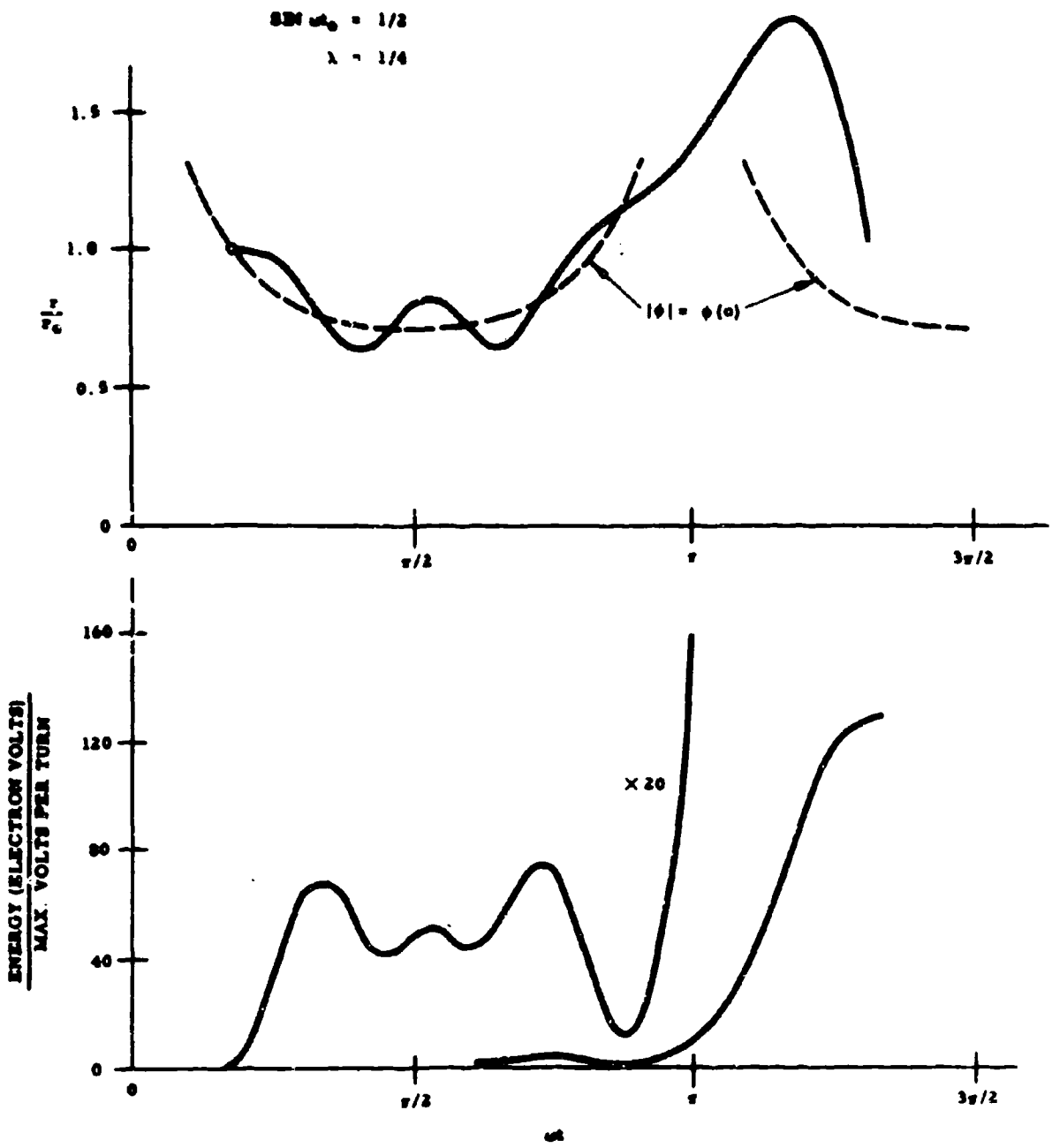


Figure 7. Motion in a Uniform Field, $\lambda = 1/4$, Sin $\omega t_o = 1/2$

BIBLIOGRAPHY

1. C. Störmer, Astrophysica Norvegica II, (1936).
2. L. Spitzer Jr., Physics of Fully Ionized Gases, Interscience Publishers Inc., London (1956).
3. A. S. Penfold, Determining Axially Symmetric Magnetic Field Patterns, AFOSR TN-60-842 (May 1960).
4. A. S. Penfold, Particle Motion in an Axially Symmetric Magnetic Field, AFOSR TN-60-841 (May 1960).
5. A. S. Penfold, A Model for the Motion of a Rarified Plasma in an Axially Symmetric Magnetic Field, AFOSR TN-60-961 (July 1960).

APPENDIX

It is the purpose of this appendix to sketch the development leading to Eqs. (1) through (4) in the text. A cylindrical coordinate system is considered with the z-axis taken as an axis of symmetry for the magnetic field. The field is described by a time-dependent vector potential $\vec{A}$, which has the following form:

$$\vec{A} = \hat{\theta} A_\theta (r, z, t) \tag{1}$$

From this potential and the equations $\vec{B} = \text{curl } \vec{A}$, $\vec{E} = -\frac{\partial \vec{A}}{\partial t}$ the field components are obtained. The only components that are different from zero are the components B_r, B_z, and E_θ.

A quantity ϕ can be defined. The defining equation plus its relationship to the vector potential is given below:

$$\phi \equiv \int_0^r dr\ r B_z (r, z, t) = r A_\theta \tag{2}$$

The basic equation of motion for a particle of mass m, charge q, and momentum $\vec{P}$ is:

$$\frac{d\vec{P}}{dt} = q\left[\vec{v} \times \vec{B} + \vec{E}\right] \tag{3}$$

The θ-component of this equation can be reduced to the following:

$$\frac{d(m r^2 \dot{\theta})}{dt} = -q \frac{d\phi}{dt} \tag{4}$$

This can be immediately integrated to yield:

$$P_\theta \equiv m r \dot{\theta} = -q\left[\frac{\phi - \phi(0) - \frac{J(0)}{q}}{r}\right] \tag{5}$$

In (5) the quantities $\phi(0)$ and $J(0)$ are constants of integration, and the latter represents the angular momentum of the particle with respect to the axis of symmetry at time zero.

If the r and z components of (3) are now written, and use is made of (5), it is found that they can be expressed in the form shown by Eqs. (1) and (2) in the text.

A more detailed development may be found in references 4 and 5 of the text.

APPENDIX F

DETERMINING AXIALLY SYMMETRIC MAGNETIC FIELD PATTERNS

PREFACE

This appendix contains the reproduction of a document published as AFOSR TN-60-842 in May 1960, which describes a method for experimentally determining the shape of an axially symmetric magnetic field pattern.

AFOSR TN-60-842 Research Study 29.14

Contract AF 49(638)-759

Project No. 9752
Task No. 37521

DETERMINING AXIALLY SYMMETRIC MAGNETIC FIELD PATTERNS

by

Alan S. Penfold

Space Research Laboratories
Litton Industries
Beverly Hills, California

Prepared for

AIR FORCE OFFICE OF SCIENTIFIC RESEARCH
AIR RESEARCH AND DEVELOPMENT COMMAND
UNITED STATES AIR FORCE
Washington, D. C.

24 May 1960

ABSTRACT

A simple method for the determination of some of the properties of a magnetic field is described. The method is applicable provided the field has a certain symmetry about one axis. The required symmetry is not seriously restricting and many field configurations of practical importance are amenable to this technique.

I INTRODUCTION

A simple method for the determination of some of the properties of a magnetic field is described. The method is applicable provided the field has a certain symmetry about one axis. Although the method is undoubtedly not a new one, it is certainly not generally recognized and this justified the present report.

The restriction to situations with a special symmetry does not severely limit the method since many situations of practical importance have this property. In many other cases (e. g., helical coils with a small pitch angle) there is near symmetry and the method will give satisfactory results.

The method is directly applicable to determining time-dependent fields which are produced by in-phase currents flowing in an array of coils. Application to other situations is discussed.

II DESCRIPTION OF THE METHOD

Consider a cylindrical coordinate system with unit vectors $\hat{r}$, $\hat{\theta}$, and $\hat{z}$. Suppose that the z-axis is the axis of symmetry and that the magnetic field has the following general form:

$$\vec{B} = \hat{r}\, B_r (r, z, t) + \hat{z}\, B_z (r, z, t) \tag{1a}$$

The corresponding induced electric field will have the form:

$$\vec{E} = \hat{\theta}\, E_\theta (r, z, t) \tag{1b}$$

The above two equations define the required symmetry. The $\vec{E}$ and $\vec{B}$ fields are related to each other through the Maxwell equation for curl $\vec{E}$:

$$\frac{\partial}{\partial r}[rE_\theta] = -r\frac{\partial}{\partial t}[B_z] \tag{2a}$$

$$\frac{\partial}{\partial z}[E_\theta] = \frac{\partial}{\partial t}[B_r] \tag{2b}$$

If a single-turn coil of wire is placed with its center on the z-axis, its plane perpendicular to the z-axis then the voltage induced in it will be:

$$V (r, z, t) = 2\pi r E_\theta \tag{3}$$

A second coil, with radius r + dr, placed at position z + dz will have an induced voltage V′. For V′ = V the following relationship must hold:

$$\frac{\partial V}{\partial r}\, dr + \frac{\partial V}{\partial z}\, dz = 0 \tag{4}$$

Substituting (2b), and (2b), and (3) into (4) gives

$$\frac{\partial B_z}{\partial t}\, dr = \frac{\partial B_r}{\partial t}\, dz \qquad (5)$$

In the simplest case the time dependence of B_r and B_z is everywhere the same. This situation is true if the field is produced by a set of in-phase currents flowing in an array of coils. Eq. (5) can then be simplified to read as follows:

$$\frac{dr}{dz} = \frac{B_r}{B_z} \qquad (6)$$

The last equation gives the result that the direction of a line joining the periphery of a series of coils having the same induced voltage is the same as the direction of the magnetic field at that point.

A magnetic field can thus be mapped with a series of coils which are all concentric with the axis of symmetry of the field. The various induced voltages are plotted on an r - z diagram and the constant voltage contours are identical with the magnetic field lines.

If the above measurements are each divided by the appropriate value of $2\pi r$ and plotted again, then the constant-value contours are (by Eq. (3)) contours of constant E_θ.

The magnitude of $\vec{B}$ at each point can be found, if desired, by applying Eq. (2a) and (2b).

So far the discussion has dealt with the special case of a time-dependent field produced by an array of coils carrying in-phase currents. The use of the method to measure dc fields and fields produced by currents having more complex time dependences is discussed briefly in the next two sections.

III THE USE OF SUPERPOSITION

If the time dependence of $\vec{B}$ is everywhere the same then it is sufficient to measure only the peak induced voltages in the survey coils. The B-field plot and the constant E_θ contours can be obtained from these data.

When the time dependence is not everywhere the same then the field pattern is moving and measurements at a whole series of times are required. This problem can be avoided by exciting the various parts of the system separately (e.g., sinusoidal excitation) and measuring the induced voltages from each part separately. A suitable linear combination of the several sets of measurements can then be made to yield the net field pattern at any desired instant of time. If this is done, one must take into consideration the electrical loading which the various parts of the system may have on each other. If there is ferromagnetic material present the technique of superposition can be applied only if this material is not operated in the region of magnetic saturation.

IV DC FIELDS

The method is applicable to dc fields provided a suitable ac analog can be constructed. If the dc system contains ferrous materials it seems difficult to apply the method, but otherwise one need only replace all metal surfaces with insulating materials.

V AN EXAMPLE

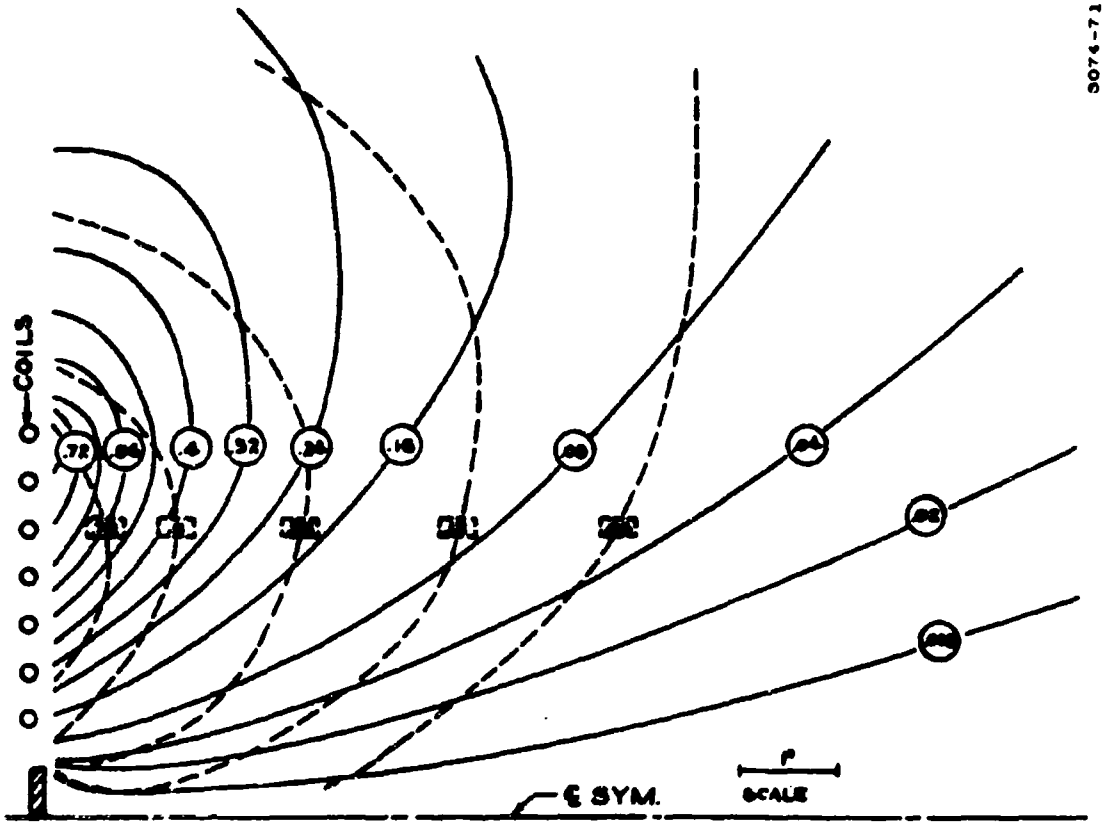
Figure 1 shows the results obtained from an application of the method to a specific situation. The field-producing elements were a series-connected array of one-turn coils of diameters 2, 3, 4, 5, 6, 7 and 8 inches arranged as shown. In addition, a 1-inch-diameter metal disc was placed on the axis of symmetry. The coils were excited at a frequency of 1 Mc. Figure 2 is a photograph of the physical test setup which was used for making the measurements. At the left of the picture can be seen the seven-turn pancake exciting coil. At the right of the picture are the concentric and independent probe or search coils. These have been mounted on a lucite plate (1/2 inch thick by 20-inch diameter). The coil spacing is 1/4 inch between adjacent wires. Thirty-nine coils have been mounted between diameters of 1/4 inch and 20 inches. The lucite plate was mounted on a board, as shown, and the whole structure on an optical bench so that the distance between the exciting coils and probing coils could be varied.

The solid lines in Figure 1 show the resulting B-field pattern. The corresponding numbers give the B-flux subtended to the axis of symmetry by each line (normalized to 1 for the flux subtended, or enclosed by the outermost coil).

The dotted lines in Figure 1 show the contours of equal E_θ field. The corresponding numbers give the value of E_θ (normalized to unity for the outermost coil).

One-quarter of the applied voltage appeared on the outermost coil and one-twentieth appeared on the innermost coil.

The shielding effect of the metal disc is clearly evident in Figure 1.



5074-71

Figure F-1. Field Patterns from an Array of Coils Excited at 1 Mc



Figure F-2. Physical Test Setup Used for Making Measurements

APPENDIX G

A RESISTOR-MESH ANALOG BOARD

APPENDIX G

A RESISTOR-MESH ANALOG BOARD

The analog board is a computer designed to study a variety of cylindrically symmetric magnetic field problems that are not amenable to exact solution. For example, the board has been used to study fringing fields of a poly-phase current system, the fields in the region around metals and ferrites of various shapes, and certain problems involving the presence of simple plasmas in the vicinity of field-producing coils. The topics treated in this appendix are listed below.

1. Mathematical development of the basic analog
2. Modifications of the basic analog
3. Plasma analog
4. Construction of the analog board and associated components.

1. MATHEMATICAL DEVELOPMENT OF THE BASIC ANALOG

The assumptions used in this development are as follows:

1. All applied currents and all fields are axially symmetric
2. All physical objects have axial symmetry
3. Displacement currents are negligible.

The MKS System of units is used throughout.

Maxwell's equations for an isotropic, homogeneous medium yield:

$$\frac{\partial Hz}{\partial z} + \frac{1}{r}\frac{\partial}{\partial r}(r H_r) = 0 \qquad \text{(G. 1)}$$

$$\frac{\partial Hr}{\partial z} - \frac{\partial Hz}{\partial r} = j(r, z) \qquad \text{(G. 2)}$$

where $j(r, z)$ is the azimuthal current density.

Eq. (G. 1) is satisfied identically if there exists a function,

$$Hz = \frac{1}{r} \frac{\partial \psi}{2r} \qquad (G. 3)$$

$$Hr = -\frac{1}{r} \frac{\partial \psi}{\partial z}$$

Substituting these into Eq. (G. 2) yields:

$$\frac{\partial}{\partial r}\left(\frac{1}{r} \frac{\partial \psi}{\partial r}\right) + \frac{1}{r} \frac{\partial^2 \psi}{\partial z^2} = -j(r, z) \qquad (G. 5)$$

The preceding equations could have been derived using the magnetic induction, B, where:

$$\vec{B} = \mu \vec{H} \qquad (G. 6)$$

in a simple medium. The magnetic flux, Φ, is defined by:

$$\Phi(r, z) = 2\pi \int_0^r r' \, Bz(r', z) \, dr'$$

and it can easily be shown that:

$$\Phi(r, z) = 2\pi\mu \, \psi(r, z) \qquad (G. 7)$$

We may re-write the current density, $j(r, z)$, as follows:

$$j(r, z) = \frac{\partial^2 I(r, z)}{\partial r \, \partial z} \qquad (G. 8)$$

If we integrate Eq. (G. 8) over the rectangle given by:

$$\left.\begin{array}{l} a \leq r \leq b \\ c \leq z \leq d \end{array}\right| \qquad (G. 9)$$

and we obtain:

$$I_R = \int_a^b dr \int_c^d dz\, j(r, z) \qquad \text{(G. 10)}$$

and we see that I_R is just the total current flowing into the rectangle. Then Eq. (G. 5) becomes:

$$\frac{\partial}{\partial r}\left(\frac{1}{r}\frac{\partial \psi}{\partial r}\right) + \frac{1}{r}\frac{\partial^2 \psi}{\partial z^2} = -\frac{\partial^2 I}{\partial r \partial z} \qquad \text{(G. 11)}$$

The analog is constructed in order to solve Eq. (G. 11). To do this we make a transformation from the (r, z) coordinate system to an (n, m) coordinate system. The motivation for this tranformation will become clear shortly. The transformation equations are the following:

$$r = r_o \sqrt{\frac{n}{n_o}} \; ; \; 0 \leqq n \leqq n_o \qquad \text{(G. 12)}$$

$$r = r_o \exp\left(\frac{n - n_o}{2n_o}\right) \; ; \; n > n_o \qquad \text{(G. 13)}$$

$$z = z_o\, m \; ; \text{ for all } m. \qquad \text{(G. 14)}$$

It is convenient to define

$$K \equiv \frac{r_o^2}{4 n_o z_o^2} \qquad \text{(G. 15)}$$

Using the transformation equations one can derive two differential equations from Eq. (G. 11). These new equations hold in the (n, m) system.

$$\frac{1}{K}\frac{\partial^2 \psi^*}{\partial n^2} + \frac{1}{n}\frac{\partial^2 \psi^*}{\partial m^2} = -\frac{\partial^2 I^*}{\partial m\, \partial n} \; ; \; 0 \leqq n \leqq n_o \qquad \text{(G. 16)}$$

$$\frac{1}{K}\frac{\partial}{\partial n}\left[\exp\left[-\left(\frac{n-n_o}{n_o}\right)\right]\frac{\partial \psi^*}{\partial n}\right] - \frac{1}{n_o}\frac{\partial^2 \psi^*}{\partial m^2} = -\frac{\partial^2 I^*}{\partial m\,\partial n}\,;\quad n > n_o \qquad \text{(G. 17)}$$

where we denote a function in the (n, m) system by an asterisk (*). In Eq. (G. 15) and (G. 16);

$$I^*(n, m) = I(r(n),\ z(m)) \qquad \text{(G. 18)}$$

$$\psi^*(n, m) = \frac{\psi(r(n),\ z(m))}{2z_o} \qquad \text{(G. 19)}$$

We introduce the operator, £;

$$\pounds \equiv \int_{N-\frac{1}{2}}^{N+\frac{1}{2}} dn \int_{M-\frac{1}{2}}^{M+\frac{1}{2}} dm, \qquad \text{(G. 20)}$$

where N and M are particular values of n and m. £ integrates over the rectangle of Figure G-1. We write

$$N+ \equiv N + \frac{1}{2} \qquad M+ \equiv M + \frac{1}{2}$$

$$N- \equiv N - \frac{1}{2} \qquad M- \equiv M - \frac{1}{2}$$

and by applying £ to E. (G. 16) and (G. 17) we obtain:

$$\frac{1}{K}\int_{M-}^{M+} dm\,\frac{\partial \psi^*}{\partial n}\exp\left[-\left(\frac{n-n_o}{n}\right)\right]\Bigg|_{N-}^{N+} + \frac{1}{n_o}\int_{N-}^{N+} dn\,\frac{\partial \psi^*}{\partial m}\Bigg|_{M-}^{M+} = -I_R(N, M) \qquad \text{(G. 22)}$$

$$;\ N > n_o$$

where, for example,

$$\frac{\partial \psi^*}{\partial m}\Bigg|_{M-}^{M+} \equiv \left(\frac{\partial \psi^*}{\partial m}\right)_{m=M+} - \left(\frac{\partial \psi^*}{\partial m}\right)_{m=M-} \qquad \text{(G. 23)}$$

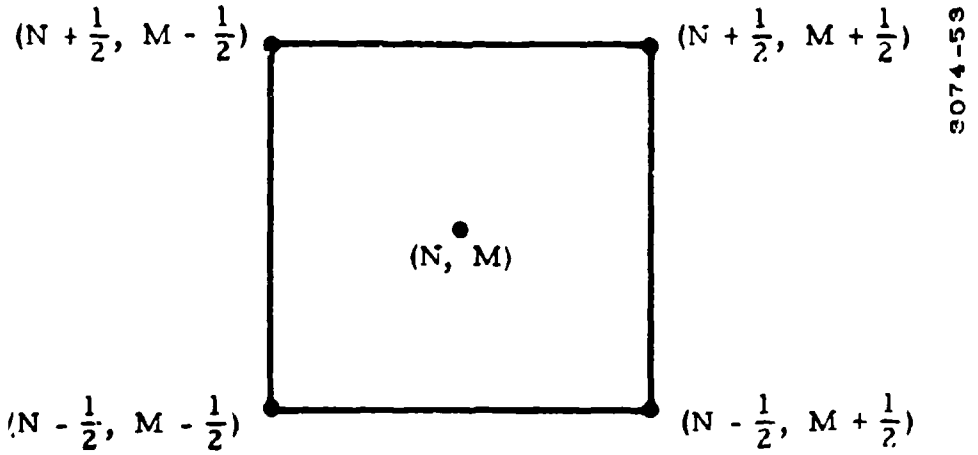


Figure G-1. Rectangle of Integration

The analog is developed by expanding ψ^* in a power series about four points on the boundary of the rectangle of integration. Figure G-2 shows the four points as crosses and also shows the notation used.

The expansion notation is illustrated below for the expansion about the point (+, 0).

$$\psi^* (n, m) = \sum_{i=0}^{\infty} \sum_{j=0}^{\infty} C_{ij} (+, 0) (n - N_+)^i (m - M)^j \qquad (G.24)$$

The validity of the analog depends on the choice of the cutoff of the power series. We neglect all terms higher than quadratic.

When Eq. (G.21) and G.22) are evaluated using these expansions, the results are the following:

$$\frac{C_{10} (+, 0) - C_{10} (-, 0)}{K} + \frac{C_{01} (0, +) - C_{01} (0, -)}{1/\ln \left[\frac{N + \frac{1}{2}}{N - \frac{1}{2}}\right]} = - I_R (N, M)$$

$$; N \leqq n_o \qquad (G.25)$$

$$\frac{C_{10} (+, 0) - C_{10} (-, 0)\, e^1}{K \exp\left(\frac{N - n_o + \frac{1}{2}}{n_o}\right)} + \frac{C_{01} (0, +) - C_{01} (0, -)}{n_o} = - I_R (N, M)$$

$$; N > n_o \qquad (G.26)$$

In order to get Eq. (G.25) we have neglected the term:

$$\left[C_{11} (0, +) - C_{11} (0, -)\right]\left[1 - N \ln\left(\frac{N + \frac{1}{2}}{N - \frac{1}{2}}\right)\right]$$

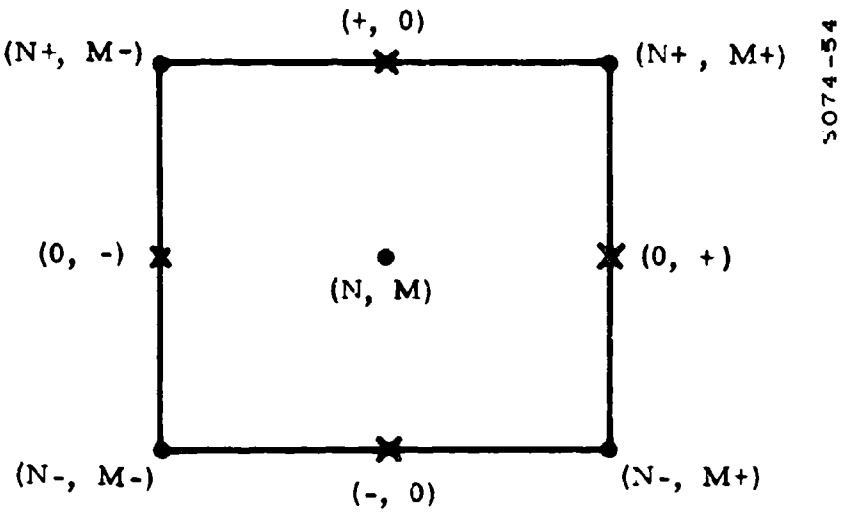


Figure G-2. Power Series Expansion Points

The second factor is small as can be seen by substituting numbers. For small values of N, ψ^* is mostly quadratic in form, depending primarily on n^2. (Small values of N are close to the axis of symmetry).

The coefficients (C_{ij}) can be evaluated from equations like Eq. (G. 24). For example, Eq. (G. 24) yields:

$$C_{10}(+, 0) = \psi^*(1, 0) - \psi^*(0, 0) \tag{G. 27}$$

where the notation $\psi^*(1, 0)$ means to take the value of $\psi^*(n, m)$ at $n = N + 1$, $m = M$.

In order to get an electrical analog, we introduce a constant, R_o, which has the dimensions of a resistance, and define resistor values in the following way:

$$R_n(N) = K R_o; \; N \leqq n_o \tag{G. 28}$$

$$R_n(N) = K R_o \exp\left(\frac{N - n_o - \frac{1}{2}}{n_o}\right); \; N > n_o \tag{G. 29}$$

$$R_m(N) = R_o \left[\ln\left(\frac{N + \frac{1}{2}}{N - \frac{1}{2}}\right)\right]^{-1}; \; N \leqq n_o \tag{G. 30}$$

$$R_m(N) = R_o n_o; \; N > n_o \tag{G. 31}$$

Since the units of ψ^* are amperes (See Eq. (G. 16), a voltage function $V^*(n, m)$ can be defined by:

$$V^*(n, m) \equiv R_o \psi^*(n, m), \tag{G. 32}$$

and (from Eq. (G. 7)) the magnetic flux, Φ, can be expressed:

$$\Phi[(\;), z(m)] = \frac{4\pi \mu z_o}{R_o} V^*(n, m) \tag{G. 33}$$

Using the above-cited equations, Eq. (G. 25) and (G. 26) can be expressed as one equation:

$$\frac{V^*(0,0) - V^*(-1,0)}{R_n(N)} + \frac{V^*(0,0) - V^*(+,0)}{R_n(N+1)} + \frac{V^*(0,0) - V^*(0,-1)}{R_m(N)} + \frac{V^*(0,0) - V^*(0,1)}{R_m(N)} = I_R(N,M) \tag{G. 34}$$

Eq. (G. 34) is the basic analog equation. It is the equation describing the system of voltages, currents, and resistors of Figure G-3.

A consideration of the equations for neighboring points yields additional resistors and voltages compatible with the network of Figure G-3.

Furthermore, from a consideration of Eq. (G. 3) and (G. 4), one can derive the following expressions for the magnetic field components:

$$\int_{M_-}^{M_+} dm\, H_z\left[r(N_-),\ z(m)\right] = \frac{1}{z_o}\left[\frac{V^*(0,0) - V^*(-1,0)}{R_n(N)}\right] \tag{G. 35}$$

$$\int_{N_-}^{N_+} dn\, H_r\left[r(n),\ z(M_-)\right] = -\frac{1}{z_o}\left[\frac{2R_m(N)}{R_n(N+1) + R_n(N)}\right]^{1/2}\left[\frac{V^*(0,0) - V^*(0,-1)}{R_m(N)}\right] \tag{G. 36}$$

The average value of H_z is proportional to the current in the n-direction, and the average value of H_r is proportional to the current in the m-direction.

In some problems it is more useful to obtain a plot of the lines of constant magnetic flux, since the slope of these lines gives the direction of the magnetic field, (see Appendix F).

From Eq. (G. 33) it can be seen that the magnetic flux is proportional to V^*, the analog board voltage. Therefore, a line of constant V^* on the resistor mesh is a line of constant Φ in the (r, z) space.

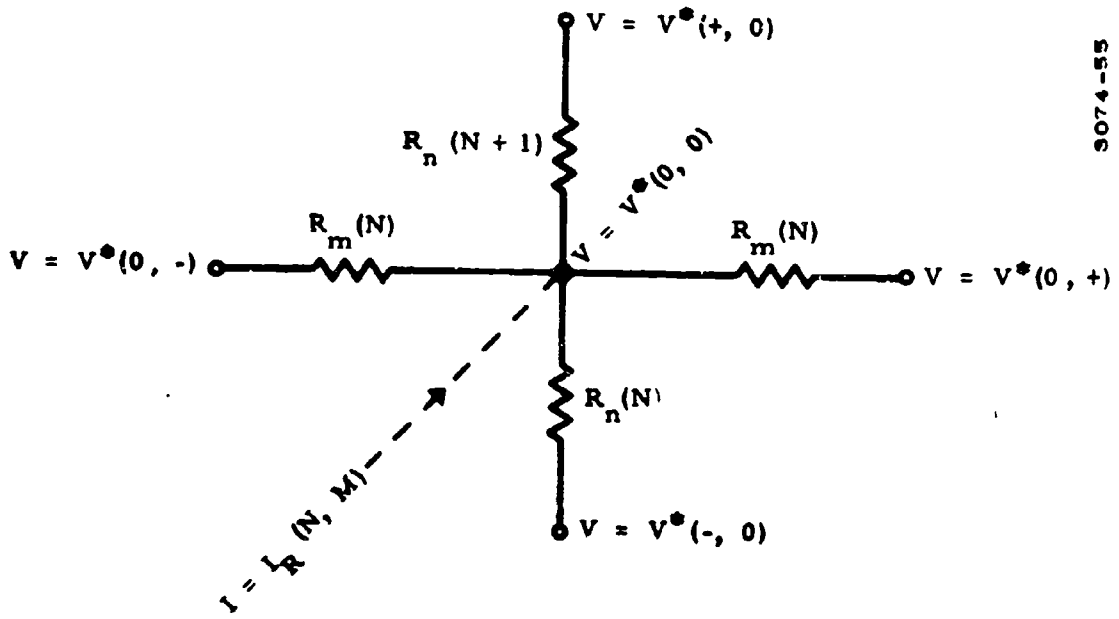


Figure G-3. Basic Analog

The advantages of having transformed to the (n, m) system are:

1. R_n is constant when $N \leqq n_o$
2. R_m is constant when $N > n_o$
3. R_n varies like e^{n/n_o} for $N > n_o$ and this variation can be made to coincide with the standard resistor sizes which vary like $e^{n/10.41}$.

The constants of the analog board were chosen as follows:

$$n_o = 5.2 \tag{G. 37}$$

$$R_o = 19.2 \text{ ohms} \tag{G. 38}$$

$$\frac{r_o}{z_o} = 5.775 \tag{G. 39}$$

Using these numbers the transformation equations become:

$$r = 2.53\, z_o \sqrt{n}\,; \; n \leqq 5.2 \tag{G. 40}$$

$$r = 5.775 \exp\left[\frac{n - 5.2}{10.4}\right] \; ; \; n > 5.2 \tag{G. 41}$$

$$z = z_o\, m; \text{ for all } m \tag{G. 42}$$

and Eq. (G. 33) becomes:

$$\Phi = 0.655\, \mu\, z_o\, V^* \tag{G. 43}$$

On the analog board the axis of symmetry coincides with zero flux and so:

$$V^*(0, m) = 0 \tag{G. 44}$$

All $n = 0$ mesh points are joined by a wire and all voltages are referred to it.

The motivation for the form of the transformation can be made clearer. The exponential dependence is desireable because of the resistor sizes, but this function does not go to zero as n goes to zero. However it can be matched to one which does. Indeed both the function and its first derivative can be matched.

If we write:

$$r = k\, n^{a};\ n \leqq n_o$$

$$r = k'\, \exp\left(\frac{n - n_o}{2n_o}\right);\ n > n_o$$

Then:

$$\frac{dr}{dn} = a\, k\, n^{a-1};\ n \leqq n_o$$

$$\frac{dr}{dn} = \frac{k'}{2n_o}\, \exp\left(\frac{n - n_o}{2n_o}\right);\ n > n_o$$

Equating these at $n = n_o$ we find

$$a = \frac{1}{2} \text{ and } k = k'\sqrt{n_o}\ ,$$

and this gives the final form to the transformation.

An important feature of the coordinate transformation should be noted. The constant n_o, and the relation between r_o and z_o, is determined by the construction of the board. The only free parameter left is z_o itself and it appears in both the r and z transformations. Now z_o is a scaling factor to be chosen for a particular problem, i. e., some length in the problem is transformed into an analog length (say in the m-direction). Since z_o appears in both coordinates, the problem automatically scales in the n-direction. For this reason it is usually not possible to perfectly map the geometry of a given problem into the analog space.

2. MODIFICATIONS OF THE BASIC ANALOG

Modifications of the basic analog are required in order to represent certain current-carrying wires, metal structures and ferrite structures. The cases which have been analyzed are listed below:

1. Ferrites whose boundaries are coincident with mesh points
2. Sheet currents:
   a. Extending in the axial direction
   b. Extending in the radial direction
3. Metallic objects (nonferrous)

Only some results of the analysis will be given.

2.1 Ferrites

These results hold only if the boundaries of the ferrites coincide with mesh points. The analog is not accurate otherwise.

If the ferrites ($\mu = \mu_2$) are immersed in a medium ($\mu = \mu_1$), then:

1. In region μ_1 the resistors are the same as the basic analog
2. In region μ_2 the values of the resistors are increased by μ_2/μ_1
3. The resistors on the boundary are
   a. Increased by $2\mu_2/(\mu_1 + \mu_2)$ for radial resistors and by the same factor for axial resistors provided the boundary is located at $n > n_o$
   b. The values of axial resistors are raised by

$$\frac{\ln\left(\frac{n+\frac{1}{2}}{n-\frac{1}{2}}\right)}{\ln\frac{n+\frac{1}{2}}{n}+\left(\frac{\mu_1}{\mu_2}\right)\ln\frac{n}{n-\frac{1}{2}}}$$

; if $n < n_o$

2.2 Sheet Currents

The concept of a field-producing sheet current can be used provided that the diameter of the wire is small compared to a mesh size, and if the coil turn-spacing is small. The currents to be fed into the board consist of two terms, I_R and I_C. I_C is a correction term which is used when the coil current is not uniform. Only one example of I_C will be given.

1. For sheet currents extending in the axial direction:

$$I_R = \int_{z(M_-)}^{z(M_+)} dz\, j\,[r(N),\ z] \tag{G.45}$$

$$I_C = \left(\frac{r(N)}{4n_o z_o}\right)^2 z_o \left\{ j\,(r,\ z(M)) - \frac{j\left(r,\ z(M+1)\right) + j\left(r,\ z(M-1)\right)}{2} \right\} \tag{G.46}$$

$$; \quad N > n_o$$

and a similar term for I_C if $N \leq n_o$.

Notice we have used the real current density, not a transformed current density.

This expressions for I_C holds provided the current passes through the point (N, M) but does not terminate there.

2. For sheet currents extending in the radial direction:

$$I_R = \int_{r(N_-)}^{r(N_+)} dr\, j\left(r,\ z(M)\right) \tag{G.47}$$

and, there are similar correction terms.

In both cases the correction terms are different if the currents terminate at a mesh point.

2.3 Metal Objects

Consider the one-turn metal strap of Figure G-4 and suppose that the gap, d, is so narrow that the cylindrical symmetry of the magnetic field is essentially undisturbed. The conductivity and permeability of the metal will be assumed to be uniform with values σ and μ_o, where the permeability is the same as that of free space.

The gap may be connected to a voltage source, or a current source, and the connection will always be taken to be ideal in the sense that it forces no lack of uniformity of current in the metal strap. Displacement currents will be ignored.

The distribution of current in the strap may not be uniform, however, due to the effects of the magnetic field. Two extreme cases can be cited:

1. The rate of change of the field is so slow that eddy currents in the metal are negligible. In this case any current that exists in the metal is due entirely to sources which are connected across the gap and so the current density in the metal is uniform. The effect on the metal of the magnetic field is negligible, and the basic analog equation, (G. 34), is valid.
2. The rate of change of the field is very rapid and strong eddy currents flow in the metal. A complete skin effect then exists and the surface of the metal is a constant-flux surface. The distribution of current in the metal is such as to prevent any of the field from penetrating.

The result of this analysis is an analog which includes in it both cases (1) and (2).

The voltage drop in the strap due to ohmic losses is $2\pi rj/\sigma$, and if $\epsilon(t)$ is the applied voltage on the gap then:

$$\frac{2\pi r}{\sigma} j = \epsilon(t) - \frac{\partial \Phi (r, z, t)}{\partial t} \qquad \text{(G. 48)}$$

where the last term is the voltage of induction. As before we let

$$\Phi = 2\pi \mu_o \psi \qquad \text{(G. 49)}$$

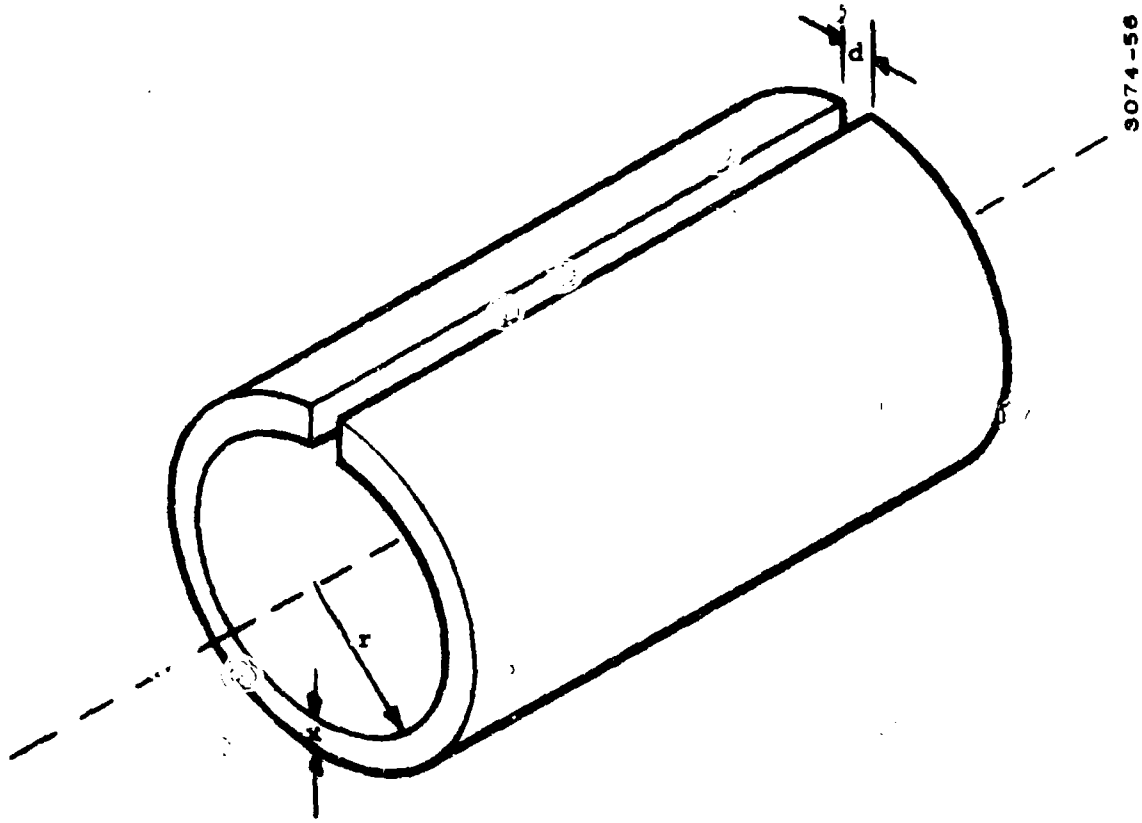


Figure G-4. One-turn Strap

Eq. (G. 5) now becomes:

$$\frac{\partial}{\partial r}\frac{1}{r}\frac{\partial \psi}{\partial r} + \frac{1}{r}\frac{\partial^2 \psi}{\partial z^2} - \frac{\sigma \mu_o}{r}\frac{\partial \psi}{\partial t} = -\frac{\sigma}{2\pi r}\varepsilon(t) \qquad \text{(G. 50)}$$

The above equation can be transformed to the (n, m) coordinate system with the aid of Eq. (G. 12) through (G. 15). A transformed time is also used as defined by

$$\tau = t/a \qquad \text{(G. 51)}$$

The result of the transformation of Eq. (G. 50) is:

$$\frac{1}{K}\frac{\partial^2 \psi^*}{\partial n^2} + \frac{1}{n}\frac{\partial^2 \psi^*}{\partial m^2} - \frac{n_c C R_o}{n}\frac{\partial \psi^*}{\partial \tau} = -\frac{\Omega n_o}{n}\varepsilon(\tau) \qquad \text{(G. 52)}$$

$$\text{for } n \leq n_o$$

and

$$\frac{1}{K}\frac{\partial}{\partial n}\left\{\left[\exp\left(-\frac{n - n_o}{n_o}\right)\right]\frac{\partial \psi^*}{\partial n}\right\} + \frac{1}{n_o}\frac{\partial^2 \psi^*}{\partial m^2}$$

$$- C R_o \frac{\partial \psi^*}{\partial \tau} = -\Omega \varepsilon(\tau)$$

$$\text{for } n > n_o$$

where

$$C \equiv \frac{\mu_o z_o^2 \sigma}{n_o 2 R_o} \qquad \text{(G. 54)}$$

$$\Omega \equiv \frac{\sigma z_o}{4\pi n_o} \qquad \text{(G. 55)}$$

It is noted that C is a characteristic capacity of the analog (farads) and Ω is a characteristic conductance (mho). C/Ω is independent of σ and is a characteristic time constant.

The same procedure as before is used to develop the analog and the result is shown in Figure G-5. Each node point is seen to be connected to ground (i. e., the axis $\psi^* = 0$) by a capacitor. Thus, when the magnetic field around the strap varies very quickly, the field inside the strap is highly attenuated.

The values for C and I_N (Figure G-5) are found from

$$\left.\begin{aligned} C_N &= C \ln \frac{N + \frac{1}{2}}{N - \frac{1}{2}} \\ I_N &= \frac{C_N}{C} \Omega \, \epsilon(\tau) \end{aligned}\right\} \quad N \leqq n_o \qquad \text{(G. 56)}$$

$$\left.\begin{aligned} C_N &= C \\ I_N &= \Omega \, \epsilon(\tau) \end{aligned}\right\} \quad N > n_o \qquad \text{(G. 57)}$$

The scale factor for the time, a, can be chosen to have any convenient value.

If the analog is more useful when expressed in terms of a constant-voltage generator rather than a constant-current generator, one can replace $\epsilon(\tau)$ by:

$$\epsilon(\tau) \equiv \frac{C}{\Omega} \frac{\partial V_g(\tau)}{\partial \tau} \qquad \text{(G. 58)}$$

where $V_g(\tau)$ is defined by the above. Substitution of the above into Eq. (G. 50) yields the analog shown in Figure G-6. Since V_g is independent of position the capacitors from all nodes can be connected to the same generator.

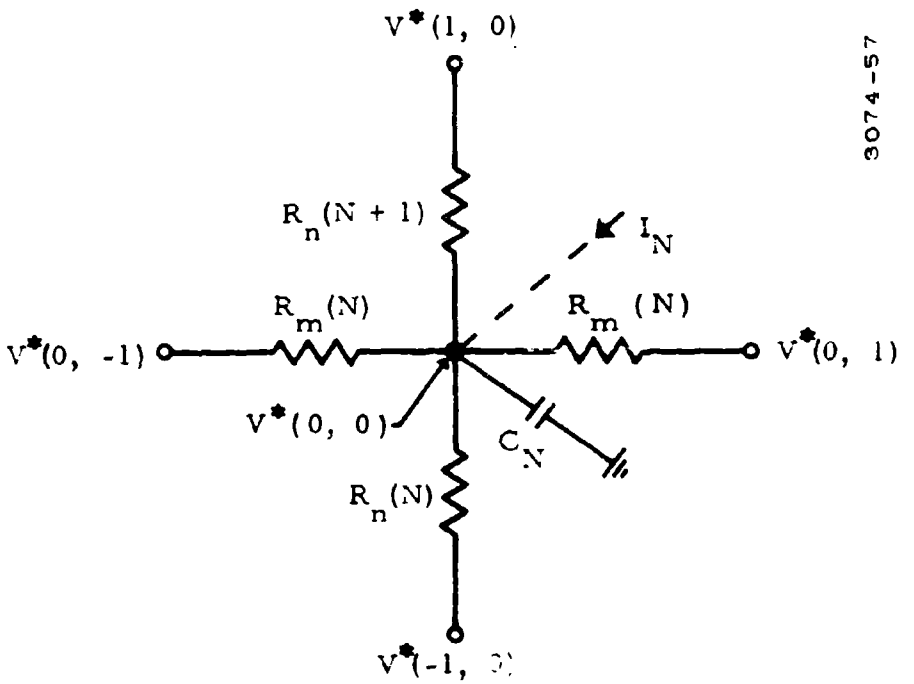


Figure G-5. Analog for Metal Objects

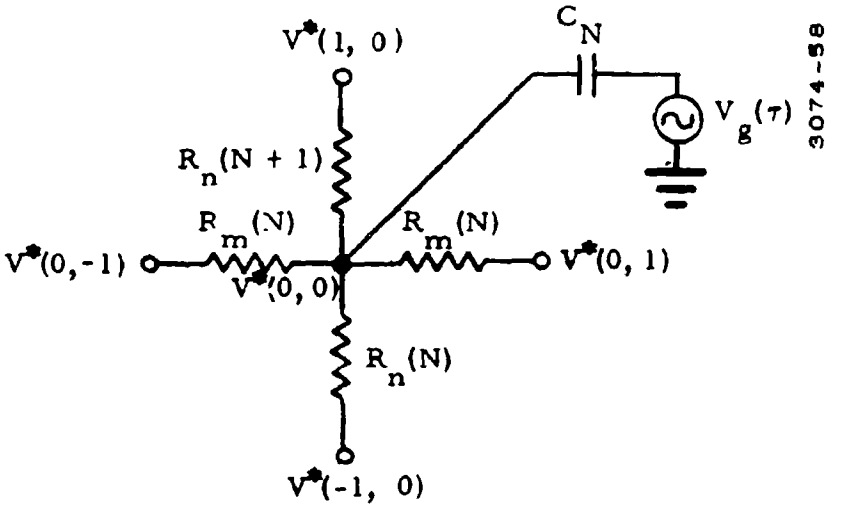


Figure G-6. Constant-Voltage Analog

Calculation shows that if (N, M) lies along an edge of the metal then the appropriate value for the capacitor is $C_N/2$ rather than C_N. If it lies on a corner, the appropriate value is $C_N/4$. These apply if $N > n_o$. The results for $N < n_o$ are tedious and will not be given here.(See Figure G-7.)

The qualitative behavior of the analog can be discovered by considering its response to a voltage step. The step is assumed to occur at $\tau = 0$ and to have amplitude ε_o. Then

$$V_g(\tau) = 0;\ \tau < 0 \qquad \text{and} \qquad V_g(\tau) = \frac{\Omega}{C}\,\varepsilon_o\,\tau;\ \tau > 0$$

In response to this voltage, the voltage at the mesh points will rise from zero to some steady-state value with a time constant proportional to C. On the other hand, for small values for τ one finds that

$$V^*(N, M) = \frac{\Omega}{C}\,\varepsilon_o\,\tau$$

This result can be rewritten in terms of the magnetic flux through the use of Eq. (G. 49) and the result is:

$$\Phi(r(N), z(M)) = \varepsilon_o t \qquad \text{(G. 59)}$$

this result holds for small values of time when the inductive behavior of the metal dominates. At large values of time the conductivity dominates. One then finds that the current flowing into each mesh point is

$$I \cong \sigma\,\frac{\Delta z\,\Delta r}{2\pi r}\,\varepsilon_o \qquad \text{(G. 60)}$$

where $\Delta z\ \Delta r$ is the area represented by one mesh point. This is Ohm's law.

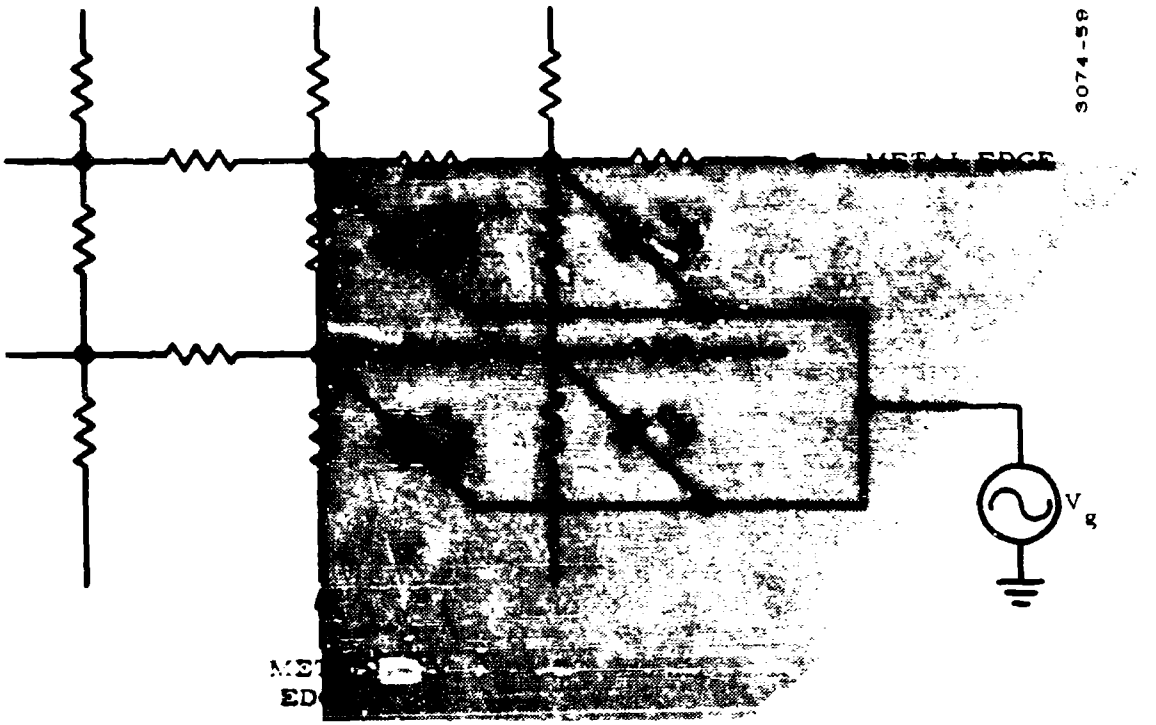


Figure G-7. Analog of Metal Corner

3. PLASMA ANALOG

We will consider the electrical analog for a magnetic field in a region containing plasma. Let the electron density be N^e. Cylindrical symmetry is assumed and N^e is assumed independent of time. This is very restrictive but still, the analog yields useful information.

The current is due almost entirely to the electrons. If e is the absolute magnitude of the electronic charge and if $< W_\theta >^e$ is the average azimuthal electron speed then the current density is

$$j = - e N^e < W_\theta >^e \qquad \text{(G. 61)}$$

where all the quantities are functions of r and z.

Let M^e be the electron mass, E_θ be the electric field of induction, and T be the average time for 90° scattering of an electron. Then:

$$\frac{\partial j}{\partial t} + \frac{j}{T} = \frac{e^2 N^e}{M^e} E_\theta \qquad \text{(G. 62)}$$

If E_θ is zero then j dies away exponentially with time constant T.

Strictly speaking T is not a constant, but it varies little over one or two collision times if the mean electron speed is constant (constant electron temperature) over a time on the order of 2T.

The situation is discussed in more detail in Section 3 of this report.

Assuming a constant value for T one finds:

$$j(t) = j(t = 0) e^{-t/T} + \frac{e^2 N^e}{M^e} \int_o^t e^{-\frac{t - t'}{T}} E_\theta(t')\, dt' \qquad \text{(G. 63)}$$

If T is very small then

$$j = \frac{e^2 N^e}{M^e} T E_\theta \qquad \text{(G. 64)}$$

which is just Ohm's law. If T is very large then

$$j = j(t=0) - \frac{e^2 N^e}{2\pi r M^e} \left[\Phi(t) - \Phi(t=0) \right] \qquad \text{(G. 65)}$$

and the current density is in phase with the magnetic flux. The plasma is then inertially dominated as is discussed in Section 3.

Eq. (G. 63) can be transformed to the (n, m) coordinate system with the result:

$$\frac{\partial^2 I^*}{\partial r \partial z} = - \frac{R_o}{R_p(n, m)} \int_o^t e^{- \frac{a(\tau - \tau')}{T}} \frac{\partial \psi^*}{\partial \tau'} d\tau' + \frac{\partial^2 I^*(t=0)}{\partial r \partial z} e^{-a\tau/T} \qquad \text{(G. 66)}$$

where:

$$R_p = \frac{R_o n}{4\pi R_e z_o^2 N^e (r(n), z(m))} \text{ (ohm)} \qquad \text{(G. 67)}$$

for $n \leq n_o$

$$R_p = \frac{R_o n_o}{4\pi R_e z_o^2 N^e (r(n), z(m))} \text{ (ohm)} \qquad \text{(G. 68)}$$

for $n > n_o$

and

$$R_e = \frac{e^2 \mu_o}{4\pi M^e} = 2.80 \times 10^{-15} \text{ meter.}$$

Note that R_e is the classical electron radius. The characteristic collision time, T, may vary from place to place in the plasma. For each place a characteristic capacity, C_p may be defined. It is:

$$C_p = \frac{T}{a R_p} \qquad \text{(G. 69)}$$

The current density , $\partial^2 I^*/\partial r \partial z$, may now be inserted into Eq. (G.16) and (G.17) and the analog derived. The result is shown in Figure G-8.

The plasma is seen to have the effect of shorting each mesh point to ground through a series RC circuit whose time constant equals the mean time for 90° collisions. The node resistors, R_p, give the self-field effects which are appreciable if

$$N^e > 3 \times 10^{17} \text{ electrons/meter}^3$$

4. CONSTRUCTION OF THE ANALOG BOARD

An analog board was constructed. Thirty-six independent current sources with a range 0 - 10 ma are provided. The current sources are zener-diode stabilized pentode tubes whose plate and cathodes are made available for connection to the analog board. The complete unit is shown in Figure G-9 and a close-up of the resistor mesh is shown in Figure G-10. It can be seen that the node points can be easily disconnected.

The board reader is essentially a bridge circuit as indicated in Figure G-11. The potentiometer R_2 is set to a value and the corresponding voltage contour is found, on the board, through the use of the probe containing the potentiometer R_1. The latter is for interpolation between the mesh points.

The null bridge is similar in design to the bridge discussed in Appendix M. It has an extremely high input impedance and so draws a negligible current from the board. A photograph of the reader is shown in Figure G-12. In order to facilitate the transformation of quantities into, and out of, the (n, m) system a slide rule was designed. It is shown in Figure G-13.

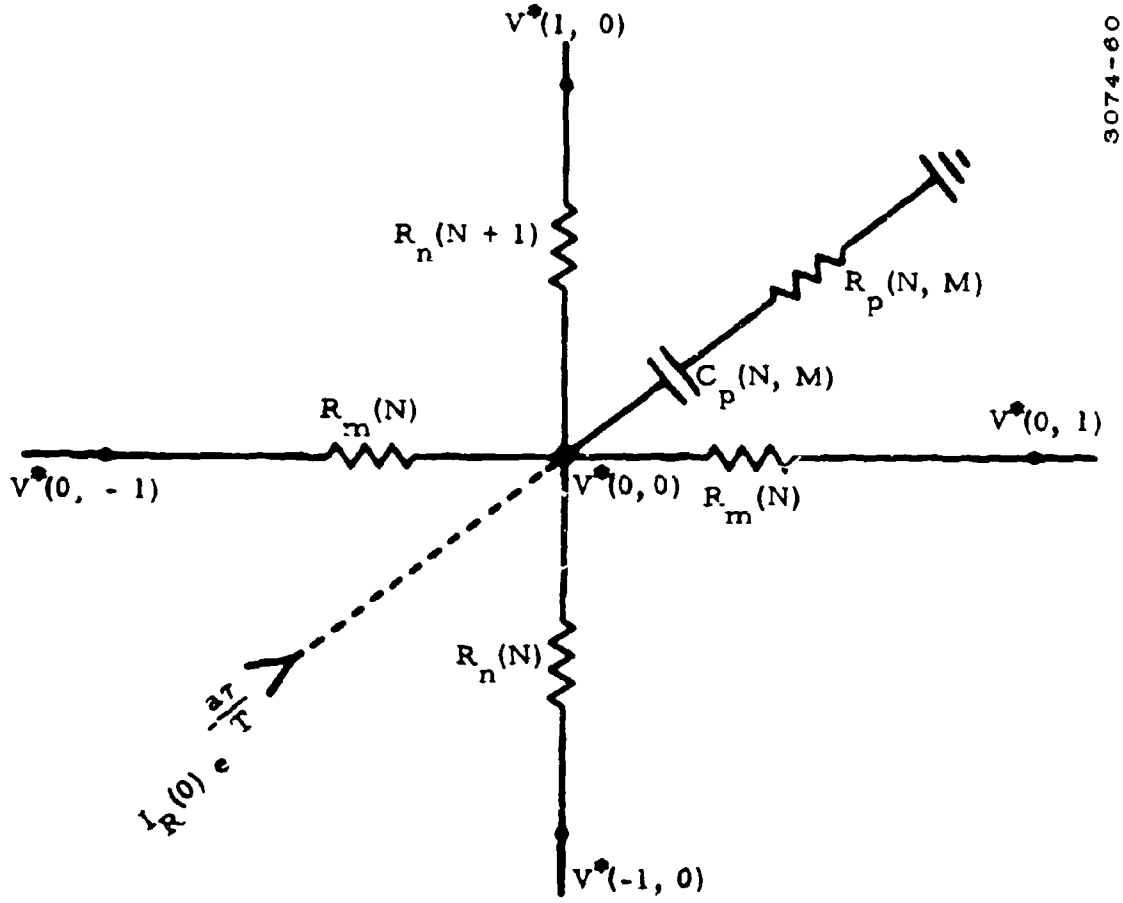


Figure G-8. Plasma Analog

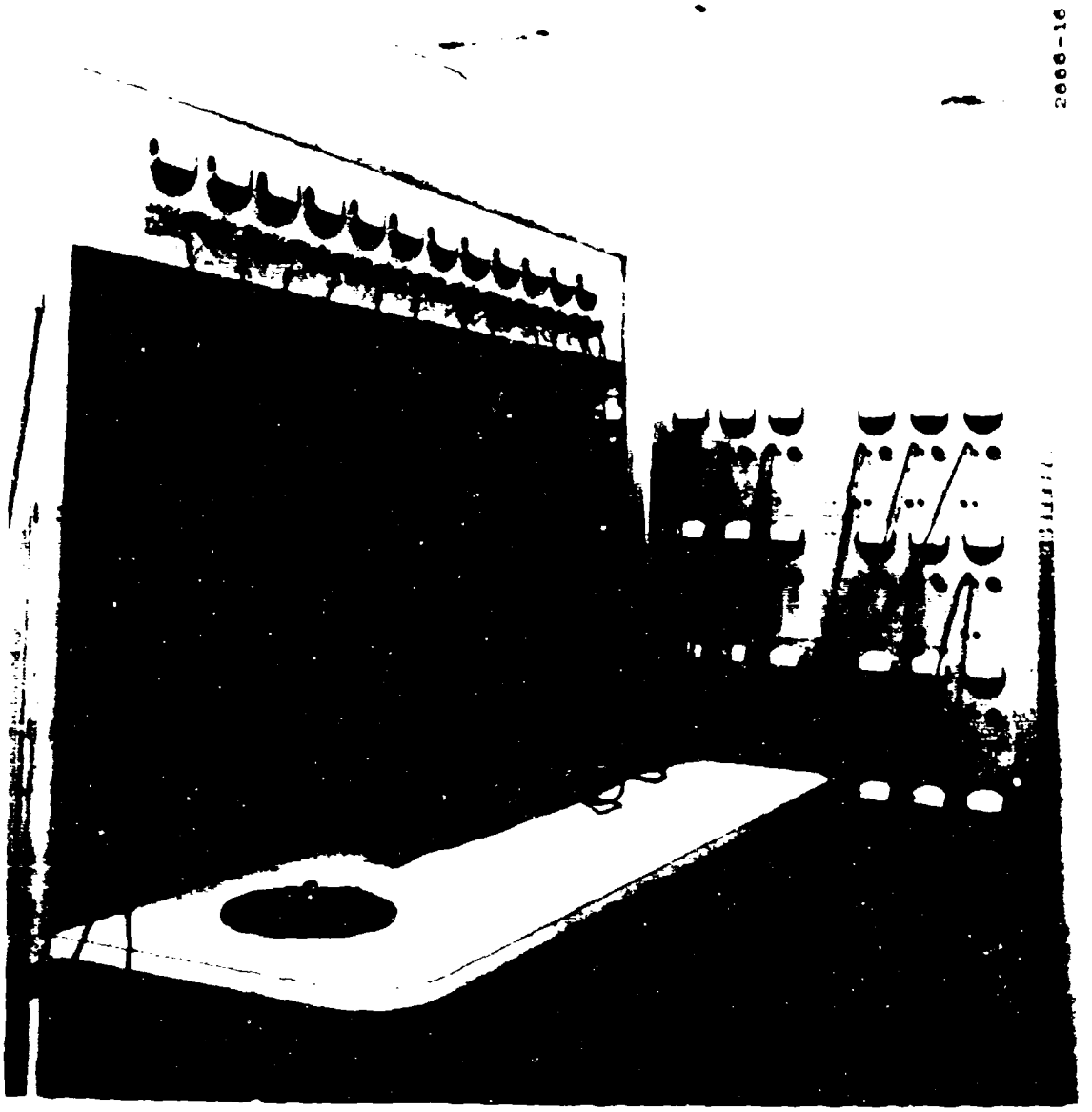


Figure G-9. Completed Analog Board



Figure G-10. Closeup of Resistor Mesh

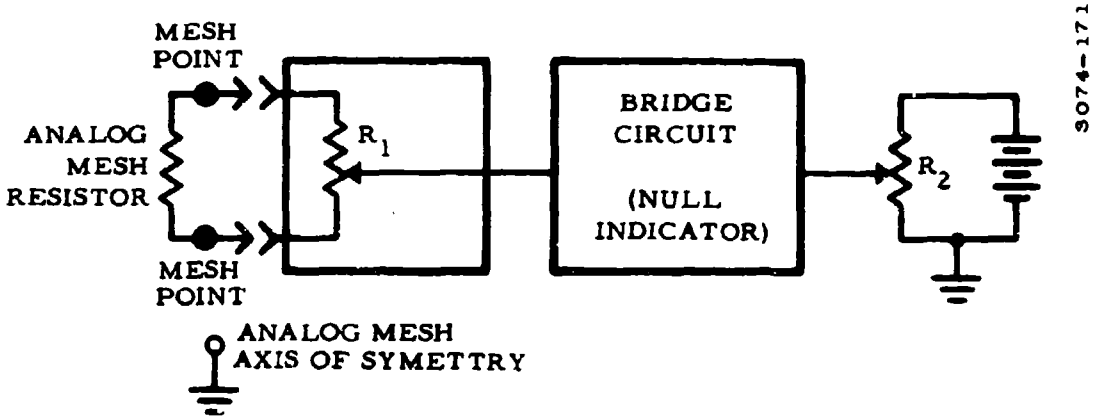


Figure G-11. Block Diagram of Board Reader

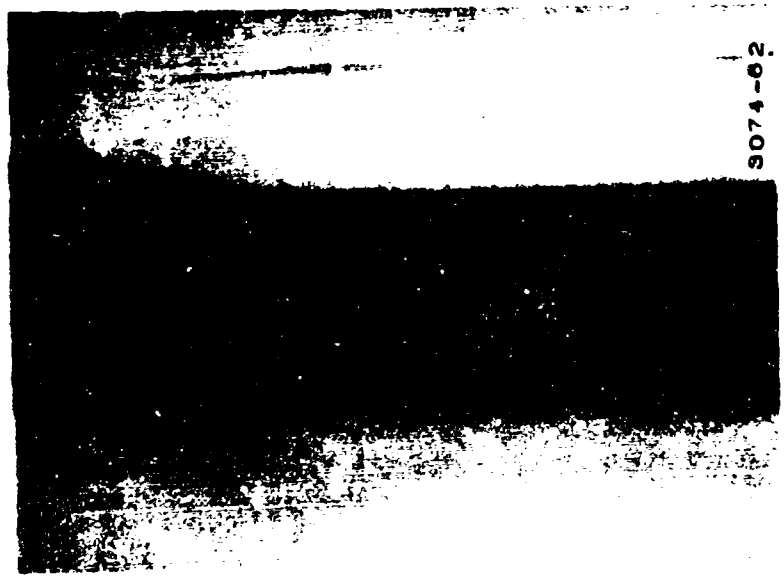


Figure G-12. Analog Board Reader



Figure G-13. Analog Board Slide Rule

REFERENCES

Note: The following references describe resistor mesh analog computers, but the exponential transform described here is not employed. As a result, the standard resistor sizes can not be employed and in addition, certain approximations to the basic analog must be made.

1. Cristensen, U. ; "An Analog Board for Time-Varying Axial Symmetrical Fields", Proc. of Symp. on Magnetic Field Design (1958), Gatlinburg, Tenn., ORNL-2745.

2. Wakefield, K. E. ; "A Resistance Analog Device for Studying Axially Symmetric Magnetic Fields", Project Matterhorn Report PM-S-23. (1958).

3. Wakefield, K. E. ; "The Use of Analog Computers in the Design of Magnetic Field Systems", ORNL-2745 (1958).

APPENDIX H

MECHANICAL DESIGN OF THE MARK II ACCELERATOR

APPENDIX H

MECHANICAL DESIGN OF THE MARK II ACCELERATOR

This appendix deals principally with the details of the mechanical design of the various subsystems of the experimental equipment in the Accelerator laboratory (Figure H-1).

The following topics are covered in this appendix:

1. Mechanical Structure of the Accelerator
   - 1.1 The Field Coils
   - 1.2 The Ferrites
2. The Vacuum System
3. The Oil System
4. The Mercury Feed System

1. THE MECHANICAL STRUCTURE OF THE ACCELERATOR

Basically the accelerator consists of two sets of coils, a vacuum channel, and a central ferrite rod. Assembly problems and anticipated needs for additions and adjustments led to the design shown in Figure H-2.

This figure is a vertical cross section of the device as it was finally realized. A few details have been omitted for clarity.

The accelerator is housed in a steel box (18) * of dimensions 2 feet × 2 feet × 7 feet, which is filled with a dielectric oil. The top and sides of the box are seperately removable, being sealed with neoprene gaskets.

*Circled numerals refer to numbers in Figure H-2.

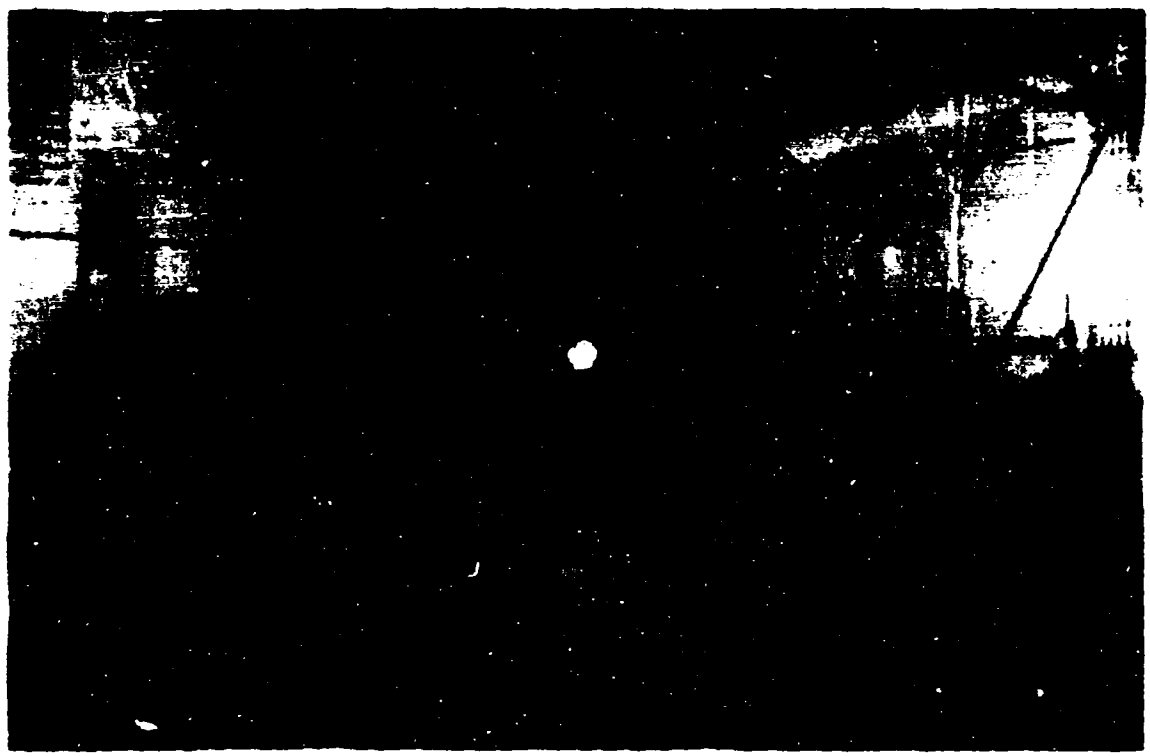
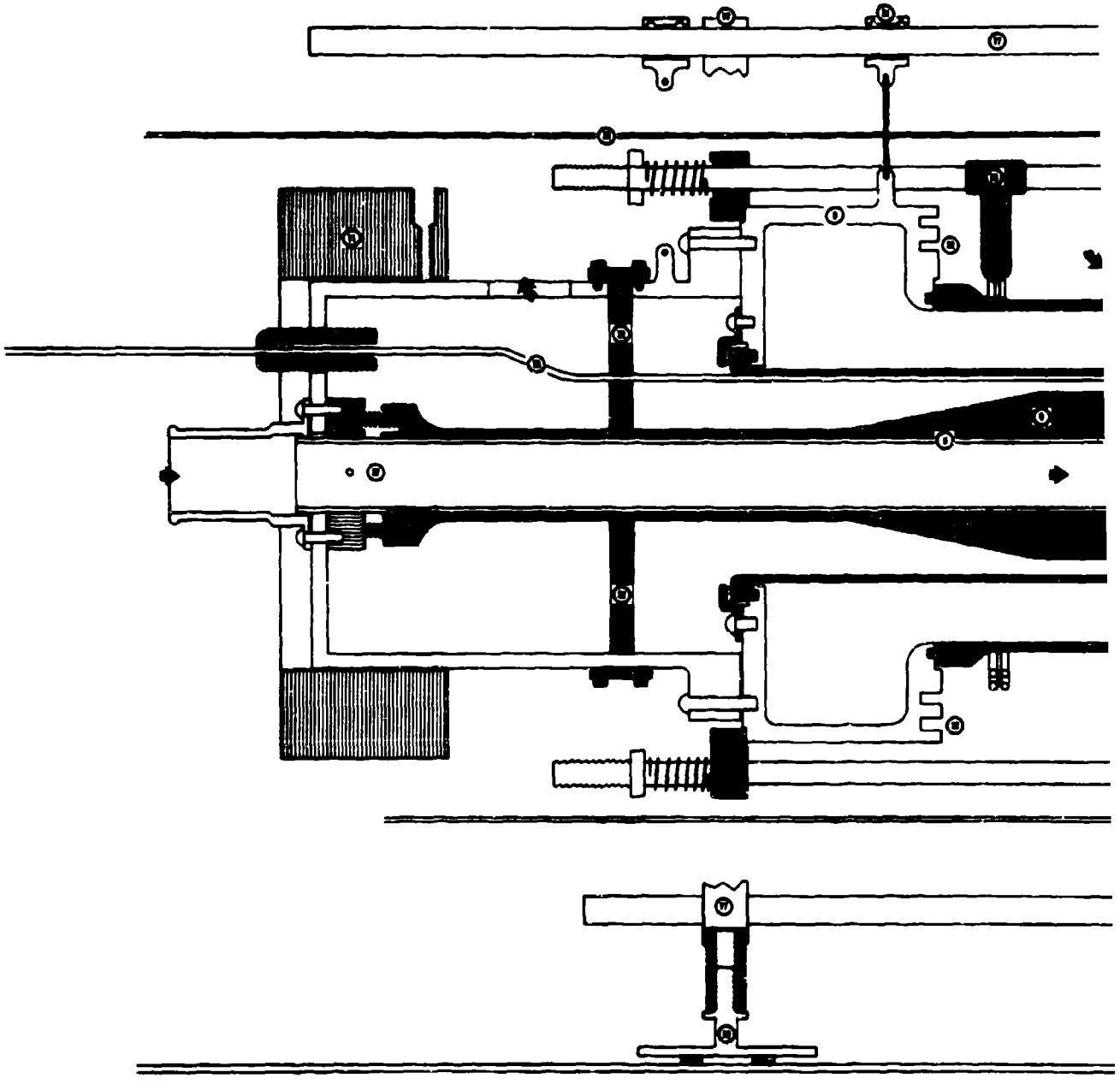


Figure H-1. View of Accelerator Laboratory

1. Vacuum Chamber
2. Outer Field Coil
3. Inner Field Coil
4. Ferrite Core
5. Stainless Steel Support Tube
6. Phenolic Spacer
7. Outer Vacuum Chamber Wall
8. Inner Vacuum Chamber Wall
9. Connector for Hg Gather
10. Tie Rod
11. Adjustable Counter Weight
12. Stainless Steel Bellows Assembly
13. Outer Coil Adjuster
14. Oil Outflow Line
15. Phenolic Outer Coil Holder
16. Phenolic Flux Bumper Support
17. Support Assembly
18. Wall of Steel Outer Box
19. Height Adjustment
20. Coil Clamp
21. Sliding Supports
22. Ferrite Core Supporting Adjustment
23. Typical Coil Leads
24. Flexible Oil Container
25. Flexible Oil Baffle
26. Phenolic Pass-Through
27. Pin For Ferrite Support Tube
28. Hanger Support
29. Transparent Oil Baffle
30. Flange on Vacuum Tank
31. Adjustable Stop
32. Cooling Channel



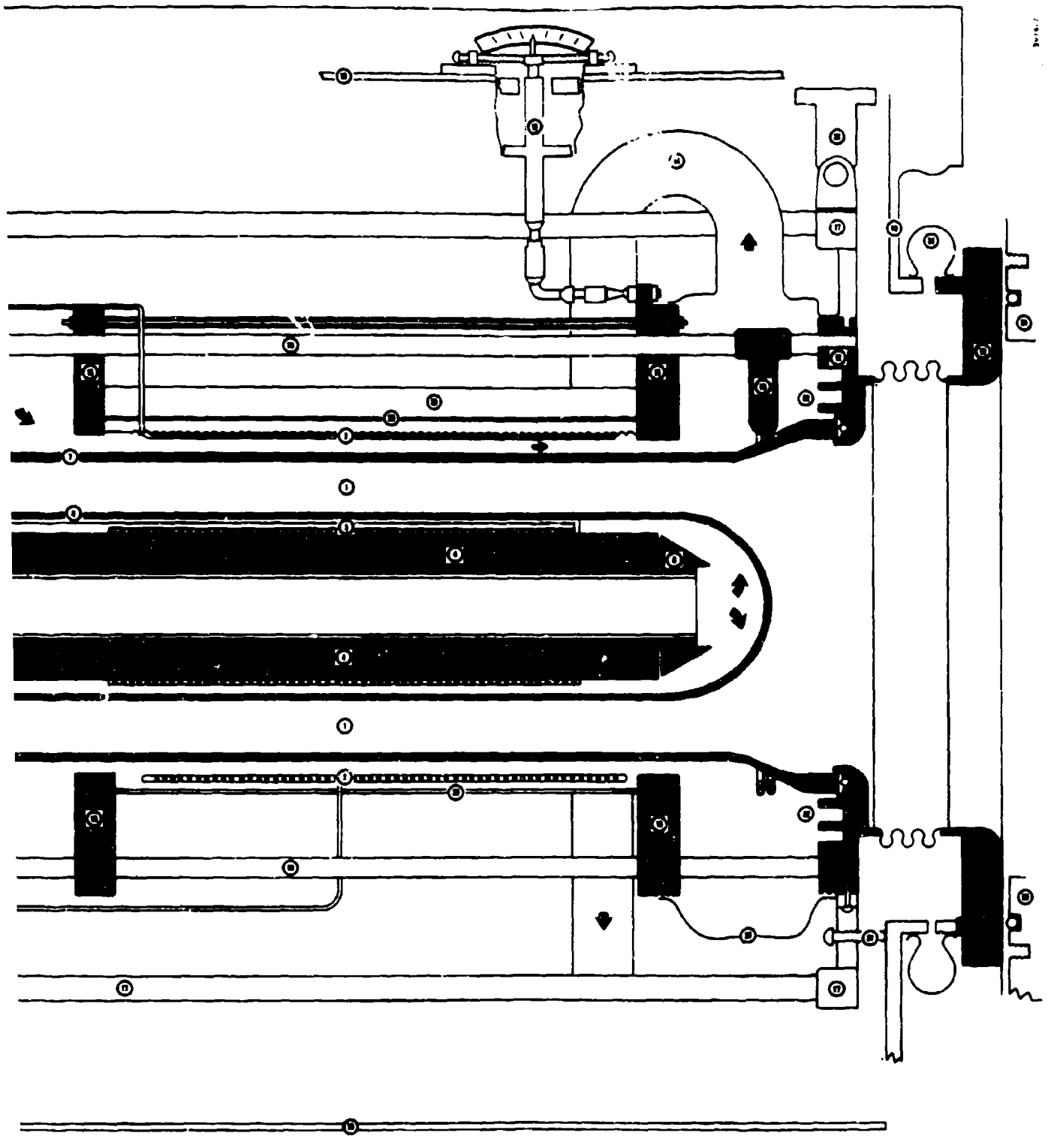


Figure H-2. Accelerator Cross Section

Each of the sides has a pyrex glass window 6 in. × 12 in. for viewing the coil region during operation. The box is reinforced with steel tubing to prevent bulging in case of excessive oil pressures, which may occur by mischance. One end of the box (not included in Figure H-2) has 24 Crouse-Hinds pass-throughs, which permit access to the insulated wires carrying the coil currents. It also has 24 small-diameter coaxial pass-throughs for temperature sensors or other signal-carrying leads. The box stands on legs with leveling screws, and these are mounted on a wheeled frame. A set of rails runs the length of the laboratory.

The accelerator is attached to the vacuum tank (30) via connecting flanges and bellows (12). This is a single welded assembly. Both flanges and bellows are made of nonmagnetic stainless steel. The bellows has a wall thickness of 0.010 inch, so it is important that it not directly contact the plasma beam. Since the steel box is filled with oil, an additional flexible oil container (24) is provided between the box and the bellows flange. The oil container is banded to the flanges with large hose clamps.

The entire accelerator structure is supported at two points: it is hung from the support (28) and the support (21). The former is attached to the box (18) whereas the latter rests on the frame (17). An adjustable leg (19) is placed between the frame (17) and the box. It bears part of the weight of the accelerator. A ball bearing race, between the leg and the box, facilitates movement of the system during assembly. In effect, the accelerator hangs in the frame (17).

One major problem was the ferrite rod (4), which weighs about 20 pounds and which had to be cantilevered from one end. The solution chosen was to use a sliding counterweight (11) to balance the ferrite rod, and adjustable fingers (22) to center it. This weight also facilitates the task of moving the central assembly backward during disassembly.

All vacuum seals are Viton-A O-rings. Viton-A may be expected to be trouble-free up to 250 C. The actual average temperature is not expected to exceed 80 C. Certain regions, such as the stainless steel bellows, may reach much higher temperatures because of ohmic heating by induced currents and plasma impingement. Cooling channels (32) were cut in these places to alleviate this problem. In addition shorted turns of copper wire (16) were provided to partially prevent the flux from reaching these regions.

The integrity of the annular vacuum channel (1) is maintained by six spring-loaded tie rods (10). They have proved extremely useful during preliminary electrical testing when the vacuum system has been up to air and the box filled with oil. When the system is pumped down, the pressure differences that develop tighten the vacuum seals. In addition, the bellows would contract under these forces, so several adjustable stops (31) were provided. Axial thermal expansion of the vacuum channel walls is taken up by increased spring compression.

It was felt that the best chance of minimizing wall heating problems at the exit end of the device was to flare the outer vacuum channel wall (7). We experienced a good deal of trouble in obtaining quartz tubes with the smooth flare-out, and several walls had to be rejected. The quartz walls were finally obtained from Thermal American Fused Quartz Co. of New Jersey and are extremely well made. (Figure H-3).

The support (15) for the outer coil moves along the tie rods and has a free motion of about four centimeters. The distance moved is measured by the scale and pointer (13) external to the box. The outer coil is moved through the flexible linkage shown attached to the pointer.

The arrows indicate the oil flow. Oil is introduced through the rear of the box, and a hose leads directly to the hollow ferrite support tube (5). Oil flows up this tube and returns, passing over the ferrite and the inner coil (3). It flows out a series of holes and enters the box. The oil is then forced to flow over the outer coil (2) by a thin circumferential sheet of neutral gray spotlight-filter film (29) which is slit to allow passage to the coil leads. This material was chosen for its transparency and high-temperature characteristics. The oil then enters the outflow pipe (14), which is connected to the oil pump.

At the time that the mechanical design had to be frozen, space was provided by (9) for the introduction of the mercury vapor feed.

Figure H-4 and H-5 are views of the accelerator.

1.1 THE FIELD COILS

The field coils, both inner and outer, are made of number 12 solid Formvar-coated wire. This small a wire size (diameter = 0.187 inch) so simplifies the winding of the coils that it was felt that the ohmic losses could be accepted, especially since the coils are oil-cooled.

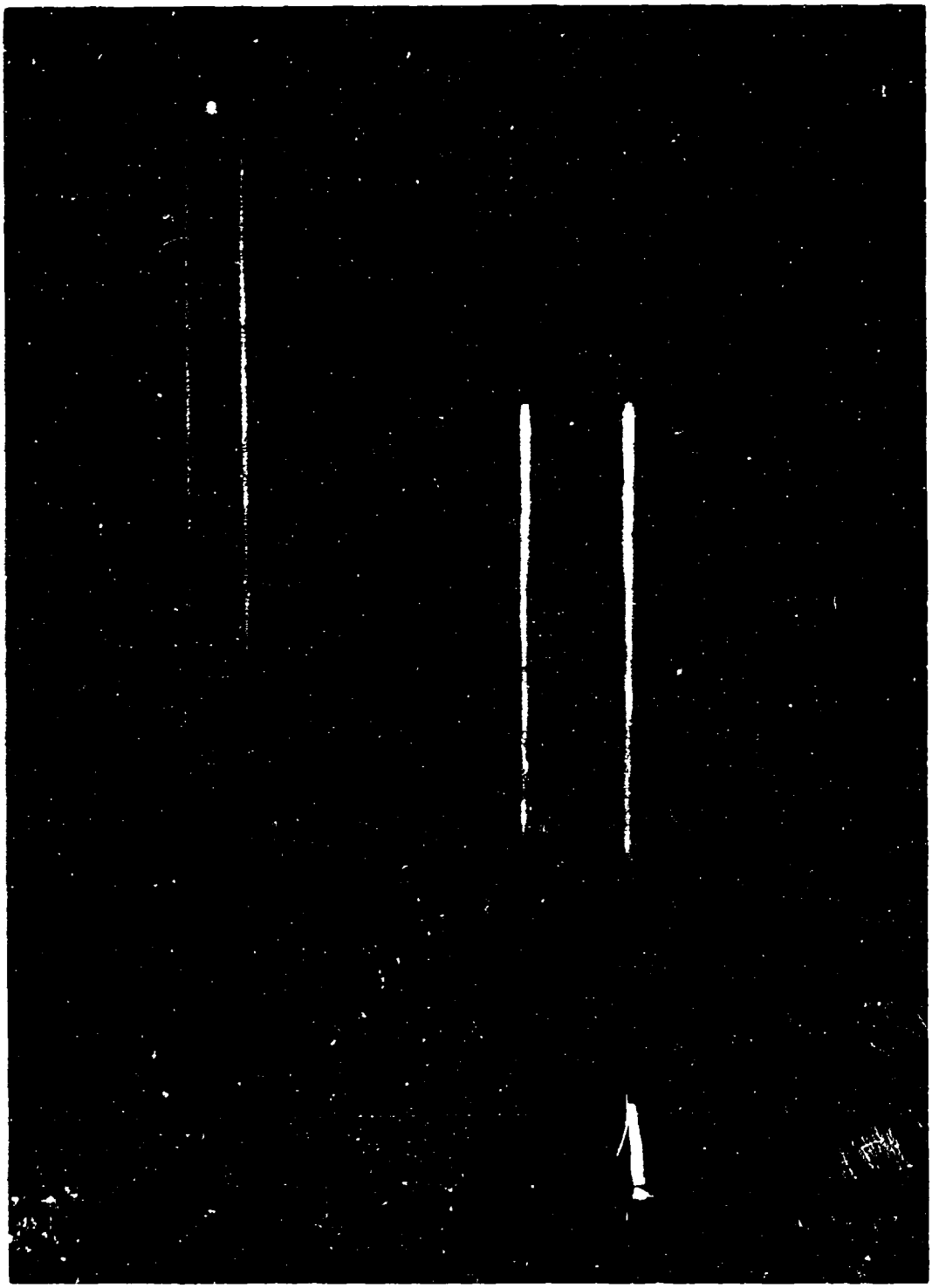


Figure H-3. Vacuum Channel Walls

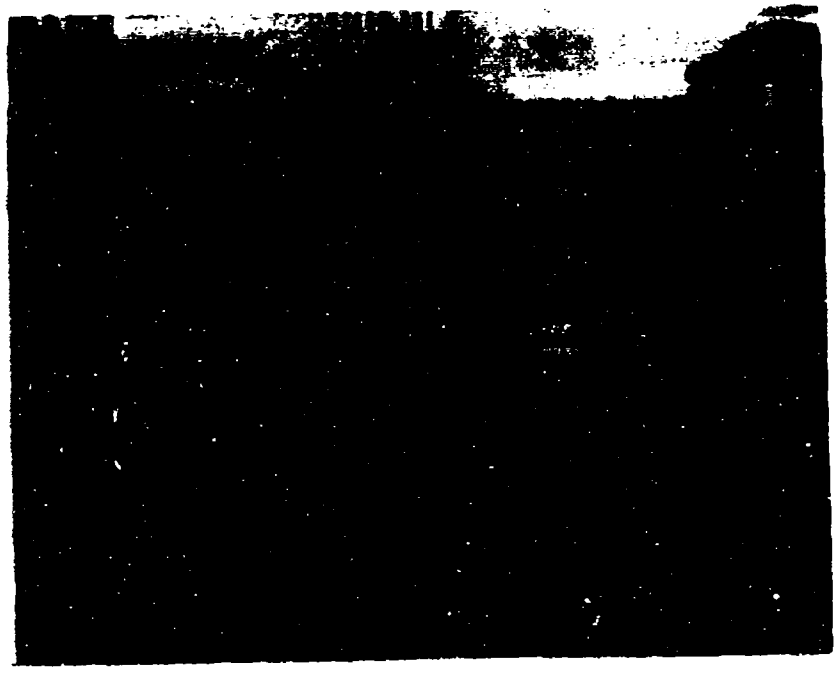


Figure H-4. Accelerator in Assembly Stage

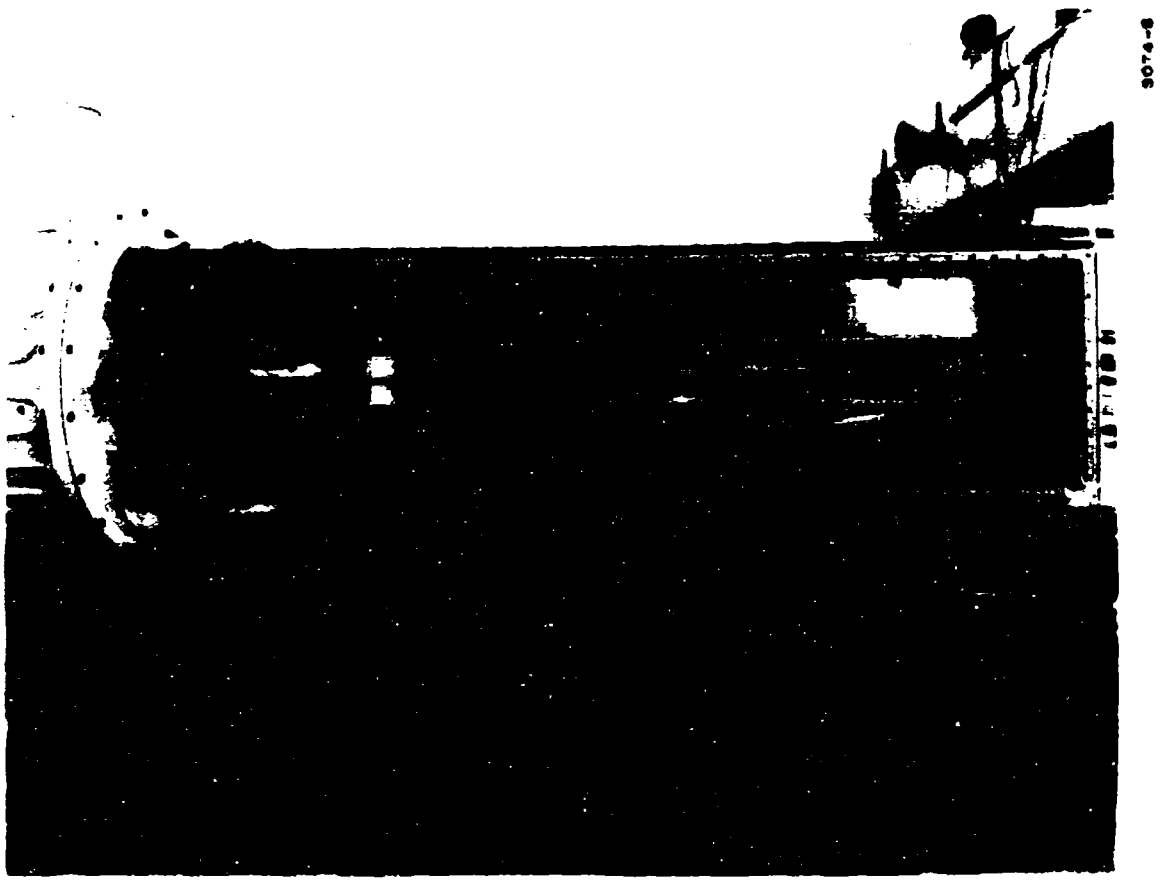


Figure H-5. Assembled Accelerator

Each coil group consists of five turns of wire, spaced one wire diameter apart. A second coil group is wound in the same sense as the first but connected physically so that if the current flow in the first group is clockwise, the current flow in the second is counterclockwise (see Figure H-6).

There are four such composites of coils. There is a fifth, which is comprised of three coil groups. The fifth contains the first coil of the device (the injection end), a middle coil, and the last coil (the exit end). They are connected in order: clockwise — counterclockwise — clockwise. The last clockwise group was added to correct somewhat for end effects.

The five composite groups of coils were wound on a split mandrel (Figure H-7) using five lengths of wire. The mandrel was collapsed and removed, leaving the entire coil system assembled.

The leads to and from the windings are held semirigidly inside the accelerator box by a web of lacing tape to prevent accidental short circuits. At all points where they are unavoidably close to supporting members, they are well insulated.

1.2 FERRITES

The ferrite used in the Mark II was obtained from Stackpole Carbon Co. of Pennsylvania. The particular type is called Ceramag 27. It is in the form of tori of outside diameter 2.760 inches, thickness 0.500 inch and with a central hole diameter of 1.00 inch. The discs have ground faces that allow close stacking without gaps. Twenty-five ferrites are stacked to make the central rod of the accelerator. This particular ferrite has a curie point temperature of 224 C and has a maximum permeability (with respect to free space) of 2390 at 4 kc. It is absolutely necessary, in a device in which the ferrite is going to heat, to have a high curie point or else the permeability is liable to fall drastically.

The manufacturer's data give a Q of this material at 250 kc of about 1300 which means it is not lossy. Above 500 kc the Q falls rapidly, but this is not of special interest for the Mark II.

2. THE VACUUM SYSTEM AND ASSOCIATED COMPONENTS

The main vacuum chamber is a cylindrical tank 30 inches in diameter and 5 feet long. The tank is flanged on both ends — the rear flange

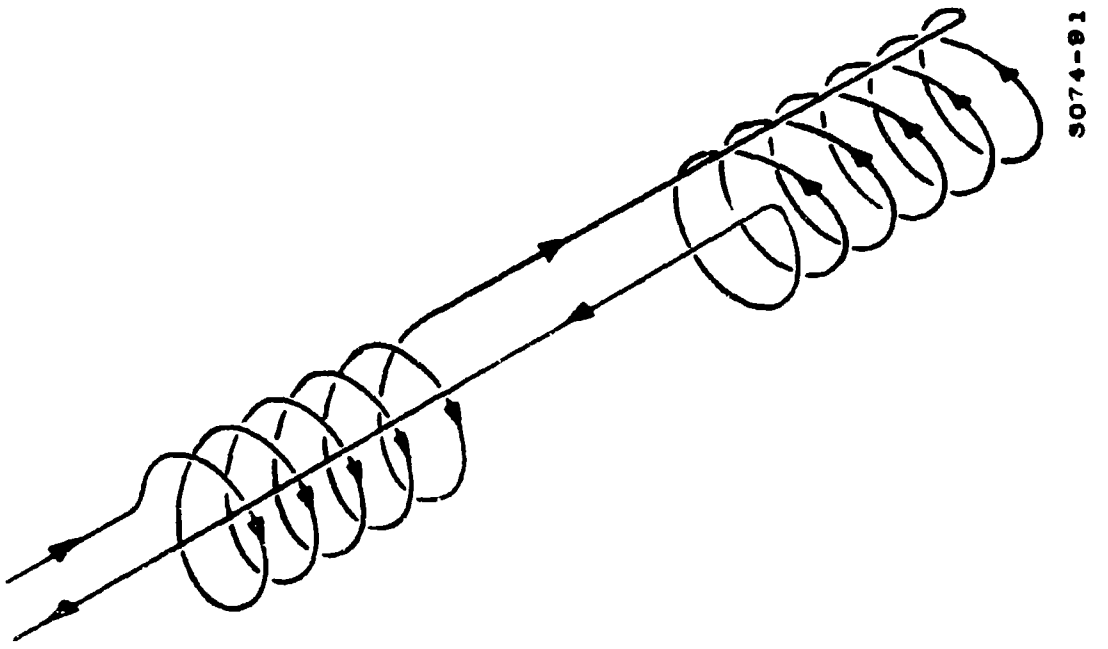


Figure H-6. Field Coil Winding

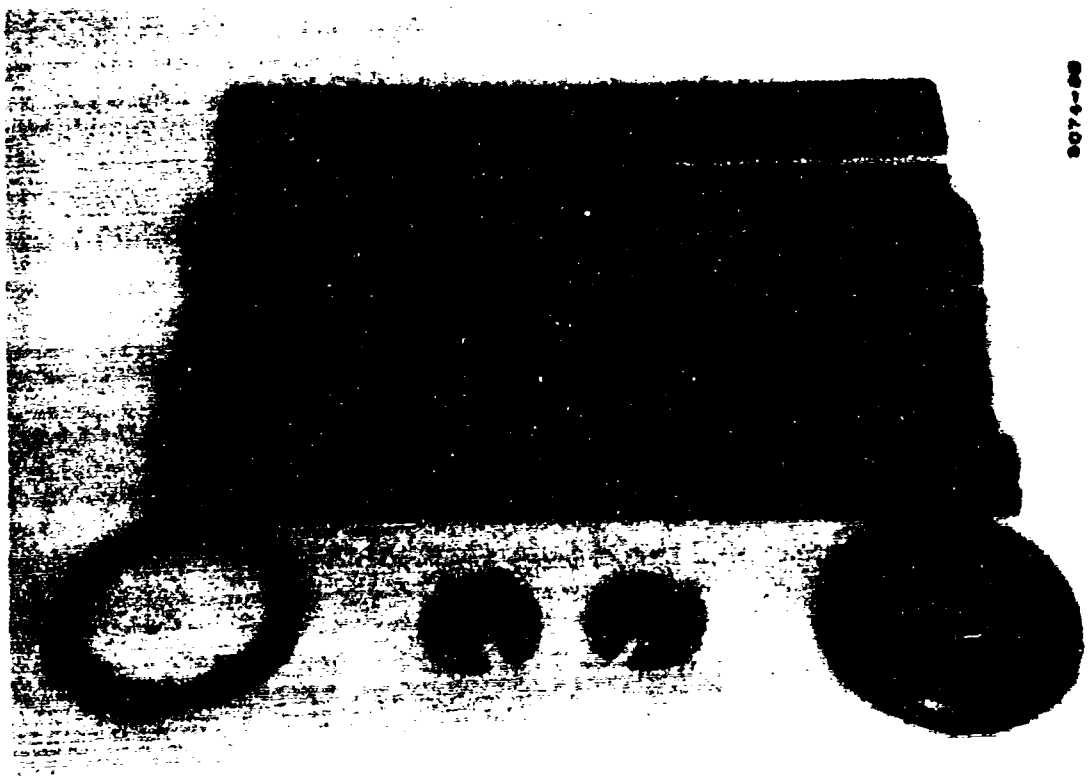


Figure H-7. Coil Winding Mandrels

carrying the pumps and the front flange connecting, via a bellows assembly, to the accelerator. (See Figure H-8).

The tank is supplied with seven observation ports, a tower intended to house diagnostic gear, and an exhaust pipe and blower that are connected to a vacuum gate valve at the top of the tank. The purpose of this is to exhaust air from the tank whenever the tank is open to the laboratory. This will keep a gentle stream of air going from the laboratory to the tank opening, and it is hoped that this will hold down the amount of mercury vapor escaping into the laboratory. Other precautions for personnel protection have been taken.

Because of the necessity of stopping the plasma beam, it is not possible to get a direct axial view of the beam. Instead four 45° viewing ports are provided: two on the tank and two on the front flange of the tank. The inside surface of the front flange has supports for diagnostics, and there is a hanger rail in the tank for the same purpose.

The tank is provided with four parallel cooling coils brazed to the tank wall. Oil is pumped through the coils.

The frame to which the tank is welded rides on wheels and on the same set of rails as the accelerator box.

2.1 PUMPING

The pumping system consists of two CEC PMC-1440 oil diffusion pumps in parallel, connected through six-inch gate valves to a common manifold on the rear flange of the tank. They are backed by two Hereus E-35 single-stage forepumps. The foreline system and foreline valves are copper and brass and, to prevent any attack by residual mercury, the foreline assembly has been heavily nickel-plated. There is a nickel-plated, freon-cooled baffle, Figures H-9 and H-10, of double chevron design just ahead of the diffusion pumps. Its principal purpose is to condense mercury vapor before it gets to the pumping system (it, of course, serves also as a barrier to pump oil). The baffle is optically opaque and was designed so that its conductance matched the combined speed of the pumps. The effective speed of the baffle-pump system is about 1500 liters/sec at 10^{-4} Torr. The base pressure of the system (without mercury), as measured on a Veeco RG-75 gauge, was about 5×10^{-6} Torr, which is several orders of magnitude lower than the base pressure after mercury has been introduced. Since the outgassing effects

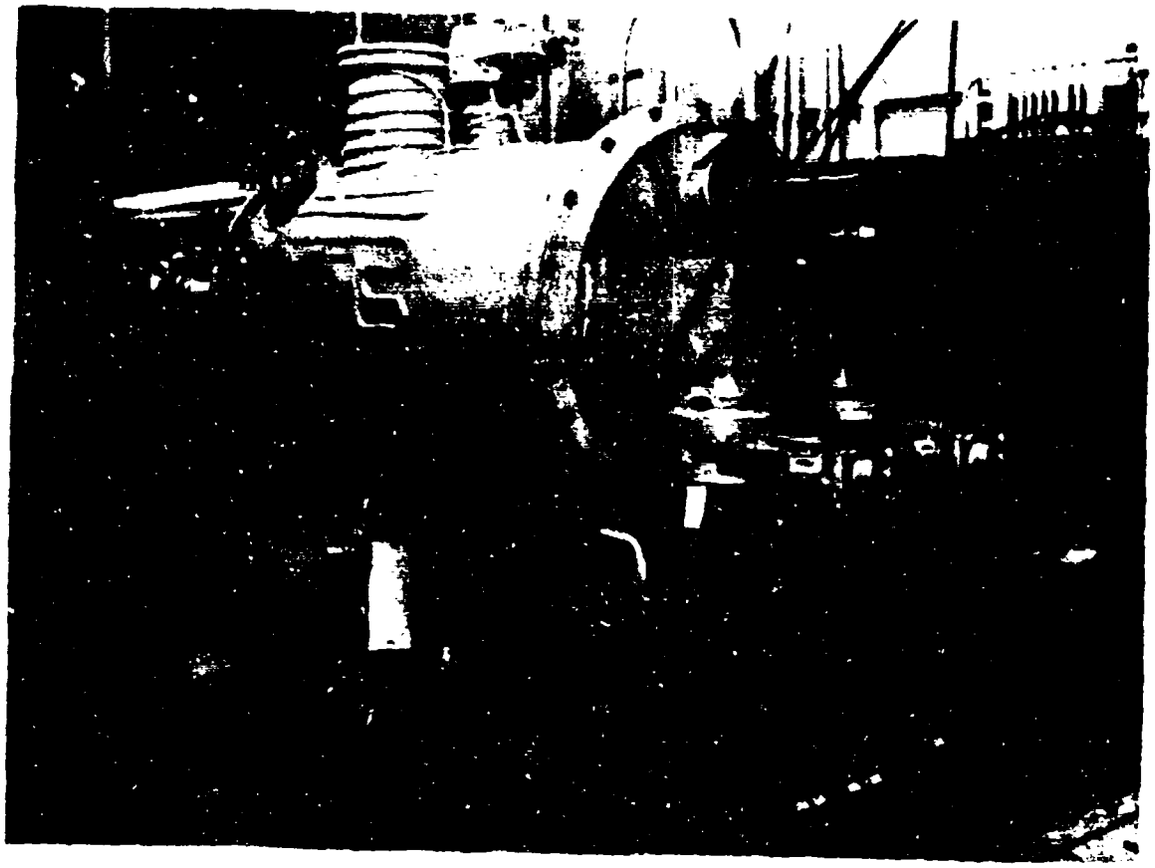


Figure H-8. Vacuum Tank



Figure H-9. Plates of the Freon Baffle



Figure H-10. Freon Baffle

caused by the impingement of a high-energy plasma beam are unknown, it is not absolutely clear that the pumping speed is adequate; but it was not felt that a faster (and much more expensive) system was justified.

2.2 CIRCUITRY OF VACUUM SYSTEM (Figure H-11)

The circuit, beside supplying the necessary pump power, incorporates several protective devices. The circuit works as follows.

A normally open, spring-loaded switch momentarily supplies line voltage to relay C′, which closes contact C, completing the main circuit loop and also closing contacts C_1 and C_2, thereby supplying power to the diffusion pumps. Note that this loop is inoperative unless switch (A) has been closed by the foreline power. Switch (W) is normally closed, and the bell is activated. When contacts C_1 and C_2 close, relay (W) opens (W) and the bell alarm ceases. Thereafter the bell will ring whenever C_1 and C_2 open for any reason. In case either diffusion pump heater should open, transformers (X) or (X′) open the relay X, thereby opening C_1 and C_2 and setting off the alarm bell. Both diffusion pumps have Fenwall thermoswitches in their water supply, and in case of overheating either Fenwall will open relay Y. The relay Z is opened by a device that monitors the forepressure of the vacuum system.

2.3 PRESSURE MEASUREMENTS

We employ a Westinghouse Shulz-Phelps ionization gauge to measure the background pressure with mercury in the system. This gauge was chosen after much searching. It appears that little has been done in the way of gauge calibrations for mercury; and, of course, most common gauges can not be used, either because mercury is condensible or because the gauges contain material that will be rapidly and destructively attacked by mercury vapor. This ionization gauge is a fairly recent development and is capable of reading in the range 1 Torr to 10^{-4} Torr, which is considerably higher than the range of a conventional ionization gauge. We have not attempted to calibrate this gauge for mercury vapor. We accept a report that the sensitivity of various configurations of ionization gauges is only weakly geometry-dependent*, and we take the sensitivity of the Shulz-Phelps gauge for mercury to be 3.4* times its sensitivity for nitrogen (which is given by the manufacturer).

*S. Dushman Scientific Foundations of Vacuum Technique, John Wiley and Sons, Inc. (1949)

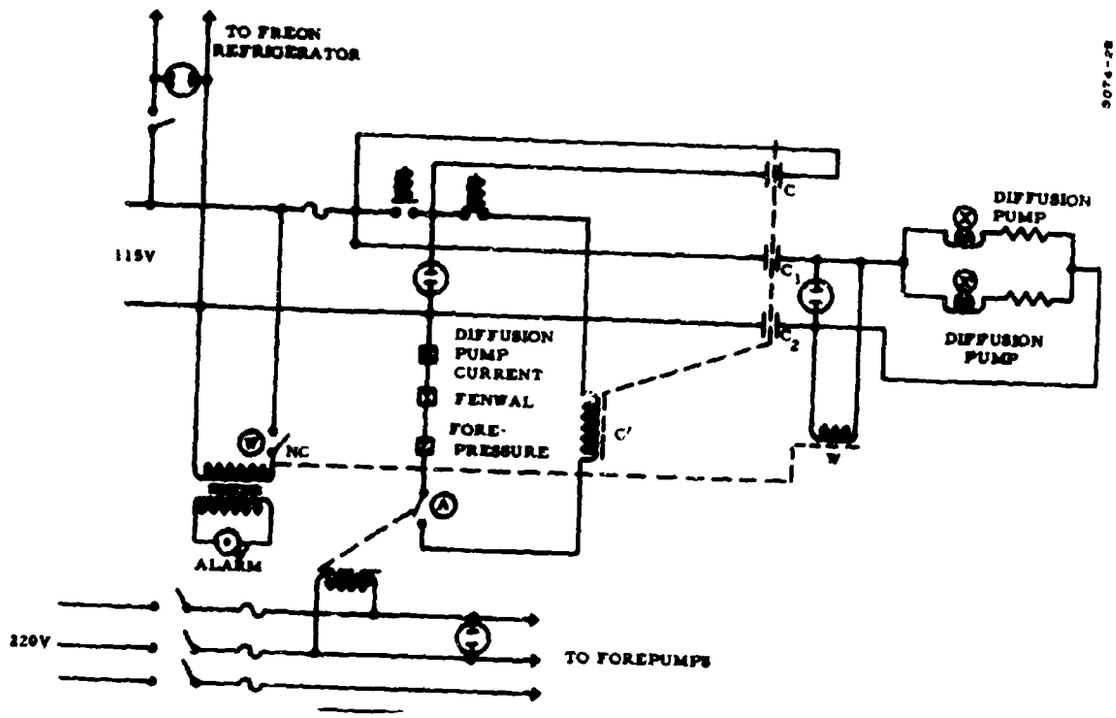


Figure H-11. Schematic of Vacuum System Circuitry

We have compared the Westinghouse calibration for nitrogen against a thermocouple gauge and found good agreement.

2.4 BEAM STOP

This is a special, optically opaque baffle located in the middle of the vacuum tank and is the intercepting surface for the plasma beam. It consists of a set of parallel, flattened, hollow, stainless steel tubes of 0.050-inch wall thickness. · These tubes are welded at their extremities to two rectangular manifolds. Figure H-12 is a schematic of the baffle.

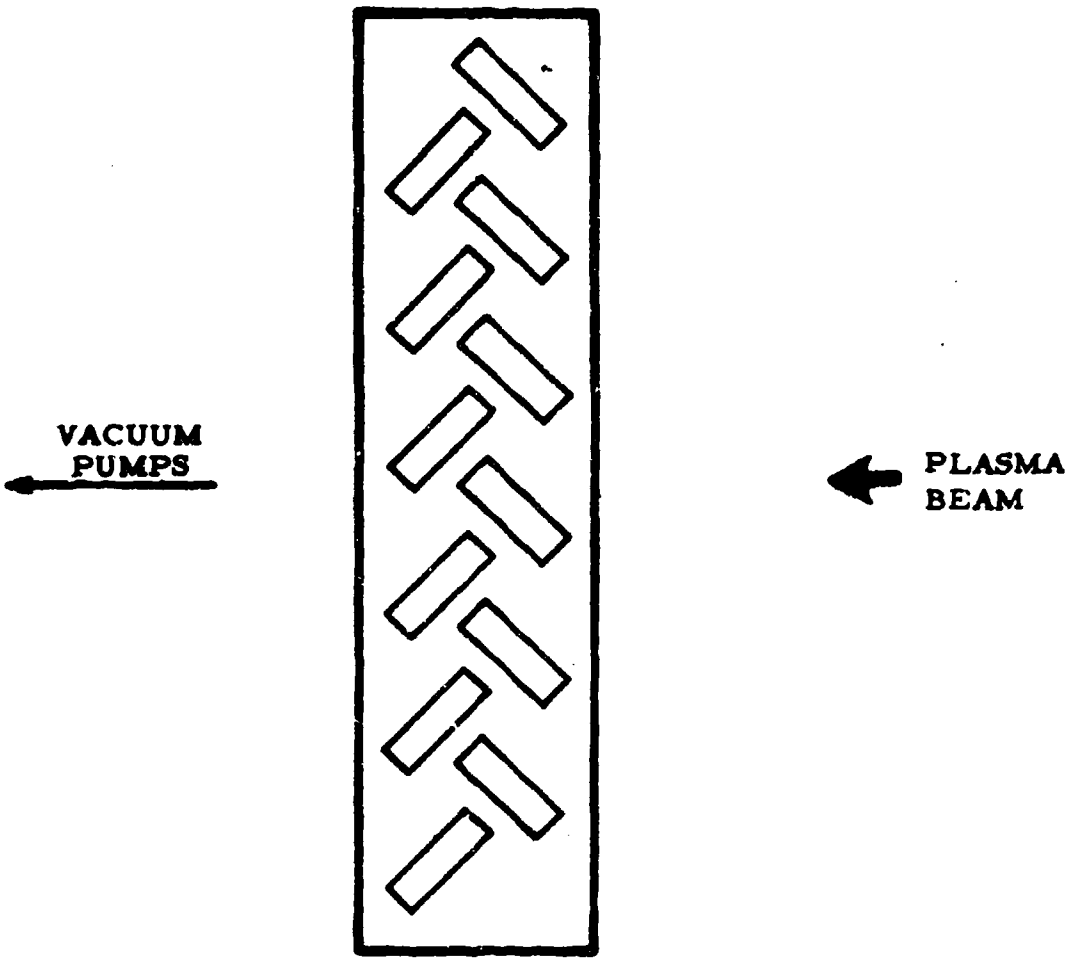
The upper and lower manifolds have, respectively, an outflow and an inflow tube that go out of the vacuum system through Crouse-Hinds fittings in the rear flange of the vacuum tank. Oil is pumped through this baffle to carry off the energy of the beam.

Figure H-13 shows the baffle seen from the pump end of the vacuum tank.

3. THE OIL SYSTEM

Early in the design stage it was decided to use oil, both as a coolant fluid and as insulation against the radio-frequency voltages. We chose Shell Diala-AX which is inexpensive and has desirable electrical properties (it is a standard transformer oil). Several other fluids were considered, including silicone oil and fluorochemicals. The cost of these is prohibitive in the quantities we are using, because the accelerator box holds about three barrels. Also the fluorochemicals have exceptionally low viscosities, which cause difficult sealing problems.

A 50-kw fluid-air heat exchanger was purchased from Electro-Impulse Laboratory of N. J. and was modified to meet our requirements. Essentially it consists of a large radiator with fan, motor, and gear pump, and a thermopile for power measurement. The radiator was mounted near the roof of the laboratory, and entrance and exit ducting was installed to allow the outside air to carry off the heat. This caused the system to be somewhat dependent on outside temperatures. Provision can be made to add water vapor for additional cooling, but tests indicate that this probably will not be necessary.



3074-82

Figure H-12. Schematic of Beam Stop



Figure H-13. View of the Beam Stop

The cooling system is divided into three separate flow subsystems.

1. Accelerator box
2. Beam-stop baffle
3. Vacuum tank walls

Figure H-14 is a schematic of the system.

The tank noted on the right of the diagram is 2-1/2 feet in diameter and 17 feet tall. It provides storage space for all the oil needed in the system. At the bottom is a manifold feeding three separate subsystems. The system contains four Sears-Roebuck 3/4-hp, centrifugal pumps and one high-pressure (100 psi, 8-1/2 gallon per minute) gear pump. The heat exchanger is mounted next to the storage tank. Refer now to Figure H-14.

The subsystems are so designed that the flow can be reversed and all systems evacuated into the storage tank. Valve A is a four-way valve. The pump is mounted across this valve in such a way that switching the valve effectively reverses the pump in the flow line. From valve A the line continues to junction X and splits into two lines. One line is a fluid by-pass controlled by a gate valve allowing fluid to be shunted around the load. The other side of the line continues to the load, and line R is a return to the storage tank. Valve V allows the return to go directly to the tank or into the flowmeter, which also dumps into the tank. The accelerator box needs an extra valve (V′), since the feed point is in the middle of the tank and cannot be used as a drain. Pump-out is accomplished by switching V′ to a line running into the bottom of the accelerator box and reversing valve A. Valve S is closed and a small air bleed (b) ahead of the valve is opened. It has proved convenient to add an additional pump to the outflow line of the accelerator box. Figure H-15 is a photograph of the flow control panel.

The heat-exchanger is run on a separate pump, which circulates hot oil from the storage tank, through the fan-radiator and back to the tank.

A test was made of the entire cooling system by putting 52 kw into a resistive load cooled by the oil circulating through the heat exchanger. In a 50-minute run the temperature rose from 32 C to 66 C and was leveling off when the run was terminated because of oil seal failure in the load. No additional tests were deemed necessary. The oil storage tank discussed above is shown in Figure H-16.

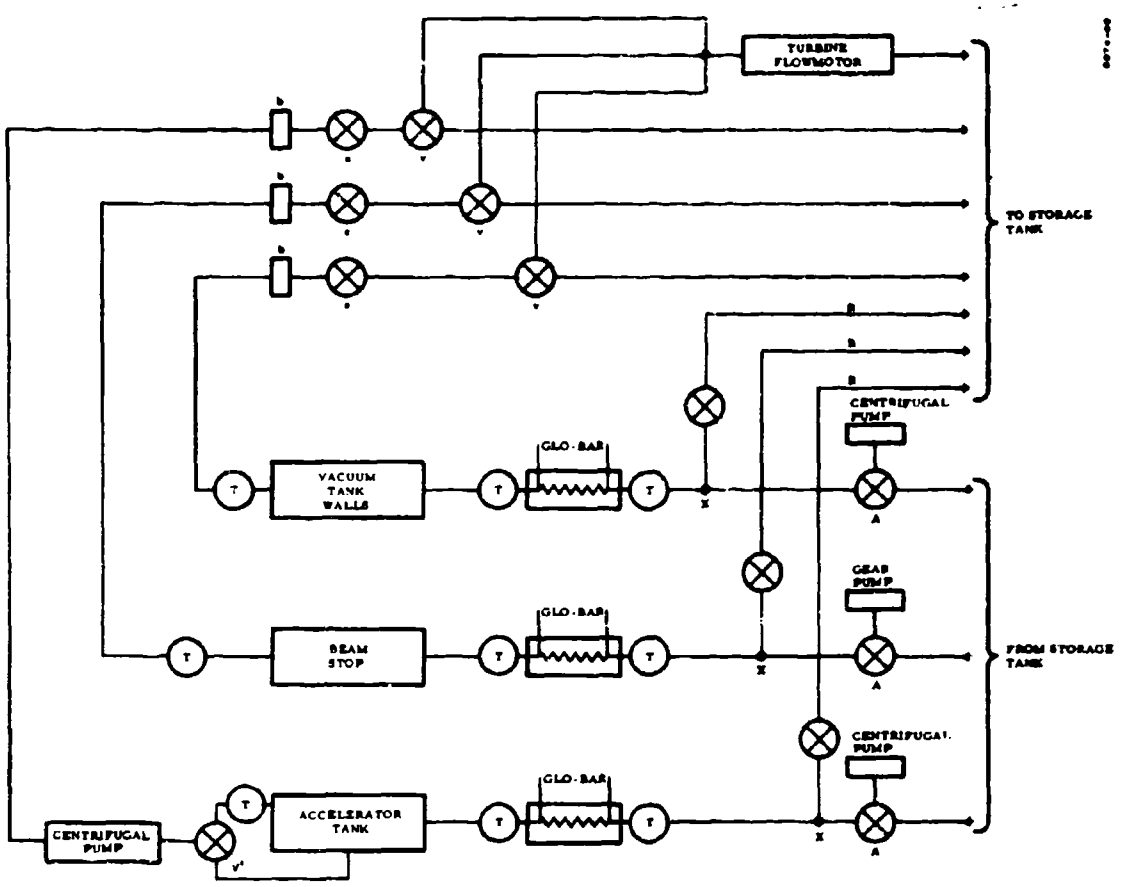


Figure H-14. Schematic of Cooling System

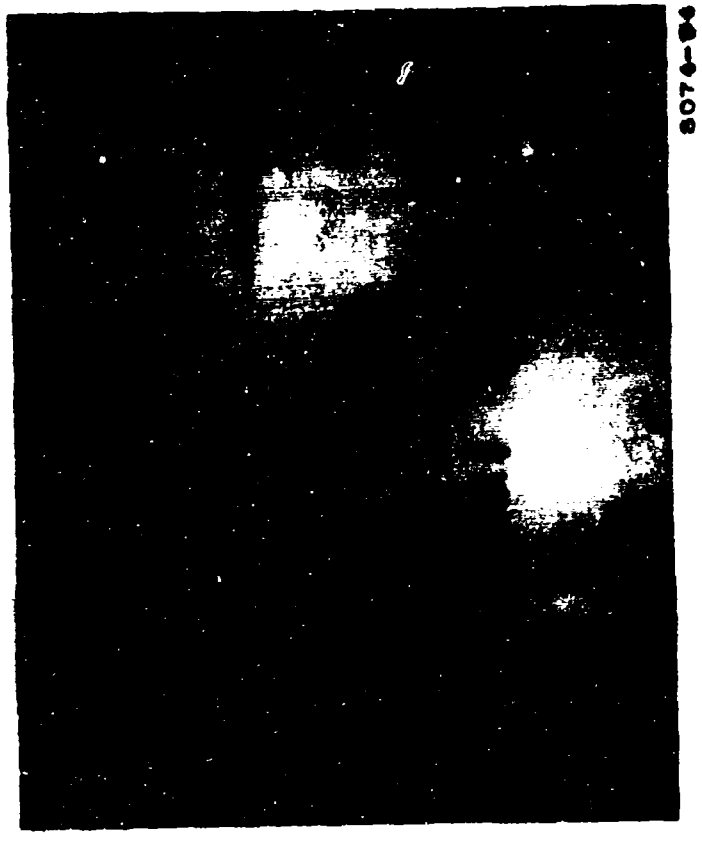


Figure H-15. Oil Flow Control Panel

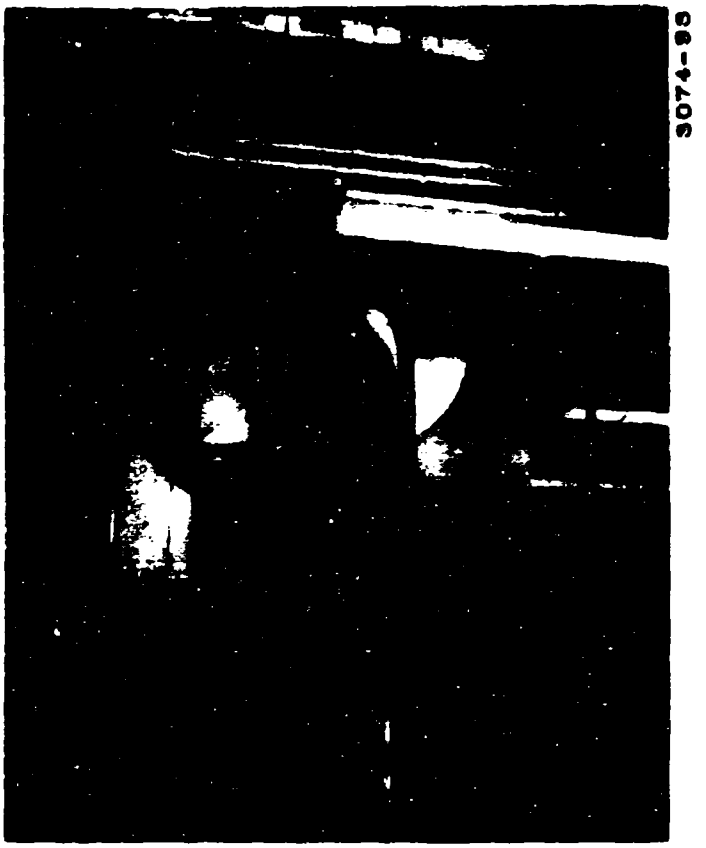


Figure H-16. Oil Storage Tank

3.1 FLOW MEASUREMENT

The flow is measured with a Fisher-Porter precision turbine flowmeter. This instrument puts out an electrical signal whose frequency is proportional to the flow rate. It has a calibration for viscosity corrections. A special calibration for the kinematic viscosity range of Diala AX was made by Fisher-Porter. The viscosity-temperature characteristics of the oil are known and are used for the correction to the flowmeter measurement. The flowmeter manifold was designed so that the path through the flowmeter had approximately the same impedance as the by-pass around it. Thus the flowmeter should have negligible effect on the flow. The flows from all three subsystems can be sent separately through the flowmeter.

3.2 POWER MEASUREMENT

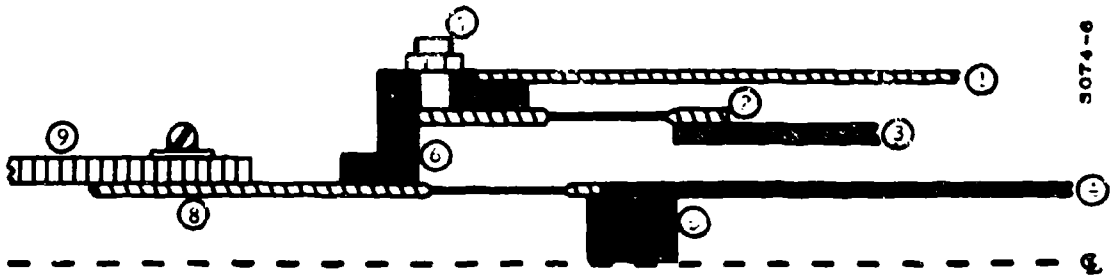
Each flow line contains an 8-ohm Glo-bar hollow carborundum resistor. A cross section of the resistor mount is shown in Figure H-17.

The resistor is fed from a 220-volt, 50-ampere Variac. The power delivered to the resistor is measured on a one-percent, 10-kw wattmeter mounted on the oil flow control panel. In this way an accurately known power can be put into any flow line. Figure H-18 is a photograph of the resistor manifold.

The power measurement is made by reading temperature differences in the flow line at points labeled (T) in Figure H-14. The temperature sensors are zener diodes. The temperature measuring system is described in detail in Appendix M. Combining these temperature differences with the flowmeter reading yields the dissipated power producing the temperature difference. The resistors, to which a known power can be applied, provide a calibration for the power measurement.

4. MERCURY FEED SYSTEM

In order that the mass flow rate of mercury be accurately determined, we have built a feed system that determines the flow rate by means of a variable speed piston driven at an accurately known rate. Figure H-19 is a schematic of the system. A photograph of the system is shown in Figure H-20.



1. OUTER COPPER JACKET
2. GLO-BAR HOLDER
3. GLO-BAR RESISTOR
4. STEEL CORE
5. PHENOLIC CASE HOLDER
6. PHENOLIC END
7. SCREW FOR CURRENT FEED-IN
8. RUBBER HOSE
9. COPPER TUBE

Figure H-17. Cross Section of Resistor Mount

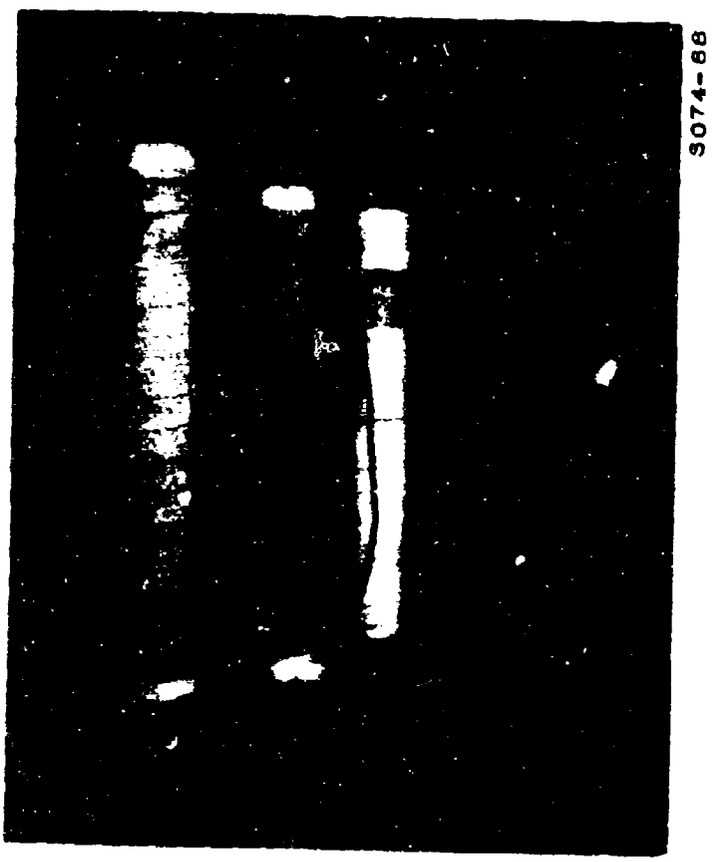


Figure H-18. Resistor Manifold

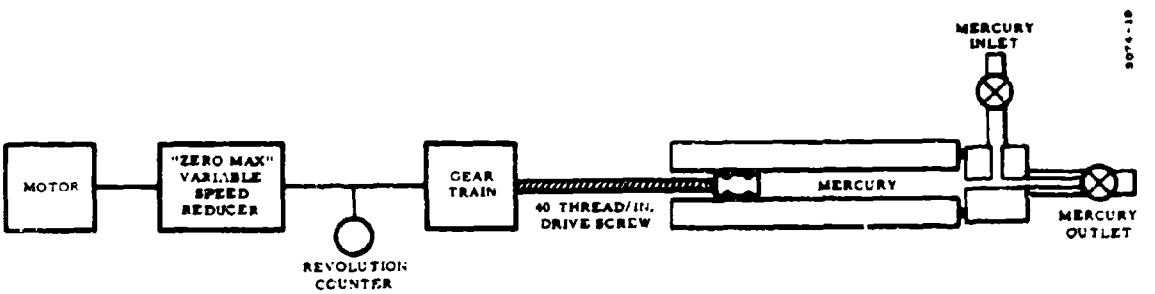


Figure H-19. Schematic of Mercury System



Figure H-20. Mercury Feed System

The variable speed-reducer driven by a synchronous motor allows a shaft speed at the revolution counter ranging continuously from zero to one-quarter of the motor speed. A further fixed reduction follows the counter and precedes the screw and piston. The output flow rate of mercury can be continuously varied from zero to 1.2 grams/min. The piston is stainless steel with a double O-ring seal between it and the plexiglass case. A transparent case was necessary for observation since a leak of mercury past the piston would result in an incorrect and unknown delivery rate.

This system was actually the second system to be designed. The first system incorporated a small gear pump to deliver the mercury. This was designed to operate on a continuous basis; recharging of the reservoir could be done without stopping the pump. However it proved not to be feasible, as the necessary tolerances were impossible to maintain. The present system will run for four hours at the maximum rate before it must be stopped for recharging. This is felt to be quite adequate.

The mercury boiler and vapor delivery system are now under construction. The problem of delivering a known rate of liquid mercury has been solved as mentioned above, but this does not solve the problem of a known rate of vapor delivery.

Two approaches have been investigated.

1. The liquid is delivered to an extremely hot surface which immediately vaporizes the liquid (a flash boiler).
2. The liquid is delivered to an oven heated to such a degree that an equilibrium surface of liquid is established. The surface remains stationary even though liquid is being delivered to the oven, since the mercury is vaporizing at the delivery rate.

In both cases any part of the system between the oven and the delivery point (in the vacuum channel) must be maintained at a high enough temperature so that no condensation can occur. It appears, at this point, that system number 2 is better and has been selected as the operational system.

The total mass of heated mercury must be kept small so that the vapor flow rate can be varied in an acceptably small time.

APPENDIX I

POWER SOURCE MODIFICATION

FOREWORD

The Appendix describes the installation and modification of six Class C power supplies. The total power capability, and the frequency range are in excess of the requirements of AF 49(638)-759 since the installation was designed to be used for the work requirements of several Air Force contracts. The burden of installation and modification was shared by the several contracts.

APPENDIX I

POWER SOURCE MODIFICATION

1. INTRODUCTION

In order to equip the laboratory with the power sources necessary to perform high-power radio frequency experiments, six surplus Navy TBC transmitters were acquired. Each transmitter has a 50-kw capability and was initially designed to operate over the frequency range of 4 to 26 Mc. These transmitters had served the Navy for many years as long-range communication equipment. The major modification for laboratory use was one of extending the low-frequency limit to 500 cycles/sec, without a significant decrease in efficiency or power capability. The transmitters were acquired in the fall of 1961 and were found to be on the average, in fair condition. After acquisition it was found that the six TBC included four different models. Considerable time and effort was spent in reworking or changing damaged components. All in all, it was only in the spring of 1963 that the reworking and modifications were completed and the installation operative. Since then modifications have proved necessary, even though these were in the nature of refinements. From experience we know that further refinements of this equipment may be expected.

2. MODIFICATIONS

2.1 Push-Pull to Single-Ended Operation

The transmitters as received, were found to operate with a push-pull output, and it was decided to convert the 893 output tubes to single-ended operation. One of the reasons for this was that the physical construction of the 893 plate circuit did not lend itself to low-frequency push-pull operation. The accelerator load also dictated a single-ended drive from each transmitter.

To convert a piece of electronics as massive as the output amplifier of a TBC transmitter presented some challenging problems. Figure I-1

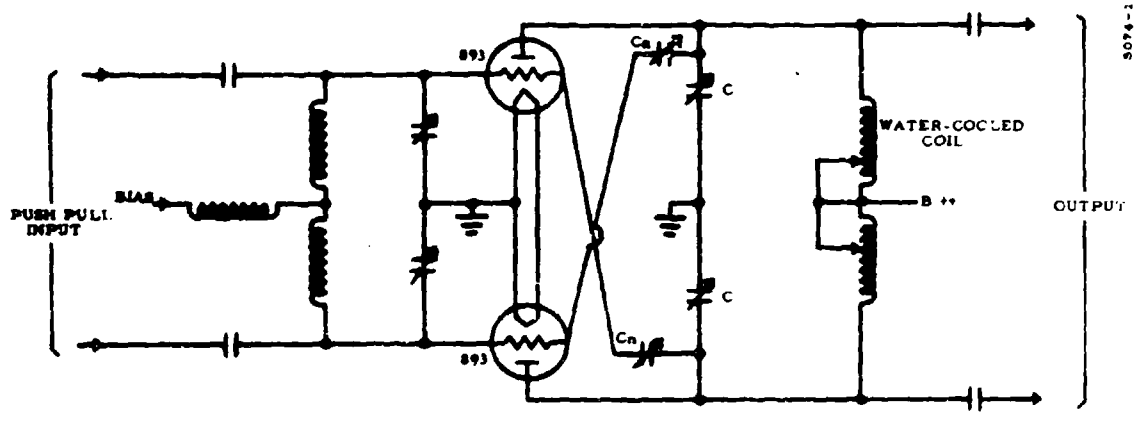


Figure I-1. Simplified Schematic of TBC Power Amplifier (Unmodified)

shows a highly simplified schematic of the TBC final amplifier before modification. Single-ended operation required paralleling the 893 output tubes. Physically connecting the tubes in parallel was simple since the plates and filaments were already connected. The plate circuit has a water-cooled inductance shunting the two plates, but this is effectively a short circuit over the frequency range of interest. Paralleling the grids of the 893 was also not difficult, but as might be expected, a number of spurious oscillations appeared when power was applied.

There are four types of spurious oscillations that can be present in a class C-operated amplifier with parallel output tubes operated in a single-ended mode. The four types encountered in modifying the circuit of Figure I-1 were the following.

1. Very-high frequency (VHF) oscillations caused by parallel operation of the tubes
2. Oscillations in the neighborhood of 2-3 Mc caused by unterminated transmission lines
3. Oscillations at the driving frequency caused by improper neutralization
4. Low-frequency oscillations caused by elements of the output circuit resonating at frequencies lower than the operating frequency.

A detailed description of the changes made to reduce the spurious oscillations follows.

2.1.1 VHF Oscillations

VHF oscillations usually occur when two tubes are operated in parallel. The lead inductances and stray capacity of the grid and plate connections form the necessary conditions for a push-pull tuned-grid, tuned-plate oscillator. The method chosen to eliminate this oscillation was to add two 50-ohm, 50-watt resistors in series with and in close proximity to the grids of the 893's. A resistor (R_2 of Figure I-2. (20,000 ohms and 100 watts) was also added directly between the two plates of the 893's to further reduce the possibility of VHF oscillation. The three resistors serve the function of introducing losses to the grid and plate resonant circuits formed by stray inductance and capacity. The Q of these tank circuits are thereby reduced to a point where VHF oscillations can no longer be sustained.

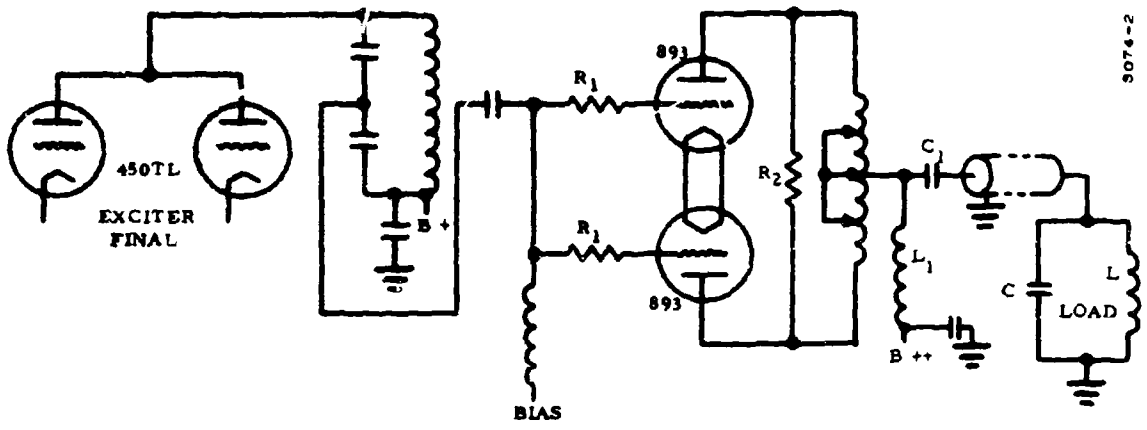


Figure I-2. Modified Output Circuit with Parasitic Resistors

2.1.2 Oscillations Caused by Transmission Lines

As Shown in Figure I-2, the load tank circuit is connected to the transmitters by means of an unmatched transmission line. For a typical application the transmission line length was about 100 feet. As the line was not terminated in its characteristic impedance, it appeared to the transmitter as a high-Q resonant circuit with a resonant frequency of 2-3 Mc. The circuit shown in Figure I-2 exhibited oscillations at this frequency.

One solution to this problem would be to terminate the lines properly. This solution was rejected since it would entail broadband matching transformers at both ends of the transmission line. The solution adopted is shown in Figure I-3. A series resonant trap, tuned to the resonant frequency of the transmission line was placed at the grids of the power amplifier tubes. The series resonant trap was made by rearranging the components of the existing grid tank circuit. In practice the trap is tuned until the oscillations vanish.

2.1.3 Neutralization

A tuned-grid, tuned-plate triode amplifier will usually oscillate because of feedback via the plate-to-grid capacity unless provision is made to neutralize the circuit. Before modification the neutralization was accomplished by cross-coupled plate-to-grid feedback capacitors, C_N as shown in Figure I-1. This simple and effective method of neutralization is possible only with a push-pull amplifier; and because we had elected to change the operating mode to single-ended, another method of neutralizing was required. The method chosen was a modification of the Rice method. Normally in Rice neutralization, the feedback signal is coupled to the grid circuit by means of a tertiary winding on the grid tank circuit. In the absence of a grid tank (see Figure I-2) an auxiliary winding, W, was added to the exciter final tank circuit and capacitors, C_N, were added to the 893 plate circuit as shown in Figure I-3. By a proper choice of the connections to the added winding, the signal fed through the 893 plate-to-grid capacity is canceled by the signal fed back through C_N and the auxiliary winding.

2.1.4 Low-Frequency Oscillations

Referring again to Figure I-3, it will be observed that the load tank circuit is shunt-fed by means of the choke, L_1, and coupling capacitor,

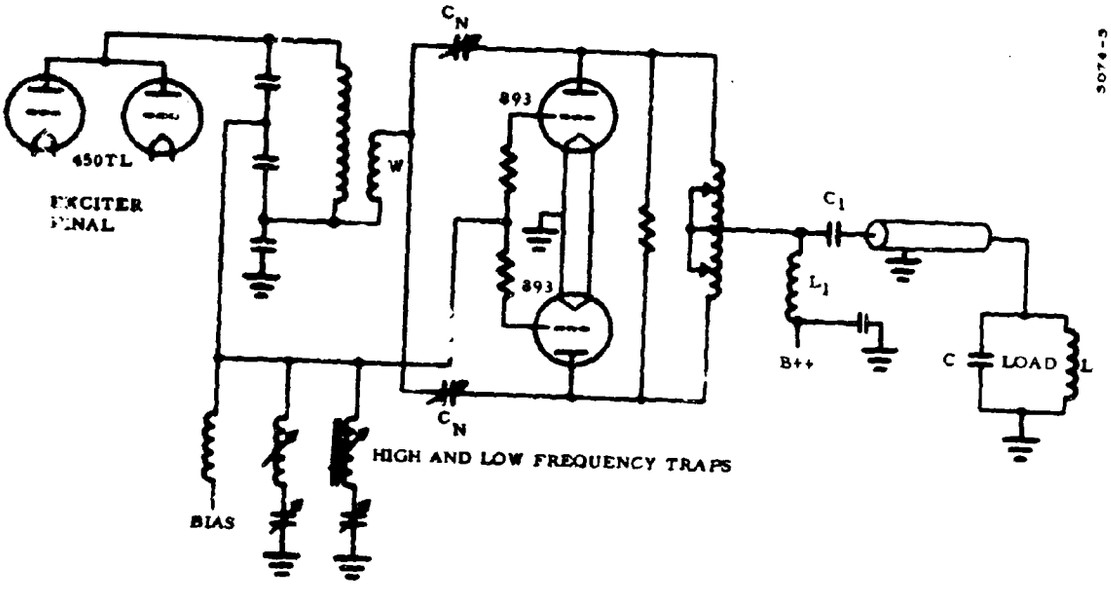


Figure I-3. Neutralization and Grid Traps

C_1. The requirements on L_1 and C_1 are that they should be at least an order of magnitude larger than L and C in order to have a negligible effect on the performance of the load tank circuit. The circuit of Figure I-3 performed well when driving a load tank circuit as shown. However, there was occasion to modify a load tank circuit to be driven push-pull by two transmitters, and during this operation low-frequency oscillations were observed.

Capacitor C of Figure I-4 is free to resonate with the shunt-feed chokes, L_1 at a much lower frequency then the natural resonant frequency of the load tank circuit. As neutralization is only effective at or near the operating frequency of the amplifier it was of no help in eliminating this type of oscillation. An additional tunable series resonant trap at the grids of the power amplifier was required. With a 55-kc push-pull tank circuit, the low-frequency oscillations occurred at about 8 kc. The tuneable element was chosen to be a variable inductance. The necessary variation of inductance was accomplished by varying the air gap spacing of the laminated iron core. Figure I-3 illustrates the placement of this low-frequency trap.

2.2 Modification of Exciter Final

The 450TL exciter final tubes were also modified from a push-pull to semiparallel operation. This modification, however, did not present the problems of oscillation experienced with the final output tubes. Parasitic (VHF) oscillations occur only when both tubes are allowed to conduct simultaneously as do the 893's. This condition is prevented for the 450TL by the form of the input drive (See Section 3, Modulation). Neutralization of this stage was unnecessary as the plate tank circuit is tuned to a much lower frequency than the grid tank circuit.

3. MODULATION

3.1 Principle of Operation

Figure I-5 shows a block diagram of a TBC-3 transmitter. The amplifier tubes operate in standard class-C mode on a continuous-wave basis. Seven tuned circuits exist between the master oscillator and the last stage of the power amplifier. In order to provide low-frequency operation, the conventional transformation would have required modification and tuning of all seven resonant circuits — a total of 42 circuits to be tuned if the operating frequency required by an experiment was to

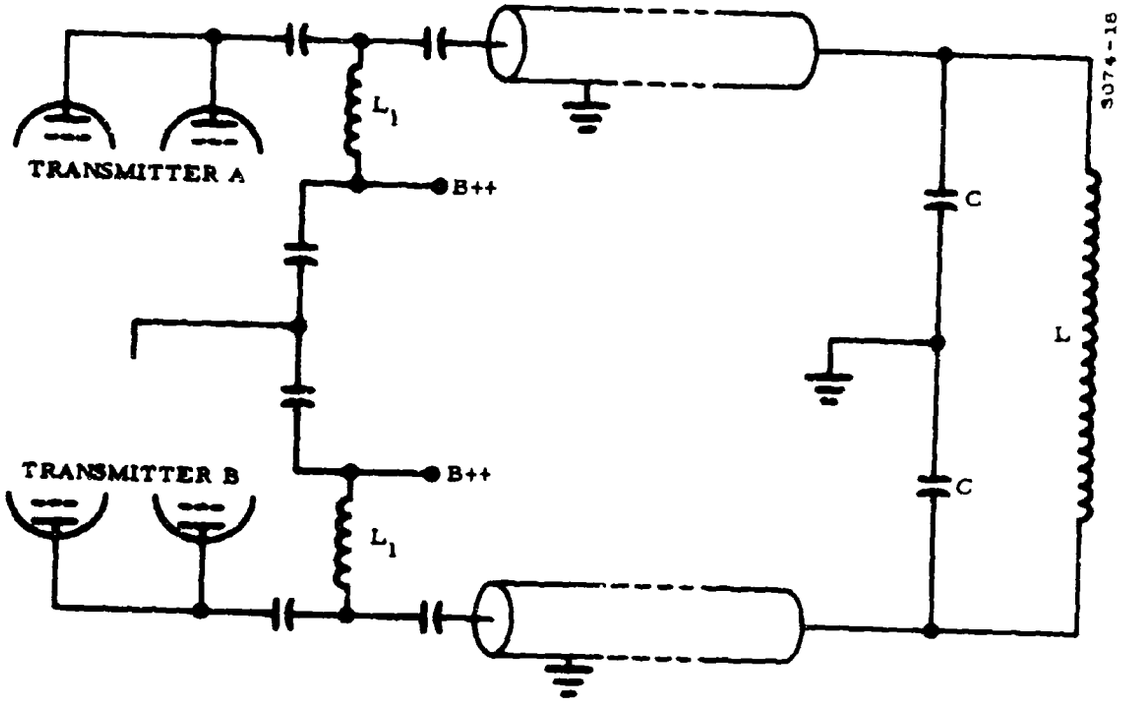


Figure I-4. Push-Pull Load Using Two Transmitters

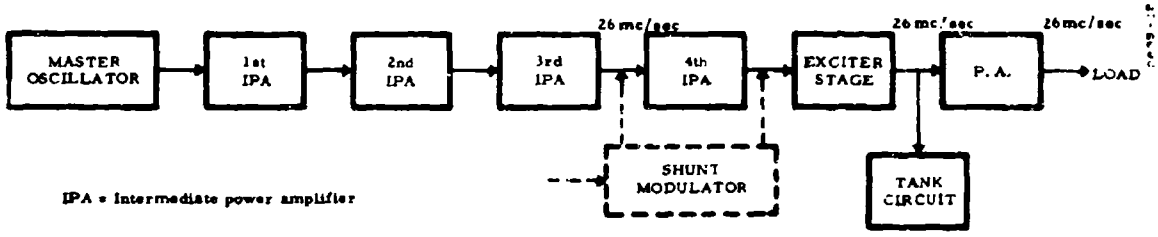


Figure I-5. Block Diagram of Unmodified TBC-3 Transmitter (Modification Shown Dotted)

be changed. To avoid this, another method, which involved modulation of a late driver stage, was selected and its general principles will be described.

Normally a class-C amplifier stage has a resonant circuit in its plate, and the frequency of the signal used to drive its grid is equal to the plate circuit resonant frequency. The conduction angle (that portion of the grid signal that drives the grid positive) is usually between 80 and 150 electrical degrees for best performance of the stage. Instead of using a pure sine wave signal to drive the grid of the class-C stage, it was reasoned that it would be driven equally well by a high-frequency carrier modulated at a frequency equal to the plate circuit resonant frequency.

Figure I-6a shows the condition of a standard class-C grid drive with positive grid regions and definition of the conduction angle indicated. Figure I-6b shows the condition of the modulated carrier grid drive introduced at the fourth intermediate power amplifier (IPA) stage. It should be observed that the modulation ratio has to be greater than 100 percent so that the conduction angle will be between 80 and 150 electrical degrees. As can be seen from Figure I-6b, the power output capability of a class-C stage is decreased by more than 50 percent when a modulated carrier grid drive is used, all other conditions being the same. However, this did not prove to be a major disadvantage, since the power capability of each stage of the TBC-3 (except for the power amplifier) was quite sufficient to compensate for this power loss.

3.2 Elimination of High Frequency Carrier

The required modifications to the transmitters included the installation of a shunt modulator and the tuning of a tank circuit between the exciter stage and the final stage of power amplification as indicated by the block diagram of Figure I-5. The tank circuit preceding the final stage of amplification is tuned to the modulating frequency and provides the driving signal to the power amplifier. It also serves the function of a filter to completely eliminate the high-frequency carrier. This can be seen from the following argument. The input to the 450TL is the modulated signal. This tube operates as class-C so it is cut off for most of the input signal. The output of the 450TL has the power amplifier's grid tank on its plate. Then the 893 grid sees the high-frequency carrier only on the negative side of its swing. The positive side is supplied by the tank circuit, since during this part of the cycle the 450TL is cut off. The 893 is also operated class-C so that it is cut off during the negative swing of its grid, which is the only region of the cycle

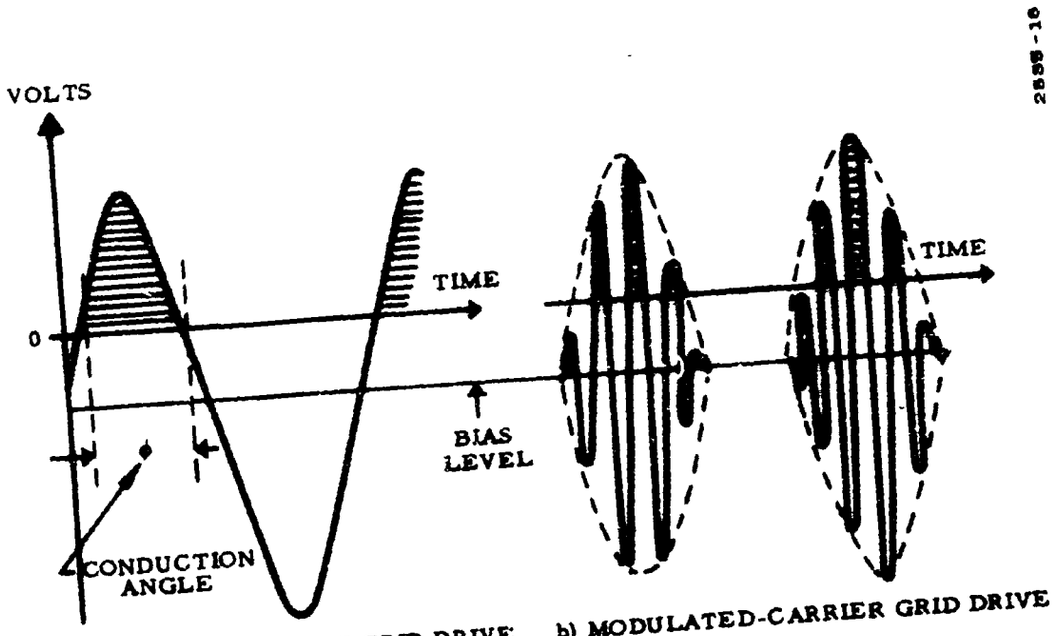


Figure I-6. Voltage of Class-C Grid Drives as a Function of Time

containing the high-frequency carrier. Thus the carrier has been completely eliminated in the final output.

3.3 Choice of Carrier Frequency

In order to achieve the highest modulation frequency possible, the carrier frequency was set at the maximum allowed by the transmitters, i.e., 26 Mc. There are two reasons for this choice.

1. Referring to Figure I-6b, the conduction angle is determined to some extent by the relationship between the phases of the carrier and modulation frequencies. As the two frequencies are not locked in any way, variations in phase can produce small variations in frequency and amplitude of the stage output. This effect becomes negligible the higher the carrier frequency with respect to the modulation frequency.
2. This reason is somewhat subtle and is concerned with the method of modulating. In order to minimize modulating power, the method chosen consisted in detuning the exciter input tank circuit (fourth IPA output) by means of a small capacitor through an electronic shunt. The recovery time (i.e., the time necessary for the signal amplitude across the tank circuit to recover its original value after the shunt has been removed) limits the maximum modulation frequency. For a constant-Q tank circuit, the number of cycles required to recover is independent of its frequency. The higher the carrier frequency, the faster is the recovery (for constant Q), allowing a higher modulating frequency. With a 26-Mc carrier, a modulating frequency as high as 500 kc can be used.

3.4 The Shunt Modulator

As indicated in the block diagram of Figure I-5, the modulator is actually connected to both the input and output of the fourth IPA stage. The 26-Mc signal appearing at these two points serves as a plate signal for the shunt clamping tubes of the modulator. These tubes act as an intermittent shunt to ground controlled by the modulating signal. During a portion of each cycle of the modulating signal, the 26-Mc is shunted to ground. The reason for simultaneously shunting the input and output tank circuits of the fourth IPA is to reduce tube dissipation and, more important, to reduce the power requirements of the shunt modulator itself. If the input shunt is not used, the 26-Mc signal to its input is always present. Shunting only the output would require that the modulator

tubes absorb excessive power during their shunt time. Excessive plate dissipation in the fourth IPA would also result, because the tube would be conducting during the time that its plate was shunted to ground. It was established that it was not sufficient to clamp only the fourth IPA input. Without a controlled shunt on the plate, the plate tank circuit oscillations would continue for an unacceptable time, negating the shunt modulator action on the input.

The shunt modulator proper consists of parallel connected pairs of 807 pentode tubes driven by a Schmidt trigger. The input signal to the Schmidt is a 20-volt sine wave. A simplified schematic of the moduiator is shown in Figure I-7.

The 26-Mc carrier is coupled by means of small capacitors, C, to the plates of pairs of 807's and serves as the plate voltage for these tubes. Plate inductance, L, and stray capacity are made to resonate in parallel at 26 Mc in order not to load the exciter stage. With the control grids of the 807's cut off (-40 volts) the transmitter is unaffected by the modulator. With the control grids at zero volts, the 807's draw plate current during each half cycle of the 26-Mc plate voltage and, consequently, both load and detune the input and output tank circuits of the fourth IPA. As an example Figure I-8 shows two oscillograms of a 26-Mc carrier signal modulated by this method at 200 kc and 55 kc. These are the signals that appear at the plate of the fourth IPA. The middle trace in both cases is the signal appearing at the grid of the power amplifier, and the lower trace is the load signal. Except for 807 screen power and a few watts for the Schmidt trigger, the modulator requires no dc input power but simply absorbs power from the transmitter. The conduction angle mentioned previously is set by changing the level of the Schmidt trigger. This is done by adjusting the potentiometer in the grid circuit of the 5687 tube.

Referring to Figure I-8 note the trace of the 26-Mc carrier in the negative half-cycle of the power amplifier grid signal.

4. TUNING

One goal of the modifications performed on the transmitters was to allow for relatively rapid changes of operating frequency. The modifications have been made so that only two tank circuits per transmitter are required when changing frequency. All other tank circuits are fixed-tuned at 26 Mc. At the input to the exciter final the 26-Mc signal is

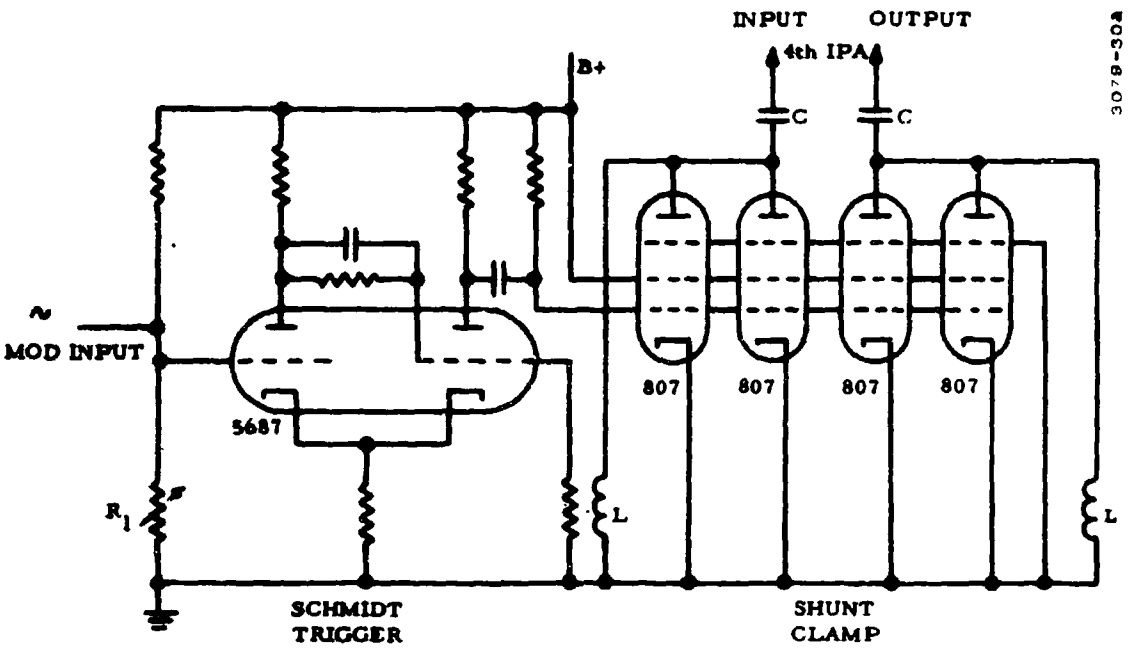
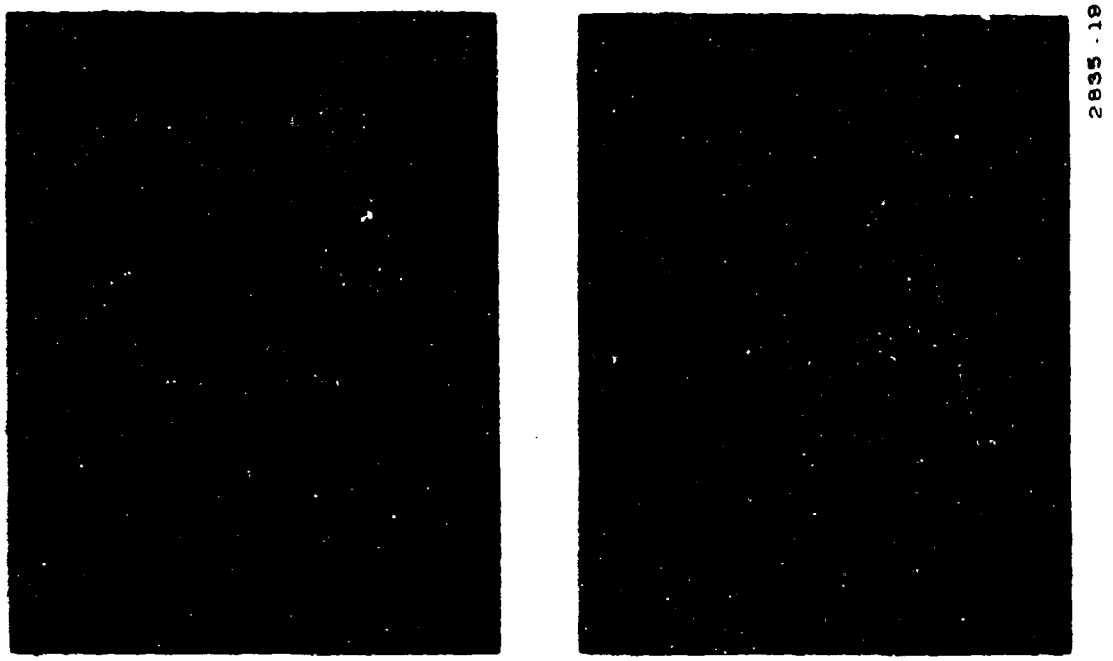


Figure I-7. Shunt Modulator



MODULATION FREQUENCY

200 Kc/sec

MODULATION FREQUENCY

55 Kc/sec

UPPER TRACE: SIGNAL AT THE PLATE OF 4th IPA

MIDDLE TRACE: SIGNAL AT GRID OF POWER AMPLIFIER

LOWER TRACE: LOAD SIGNAL

Figure I-8. Signal Patterns at Various Stages in Modified TBC Transmitter

It is noted that C is a characteristic capacity of the analog (farads) and Ω is a characteristic conductance (mho). C/Ω is independent of σ and is a characteristic time constant.

The same procedure as before is used to develop the analog and the result is shown in Figure G-5. Each node point is seen to be connected to ground (i. e., the axis $\psi^* = 0$) by a capacitor. Thus, when the magnetic field around the strap varies very quickly, the field inside the strap is highly attenuated.

The values for C and I_N (Figure G-5) are found from

$$\left.\begin{aligned} C_N &= C \ln \frac{N + \frac{1}{2}}{N - \frac{1}{2}} \\ I_N &= \frac{C_N}{C} \Omega \, \varepsilon(\tau) \end{aligned}\right\} \quad N \leqq n_o \qquad \text{(G. 56)}$$

$$\left.\begin{aligned} C_N &= C \\ I_N &= \Omega \, \varepsilon(\tau) \end{aligned}\right\} \quad N > n_o \qquad \text{(G. 57)}$$

The scale factor for the time, a, can be chosen to have any convenient value.

If the analog is more useful when expressed in terms of a constant-voltage generator rather than a constant-current generator, one can replace $\varepsilon(\tau)$ by:

$$\varepsilon(\tau) \equiv \frac{C}{\Omega} \frac{\partial V_g(\tau)}{\partial \tau} \qquad \text{(G. 58)}$$

where $V_g(\tau)$ is defined by the above. Substitution of the above into Eq. (G. 50) yields the analog shown in Figure G-6. Since V_g is independent of position the capacitors from all nodes can be connected to the same generator.

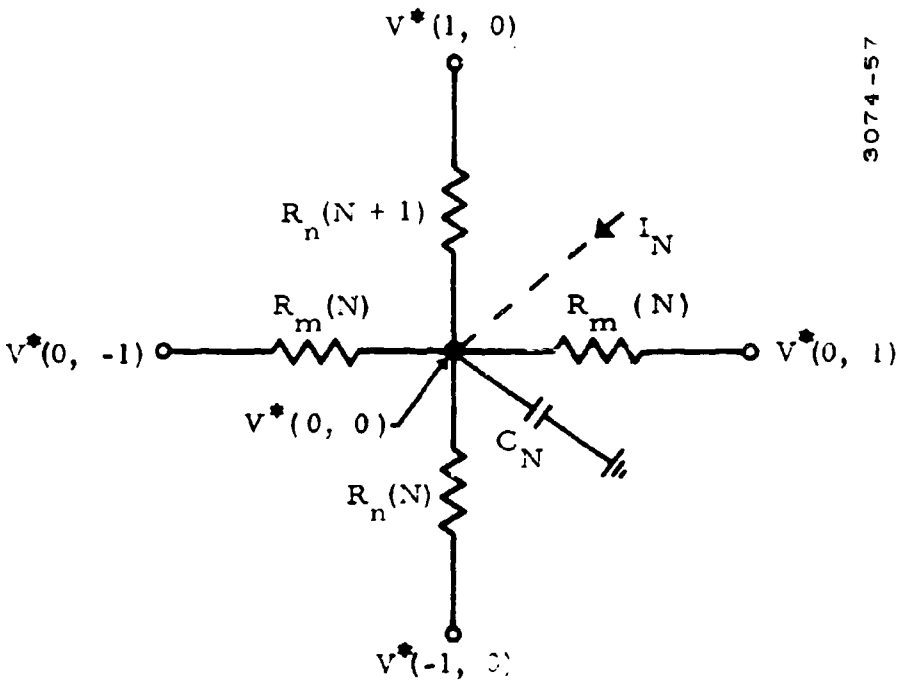


Figure G-5. Analog for Metal Objects

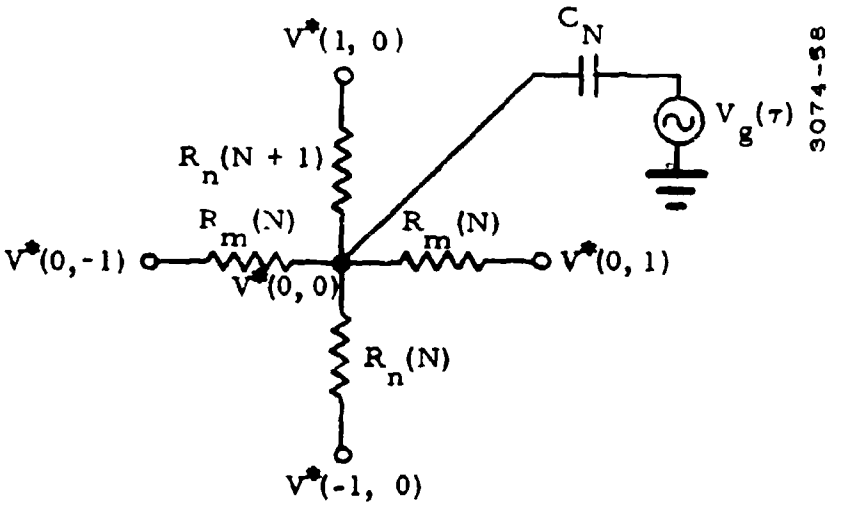


Figure G-6. Constant-Voltage Analog

Calculation shows that if (N, M) lies along an edge of the metal then the appropriate value for the capacitor is $C_N/2$ rather than C_N. If it lies on a corner, the appropriate value is $C_N/4$. These apply if $N > n_o$. The results for $N < n_o$ are tedious and will not be given here.(See Figure G-7.)

The qualitative behavior of the analog can be discovered by considering its response to a voltage step. The step is assumed to occur at $\tau = 0$ and to have amplitude ε_o. Then

$$V_g(\tau) = 0;\ \tau < 0 \qquad \text{and} \qquad V_g(\tau) = \frac{\Omega}{C}\,\varepsilon_o\,\tau;\ \tau > 0$$

In response to this voltage, the voltage at the mesh points will rise from zero to some steady-state value with a time constant proportional to C. On the other hand, for small values for τ one finds that

$$V^*(N, M) = \frac{\Omega}{C}\,\varepsilon_o \tau$$

This result can be rewritten in terms of the magnetic flux through the use of Eq. (G. 49) and the result is:

$$\Phi(r(N), z(M)) = \varepsilon_o t \qquad \text{(G. 59)}$$

this result holds for small values of time when the inductive behavior of the metal dominates. At large values of time the conductivity dominates. One then finds that the current flowing into each mesh point is

$$I \cong \sigma\,\frac{\Delta z\,\Delta r}{2\pi r}\,\varepsilon_o \qquad \text{(G. 60)}$$

where $\Delta z\,\Delta r$ is the area represented by one mesh point. This is Ohm's law.

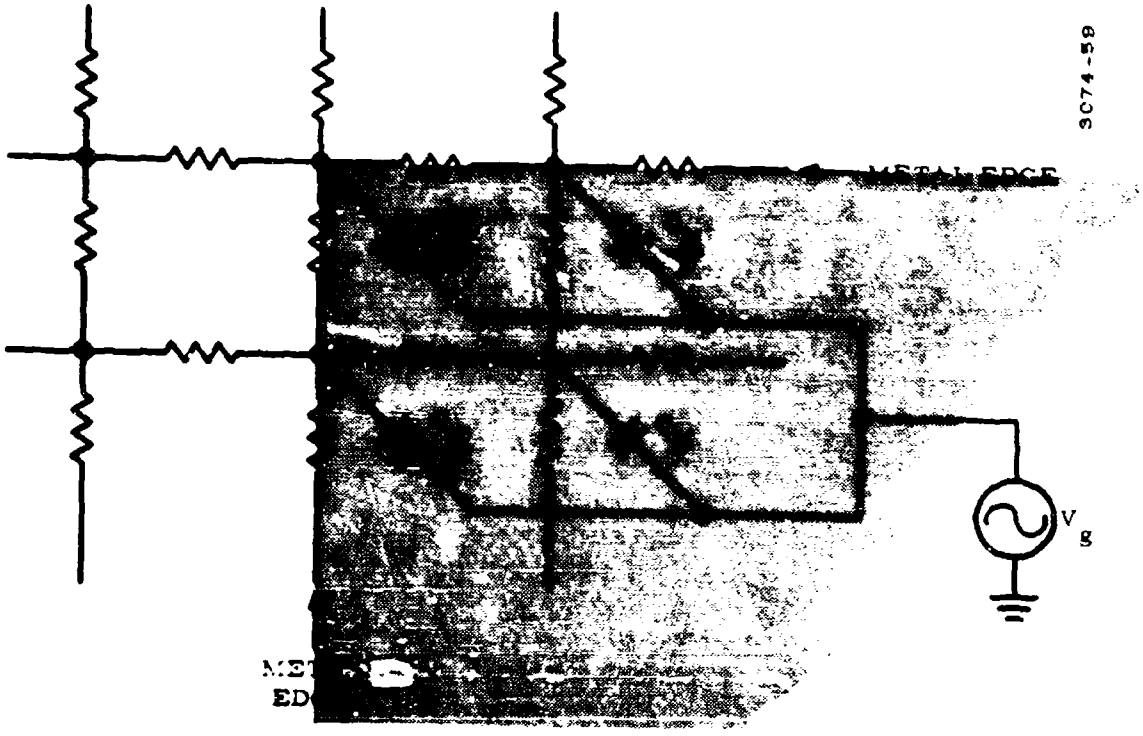


Figure G-7. Analog of Metal Corner

3. PLASMA ANALOG

We will consider the electrical analog for a magnetic field in a region containing plasma. Let the electron density be N^e. Cylindrical symmetry is assumed and N^e is assumed independent of time. This is very restrictive but still, the analog yields useful information.

The current is due almost entirely to the electrons. If e is the absolute magnitude of the electronic charge and if $\langle W_\theta \rangle^e$ is the average azimuthal electron speed then the current density is

$$j = -eN^e \langle W_\theta \rangle^e \qquad \text{(G. 61)}$$

where all the quantities are functions of r and z.

Let M^e be the electron mass, E_θ be the electric field of induction, and T be the average time for 90° scattering of an electron. Then:

$$\frac{\partial j}{\partial t} + \frac{j}{T} = \frac{e^2 N^e}{M^e} E_\theta \qquad \text{(G. 62)}$$

If E_θ is zero then j dies away exponentially with time constant T.

Strictly speaking T is not a constant, but it varies little over one or two collision times if the mean electron speed is constant (constant electron temperature) over a time on the order of 2T.

The situation is discussed in more detail in Section 3 of this report.

Assuming a constant value for T one finds:

$$j(t) = j(t=0)e^{-t/T} + \frac{e^2 N^e}{M^e} \int_0^t e^{-\frac{t-t'}{T}} E_\theta(t')\, dt' \qquad \text{(G. 63)}$$

If T is very small then

$$j = \frac{e^2 N^e}{M^e} T E_\theta \qquad \text{(G. 64)}$$

which is just Ohm's law. If T is very large then

$$j = j(t=0) - \frac{e^2 N^e}{2\pi r M^e}\left[\Phi(t) - \Phi(t=0)\right] \qquad \text{(G. 65)}$$

and the current density is in phase with the magnetic flux. The plasma is then inertially dominated as is discussed in Section 3.

Eq. (G. 63) can be transformed to the (n, m) coordinate system with the result:

$$\frac{\partial^2 I^*}{\partial r \partial z} = -\frac{R_o}{R_p(n, m)} \int_o^t e^{-\frac{a(\tau - \tau')}{T}} \frac{\partial \psi^*}{\partial \tau'} d\tau' + \frac{\partial^2 I^*(t=0)}{\partial r \partial z} e^{-a\tau/T} \qquad \text{(G. 66)}$$

where:

$$R_p = \frac{R_o n}{4\pi R_e z_o^2 N^e(r(n), z(m))} \text{ (ohm)} \qquad \text{(G. 67)}$$

for $n \leq n_o$

$$R_p = \frac{R_o n_o}{4\pi R_e z_o^2 N^e(r(n), z(m))} \text{ (ohm)} \qquad \text{(G. 68)}$$

for $n > n_o$

and

$$R_e = \frac{e^2 \mu_o}{4\pi M^e} = 2.80 \times 10^{-15} \text{ meter.}$$

Note that R_e is the classical electron radius. The characteristic collision time, T, may vary from place to place in the plasma. For each place a characteristic capacity, C_p may be defined. It is:

$$C_p = \frac{T}{a R_p} \qquad \text{(G. 69)}$$

The current density , $\partial^2 I^* / \partial r \partial z$, may now be inserted into Eq. (G. 16) and (G.17) and the analog derived. The result is shown in Figure G-8.

The plasma is seen to have the effect of shorting each mesh point to ground through a series RC circuit whose time constant equals the mean time for 90° collisions. The node resistors, R_p, give the self-field effects which are appreciable if

$$N^e > 3 \times 10^{17} \text{ electrons/meter}^3$$

4. CONSTRUCTION OF THE ANALOG BOARD

An analog board was constructed. Thirty-six independent current sources with a range 0 - 10 ma are provided. The current sources are zener-diode stabilized pentode tubes whose plate and cathodes are made available for connection to the analog board. The complete unit is shown in Figure G-9 and a close-up of the resistor mesh is shown in Figure G-10. It can be seen that the node points can be easily disconnected.

The board reader is essentially a bridge circuit as indicated in Figure G-11. The potentiometer R_2 is set to a value and the corresponding voltage contour is found, on the board, through the use of the probe containing the potentiometer R_1. The latter is for interpolation between the mesh points.

The null bridge is similar in design to the bridge discussed in Appendix M. It has an extremely high input impedance and so draws a negligible current from the board. A photograph of the reader is shown in Figure G-12. In order to facilitate the transformation of quantities into, and out of, the (n, m) system a slide rule was designed. It is shown in Figure G-13.

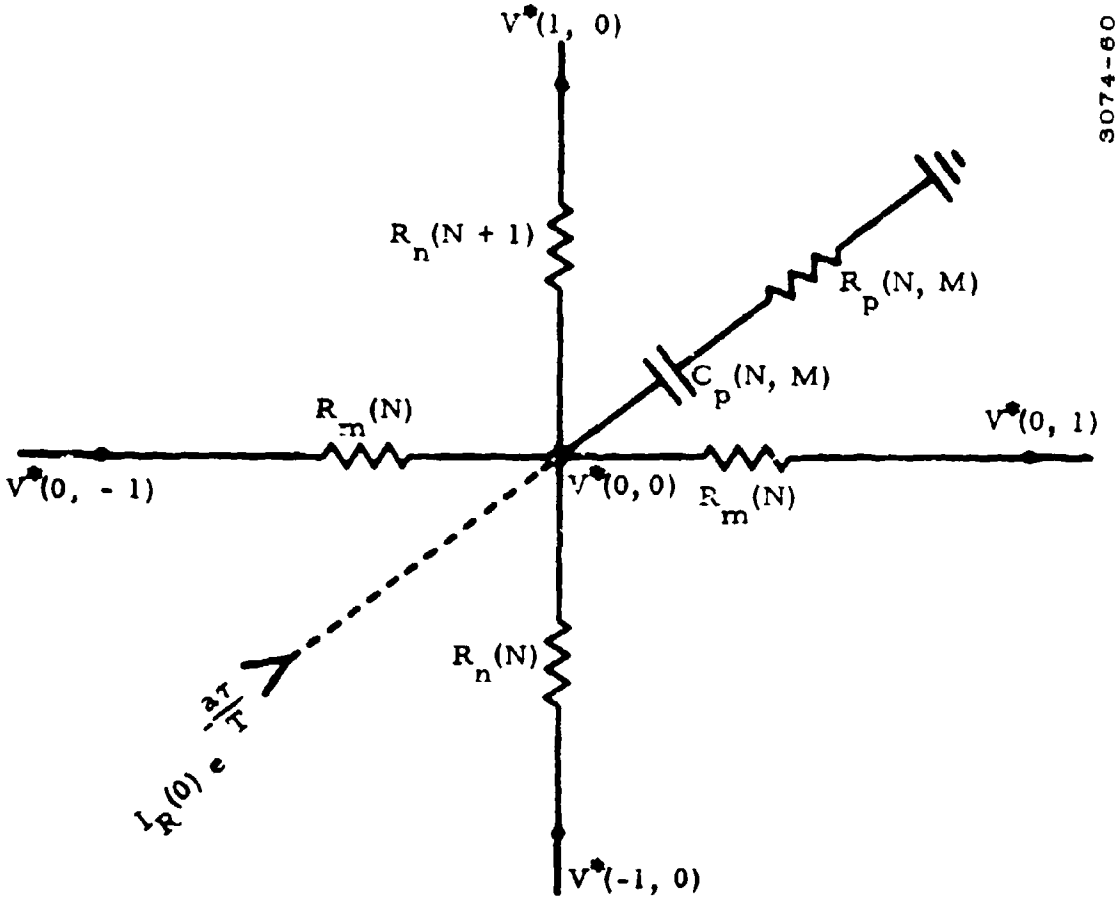


Figure G-8. Plasma Analog

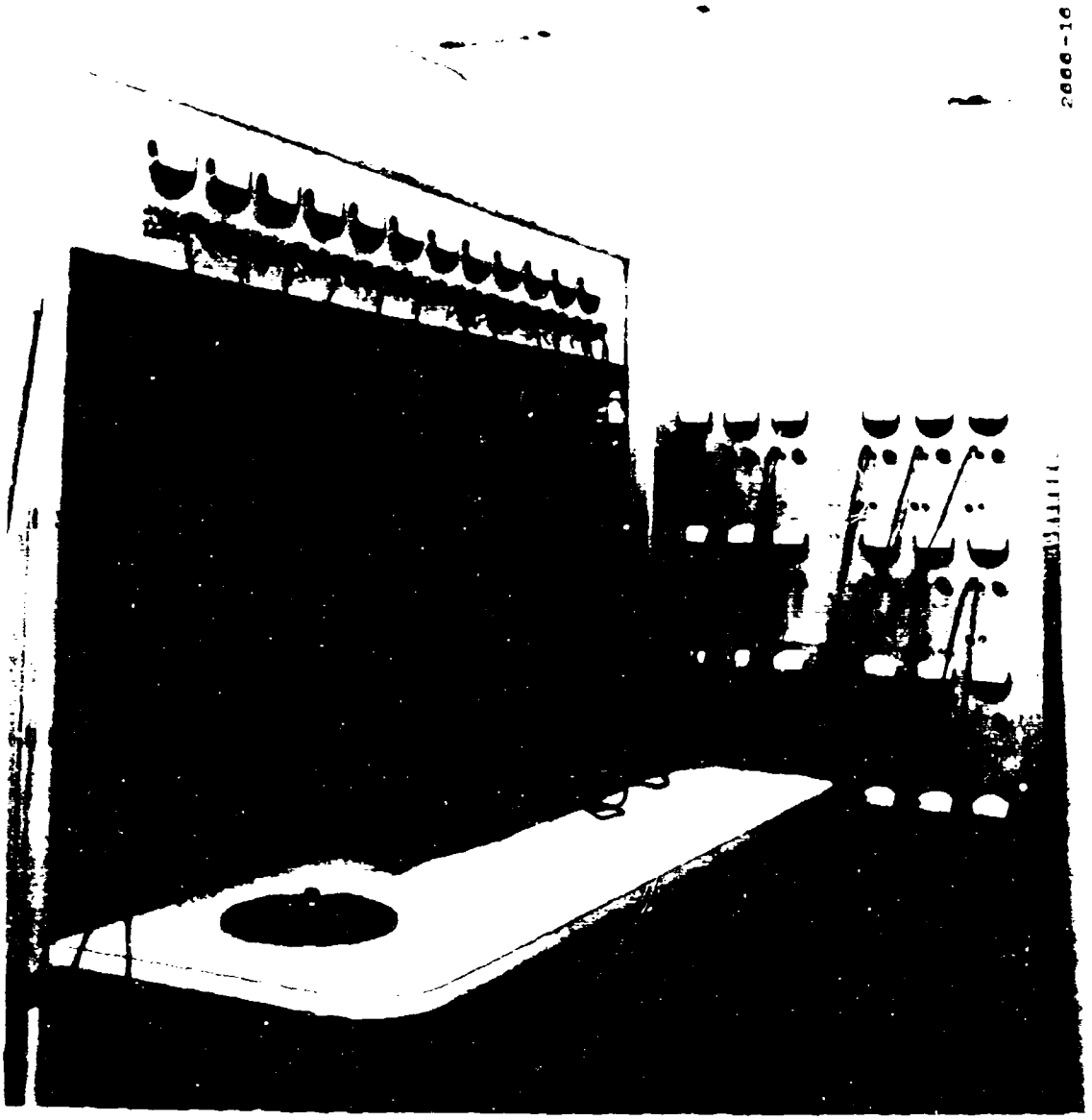


Figure G-9. Completed Analog Board



Figure G-10. Closeup of Resistor Mesh

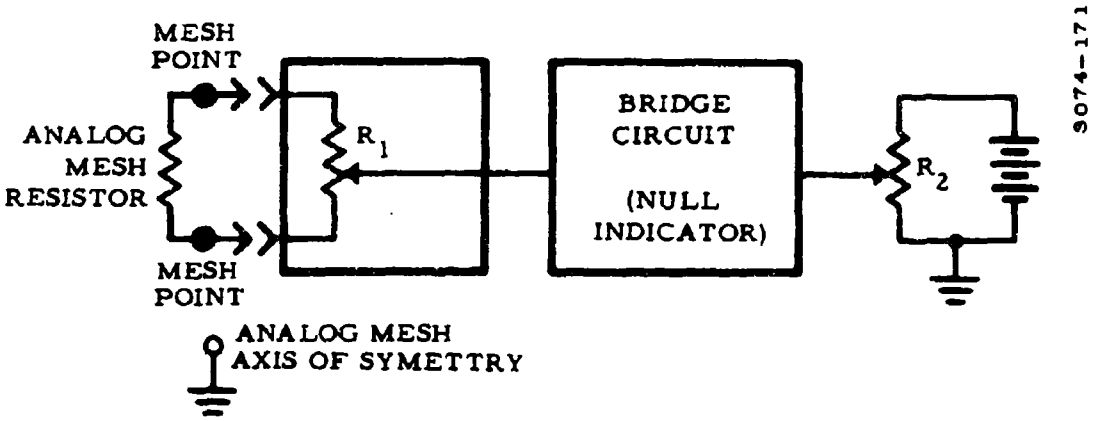


Figure G-11. Block Diagram of Board Reader

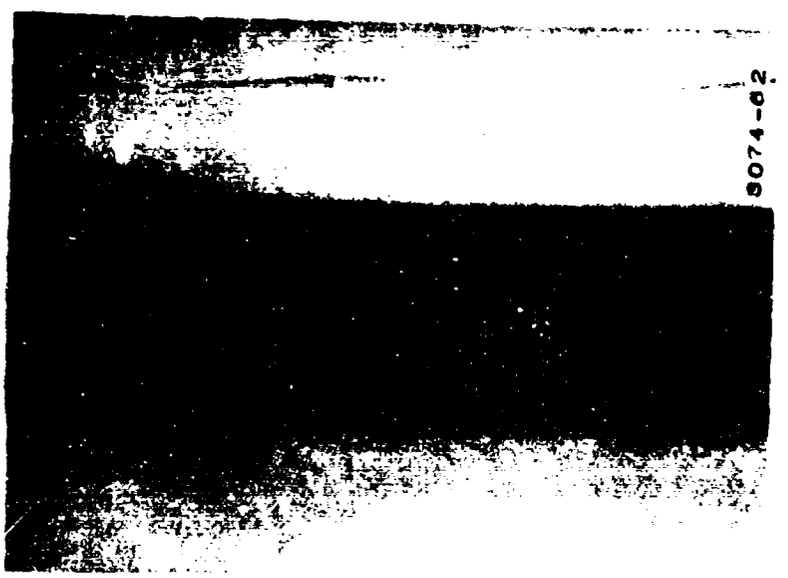


Figure G-12. Analog Board Reader



Figure G-13. Analog Board Slide Rule

REFERENCES

Note: The following references describe resistor mesh analog computers, but the exponential transform described here is not employed. As a result, the standard resistor sizes can not be employed and in addition, certain approximations to the basic analog must be made.

1. Cristensen, U.; "An Analog Board for Time-Varying Axial Symmetrical Fields", Proc. of Symp. on Magnetic Field Design (1958), Gatlinburg, Tenn., ORNL-2745.

2. Wakefield, K. E.; "A Resistance Analog Device for Studying Axially Symmetric Magnetic Fields", Project Matterhorn Report PM-S-23. (1958).

3. Wakefield, K. E.; "The Use of Analog Computers in the Design of Magnetic Field Systems", ORNL-2745 (1958).

APPENDIX H

MECHANICAL DESIGN OF THE MARK II ACCELERATOR

APPENDIX H

MECHANICAL DESIGN OF THE MARK II ACCELERATOR

This appendix deals principally with the details of the mechanical design of the various subsystems of the experimental equipment in the Accelerator laboratory (Figure H-1).

The following topics are covered in this appendix:

1. Mechanical Structure of the Accelerator
   - 1.1 The Field Coils
   - 1.2 The Ferrites
2. The Vacuum System
3. The Oil System
4. The Mercury Feed System

1. THE MECHANICAL STRUCTURE OF THE ACCELERATOR

Basically the accelerator consists of two sets of coils, a vacuum channel, and a central ferrite rod. Assembly problems and anticipated needs for additions and adjustments led to the design shown in Figure H-2.

This figure is a vertical cross section of the device as it was finally realized. A few details have been omitted for clarity.

The accelerator is housed in a steel box (18) * of dimensions 2 feet × 2 feet × 7 feet, which is filled with a dielectric oil. The top and sides of the box are seperately removable, being sealed with neoprene gaskets.

*Circled numerals refer to numbers in Figure H-2.

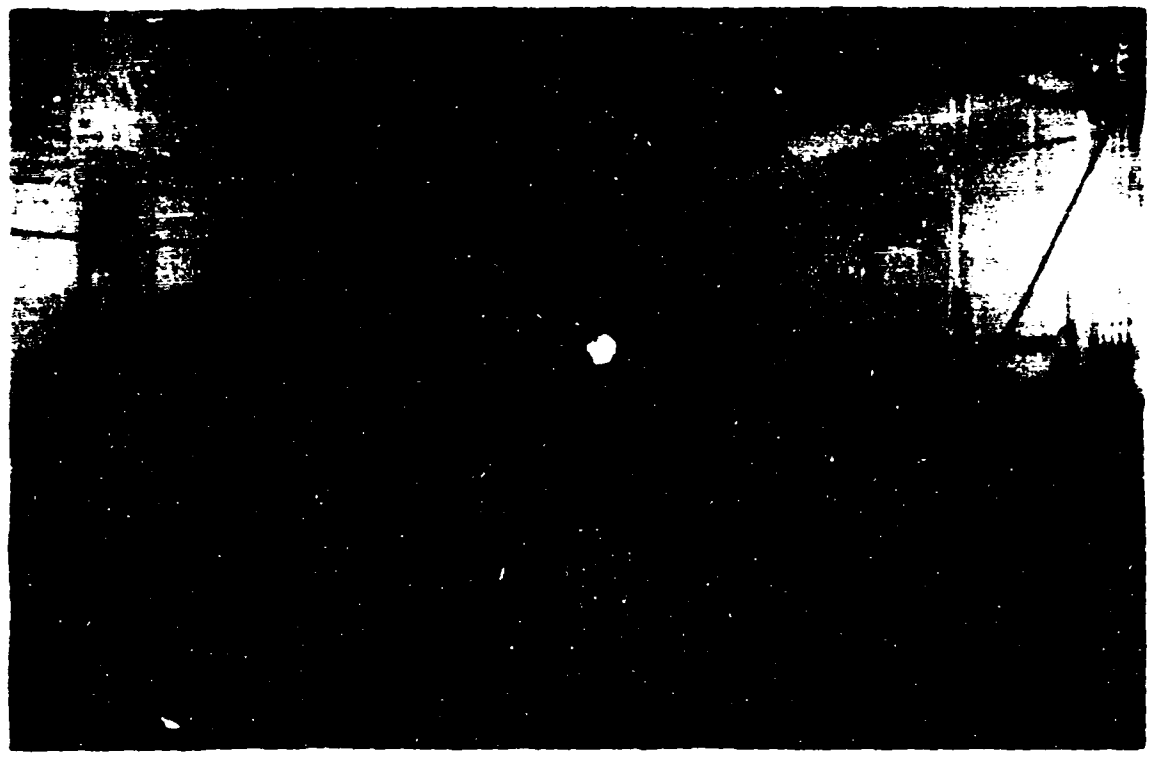
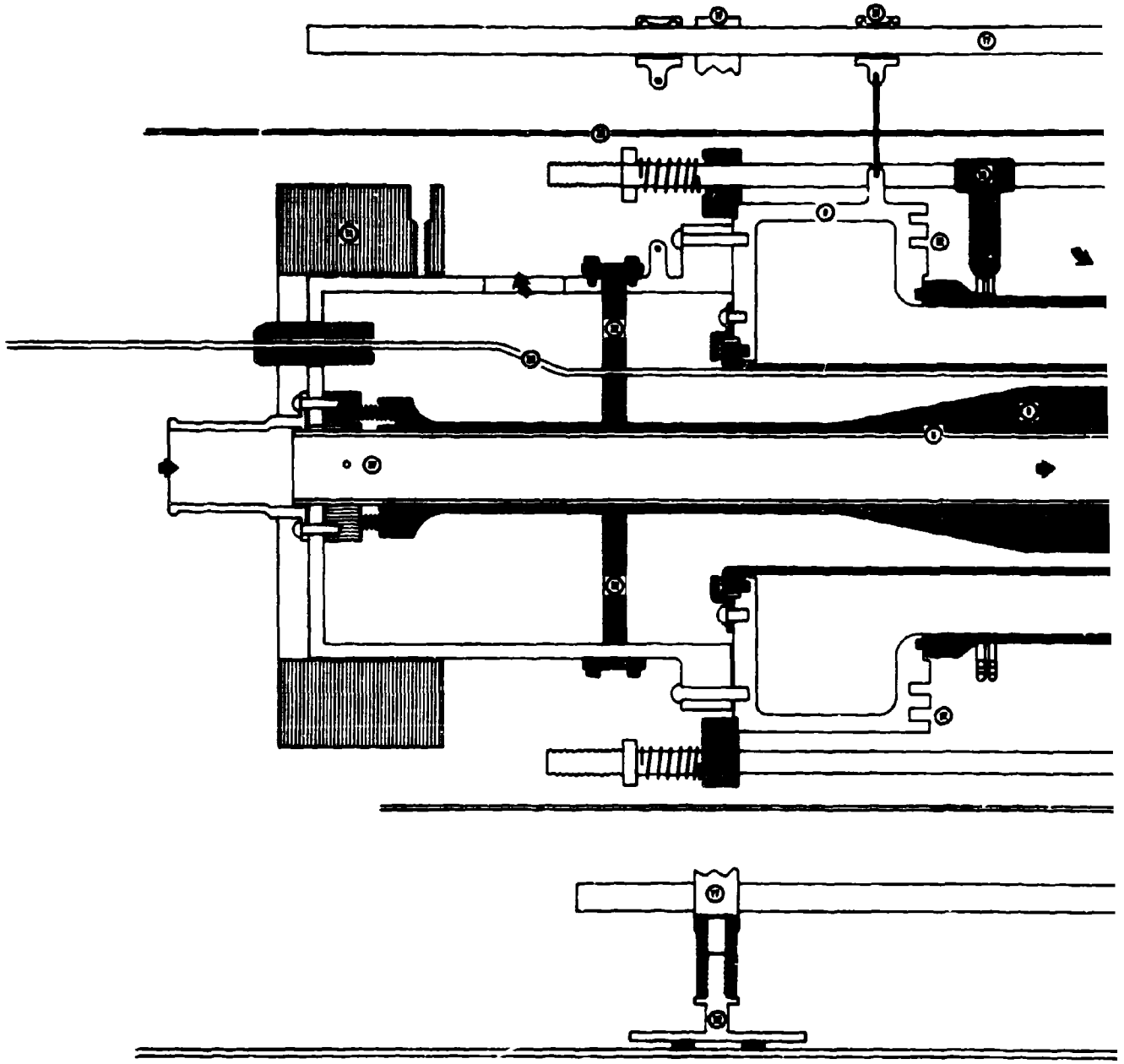


Figure H-1. View of Accelerator Laboratory

1. Vacuum Channel
2. Outer Field Coil
3. Inner Field Coil
4. Ferrite Core
5. Stainless Steel Support Tube
6. Phenolic Spacer
7. Outer Vacuum Channel Wall
8. Inner Vacuum Channel Wall
9. Container for Rig Water
10. Tie Rod
11. Adjustable Counter Weight
12. Stainless Steel Bellows Assembly
13. Outer Coil Adjuster
14. Oil Overflow Line
15. Phenolic Outer Coil Holder
16. Phenolic Pole Bumper Support
17. Support Assembly
18. Wall of Steel Outer Box
19. Height Adjustment
20. Coil Clamp
21. Sliding Supports
22. Ferrite Core Bearing Adjustment
23. Typical Coil Leads
24. Flexible Oil Container
25. Flexible Oil Baffle
26. Phenolic Pass-Through
27. Pin For Ferrite Support Tube
28. Hanger Support
29. Transparent Oil Baffle
30. Flange on Vacuum Tank
31. Adjustable Stop
32. Cooling Channel



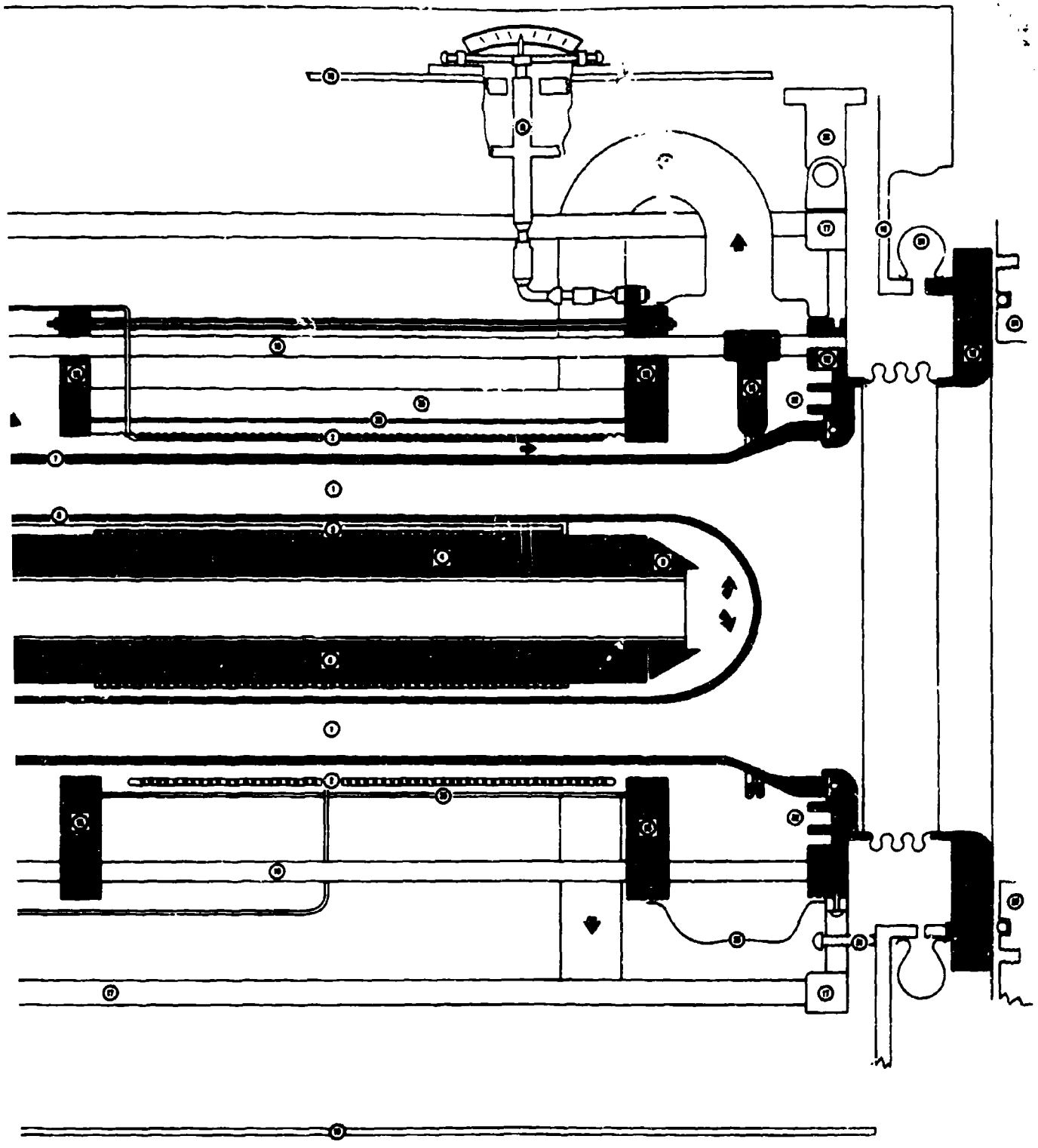


Figure H-2. Accelerator Cross Section

Each of the sides has a pyrex glass window 6 in. × 12 in. for viewing the coil region during operation. The box is reinforced with steel tubing to prevent bulging in case of excessive oil pressures, which may occur by mischance. One end of the box (not included in Figure H-2) has 24 Crouse-Hinds pass-throughs, which permit access to the insulated wires carrying the coil currents. It also has 24 small-diameter coaxial pass-throughs for temperature sensors or other signal-carrying leads. The box stands on legs with leveling screws, and these are mounted on a wheeled frame. A set of rails runs the length of the laboratory.

The accelerator is attached to the vacuum tank (30) via connecting flanges and bellows (12). This is a single welded assembly. Both flanges and bellows are made of nonmagnetic stainless steel. The bellows has a wall thickness of 0.010 inch, so it is important that it not directly contact the plasma beam. Since the steel box is filled with oil, an additional flexible oil container (24) is provided between the box and the bellows flange. The oil container is banded to the flanges with large hose clamps.

The entire accelerator structure is supported at two points: it is hung from the support (28) and the support (21). The former is attached to the box (18) whereas the latter rests on the frame (17). An adjustable leg (19) is placed between the frame (17) and the box. It bears part of the weight of the accelerator. A ball bearing race, between the leg and the box, facilitates movement of the system during assembly. In effect, the accelerator hangs in the frame (17).

One major problem was the ferrite rod (4), which weighs about 20 pounds and which had to be cantilevered from one end. The solution chosen was to use a sliding counterweight (11) to balance the ferrite rod, and adjustable fingers (22) to center it. This weight also facilitates the task of moving the central assembly backward during disassembly.

All vacuum seals are Viton-A O-rings. Viton-A may be expected to be trouble-free up to 250 C. The actual average temperature is not expected to exceed 80 C. Certain regions, such as the stainless steel bellows, may reach much higher temperatures because of ohmic heating by induced currents and plasma impingement. Cooling channels (32) were cut in these places to alleviate this problem. In addition shorted turns of copper wire (16) were provided to partially prevent the flux from reaching these regions.

The integrity of the annular vacuum channel (1) is maintained by six spring-loaded tie rods (10). They have proved extremely useful during preliminary electrical testing when the vacuum system has been up to air and the box filled with oil. When the system is pumped down, the pressure differences that develop tighten the vacuum seals. In addition, the bellows would contract under these forces, so several adjustable stops (31) were provided. Axial thermal expansion of the vacuum channel walls is taken up by increased spring compression.

It was felt that the best chance of minimizing wall heating problems at the exit end of the device was to flare the outer vacuum channel wall (7). We experienced a good deal of trouble in obtaining quartz tubes with the smooth flare-out, and several walls had to be rejected. The quartz walls were finally obtained from Thermal American Fused Quartz Co. of New Jersey and are extremely well made. (Figure H-3).

The support (15) for the outer coil moves along the tie rods and has a free motion of about four centimeters. The distance moved is measured by the scale and pointer (13) external to the box. The outer coil is moved through the flexible linkage shown attached to the pointer.

The arrows indicate the oil flow. Oil is introduced through the rear of the box, and a hose leads directly to the hollow ferrite support tube (5). Oil flows up this tube and returns, passing over the ferrite and the inner coil (3). It flows out a series of holes and enters the box. The oil is then forced to flow over the outer coil (2) by a thin circumferential sheet of neutral gray spotlight-filter film (29) which is slit to allow passage to the coil leads. This material was chosen for its transparency and high-temperature characteristics. The oil then enters the outflow pipe (14), which is connected to the oil pump.

At the time that the mechanical design had to be frozen, space was provided by (9) for the introduction of the mercury vapor feed.

Figure H-4 and H-5 are views of the accelerator.

1.1 THE FIELD COILS

The field coils, both inner and outer, are made of number 12 solid Formvar-coated wire. This small a wire size (diameter = 0.187 inch) so simplifies the winding of the coils that it was felt that the ohmic losses could be accepted, especially since the coils are oil-cooled.

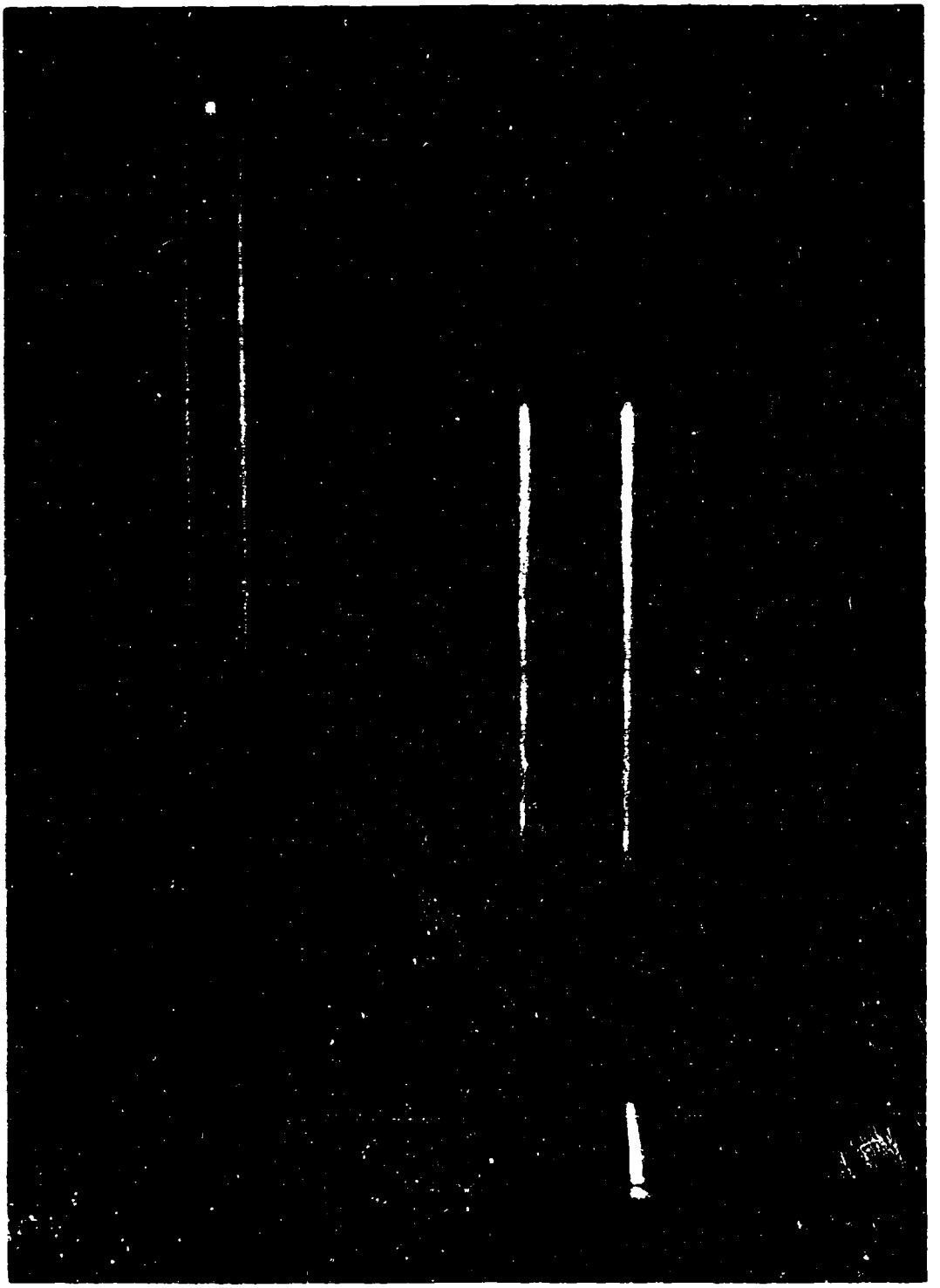


Figure H-3. Vacuum Channel Walls

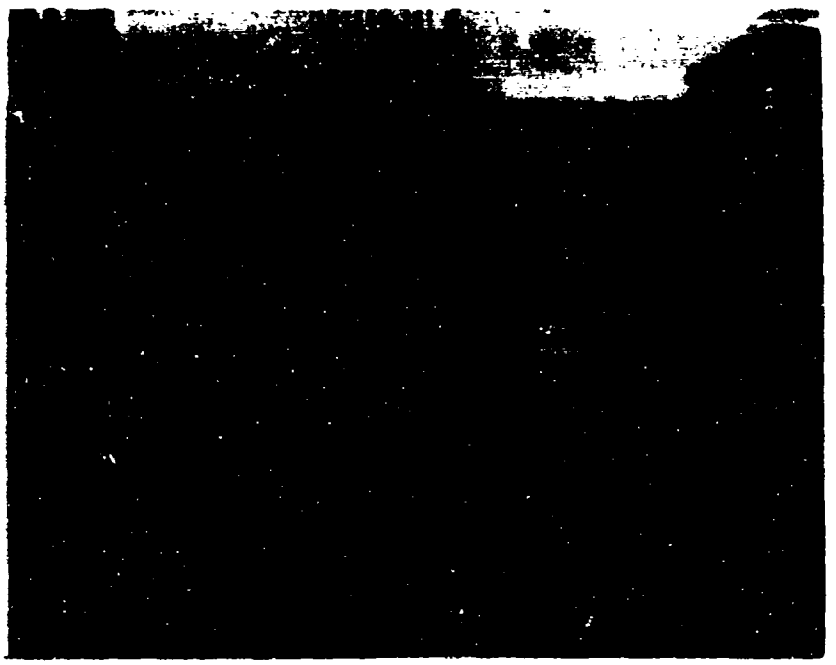


Figure H-4. Accelerator in Assembly Stage

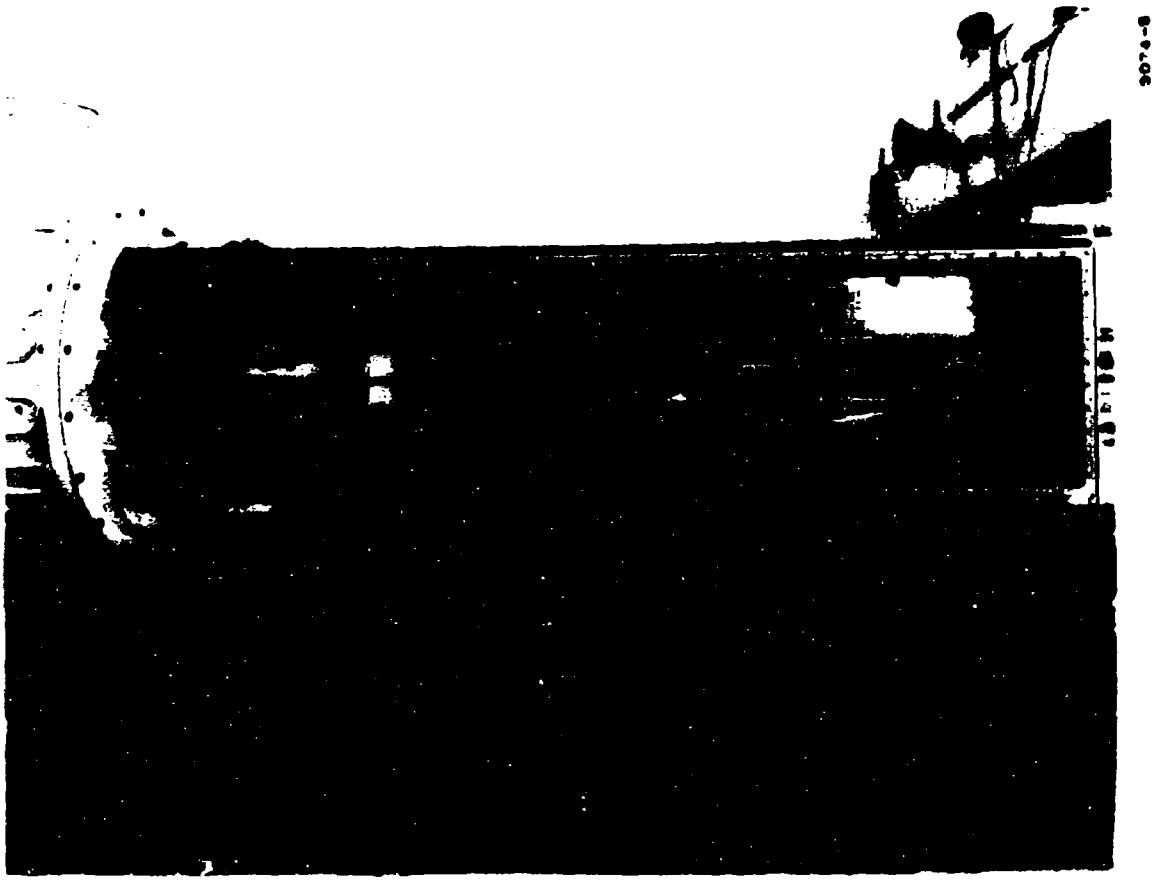


Figure H-5. Assembled Accelerator

Each coil group consists of five turns of wire, spaced one wire diameter apart. A second coil group is wound in the same sense as the first but connected physically so that if the current flow in the first group is clockwise, the current flow in the second is counterclockwise (see Figure H-6).

There are four such composites of coils. There is a fifth, which is comprised of three coil groups. The fifth contains the first coil of the device (the injection end), a middle coil, and the last coil (the exit end). They are connected in order: clockwise — counterclockwise — clockwise. The last clockwise group was added to correct somewhat for end effects.

The five composite groups of coils were wound on a split mandrel (Figure H-7) using five lengths of wire. The mandrel was collapsed and removed, leaving the entire coil system assembled.

The leads to and from the windings are held semirigidly inside the accelerator box by a web of lacing tape to prevent accidental short circuits. At all points where they are unavoidably close to supporting members, they are well insulated.

1.2 FERRITES

The ferrite used in the Mark II was obtained from Stackpole Carbon Co. of Pennsylvania. The particular type is called Ceramag 27. It is in the form of tori of outside diameter 2.760 inches, thickness 0.500 inch and with a central hole diameter of 1.00 inch. The discs have ground faces that allow close stacking without gaps. Twenty-five ferrites are stacked to make the central rod of the accelerator. This particular ferrite has a curie point temperature of 224 C and has a maximum permeability (with respect to free space) of 2390 at 4 kc. It is absolutely necessary, in a device in which the ferrite is going to heat, to have a high curie point or else the permeability is liable to fall drastically.

The manufacturer's data give a Q of this material at 250 kc of about 1300 which means it is not lossy. Above 500 kc the Q falls rapidly, but this is not of special interest for the Mark II.

2. THE VACUUM SYSTEM AND ASSOCIATED COMPONENTS

The main vacuum chamber is a cylindrical tank 30 inches in diameter and 5 feet long. The tank is flanged on both ends — the rear flange

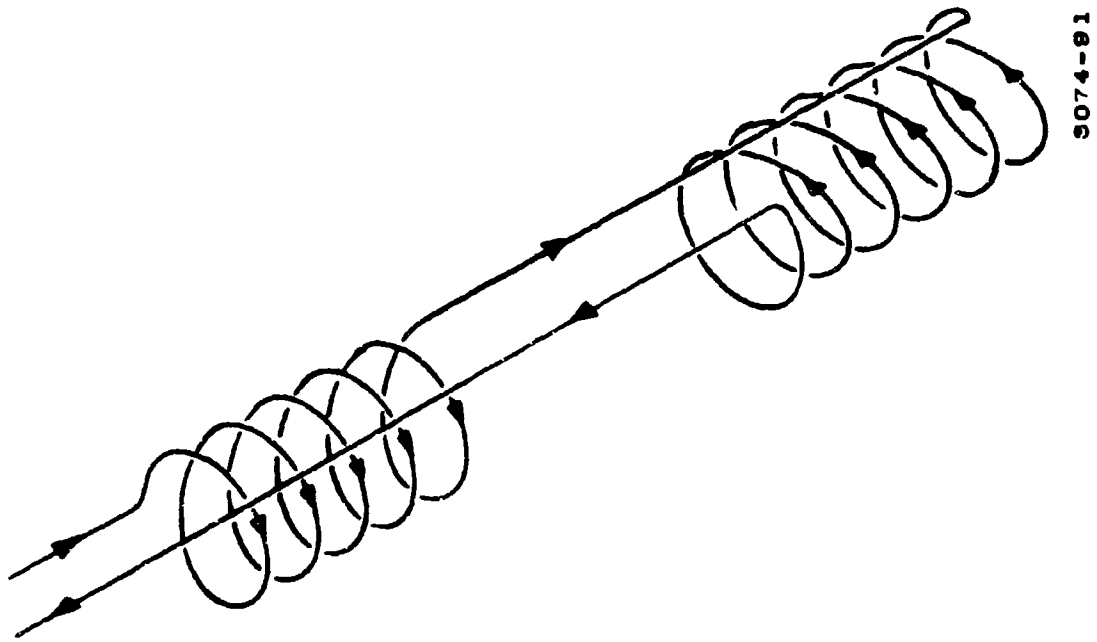


Figure H-6. Field Coil Winding

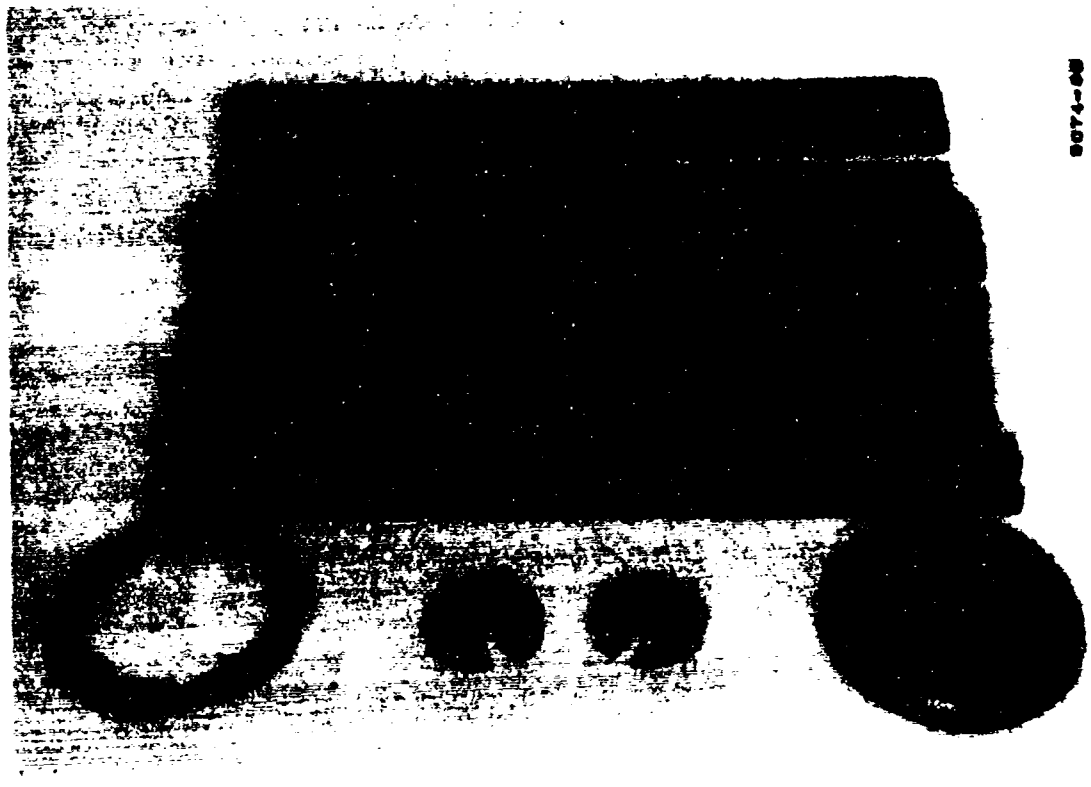


Figure H-7. Coil Winding Mandrels

carrying the pumps and the front flange connecting, via a bellows assembly, to the accelerator. (See Figure H-8).

The tank is supplied with seven observation ports, a tower intended to house diagnostic gear, and an exhaust pipe and blower that are connected to a vacuum gate valve at the top of the tank. The purpose of this is to exhaust air from the tank whenever the tank is open to the laboratory. This will keep a gentle stream of air going from the laboratory to the tank opening, and it is hoped that this will hold down the amount of mercury vapor escaping into the laboratory. Other precautions for personnel protection have been taken.

Because of the necessity of stopping the plasma beam, it is not possible to get a direct axial view of the beam. Instead four 45° viewing ports are provided: two on the tank and two on the front flange of the tank. The inside surface of the front flange has supports for diagnostics, and there is a hanger rail in the tank for the same purpose.

The tank is provided with four parallel cooling coils brazed to the tank wall. Oil is pumped through the coils.

The frame to which the tank is welded rides on wheels and on the same set of rails as the accelerator box.

2.1 PUMPING

The pumping system consists of two CEC PMC-1440 oil diffusion pumps in parallel, connected through six-inch gate valves to a common manifold on the rear flange of the tank. They are backed by two Hereus E-35 single-stage forepumps. The foreline system and foreline valves are copper and brass and, to prevent any attack by residual mercury, the foreline assembly has been heavily nickel-plated. There is a nickel-plated, freon-cooled baffle, Figures H-9 and H-10, of double chevron design just ahead of the diffusion pumps. Its principal purpose is to condense mercury vapor before it gets to the pumping system (it, of course, serves also as a barrier to pump oil). The baffle is optically opaque and was designed so that its conductance matched the combined speed of the pumps. The effective speed of the baffle-pump system is about 1500 liters/sec at 10^{-4} Torr. The base pressure of the system (without mercury), as measured on a Veeco RG-75 gauge, was about 5×10^{-6} Torr, which is several orders of magnitude lower than the base pressure after mercury has been introduced. Since the outgassing effects

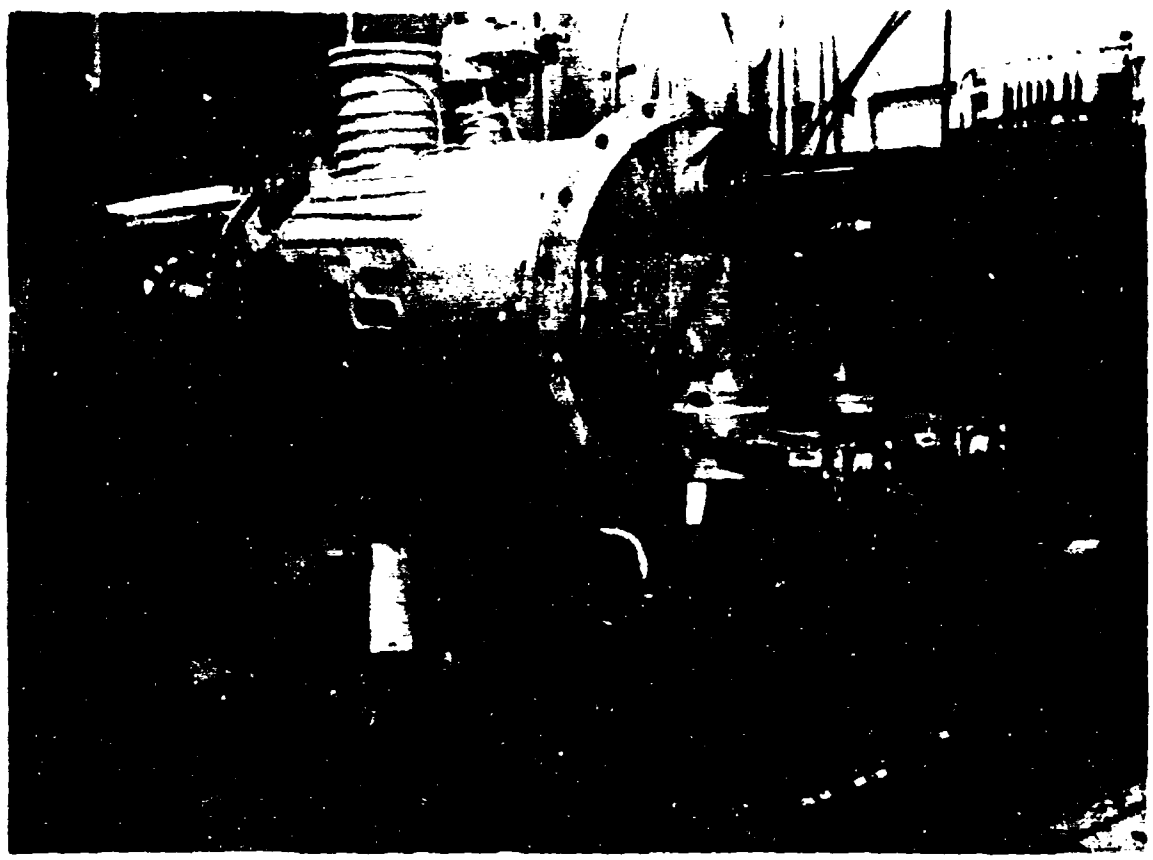


Figure H-8. Vacuum Tank

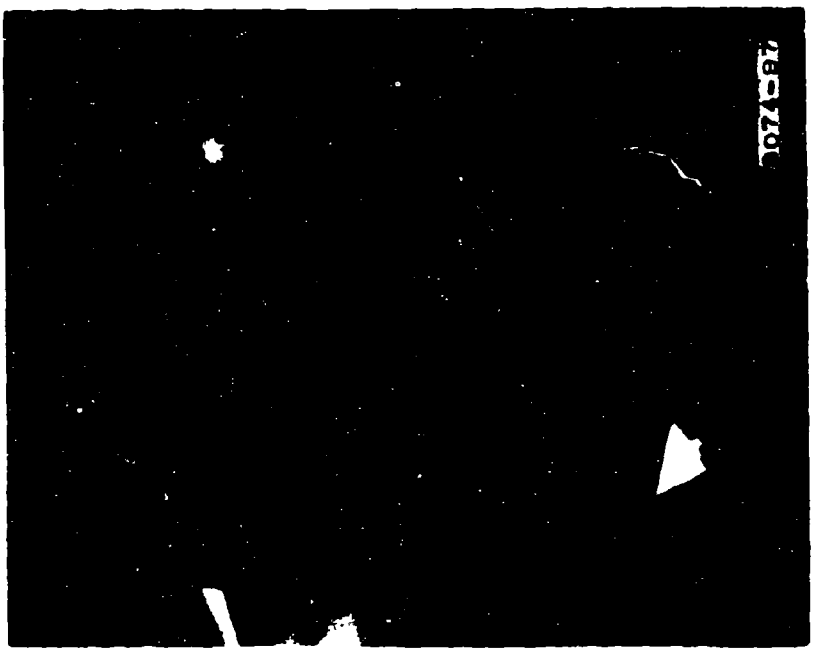


Figure H-9. Plates of the Freon Baffle



Figure H-10. Freon Baffle

caused by the impingement of a high-energy plasma beam are unknown, it is not absolutely clear that the pumping speed is adequate; but it was not felt that a faster (and much more expensive) system was justified.

2.2 CIRCUITRY OF VACUUM SYSTEM (Figure H-11)

The circuit, beside supplying the necessary pump power, incorporates several protective devices. The circuit works as follows.

A normally open, spring-loaded switch momentarily supplies line voltage to relay C′, which closes contact C, completing the main circuit loop and also closing contacts C_1 and C_2, thereby supplying power to the diffusion pumps. Note that this loop is inoperative unless switch (A) has been closed by the foreline power. Switch (W) is normally closed, and the bell is activated. When contacts C_1 and C_2 close, relay (W) opens (W) and the bell alarm ceases. Thereafter the bell will ring whenever C_1 and C_2 open for any reason. In case either diffusion pump heater should open, transformers (X) or (X′) open the relay X, thereby opening C_1 and C_2 and setting off the alarm bell. Both diffusion pumps have Fenwall thermoswitches in their water supply, and in case of overheating either Fenwall will open relay Y. The relay Z is opened by a device that monitors the forepressure of the vacuum system.

2.3 PRESSURE MEASUREMENTS

We employ a Westinghouse Shulz-Phelps ionization gauge to measure the background pressure with mercury in the system. This gauge was chosen after much searching. It appears that little has been done in the way of gauge calibrations for mercury; and, of course, most common gauges can not be used, either because mercury is condensible or because the gauges contain material that will be rapidly and destructively attacked by mercury vapor. This ionization gauge is a fairly recent development and is capable of reading in the range 1 Torr to 10^{-4} Torr, which is considerably higher than the range of a conventional ionization gauge. We have not attempted to calibrate this gauge for mercury vapor. We accept a report that the sensitivity of various configurations of ionization gauges is only weakly geometry-dependent*, and we take the sensitivity of the Shulz-Phelps gauge for mercury to be 3.4* times its sensitivity for nitrogen (which is given by the manufacturer).

---

*S. Dushman Scientific Foundations of Vacuum Technique, John Wiley and Sons, Inc. (1949)

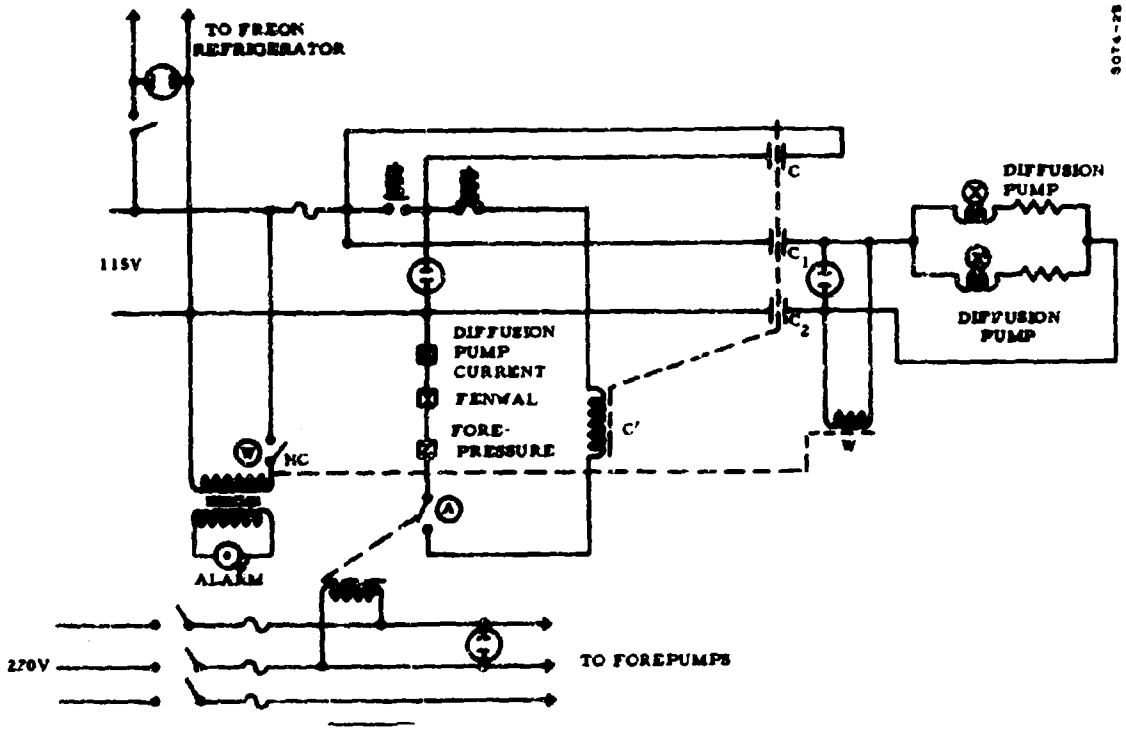


Figure H-11. Schematic of Vacuum System Circuitry

We have compared the Westinghouse calibration for nitrogen against a thermocouple gauge and found good agreement.

2.4 BEAM STOP

This is a special, optically opaque baffle located in the middle of the vacuum tank and is the intercepting surface for the plasma beam. It consists of a set of parallel, flattened, hollow, stainless steel tubes of 0.050-inch wall thickness. · These tubes are welded at their extremities to two rectangular manifolds. Figure H-12 is a schematic of the baffle.

The upper and lower manifolds have, respectively, an outflow and an inflow tube that go out of the vacuum system through Crouse-Hinds fittings in the rear flange of the vacuum tank. Oil is pumped through this baffle to carry off the energy of the beam.

Figure H-13 shows the baffle seen from the pump end of the vacuum tank.

3. THE OIL SYSTEM

Early in the design stage it was decided to use oil, both as a coolant fluid and as insulation against the radio-frequency voltages. We chose Shell Diala-AX which is inexpensive and has desirable electrical properties (it is a standard transformer oil). Several other fluids were considered, including silicone oil and fluorochemicals. The cost of these is prohibitive in the quantities we are using, because the accelerator box holds about three barrels. Also the fluorochemicals have exceptionally low viscosities, which cause difficult sealing problems.

A 50-kw fluid-air heat exchanger was purchased from Electro-Impulse Laboratory of N.J. and was modified to meet our requirements. Essentially it consists of a large radiator with fan, motor, and gear pump, and a thermopile for power measurement. The radiator was mounted near the roof of the laboratory, and entrance and exit ducting was installed to allow the outside air to carry off the heat. This caused the system to be somewhat dependent on outside temperatures. Provision can be made to add water vapor for additional cooling, but tests indicate that this probably will not be necessary.

3074-92

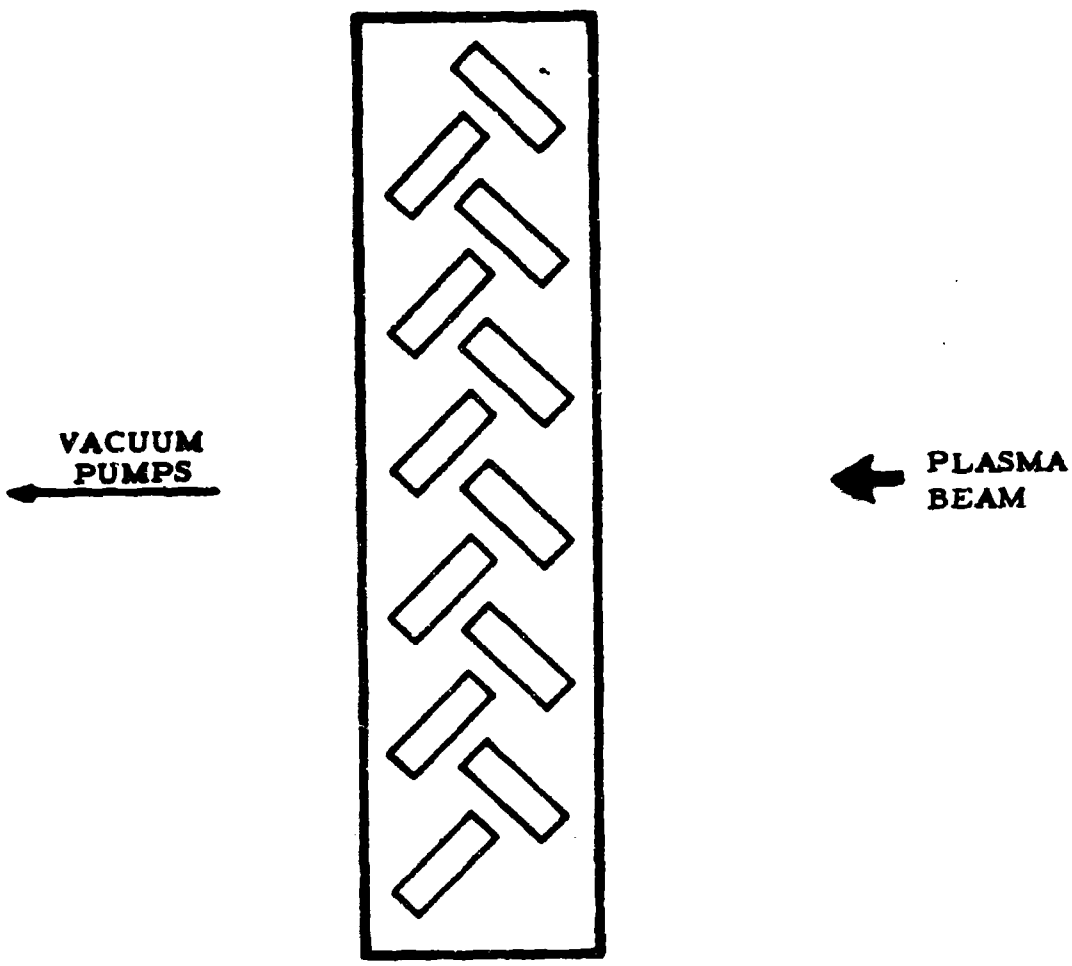


Figure H-12. Schematic of Beam Stop



Figure H-13. View of the Beam Stop

The cooling system is divided into three separate flow subsystems.

1. Accelerator box
2. Beam-stop baffle
3. Vacuum tank walls

Figure H-14 is a schematic of the system.

The tank noted on the right of the diagram is 2-1/2 feet in diameter and 17 feet tall. It provides storage space for all the oil needed in the system. At the bottom is a manifold feeding three separate subsystems. The system contains four Sears-Roebuck 3/4-hp, centrifugal pumps and one high-pressure (100 psi, 8-1/2 gallon per minute) gear pump. The heat exchanger is mounted next to the storage tank. Refer now to Figure H-14.

The subsystems are so designed that the flow can be reversed and all systems evacuated into the storage tank. Valve A is a four-way valve. The pump is mounted across this valve in such a way that switching the valve effectively reverses the pump in the flow line. From valve A the line continues to junction X and splits into two lines. One line is a fluid by-pass controlled by a gate valve allowing fluid to be shunted around the load. The other side of the line continues to the load, and line R is a return to the storage tank. Valve V allows the return to go directly to the tank or into the flowmeter, which also dumps into the tank. The accelerator box needs an extra valve (V′), since the feed point is in the middle of the tank and cannot be used as a drain. Pump-out is accomplished by switching V′ to a line running into the bottom of the accelerator box and reversing valve A. Valve S is closed and a small air bleed (b) ahead of the valve is opened. It has proved convenient to add an additional pump to the outflow line of the accelerator box. Figure H-15 is a photograph of the flow control panel.

The heat-exchanger is run on a separate pump, which circulates hot oil from the storage tank, through the fan-radiator and back to the tank.

A test was made of the entire cooling system by putting 52 kw into a resistive load cooled by the oil circulating through the heat exchanger. In a 50-minute run the temperature rose from 32 C to 66 C and was leveling off when the run was terminated because of oil seal failure in the load. No additional tests were deemed necessary. The oil storage tank discussed above is shown in Figure H-16.

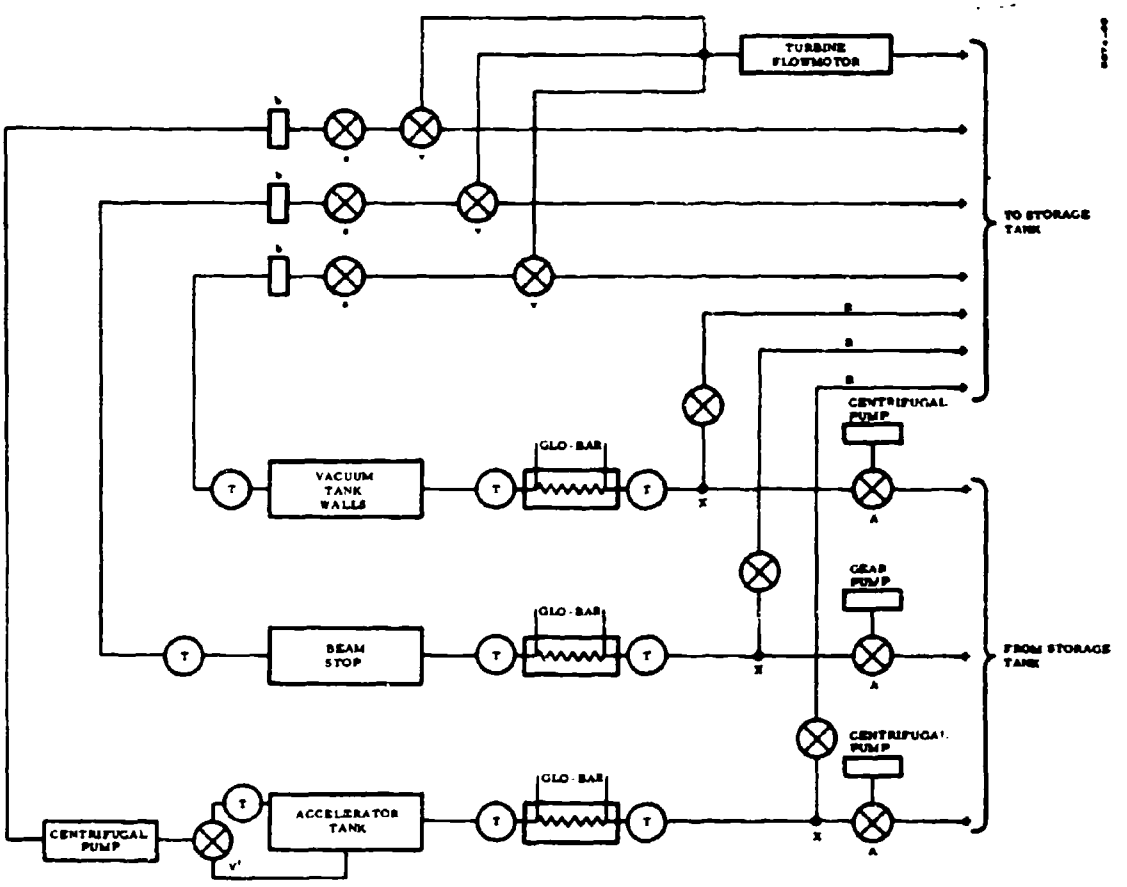


Figure H-14. Schematic of Cooling System



Figure H-15. Oil Flow Control Panel

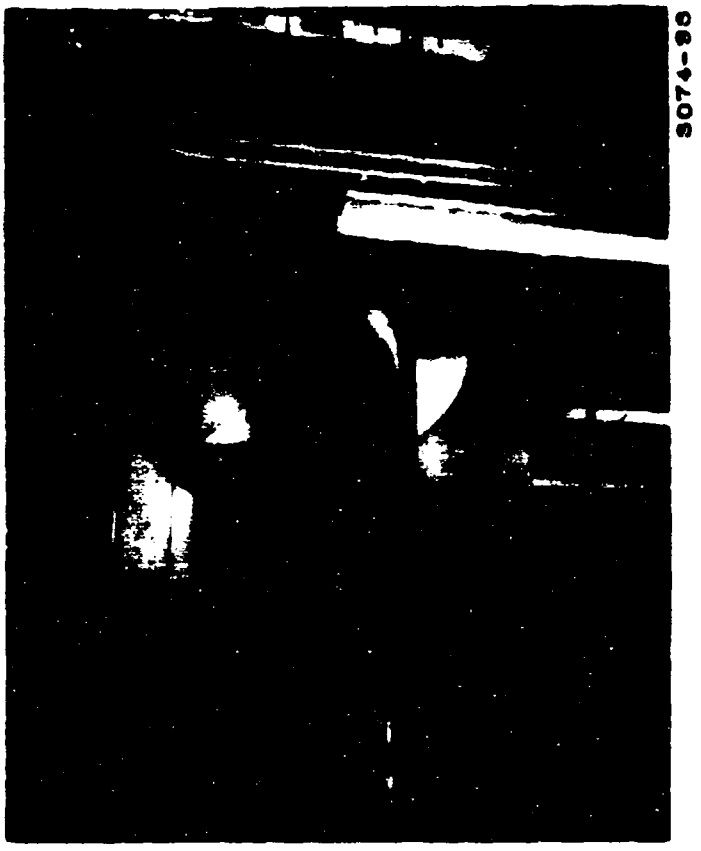


Figure H-16. Oil Storage Tank

3. 1 FLOW MEASUREMENT

3. 1 FLOW MEASUREMENT

The flow is measured with a Fisher-Porter precision turbine flowmeter. This instrument puts out an electrical signal whose frequency is proportional to the flow rate. It has a calibration for viscosity corrections. A special calibration for the kinematic viscosity range of Diala AX was made by Fisher-Porter. The viscosity-temperature characteristics of the oil are known and are used for the correction to the flowmeter measurement. The flowmeter manifold was designed so that the path through the flowmeter had approximately the same impedance as the by-pass around it. Thus the flowmeter should have negligible effect on the flow. The flows from all three subsystems can be sent separately through the flowmeter.

3. 2 POWER MEASUREMENT

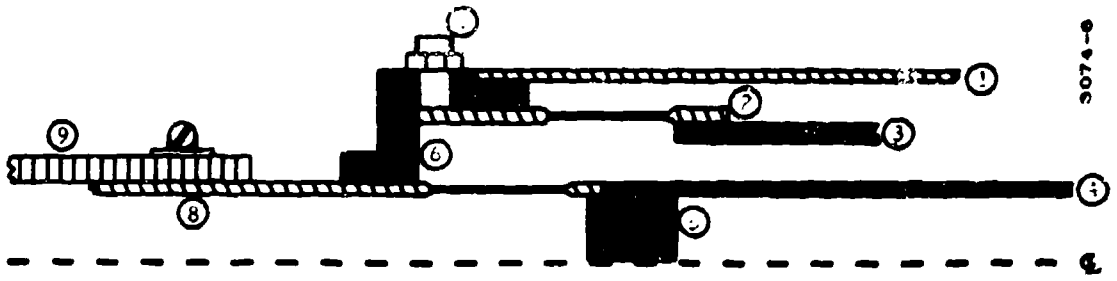
Each flow line contains an 8-ohm Glo-bar hollow carborundum resistor. A cross section of the resistor mount is shown in Figure H-17.

The resistor is fed from a 220-volt, 50-ampere Variac. The power delivered to the resistor is measured on a one-percent, 10-kw wattmeter mounted on the oil flow control panel. In this way an accurately known power can be put into any flow line. Figure H-18 is a photograph of the resistor manifold.

The power measurement is made by reading temperature differences in the flow line at points labeled (T) in Figure H-14. The temperature sensors are zener diodes. The temperature measuring system is described in detail in Appendix M. Combining these temperature differences with the flowmeter reading yields the dissipated power producing the temperature difference. The resistors, to which a known power can be applied, provide a calibration for the power measurement.

4. MERCURY FEED SYSTEM

In order that the mass flow rate of mercury be accurately determined, we have built a feed system that determines the flow rate by means of a variable speed piston driven at an accurately known rate. Figure H-19 is a schematic of the system. A photograph of the system is shown in Figure H-20.



1. OUTER COPPER JACKET
2. GLO-BAR HOLDER
3. GLO-BAR RESISTOR
4. STEEL CORE
5. PHENOLIC CASE HOLDER
6. PHENOLIC END
7. SCREW FOR CURRENT FEED-IN
8. RUBBER HOSE
9. COPPER TUBE

Figure H-17. Cross Section of Resistor Mount

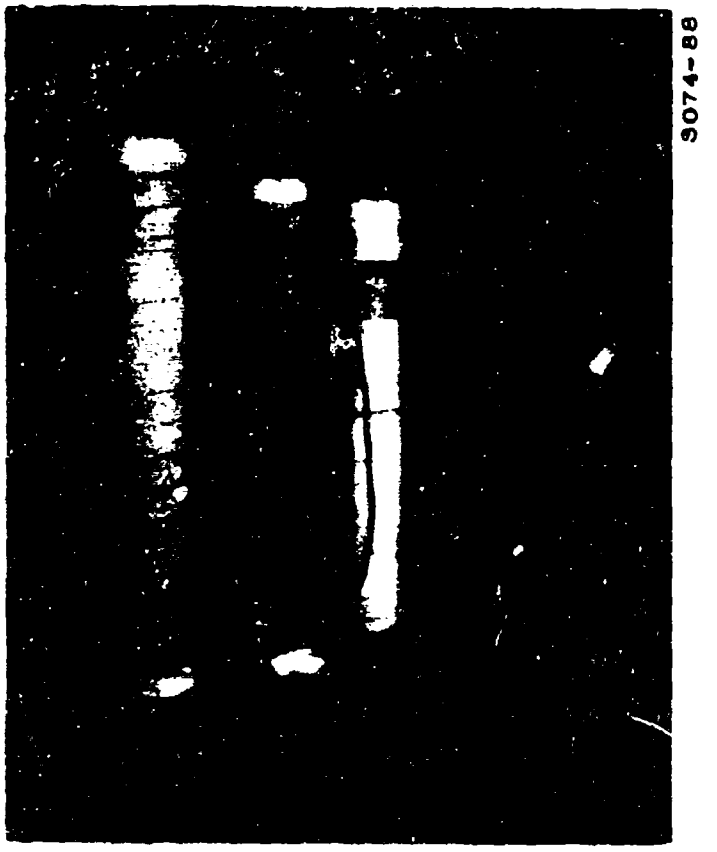


Figure H-18. Resistor Manifold

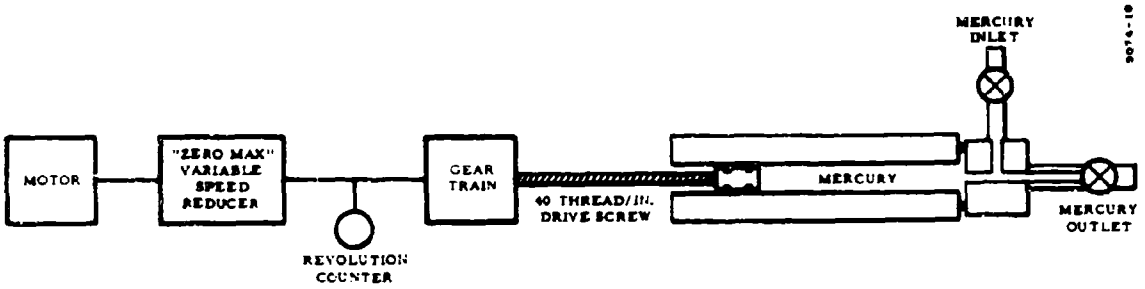


Figure H-19. Schematic of Mercury System

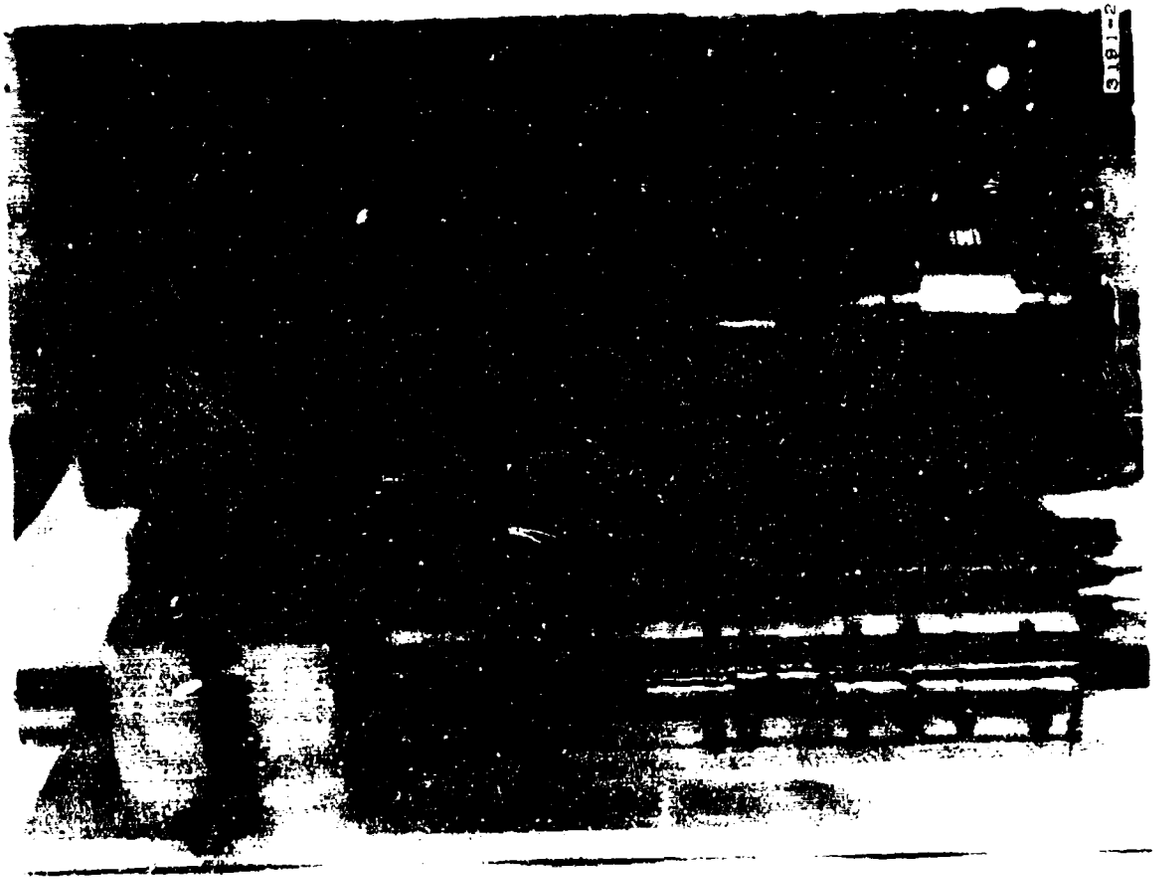


Figure H-20. Mercury Feed System

The variable speed-reducer driven by a synchronous motor allows a shaft speed at the revolution counter ranging continuously from zero to one-quarter of the motor speed. A further fixed reduction follows the counter and precedes the screw and piston. The output flow rate of mercury can be continuously varied from zero to 1.2 grams/min. The piston is stainless steel with a double O-ring seal between it and the plexiglass case. A transparent case was necessary for observation since a leak of mercury past the piston would result in an incorrect and unknown delivery rate.

This system was actually the second system to be designed. The first system incorporated a small gear pump to deliver the mercury. This was designed to operate on a continuous basis; recharging of the reservoir could be done without stopping the pump. However it proved not to be feasible, as the necessary tolerances were impossible to maintain. The present system will run for four hours at the maximum rate before it must be stopped for recharging. This is felt to be quite adequate.

The mercury boiler and vapor delivery system are now under construction. The problem of delivering a known rate of liquid mercury has been solved as mentioned above, but this does not solve the problem of a known rate of vapor delivery.

Two approaches have been investigated.

1. The liquid is delivered to an extremely hot surface which immediately vaporizes the liquid (a flash boiler).
2. The liquid is delivered to an oven heated to such a degree that an equilibrium surface of liquid is established. The surface remains stationary even though liquid is being delivered to the oven, since the mercury is vaporizing at the delivery rate.

In both cases any part of the system between the oven and the delivery point (in the vacuum channel) must be maintained at a high enough temperature so that no condensation can occur. It appears, at this point, that system number 2 is better and has been selected as the operational system.

The total mass of heated mercury must be kept small so that the vapor flow rate can be varied in an acceptably small time.

BLANK PAGE

FOREWORD

The Appendix describes the installation and modification of six Class C power supplies. The total power capability, and the frequency range are in excess of the requirements of AF 49(638)-759 since the installation was designed to be used for the work requirements of several Air Force contracts. The burden of installation and modification was shared by the several contracts.

APPENDIX I

POWER SOURCE MODIFICATION

1. INTRODUCTION

In order to equip the laboratory with the power sources necessary to perform high-power radio frequency experiments, six surplus Navy TBC transmitters were acquired. Each transmitter has a 50-kw capability and was initially designed to operate over the frequency range of 4 to 26 Mc. These transmitters had served the Navy for many years as long-range communication equipment. The major modification for laboratory use was one of extending the low-frequency limit to 500 cycles/sec, without a significant decrease in efficiency or power capability. The transmitters were acquired in the fall of 1961 and were found to be on the average, in fair condition. After acquisition it was found that the six TBC included four different models. Considerable time and effort was spent in reworking or changing damaged components. All in all, it was only in the spring of 1963 that the reworking and modifications were completed and the installation operative. Since then modifications have proved necessary, even though these were in the nature of refinements. From experience we know that further refinements of this equipment may be expected.

2. MODIFICATIONS

2.1 Push-Pull to Single-Ended Operation

The transmitters as received, were found to operate with a push-pull output, and it was decided to convert the 893 output tubes to single-ended operation. One of the reasons for this was that the physical construction of the 893 plate circuit did not lend itself to low-frequency push-pull operation. The accelerator load also dictated a single-ended drive from each transmitter.

To convert a piece of electronics as massive as the output amplifier of a TBC transmitter presented some challenging problems. Figure I-1

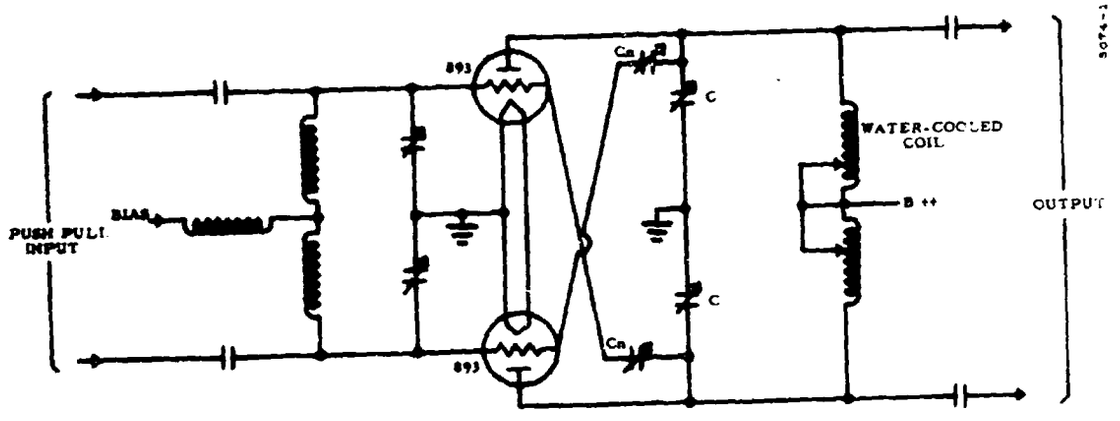


Figure I-1. Simplified Schematic of TBC Power Amplifier (Unmodified)

shows a highly simplified schematic of the TBC final amplifier before modification. Single-ended operation required paralleling the 893 output tubes. Physically connecting the tubes in parallel was simple since the plates and filaments were already connected. The plate circuit has a water-cooled inductance shunting the two plates, but this is effectively a short circuit over the frequency range of interest. Paralleling the grids of the 893 was also not difficult, but as might be expected, a number of spurious oscillations appeared when power was applied.

There are four types of spurious oscillations that can be present in a class C-operated amplifier with parallel output tubes operated in a single-ended mode. The four types encountered in modifying the circuit of Figure I-1 were the following.

1. Very-high-frequency (VHF) oscillations caused by parallel operation of the tubes
2. Oscillations in the neighborhood of 2-3 Mc caused by unterminated transmission lines
3. Oscillations at the driving frequency caused by improper neutralization
4. Low-frequency oscillations caused by elements of the output circuit resonating at frequencies lower than the operating frequency.

A detailed description of the changes made to reduce the spurious oscillations follows.

2.1.1 VHF Oscillations

VHF oscillations usually occur when two tubes are operated in parallel. The lead inductances and stray capacity of the grid and plate connections form the necessary conditions for a push-pull tuned-grid, tuned-plate oscillator. The method chosen to eliminate this oscillation was to add two 50-ohm, 50-watt resistors in series with and in close proximity to the grids of the 893's. A resistor (R_2 of Figure I-2. (20,000 ohms and 100 watts) was also added directly between the two plates of the 893's to further reduce the possibility of VHF oscillation. The three resistors serve the function of introducing losses to the grid and plate resonant circuits formed by stray inductance and capacity. The Q of these tank circuits are thereby reduced to a point where VHF oscillations can no longer be sustained.

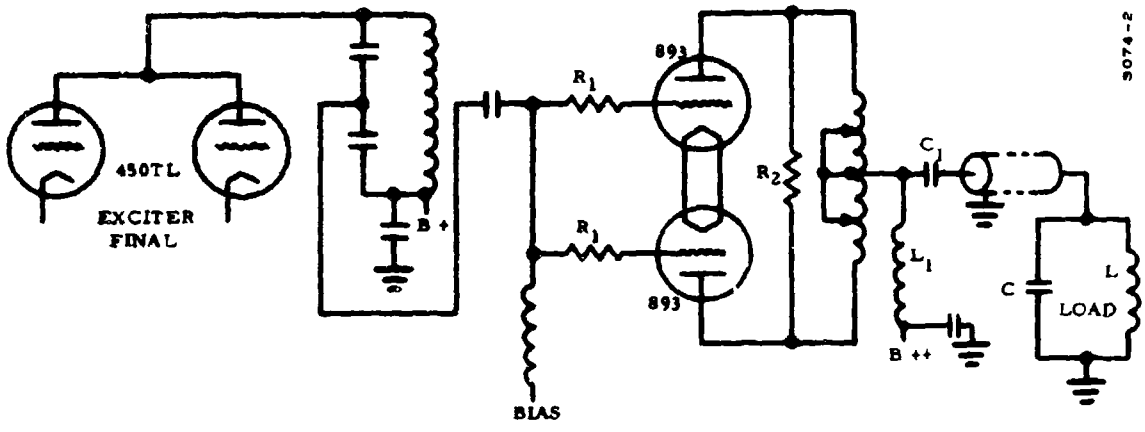


Figure I-2. Modified Output Circuit with Parasitic Resistors

2. 1. 2 Oscillations Caused by Transmission Lines

As Shown in Figure I-2, the load tank circuit is connected to the transmitters by means of an unmatched transmission line. For a typical application the transmission line length was about 100 feet. As the line was not terminated in its characteristic impedance, it appeared to the transmitter as a high-Q resonant circuit with a resonant frequency of 2-3 Mc. The circuit shown in Figure I-2 exhibited oscillations at this frequency.

One solution to this problem would be to terminate the lines properly. This solution was rejected since it would entail broadband matching transformers at both ends of the transmission line. The solution adopted is shown in Figure I-3. A series resonant trap, tuned to the resonant frequency of the transmission line was placed at the grids of the power amplifier tubes. The series resonant trap was made by rearranging the components of the existing grid tank circuit. In practice the trap is tuned until the oscillations vanish.

2. 1. 3 Neutralization

A tuned-grid, tuned-plate triode amplifier will usually oscillate because of feedback via the plate-to-grid capacity unless provision is made to neutralize the circuit. Before modification the neutralization was accomplished by cross-coupled plate-to-grid feedback capacitors, C_N as shown in Figure I-1. This simple and effective method of neutralization is possible only with a push-pull amplifier; and because we had elected to change the operating mode to single-ended, another method of neutralizing was required. The method chosen was a modification of the Rice method. Normally in Rice neutralization, the feedback signal is coupled to the grid circuit by means of a tertiary winding on the grid tank circuit. In the absence of a grid tank (see Figure I-2) an auxiliary winding, W, was added to the exciter final tank circuit and capacitors, C_N, were added to the 893 plate circuit as shown in Figure I-3. By a proper choice of the connections to the added winding, the signal fed through the 893 plate-to-grid capacity is canceled by the signal fed back through C_N and the auxiliary winding.

2. 1. 4 Low-Frequency Oscillations

Referring again to Figure I-3, it will be observed that the load tank circuit is shunt-fed by means of the choke, L_1, and coupling capacitor,

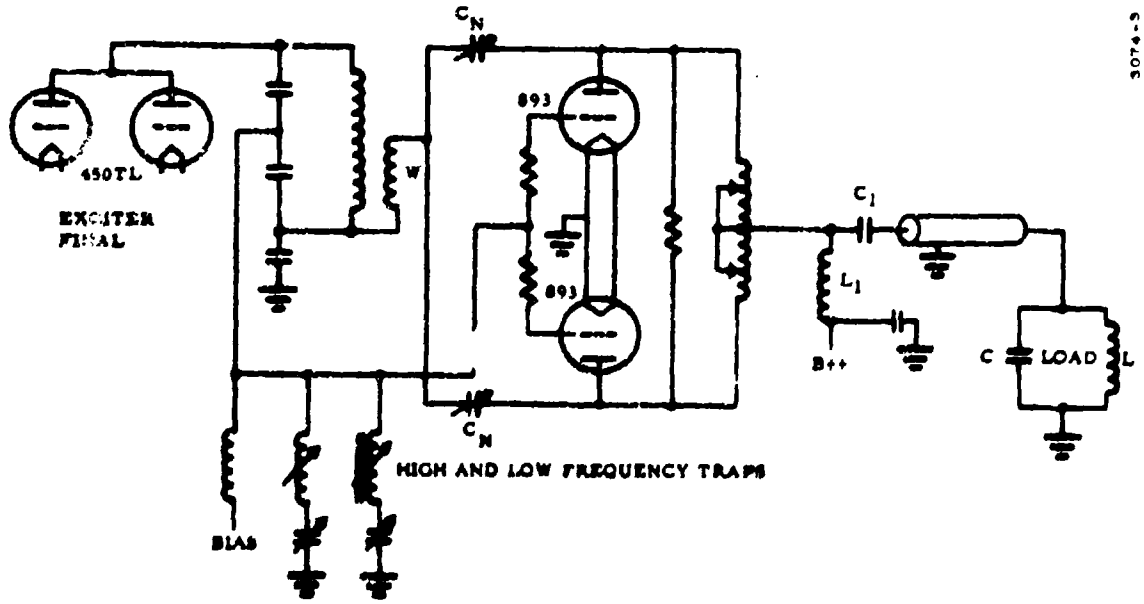


Figure I-3. Neutralization and Grid Traps

C_1. The requirements on L_1 and C_1 are that they should be at least an order of magnitude larger than L and C in order to have a negligible effect on the performance of the load tank circuit. The circuit of Figure I-3 performed well when driving a load tank circuit as shown. However, there was occasion to modify a load tank circuit to be driven push-pull by two transmitters, and during this operation low-frequency oscillations were observed.

Capacitor C of Figure I-4 is free to resonate with the shunt-feed chokes, L_1 at a much lower frequency then the natural resonant frequency of the load tank circuit. As neutralization is only effective at or near the operating frequency of the amplifier it was of no help in eliminating this type of oscillation. An additional tunable series resonant trap at the grids of the power amplifier was required. With a 55-kc push-pull tank circuit, the low-frequency oscillations occurred at about 8 kc. The tuneable element was chosen to be a variable inductance. The necessary variation of inductance was accomplished by varying the air gap spacing of the laminated iron core. Figure I-3 illustrates the placement of this low-frequency trap.

2.2 Modification of Exciter Final

The 450TL exciter final tubes were also modified from a push-pull to semiparallel operation. This modification, however, did not present the problems of oscillation experienced with the final output tubes. Parasitic (VHF) oscillations occur only when both tubes are allowed to conduct simultaneously as do the 893's. This condition is prevented for the 450TL by the form of the input drive (See Section 3, Modulation). Neutralization of this stage was unnecessary as the plate tank circuit is tuned to a much lower frequency than the grid tank circuit.

3. MODULATION

3.1 Principle of Operation

Figure I-5 shows a block diagram of a TBC-3 transmitter. The amplifier tubes operate in standard class-C mode on a continuous-wave basis. Seven tuned circuits exist between the master oscillator and the last stage of the power amplifier. In order to provide low-frequency operation, the conventional transformation would have required modification and tuning of all seven resonant circuits — a total of 42 circuits to be tuned if the operating frequency required by an experiment was to

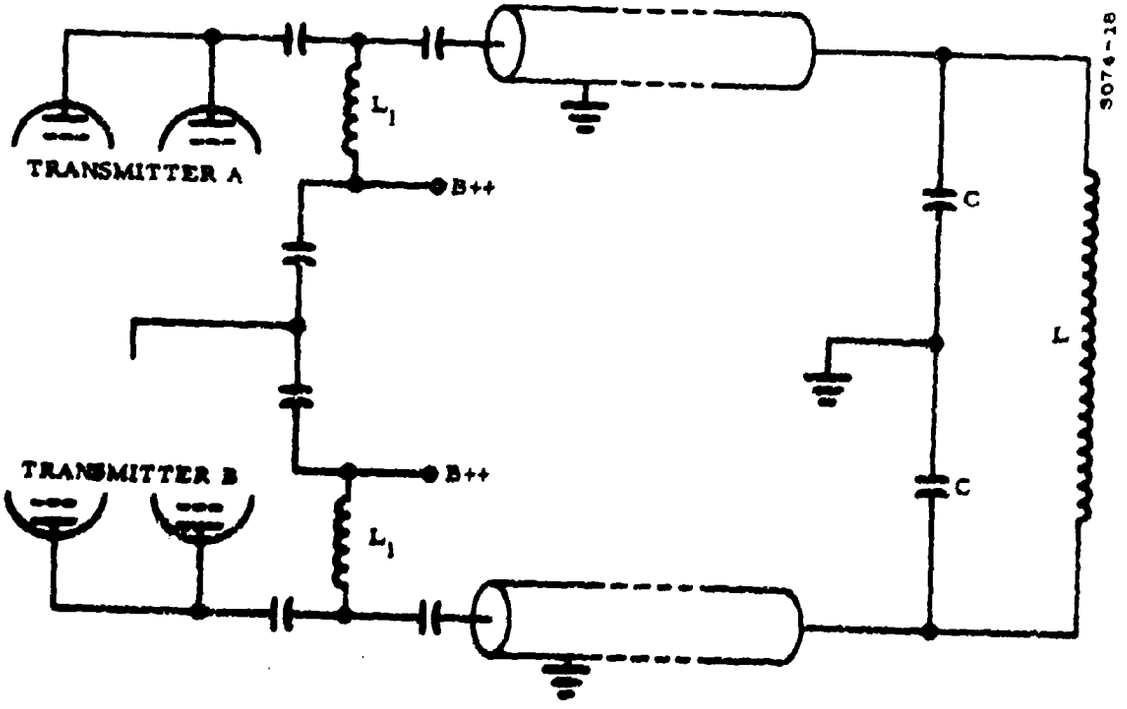


Figure 1-4. Push-Pull Load Using Two Transmitters

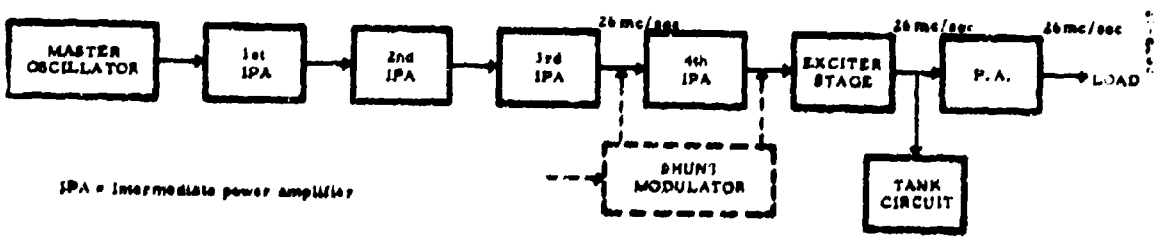


Figure I-5. Block Diagram of Unmodified TBC-3 Transmitter (Modification Shown Dotted)

be changed. To avoid this, another method, which involved modulation of a late driver stage, was selected and its general principles will be described.

Normally a class-C amplifier stage has a resonant circuit in its plate, and the frequency of the signal used to drive its grid is equal to the plate circuit resonant frequency. The conduction angle (that portion of the grid signal that drives the grid positive) is usually between 80 and 150 electrical degrees for best performance of the stage. Instead of using a pure sine wave signal to drive the grid of the class-C stage, it was reasoned that it would be driven equally well by a high-frequency carrier modulated at a frequency equal to the plate circuit resonant frequency.

Figure I-6a shows the condition of a standard class-C grid drive with positive grid regions and definition of the conduction angle indicated. Figure I-6b shows the condition of the modulated carrier grid drive introduced at the fourth intermediate power amplifier (IPA) stage. It should be observed that the modulation ratio has to be greater than 100 percent so that the conduction angle will be between 80 and 150 electrical degrees. As can be seen from Figure I-6b, the power output capability of a class-C stage is decreased by more than 50 percent when a modulated carrier grid drive is used, all other conditions being the same. However, this did not prove to be a major disadvantage, since the power capability of each stage of the TBC-3 (except for the power amplifier) was quite sufficient to compensate for this power loss.

3.2 Elimination of High Frequency Carrier

The required modifications to the transmitters included the installation of a shunt modulator and the tuning of a tank circuit between the exciter stage and the final stage of power amplification as indicated by the block diagram of Figure I-5. The tank circuit preceding the final stage of amplification is tuned to the modulating frequency and provides the driving signal to the power amplifier. It also serves the function of a filter to completely eliminate the high-frequency carrier. This can be seen from the following argument. The input to the 450TL is the modulated signal. This tube operates as class-C so it is cut off for most of the input signal. The output of the 450TL has the power amplifier's grid tank on its plate. Then the 893 grid sees the high-frequency carrier only on the negative side of its swing. The positive side is supplied by the tank circuit, since during this part of the cycle the 450TL is cut off. The 893 is also operated class-C so that it is cut off during the negative swing of its grid, which is the only region of the cycle

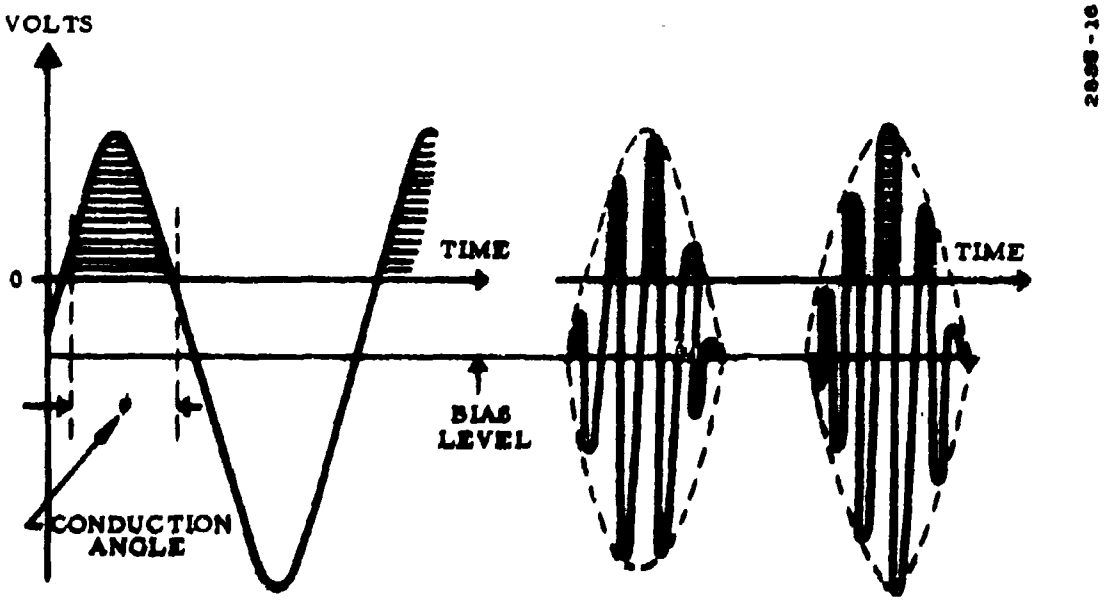


Figure I-6. Voltage of Class-C Grid Drives as a Function of Time

containing the high-frequency carrier. Thus the carrier has been completely eliminated in the final output.

3.3 Choice of Carrier Frequency

In order to achieve the highest modulation frequency possible, the carrier frequency was set at the maximum allowed by the transmitters, i.e., 26 Mc. There are two reasons for this choice.

1. Referring to Figure I-6b, the conduction angle is determined to some extent by the relationship between the phases of the carrier and modulation frequencies. As the two frequencies are not locked in any way, variations in phase can produce small variations in frequency and amplitude of the stage output. This effect becomes negligible the higher the carrier frequency with respect to the modulation frequency.
2. This reason is somewhat subtle and is concerned with the method of modulating. In order to minimize modulating power, the method chosen consisted in detuning the exciter input tank circuit (fourth IPA output) by means of a small capacitor through an electronic shunt. The recovery time (i.e., the time necessary for the signal amplitude across the tank circuit to recover its original value after the shunt has been removed) limits the maximum modulation frequency. For a constant-Q tank circuit, the number of cycles required to recover is independent of its frequency. The higher the carrier frequency, the faster is the recovery (for constant Q), allowing a higher modulating frequency. With a 26-Mc carrier, a modulating frequency as high as 500 kc can be used.

3.4 The Shunt Modulator

As indicated in the block diagram of Figure I-5, the modulator is actually connected to both the input and output of the fourth IPA stage. The 26-Mc signal appearing at these two points serves as a plate signal for the shunt clamping tubes of the modulator. These tubes act as an intermittent shunt to ground controlled by the modulating signal. During a portion of each cycle of the modulating signal, the 26-Mc is shunted to ground. The reason for simultaneously shunting the input and output tank circuits of the fourth IPA is to reduce tube dissipation and, more important, to reduce the power requirements of the shunt modulator itself. If the input shunt is not used, the 26-Mc signal to its input is always present. Shunting only the output would require that the modulator

tubes absorb excessive power during their shunt time. Excessive plate dissipation in the fourth IPA would also result, because the tube would be conducting during the time that its plate was shunted to ground. It was established that it was not sufficient to clamp only the fourth IPA input. Without a controlled shunt on the plate, the plate tank circuit oscillations would continue for an unacceptable time, negating the shunt modulator action on the input.

The shunt modulator proper consists of parallel connected pairs of 807 pentode tubes driven by a Schmidt trigger. The input signal to the Schmidt is a 20-volt sine wave. A simplified schematic of the modulator is shown in Figure I-7.

The 26-Mc carrier is coupled by means of small capacitors, C, to the plates of pairs of 807's and serves as the plate voltage for these tubes. Plate inductance, L, and stray capacity are made to resonate in parallel at 26 Mc in order not to load the exciter stage. With the control grids of the 807's cut off (-40 volts) the transmitter is unaffected by the modulator. With the control grids at zero volts, the 807's draw plate current during each half cycle of the 26-Mc plate voltage and, consequently, both load and detune the input and output tank circuits of the fourth IPA. As an example Figure I-8 shows two oscillograms of a 26-Mc carrier signal modulated by this method at 200 kc and 55 kc. These are the signals that appear at the plate of the fourth IPA. The middle trace in both cases is the signal appearing at the grid of the power amplifier, and the lower trace is the load signal. Except for 807 screen power and a few watts for the Schmidt trigger, the modulator requires no dc input power but simply absorbs power from the transmitter. The conduction angle mentioned previously is set by changing the level of the Schmidt trigger. This is done by adjusting the potentiometer in the grid circuit of the 5687 tube.

Referring to Figure I-8 note the trace of the 26-Mc carrier in the negative half-cycle of the power amplifier grid signal.

4. TUNING

One goal of the modifications performed on the transmitters was to allow for relatively rapid changes of operating frequency. The modifications have been made so that only two tank circuits per transmitter are required when changing frequency. All other tank circuits are fixed-tuned at 26 Mc. At the input to the exciter final the 26-Mc signal is

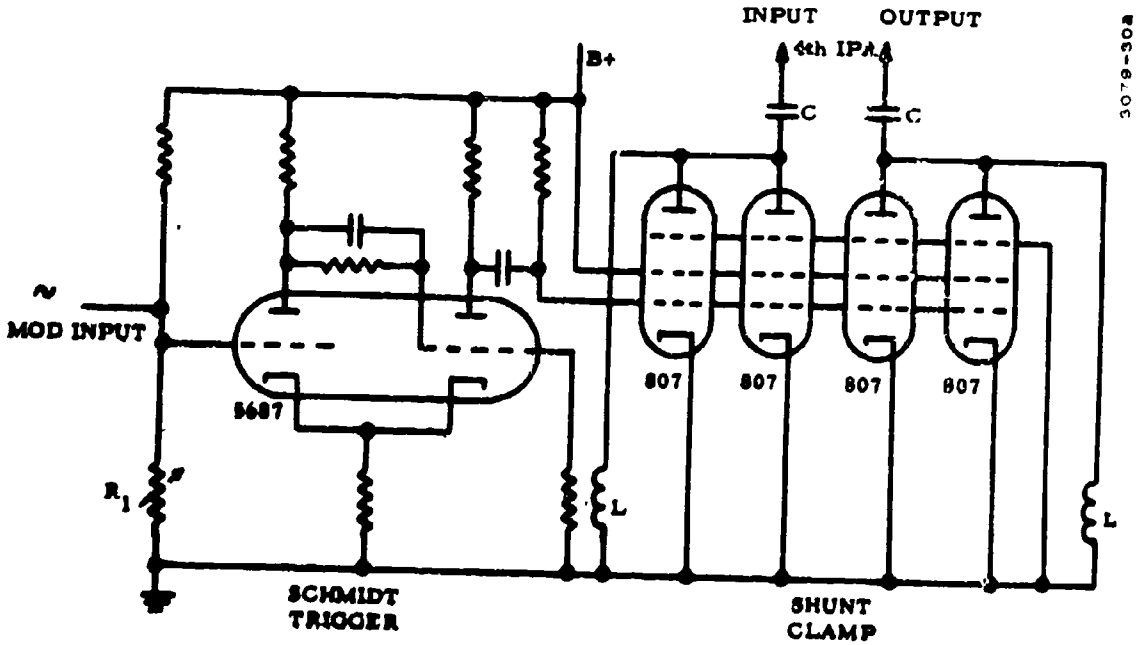
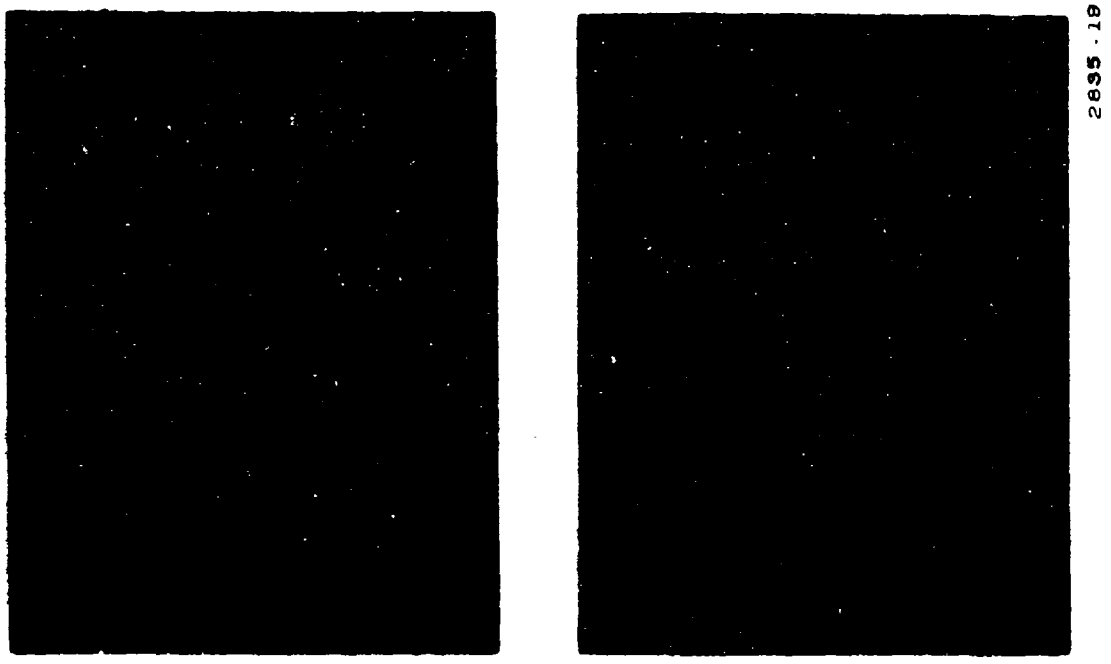


Figure I-7. Shunt Modulator



2835-19

MODULATION FREQUENCY

200 Kc/sec

MODULATION FREQUENCY

55 Kc/sec

UPPER TRACE: SIGNAL AT THE PLATE OF 4th IPA

MIDDLE TRACE: SIGNAL AT GRID OF POWER AMPLIFIER

LOWER TRACE: LOAD SIGNAL

Figure I-8. Signal Patterns at Various Stages in Modified TBC Transmitter

modulated at the desired operating frequency, and a tank circuit tuned to this frequency is driven by the exciter final. Two methods can be used to tune the exciter final tank: the capacity or the inductance can be varied. In order to cover the frequency range 50kc - to 300 kc, a coarse frequency setting is made by the proper series - parallel connection of eight 0.045-μ farad transmitting capacitors. Fine tuning is accomplished by sliding a tap on the copper tubing comprising the tank inductance. This inductance consists of 30 turns of 1/2-inch-diameter tubing wound into a cylinder 1 foot in diameter and 2-1/2-feet long. The tank is tuned initially to the desired operating frequency using an oscilloscope and signal generator, the exact frequency being indicated by a decade frequency counter driven by the generator.

5. CONCLUSION

Successful operation has been achieved at frequencies between 500 cycles/sec and 500 kc using the technique of broadband modulation. The transmitters have supplied (in a polyphase system) up to 20,000 volts per phase with circulating currents in the load tank circuits of more than 200 peak-to-peak amperes per phase at a frequency of 55 kc.

Figure I-9 (a through c) shows the transmitters during installation in the laboratory. Figure I-9d shows some of the heat exchangers of the transmitters. Figure I-10 shows three of the six transmitters after the completion of the installation.

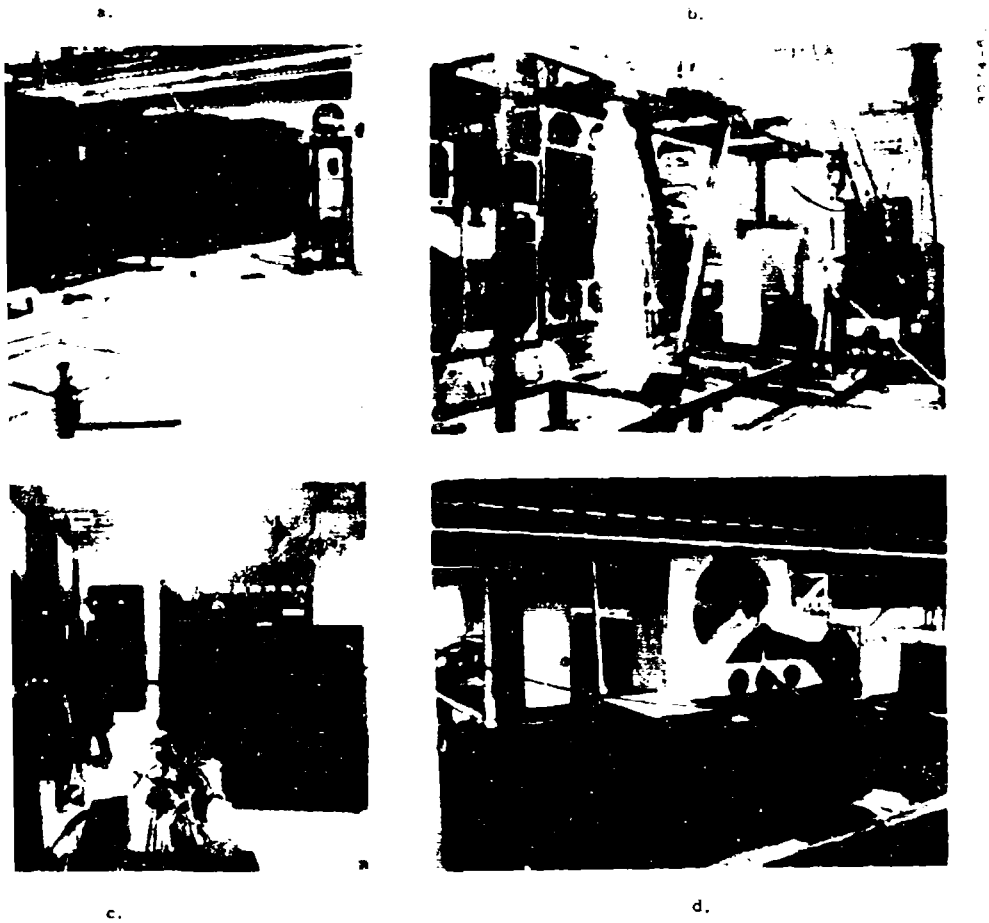


Figure I-9. Transmitters During Installation



Figure I-10. Transmitters Installed

APPENDIX J
CONTROL AND MONITORING METHODS

APPENDIX J

CONTROL AND MONITORING METHODS

This appendix deals with the details of various control and monitoring circuitry developed for the Mark II accelerator. The items discussed are:

1. The Master Frequency Source
2. The Phase Control Circuits
3. The Polyphase Generator
4. The Phase Display Circuits

1. MASTER FREQUENCY SOURCE

Successful operation of the TBC transmitters as power sources for a polyphase-driven device requires a very stable frequency source. The phase relation of the currents in the accelerator needs to be accurately established in order that the traveling wave proceed as smoothly as possible. High-Q resonant circuits are used not only in the accelerator proper but in the power sources themselves. A high-Q circuit, at resonance, will transform small frequency shifts into large phase shifts. Given a small frequency shift there is no guaranty that all the phase shifts of all phases in the system will be equal; therefore, stability of the master frequency source is necessary.

Not only must the frequency source be stable (one part in 10^4 or better), but the frequency should be variable in increments of 1000 cycles/sec for experimental purposes.

The use of a multiplicity of crystal oscillators with mixing was considered as a solution as well as the use of a harmonic generator using a single low-frequency crystal or tuning fork. Either solution would be

realizable but complex. The system that was finally adopted is believed to have novel features, even though the concept is well-known.

A decade-frequency counter was employed to servo a standard signal generator. The frequency range achieved was 1 kc to 600 kc. The stability of the servoed frequency is as good as the stability of the crystal reference oscillator in the decade counter (one part in 10^6). A block diagram of this system is shown in Figure J-1.

As in any standard decade counter, a crystal oscillator is employed as the basic time reference. Usually a 1-Mc crystal is counted down in decade steps to either 1 cycle/sec or 1/10 cycle/sec. A 1-kc pulse train is obtainable either directly as an output or from within the counter. The pulses are fed through a buffer invertor to a blocking oscillator. The function of the blocking oscillator is to shape the output pulses of the frequency counter in order that the diode gate controlled by the blocking oscillator is open for only 0.2 microsecond. A narrow pulse is required in order that only a fraction of a cycle of the signal generator output be allowed through the gate. The opening of the diode gate allows the RC integrator (time constant of about 1 millisecond) to sample, at a 1-kc rate, the instantaneous value of the output signal of the signal generator. A dc signal is thus generated whose amplitude is a function of the time relation of the blocking oscillator pulse to the signal generator sine wave. If the signal generator frequency is exactly an integral multiple of the frequency counter output, then the integrator output will be of constant amplitude. The servo loop is completed by feeding the integrator output to a varicap (variable capacitance; semiconductor) which shunts a capacitor in the tuning circuit of the signal generator. As the frequency of the signal generator tries to drift, the phase of its output signal varies with respect to the frequency counter pulses. This phase change is converted to an amplitude change by the RC integrator. This change in amplitude changes the capacity of the varicap. Since the varicap is part of the frequency-determining circuitry of the signal generator, the attempt to change frequency is compensated, and the generator remains locked at an integral multiple of the frequency counter output.

As long as the sampling pulse from the blocking oscillator is considerably narrower than half a cycle of the servoed frequency, an error signal will be generated as the signal generator tries to drift. A 0.2-microsecond pulse allows a servoed frequency range of 1 kc to over 600 kc in 1-kc steps.

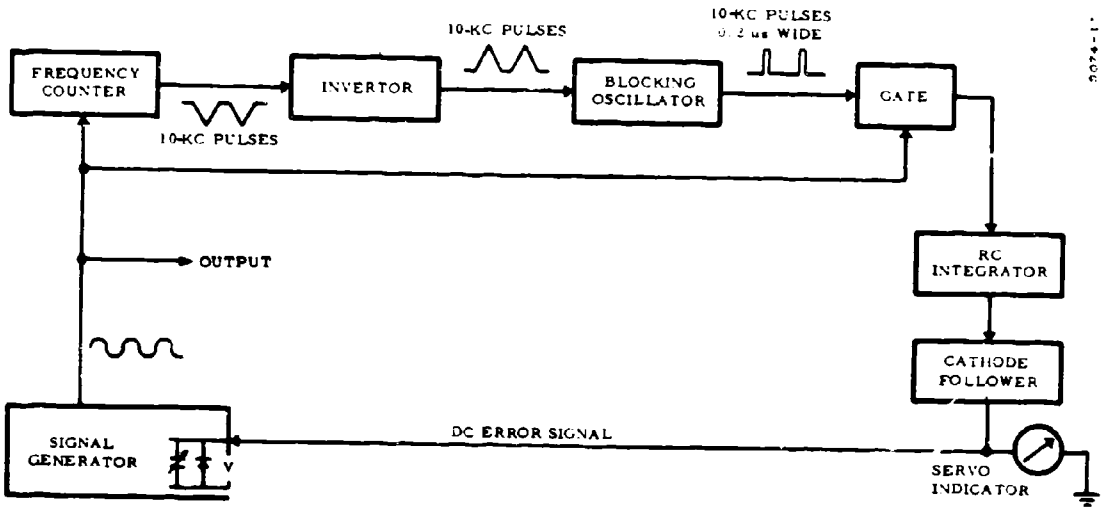


Figure J-1. Block Diagram of the Stable Frequency Source

Thus, with two tubes and a few diodes, it was found possible to convert two standard pieces of laboratory equipment to a system capable of generating over 600 different frequencies, each as stable as the master oven-controlled crystal. The generated frequency is also displayed by the frequency counter, avoiding any possibility of ambiguity of output frequency.

2. PHASE CONTROL

Because of the expected changes in the resonant frequency of the circuits of the accelerator when ionized gas is in the device, it was felt necessary to have a system that would lock the phases of the coil currents in their correct relationship. In broad outline this phase-servo system senses the coil currents and compares their phases with a set of standard signals. If the correct relation does not hold, an error signal is generated, and the appropriate phase is shifted until the correct relationship obtains. A 40-degree shift in phase can be reduced to about a one-degree shift using this servo. A block diagram of the system is shown in Figure J-2.

2.1 The Feedback Element

This detects the phase of the coil currents in the accelerator. It is most desirable that this element be a small noninductive resistor in series with the coil. The voltage across this resistor would be exactly in phase with the coil current. Several 0.1-ohm resistors were built, but the inductance could not be reduced to a suitably low value; so instead, three-turn pickup coils centered inside the pad inductors are used. The feedback signal is now 90° out of phase with the coil currents, but the phase servo was modified to use this signal.

2.2 The Shaping Circuit

The function of this circuit is to provide a signal to the phase servo that is independent of the feedback signal amplitude. This is done by amplifying and diode-clipping the sine-wave output of the pickup coil.

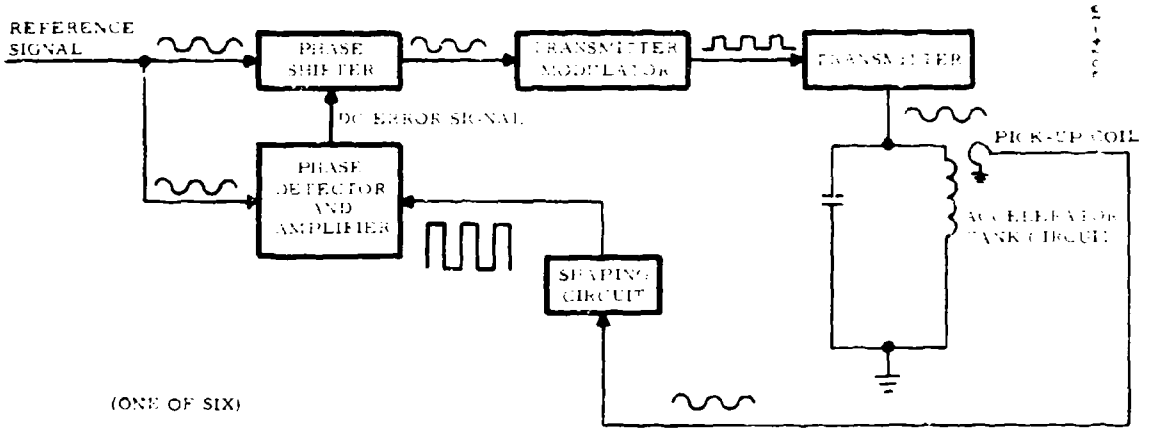


Figure J-2. Phase Control System

2.3 The Phase Detector

The phase detector compares the phase of the clipped feedback signal with a reference signal and generates a dc error voltage if the phases vary from a (preset) standard difference. The phase-detector used is shown in Figure J-3.

The operation of the detector can be seen by reference to Figures J-3 and J-4.

Curve one of Figure J-4 shows the a signal exactly 90° out of phase with the square wave. During the time the square wave is negative both capacitors, C_1 and C_2, come to the same negative voltage. When the two signals are slightly phase shifted, as in curve two, capacitor C_1 charges to a slightly less negative voltage then in the first case while C_2 charges to the same voltage. Therefore a voltage difference appears at the input to the dc amplifier. This difference is the error signal.

2.4 The DC Amplifier

The loop gain of the servo is furnished by a single-stage differential amplifier (Figure J-5).

Cathode followers are used for isolation, and the differential gain of the amplifier is 80.

2.5 The Phase Shifter

The function of the phase shifter is to shift the phase of the signal to the transmitter modulator by an amount determined by the phase error. The phase shifting element in this circuit is a varicap (as in the frequency servo). The varicap is a useful device for converting a voltage variation into a reactance variation. The capacity is inversely proportional to the 3/2 power of the applied voltage, making the conversion nonlinear. To make full use of the varicap, the mean operating point was selected to allow equal variation of capacity on either side of the operating point (see Figure J-6).

The phase-shifting circuit used is shown in Figure J-7.

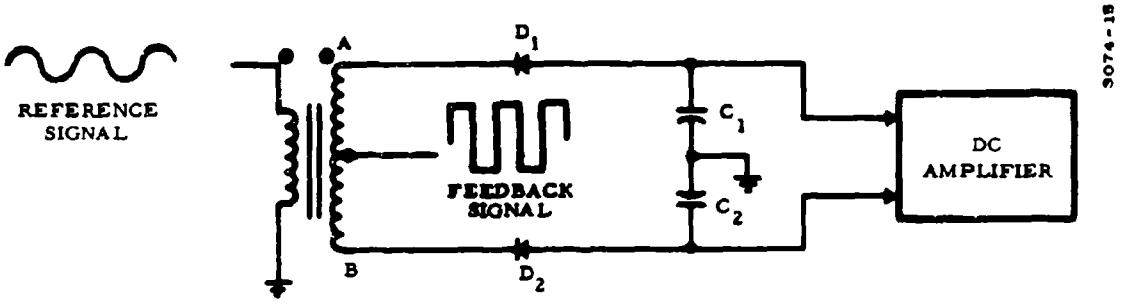


Figure J-3. Phase Detector

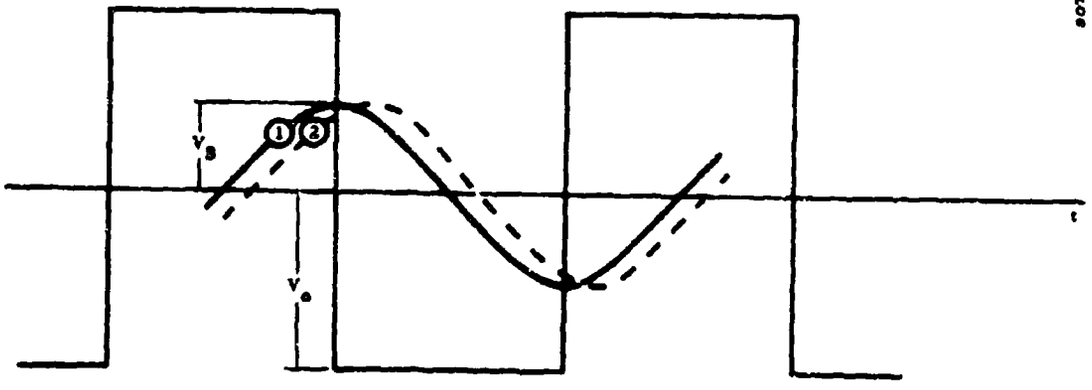


Figure J-4. Phase Detector Signals

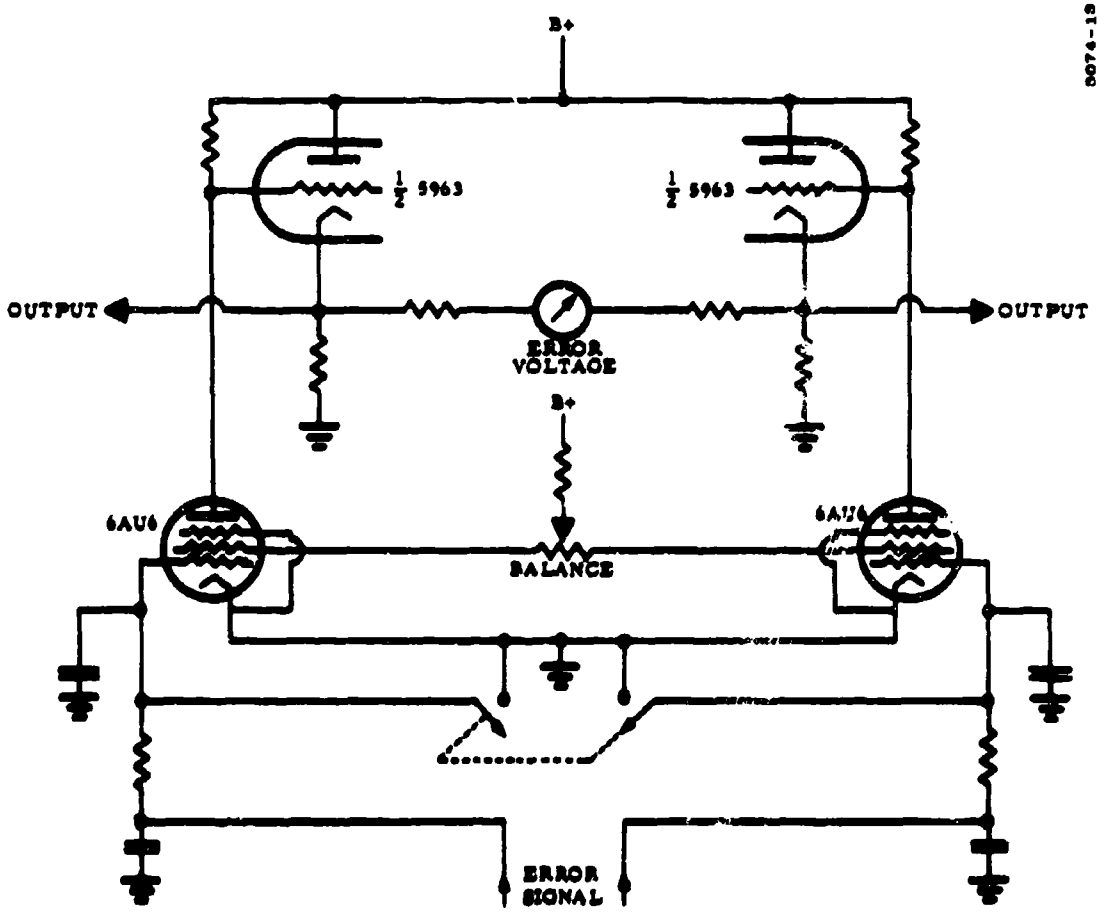


Figure J-5. Differential Amplifier

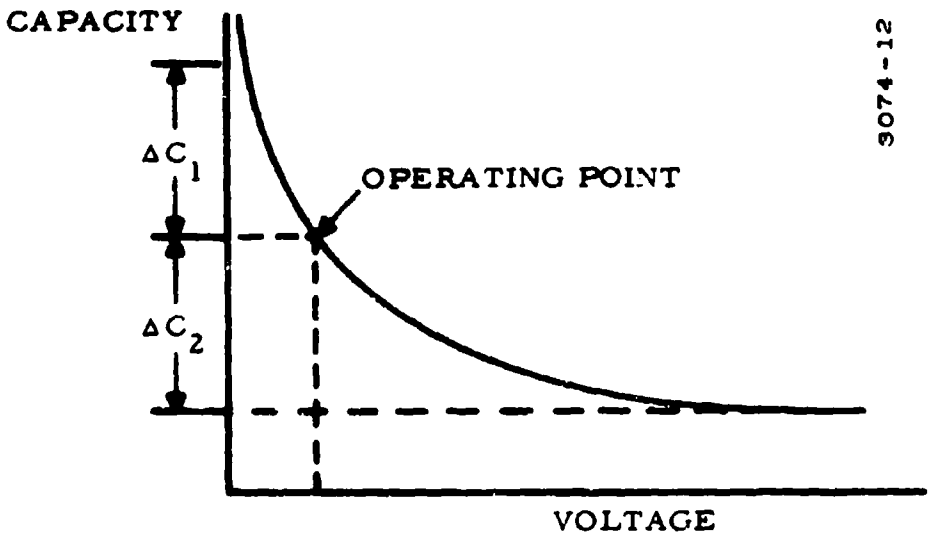


Figure J-6. Typical Operating Characteristics of a Voltage-Variable Capacitor

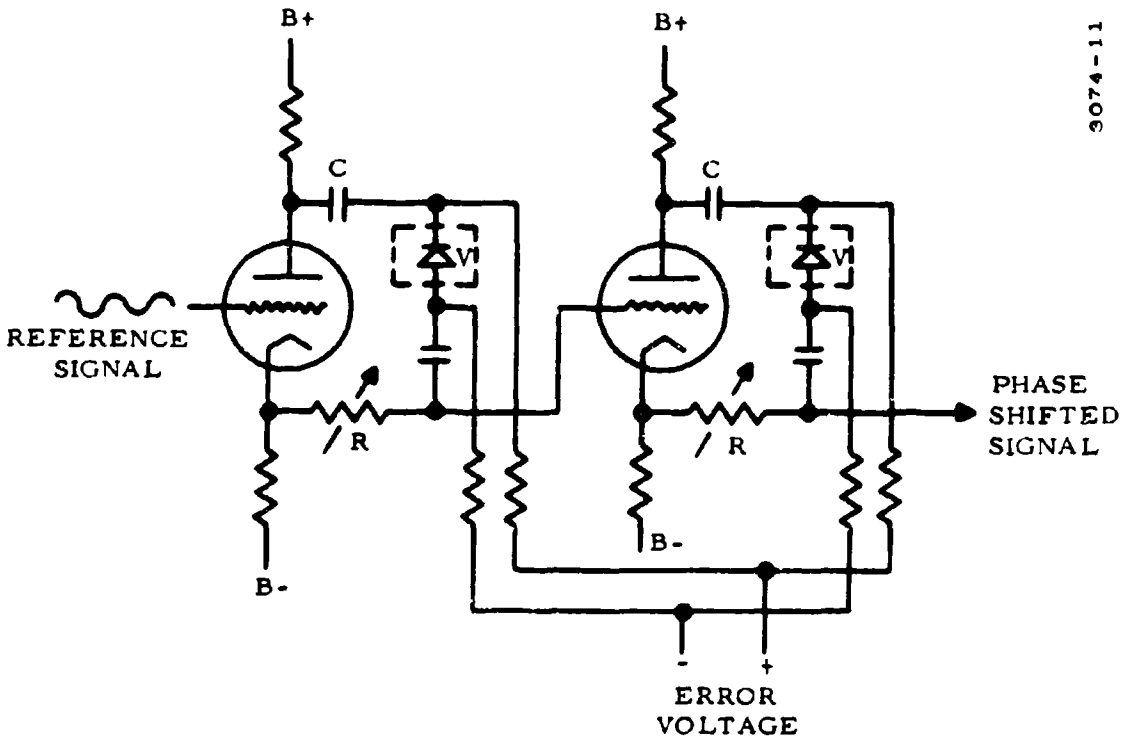


Figure J-7. Phase-Shifting Circuit

The varicap is represented by the diode with a "V". Two stages of phase shift were used to double the effective gain of the servo. A split-load, unity-gain amplifier drives an RC phase-shifting network containing the varicap and a manually variable resistor, R. The circuit is frequency-dependent, and the resistor is used to allow the operating frequency to be charged. The varicap is initially back-biased with a voltage equal to its mean operating point. The resistor is adjusted (with zero error voltage) to produce a phase shift of 90° per stage, presetting the servo to a zero phase error condition. The circuit is able to compensate for phase shiftr of ±40°

3. POLYPHASE GENERATOR

The connecting element between the phase servos and the frequency generator is called the polyphase generator. The function of this generator is to take the output of the frequency generator and convert it to a polyphase signal. The circuit was required to generate phase-accurate signals and to be capable of operating over a wide frequency range (5 kc to 500 kc). It was not possible to design a single circuit to accomplish the wide frequency range of operation without the use of band-switching. There are two bands, 5 kc to 50 kc and 50 kc to 500 kc. In each of these bands there are frequency ranges based on multiples of 3/2 (i.e., 50-75 kc, 75-112 kc, etc.). A block diagram of the polyphase generator is shown in Figure J-8.

The polyphase generator was designed to serve as a source for two polyphase systems: a three-phase system of phases 0°, -120°, and -240° and a five-phase system of phases 0°, -72°, -144°, -216°, and -288°. A resistor matrix was chosen as the most practical way of generating a large number of phases over a very wide frequency range. The matrix is driven by four quadrature signals. Any phase angle can be generated by two resistors summing the appropriate quadrature voltages. For the circuit of Figure J-9 it can easily be shown that $V = V_o \sin(\omega t - \psi)$

where

$$\tan \psi = \frac{\sin \phi}{\frac{R_2}{R_1} + \cos \phi}$$

ψ can be varied continuously between 0° and ϕ by varying $\frac{R_2}{R_1}$.

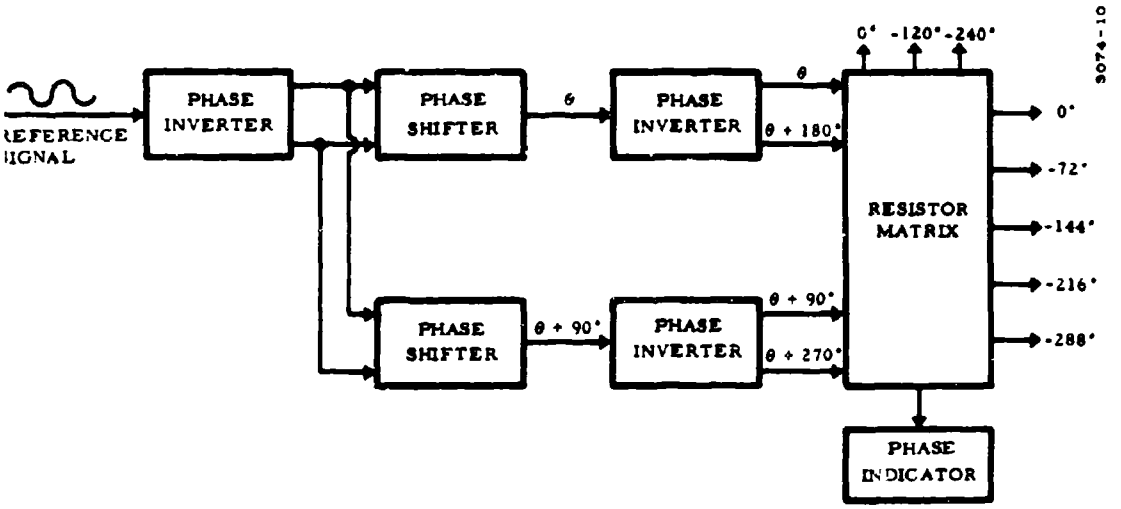


Figure J-8. Polyphase Generator

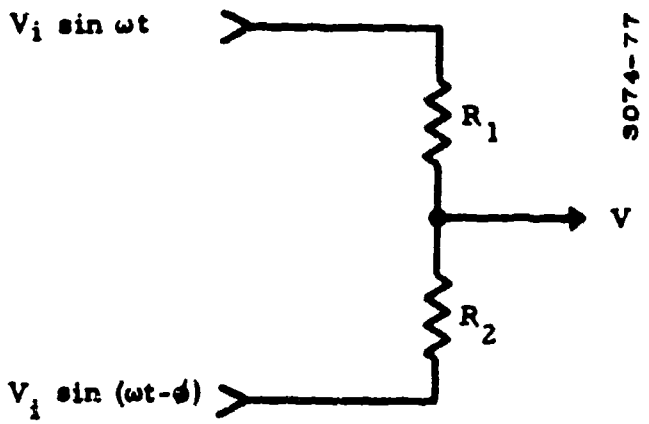


Figure J-9. Matrix Element of Phase Generator

The output phase-shifted signals are resistor-attenuated to be equal in amplitude. A 10-volt peak-to-peak output was chosen as the standard output amplitude. Trim potentiometers are used as the resistor elements in the matrix in order to adjust the matrix for phase and amplitude of the output. The driving signals to the resistor matrix are obtained from two split-load amplifiers. Equal plate and cathode resistors are used to insure equal output signals from each amplifier.

The band switching mentioned earlier is in the phase shifter blocks of Figure J-8. The outputs from the two phase shifters (Figure J-8) differ in phase by 90° (over a frequency range from 5 kc to 500 kc). In practice the phase error can be held to ±1° over the frequency range with suitable band switching.

The phase-shifting elements consist of two series RC circuits connected across supplementary phase-opposed input signals. The output signal is referenced to ground. The circuit contains a reactive element and is therefore frequency-dependent. If the frequency is changed then, for a fixed resistor-capacitor combination, the phase relationship between input and output is altered. Two phase-shifting circuits are used to minimize this situation. The resistor-capacitor combination of each phase shifter is preset at a given frequency, f, so that a 90° relation exists between the two outputs. This condition is realized when the phase shifts produced by the two circuits are 45° and 135° respectively. Figure J-10 illustrates this condition.

Since the loci of the two output vectors form a semicircle as a function of frequency, the amplitude of the two outputs is independent of frequency. The relative phase of the outputs is frequency-dependent, but the dependency is minimal for the condition shown in Figure J-10.

If the frequency variation, Δf, is less than $0.5f$ where f is the mid-frequency, then the relative phase variation of the two outputs will be less than ± 1°. In the actual circuit both R and C are varied in steps to cover the range 5 kc to 500 kc. Six resistor changes in combination with two capacitor changes are required.

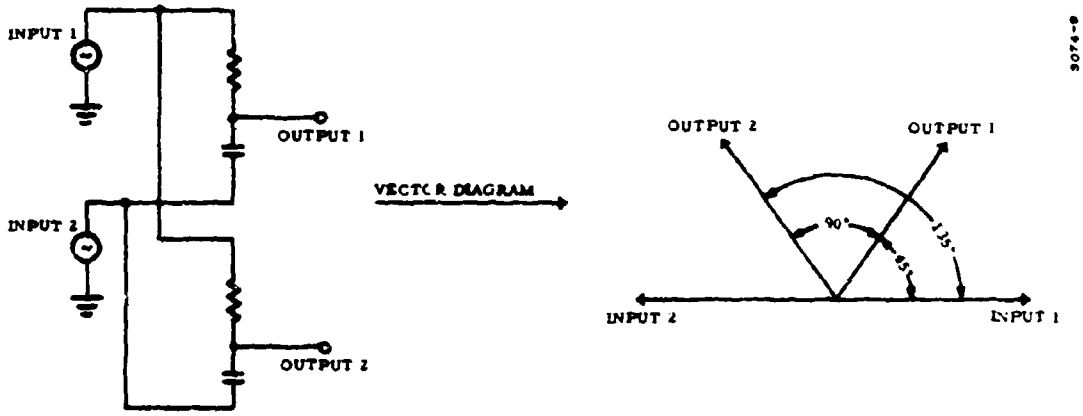


Figure J-10. Vector Relations

4. PHASE DISPLAY

Two types of phase-monitoring circuits were designed. It was felt desirable to display relative phase on a meter calibrated in degrees and also an oscilloscope where all phases were displayed simultaneously. The meter display will be discussed first.

4.1 Meter Display

The purpose of the meter display was as to monitor the standard phases from the resistor matrix. By appropriate switching, the meter indicates the relative phase between any two adjacent phases. In this particular application the phase generator divides 360 electrical degrees into equal parts. The meter indication therefore should be constant, as it is switched between adjacent phases if the phase generator is operating correctly. Confidence in this method of aligning and checking the phase generator is achieved by making the switched monitoring circuitry independent of input amplitude and thus dependent only on phase. The circuit for the phase monitor is shown in Figure J-11.

The phase monitor consists of two squaring amplifiers driving the suppressor and control grid of a double-grid gate tube such as a 6AS6. Either grid signal is capable of totally inhibiting the plate current of the tube. Plate current exists if and only if both grids are near zero bias. The meter in the plate circuit of the gate tube reads the average value of the plate current, which, if it were not for the finite rise-time of the grid signals, would be inversely proportional to the phase difference between the two input signals. The meter is calibrated to read $180° - \theta°$ where θ is the relative phase angle between the two inputs.

4.2 Oscilloscope Display

This system provides a visual output of the polyphase coil currents in the accelerator. It should be said here that the tuning of the accelerator would be practically impossible without a device of this sort. This display was designed to present a composite picture of both phase and amplitude of the polyphase currents.

The driving signals for the display are the feedback signals from the sensing coils used in the phase servo system. A diagram of the system is given in Figure J-12.

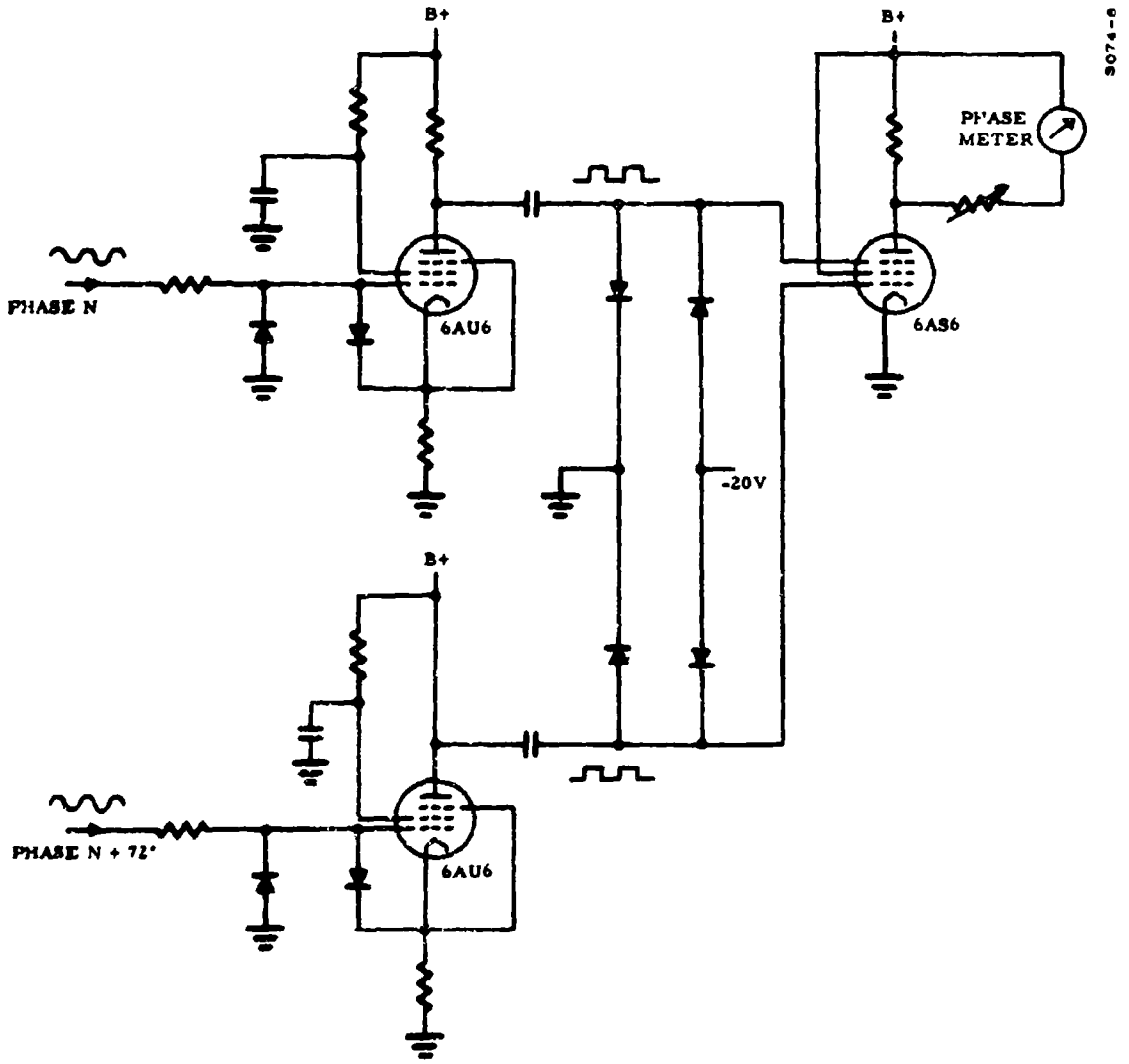


Figure J-11. Phase-Monitoring Circuit

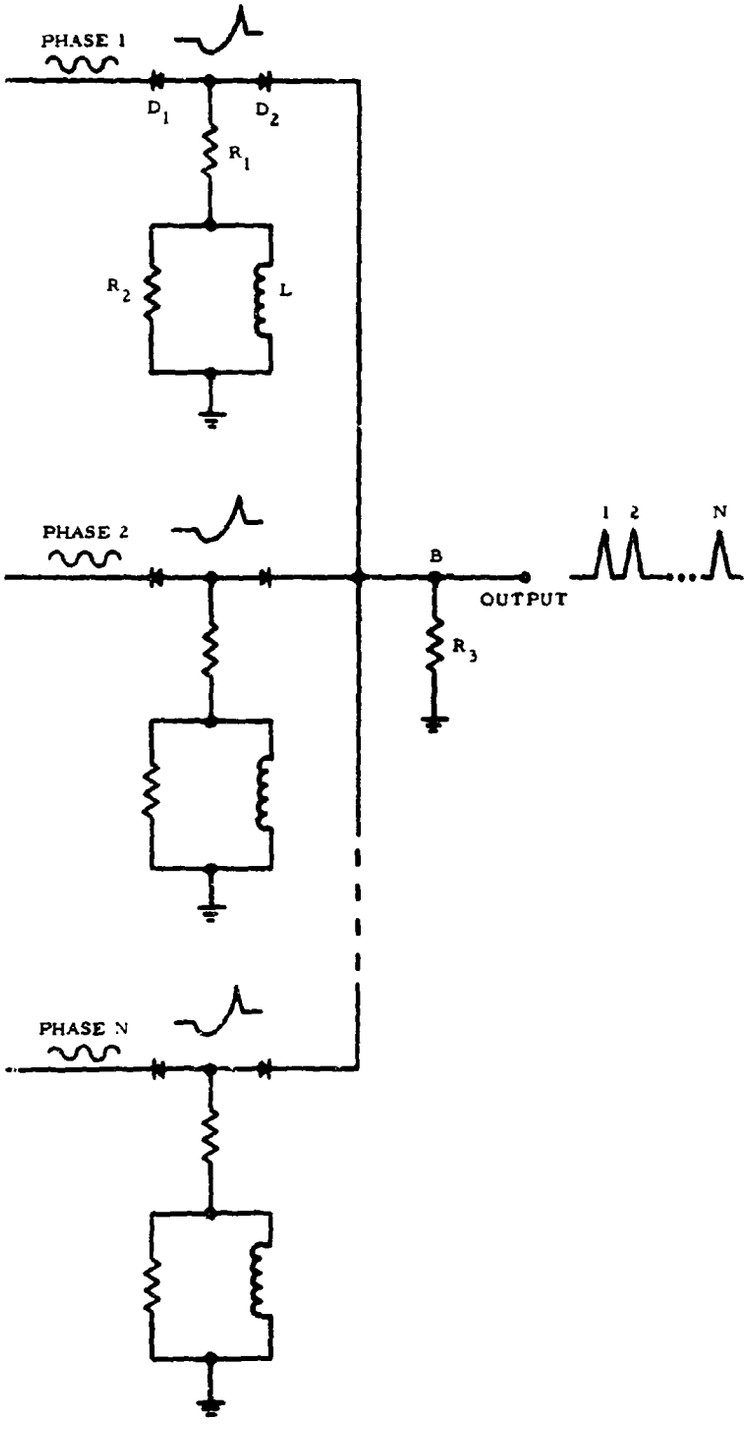


Figure J-12. Multiphase Display

A sine wave signal from each phase drives a passive circuit consisting of two diodes, two resistors, and an inductance.

The essential property of this circuit can be seen from the following argument. (See Figures J-13 and J-14).

During the conduction cycle of D_1, $V_i \sim V$. The current, i, phase-lags V by an amount arc tan $\frac{2\pi fL}{r}$ (see Figure J-14). At time t_1, V = 0 but current is still running in D_1. V becomes positive and D_2 conducts during the interval t_2-t_1. At time t_2, i = 0 and D_1 shuts off. The voltage V_o then rapidly falls to zero.

The resistor, R, is common to the five display circuits (Figure J-13), and the composite signal is a series of sharp, peaked, positive pulses as shown in Figure J-12.

Each pulse is representative of a phase. The amplitude of the pulse is proportional to the input amplitude, and the relative position of its peak is proportional to the relative phase. The function of the resistors, R_2, in Figure J-12 is to critically damp the inductance L. If L were allowed to ring with its stray capacity, a series of pulses would be produced — an undesirable situation.

Two oscillograms of the phase display are shown in Figure J-15. One shows the display at a time when the accelerator was not perfectly adjusted and the phase-servo circuit was not working. The other shows the same display after the phase-servo circuit was turned on.

Figure J-16 is a photograph of the control console which contains the frequency and phase servo systems and the display system (the unit to the left). The unit to the right is the remote control for the six TBC transmitters.

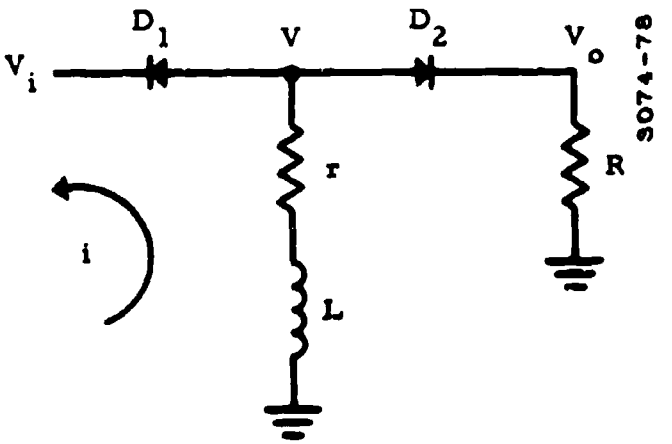


Figure J-13. Circuit to Illustrate Operation of Phase Display

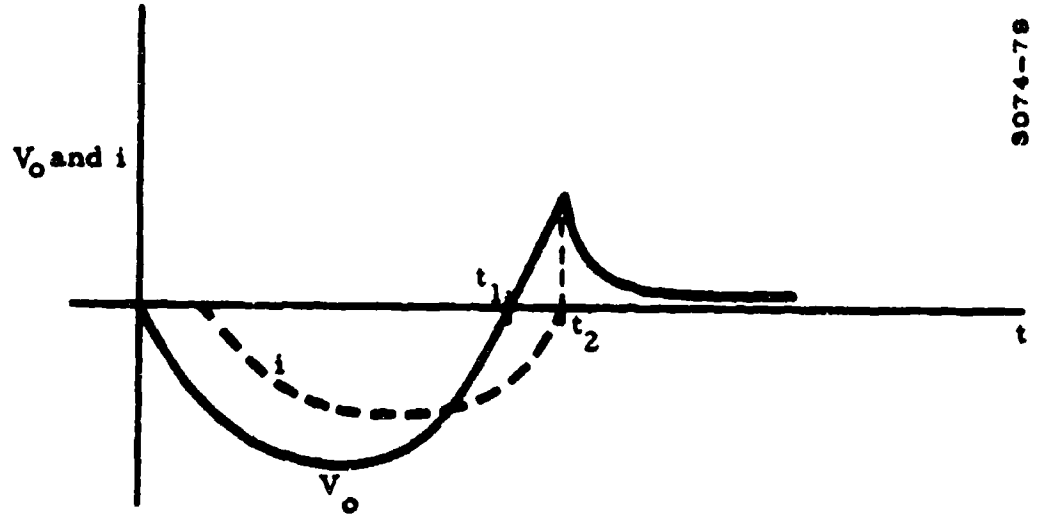


Figure J-14. Voltage and Current in Display Circuit



5191-4

WITHOUT SERVOS



WITH SERVOS

Figure J-15. Five-Phase Oscillograms

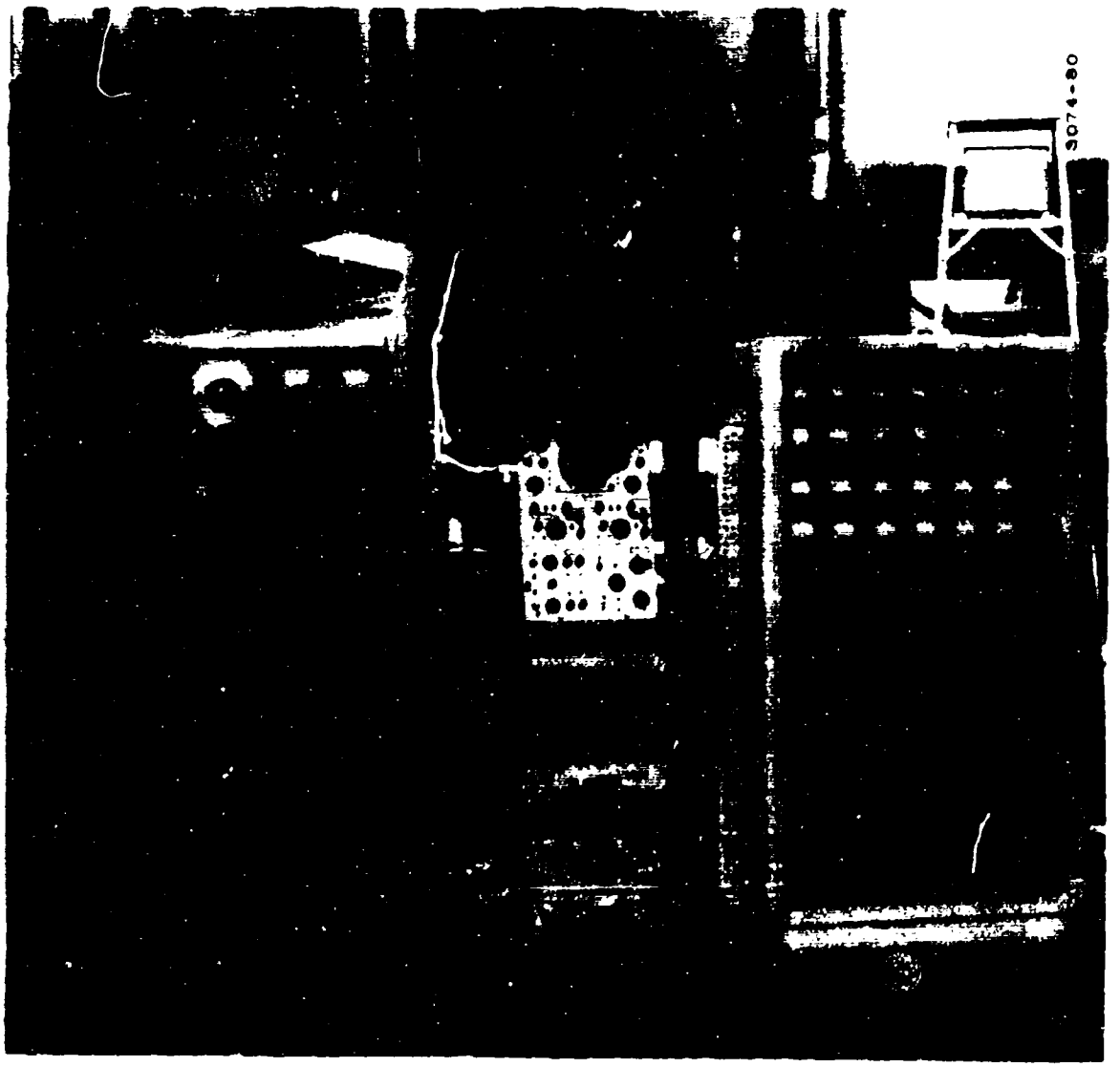


Figure J-16. Control Console

APPENDIX K

DESIGN OF A CURRENT-FORCING TRANSFORMER

APPENDIX K

DESIGN OF A CURRENT-FORCING TRANSFORMER

1. THE PROBLEM

The currents in the inner set of coils on the Mark II accelerator have fixed amplitude and phase relations to the currents in the outer set. In order to keep the number of controls to a minimum, it is desirable that the circuit that couples the inner and outer coils be of such a nature that the desired phase and amplitude relations are automatically achieved. This can be accomplished with a tuned current transformer, connected as described in Section 4. 2. 3. However, because of the high frequency (240 kc) and voltage involved, the design of this transformer is special enough to warrant description.

Consider the simple transformer shown in Figure K-1. The primary inductance of the transformer is L_1, the secondary inductance is L_2, and the mutual inductance between primary and secondary is M. The equivalent circuit for the transformer is also shown in Figure K-1.

Suppose that the load to be connected to the secondary has an impedance, Z, where, in the case of the Mark II accelerator, Z is predominantly inductive. The current-voltage relations for the transformer can then be written as follows:

$$\begin{bmatrix} E_1 \\ \\ I_1 \end{bmatrix} = \begin{bmatrix} M/L_1 & j\omega\,(L_1L_2 - M^2)/M \\ \\ 1/j\omega M & L_2/M \end{bmatrix} \begin{bmatrix} E_2 = I_2Z \\ \\ I_2 \end{bmatrix} \qquad \text{(K. 1)}$$

The so-called coefficient of coupling, k, is given by

$$k^2 = M^2/L_1L_2 \qquad \text{(K. 2)}$$

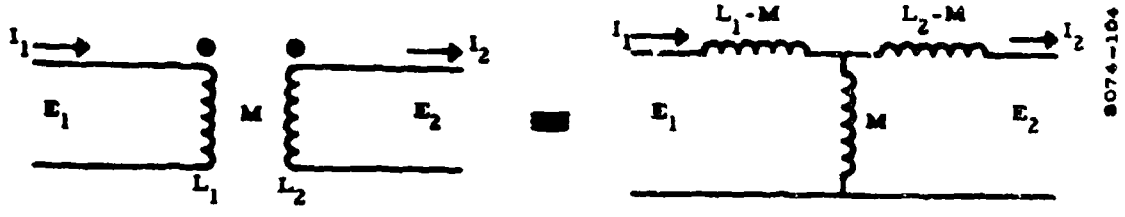


Figure K-1. Transformer and Its Equivalent Circuit

From Eq. (K. 1) the ratio of primary to secondary current is

$$I_1/I_2 = \frac{Z}{j\omega M} + \frac{L_2}{M} \qquad \text{(K. 3)}$$

In order for this ratio to be determined by the transformer only and not by the load (since the load impedance varies with plasma loading), it is necessary that

$$|Z| << M \qquad \text{(K. 4)}$$

In the case of the Mark II accelerator $|Z|$ is about 60 ohms (i. e. 40 microhenry at 240 kc). Then, to satisfy Eq. (K. 4), M would have to be very large compared to 40 microhenrys. At the frequency and voltage involved this is a difficult requirement. In fact, from a practical standpoint, it is nearly impossible.

2. THE SOLUTION

Consider the circuit shown in Figure K-2. In matrix notation the current-voltage relations are

$$\begin{bmatrix} E_1 \\ I_1 \end{bmatrix} = \begin{bmatrix} 1 & 0 \\ j\omega C_1 & 1 \end{bmatrix} \begin{bmatrix} M/L_1 & j\omega(L_1L_2 - M^2)M \\ 1/j\omega M & L_2/M \end{bmatrix} \begin{bmatrix} 1 & 0 \\ j\omega C_2 & 1 \end{bmatrix} \begin{bmatrix} E_2 = I_2 Z \\ I_2 \end{bmatrix} \qquad \text{(K. 5)}$$

$$\equiv \begin{bmatrix} A_1 & A_2 \\ A_3 & A_4 \end{bmatrix} \begin{bmatrix} E_2 = I_2 Z \\ I_2 \end{bmatrix}$$

The desired fixed relation between I_1 and I_2 can be achieved if the matrix element A_3 can be reduced to zero. It is found that this requires the following relation to hold:

$$\omega^2 C_1 \frac{M^2}{L_1} + \omega^2 C_2 L_2 - \omega^4 C_1 C_2 (L_1 L_2 - M^2) = 1 \qquad \text{(K. 6)}$$

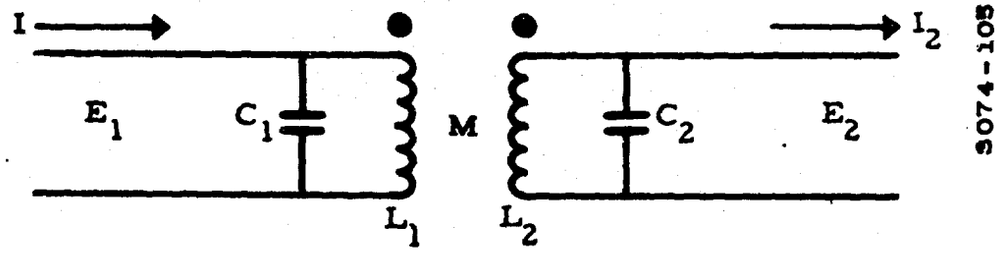


Figure K-2. Tuned Transformer

This is a resonance relation and, when it holds, the current ratio is

$$\frac{I_1}{I_2} = \frac{L_2}{M} - \omega^2 C_1 \left[\frac{L_1 L_2 - M^2}{M}\right] \qquad \text{(K. 7)}$$

Thus, when $I_2 = 0$ (i. e. there is no load connected to the transformer) then I_1 is also zero. This means that the desired adjustment corresponds to an impedance maximum (a resonance) as seen from the primary circuit. In practice the impedance is not infinite, as Eq. (K. 7) implies, due to the effect of resistance in the windings.

When written in terms of the coefficient of coupling, k, Eq. (K. 7) becomes:

$$\frac{I_1}{I_2} = \frac{1}{k}\sqrt{\frac{L_2}{L_1}}\left[1 - (1 - k^2)\,\omega^2 C_1 L_1\right] \qquad \text{(K. 8)}$$

It is desirable to keep the coefficient of coupling as near to unity as possible. Small values of k lead to:

1. An unwanted frequency dependance in the current ratio
2. A current ratio that depends sensitively on the geometry of the transformer rather than just the primary-to-secondary turns ratio.

At 240 kc one must give serious consideration to the skin effect and to wire-to-wire proximity effects. Iron cores are too lossy to be used, and the transformers are too large for ferrite cores. In addition, the transformers must be capable of handling about 4000 volts and currents of 70 amperes. When all these factors are considered it becomes difficult to make a transformer with a high coefficient of coupling. For example, a transformer made from two, concentric, air-core coils of copper tubing would typically have a coefficient of coupling less than 0. 6.

A solution to the problem was found in the form of transformers made of coaxial cable. The coefficient of coupling for these was experimentally determined to be about 0. 97, and the ratio $\sqrt{L_2/L_1}$ was equal to the turns-ratio to within a few percent.

The basic scheme is illustrated in Figure K-3. A helical coil made from two parallel strands of coaxial cable is shown. The per-strand inductance of the helix is L, and the per-strand capacitance of the cable is C.

The center wires of the cable are connected in series, whereas the coaxial braids are connected in parallel. The transformer then has a primary-to-secondary voltage ratio of 1:2. The equivalent electrical circuit of the arrangement is shown in Figure K-4. The stray inductances, $L_1 - M$ and $L_2 - M$, (see Figure K-1) are very small. The only contribution to inductance comes from the magnetic field that exists between the center wires and their coaxial braids. Experimental measurement showed that the stray inductance was three percent of the primary inductance in a typical case.

The transformer shown in Figure K-3 is connected in such a way that it inverts the signal. If connected in a noninverting fashion, a different capacity is effective. The equivalent circuit then changes from that of Figure K-4 to that of Figure K-5.

In the case of the Mark II accelerator the primary-to-secondary current ratio which is required is 5:1; so five strands of cable were used in the transformers. The five strands were twisted together and taped. Then the coil was wound. The coil diameter (i.e. the diameter of the transformer) is about 18 inches and the coil has six turns, giving an inductance, L, of about 15 microhenrys. The cable used was RG-8/U which has an insulation strength in excess of 20 kilovolts and a current-carrying capacity, at 240 kc, of about 15 amperes rms (experimental determination).

With the design as above and with the transformer connected to invert the signal, the effective capacity (referred to the secondary) is about 11/5 C. This is just about enough to achieve the desired resonance (to make $A_3 = 0$; Eq. (K. 5)) automatically. A small additional amount of capacity was added to perfect the tuning adjustment.

Five such transformers were constructed. They are the black coils visible in Figure 4-17 of this report. The frequency of operation can be varied by ±5 kc without the necessity of retuning the transformers.

The transformers have an experimentally determined Q of about 80, so the Joule heating losses in them are acceptably small.

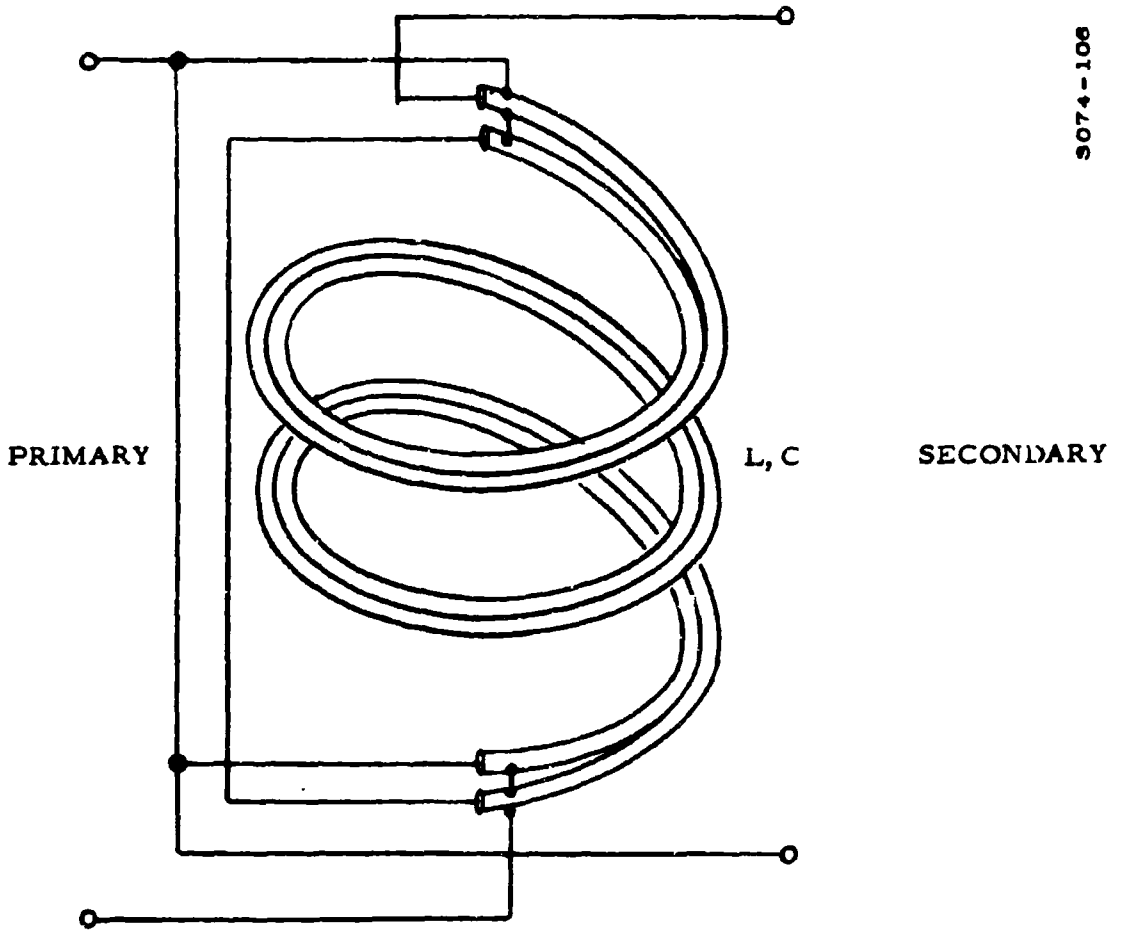


Figure K-3. A 2:1 Transformer of Coaxial Cable

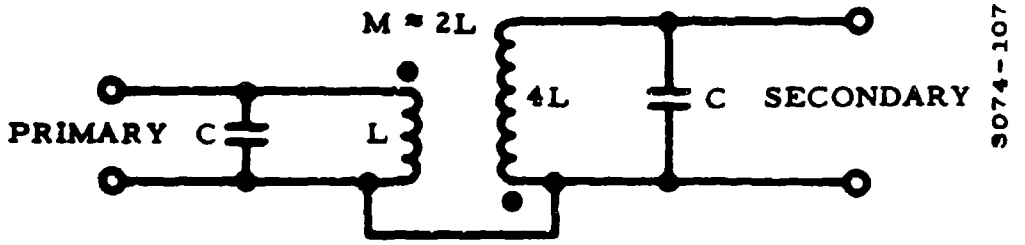


Figure K-4. Equivalent Circuit of the Transformer in Figure K-3

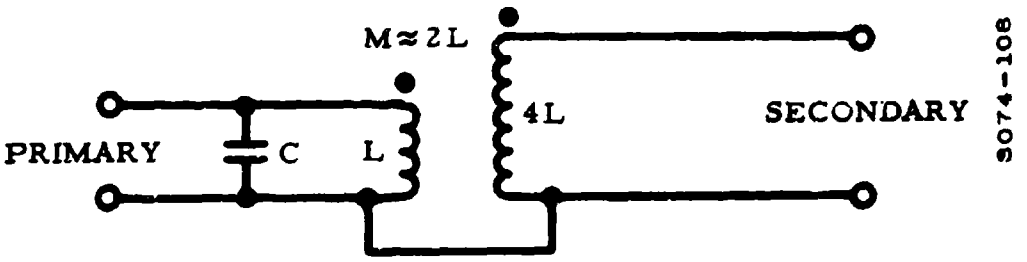


Figure K-5. Equivalent Circuit

3. OTHER APPLICATIONS FOR COAXIAL CABLE

Various other uses are possible for a helix of coaxial cable. Some of these are illustrated in Figure K-6. Each drawing in this figure shows the electrical connections and the corresponding equivalent circuit.

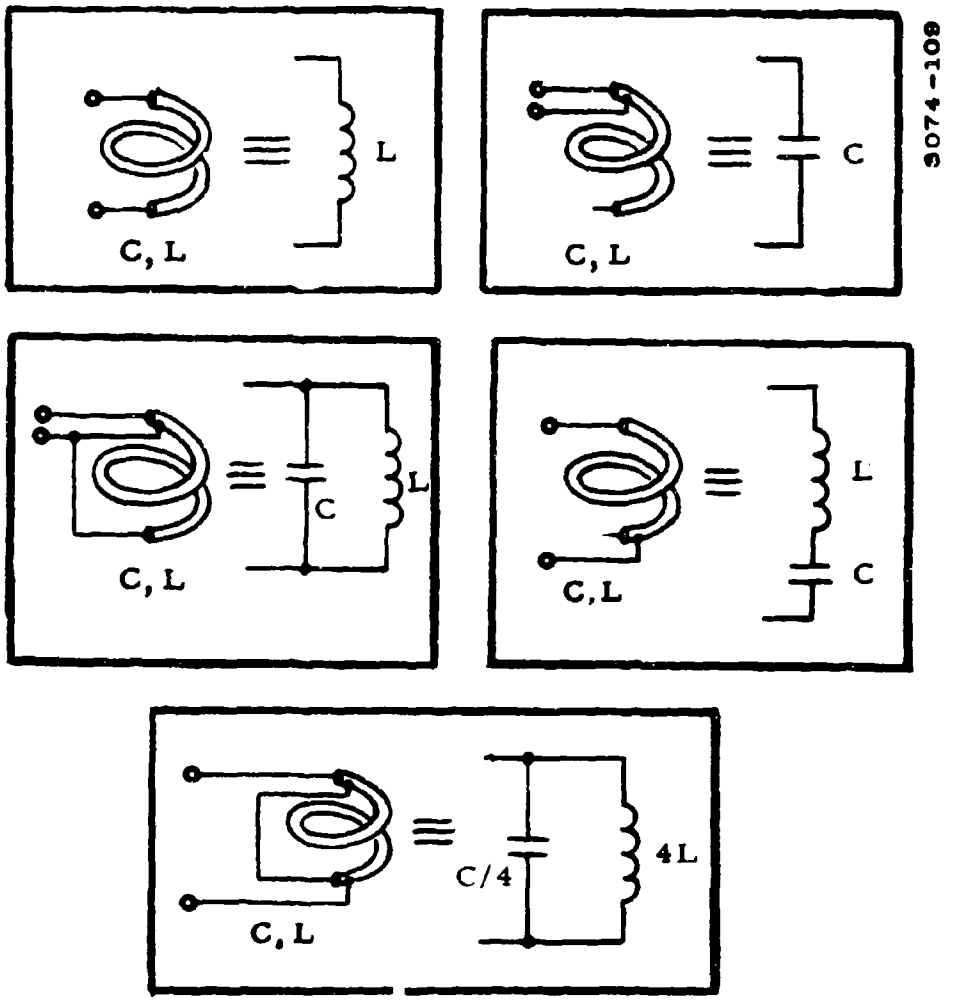


Figure K-6. Possible Connections of a Helix of Coaxial Cable

APPENDIX L

ANALYSIS OF A RING COUPLING-CIRCUIT

APPENDIX L

ANALYSIS OF A RING COUPLING-CIRCUIT

1. INTRODUCTORY REMARKS

The coupling network that connects the coils of a traveling-wave accelerator to the sources of power must be properly designed. Otherwise the desired magnetic field cannot be established in the accelerator. It will be assumed here that the proper magnetic field is established when:

1. The coil currents are equal in magnitude.
2. The coil currents have symmetrically disposed phase relations with respect to 360° of phase.

The first requirement is established by the physical construction of the accelerator itself; while the second not only satisfies the requirements of the accelerator but, in addition, reduces the current that flows in the ground return path of the coupling network to zero. The requirements of the accelerator alone can be satified by coil currents that have phases which are symmetric with respect to 180°.

In order to supply large amounts of power, the power sources consist of hard-vacuum tubes operating in the class-C mode. With this type of source the characteristics of the coupling network, when properly adjusted, must be such that:

1. Each power source is presented with an impedance that is purely real.
2. A direct capacitive path exists between the ground return line and the point to which each power source is connected.

The purpose of this discussion is to demonstrate that the coupling circuit used on the Mark II accelerator has the desired properties. The

variable elements in this network are a set of ten capacitors. It will be shown that the circuit does have the desired properties and that, in addition:

1. The circuit allows the power load to be apportioned among the power supplies in any of a wide variety of ways.
2. The value of any one of the variable capacitors can be chosen arbitrarily (within certain limits). The remaining capacitors are then uniquely determined by the requirement of a real impedance and the power apportioning scheme that is desired.

For simplicity the network that will be analysed is a three-phase network rather than the five-phase network used on the Mark II. The conclusions are the same in either case.

2. THE CIRCUIT

The circuit to be analysed is shown in Figure L-1. It is a star-delta arrangement where the elements of the delta are three variable capacitors, denoted in the figure as C_{AC}, C_{CB}, and C_{BA}. The arms of the star each consist of a variable capacitor in parallel connection with the coils of the accelerator. The latter have both inductive and resistive properties as indicated in the figure. The power sources are connected between ground and each of the three nodes labeled A, B, and C.

The inductive elements, while shown as simple inductors in Figure L-1, are in reality a mutually coupled set. The coupling occurs in the accelerator structure and it is a consequence of the close proximity of the coils. Close proximity is required when a smoothly moving magnetic field is desired. The mutual inductances between L_A, L_B, and L_C (the self-inductances of the coil systems) will be denoted by L_{AB}, L_{AC}, and so on. The mutual inductances are not shown in Figure L-1.

The self-inductances, mutual inductances and resistances all vary with the behavior of the plasma in the accelerator. However, insofar as the present analysis is concerned, their values can be considered to be fixed. The analysis will, in addition, sume that the magnitudes of the currents flowing in L_A, L_B, and L_C are equal and that they are sinusoidally varying with the following disposition of phase relations: 0°, 120°, 240°. Thus, the following relations hold:

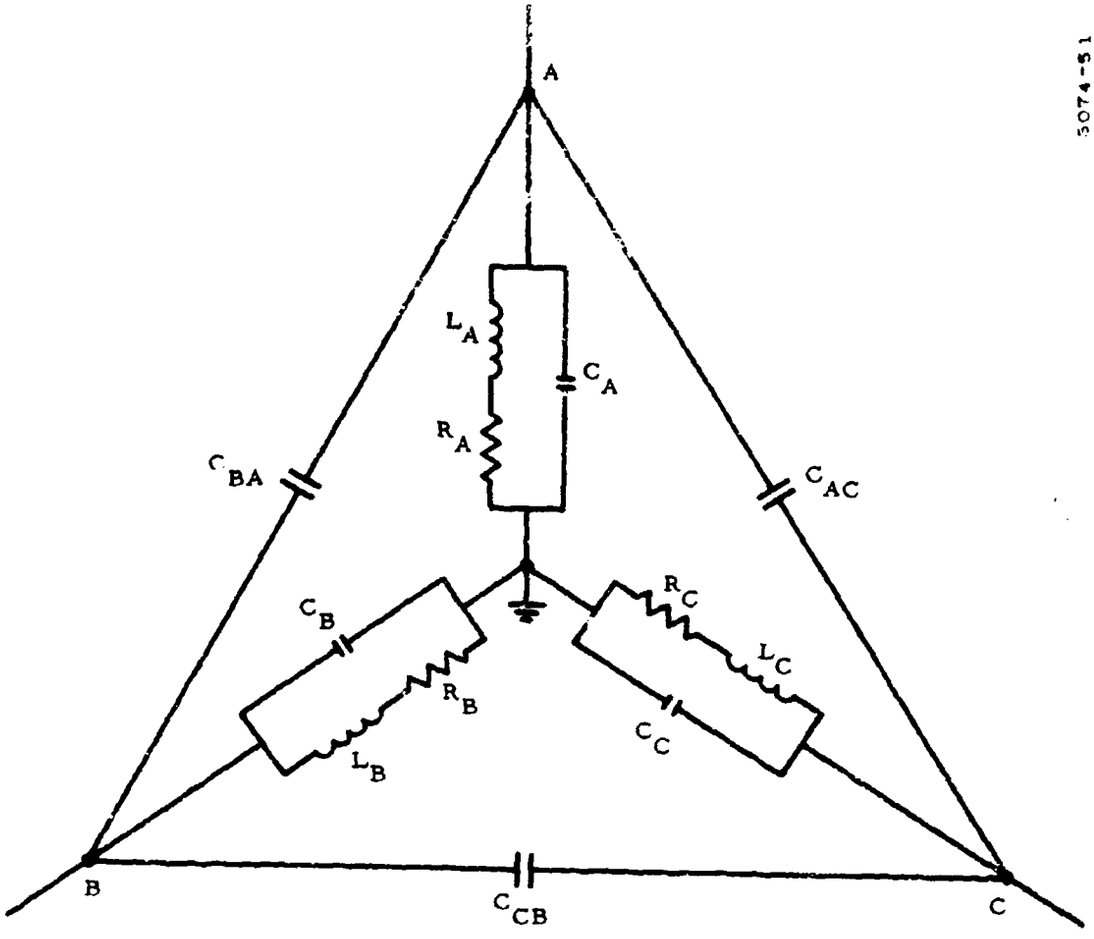


Figure L-1. Ring Circuit

$$I_b/I_a = e^{j\phi};\ \phi = \frac{2\pi}{3} \qquad \text{(L. 1)}$$

$$I_a/I_c = e^{j\phi} \qquad \text{(L. 2)}$$

$$I_c/I_b = e^{j\phi} \qquad \text{(L. 3)}$$

$$|I_a| = |I_b| = |I_c| \equiv I \qquad \text{(L. 4)}$$

where I_a, I_b, and I_c are the currents flowing in L_A, L_B and L_C respectively. The currents flowing from the power sources to the nodes will be denoted by I_A, I_B, and I_C, and the voltages at the nodes by E_A, E_B, and E_C.

The impedances seen by the power sources will be denoted by Z_A, Z_B, and Z_C; where, for example,

$$Z_A = E_A/I_A \qquad \text{(L. 5)}$$

3. POWER RELATIONS

The power being supplied by the supply connected to node A is

$$\begin{aligned} P_A &= \text{Real part of } (E_A I_A) \\ &= \text{Real part of } (E_A^2/Z_A) \end{aligned} \qquad \text{(L.6)}$$

However, for proper operation of the power supplies E_A and I_A must be in phase. This can only be true if

$$\text{Imaginary part of } Z_A = 0 \qquad \text{(L. 7)}$$

Similar relations hold for Z_B and Z_C. When all the node impedances are real the following equation, which expresses conservation of energy, must hold:

$$\frac{|E_A|^2}{Z_A} + \frac{|E_B|^2}{Z_B} + \frac{|E_C|^2}{Z_C} = I^2 (R_A + R_B + R_C) \qquad \text{(L. 8)}$$

4. PROPERTIES OF THE ACCELERATOR

The relations between the node voltages and the currents in L_A, L_B, and L_C can be expressed in matrix notation as follows:

$$\begin{bmatrix} E_A \\ E_B \\ E_C \end{bmatrix} = j\omega \begin{bmatrix} L_A & L_{BA} & L_{AC} \\ L_{BA} & L_B & L_{CB} \\ L_{AC} & L_{CB} & L_C \end{bmatrix} \begin{bmatrix} I_a \\ I_b \\ I_c \end{bmatrix} + \begin{bmatrix} R_A & 0 & 0 \\ 0 & R_B & 0 \\ 0 & 0 & R_C \end{bmatrix} \begin{bmatrix} I_a \\ I_b \\ I_c \end{bmatrix} \qquad \text{(L. 9)}$$

Consider the equation for E_A out of the set expressed by (L. 9). It will contain I_b and I_c in addition to I_a; however the former two may be expressed in terms of I_a through the use of Eq. (L. 1) and (L. 2).

After some algebraic manipulation it is found that E_A and I_a are related in the following way:

$$E_A = \left[j\omega \ell_A + r_A \right] I_a \qquad \text{(L. 10)}$$

where:

$$\ell_A \equiv L_A + \left(L_{BA} + L_{AC} \right) \cos \phi \qquad \text{(L. 11)}$$

$$r_A \equiv R_A + \omega \left(L_{AC} - L_{BA} \right) \sin \phi \qquad \text{(L. 12)}$$

Similar relations can be derived for nodes B and C by cyclic permutation. Thus, there exist quantities ℓ_B, ℓ_C, r_B, and r_C. These quantities are the effective values of inductance and resistance with the mutual coupling of the circuits properly accounted for. It should be noted that the values of these quantities will change if the currents I_a, I_b, and I_c are not equal in magnitude and properly phased, as assumed.

Eq. (L. 10), and the other two similar equations, are identical to the current-voltage relation for simple series-connected inductor-resistor circuits. The "Q" at node A is:

$$Q_A \equiv \frac{\omega \ell_A}{r_A} \qquad \text{(L. 13)}$$

Similar equations exist for nodes B and C. Because of the mutual coupling Q_A, Q_B, and Q_C have very different values, and they may even be negative. If for example, Q_A is negative, then r_A is negative. A negative resistor is equivalent to a source of energy (i. e., a generator) rather than a sink of energy. The spectacular variations which are found in the values of Q give an indication of the importance of having a proper coupling network.

From here on the analysis will make use of the effective values of inductance and resistance. The following relation is important:

$$r_A + r_B + r_C = R_A + R_B + R_C \qquad \text{(L. 14)}$$

It can be derived from Eq. (L. 12) and its counterpart equations.

5. PROPERTIES OF THE COUPLING CIRCUIT

The current-voltage relations at node B are shown in Figure L-2. The real values of L_B and R_B are shown in the figure but the analysis will use ℓ_B and r_B in order to account for the mutual coupling.

Conservation of current requires that $I_B = I_1 + I_b + I_3 + I_4$. From this one finds that:

$$\frac{1}{Z_B} = \frac{I_b}{E_B} + j\omega \left[C_{CB} + C_B + C_{BA} \right] - j\omega C_{CB} \left(\frac{E_C}{I_c} \right) \left(\frac{I_b}{E_B} \right) \left(\frac{I_c}{I_b} \right) - j\omega C_{BA} \left(\frac{E_A}{I_a} \right) \left(\frac{I_b}{E_B} \right) \left(\frac{I_a}{I_b} \right) \qquad \text{(L. 15)}$$

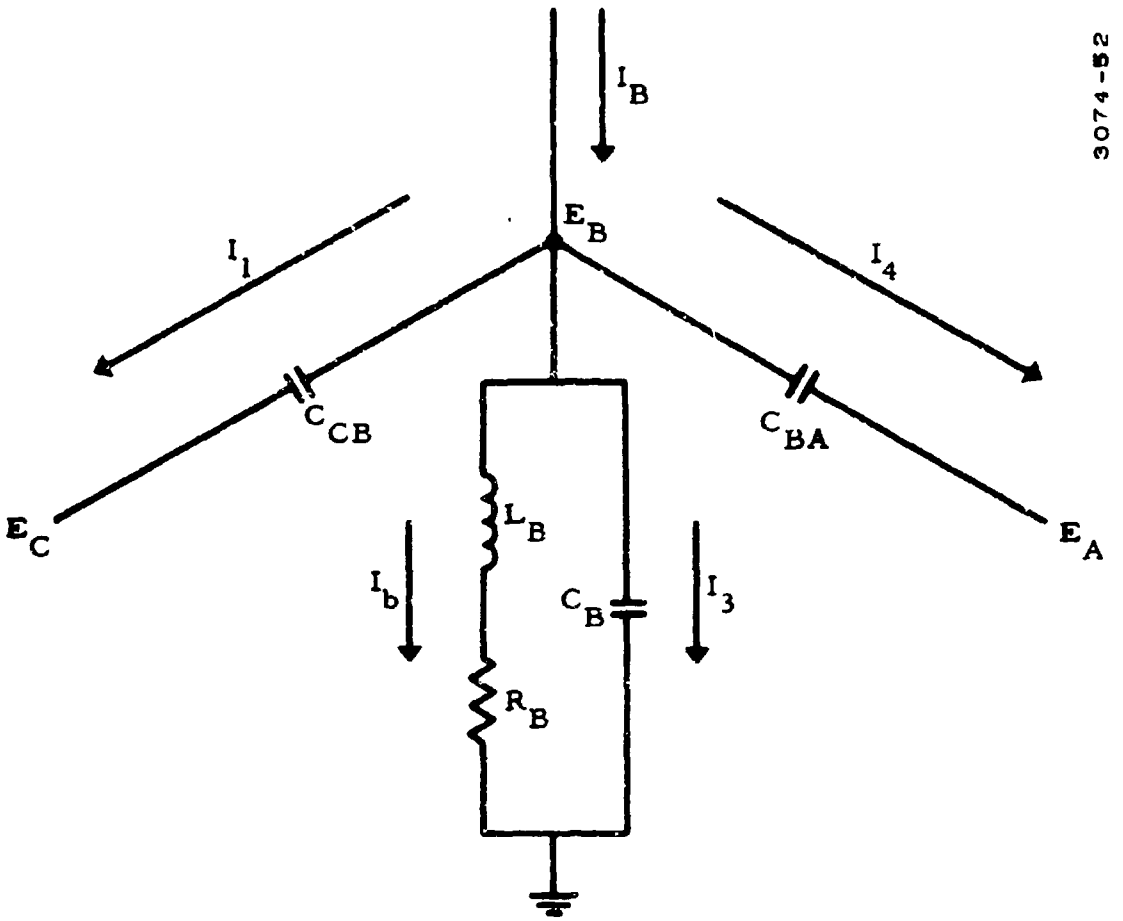


Figure L-2. Notation at Node B

The voltage-current ratios, which appear in Eq. (L.15), are determined by Eq. (L. 10) and its counterpart equations. The resulting equation for $1/Z_B$ is complex, but we must set the imaginary part equal to zero to accord with the requirements previously discussed. As a result, two equations are obtained. The algebraic manipulation is involved and will not be given here. The equations obtained are:

$$a^B C_B + a^B_{BA} C_{BA} + a^B_{CB} C_{CB} = \frac{1}{\omega^2 \ell_B} \tag{L 16}$$

$$- a_{BA} C_{BA} + a_{CB} C_{CB} = K_B \tag{L.17}$$

where the various values of a represent constants. Similar equations can be found for node A and node C. The values of a are:

$$a^B = \frac{1 + Q_B^2}{Q_B^2} \tag{L.18}$$

$$a^B_{BA} = \frac{1 + Q_B^2}{Q_B^2} - \frac{\ell_A}{\ell_B}\left(\frac{1 + Q_A Q_B}{Q_A Q_B}\right) \cos \phi$$

$$- \frac{\ell_A}{\ell_B}\left(\frac{Q_A - Q_B}{Q_A Q_B}\right) \sin \phi \tag{L.19}$$

$$a_{BA} = \ell_B \ell_A \left[\left(\frac{Q_B - Q_A}{Q_A Q_B}\right) \cos \phi + \left(\frac{1 + Q_A Q_B}{Q_A Q_B}\right) \sin \phi \right] \tag{L. 20}$$

$$K_B = \frac{1}{\omega} \ell_B^2 \left[\left(\frac{1 + Q_B^2}{Q_B^2}\right) \frac{1}{Z_B} - \frac{1}{\omega \ell_B Q_B} \right] \tag{L. 21}$$

and the remaining values can be found by cyclic permutation. With the aid of the relations derived earlier one can show that

$$K_B = \frac{1}{I^2\omega^3}\left[\frac{|E_B|^2}{Z_B} - I^2 r_B\right] \qquad \text{(L. 22)}$$

with similar relations for K_A and K_C

With the aid of Eq. (L. 8) and (L. 14) one finds that

$$K_A + K_B + K_C = 0 \qquad \text{(L. 23)}$$

When Eq. (L. 17) and its counterpart equations are assembled in matrix form one finds:

$$\begin{bmatrix} a_{BA} & 0 & -a_{AC} \\ -a_{BA} & a_{CB} & 0 \\ 0 & -a_{CB} & a_{AC} \end{bmatrix} \begin{bmatrix} C_{BA} \\ C_{CB} \\ C_{AC} \end{bmatrix} = \begin{bmatrix} K_A \\ K_B \\ K_C \end{bmatrix} \qquad \text{(L. 24)}$$

From this one gets

$$\begin{bmatrix} C_{BA} \\ C_{CB} \\ C_{AC} \end{bmatrix} = \frac{\left(K_A + K_B + K_C\right)\begin{bmatrix} (a_{AC}a_{CB}) \\ (a_{BA}a_{AC}) \\ (a_{BA}a_{CB}) \end{bmatrix}}{D} \qquad \text{(L. 25)}$$

where D is the determinant of the 3 × 3 matrix. According to Eq. (L. 23) the numerator of Eq. (L. 25) is zero. The denominator is easily shown to be zero also. The meaning of this result is that the system of equations for the C_{IJ} is indeterminate, and one of the capacitors can be chosen to have any value at all. Eq. (L. 24) can then be used to obtain the values of the others. Following this, Eq. (L. 16) and its counterpart equations can be used to find C_A, C_B, and C_C. The only restriction is that none of the values can be allowed to be negative (in the complex notation a negative capacitor is an inductor).

On the other hand, in Eq. (L. 16) one may choose C_B arbitrarily. Then Eq. (L. 16) determines a relation between C_{BA} and C_{CB} which removes the indeterminacy from Eq. (L. 24). Therefore, one and only one of the ten capacitors is arbitarily chosen, provided the values of K_A, K_B, and K_C are specified.

However, if K_A, K_B, and K_C are not specified then any <u>two</u> of the capacitors are arbitrary. For example, from Eq. (L. 24) one sees that, if C_{BA} and C_{AC} are chosen arbitrarily, the first equation determines K_A, the second two combine to determine K_B, and Eq. (L. 23) determines K_C. Eq. (L. 16) and counterparts determine C_A, C_B, and C_C.

6. CONCLUSIONS

The conclusions are: if the node impedances are real then

1. If the power sharing is to be a prescribed way one capacitor is arbitrary.
2. If two capacitors are arbitrarily chosen the power sharing can no longer be prescribed.

APPENDIX M

ZENER DIODES AS TEMPERATURE-SENSING DEVICES

APPENDIX M

ZENER DIODES AS TEMPERATURE-SENSING DEVICES

1. INTRODUCTORY REMARKS

Proper knowledge of the operating characteristics of the Mark II accelerator can be obtained only if the relative amounts of power that are dissipated, as heat, in the various parts of the system are known. All the heat eventually appears in the flow of cooling oil; so the required power distribution can be inferred if the oil temperature is measured at a sufficient number of places. In addition it is necessary to monitor the temperature of the walls of the annular accelerating channel.

The places where temperature measurements are required are, in general, so located that mercury thermometers cannot be used. Ordinarily, the problem would be solved by using thermocouples with a sensitive bridge-type readout device.

However, the accelerator structure and, in fact, the whole laboratory are located in the ground wave of the power supplies (operated at 240 kc). It has been found by experience that sensitive instruments (i. e., instruments designed to detect signals in the microvolt range) do not operate properly under such conditions.

Consequently, a study was made to determine whether some device other than a thermocouple could be employed. The basic accuracy required was estimated to be about ± 0. 1C.

Table M-1 compares the sensitivity of zener diodes, thermocouples, and thermistors as temperature sensors under typical conditions of operation.

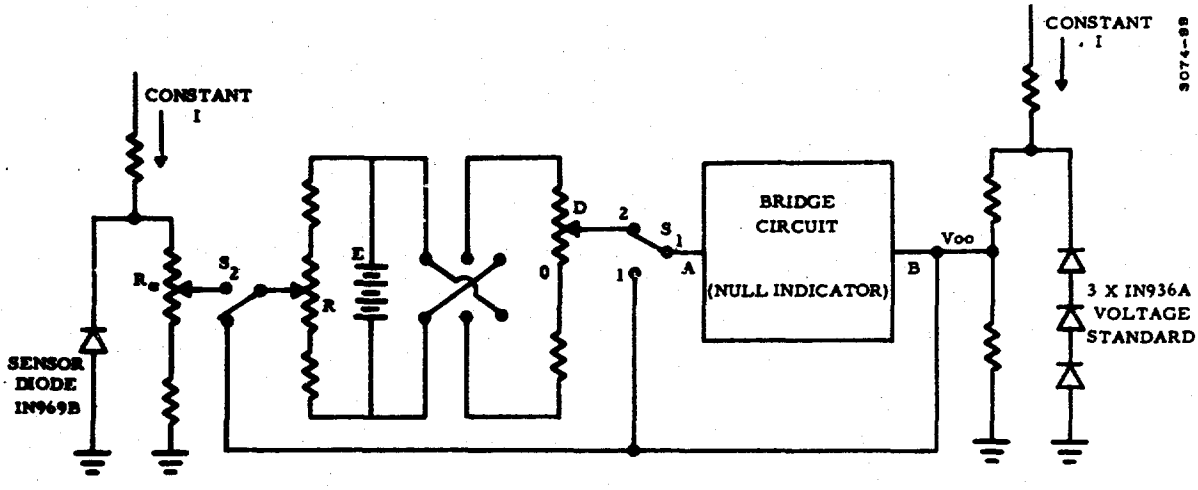


Figure M-1. Basic Arrangement of Sensing Circuit

TABLE M-1

COMPARISON OF TEMPERATURE-SENSING ELEMENTS

Type	Sensitivity (millivolt/°C)
Thermocouple	~ 0.04
Thermistor	~ 4.0
Zener Diode	~ 20.0

The zener diode is seen to be much more sensitive than the thermocouple and comparable in sensitivity to a thermistor. The response of a thermistor is nonlinear, making it difficult to record temperature differences with accuracy. For these reasons a study was initiated to determine whether zener diodes made suitable sensing elements.

2. PROPERTIES OF ZENER DIODES

The zener diode is a voltage-regulating device that operates at a current of 3 or 4 ma (typically) with a dynamic resistance on the order of 30 ohms.

The temperature coefficient varies with the type of diode and has a maximum, of about 20 mv/°C, for diodes designed to operate at 25 volts. The temperature range over which satisfactory operation is obtained is typically -65C to +175C.

The small, glass-encapsulated zener diodes have a very small mass, and the thermal time constant was experimentally determined to be about three seconds.

Specially constructed zener diodes are available with a temperature coefficient that is less than 1/20 that of the usual zener. These can be used to supply a reference voltage that can be interpreted as a standard temperature.

For convenience we adopt 0C as the reference temperature. Then, the voltage of a zener as a function of temperature, T, can be represented as follows:

$$V = V_o + \alpha T + \beta T^2 + \ldots\ldots \qquad (M.1)$$

If the zener is to make a satisfactory temperature sensor one requires

1. That V_o be stable and vary little from diode to diode.
2. That α be stable and vary little from diode to diode.
3. That β and all higher-order terms be effectively zero.
4. That the same equation hold no matter whether the temperature is increasing or decreasing.

All of the requirements were found, by experiment, to be satisfied. The unit-to-unit variations in V_o are given by the diode manufacturers, and 5 percent is a typical tolerance. No information on the tolerance of α or the value of β is available in the manufacturers' literature. Experimentally it was found that α varied by 2 or 3 percent from unit-to-unit and that β was too small to be detected by the experimental equipment. No hysteresis could be detected that was attributable to a hysteresis in the value of α.

The variation of V_o with diode current is computed from the dynamic resistance. For the diodes selected (type IN 969B) V_o varies at a rate of 30 mv per ma. In order to keep V_o stable to 1 mv (corresponding to a temperature variation of 0.05C) the diode current must be held constant to 0.03 ma (out of about 3 ma). Thus, the diode current supply has to be stable to about 1 percent. This kind of stability is rather easily obtained.

3. THE SENSING CIRCUIT

A temperature-compensated zener diode (three type IN 936A diodes in series) supplies a voltage standard, V_{oo}, which is taken to represent 0C.

Figure M-1 shows the essential details of the circuit employed. The temperature of the sensor diode is determined from the setting of potentiometer, D. The null-indicating bridge circuit, which indicates when the voltages at A and B are equal, is used to determine when D is correctly adjusted. The bridge itself is adjusted when the switch S_1 is set to position 1, so that equal voltages are applied to A and B.

Potentiometers R and D allow any fraction of the floating voltage, E, to be added in series with the voltage of the sensor diode. The reversing switch is used when the sensor voltage is less than V_{oo} (i. e., when the sensor temperature is less than 0C). It is also used when measuring temperature differences as will be described later.

The potentiometer R_a gives a way of changing the apparent temperature coefficient of the sensor diode. By suitable adjustment the apparent coefficients of many sensors can be made equal. Potentiometer R allows the apparent value of V_o (see Eq. (M. 1))of many sensor diodes to be made equal. Only one potentiometer, R, is used; but a separate R_a is used for each sensor. The setting of R for each sensor is recorded and used as needed.

Switch S_2 allows the zero setting of R to be determined.

The calibration procedure is fairly simple. First the sensor is placed in an ice bath, and, with D set to zero, R is adjusted to give a null reading on the bridge. Then the sensor is placed in a hot bath of known temperature, and the temperature coefficient a is determined. Suppose this has to be reduced to agree with the chosen standard value, a_{oo}.

Return the sensor to the ice bath and vary R. Rebalance with D. Then increase D in the ratio a_{oo}/a and rebalance with R_a. The latter is now set correctly. Return D to zero and rebalance with R. Record the value of the latter. The calibration is now complete.

Temperature differences can be measured directly by connecting one sensor to input A and a second to input B. Switches for accomplishing these connections are not shown. When this is done R must be set to the difference of the recorded settings for the two sensors.

4. THE NULL INDICATOR

The circuit that has been described will function properly only if the null-indicating bridge draws no current from the rest of the circuit. That is, inputs A and B (see Figure M-1) must be high impedance inputs.

The circuit that was used typically draws less than 2×10^{-10} amperes and has a (static) input impedance greater than 10^{12} ohms. The circuit achieved this performance with the use of common, inexpensive, vacuum tubes. The operation of this circuit will now be described.

The basic elements of the circuit are shown in Figure M-2. The bridge is formed by two triode vacuum tubes and their plate resistors. Switches S, S' are normally closed so the high-valued resistors are short-circuited and have no effect.

First, grids G and H are connected together, and R_B is adjusted until the meter reading is zero. Then they are connected as shown to voltages V_A and V_B, where $V_A = V_B$. Switch S is opened, and if the meter reading is observed to jump, potentiometer R is adjusted. When properly adjusted the meter reading is invariant to the state of S. Potentiometer R' is adjusted in a similar manner. When these adjustments have been made the bridge draws no current from the voltage sources V_A and V_B.

The possibility of achieving such a condition is shown by the following reasoning. Suppose input A is disconnected from the voltage source, V_A, and suppose that it then assumes a voltage, V_A'. The relation between V_A' and V_B is the following:

$$V_A' = V_B + e_{KH} - IR = i_g R_g \qquad (M.2)$$

where i_g is the grid current of the tube.

Clearly, V_A' can be made equal to V_A if R is adjusted so that

$$R = \frac{1}{I}\left[V_B - V_A + e_{KH} - i_g R_g\right] \qquad (M.3)$$

If V_A' is made equal to V_A by this adjustment then input A can be reconnected to the voltage source V_A without disturbing the latter in any way. That is, the circuit will draw no current from V_A. When this condition holds, switch S has no effect on the meter reading. Thus we have shown that adjustment for zero current to the bridge is always possible regardless of tube characteristics or leakage.

5. THE ACTUAL CIRCUIT

The actual circuit that was built is shown in Figure M-3. The bridge can detect a voltage difference of 4×10^{-4} volt, corresponding to a temperature difference of 0.02C.

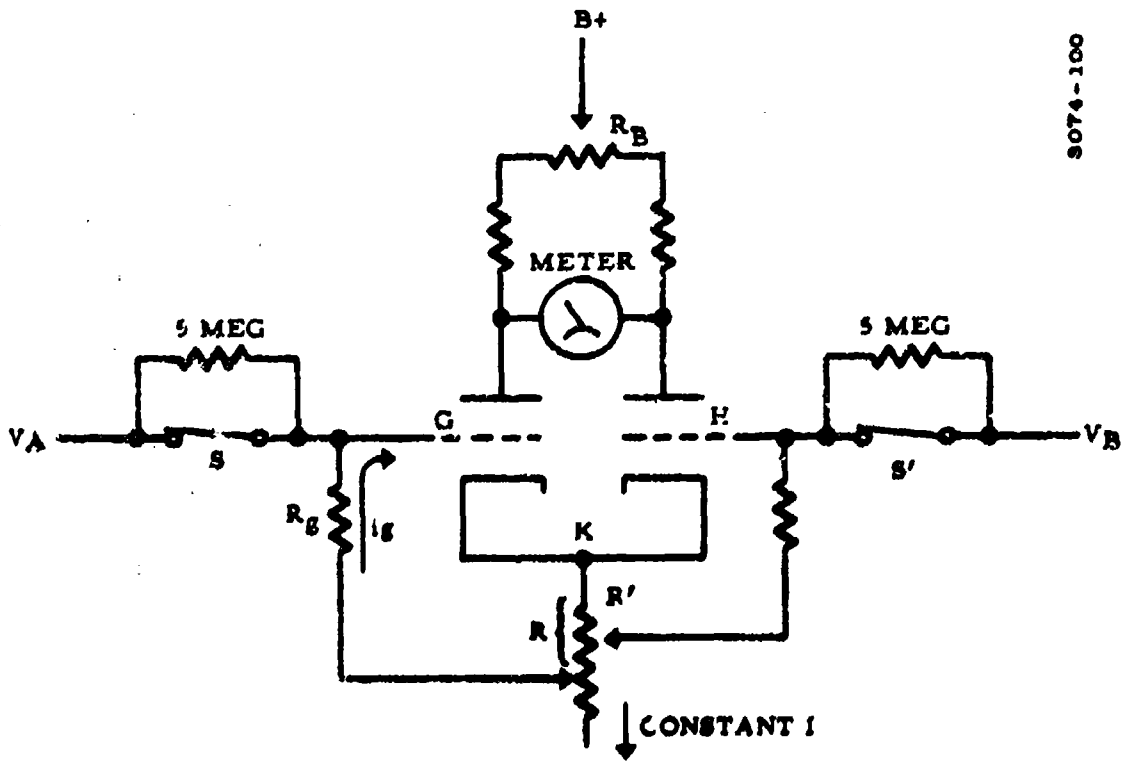


Figure M-2. Basic Circuit of Null-Indicating Bridge

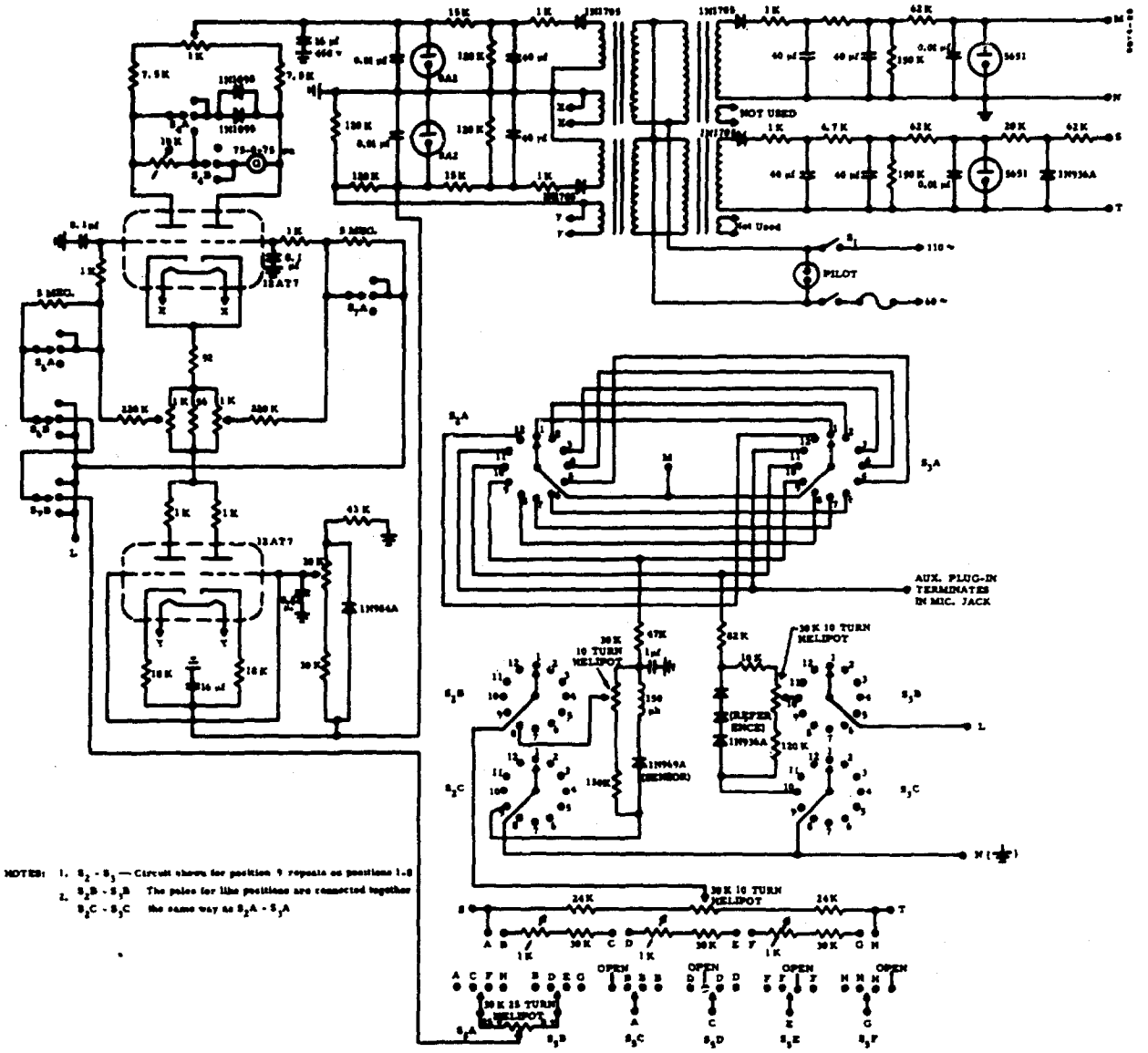


Figure M-3. Temperature-Sensing Circuit

An RC filter is located in the grid line of each bridge tube, and an LC filter is used in series with each sensor. These components reduce the amplitude of unwanted electrical noise. It is important that the unwanted noise be less than 0.2 volt peak-to-peak as measured across the meter circuit. Otherwise the meter-protecting diodes* conduct on the noise signal, and the sensitivity of the circuit is decreased. If necessary, filtering can be added at the meter circuit itself.

The readout device is a 25-turn potentiometer (linear to 0.05 percent) with an associated range-changing switch.

Any one of ten sensors can be compared to the 0C reference, or any pair of the ten can be employed to make difference readings.

The panel arrangement of the completed circuit is shown in Figure M-4.

The bridge tubes require a warmup time of about 30 minutes before drifts in the balance setting become undetectable.

When temperature difference measurements are made, and the mean temperature is significantly different from 0C, the grid current compensating potentiometers may require readjustment. This is particularly true if an accuracy of 0.1C is to be maintained (for this accuracy the bridge must draw less than 2×10^{-8} amperes input current).

6. EXPERIMENTAL TESTS

Various experimental tests were performed to check the operation of the bridge and the behavior of the sensors.

6.1 Drift

If the bridge is balanced with both inputs connected to the reference voltage the imbalance due to drifts is less than 0.02C in three hours.

*A. S. Penfold and E. L. Garwin, Rev. Sci. Inst., 29, 252 (1958).

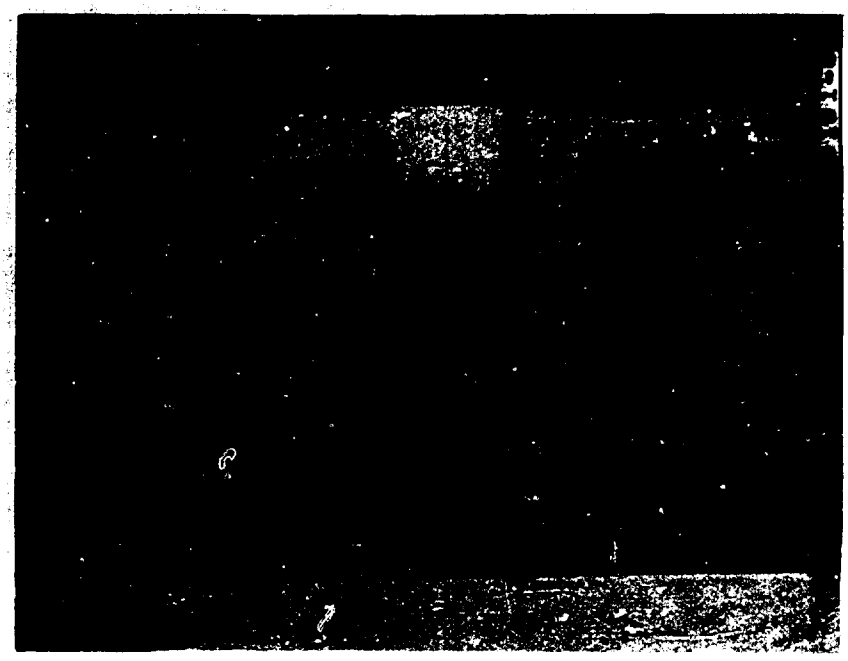


Figure M-4. Front Panel of Temperature-Sensing Circuit

6.2 Symmetry

If a temperature difference is measured and the connections of the sensors to the bridge are reversed, the same reading is obtained (but with opposite algebraic sign) to within ± 0.1C.

6.3 Reproducibility

Repeated measurements from several sensors, extending over a period of several days, indicated that the sensors are stable and that their voltage is reproducible to within 0.1C. Some difficulty was experienced in reproducing the temperature of the oil bath (used for the tests) to this accuracy.

6.4 Hysteresis

Heating and cooling measurements were made at rates of 40C/hr and 20 C/hr. A difference of 0.1 C was observed between the ascending and descending readings in the former case and 0.05 C in the latter. The entire effect is thought to be due to a slight thermal lag of the mercury theromometer employed as the standard.

6.5 Linearity

Figure M-5 shows the results of a typical linearity check. The output reading (dial reading) for two zener sensors is shown as a function of temperature. The curves were measured concurrently at a heating rate of 13 C/hr. The standard deviation of the points from best-fit straight lines is less than ± 0.05 C. No significant deviation from linearity occurs. The difference of the two curves is also shown. Since, when the tests were made, neither diode had been corrected for variations in V_o or α (Eq. (M.1)), the difference curve is expected to be a straight line. This is observed. The value of α for the two sensors differs by two percent. This is a typical result.

Finally, ten sensors were calibrated for the range 0 C-100 C, and their readings over this range were compared. They agreed to within ± 0.15 C. The experimental array of the ten sensors is shown in Figure M-6.

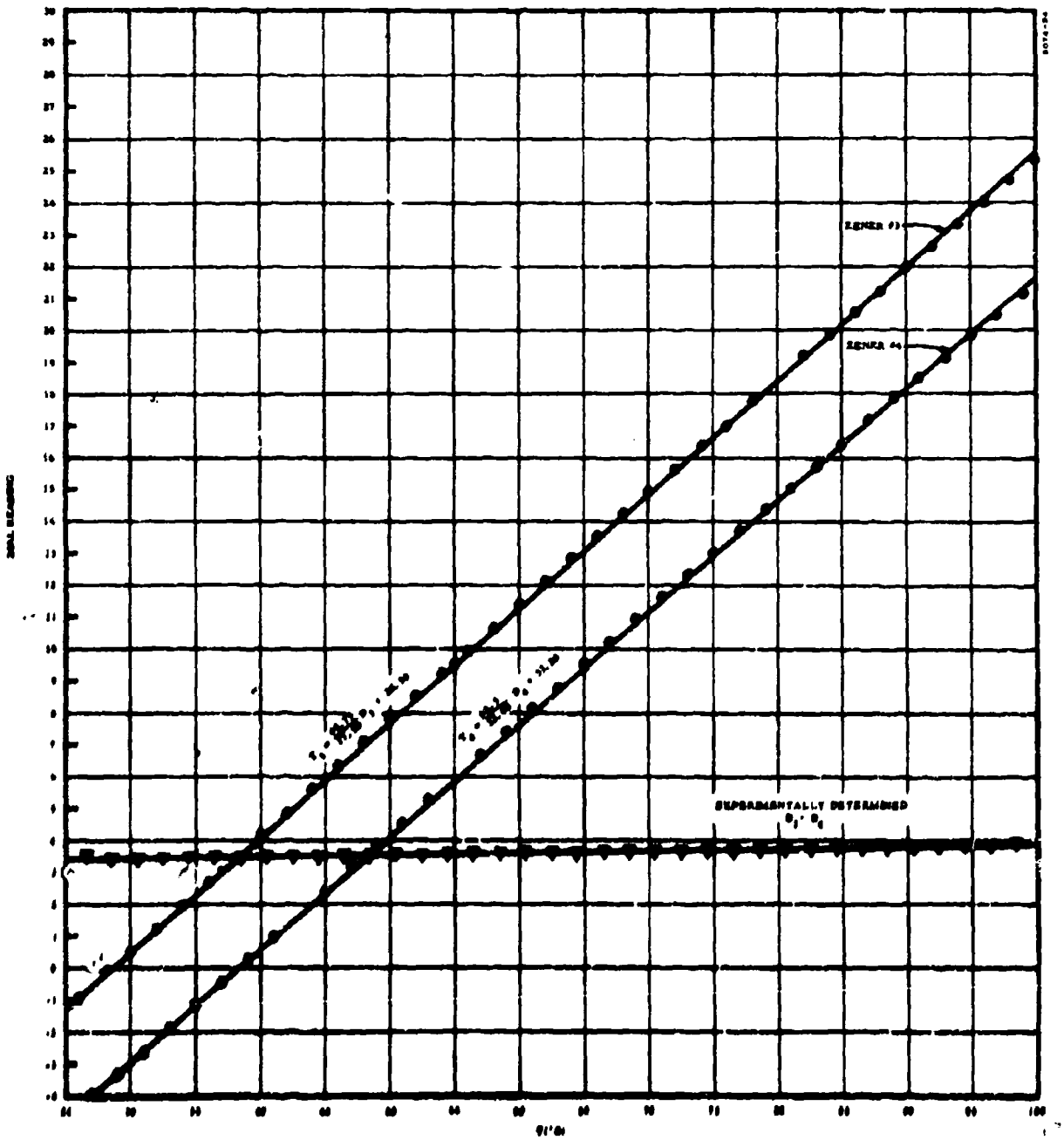
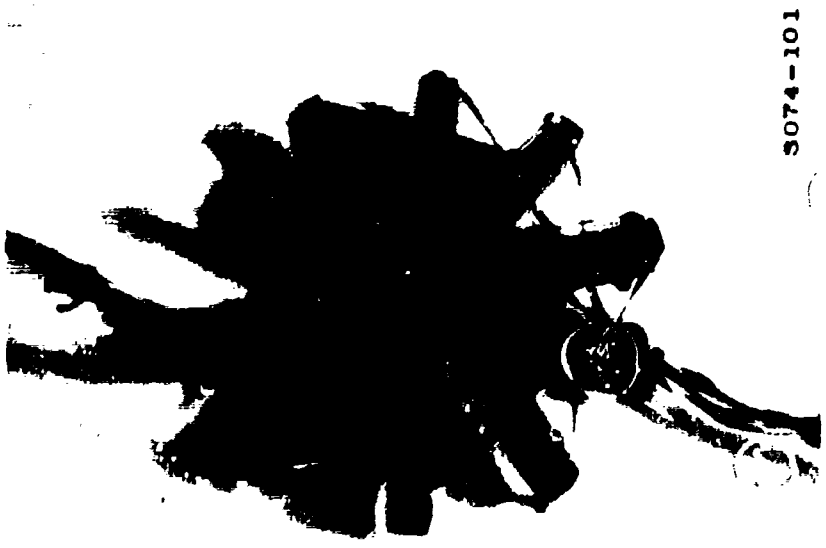


Figure M-5. Plot of Temperature vs. Dial Reading for Two Zener Diodes



3074-101

Figure M-6. Zener Diode Test Mount

APPENDIX N

SHIELDING AGAINST CAPACITIVE ELECTRIC FIELDS

APPENDIX N

SHIELDING AGAINST CAPACITIVE ELECTRIC FIELDS

1. INTRODUCTION

When a time-dependent voltage is applied to a set of coils, two electric field patterns exist within the geometry: that due to the time rate of change of magnetic flux and that due to the accumulation of charges on various parts of the system. The first type of field is the inductive electric field, and the second type is the capacitive electric field. The net field that acts on charged particles is the vector sum of the two fields.

In a plasma research device the capacitive field is a complicating factor that sometimes needs to be eliminated. Some of the confusion that arose in early studies of gaseous discharges because of this field has been described by MacKinnon[1] in a paper on the origin of the electrodeless discharge. Fortunately, in many situations of interest, the capacitive electric field can be strongly attenuated without seriously affecting the inductive field. The desired attenuation may be accomplished by applying a very thin coating of conducting material to the walls of the vacuum envelope that surrounds the volume of interest. The resistivity of the coating is usually noncritical, and variations of several orders of magnitude can be tolerated.

The possibility of this type of shielding has been recognized for some time and has been employed in experimental devices,[2,3] but very little information concerning it has been published.

The MKS system of units is used throughout this paper.

2. GEOMETRY

The geometrical arrangement chosen for the calculations that follow is shown in Figure N-1 and it is similar to the geometry used in the Mark II traveling wave plasma accelerator. The coils are sets of

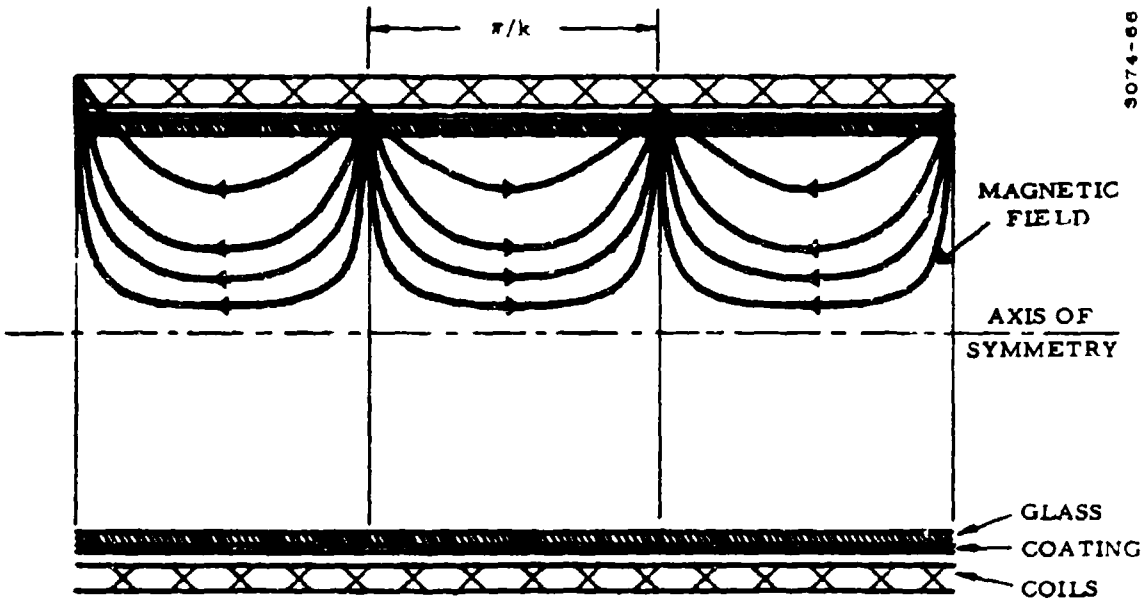


Figure N-1. Geometry

windings excited by a polyphase source of power, and the magnetic field pattern travels in the axial direction with speed ω/k, where ω is the circular frequency and k is the wave number.

The shielding effect caused by the coating on the glass is exactly the same for a traveling wave as for a standing wave of the same frequency and wavelength. For simplicity of calculation a standing wave is considered and, in addition, the following assumptions are made:

1. The magnetic field arises from an azimuthal sheet current that is distributed sinusoidally along the glass surface.
2. The capacitive electric field arises from a surface charge that is distributed sinusoidally along the glass surface.
3. Radiation can be neglected.
4. The coating has a uniform surface resistivity, η, and a thickness less than the skin depth for all frequencies of interest.
5. The sheet current, surface charge, and coating are very close to each other and all can be taken to be at radius $r = r_o$.
6. The vacuum region is free of plasma.

By virtue of the above-cited assumptions the voltage applied to the coils is also distributed sinusoidally along the glass. This condition is usually not satisfied since the distribution of voltage depends on the exact way in which the coils are connected to the power source. However, nonsinusoidal distributions can be studied by making a Fourier analysis and then applying the present results.

3. SUMMARY OF RESULTS

The sheet-current density and the surface-charge density are taken to have the following forms:

$$\vec{J} = \hat{\theta}\, J_o \sin(kz)\, e^{i\omega t} \qquad \text{(N. 1)}$$

$$\rho = \rho_o \cos(kz)\, e^{i\omega t} \qquad \text{(N. 2)}$$

It can be shown (Attachment 1) that both the magnetic field and the inductive electric field are modified by the same factor, M, due to the presence of the coating.

$$M = \frac{1}{1 + i\omega\lambda} = \frac{1}{\sqrt{1 + (\omega\lambda)^2}} e^{-i \arctan(\omega\lambda)} \qquad \text{(N. 3)}$$

The parameter, λ, is defined by the following equation

$$\lambda = \frac{1}{\omega_k} \frac{Z_o}{\eta} [I_1 K_1 kr_o] \qquad \text{(N. 4)}$$

where η is the surface resistivity of the coating, Z_o is the characteristic impedance of free space (376.7 ohms), and $\omega_k = ck$ (where c is the speed of light in vacuum). I_1 and K_1 are hyperbolic Bessel functions of first order, of argument kr, evaluated at kr_o.

M has the same form as the voltage transfer function for the simple L-R circuit shown in Figure N-2a. As the frequency is increased the initial effect on the magnetic field is a phase shift, followed, at higher frequencies, by an amplitude change.

The total effect of the coating can be described in terms of a "Q" defined by $Q = 1/\omega\lambda$. The magnitude of M is related to Q as follows:

$$|M| = \frac{Q}{\sqrt{1 + Q^2}} \qquad \text{(N. 5)}$$

In order that the Q be larger than a given value, the resistivity must satisfy the following condition:

$$\eta > QZ_o \left(\frac{\omega}{\omega_k}\right) I_1 K_1 kr_o \qquad \text{(N. 6)}$$

In the special case of a traveling wave, ω/ω_k is equal to v_f/c, where v_f is the speed of the field pattern and c is the speed of light.

It can be shown (Attachment 2) that the capacitive electric field is modified by a factor, E.

$$E = \frac{1}{1 - \frac{i}{\omega\delta}} = \frac{\omega\delta}{\sqrt{1 + (\omega\delta)^2}} e^{i \arctan\left(\frac{1}{\omega\delta}\right)} \qquad \text{(N. 7)}$$

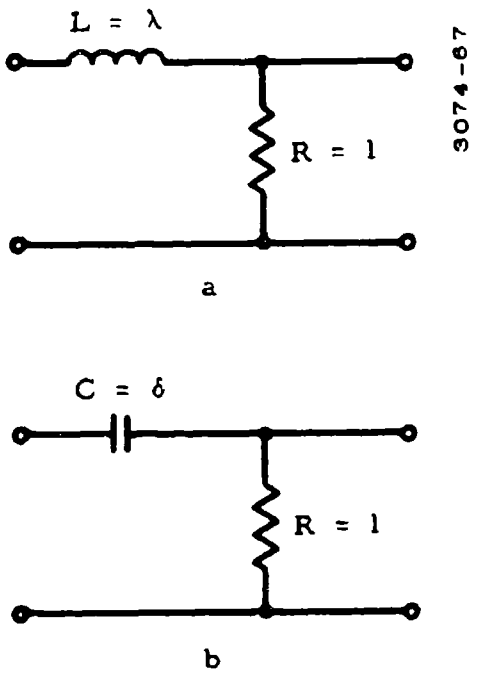


Figure N-2. Equivalent Circuits

The parameter, δ, is defined by the following equation:

$$\frac{1}{\delta} = \omega_k \frac{Z_o}{\eta} [I_o K_o kr_o] \qquad (N.8)$$

where I_o and K_o are hyperbolic Bessel functions of zero order and argument kr, evaluated at kr_o.

E has the same form as the voltage transfer function for the simple R-C circuit shown in Figure N-2b. As the frequency is increased the attenuation of the capacitive field decreases. In order that $|E|$ be less than a given value the resistivity must satisfy the following condition:

$$\eta < \frac{|E|}{\sqrt{1 - |E|^2}} Z_o \left(\frac{\omega_k}{\omega}\right) I_o K_o kr_o \qquad (N.9)$$

Eq. (N. 6) and (N. 9) show the possibility of choosing η so that $|E|$ is quite small while Q is still large.

A plot of the quantities $I_oK_okr_o$ and $I_1K_1kr_o$ as a function of kr_o is given in Figure N-3[4, 5]. It is seen that if kr_o is greater than unit then both quantities may be replaced by 1/2 with negligible error. When this is done Eq. (N. 6) and (N. 9) become the following:

$$\eta > \frac{QZ_o}{2} \left(\frac{\omega}{\omega_k}\right) \qquad (N.10)$$

$$\eta < \frac{|E|}{\sqrt{1 - |E|^2}} \frac{Z_o}{2} \left(\frac{\omega_k}{\omega}\right) \qquad (N.11)$$

If these equations are written as equalities the graphical representation of Figure N-4 can be drawn.

The analysis leading to Eq. (N. 10) is independent of that leading to Eq. (N. 11), and therefore the value of ω_k used in each may be chosen independently. For example, if the coil voltage is not distributed sinusoidally along the glass then a Fourier series can be employed, and the value of ω_k used in Eq. (N. 11) can be taken to be that corresponding to the longest wavelength in the Fourier series.

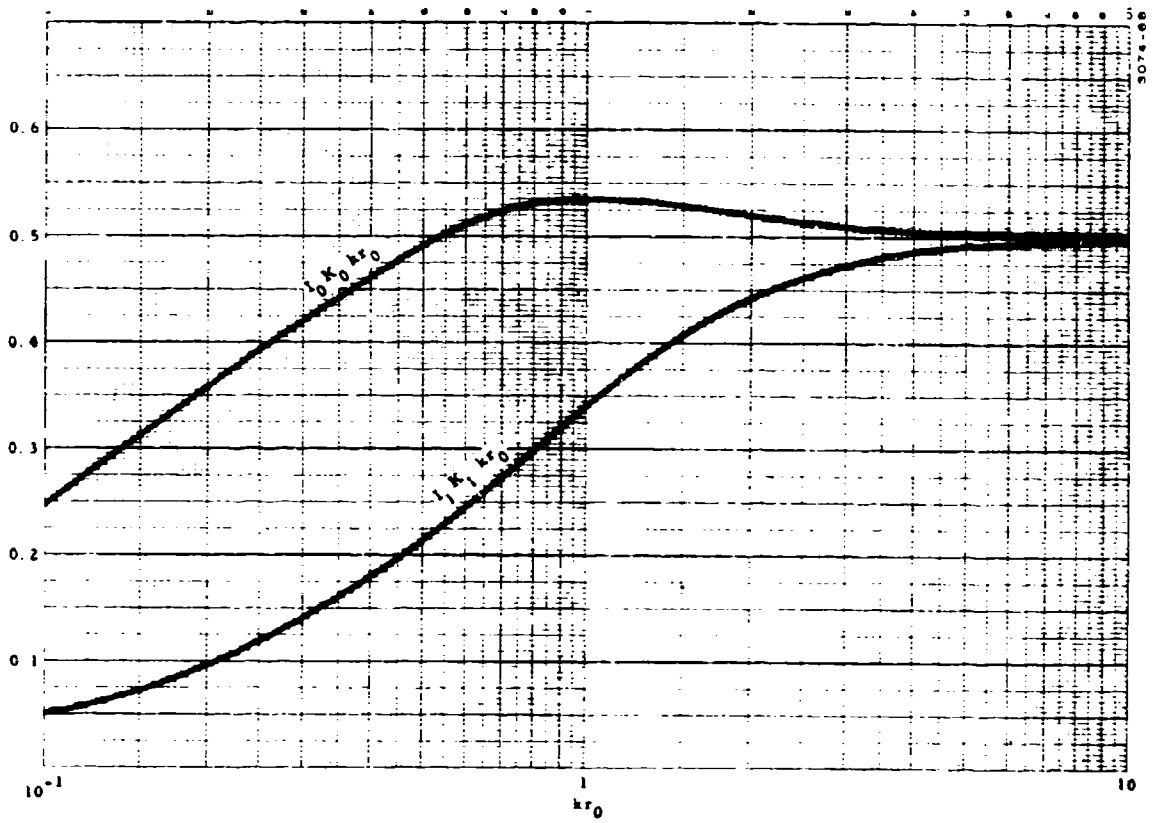


Figure N-3. Plot of $I_oK_okr_o$ and $I_1K_1kr_o$ vs kr_o

Example

In many cases of practical importance a wide variation of η is allowable. The following example is given to illustrate this fact.

Consider a traveling-wave device with a diameter of 0.16 meter, a wavelength of 0.2 meter, and an operating frequency of 250 kc. The following conditions apply:

$$v_f = \text{field speed} = 5 \times 10^4 \text{ meters/sec.}$$
$$k = \text{wave number} = 31.4 \text{ meter}^{-1}$$
$$v_f/c = \omega/\omega_k = 1.67 \times 10^{-4}$$
$$kr_o = 2.5$$

In addition, we will demand the following conditions:

$$Q \geq 100 \quad (|M| \geq 0.995)$$
$$|E| \leq 0.01$$

Since kr_o is larger than unity, the data of Figure N-4 can be used, and one finds that the required degree of shielding can be obtained with any value of η that falls in the range shown below.

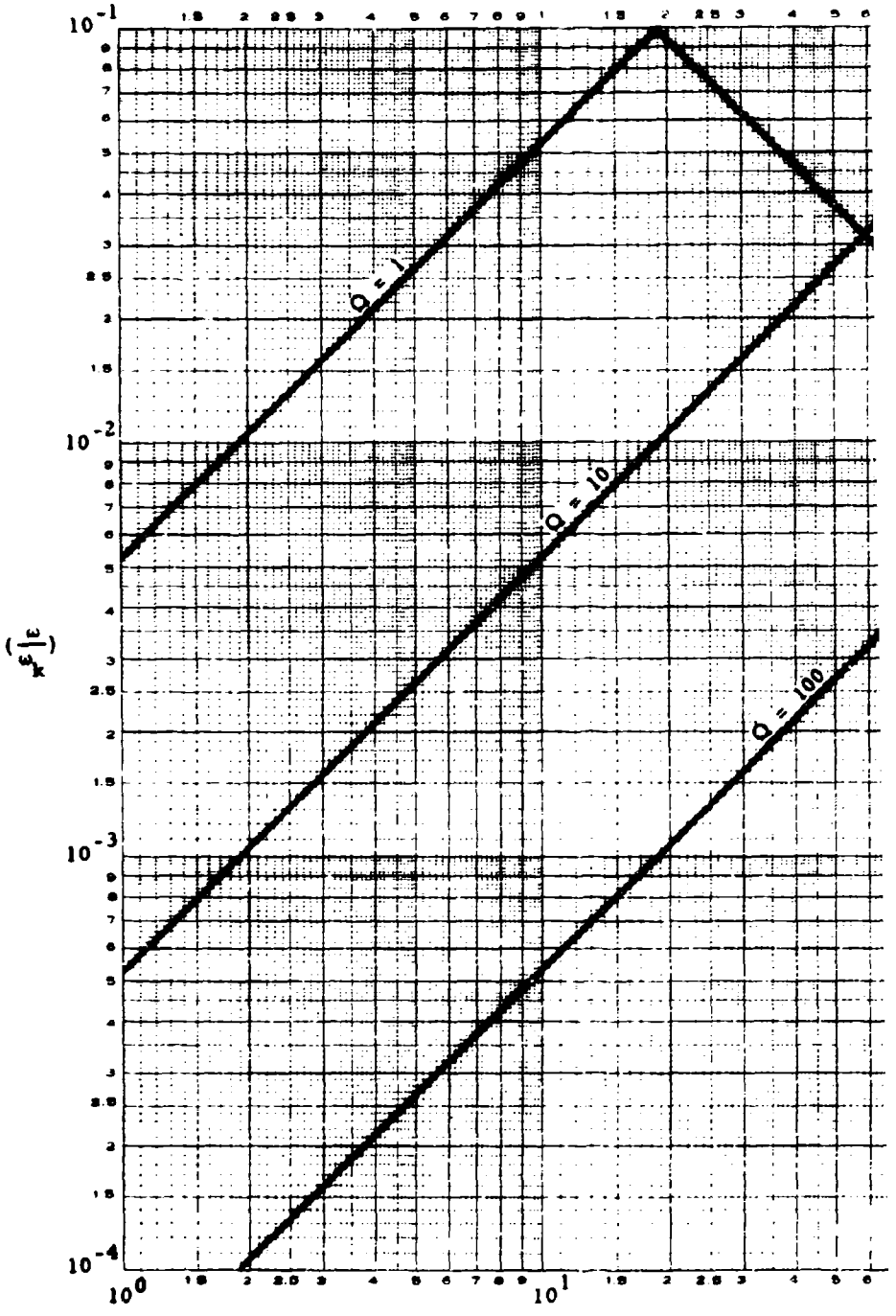
$$3.1 \leq \eta \leq 11,500 \text{ (ohms)}$$

4. TRANSIENT BEHAVIOR

The degree of shielding that can be obtained for transient conditions can be estimated through the use of L-R and R-C time constants derived from the equivalent circuits of Figure N-2. The time constant for the appearance of the magnetic field, τ_M, and for the disappearance of the capacitive field, τ_E, are found to be:

$$\tau_M = \frac{Z_o}{\eta\omega_k} I_1 K_1 kr_o \approx \frac{188.3}{\eta\omega_k} \qquad \text{(N. 12)}$$

$$\tau_E = \frac{\eta}{Z_o\omega_k} [I_o K_o kr_o]^{-1} \approx \frac{\eta}{188.3\,\omega_k} \qquad \text{(N. 13)}$$


10^{-1}
10^{-2}
10^{-3}
10^{-4}
10^{0}
10^{1}
Q = 1
Q = 10
Q = 100
$(\frac{\omega}{\omega_k})$

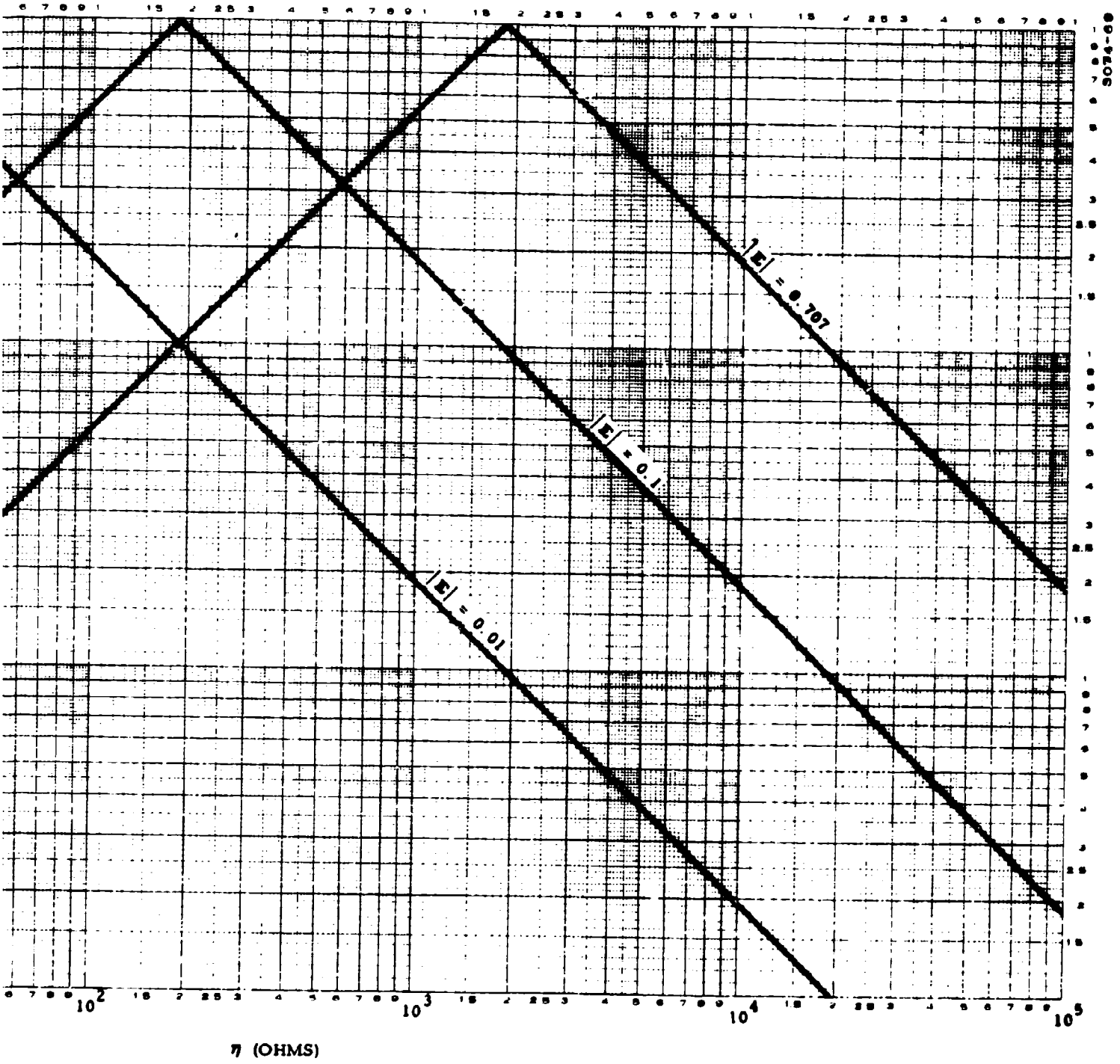


Figure N-4. Plot of ω/ω_k vs η

For the previous example, taking $\eta = 10^3$ ohms

$$\tau_M = 2 \times 10^{-9} \text{ sec}$$

$$\tau_E = 6 \times 10^{-8} \text{ sec}$$

REFERENCES

1. MacKinnon, K. A., "On the Origin of the Electrodeless Discharge", Phil. Mag., S. 7, Vol. 8, No. 52; Nov 1929.

2. Rogers, Dr. K. C., private communication; Feb. 1961.

3. Stevens Institute of Technology, Investigation of Plasma Acceleration, Final Report, SIT P37 (6/61); 1961.

4. Jahnke, E. and Emde, F., Tables of Functions, Dover Publications.

5. Dwight, H. B., Mathematical Tables, 2nd Edition, Dover Publications; 1958.

APPENDIX N

ATTACHMENT 1

In this attachment the expression for M given in Eq. (N. 3) is derived, using the fact that the applied sheet-current density is:

$$\vec{J} = \hat{\theta} J_o \sin(kz)\, e^{i\omega t} \qquad \text{(N1. 1)}$$

The vector potential for the field has only an azimuthal component, $A_\theta(r, z, t)$, and its axial dependence must be the same as that of the sheet current. Thus, we assume that

$$A_\theta \sim R(r) \sin(kz)\, e^{i\omega t} \qquad \text{(N1. 2)}$$

Except at $r = r_o$ (the radius of the sheet current and the conducting layer) the vector potential must satisfy:

$$\text{curl curl } \vec{A} = 0 \qquad \text{(N1. 3)}$$

When Eq. (N1. 2) is substituted into Eq. (N1. 3) a differential equation for R(r) results:

$$\frac{d}{dr}\left[\frac{1}{r}\frac{drR}{dr}\right] - k^2 R = 0 \qquad \text{(N1. 4)}$$

The solutions of the equation above are hyperbolic Bessel functions of order one, and one must select those that yield finite values of A_θ everywhere. If A and B are constants (whose values are yet to be determined) the solutions for A_θ are

$$A_\theta = AI_1(kr) \sin(kz)\, e^{i\omega t};\ r < r_o \qquad \text{(N1. 5)}$$

$$A_\theta = BK_1(kr) \sin(kz)\, e^{i\omega t};\ r > r_o \qquad \text{(N1. 6)}$$

Now A_θ is continuous at $r = r_o$; so B is determined by

$$B = \frac{I_1 (kr_o)}{K_1 (kr_o)} A \qquad \text{(N1. 7)}$$

The axial field component is easily obtained and is described by zero-order Bessel functions:

$$B_z = A k I_o (kr) \sin(kz) e^{i\omega t}; \; r < r_o \qquad \text{(N1. 8)}$$

$$B_z = - \frac{I_1 (kr_o)}{K_1 (kr_o)} A k K_o (kr) \sin(kz) e^{i\omega t}; \; r > r_o \qquad \text{(N1. 9)}$$

The axial field component is discontinuous at $r = r_o$ where it satisfies the following equation:

$$B_z \text{ (inside)} - B_z \text{ (outside)} = \mu_o [J + J'] \qquad \text{(N1. 10)}$$

J is the magnitude of the applied sheet current, and J' is the magnitude of the sheet current induced in the conducting layer by the inductive electric field. This field is obtained from the negative time derivative of A_θ. Then, through the use of ohm's law, the induced sheet current is found:

$$J' = - \frac{A}{\eta} I_1 (kr) i\omega \sin(kz) e^{i\omega t}; \qquad \text{(N1. 11)}$$

From the foregoing equations one can derive an equation for A. It is convenient to use the relation $\mu_o = Z_o/c$ (where Z_o is the characteristic impedance of free space and c is the speed of light) and the definition $\omega_k \equiv ck$. Then, the value of A is:

$$A = M \left[\frac{Z_o K_1 (kr_o) kr_o}{\omega_k} \right] J_o \qquad \text{(N1. 12)}$$

Where

$$M = [1 + i\omega\lambda]^{-1} \qquad \text{(N1. 13)}$$

and

$$\lambda = \frac{1}{\omega_k} \frac{Z_o}{\eta} [I_1 (kr_o) K_1 (kr_o) kr_o] \qquad \text{(N1. 14)}$$

The conducting layer is seen to modify both the magnetic field components and the induced electric field by the factor, M.

APPENDIX N

ATTACHMENT 2

In this attachment the expression for E given in Eq. (N. 7) is derived, using the fact that the applied surface-charge density is:

$$\rho = \rho_o \cos(kz)\, e^{i\omega t} \qquad \text{(N2.1)}$$

The scalar potential for the electric field does not depend on azimuth because of the symmetry, and its axial dependence must be the same as that of the surface charge. Thus, we assume that

$$\phi \sim R(r) \cos(kz)\, e^{i\omega t} \qquad \text{(N2. 2)}$$

Except at $r = r_o$ (the radius of the surface charge and the conducting layer) the scalar potential must satisfy the following:

$$\text{div grad}\, \phi = 0 \qquad \text{(N2. 3)}$$

When Eq. (N2. 2) is substituted into Eq. (N2. 3) a differential equation for R(r) results:

$$\frac{1}{r} \frac{d}{dr} r \frac{dR}{dr} - k^2 R = 0 \qquad \text{(N2. 4)}$$

The solutions of the equation above are hyperbolic Bessel functions of zero order, and one must select those that yield finite values of ϕ everywhere. If C and D are constants (whose values are not yet determined) the solutions for ϕ are found to be

$$\phi = C I_o (kr) \cos(kz) e^{i\omega t};\ r < r_o \qquad \text{(N2. 5)}$$

$$\phi = D K_o (kr) \cos(kz) e^{i\omega t};\ r > r_o \qquad \text{(N2. 6)}$$

Now ϕ is continuous at $r = r_o$; so D is determined by

$$D = \frac{I_o(kr_o)}{K_o(kr_o)} C \qquad \text{(N2. 7)}$$

The radial field component is easily obtained, and it is described by first-order Bessel functions.

$$E_r = -CkI_1(kr)\cos(kz)e^{i\omega t};\ r < r_o \qquad \text{(N2. 8)}$$

$$E_r = \frac{I_o(kr_o)}{K_o(kr_o)} CkK_1(kr)\cos(kz)e^{i\omega t};\ r > r_o \qquad \text{(N2. 9)}$$

The radial field component is discontinuous at $r = r_o$ where it satisfies the following equation:

$$E_r\,(\text{outside}) - E_r\,(\text{inside}) = \frac{1}{\epsilon_o}\,[\rho + \rho'] \qquad \text{(N2. 10)}$$

Where ρ is the magnitude of the applied surface charge and ρ' is the magnitude of the surface charge induced in the conducting layer by the capacitive field. The induced surface charge is found from Ohm's law and the charge-conservation equation, and it has the following value:

$$\rho' = -C\,\frac{k^2 I_o(kr_o)}{i\omega\eta}\cos(kz)e^{i\omega t} \qquad \text{(N2.11)}$$

From the foregoing equations one can derive an equation for C. It is convenient to use the relation $\epsilon_o = (Z_o c)^{-1}$ (where Z_o is the characteristic impedance of free space and c is the speed of light) and the definition $\omega_k \equiv ck$. Then, the value of C is:

$$C = E\left[\frac{Z_o c K_o(kr_o) kr_o}{k}\right]\rho_o \qquad \text{(N2. 12)}$$

where

$$E = \left[1 + \frac{1}{i\omega\delta}\right]^{-1} \qquad \text{(N2. 13)}$$

and

$$\frac{1}{\delta} = \omega_k \frac{Z_o}{\eta} \left[I_o (kr_o) K_o (kr_o) kr_o \right] \qquad \text{(N2. 14)}$$

The conducting layer is seen to modify the electric field by the factor, E.

APPENDIX P

A SINGLE-PHASE INDUCTION PLASMA ACCELERATOR

NOTE

This appendix contains a document published in 1962 as Litton TM 62-46A.

The theoretical analysis presented in the document represents a step in the development of a theoretical model. It is now felt that the analysis was oversimplified insofar as the effects of thermal expansion are concerned.

Publication No. 2542

Technical Memorandum 62 - 46A

A SINGLE-PHASE INDUCTION PLASMA ACCELERATOR

by

D. L. Curtis and A. S. Penfold

7 December 1962

This document contains proprietary information of Litton Systems, Inc. Any reproduction, use and/or disclosure of this document and/or any portions thereof is expressly prohibited without the prior written consent of Litton Systems, Inc.

LITTON SYSTEMS, INC.
Space Sciences Laboratory
336 North Foothill Road, Beverly Hills, California

CONTENTS

I	INTRODUCTION	1
II	DISCUSSION OF EXPERIMENTS	3
	2.1 Description of the Accelerator	3
	2.2 Experimental Results	5
III	THEORETICAL DISCUSSION OF ACCELERATOR	19
	3.1 General Considerations	19
	3.2 Discussion of the Magnetic Field Pattern	21
	3.3 Extension of the Two-Fluid Model	22
	3.4 Comparison to Experiment	32
IV	CONCLUSIONS	37
	REFERENCES	39

I INTRODUCTION

In the spring of 1960 a series of experiments was begun, under Litton Systems, Inc. sponsorship, with a plasma accelerator consisting of a few turns of copper tubing wound to a conical shape. The first tests used a high-voltage dc power supply, an energy storage capacitor, and a spark-gap switch. The device was operated at the natural repetition rate of the charging circuitry - typically several discharges per second. These tests indicated that the device was capable of forming and accelerating plasma, but because of the pulsed nature of the discharge it was difficult to determine the behavior in detail.

Later tests were carried out with the device operating CW from a radio-frequency power source. Various gases including air, nitrogen, helium, argon, and carbon dioxide were successfully tried. The detailed operation of the accelerator varied with the gas used, chiefly with respect to the ease of obtaining ionization; but the qualitative features of the performance were not affected by the type of gas employed. Specific impulses in the range 400 to 2500 seconds were obtained, and thrust levels in the range 0.9×10^{-2} to 4.5×10^{-2} newton (2 to 10 millipounds) were measured. However, the efficiency seemed low, and it was supposed that there was a large neutral efflux of low velocity.

Recently, the concept of the accelerator has been subjected to a detailed re-examination, and in this process the experimental data have been re-valuated. The more careful analysis shows that the performance was much better than originally believed and that the ionizing process is particularly efficient. A figure of merit of <270 electron volts per ion pair was obtained for nitrogen. This is some two times lower than values being currently quoted for Cs ion engines and 2.8 times lower than values quoted for Hg bombardment-type ion engines.

This document examines the experimental data of one set of measurements and advances a theoretical model to explain the results.

II DISCUSSION OF EXPERIMENTS

2.1 DESCRIPTION OF THE ACCELERATOR

Figure 2-1 gives a schematic description of the accelerator. It consisted of nine turns of copper tubing wound on a pyrex funnel. The copper tubing was connected through an air-core isolating transformer to a 1.7 Mc power source. The cone-angle was 60 degrees and the mouth of the funnel was 0.1 meters across. A flow of cooling water was passed through the copper tubing, and the water system contained flow and temperature measuring gear. The isolating transformer was center-tapped to ground.

A ceramic-like material (not shown in Figure 2-1) coated the copper coils to prevent gas discharges from occuring along the outside of the funnel. Several tungsten wires were placed along the pyrex wall near the apex of the cone as indicated in Figure 2-1. These wires were observed to aid in the initiation of the gas discharge.

The gas was admitted from the stem of the funnel and was not preionized, or preheated. A flow-measuring system was devised and included in the gas line.

The accelerator was placed inside a vacuum chamber 8 feet in diameter by 15 feet long. The diffusion pumps on the chamber were able to maintain a vacuum of 0.6 micron when the gas flow-rate was 2×10^{-6} kilogram per sec. Various pieces of diagnostic equipment were manipulated in front of the accelerator by means of a small trolley and hoist system operating from an I-beam located along the top of the vacuum tank. The diagnostic gear could be positioned without breaking the vacuum.

A ballistic pendulum was employed to measure thrust. Inasmuch as the energy density in the beam was low and the specific impulse of the gas was low, the heating of the pendulum was small and the ablation of material from the pendulum was negligible. (Recently[1] a series of experimental results have indicated that data obtained with a ballistic pendulum may be seriously in error. However, these results apply to a pulsed accelerator of high

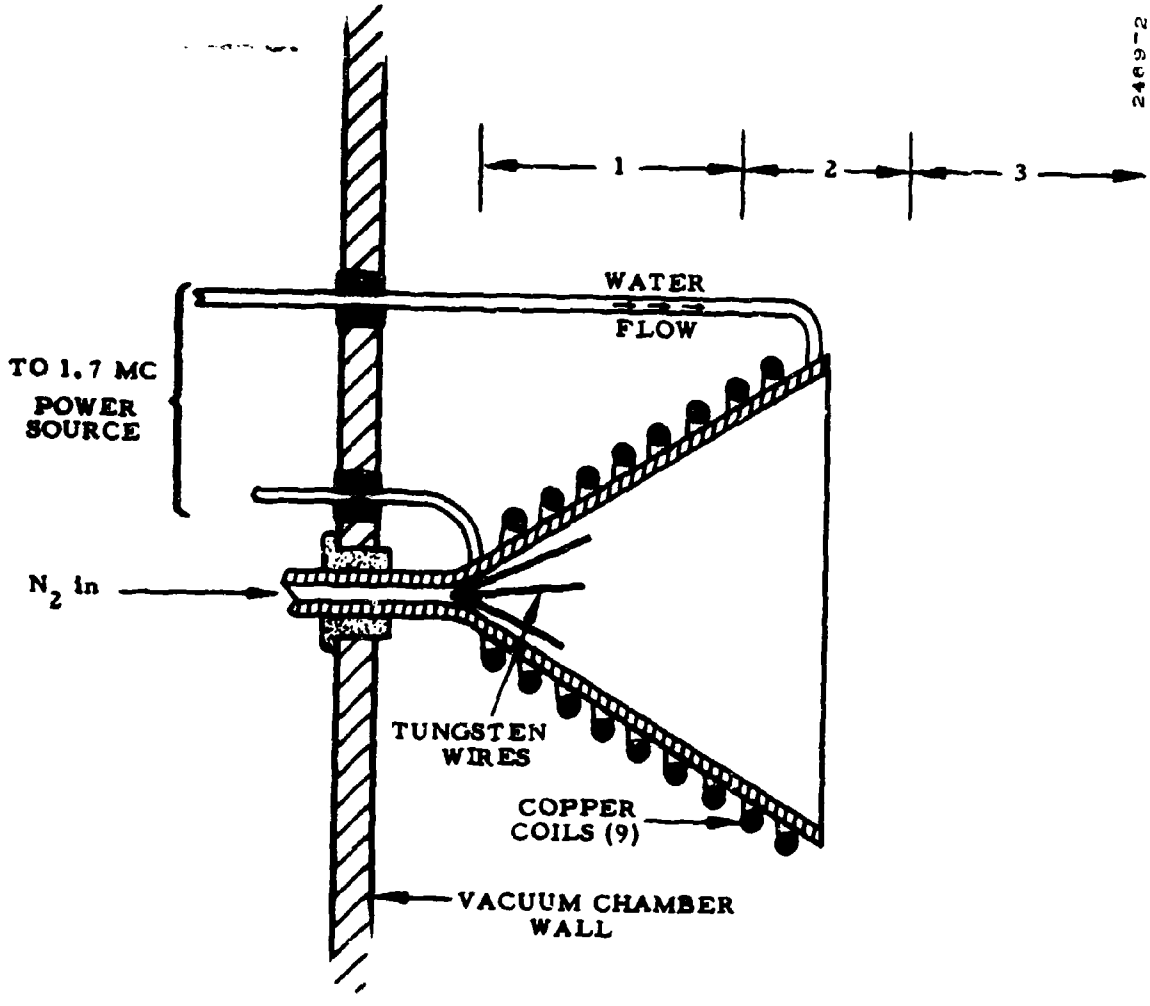


Figure 2-1. Schematic Description of Accelerator

specific impulse where the instantaneous rate of energy delivery to the pendulum is much greater than for the experiments described here.)

Figure 2-2 shows the shape of the pendulum employed. It was suspended from the ceiling of the vacuum tank by light threads and was located so that the thin neck was on the axis of symmetry of the accelerator. Thus the pendulum sampled thrust with a weighting factor proportional to distance from the axis of symmetry. This is in accord with the distribution of material in the efflux, and one can compute the total thrust with a simple multiplication factor. The pendulum intercepted 14.7% of the beam. The mass was 0.064 kilogram, and deflections up to 6 mm were observed under steady-state conditions of operation. A small thermocouple was attached to the pendulum to obtain temperature rate-of-rise data.

2.2 EXPERIMENTAL RESULTS

When gas was admitted to the accelerator nothing was observed to happen until the pressure of the gas at the apex of the funnel reached a value of several hundred microns Hg. Then a glow discharge began which quickly developed into a heavy discharge. At the same time a luminous efflux (usually blue-purple in color) appeared which extended from the mouth of the funnel and was clearly visible for several feet into the vacuum tank. The angle of divergence of the luminosity was close to 30 degrees (the half-angle of the funnel), but photographs with long time exposures indicated a faint luminosity which diverged at 60 to 70 degrees.

Simple reasoning leads one to consider three major regions of the funnel as indicated on Figure 2-1. In region 1 the magnetic field lines are nearly parallel to the axis of symmetry and would lead to acceleration in the radial direction. However, the density of gas is high and its temperature is low so collisions are frequent, and not much acceleration is expected. Thus, region 1 is the ionizing and heating region. In region 2 the magnetic field lines are fringing rapidly, and as the current through the coils rises and falls the field lines tend to move back and forth in an axial direction. Ionized material will be accelerated away from the funnel, and the gas density will drop rapidly; so region 2 is the accelerating region. In region 3 the gas is up to maximum speed, and the density is extremely low (much less than one micron Hg) so collisions are infrequent; region 3 is the free-flight region.

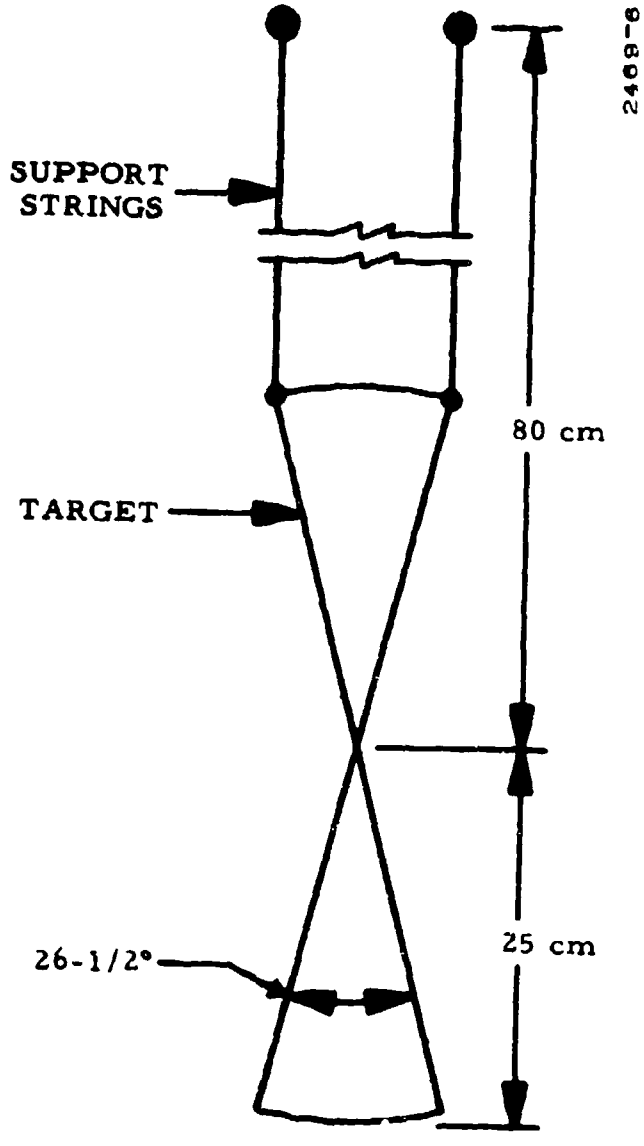


Figure 2-2. Pendulum Configuration

The simple picture presented above was checked experimentally. A small flag of compressed-mica paper was placed at various positions within and in front of the accelerator. In region 1 the flag was observed to hang vertically because of gravity. In region 2 the flag began to be deflected by the plasma wind and in region 3 the flag pointed along the plasma flow lines. These flow lines were coincident with a line drawn from the position of the flag to the apex of the funnel in agreement with the flow pattern of the luminosity.

Visual inspection of the luminosity near the apex of the funnel showed it to be concentrated around the axis of symmetry – not near the pyrex walls as one would e :pect if the ionizing process were inductive in character. In addition, when a small tungsten disc was placed on the axis of symmetry near the apex, the luminosity was observed to drop significantly, indicating that the sustaining ionization was originating from the region near the axis. This observation also speaks against an inductive process. Near the apex of the funnel the voltage was small. It was determined to be about 20 volts per turn. This is too small a voltage to cause breakdown of the gas. From all these observations one tends to conclude that some mechanism other than induction sustains the ionization.

A large, light pendulum was placed in front of the accelerator several feet from the mouth of the funnel. A strong permanent magnet was interposed between the accelerator and the pendulum. The luminosity was observed to be stopped by the magnetic field, and the deflection of the pendulum was reduced to less than 10% of the unobstructed value. A nonmagnetic object of the same cross-sectional area as the magnet was then sustituted for the magnet and the pendulum again deflected strongly. These observations lead to the following conclusions:

1. Nearly all of the high-speed gas leaving the accelerator was ionized. The neutral efflux was not heated by an amount sufficient to give significant thrust.
2. The luminosity was associated with ionized material only and was not due to excited-state transitions of neutral atoms.

An attempt was made to determine the plasma speed by using a small secondary-emission probe. The probe was placed in front of the accelerator at one meter distance, and the accelerator was operated and the probe current observed. The accelerator was then suddenly turned off; the transient probe signal was observed. A sudden change in the signal

was observed a few microseconds after turnoff, and this signal was determined to be associated with the decay of the ultraviolet light flux from the apex of the funnel as the discharge ceased. At a later time the probe signal changed again and gradually decreased to zero. The second change was taken to be associated with the arrival of the last of the plasma from the accelerator. The speeds derived in this way were larger than those derived from the pendulum by a factor of four, and they were larger than those derived from theoretical considerations by about the same factor.

The driving voltage applied to the accelerator was not shielded from the diagnostic region. An insulating material was placed over the coils to prevent a strong discharge from occuring along the outside of the funnel. None was observed to occur. However, it is possible that some material is accelerated to high speed by this capacitive electric field. If so the speed of the material would vary as the square root of total voltage applied to the accelerator. Figure 2-3 shows the result of plotting the measured speeds against the square root of voltage. It is seen that the points fall along a straight line which passes through the origin, and so the conjecture is verified.

In contrast to the behavior discussed above, the measured values of thrust should depend on the magnetic field strength. The induced currents in the plasma depend on the induced electric field and therefore on the applied voltage. The magnetic field strength depends on the applied current. Since the magnetic forces depend on the product of field and gas current, the force will vary as the voltage-current product for the coil. The impulse delivered to the plasma depends on the magnetic force; therefore,it follows that the measured thrust should vary as the voltage-current product. This relation was tested. The results are shown in Figure 2-4. A straight-line relation is obeyed. If the magnetic field served only to provide an electric field which heated the gas by Joule heating, then the energy would vary as the square of the coil voltage, and the measured thrust would depend less strongly than linearly on the applied voltage. Figure 2-4 shows that this is not the case, and that the device <u>is primarily an induction accelerator</u>.

A particular set of experimental results will be analysed in detail in the following paragraphs. The pertinent experimental information is listed in Table II-1.

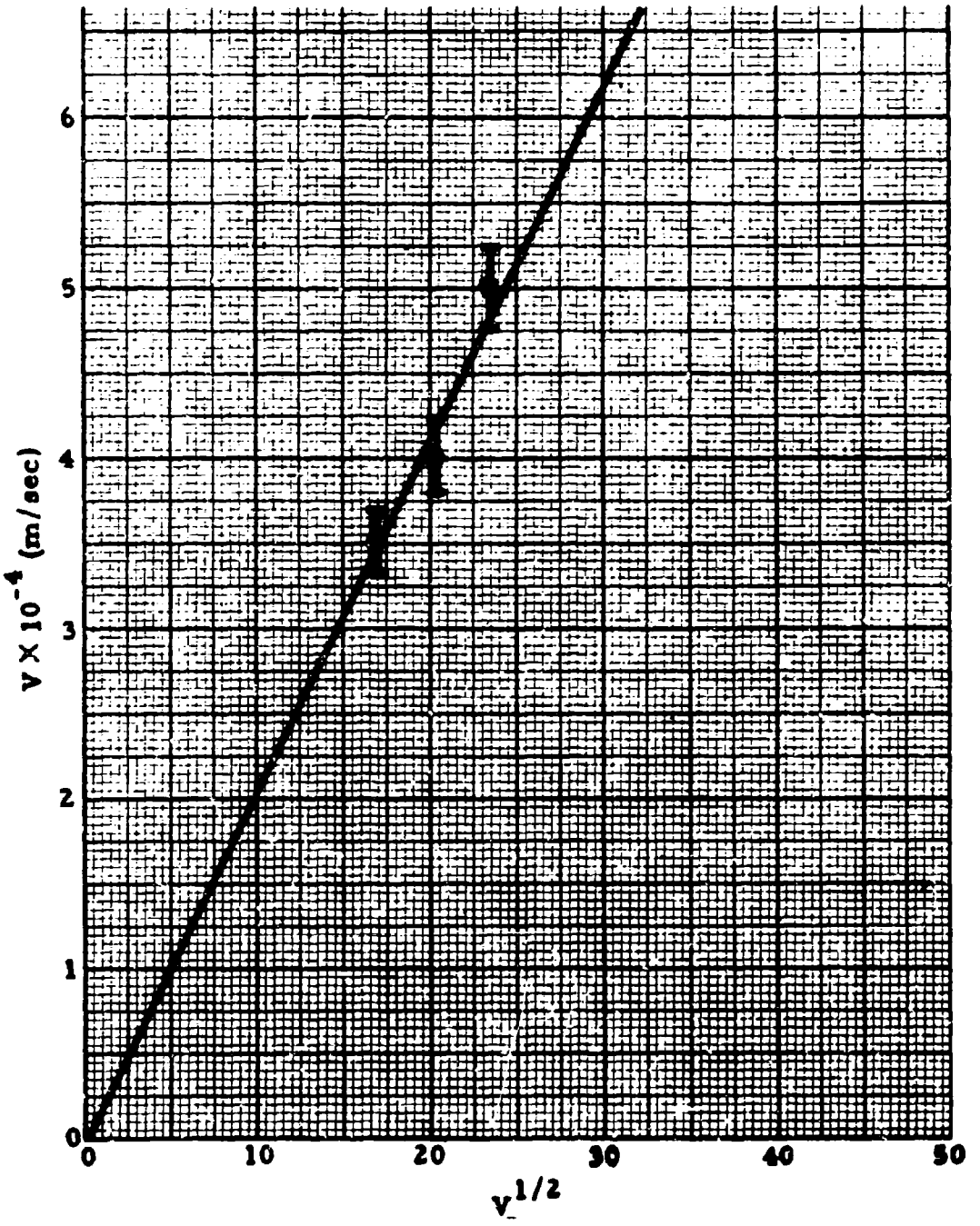


Figure 2-3. Plot of Measured Speeds vs Square Root of Voltage

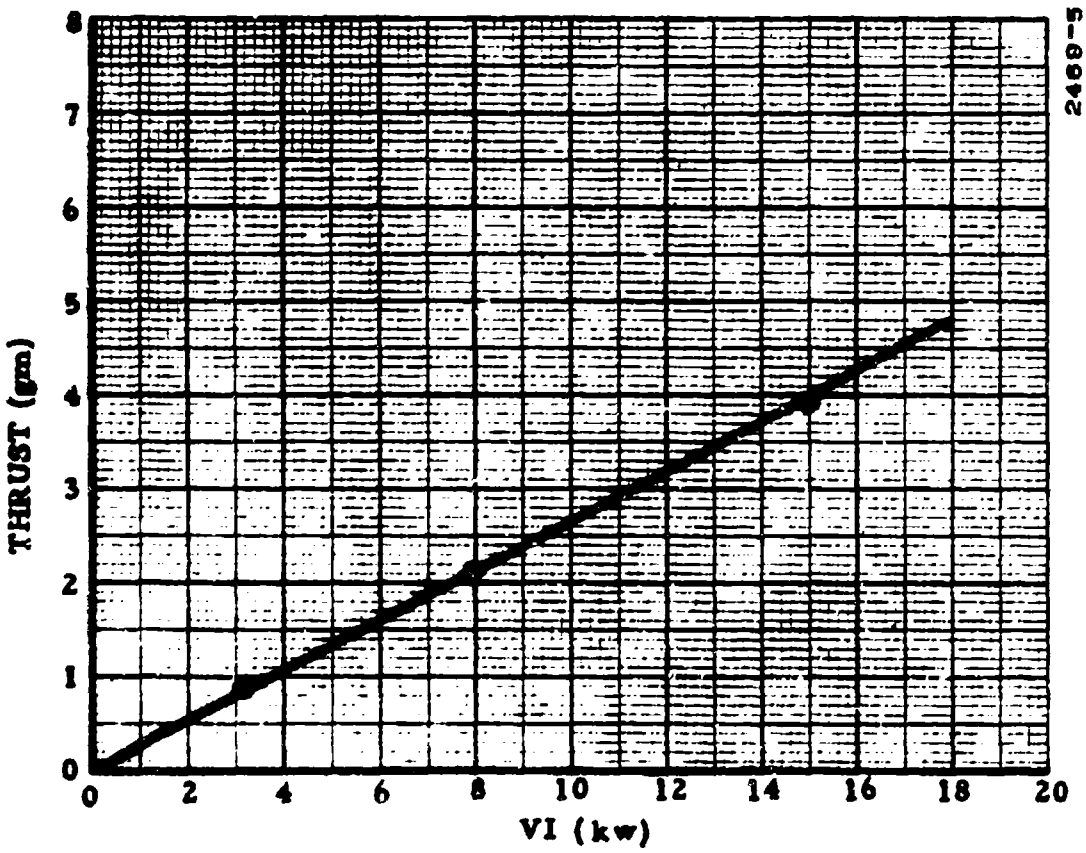


Figure 2-4. Plot of Measured Thrust vs Voltage – Current Product

TABLE II-1

EXPERIMENTAL RESULTS

Accelerator Data	
unloaded inductance	2.4×10^{-6} henry
conical angle	60°
maximum diameter (inner)	0.09 meter
Power Data	
frequency	1.7 Mc
voltage (rms)	410 v
current (rms)	19 amp
V-I phase angle	81.5°
computed input power	1150 w
Heat-Flow Data	
heat lost to funnel coolant liquid	810 w
Joule heating loss of coils (computed)	8 w
heat received by ballistic target	350 w
Thrust Data	
pendulum deflection	5×10^{-3} meter
calculated thrust	2.1×10^{-2} newton
estimated experimental error	± 10%
(1 Newton = .224 pound)	

TABLE II-1 (Cont)

Gas Flow Data

gas used	nitrogen
flow-rate	2×10^{-6} kgm/sec

(1 kgm/sec = 2.21 lb/sec)

Specific Impulse

The measured thrust divided by the measured flow-rate gives a specific impulse of 1050 seconds.

The threshold energies for the various ion species that could be present are:

N_2^+	- 15.5 volts	
N_2^{++}	- 45 volts	
N^+	- 38.8 volts	includes dissociation energy of 24.3 volts
N^{++}	- 53.8 volts	

Recently an experiment on electron bombardment of nitrogen has been reported[2]. In these experiments no N^+ yield was observed at all for bombarding energies up to 50 volts. Above that energy the experiment could not separate the N^+ yield from the N_2^{++} yield. At 100 volts the sum of the N^+ yield and twice the N_2^{++} yield was only 40% of the N_2^+ yield. These observations make it seem unlikely that there was a significant fraction of doubly ionized species in the beam from the conical accelerator. This strong suppression of dissociated species is also supported by two other experimental observations:

1. When CO_2 was used in the accelerator there was no observable carbon deposit on the pendulum or on the chamber walls. This is presumably accounted for by the tenacity of the C-O bond.

2. Experiments with nitrous oxide[3] show little yield of dissociated species because of the tenacity of the N-O bond.

In view of these arguments, and also because of the results of the experiments conducted with the deflecting magnet, it is concluded that the thrust is due to singly-charged nitrogen molecules exclusively. The power required to cause the gas input-flow to ionize completely is then computed to be 107 watts.

A value for the directed beam power can be derived from the measured thrust and the flow-rate. In order to make this calculation, one must take into consideration the average angle of impact on the ballistic pendulum (70°) and the ratio of the mean plasma speed to the root-mean-square plasma speed. Simple considerations regarding the distribution of magnetic field across the mouth of the accelerator show that there is a considerable spread of energies in the output and that the ratio is about 8/9 when the accelerator is lightly loaded, and smaller than this if the loading is heavy. In order to get a conservative value for the beam power, a value of 8/9 was assumed. It was then calculated that the directed beam power was 136 watts if all the gas was ionized.

The heat-flow data show that the sum of the power lost to the pendulum (350 watts) and that lost to the accelerator walls (810 watts) equals the input power. This provides a check on the measurements. The data also show that the Joule heating of the accelerator coils was negligible.

It is now assumed that only a fraction, X, of the molecules becomes ionized, and that the electrons in the efflux are very much hotter than the ions. Then, the power measurements discussed above can be used to obtain an equation for the heat energy in the efflux. If H is the electron heat energy in electron volts then:

$$\frac{19.7}{X} + 15.5\,X + H\,X = 50.7 \qquad (1)$$

Eq. (1) yields the curve shown by the solid line in Figure 2-5. It is seen that the heat energy is bounded and cannot exceed 17 electron volts. Also, since H cannot be negative it is seen that more than 45.5% of all the gas was ionized.

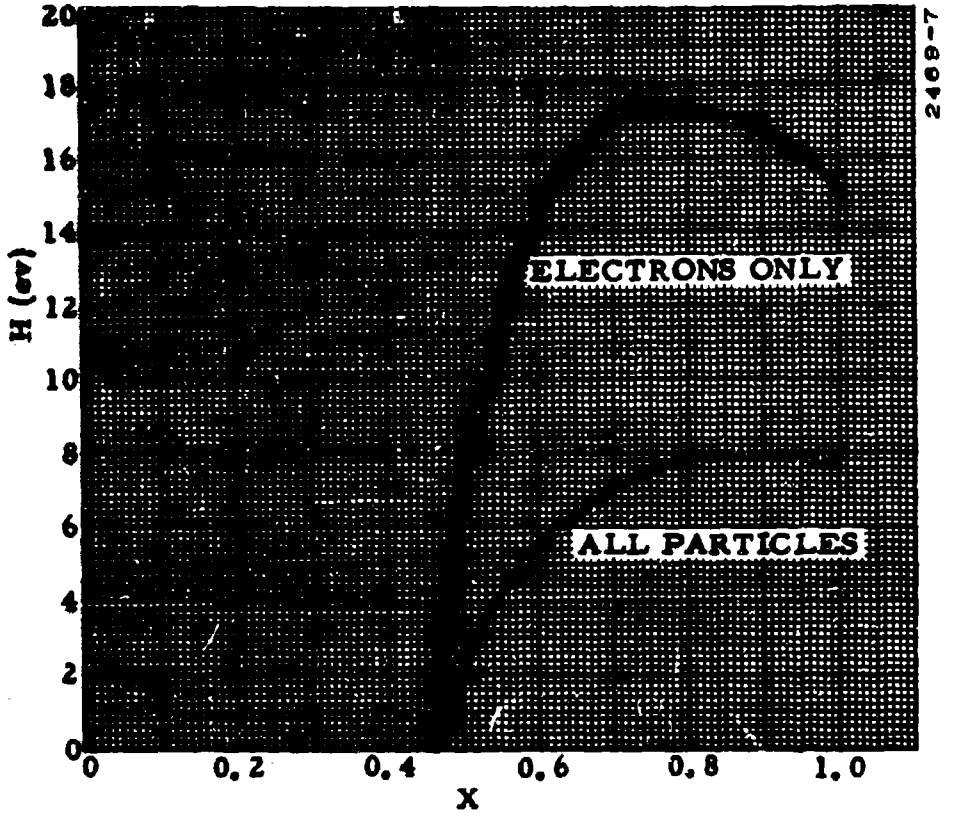


Figure 2-5. Plot of Heat Energy vs Fraction of Ionized Molecules

On the other hand, if one argues that the electrons are not much hotter than the ions, one must also assume that the un-ionized material is heated as well. In that case Eq. (1) must be rewritten:

$$\frac{19.7}{X} + 15.5\,X + \frac{X+1}{X}\,H = 50.7 \qquad (2)$$

Eq. (2) yields the curve shown by the dashed line in Figure 2-5. It shows the same cut-off point at X = 45.5%. When one remembers that one electron volt is equivalent to 10^4 degrees Kelvin, one realizes that Eq. (2) implies extremely hot material, and its use is questionable. On the other hand, the electrons can easily be much hotter than the ions and are expected to have energies roughly equivalent to the whole accelerating energy (40 volts for X = 0.5). This will be discussed further in Section III.

In a similar fashion the energy required to make an electron-ion pair can be derived from the input power and the directed power obtained from the thrust measurement. The equation obtained is

$$E_{ip} = \left|10.76 - \frac{1.27}{X}\right| \frac{15.5}{X} \text{ (ev)} \qquad (3)$$

Eq. (3) yields the curve shown in Figure 2-6. The region below X = 45.5% has been shown as a dashed curve because it is the region excluded by Figure 2-5. It is learned from Figure 2-6 that the maximum energy expended per ion-pair formed is 268 electron volts. The actual value may be as low as 185 electron volts as discussed in Section III. These figure are encouragingly small, and are considerably better than values being currently reported by other workers.

The chief difficulty with the accelerator was intense wall-heating near the apex of the funnel, which caused the material of the wall (pyrex or quartz) to melt. However, since the thermal contact to the coolant liquid following in the coils was rather poor this does not seem to be an insurmountable problem. One might ask whether a significant amount of material was ablated from the walls and passed from the accelerator so that the interpretation of the thrust measurements are wrong. The experiment with the deflecting magnet showed that all the thrust-producing materials was ionized so if ablated material affected the thrust measurements, it must have been ionized. In that case the curves of Figures 2-5 and 2-6 apply with values for X allowed to be larger than one. This would imply electron energies smaller than 15 ev and values for ev/ion pair less

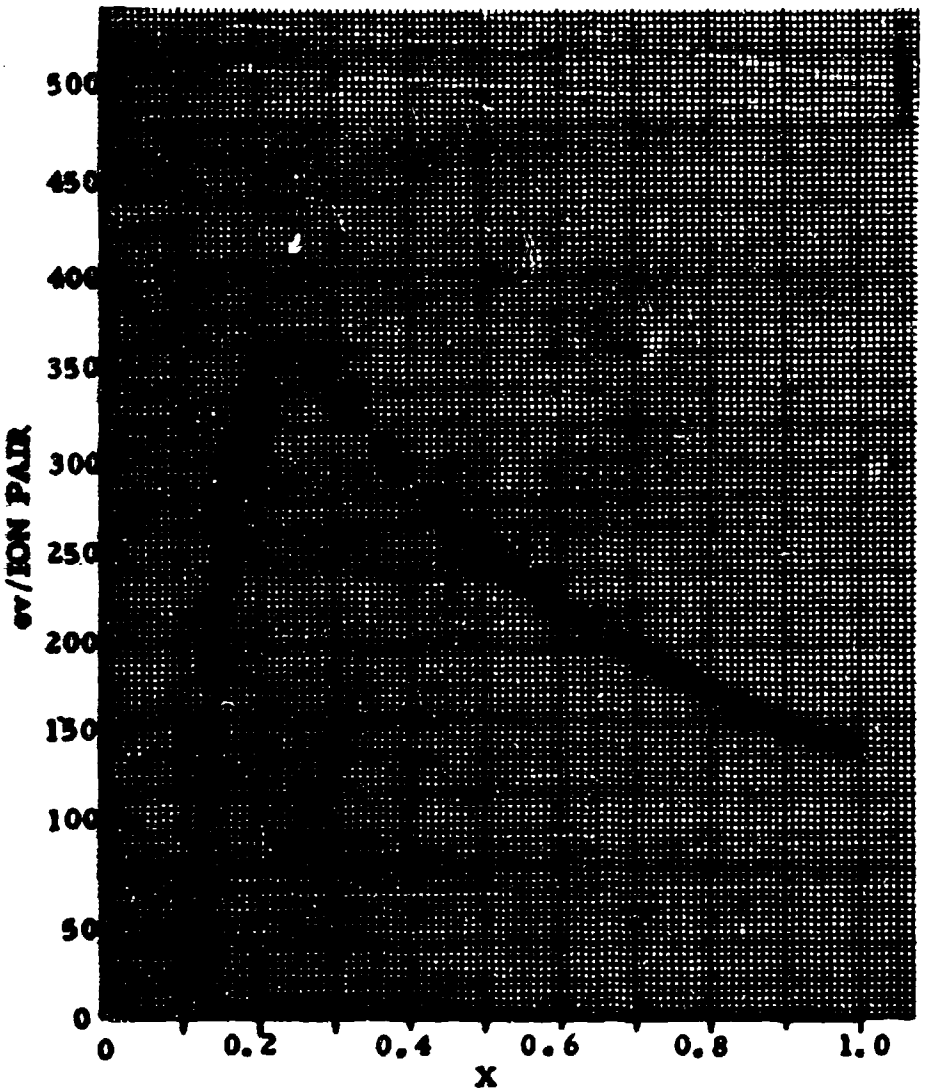


Figure 2-6. Plot of Energy vs Fraction of Ionized Molecules

than 150 ev. This seems unlikely. It is undoubtedly true that ablated material passed from the accelerator, but it would seem that it did not reach high speeds.

The efficiency of the machine, computed as the ratio of $(\text{thrust})^2$ to twice the power input times the mass flow-rate, was 9%. This is a low number in spite of the relatively small amount of energy spent to heat and ionize.

III THEORETICAL DISCUSSION OF ACCELERATOR

3.1 GENERAL CONSIDERATIONS

The mean speed of the particles in the efflux was measured to be about 10^4 meter per second, and from this the particle density near the mouth of the funnel can be calculated. The density is found to be 1.5×10^{17} particles per cubic meter. This can be compared to the particle density of 3.5×10^{19} particles per cubic meter which corresponds to a pressure of one micron at room temperature. Thus the particle density in the efflux is extremely low, and the chance for close collisions to occur amongst the particles in the beam is small. The ambient pressure in the vacuum chamber was 0.6 micron and the corresponding mean free path (at room temperature) is about 0.1 meter. The mean free path for fast molecules moving through the ambient gas is considerably larger than the mean free path at room temperature. One therefore concludes that the energy lost by the fast beam while in transit to the ballistic target was negligible.

In spite of the low density in the beam the Debye length is small, being on the order of 10^{-4} meter.

The luminosity of the beam could have been due to bremsstrahlung radiation from the hot electrons. The experimental results indicate that electron energies of about 15 electron-volts were present. A rough calculation of the bremsstrahlung radiation power[4] yields one milliwatt. This power level should be sufficient to be quite noticeable to the eye.

The axial magnetic field strength near the mouth of the funnel was determined to be about 15×10^{-4} weber per square meter (15 gauss) and this is a field which is orders of magnitude too small to accelerate nitrogen ions to the observed energies. This can easily be seen by computing the gyro radius for the ions and comparing it to the radial dimension of the accelerator. The ratio is found to be about 20/1. The corresponding ratio for electrons is only 5×10^{-5}, however; so

the field is strong enough to have a profound effect on the electrons. Because of the small value for the Debye length, the electrons cannot move on paths that will lead to significant ion-electron separation; so space charges form of sufficient magnitude to impede the electron motion and aid the ion motion so that both types of particles move together. A mathematical model describing this action has been formulated[5]. It was shown that the combined motion is identical to that for a particle having a mass that is the geometric mean of the ion and electron masses. The gyro radius for a particle of this geometric-mean mass is 1.1×10^{-2} meter when the magnetic field strength is that used in the accelerator experiment. This radius is less than the radial dimension of the funnel and one concludes that ion acceleration can occur through the mechanism of the electric fields generated by space charges.

It is interesting to compute the space-charge density required to establish a voltage sufficient to give rise to the acceleration observed in the experiment. The measured ion speed corresponds to an energy of about 20 ev, and a potential difference equal to this energy must appear across a region within the funnel. The concept of Debye length can be employed. In MKS units the Debye length, H, is:

$$H = 69\,(T/n)^{\frac{1}{2}} \qquad (4)$$

where T is the electron temperature and n is the density of nonneutralized charges. For T, one substitutes a value equivalent to 20 ev (2×10^5 degrees) and for H, a value equivalent to the distance over which acceleration occurs in the funnel (0.025 meter). The resulting value for n is:

$$n = 1.5 \times 10^{12} \text{ charges per cubic meter} \qquad (5)$$

This density is 10^5 times smaller than the density of ions leaving the funnel, and so one sees that it is easy for the system to establish the required potentials.

The process of accelerating an ion in the funnel occupies a length of time which is long compared to a half-period of the applied magnetic field. This can be demonstrated in a simple fashion: the average distance moved by an ion in attaining speed, v, is about $2\pi r$, where r is the gyro radius for a particle whose mass is the geometric mean, $(Mm)^{1/2}$, of the ion and electron masses[5]. In order that the

acceleration process occurs over many cycles of the applied field the following condition must hold:

$$\frac{2\pi r}{v} >> T \tag{6}$$

where T is the period of the applied field. However, v/r is the cyclotron-frequency, ω_c, for a particle of mass $(Mm)^{1/2}$; so Eq. (6) can be rewritten as follows:

$$\omega/\omega_c >> 1 \tag{7}$$

The funnel experiment was done under conditions for which the ratio above was equal to 9. Hence, one concludes that each ion was accelerated over many cycles, and so in order to compare with experiment, a time average must be taken of any accelerating effects predicted by a theoretical calculation.

In the following sections a theoretical calculation is made. The calculation relies heavily on a particular formulation of the equations of motion for a charged particle in an axially-symmetric, time-dependent, magnetic field[6] and also on a two-fluid-model[5] which describes the rudiments of the ion-electron coupling through the action of space-charge accumulation. Space does not permit a treatment of these basic ideas here, but rather, the calculations to be given here constitute an extension of the model.

The proposed space-charge mechanism has already been experimentally observed in other devices[7].

3.2 DISCUSSION OF THE MAGNETIC FIELD PATTERN

The magnetic flux-contours for the funnel were determined by experiment, and field-strength measurements were made. However, the results were not complete enough for theoretical purposes. Therefore a determination was also made with an electrical analog board.

A seven-turn, 60-degree funnel was analogued. A metal plane was included to analog the effects (expected to be small) of the wall of the vacuum chamber. At the frequency employed in the experiment a

strong skin effect exists at any metal surface and such surfaces become surfaces of zero flux. The inductance of the coil obtained from the analog was 2.0 microhenries; this compares well with the measured inductance of the coil (2.4 microhenries) determined with an L-C meter and also with the inductance (2.0 microhenries) deduced from the voltage-current ratio employed during the experiment.

The analog also yielded a value of 15×10^{-4} weber per square meter for the strength of the magnetic field across the mouth of the funnel. Figure 3-1 shows the magnetic field pattern obtained from the analog. The curves in that figure are labelled by the relative values of flux. The magnitude of the flux at the point indicated by the small cross was determined to be 0.84×10^{-5} weber for the conditions of the experiment. The radius at the cross is 0.045 meter.

Figure 3-2 shows a photograph of the analog board as it was set up for this problem. The board consists of 1800 resistors arranged in a rectangular mesh.

The field lines diverge less than the funnel angle in the region inside the funnel. This is true because the coils are wound in series.

3.3 EXTENSION OF THE TWO-FLUID MODEL

It can be shown[6] that the motion of a particle of mass, M, and charge, q, in a magnetic flux, Φ (r, z, t), can be determined from a consideration of an inductive potential, V_L. The radial and axial motions of a particle can be determined from this potential in the same way as for an ordinary electric potential, V_E; by computing a force from -q grad V_L. The inductive potential differs from an ordinary potential in three important respects:

1. Only the axial and radial forces can be found from the gradient of V_L (since it does not depend on azmuth because of the axial symmetry of the field). The equation of motion for the azmuthal angle, θ, is found by forming $-(2qV_L/M)^{1/2}$.
2. An ordinary potential depends on position and time only whereas V_L depends on the angular momentum of the particle (with respect to the axis of symmetry) at some previous time.

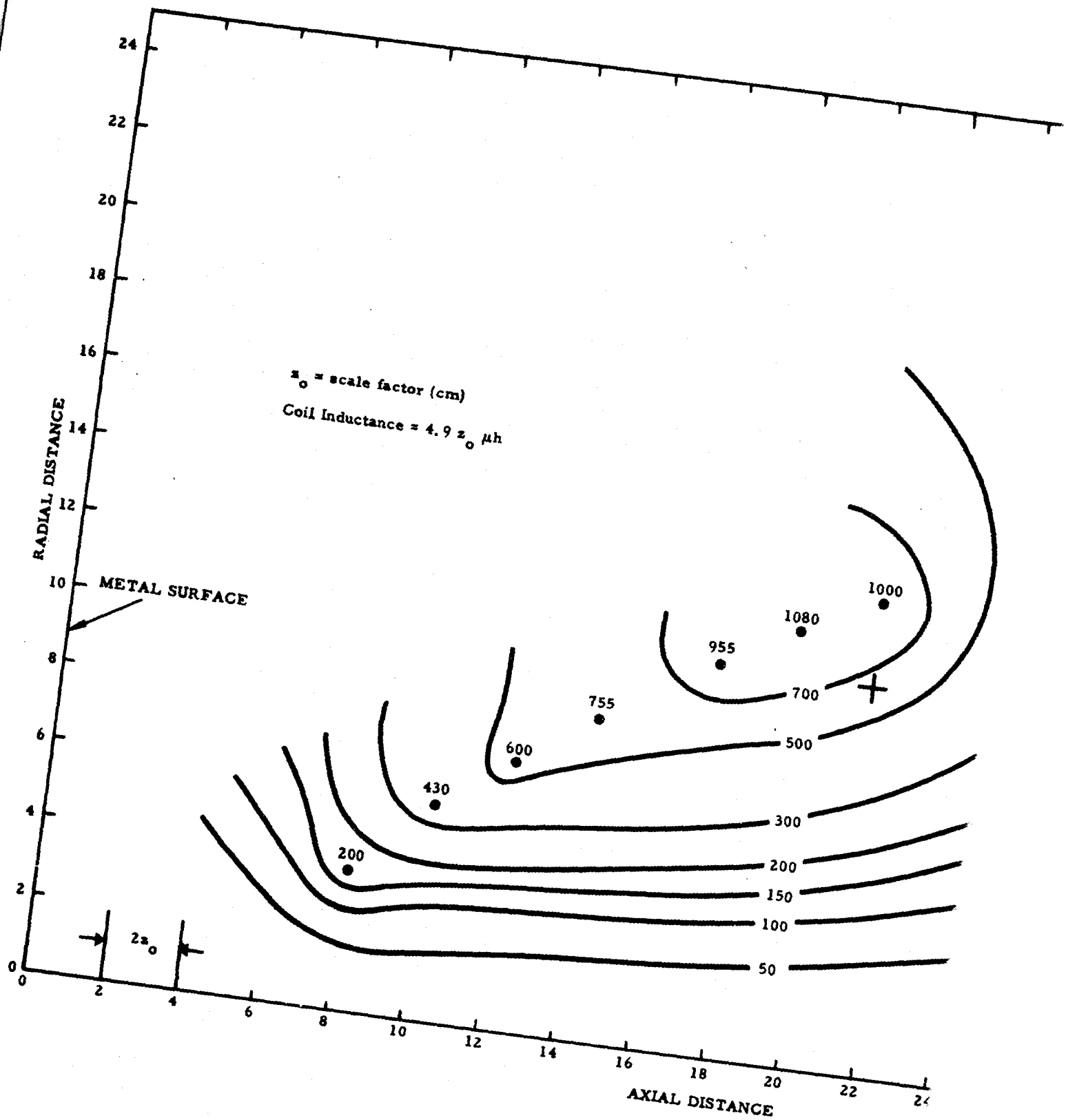

z_o = scale factor (cm)
Coil Inductance = 4.9 z_o μh
RADIAL DISTANCE
METAL SURFACE
$2z_o$
AXIAL DISTANCE
1000
1080
955
700
755
600
500
430
300
200
200
150
100
50
0
2
4
6
8
10
12
14
16
18
20
22
24

Figure 3-1

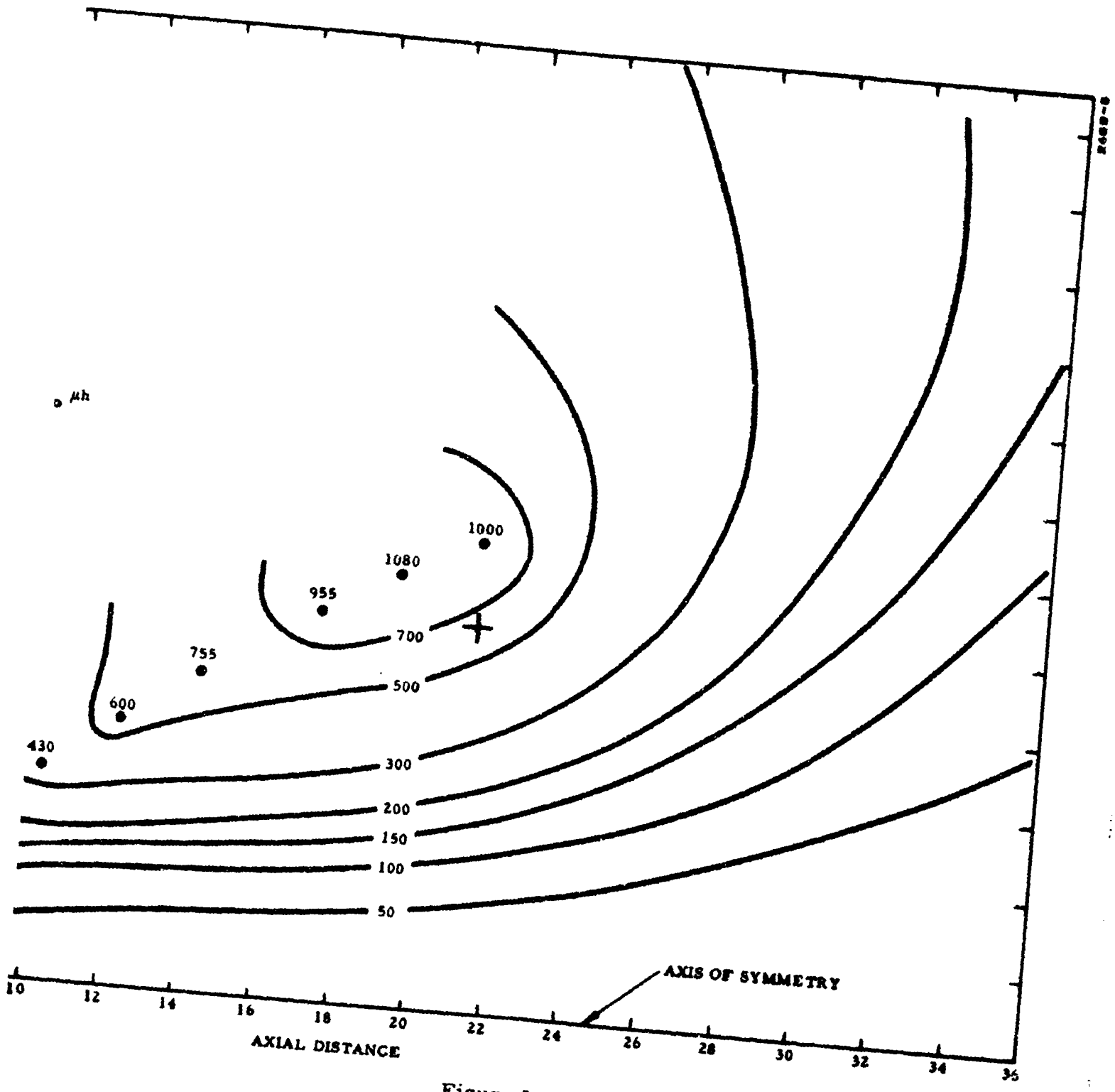


Figure 3-1. Magnetic Field Pattern

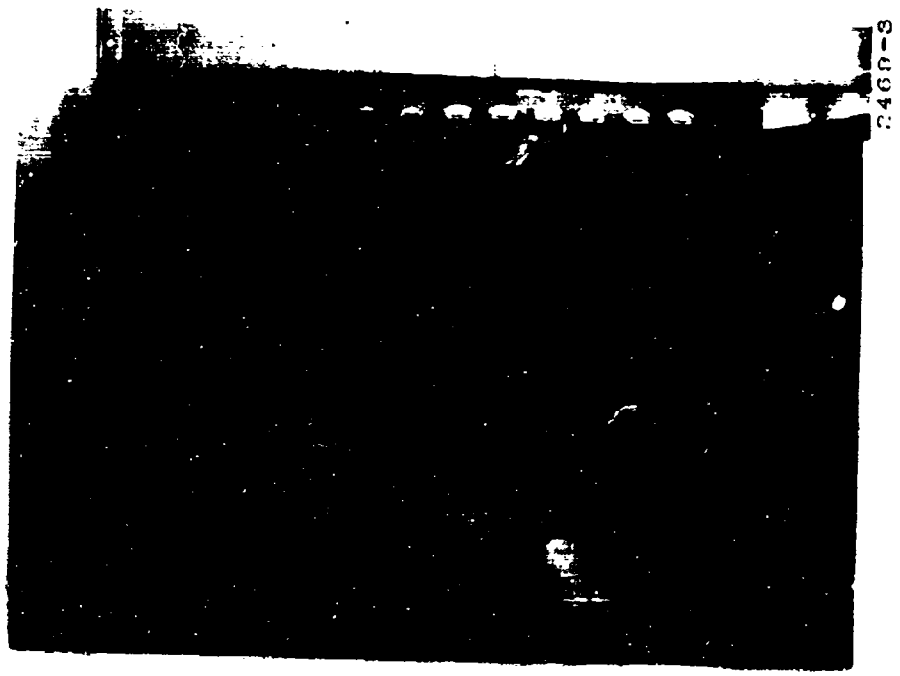


Figure 3-2. Analog Board

3. The centrifugal force is also described by V_L and so it can have nonzero values even when the magnetic field is zero.

If an electric potential is present as well as a magnetic potential then the same formalism can be used provided the electric potential does not depend on azimuthal angle. In that case, the total potential can be written as:

$$V(r,\ z,\ t) = V_L(r,\ z,\ t) + V_E(r,\ z,\ t) \tag{8}$$

where:

$$V_L = \frac{q}{8\pi^2 M}\left[\frac{\Phi - K}{r}\right]^2 \quad \text{where } \Phi = 2\pi\int_o^r dr\ rB_z \tag{9}$$

and K is a constant if there are no azimuthal forces acting on the particle at any time. K can be determined for a particle located at co-ordinates r_o, z_o, t_o by the following relation:

$$K = \frac{J(r_o,\ z_o,\ t_o)}{q} + \Phi\ (r_o,\ z_o,\ t_o) \tag{10}$$

The inductive potential formalism is capable of handling forces in the azimuthal direction only if they are of an impulsive type, such as those caused by close collisions between the constituents of a plasma. If an impulsive collision occurs at time t_o and causes the angular momentum of the particle to change from J to J', a new value of K can be derived using Eq. (10) since the particle has had no chance to change its spatial position during the collision time. For all times after the collision an entirely new potential exists for the particle! The new potential is calculated by inserting the changed value of K into Eq. (9).

A great deal of useful information can be derived by plotting the inductive potential even though the equations of motion that can be derived from it are never solved. The motion will be like that of a small sphere rolling over a landscape having the same contours as the potential. Changes of energy can also be determined without solving the equations of motion.

A derivation o. equations describing the motion of the plasma in the funnel accelerator is possible if certain assumptions are made:

1. The condition expressed by Eq. (7) is assumed so the ions experience many cycles of the applied field during acceleration.
2. Because Eq. (7) is satisfied, the density of ions, n_i, is time-independent.
3. One must allow for the presence of strong collective oscillations of electrons, but it is assumed that their frequency is high compared to the applied frequency. Thus the density of electrons averaged over the high-frequency variations, n_e, is time-independent.
4. Charge neutrality requires that $n_e = n_i$ to a high degree of approximation.
5. The accelerating phase occurs without essential disturbance of the ion trajectories by the effects of large-angle scattering events.

If M and q denote the ion mass and charge, and m and -q denote the electron mass and charge, then the total potential acting ions and on electrons is:

$$V^e = -\frac{q}{8\pi^2 m}\left[\frac{\Phi(r, z, t) - K^e}{r}\right]^2 + V_E(r, z, t) \qquad (11)$$

$$V^i = \frac{q}{8\pi^2 M}\left[\frac{\Phi(r, z, t) - K^i}{r}\right]^2 + V_E(r, z, t) \qquad (12)$$

where V_E is the potential arising from space-charge effects. The values of K^e and K^i will vary from one particle to another, but one can compute the average potential for all particles in an element of volume if the distribution functions for these quantities are known.

The azimuthal velocity of an ion is found from the following equation:

$$V_\theta^i = -\frac{q}{2\pi M}\left[\frac{\Phi - K^i}{r}\right] \qquad (13)$$

Eq. (13) it is

and a similar result will hold for an electron. From Eq. (13) it is seen that K^i is proportional to the angular momentum of the particle at those times when the applied field is zero.

$$K^i = \left[\frac{2\pi Mr}{q}\right] V_\theta^i \quad (\phi = o) \tag{14}$$

A similar result will hold for an electron. We are interested in following, in detail, the motion of an ion. K^i is constant (no close collisions) and equal to the value which it had at the beginning of the acceleration phase for the ion in question. We assume that the ion began acceleration at radius r_o.

The distribution function for K^i will be the same as that when the ion was at r_o. This distribution is that appropriate to a Maxwellian gas at temperature T^i (or temperature-energy E^i, expressed in electron volts). A bracket notation is used to denote average values, and one finds the following:

$$< K^i >_K = 0 \tag{15}$$

$$< (K^i)^2 >_K = \frac{8\pi^2 M}{3q} E^i r_o^2 \tag{16}$$

The results can be used to find the average potential acting on ions which began to accelerate at r_o.

$$< V^i >_K = \frac{q}{8\pi^2 M}\left(\frac{\Phi}{r}\right)^2 + \frac{E^i}{3}\left(\frac{r_o}{r}\right)^2 + V_E \tag{17}$$

As the ions move they will be surrounded at all times by an equal density of fast electrons. The electron motions are extremely complicated, and no attempt will be made to follow them in detail. Electrons which are in the vicinity of an ion at time, t, move away rapidly, and their place is taken by others moving in from other parts of the geometry. For each electron the value of K^e changes only slowly compared to the applied frequency. This can be checked by computing, for example, the self-collision time[8]. Although there will be some tendency toward spatial separation of electrons with values of K^e which are opposite in sign, it will be assumed that the bulk of the electrons at any given position are in a state of complete thermal equilibrium.

These assumptions imply that the values of K^e for electrons are not distributed according to a Maxwellian equation but that, instead, the values of K^e/r are so distributed. One finds the following:

$$< \frac{K^e}{r} >_K = 0 \tag{18}$$

$$< \left(\frac{K^e}{r}\right)^2 >_K = \frac{8\pi^2 m}{3q} E^e \tag{19}$$

The results can be used to find the average potential acting on the electrons.

$$< V^e >_K = - \frac{q}{8\pi^2 m} \left(\frac{\Phi}{r}\right)^2 - \frac{E^e}{3} + V_E \tag{20}$$

Notice that the term involving the electron temperature has no r-dependence in contrast to the situation for the ions. This is a consequence of the ability of the electrons to change location rapidly.

The flow of electrons and ions through any imagined surface in the plasma must be equal. Since the electron and ion densities are equal at all positions and at all times, equal flow can be obtained only if the drift velocity of the electrons is equal to the average velocity of the ions at all places. A rigorous treatment of this condition is too complicated to attempt here. However, if the condition is satisfied, the average drift energy of the electrons is small, and this will be so if $< V^e >$ is much smaller than any one of the terms on the right-hand side of Eq. (20). An equation for V_E immediately follows from this assumption.

$$V_E = \frac{q}{8\pi^2 m} \left(\frac{\Phi}{r}\right)^2 + \frac{E^e}{3} \tag{21}$$

The distribution of space-charge can be found from Eq. (21) and Poisson's law. Figure 3-3 shows a sketch of the time-dependence of V_E for an applied field that varies sinusoidally. The potential reaches a height B when the field is maximum and falls to height A when the field is zero. Height A is maintained by the electron temperature. It

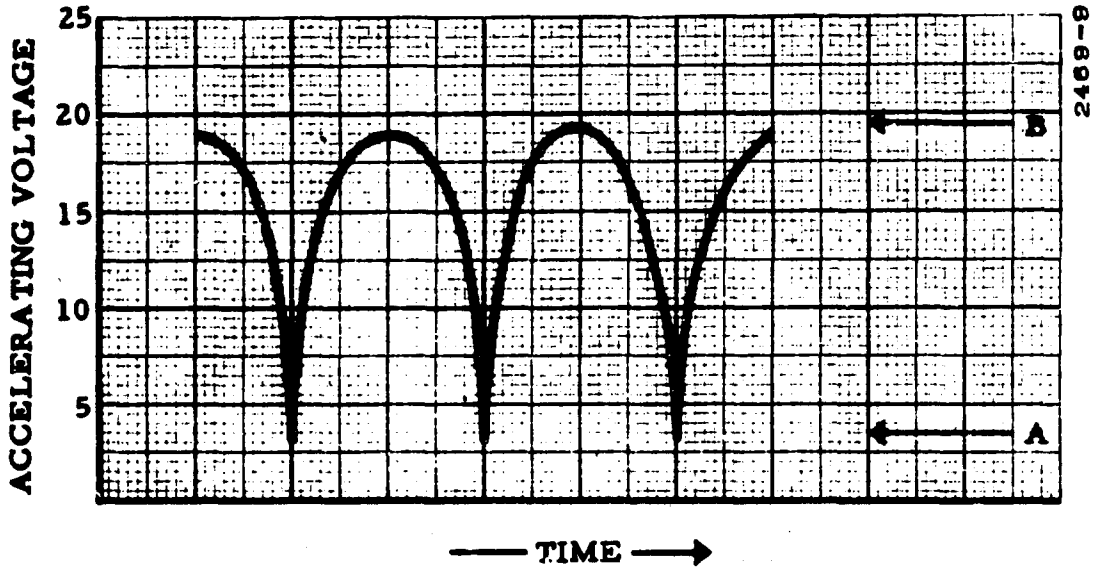


Figure 3-3. Plot of Accelerating Voltage vs Time

simply expresses the desire of the hot electron gas because of the angular momentum of the electrons, to keep ions away from the axis of symmetry.

Eq. (21) can be used in Eq. (17) to obtain the potential acting on the ions. It is only the time average of the potential that really matters; therefore that average is taken. Also, the term in 1/M can be neglected in comparison to the term in 1/m. The resulting equation is:

$$<<V^i>>_{Kt} = \frac{q}{16\pi^2 m}\left(\frac{\Phi_o}{r}\right)^2 + \left(\frac{r_o}{r}\right)^2 \frac{E^i}{3} + \frac{E^e}{3} \qquad (22)$$

where Φ_o is the peak value of the flux.

It should be noted that it is the electron mass that appears in Eq. (22), not the ion mass. This is the same as the result obtained previously[5] and leads to the conclusion that the motion of the ions in the plasma is like the motion of an isolated particle of charge q and mass $(Mm)^{1/2}$.

The value of E^e for the electrons is to be taken to be much larger than that for the ions and so the term in E^i is negligibly small except near the axis of symmetry. Near the axis it cannot be neglected, because it describes the fact that the average ion never passes through the axis of symmetry because of angular momentum acquired from thermal motion. It is convenient to neglect this term, however, in order to get a rough idea of the form of $<<V^i>>$. Figure 3-4 shows a plot of the potential without the E^i term. In the formalism being employed, a particle that is incident on the axis of symmetry is reflected from it in the manner of a light-ray. This fact should be kept in mind when interpreting Figure 3-4.

It is seen that the contours of constant potential tend to follow the same angle as the funnel. The numbers attached to the curves are values for the potential (in volts) for the conditions of the funnel experiment. The axis of symmetry is also a contour line, and the voltage there is 2.7, corresponding to an electron temperature of 8 ev. Two ion trajectories are sketched on the figure. These were not computed from the equations of motion but were determined from simple energy and ray-optic considerations.

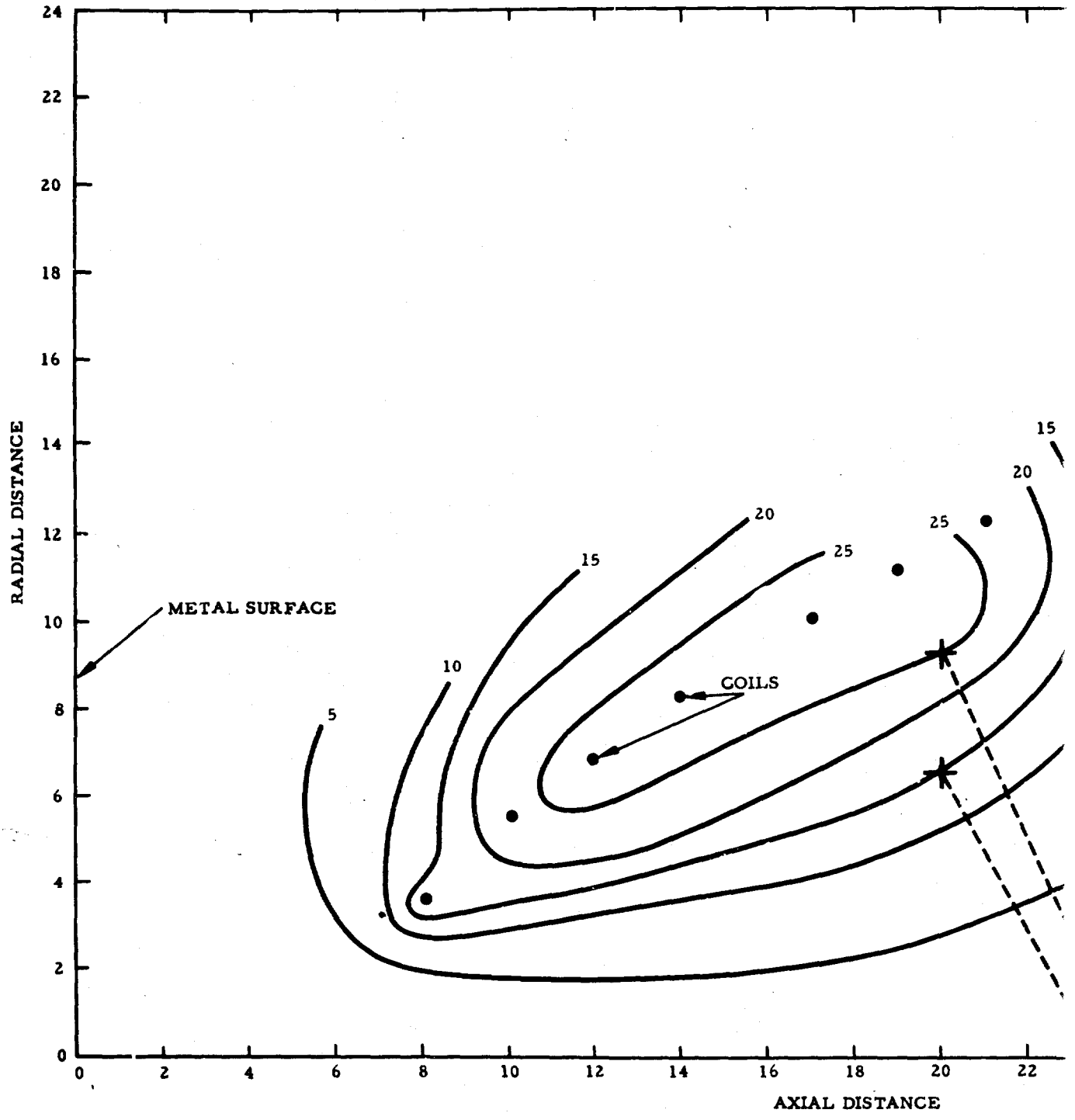
One conclusion obtained from Figure 3-4 is that all the ions are forced toward the axis of symmetry (they pass through it in Figure 3-4 , but would not if the E^i term had not been neglected.) This leads to a high value of particle density along the axis and perhaps to additional scattering and ion heating. Because of the density increase there should be increased luminosity along the axis. This has been observed experimentally and, under some conditions, the luminosity along the axis is so enhanced that a bright core appears.

The details of the motion of electrons within the plasma is far too complicated to submit to detailed analysis. However, the electrons move at all times under the combined effect of the inductive potential and the induced electric field as described by Eq. (12). Selected test plots of V^e have been made for various choices of K^e. The sign of K^e, with respect to the instantaneous sign of $\dot{\Phi}$, is the factor that determines the basic nature of the motion. When the two have the same sign the electron is accelerated toward the mouth of the funnel. When the two have opposite sign the acceleration is toward the apex of the funnel. Thus there exist counterflowing electron currents, and the direction of these currents is roughly along the magnetic field lines. Since the latter cut across the space-charge potential lines at an angle, the counterflow of electrons can involve energy exchanges twice as high as the energy of the accelerated ions. The factor of two comes from the fact that the ions are accelerated by the average potential, not by its peak value.

The ionizing mechanism is adequately explained by the arguments above, since the entering neutral gas is continually met with a barrage of electrons of high energy (up to 50 volts in the case of the funnel accelerator). These are electrons that, by occasional scattering events, suddenly find themselves at an unstable position in the field.

3.4 COMPARISON TO EXPERIMENT

The foregoing results have been applied to the experimental situation. The mean accelerating energy is obtained by averaging Eq. (22) over all values of r within the funnel at the axial distance at which the acceleration commences. This axial distance is not known, but fortunately the answer is insensitive to its choice since the space-charge potential lines are nearly parallel to the walls of the funnel, as shown


RADIAL DISTANCE
AXIAL DISTANCE
METAL SURFACE
COILS
5
10
15
20
25
15
20
25
0
2
4
6
8
10
12
14
16
18
20
22
24

F

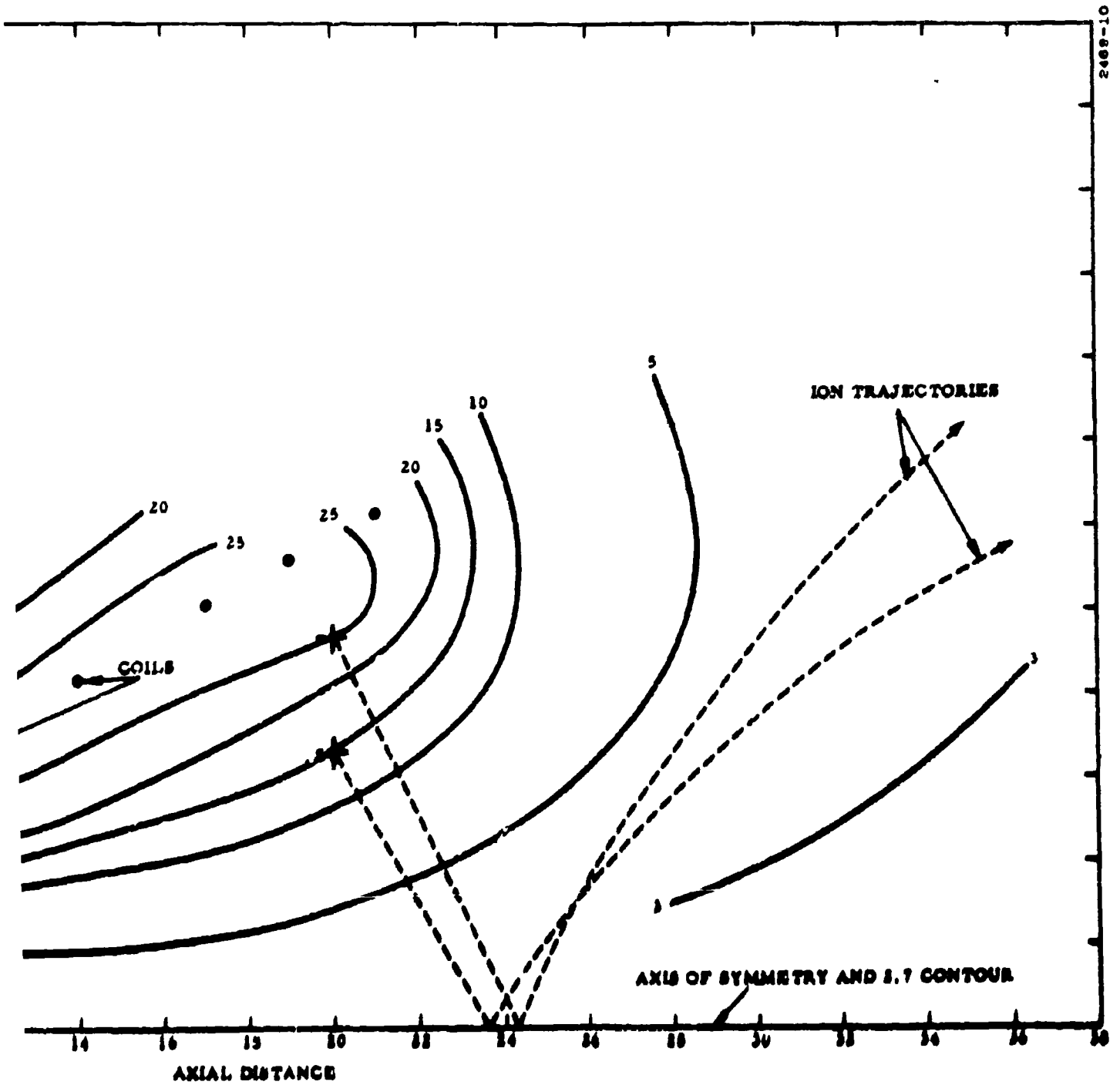


Figure 3-4. Plot of Potential Without E^1 Term

by Figure 3-4. The computed value for the thrust is insensitive to the choice of electron temperature. A value of 15 ev was assumed, and the thrust was found to be:

$$T = 2.1 \times 10^{-2} \text{ newton}$$

This value is within 1% of the measured thrust. The average accelerating voltage was found to be 22 volts. The expected power in the beam was computed by adding 15 ev of electron heat and 15.5 ev for the energy required to ionize nitrogen. The computed power was then found to be:

$$P = 360 \text{ watts}$$

This value is within 3% of the measured power. Both of these calculations provide an excellent check on the experimental measurements. The percentage ionization assumed in the calculations was 100%.

IV CONCLUSIONS

The agreement between the theoretical calculations and the experimental measurements is better than expected, because the calculations were based on a simplified model and perturbing effects were omitted. However they indicate that the measured values could not have been obtained unless the percentage ionization was extremely high.

The high degree of ionization is reasonable considering the excellent ionizing mechanism operating within the funnel.

REFERENCES

1. Gooding, T. J., Hayworth, B.R., and Lovberg, R. L. ARS Journal, 32:1599 (1962).

2. Cook, C. J. and Peterson, J. R. Phys. Rev. Letters, 9:164 (1962)

3. Brown, S. C. Basic Data of Plasma Physics, John Wiley and Sons, Inc. (1959)

4. Linhart, J. G. Plasma Physics, North-Holland Publishing Co. (1960)

5. Penfold, A. S. A Model for the Motion of a Rarified Plasma in an Axially Symmetric Magnetic Field, Technical Memorandum 61-27, Litton Systems, Inc. (1961); also AFOSR TN 60-961

6. _____. Particle Motion in an Axially Symmetric Magnetic Field, Technical Memorandum 61-25, Litton Systems, Inc. (1961); also AFOSR TN 60-841

7. Janes, G. S. Abstracts of the Fifth AFOSR Contractor Meeting on Ion and Plasma Propulsion Research (1962).

8. Spitzer, L., Jr. Physics of Fully Ionized Gases, Interscience Publishers, Inc. (1956).

AFOSR SCI. DOC. 64-1340 June 1964 UNCLASSIFIED
(LIT 3075)

Research on Electromagnetic Plasma Acceleration

This is a final report on work done under Contract AF49(638)-759 covering four years of investigation. Included in this report are the following:

(a) An experimental investigation of the acceleration of plasma toroids in a pulsed traveling wave device.

(b) A theoretical investigation of the behavior of plasma in axially-symmetric magnetic fields.

(c) A detailed description of a CW polyphase-driven traveling wave accelerator.

In addition there are a number of appendices describing various ancillary techniques and apparatuses including polyphase monitoring and control systems, an analog computer for axially-symmetric magnetic fields, and the CW power sources.

Qualified requestors may obtain copies of this report from DDC - center.

AFOSR SCI. DOC. 64-1340 June 1964 UNCLASSIFIED
(LIT 3075)

Research on Electromagnetic Plasma Acceleration

This is a final report on work done under Contract AF49(638)-759 covering four years of investigation. Included in this report are the following:

(a) An experimental investigation of the acceleration of plasma toroids in a pulsed traveling wave device.

(b) A theoretical investigation of the behavior of plasma in axially-symmetric magnetic fields.

(c) A detailed description of a CW polyphase-driven traveling wave accelerator.

In addition there are a number of appendices describing various ancillary techniques and apparatuses including polyphase monitoring and control systems, an analog computer for axially-symmetric magnetic fields, and the CW power sources.

Qualified requestors may obtain copies of this report from DDC - center.

AFOSR SCI. DOC. 64-1340 June 1964 UNCLASSIFIED
(LIT 3075)

Research on Electromagnetic Plasma Acceleration

This is a final report on work done under Contract AF49(638)-759 covering four years of investigation. Included in this report are the following:

(a) An experimental investigation of the acceleration of plasma toroids in a pulsed traveling wave device.

(b) A theoretical investigation of the behavior of plasma in axially-symmetric magnetic fields.

(c) A detailed description of a CW polyphase-driven traveling wave accelerator.

In addition there are a number of appendices describing various ancillary techniques and apparatuses including polyphase monitoring and control systems, an analog computer for axially-symmetric magnetic fields, and the CW power sources.

Qualified requestors may obtain copies of this report from DDC - center.

AFOSR SCI. DOC. 64-1340 June 1964 UNCLASSIFIED
(LIT 3075)

Research on Electromagnetic Plasma Acceleration

This is a final report on work done under Contract AF49(638)-759 covering four years of investigation. Included in this report are the following:

(a) An experimental investigation of the acceleration of plasma toroids in a pulsed traveling wave device.

(b) A theoretical investigation of the behavior of plasma in axially-symmetric magnetic fields.

(c) A detailed description of a CW polyphase-driven traveling wave accelerator.

In addition there are a number of appendices describing various ancillary techniques and apparatuses including polyphase monitoring and control systems, an analog computer for axially-symmetric magnetic fields, and the CW power sources.

Qualified requestors may obtain copies of this report from DDC - center.